Xingyi Huang · Chunyi Zhi *Editors*

Polymer Nanocomposites

Electrical and Thermal Properties

Springer

Polymer Nanocomposites

Xingyi Huang • Chunyi Zhi
Editors

Polymer Nanocomposites

Electrical and Thermal Properties

Springer

Editors
Xingyi Huang
Shanghai Key Laboratory of Electrical Insulation and Thermal Ageing
Department of Polymer Science and Engineering
Shanghai Jiao Tong University
Shanghai, China

Chunyi Zhi
Department of Physics and Materials Science
City University of Hong Kong
Hong Kong, China

ISBN 978-3-319-28236-7 ISBN 978-3-319-28238-1 (eBook)
DOI 10.1007/978-3-319-28238-1

Library of Congress Control Number: 2016936276

Springer Cham Heidelberg New York Dordrecht London
© Springer International Publishing Switzerland 2016
This work is subject to copyright. All rights are reserved by the Publisher, whether the whole or part of the material is concerned, specifically the rights of translation, reprinting, reuse of illustrations, recitation, broadcasting, reproduction on microfilms or in any other physical way, and transmission or information storage and retrieval, electronic adaptation, computer software, or by similar or dissimilar methodology now known or hereafter developed.
The use of general descriptive names, registered names, trademarks, service marks, etc. in this publication does not imply, even in the absence of a specific statement, that such names are exempt from the relevant protective laws and regulations and therefore free for general use.
The publisher, the authors and the editors are safe to assume that the advice and information in this book are believed to be true and accurate at the date of publication. Neither the publisher nor the authors or the editors give a warranty, express or implied, with respect to the material contained herein or for any errors or omissions that may have been made.

Printed on acid-free paper

Springer International Publishing AG Switzerland is part of Springer Science+Business Media (www.springer.com)

Preface

With the rapid development of electronic products and power equipment, functional materials with excellent electrical and thermal properties are highly desirable. Polymer materials are attractive because of their flexibility, light weight, ease of processing, and most importantly low cost. However, particularly filled polymer composites, rather than polymeric materials themselves, are more commonly used in various practical applications. This is because the electrical and thermal properties of the polymer composites can be significantly enhanced or tuned in a wide range by introducing specific fillers, particularly nanoparticles.

Numerous nanoparticles from 0 to 3 dimensions have been successfully fabricated and used as fillers for polymer composites, which enrich the polymer composites with new mechanisms, properties, and applications. This book aims at summarizing fundamental principles and state-of-the-art progresses in electrical and thermal properties of polymer nanocomposites.

This book consists of three parts with 12 chapters, which are contributed by well-recognized experts in each field. Part I and Part II focus on the electrical properties of polymer nanocomposites under low and high electric field, respectively. The electrical properties under low electric field mainly cover the dielectric constant (high-k and low-k), dielectric loss, percolation behaviors, and positive temperature coefficient of polymer composites, whereas the electrical properties under high electric field mainly cover breakdown strength and energy storage of polymer nanocomposites. Part III focuses on thermal properties of the polymer nanocomposites, including thermal stability, and thermomechanical, calorimetric, and flame-retardant properties.

We greatly appreciate the efforts of all contributors for bringing the community this wonderful book, which is the first comprehensive book focusing on the fundamental principles and state-of-the-art progress of the electrical and thermal properties of the polymer nanocomposites. Xingyi Huang and Chunyi Zhi would like to

thank Professor Pingkai Jiang, the National Natural Science Foundation of China, the Special Fund of the National Priority Basic Research of China, and Research Grants Council of Hong Kong for the long-time financial support on this work.

Shanghai, China — Xingyi Huang
Hong Kong, China — Chunyi Zhi

Contents

Part I
Electrical Properties of Polymer Nanocomposites Under Low Electric Field

Chapter 1
Dielectric Constant of Polymer Composites and the Routes to High-*k* or Low-*k* Nanocomposite Materials

Jinkai Yuan, Shenghong Yao, and Philippe Poulin

1.1 Introduction

The dielectric constant, k, is a physical feature related to the electric polarizability of a material [1]. Physically the greater the polarization developed in the materials, the higher the k. In comparison to the k value of silicon dioxide, which is 3.9, the dielectric materials are classified into high-k dielectrics ($k > 3.9$) and low-k dielectrics ($k < 3.9$). Besides polarizability, losses are also an important feature. They arise in dielectrics from the motion of bound charges in response to an applied electrical field. Generally the dielectric constant is treated as a complex function. It includes the contributions of inphase polarizability and losses, respectively, through the real $\varepsilon'(\omega)$ and imaginary parts $\varepsilon''(\omega)$ of the dielectric constant, where ω is the angular frequency. Losses are often quantified through the so-called $\tan(\delta)$ value which is given for a dielectric material by the ratio of $\varepsilon''(\omega)$ to $\varepsilon'(\omega)$. The k value (also sometimes referred to as relative dielectric constant) is simply given by the ratio $\varepsilon'(\omega)$ of to the permittivity of vacuum. When free charges are present, they contribute to increasing the losses via a frequency independent (in the ranges of interest) term, named DC conductivity. Low losses are important for applications and will be discussed throughout the chapter.

Recently, there is a fast-growing interest in both kinds of dielectric materials due to their wide range of applications in electronic and electrical industry. For instance, high-k dielectrics can serve as effective materials for cable insulation [2], charge-storage capacitors [3, 4], electrocaloric cooling [5, 6], and artificial muscles [7, 8]. While low-k materials are the key insulating components for isolating signal-carrying conductors from one another as well as reducing the signal propagation delay and dynamic power dissipation in the high-density and high-speed microelectronic packaging [1, 9].

J. Yuan, PhD (✉) • S. Yao, PhD • P. Poulin, PhD
Centre de Recherche Paul Pascal, CNRS, Université de Bordeaux,
115 Avenue Schweitzer, Pessac, Girond 33600, France
e-mail: yuan@crpp-bordeaux.cnrs.fr; tingsaint@gmail.com; poulin@crpp-bordeaux.cnrs.fr

© Springer International Publishing Switzerland 2016

X. Huang, C. Zhi (eds.), *Polymer Nanocomposites*,
DOI 10.1007/978-3-319-28238-1_1

Traditional dielectric materials are ceramics (e.g., mica, silicon dioxide, and $BaTiO_3$) with excellent dielectric properties, coupled with high stiffness and excellent thermal stability [10–13]. However, their applicability for practical electronic devices is largely impeded by their poor flexibility, high-density, and challenging processing conditions [14, 15]. Considering these limitations, polymeric dielectrics have been broadly explored as alternative dielectrics [16–20]. They can offer tunable dielectric properties, processing advantages including mechanical flexibility, and the capability of being molded into various configurations for electronic devices with reduced volume and weight. To satisfy distinct electronic and electrical applications, it is critical to tune the *k* values, while maintaining other excellent physical properties of polymers. In the past decade, many efforts have been devoted to tailor dielectric properties of polymers via modifying the polymeric chain architecture [9, 21], blending polymers with different high-*k* or low-*k* polymers [16, 20, 22, 23], and forming nanocomposites by dispersing ceramic or conducting nanoparticles into polymer matrices [2, 4, 15].

Polymer nanocomposites consisting of nanoparticles allow for a large tunability of the dielectric constant by varying the identity, shape, and content of nanoadditives, as well as engineering the nanoparticle–polymer interfaces. However, challenges still exist today on rationally designing optimum composite microstructures to realize a target high-*k* or low-*k* value. The relationship between the composite morphology and the dielectric properties is far from being fully understood.

To provide a comprehensive understanding to this topic and to clarify the emerging problems, we review the recent progress in the fundamentals, processes, and properties of dielectric polymer composites. Particular attention is paid on the current routes toward high-*k* or low-*k* nanocomposite materials. Some long-standing problems and topics that warrant further investigations in the near future are also addressed.

1.2 Dielectric Polarization in Polymer Composite Materials

To tune the dielectric constant of polymers, it is critical to understand the origin of dielectric constant, i.e., various types of polarization. Generally the polarization in polymer dielectrics includes interfacial, orientational (or dipolar), ionic (migration of ions over a distance beyond 10 nm), and electronic polarization. Each polarization is associated to a dielectric loss (ε'') peak at a specific frequency, as shown in Fig. 1.1. Generally the more types of polarization used, the higher the molar polarization and the *k* values. Note however that more complex frequency dependencies can be observed depending on the structure of the material. For example, dielectric spectra can exhibit a broad dispersion in so-called near-percolated materials which are of great interest in the field of high-*k* materials and which are commented further. In such systems the dielectric constant scales with frequency through particular power laws. The absence of singular modes and the broadness of the response reflect in fact the dispersity in characteristic sizes in near-percolated networks. In the following, it is addressed how various polarization is utilized for tailoring the dielectric constant.

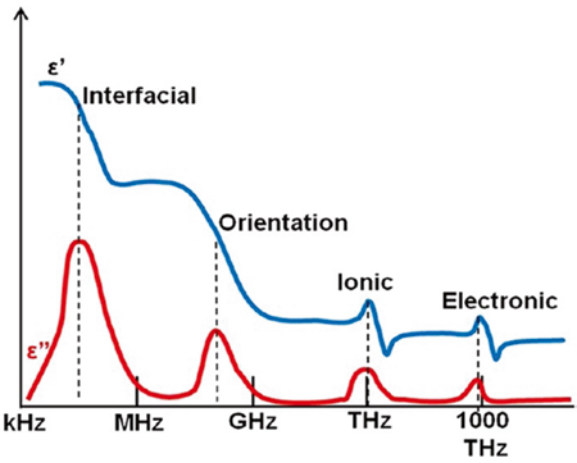

Fig. 1.1 Real (ε') and imaginary part (ε'') of the dielectric constant as a function of frequency in a polymer having interfacial, orientational, ionic, and electronic polarization (Reproduced with permission from Ref. [24]. Copyright 2013 American Chemical Society)

For polymer composites, orientational polarization refers to the reorientation of permanent molecular dipole moments, of nanoparticles, or of dipolar moieties appended to polymers [24]. The dipolar relaxation usually occurs between 0.1 and 10^7 Hz, depending on the nature of the dipoles (amorphous or crystalline), temperature, and frequency. Actually, by finely controlling the density and structure of dipoles, one can achieve dipolar glass, ferroelectric, and relaxor ferroelectric polymers which exhibit different levels of dielectric constant and dielectric losses [25].

Ionic polarization includes physical transport of incorporated ions in polymer materials. On the basis of this polarization, the polymeric electrolytes can be used to enhance the capacitive performance of gate dielectrics for organic field effect transistors [26]. The fundamental operating mechanism is forming electric double layer at the interface between the polymer electrolyte and electrode. In spite of their excellent energy storage performance, polymer electrolytes are not suitable for film capacitors because of a fundamental weakness, i.e., the high dielectric loss due to the transport of ion species over a long distance. The high dielectric losses are detrimental for the practical applicability of typical polymer dielectrics due to the huge energy waste and large risk of services. Therefore the ionic polarization should be avoided for typical polymeric dielectrics by decreasing the concentration of impurity ions during the polymerization processes.

Electronic polarization is related to the delocalization of electrons in organic polymers in response to an externally applied electric field. It should be noted that the dielectric losses corresponding to the electronic polarization are in the infrared and optical frequencies, not in the lower frequencies, which is a desirable feature for the presently discussed applications. To tailor the dielectric constant from electronic polarization, Si, Ge, and Sn are usually proposed to replace C for new dielectric polymers [25]. Synthesizing such inorganic polymers, however, is very challenging.

Maxwell–Wagner–Sillars (MWS) interfacial polarization related to reorganization of interfacial charges (e.g., electrons and holes accumulated at interfaces) in heterogeneous systems [27]. It exists in all multicomponent dielectric systems, such as semicrystalline polymers (crystal–amorphous interfaces could cause MWS effect), polymer blends, and nanocomposites consisting of high-k ceramic nanoparticles or highly polarizable conducting nanofillers. According to MWS effect [28], when a current flows across the two-material interfaces, charges can be accumulated at the interface between two dielectric materials with different relaxation time ($\tau = \varepsilon/\sigma$, where ε is the dielectric constant and σ is the conductivity). From this point of view, the large contrast in dielectric constant (for ceramic nanoparticles) or conductivity (for conducting nanoparticles) between filler and polymer matrix is highly desirable for interfacial polarization and thus affords a high dielectric constant. However, such large contrast will result in electric field intensification in the polymer matrix near the particle surface [29]. The field intensification is associated with the highly inhomogeneous electric fields and generally either enhances the local probability of dielectric failure or propagation of the discharge cascade [14, 30, 31]. Therefore a big challenge to utilize interfacial polarization consists in finding compromises that allow for high-k, high breakdown strength, and low losses in a single nanocomposite material.

1.3 High-k Polymer Composite Materials

The continuous miniaturization and increased functionality in modern electronic devices have spurred the development of easily processed materials, with improved dielectric constant, enhanced breakdown strength, and reduced dielectric losses. Conventional high-k ceramic materials such as $BaTiO_3$ (BTO) can be fabricated into thin films by using chemical solution deposition yielding a high dielectric constant of about 2500 and relatively low losses [10]. However, they require a sintering process at high temperature (900 °C), which is not compatible with most of substrate materials. Though RF magnetron sputtering can be used to make high-k ceramic nanofilms at room temperature [12], the cost is high and fabricating large area defect-free films is still very challenging because of the poor flexibility of ceramics. On the other hand, polymer-based dielectrics have large-scale processability, high electric breakdown field, and light weight, but they suffer from low dielectric constant (usually $k < 10$).

Recently, a few strategies, including modification of polymer chain structures [21, 32–34] and random composite approaches [15], have been developed to increase the dielectric constant of polymers. Chu et al. [18] obtained a very high energy density with fast discharge speed and low losses in defect modified polyvinylidene fluoride (PVDF) polymers. The resultant ferroelectric terpolymer poly(vinylidene fluoride-trifluoroethylene-chlorofluoroethylene) P(VDF-TrFE-CFE) has a dielectric constant as high as 50, the highest in known unfilled polymers. However, the use of toxic chemicals, needed for the synthesis of the above polymers, is not favorable from environmental and health points of view. Thakur et al. [35], for

the first time, successfully realized an environmentally friendly aqueous functionalized PVDF through a refluxing method. The dielectric constant and loss tangent for the dopamine functionalized PVDF have been found to be of 32 (higher than 10 for pristine PVDF) and 0.04, respectively.

Among all the approaches to increase the dielectric constant of polymers, the composite technology is most intensively studied due to its easy processing and a large tunability of dielectric properties by selection of the fillers with various properties (e.g., size, shape, and conductivity, etc.) as well as control of the microstructures of composites (e.g., filler dispersion and distribution, polymer matrix morphology). Approaches include adding high-*k* inorganic fillers and conductive/semiconductive fillers to polymers.

1.3.1 High-k Ceramic Nanoparticle–Polymer Composites

The introduction of ceramic nanoparticles into polymer matrices to form so-called 0-3 dielectric nanocomposites represents one of most promising and exciting avenues in this field [36, 37]. The created nanocomposites combine the advantages of ceramics and polymers and represent a novel type of material that is flexible, easy to process, and of relatively high dielectric permittivity and high breakdown strength. A vast amount of research has in past years succeeded in improving dielectric constant of polymers using ferroelectric metal oxides as filler, such as TiO_2 [38, 39], ZrO_2 [40], BTO [41], and $CaCu_3Ti_4O_{12}$ (CCTO) [42–45]. It was found in the simulation and experimental work that the dielectric constant of composite largely increases only as approaching the percolation threshold of inorganic nanoparticles [46, 47]. For spherical fillers, the percolation threshold is as high as ~30–35 vol% [46, 47]. That's why a very high filler loading is in general necessary to realize a high enough *k* value. For instance, Dang et al. [42] developed advanced high-*k* CCTO/polyimide (PI) functional hybrid films using an in situ polymerization process. A high dielectric constant [48] is obtained at 100 Hz at a concentration of spherical CCTO filler as high as 40 vol%, as shown in Fig. 1.2a. Such high loading of ceramic powders significantly deteriorates the mechanical performance of final composites. Furthermore, it is very difficult to process such composite dielectrics into defect-free and a few micrometers thick films. The porosity caused by high loading even dramatically decreases the dielectric properties of the composites.

To circumvent this problem, it is desirable to use rodlike nanoparticles as alternative fillers, such as BTO nanofibers [48–50], $Pb(Zr,Ti)O_3$ (PZT) nanowires [51], and $Ba_{0.6}Sr_{0.4}TiO_3$ (BST) nanotubes [52]. As predicted by a finite element analysis [46], the percolation threshold in a polymer matrix can decrease to 18 vol% as the aspect ratio of particles increases to 3. Recently, electrospun BTO nanofibers with a large aspect ratio were used as dielectric fillers in poly(vinylidene fluoride-trifluoroethylene) (PVDF-TrFE)-based nanocomposites [48]. Because of the reduced percolation threshold, the nanocomposites show a dielectric constant of 30 at a much smaller filler loading (10.8 vol%), as shown in Fig. 1.2b.

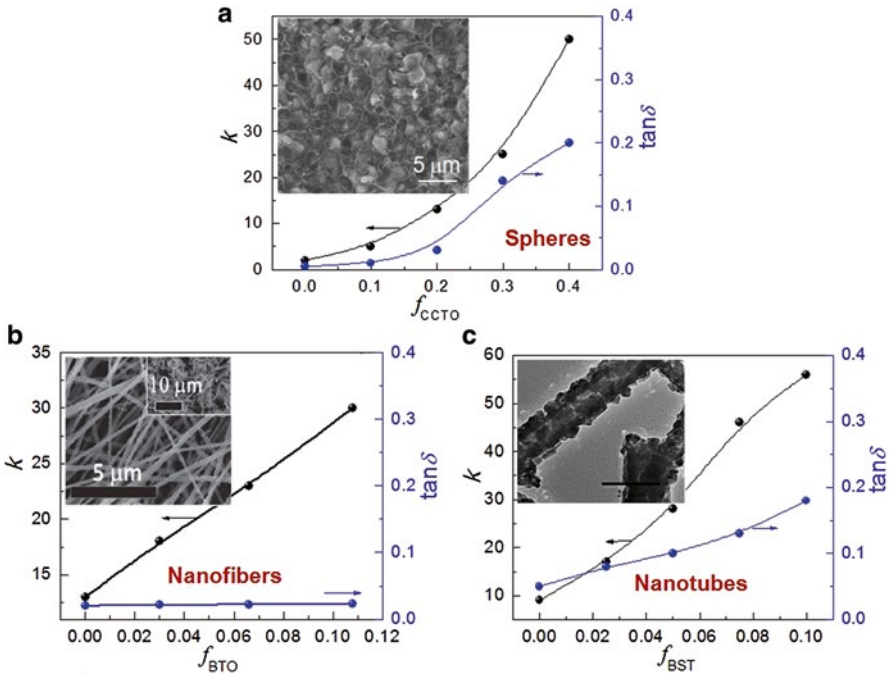

Fig. 1.2 (**a**) Variation of dielectric constant, k, and loss tangent, tanδ, of the CCTO/PI hybrid films as a function of the volume fraction of CCTO filler at 100 Hz and room temperature (The data plotted are taken from Ref. [42]). Inset of (**a**) shows the SEM image of the fractured cross-surface of the CCTO/PI hybrid film with 40 vol% spherical CCTO fillers (Reproduced with permission from Ref. [42] Copyright 2009 Wiley-VCH). (**b**) Dependence of k, and tanδ, on the volume fraction of $BaTiO_3$ nanofibers in epoxy-based composites, measured at 1 kHz. Data are taken from the work by Song et al. [48]. Inset of (**b**) is SEM image of the $BaTiO_3$ nanofibers (Reproduced with permission from Ref. [48]. Copyright 2012 Royal Society of Chemistry). (**c**) The k, and tanδ of BST nanotube/PVDF composite film loaded with various concentrations of nanotube fillers, measured at 100 Hz (The data plotted are taken from Ref. [52]) Inset of (**c**) is the TEM image of BST nanotube (Reproduced with permission from Ref. [52]. Copyright 2014 Royal Society of Chemistry)

Being similar with the nanorods that have 1D morphology, tubular nanostructures also have large aspect ratio yet much smaller density in mass. Such unique features render 1D perovskite BST nanotubes more efficient in enhancing the dielectric constants of composites [52]. It has been demonstrated that the surface hydroxylated BST nanotubes/PVDF nanocomposite flexible films exhibit a high dielectric constant of 58 at 100 Hz at content as low as 10 vol% fillers (see Fig. 1.2c). The key to achieve such high-k nanocomposites is realizing a compact and uniform morphology of the tubular nanostructures by optimizing electrospinning conditions. In addition, if not impossible, exploring 2D high-k nanoplatelets is also very promising for enhancing the dielectric constant of polymers. But to our knowledge, the high-k 2D ceramic platelets/polymer nanocomposites are still in blank up to now.

Although a high dielectric constant can be achieved in polymer composites by loading various high-*k* ceramic particles, there are still many technological and scientific challenges in realizing high-performance nanocomposites. Typical challenges involve achieving uniform dispersion of inorganic nanoparticles and finely controlling the filler–matrix interfacial morphologies to achieve desirable interfacial polarization. A straightforward way is to use small modifiers (e.g., coupling agents [53] and surfactants [54]) to tailor surface properties of nanoparticle in order to improve their compatibility with host polymers and consequently the apparent dielectric performance of the nanocomposites. The modifiers indeed afford an enhancement in the dispersion of inorganic nanoparticles, but they themselves may not contribute to the enhancement of dielectric properties. In some cases, the modifiers even adversely affect the bulk dielectric properties by inducing discontinuous variations in the local electric field and thereby resulting in a significantly reduced dielectric strength [14, 55].

An alternative strategy consists in designing and synthesizing core–shell nanoparticles. The basic idea is introducing one or multi-insulating shells onto individual raw nanoparticles to prevent them from aggregating and forming infinite percolating pathways as well. Consequently core–shell nanoparticles largely enhance the dielectric constant of composites meanwhile well preserving the intrinsic high dielectric strength of polymers by mitigating the propagation of breakdown paths of particles. Recently, Huang et al. [2] reviewed the general methods (Fig. 1.3) developed in the past years for preparing high-*k* nanocomposites based on the core–shell strategy. The core–shell nanoparticles can be prepared by grafting polymer brushes via "grafting from" or "grafting to" routes as well as by coating inorganic shells.

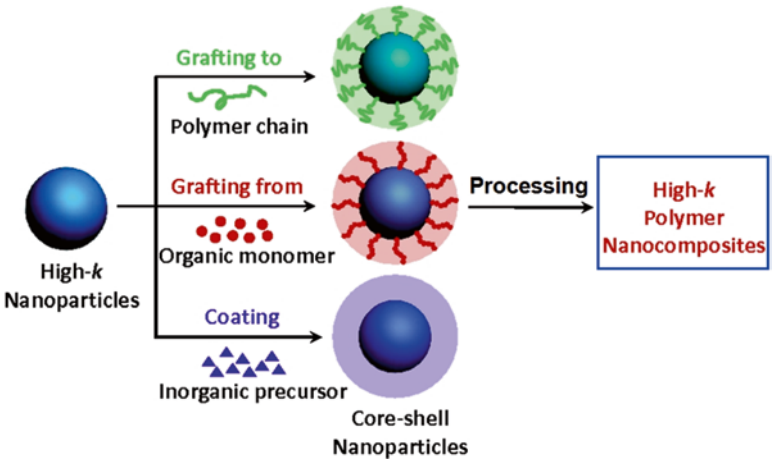

Fig. 1.3 Approaches used to prepare core–shell nanoparticles for high-*k* polymer nanocomposites (Reproduced with permission [2]. Copyright 2015 Wiley-VCH)

The "grafting from" strategy relies on the in situ polymerization of monomers on the initiator-functionalized nanoparticles surfaces. This technology enables the direct formation of high-*k* nanocomposites by using the shell layer as matrix without mixing any additional polymers. This allows for the preparation of very thin and defect-free nanocomposites bearing high filler loadings. For instance, Xie et al. [56] successfully prepared core–shell BTO/poly(methyl methacrylate) (PMMA) nanocomposites via in situ atom transfer radical polymerization (ATRP) of methyl methacrylate (MMA) from the surface of BTO nanoparticles by using silane monolayers as initiators. The BTO core affords a high-*k* (~15 at 1 kHz), while the flexible PMMA shell endows the material with good dispersibility and inherent low loss of the host polymer (~0.037 at 1 kHz) by retarding charge carriers movement in composites. Such core–shell structure can lead to suppressed losses compared to the conventional ceramic particle/polymer nanocomposites [36, 53]. Very recently, Paniagua et al. [57] used a phosphonic acid (PA) as surface initiator for the growth of polystyrene (PS) and PMMA from BTO nanoparticles through ATRP with activators regenerated by electron transfer. The process is schematically illustrated in Fig. 1.4a. By covalently attaching the polymer matrix to the nanoparticles, one can

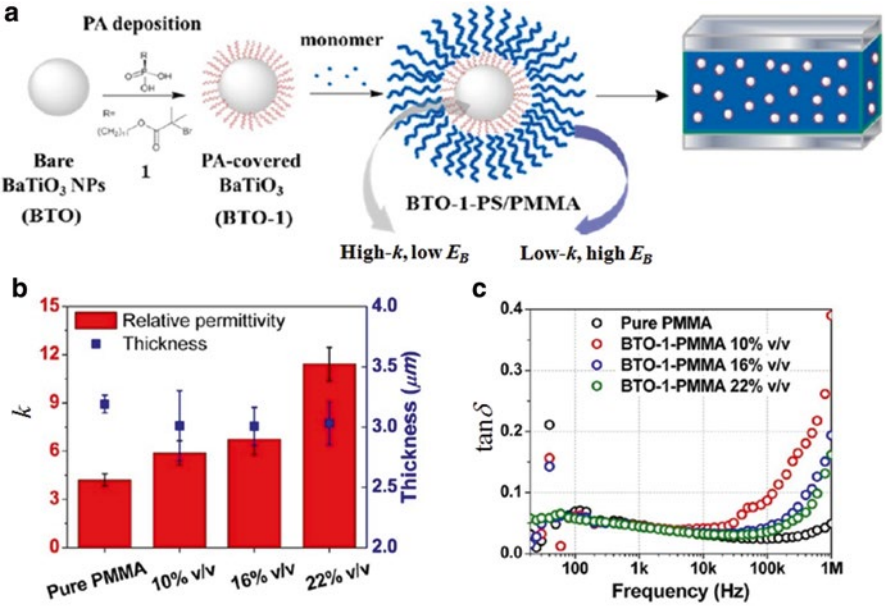

Fig. 1.4 (**a**) Schematic illustration for creating core–shell nanoparticles by "grafting from" route. A capacitor dielectric can be prepared without mixing any additional polymer, and without the need for ball milling or ultrasonication. (**b**) The dielectric constant, *k*, at 1 kHz as a function of volume fraction of BTO nanoparticles. The nanocomposite films have a similar thickness~3 μm. (**c**) Frequency dependence of loss tangent, tan*δ* for the nanocomposites with various BTO loadings (Reproduced with permission from Ref. [57]. Copyright 2014 American Chemical Society)

create a one-component system with three constituents. The dielectric constant can reach 11.4 at 1 kHz (Fig. 1.4b) for 22 vol% BTO particle, while the loss tangent remains at the same low level (Fig. 1.4c) as polymer matrix.

The "grafting to" strategy deals with grafting polymer chains onto the nanoparticle surfaces via a reaction between the functional groups of polymers and nanoparticles. This approach is more commonly found in the literature given its simplicity and large tunability of the grafted polymer chains according to the desired properties of nanocomposites.

Tchoul et al. [59] used click chemistry to attach PS to TiO_2 nanorods and reported a dielectric constant of 6.4 at 1 kHz, while the loss tangent was as low as 0.625 %. State-of-the-art results for polymers attached to ceramic nanoparticles were reported by Jung et al. [58]. They investigated the dielectric properties in a PS nanocomposite comprising core–shell $BaTiO_3$ particles with diblock copolymer shielding layers. The adoption of diblock copolymer resulted in a well-defined layered polymer shell through two-step processes, as illustrated in Fig. 1.5a. A weakly adsorbed layer was first

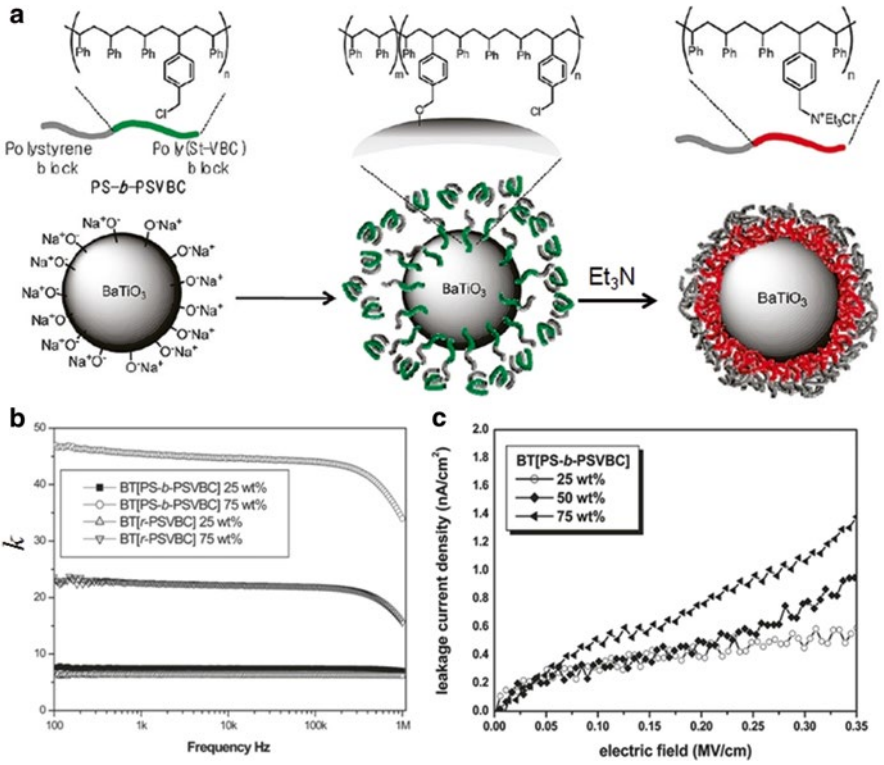

Fig. 1.5 (**a**) Scheme for preparing core–shell nanoparticles by "grafting to" method. A diblock copolymer PS-*b*-PSVBC was covalently attached on the surfaces of BTO particles. (**b**) The dielectric constant, *k*, as a function of volume fraction of BTO nanoparticles. (**c**) The leakage current density as a function of applied electric fields for BTO@PS-*b*-PSVBC/PS nanocomposites (Reproduced with permission from Ref. [58]. Copyright 2010 American Chemical Society)

formed by reacting the chloromethyl group of polystyrene-block-poly(styrene-co-vinylbenzylchloride) (PS-*b*-PSVBC) with the oxy anion on the $BaTiO_3$ surface. The nonpolar chloromethyl functional blocks were subsequently transformed to the polar ammonium blocks and formed a dense layer that interacted strongly with the $BaTiO_3$ particle surfaces. This unique feature not only benefits to good dispersibility in a nonpolar medium but also affords a high dielectric strength at high applied electric field. As shown in Fig. 1.5b, c, the diblock copolymer coated $BaTiO_3$ nanocomposite afforded a high dielectric permittivity (~44 at 10 kHz) and a significantly low leakage current density of 0.76 nA/cm^2, even with a fraction of $BaTiO_3$ particle as large as 75 wt%.

In addition to the polymer shells, a very thin ceramic layer has been also realized on the metal oxide nanoparticles, which provides a route toward decreased permittivity contrast between filler and matrix, and thus addresses the problem of electric field intensification that occurred in conventional ceramic/polymer composites. It was speculated that this ceramic layer formed between the ceramic nanoparticles and polymer phases served as effective electron scatters and trapping centers to reduce the breakdown probability [60]. As illustrated in Fig. 1.6a, Lanagan et al. [61] employed a layer-by-layer methylaluminoxane (MAO) coating process to prepare Al_2O_3 encapsulated metal oxide core–shell nanoparticles. The Al_2O_3 shell thickness can be varied depending on the cycles of MAO coating. These core–shell nanoparticles subsequently served as metallocene catalyst support for the following in situ propylene (PP) polymerization. The thickness of the Al_2O_3 coating actually had little effect on the dielectric constant, only showing a marginal increase upon increasing the shell thickness (Fig. 1.6b). Still, the presence of Al_2O_3 shell

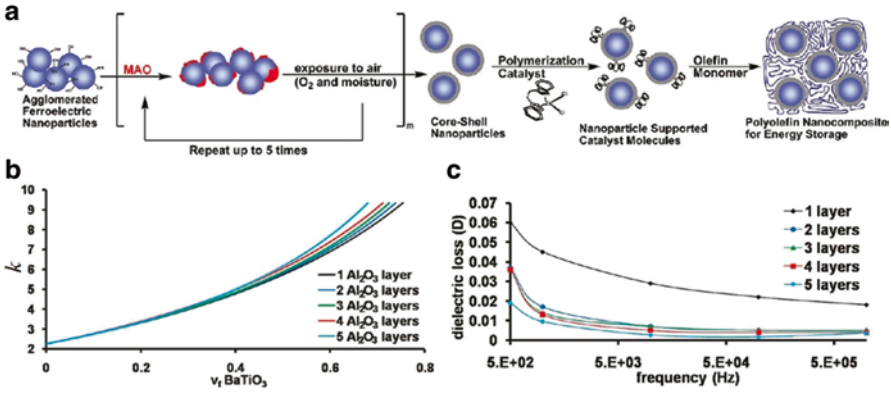

Fig. 1.6 (**a**) A route to aluminum oxide encapsulated high-*k* metal oxide core–shell nanoparticles and catalytically synthesized nanocomposites via in situ supported metallocene olefin polymerization process. (**b**) Dielectric constant versus the volume fraction of the $BaTiO_3$-Al_2O_3 core–shell nanoparticles with various shell thicknesses. (**c**) Frequency dependence of the dielectric loss of $BaTiO_3$-Al_2O_3/PP nanocomposites (Reproduced with permission [61]. Copyright 2010, American Chemical Society)

dramatically suppressed the leakage current and high-field dielectric loss in nanocomposites (Fig. 1.6c).

Most of core–shell nanoparticles currently studied are based on the spherical high-*k* ceramics. The high aspect ratio 1D or 2D core–shell nanoparticles may have superior dielectric properties at low filler loading because of their large dipole moments and low percolation threshold and therefore deserve more attention in the future.

1.3.2 High-k Conducting Nanoparticle–Polymer Composites

Conducting materials, like metal particles, have a negative dielectric constant (in the frequency range of interest which is below the so-called plasma frequency). Owing to the particular response of the particles, conducting particle/polymer nanocomposites are expected to possess much higher dielectric constant than their ceramic counterparts. In fact, exceptionally high dielectric constant has been achieved as the particle loading is very close to but does not exceed the percolation threshold [62]. This divergent behavior can be explained by employing the microcapacitor model based on the near-percolated networks (Fig. 1.7) [63].

Up to now, very high-*k* values have been reported in various systems made by randomly mixing polymers with conducting particles, such as metal spheres [64], carbon nanofiber [65], carbon nanotubes (CNTs) [62, 66], and graphene [67, 68]. For instance, Dang et al. [64] first reported a percolative Ni/PVDF composite bearing a *k* value as high as 400 as approaching the percolation threshold of 17 vol%

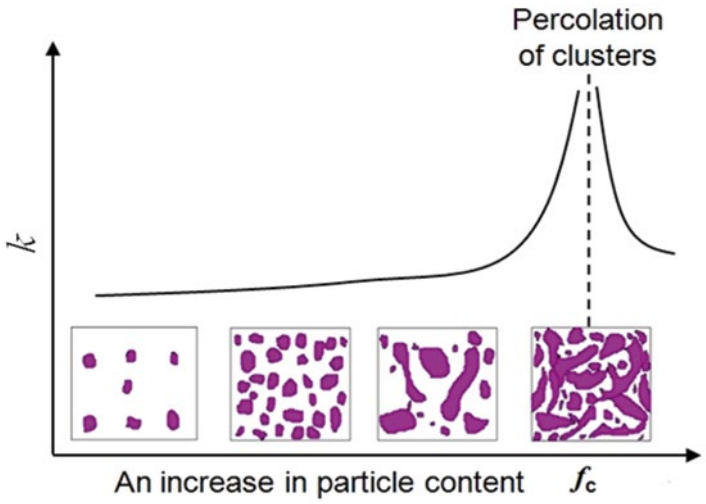

Fig. 1.7 Microstructure evolution with increasing particle concentration in a polymer matrix. Particles in a composite near percolation can form numerous microcapacitors that would contribute to an abnormally large capacitance of the composite, consequently give rise to a large increase of the dielectric constant

from below. As compared to the spherical conductive particle, one-dimensional carbon materials with large aspect ratios can lead to a much lower percolation level. Yuan et al. [62] employed CNTs as nanofiber to pursue high-*k* polymer nanocomposites. The nanocomposites were prepared by melt mixing multi-walled carbon nanotubes (MWNT) within PVDF host polymer. A remarkable interaction at molecular level is achieved by establishing donor–acceptor complexes between the delocalized "π-electron" clouds of MWNTs and strongly electrophilic F groups of PVDF chains (inset of Fig. 1.8d). This strong interfacial interaction is confirmed by the formation of thin PVDF layers on the MWNT surface (Fig. 1.8a). It creates an advanced material with individual nanotube dispersion (Fig. 1.8b). As approaching a critical concentration, the established near-percolated network allows for the formation of microcapacitors with neighboring nanotubes as electrodes and polymer in between as dielectric (Fig. 1.8c). This network morphology has two significant benefits. First it fully takes the advantage of the high specific surface area of nanotubes and results in a huge interfacial area which is considered as the site for additional

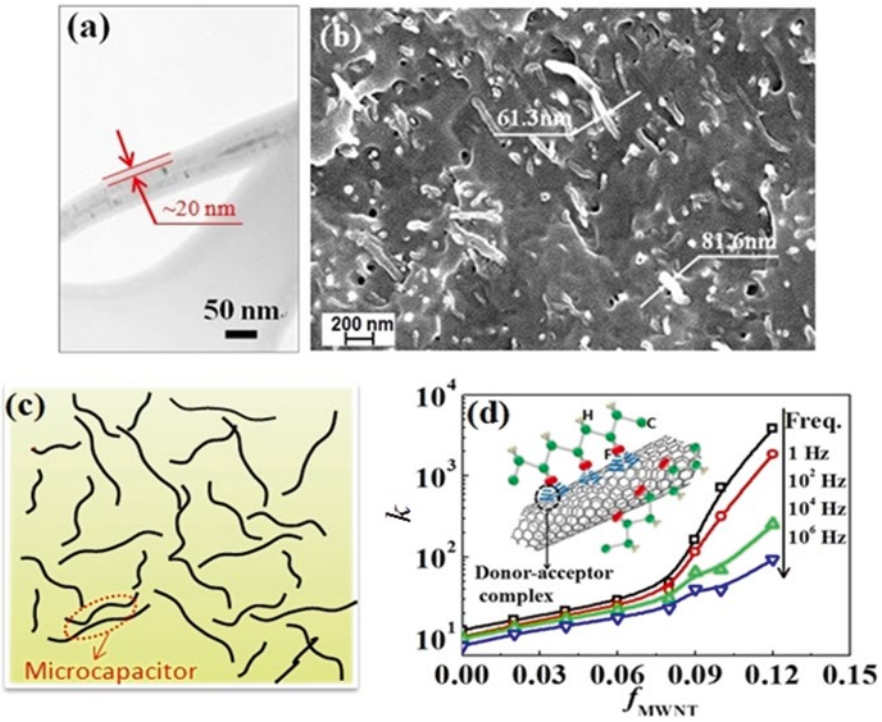

Fig. 1.8 (**a**) TEM image of MWNT with a 20 nm thick PVDF layer. (**b**) SEM image of fractured surface of MWNT/PVDF nanocomposite with f_{MWNT}=10 vol%. (**c**) Schematic illustration of a near-percolated network based on individual CNTs. (**d**) Dependence of the dielectric constant of nanocomposites on the MWNT volume fraction at different frequencies (Reproduced with permission [62]. Copyright 2011 American Chemical Society)

polarizability. Second, the interfacial polarization, within the microcapacitors, can be significantly reinforced because of the formation of the donor–acceptor complexes. The delocalized "π-electron" clouds of MWNTs provide large domains for nomadic electrons, and the electrophilic F groups strongly attract these electrons. These unique features of individual CNT networks consequently give rise to a very high dielectric constant of 3800 at 1 Hz (Fig. 1.8d). Another promising candidate for creating high-*k* percolative composites is two-dimensional conductive filler with a disk or plate shape. He et al. [69] employed such design and demonstrated a graphite nanoplatelet/PVDF nanocomposite. A large dielectric constant of 2700 was observed near percolation threshold as low as 1.0 vol%.

As discussed above, the large *k* values in conducting particle/polymer composites are afforded by interfacial polarization, also known as the MWS effect [62, 70]. However, the charges stored inside the composite would be possibly delocalized either by tunneling or by ohmic conduction. Both lead to a quite high loss dissipation factor, which is not desirable for the practical applications of high-*k* materials [15, 70, 71]. Thus, besides largely increasing the dielectric constant, the dielectric losses should be kept as low as possible.

During past years, many efforts have been devoted to address this issue. One potential strategy is to introduce inter-particle barrier layer into percolative polymer composites. As such, the tunneling current between neighboring conductive nanoparticles can be suppressed and hence affords much lower dielectric losses [72–76]. For instance, Liu et al. [76] made an organic polysulfone (PSF) dielectric shell on MWNTs by employing a simple electrospinning method (Fig. 1.9a). The PSF shell served not only as a barrier to prevent MWNTs from direct contact but also as a polymer matrix after fusion by hot pressing. The resultant MWNT/PSF composites showed a high dielectric constant (ca. 58) when the nanotube content

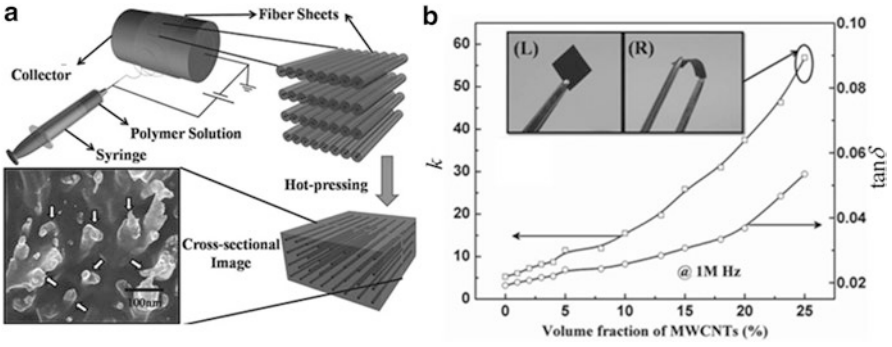

Fig. 1.9 (**a**) Schematic image for the formation of MWNT/PSF composites. The inset is the SEM image of cross section of the composites perpendicular to the fiber direction, MWNTs are indicated by arrows. (**b**) Dependence of the dielectric constant and loss tangent of the composites on the MWNT loading, measured at 1 MHz. The photograph in the inset of (**b**) shows that the composite can be largely deformed (Reproduced with permission [76]. Copyright 2011 Wiley-VCH)

reached 25 vol%, while there was only a slight change in loss tangent from 0.02 to 0.05 (Fig. 1.9b).

Realizing heterogeneous spatial distribution of conducting particles can be another promising strategy [65, 77, 78]. Recently, Gu et al. [78] have developed MWNT/cyanate ester (CE) composite with a gradient dielectric constant via the gradient distribution of MWNT along the direction of the thickness. The CE-rich region can break the conducting path along the direction of electric field (thickness direction), which leads to a far lower loss as compared with randomly dispersed MWNT/CE composites. Yuan et al. [79] reported a more general strategy for dielectric constant enhancement by employing vertically aligned CNT arrays as filler. These CNT arrays naturally form effective microcapacitors in series to store charges if polymer matrix can be completely penetrated into them. More importantly, they can avoid the relaxation of charges stored if the hybrids are well isolated to each other. The key to this strategy is uniformly dispersing CNT arrays into polymer matrix without disturbing the given CNT parallel structures. The integrity of the CNT arrays was retained during composite fabrication in the means of attaching them onto a rigid microplatelet. By varying CVD conditions, two different SiC-CNT hybrids were realized [80]: (i) CNT arrays were grown uniformly along a single direction (denoted as "single-direction" hybrid, Fig. 1.10a) and (ii) the growth of CNT arrays was along two opposite directions perpendicular to the flat surfaces of SiC particles (denoted as "two-direction" hybrid, Fig. 1.10b). After blending with PVDF matrix, the unique architecture of hybrids can be retained. A much more effective microcapacitor network with parallel CNTs as electrode can then be formed

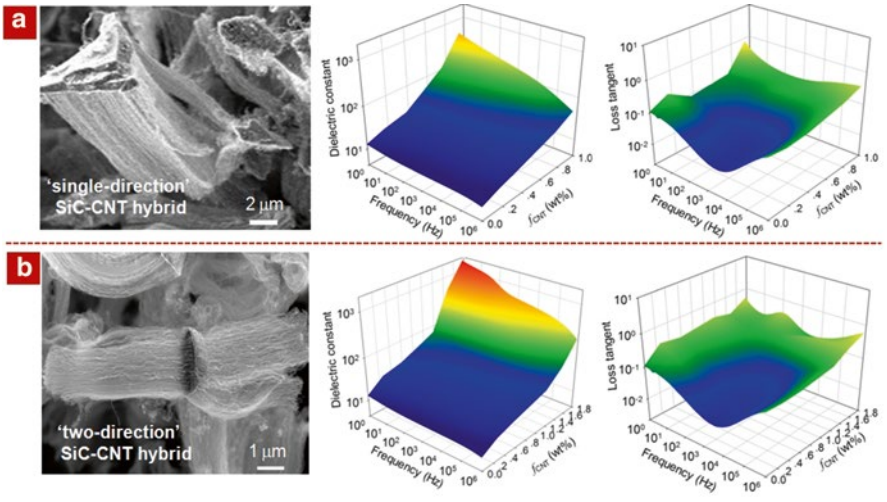

Fig. 1.10 (**a**) SEM images of "single-direction" hybrid and the dielectric properties of their PVDF composites at various CNT contents and frequencies. (**b**) SEM pictures of "two-direction" hybrid and the dielectric spectra of their PVDF composites (Reproduced with permission [79]. Copyright 2014 American Chemical Society)

near percolation, which has a strong effect on the dielectric constant improvement. The produced CNT arrays afford a dielectric constant as high as 1627 at 1 Hz while keeping the loss tangent as low as 0.43 in PVDF composites. More importantly, these improvements were achieved at a very low loading, showing a much higher figure of merit (which describes the relative dielectric constant enhancement with respect to the conducting particle content) than the state-of-the-art nonpercolated polymer composites [79].

In spite of great improvement in enhancing the dielectric constant and lowering the losses, challenges still exist today on finely controlling the network morphology of conducting particles near percolation. In particular, the manufacturing of nanocomposites is often dictated by intuitive expectations or empirical approaches following trials and errors. It is clear that modeling should be further developed to guide more rationally the design of optimal structures. This need becomes even timelier when we consider that formulation and microfabrication technologies are progressing fast. Implementing new technologies such as ink-jet printing and 3D printing, for example, could help in achieving highly controlled structures with enhanced properties. In addition, how to improve the high-field dielectric properties of percolative polymer composites is still not clear. This open question deserves more attention in the future.

1.4 Low-k Polymer Nanocomposite Materials

The rapid development of electronics and electric technologies is associated to a growing need of high-density, high-speed, and high-frequency microelectronic packing [9]. Developing desirable microelectronic packing materials have received much scientific and technological interest. In the past, silica films with a dielectric constant of 3.9 were used. However, continuous miniaturization of electronic device requires the film with lower dielectric constant to reduce both signal propagation delay and dynamic power consumption [81]. The dielectric constant, k, is a key factor that influences the operational speed of integrated circuit (IC). The propagation delay time T_d of IC signal is described as follows:

$$T_d = (k)^{0.5} l / C$$

where l and C are the signal transmission distance and the speed of the light, respectively. Therefore, the lower the dielectric constant of the transmission medium is, the smaller the signal propagation delay time is. The international technology roadmap for semiconductors (ITRS) indicates that future electronics will require an effective k of 2.1–2.5 [82]. Actually realizing such low-k dielectric films is very challenging, in particular combining with other manufacturing requirements, such as high thermal conductivity, low losses, strong mechanical strength, and easy processing. Since water has a high dielectric constant (k~80),

minimizing the moisture content or alternatively improving hydrophobicity of materials is also critical.

Among novel materials, polymer-based low-*k* materials are arousing more and more attention due to their excellent mechanical and physicochemical properties. Typical low-*k* polymers include fluoropolymers, heteroaromatic polymers, poly(aryl ether)s, polyimides, and hydrocarbon polymers without any polar group [9].

There are two possible ways to lower the dielectric constant of polymers, i.e., decreasing dipole strength or the number of dipoles (Fig. 1.11). In more details, decreasing the molecular polarizability can be realized by designing low polarizability chemical structure of polymers. For example, introducing fluorinated substituent into polymer chains could effectively decrease the *k* values due to the small dipole and the low polarizability of the C-F bond. Tao et al. [83] synthesized a fluorinated epoxy resin that can bear a dielectric constant lower than 3.3 without affecting the mechanical properties and chemical stability of plain epoxy resin. However, the fluorination process is technologically complicated, time- and energy consuming, and usually of high cost. These features are not desirable for the large-scale production of low-*k* films.

An alternative approach to prepare low-*k* polymers is to decrease the dipole density. The density of a material can be decreased by increasing the free volume through rearranging the material structure (constitutive porosity) or removing part of the material (subtractive porosity) [84]. By taking the advantage of the low dielectric constant of air ($k=1$, so-called air gaps) in the pores, a mesoporous organic polymer can exhibit an ultralow dielectric constant. The nano/mesopores are generally produced by methods including reprecipitation, sol–gel, thermolysis, supercritical foaming, and electrochemical etching [85]. The pore size and size distribution are critical to the mechanical and dielectric properties of bulk materials and thus need to be finely controlled during pore processing. Jiang et al. [86] prepared a low-*k* nanoporous PI films by first preparing silica/PI nanocomposites via sol–gel process and subsequently treating the nanocomposites with hydrofluoric acid to remove the dispersed silica particles, leaving pores with diameters between

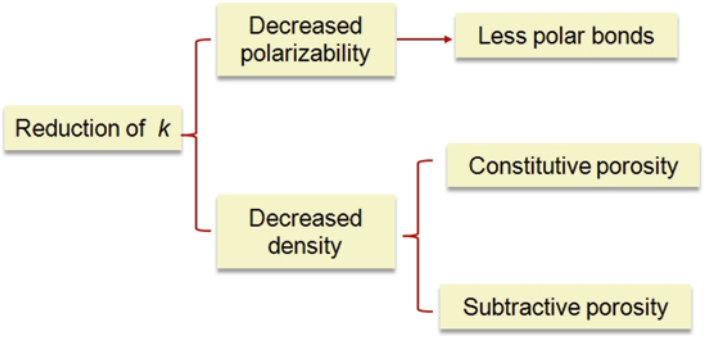

Fig. 1.11 Possibilities for reducing the *k* value of polymer dielectrics

20 and 120 nm. The dielectric constant decreased from 3.4 to 1.8 as the pore content reached up to 20 %, the film kept a tensile strength about 95 MPa.

Despite the achievement of very low dielectric constant ($k \sim 2$) in porous polymers, the aforementioned approaches commonly result in a broad pore size distribution and open pore structures, which detrimentally affect the mechanical properties of polymers and thus limit their use. Furthermore, polymer sole actually cannot meet the multirequirements expected for low-*k* materials in advanced microelectronic packing because of their low thermal conductivity (0.2 $Wm^{-1}K^{-1}$). The manufacturable solutions may rely on the nanocomposite approaches consisting of dispersing hollow particles or high thermal conductivity core–shell nanoparticles into polymer matrix to find compromises of dielectric, mechanical, and thermal properties.

1.4.1 Low-k Hollow Particle/Polymer Nanocomposite Materials

Comparing with introducing subtractive porosity, dispersing ordered mesoporous particles allows for much easier control over the size and distribution of pores in polymers. Decreased dielectric constant and improved mechanical properties can be simultaneously achieved in nanocomposites filled with mesoporous silica materials such as MCM-41 [87, 88] and SBA-15 [89, 90]. This new family of mesoporous materials has attracted considerable interests due to their highly ordered and uniform mesoporosity (Fig. 1.12a, b). The typical pore size ranges from 2 to 10 nm and the surface areas are as high as ~1000 $m^2\ g^{-1}$. These unique features can largely decrease the dipole density of polymers as they are used as fillers in nanocomposites. Dang's group [87] reported a low dielectric constant ($k = 2.6$) in nanohybrid PI films filled with 3.0 wt% MCM-41. Similarly, Min et al. synthesized a series of PI composite thin films composed of SBA-15 modified with functional groups of

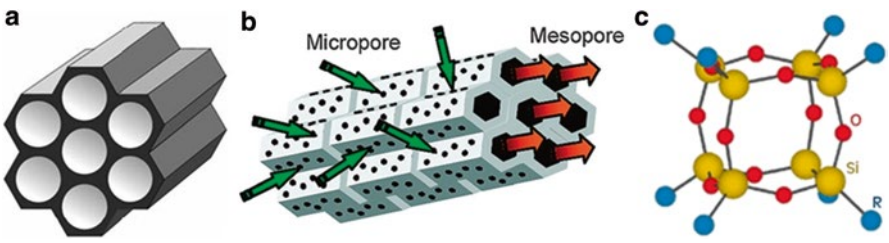

Fig. 1.12 Schematic diagram of (**a**) MCM-41, (**b**) SBA-15 with micropores in walls and mesoporous channels, and (**c**) molecular structure of POSS. R may be a hydrogen atom or an organic functional group, e.g., alkyl, alkylene, acrylate, hydroxyl, or epoxide unit (Reproduced with permission [91]. Copyright 2014 Royal Society of Chemistry)

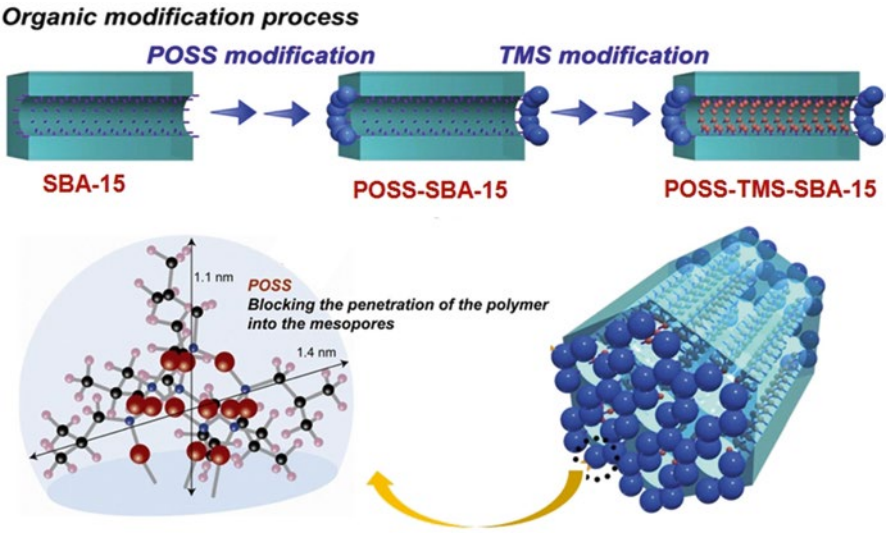

Fig. 1.13 Schematic illustration of preparation of POSS-capped mesoporous silica particles. Epoxy polymer cannot enter into the inner channels due to the steric hindrance of isobutyl groups (Reproduced with permission [88]. Copyright 2011 Elsevier)

octyltrimethoxysilane (OTMS) or 3-aminopropyl trimethoxy silane (ATS). They systematically investigated the modification effect on the mechanical and dielectric properties as well as the thermal stability of thin films. It was found that the tensile strength and elongation of the composite films containing SBA-15 modified with ATS were much higher than those of composite without modification while the dielectric constant was significantly reduced to 2.7.

Although mesoporous silica has been successfully used to lower k values, two tricky problems still exist to restrict their application in fabricating advanced low-k polymeric hybrids [89]. First, the size of the inner channels of mesoporous silica is generally so large that the resin molecule can enter into the channels and decrease the porosity density. Second, the existence of rich polar and hydrophilic silanol groups in the inner channels renders mesoporous silica capable of adsorbing moisture. As water has a high k~80, mesoporous silica particles usually show a high dielectric constant. Therefore further lowering the dielectric constant of the resultant hybrid nanocomposites is limited. Using smart molecular caps to block the entrance of channels in mesoporous silica particles is a promising method to address this issue. Suzuki et al. [88] first modified the entrance of the mesopores by polyhedral oligomeric silsesquioxane (POSS) molecules. Trimethylsilyl (TMS) agents are grafted onto silanol groups at the inner mesopores to reduce the polarity. The process is schematically illustrated in Fig. 1.13. Subsequently they added the capped particles into epoxy resin and found that the dielectric constant of the hybrid with 20 wt% particles is as low as 2.5.

Being similar with mesoporous silica, POSS is also referred to as a silica nanoparticle consisting of a silica cage core, as well as organic functional groups attached to the corners of the cage (Fig. 1.12c) [92]. Nanoporous POSS has received extensive research attention as a filler to reduce the dielectric constant of hybrid nanocomposites [93–96] because its unique nanometersized cage provides POSS composites with a very low dielectric constant. In addition, owing to the variable reactive external groups, the POSS moieties can be chemically bond to the organic matrix and uniformly distributed within the polymeric system at molecular level and thus enhance the thermal and mechanical properties of the resultant hybrid materials. Therefore, formation of polymer/POSS nanocomposites could simultaneously lower the dielectric constants and enhance the mechanical properties of polymers [92, 97]. For example, Yang et al. prepared three-dimensional organic–inorganic network hybrids via hydrosilylative addition reaction of octahydridosilsesquioxanes with dienes to form chemical bonds between two monomers. As such, POSS molecules were uniformly dispersed into the polymeric system at the nanoscale. The resultant hybrid films exhibited enhanced mechanical properties (elastic modulus of 8.9 GPa) and a reduced dielectric constant (k ~2.43). This strategy offers the advantage of tunability of dielectric and mechanical properties by adjusting the length and the structure of the linking chain between POSS cages.

1.4.2 Low-k Hybrid Particle/Polymer Nanocomposite Materials

As discussed above, in addition to the high mechanical strengths and extremely low dielectric constant, the advanced microelectronic packing materials should also have high thermal conductivity to dissipate the generated heat. Recent studies have shown that ceramic nanoparticles with high thermal conductivity (e.g., boron nitride nanosheets [98] and aluminum oxide spheres [99]) can afford an efficient thermal conduction in polymer composites. However, most of the ceramic particles with high thermal conductivity usually lead to a high dielectric constant of polymer composites because of the lack of porosity. Therefore it is urgent to seek solutions to simultaneously improve thermal conductivity and decrease the dielectric constant of polymers.

Designing and synthesizing novel hybrid nanoparticles can meet this end by combining high thermal conductivity particles with low-*k* particles. Recently, Huang and Zhi [100] achieved an ideal dielectric thermally conductive epoxy nanocomposite using POSS-functionalized boron nitride nanotubes as fillers (Fig. 1.14a). The unique hybrid structure afforded a decreased dielectric constant (Fig. 1.14b) due to the intrinsic low-*k* in boron nitride nanotubes and POSS molecules, while the thermal conductivity was dramatically improved by 1360 % as compared with the pristine epoxy resin (Fig. 1.14c). However, to further lower the dielectric constant of such composites, the key relies on well preserving the porosity of boron nitride nanotubes.

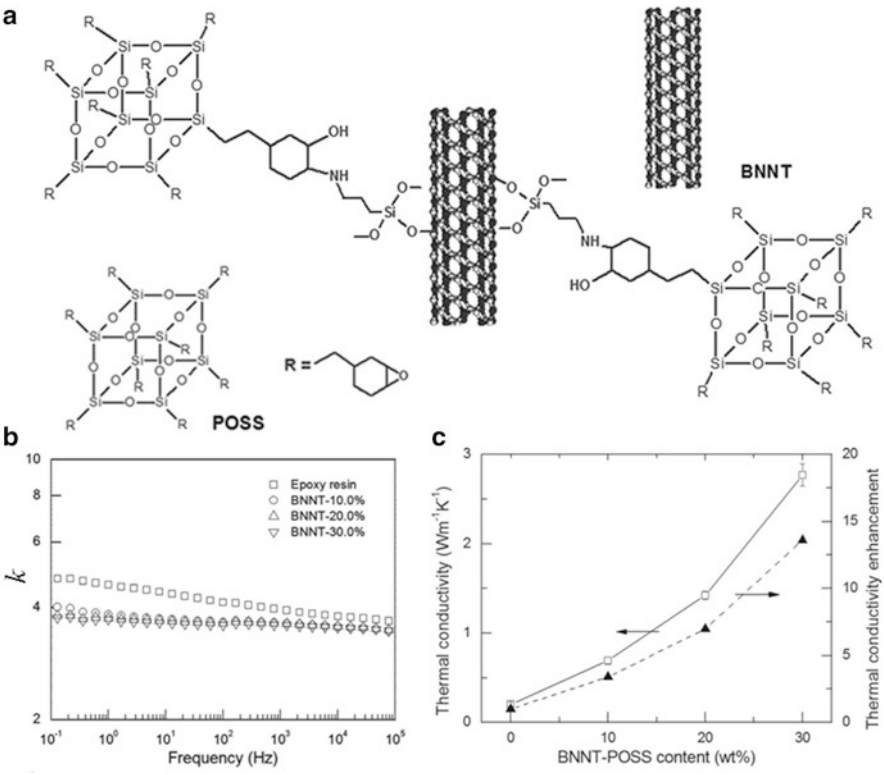

Fig. 1.14 (**a**) Schematic diagram of preparation of POSS-functionalized boron nitride nanotubes. (**b**) Frequency dependence of the dielectric constant of the epoxy composites filled with POSS-functionalized boron nitride nanotubes. (**c**) The composites' thermal conductivity varies as a function of the filler loading (Reproduced with permission [100]. Copyright 2013 Wiley-VCH)

1.5 Conclusions

Polymer nanocomposites allow for a large tunability of dielectric constant by properly selecting the identity, size, shape, property of filler and by controlling the morphology of polymer matrices, and engineering the interfaces between filler and matrix. To make high-*k* nanocomposites, ceramic or conducting particles with high dielectric constant are usually used as filler to improve the dielectric constant of composites, but attention should be paid in avoiding the formation of conducting path of particles so as to suppress the high loss tangent and preserve the intrinsic high dielectric strength of polymers. On the other hand, decrease of the dielectric constant of polymer to fabricate low-*k* nanocomposite materials relies on introducing uniformly sized pores. Simultaneously achieving a low dielectric constant, improved mechanical strength, and high thermal conductivity is the big challenge in the field. Potential solution to this problem is designing and synthesizing novel and

multifunctional hybrid fillers. From a more general point of view, it can be noted that manufacturing of nanocomposites is often guided by intuitive expectations and empirical approaches. Advanced modeling should be further developed in order to provide a more rational guidance of experimental efforts. In addition, it is expected that the development of new formulation and microfabrication technologies will help in the optimization and control of nanocomposite structures to achieve enhanced properties in the years to come.

Acknowledgments This work was financially supported by France ANR and Solvay through the Project ELENA.

References

1. Nalwa H (1999) Handbook of Low and High Dielectric Constant Materials and Their Applications. Academic, London
2. Huang X, Jiang P (2015) Core-shell structured high-*k* polymer nanocomposites for energy storage and dielectric applications. Adv Mater 27(3):546–554
3. Rao Y, Wong CP (2004) Material characterization of a high-dielectric-constant polymer-ceramic composite for embedded capacitor for RF applications. J Appl Polym Sci 92(4): 2228–2231
4. Dang ZM, Yuan JK, Yao SH et al (2013) Flexible nanodielectric materials with high permittivity for power energy storage. Adv Mater 25(44):6334–6365
5. Neese B, Chu B, Lu SG, Wang Y, Furman E, Zhang QM (2008) Large electrocaloric effect in ferroelectric polymers near room temperature. Science 321(5890):821–823
6. Zhang G, Li Q, Gu H, Jiang S, Han K, Gadinski MR et al (2015) Ferroelectric polymer nanocomposites for room-temperature electrocaloric refrigeration. Adv Mater 27(8):1450–1454
7. Zhang QM, Li HF, Poh M, Xia F, Cheng ZY, Xu HS et al (2002) An all-organic composite actuator material with a high dielectric constant. Nature 419(6904):284–287
8. Brochu P, Pei Q (2010) Advances in dielectric elastomers for actuators and artificial muscles. Macromol Rapid Comm 31(1):10–36
9. Maier G (2001) Low dielectric constant polymers for microelectronics. Prog Polym Sci 26(1):3–65
10. Ihlefeld J, Laughlin B, Hunt-Lowery A, Borland W, Kingon A, Maria JP (2005) Copper compatible barium titanate thin films for embedded passives. J Electroceram 14(2):95–102
11. Barber P, Balasubramanian S, Anguchamy Y, Gong S, Wibowo A, Gao H et al (2009) Polymer composite and nanocomposite dielectric materials for pulse power energy storage. Materials 2(4):1697–1733
12. Yao SH, Yuan JK, Gonon P, Bai J, Pairis S, Sylvestre A (2012) Effect of oxygen vacancy on the dielectric relaxation of BaTiO3 thin films in a quenched state. J Appl Phys 111(10):104109
13. Wu JB, Nan CW, Lin YH, Deng Y (2002) Giant dielectric permittivity observed in Li and Ti doped NiO. Phys Rev Lett 89:217601
14. Li JY, Zhang L, Ducharme S (2007) Electric energy density of dielectric nanocomposites. Appl Phys Lett 90:132901
15. Dang Z-M, Yuan J-K, Zha J-W, Zhou T, Li S-T, Hu G-H (2012) Fundamentals, processes and applications of high-permittivity polymer matrix composites. Prog Mater Sci 57(4): 660–723
16. Wang Y, Zhou X, Chen Q, Chu B, Zhang Q (2010) Recent development of high energy density polymers for dielectric capacitors. IEEE Trans Dielectr Electr Insul 17(4):1036–1042

17. Job AE, Alves N, Zanin M, Ueki MM (2003) Increasing the dielectric breakdown strength of poly(ethylene terephthalate) films using a coated polyaniline layer. J Phys D-Appl Phys 36(12):1414–1417
18. Chu B, Zhou X, Ren K, Neese B, Lin M, Wang Q et al (2006) A dielectric polymer with high electric energy density and fast discharge speed. Science 313(5785):334–336
19. Tuncer E, Sauers I, Randy James D, Ellis AR, Parans Paranthaman M, Goyal A et al (2007) Enhancement of dielectric strength in nanocomposites. Nanotechnology 18:325704
20. Rahimabady M, Chen S, Yao K, Tay FEH, Lu L (2011) High electric breakdown strength and energy density in vinylidene fluoride oligomer/poly(vinylidene fluoride) blend thin films. Appl Phys Lett 99:142901
21. Wu S, Li W, Lin M, Burlingame Q, Chen Q, Payzant A et al (2013) Aromatic polythiourea dielectrics with ultrahigh breakdown field strength, low dielectric loss, and high electric energy density. Adv Mater 25(12):1734–1738
22. Islam MS, Qiao Y, Tang C, Ploehn HJ (2015) Terthiophene-containing copolymers and homopolymer blends as high-performance dielectric materials. ACS Appl Mater Interfaces 7(3):1967–1977
23. Tan L, Liu S, Zeng F, Zhang S, Zhao J, Yu Y (2011) A low dielectric constant polyimide/ polyoxometalate composite. Polym Adv Technol 22(2):209–214
24. Fredin LA, Li Z, Lanagan MT, Ratner MA, Marks TJ (2013) Sustainable high capacitance at high frequencies: metallic aluminum – polypropylene nanocomposites. ACS Nano 7(1): 396–407
25. Zhu L (2014) Exploring strategies for high dielectric constant and low loss polymer dielectrics. J Phys Chem Lett 5(21):3677–3687
26. Kim SH, Hong K, Xie W, Lee KH, Zhang S, Lodge TP et al (2013) Electrolyte-gated transistors for organic and printed electronics. Adv Mater 25(13):1822–1846
27. Kremer F, Schönhals A (2003) Broadband dielectric spectroscopy. Springer, New York
28. Tamura R, Lim E, Manaka T, Iwamoto M (2006) Analysis of pentacene field effect transistor as a Maxwell-Wagner effect element. J Appl Phys 100(11):114515
29. Ducharme S (2009) An inside-out approach to storing electrostatic energy. ACS Nano 3(9):2447–2450
30. Li JY, Huang C, Zhang QM (2004) Enhanced electromechanical properties in all-polymer percolative composites. Appl Phys Lett 84:3124
31. Cheng Y, Chen X, Wu K, Wu S, Chen Y, Meng Y (2008) Modeling and simulation for effective permittivity of two-phase disordered composites. J Appl Phys 103:034111
32. Chu B, Zhou X, Neese B, Zhang QM, Bauer F (2006) Relaxor ferroelectric poly(vinylidene fluoride-trifluoroethylene-chlorofluoroethylene) terpolymer for high energy density storage capacitors. IEEE Trans Dielectrics Electrical Insulation 13(5):1162–1169
33. Qiao Y, Islam MS, Han K, Leonhardt E, Zhang J, Wang Q et al (2013) Polymers containing highly polarizable conjugated side chains as high-performance all-organic nanodielectric materials. Adv Funct Mater 23(45):5638–5646
34. Burlingame Q, Wu S, Lin M, Zhang QM (2013) Conduction mechanisms and structure-property relationships in high energy density aromatic polythiourea dielectric films. Adv Energy Mater 3(8):1051–1505
35. Thakur VK, Lin M-F, Tan EJ, Lee PS (2012) Green aqueous modification of fluoropolymers for energy storage applications. J Mater Chem 22(13):5951–5959
36. Dang ZM, Xu HP, Wang HY (2007) Significantly enhanced low-frequency dielectric permittivity in the BaTiO3/poly(vinylidene fluoride) nanocomposite. Appl Phys Lett 90(1):012901
37. Arbatti M, Shan XB, Cheng ZY (2007) Ceramic-polymer composites with high dielectric constant. Adv Mater 19(10):1369–1372
38. Balasubramanian B, Kraemer KL, Reding NA, Skomski R, Ducharme S, Sellmyer DJ (2010) Synthesis of monodisperse TiO_2-paraffin core-shell nanoparticles for improved dielectric properties. ACS Nano 4(4):1893–1900

39. Dang Z-M, Xia Y-J, Zha J-W, Yuan J-K, Bai J (2011) Preparation and dielectric properties of surface modified TiO_2/silicone rubber nanocomposites. Mater Lett 65(23-24):3430–3432
40. Zou C, Kushner D, Zhang S (2011) Wide temperature polyimide/ZrO_2 nanodielectric capacitor film with excellent electrical performance. Appl Phys Lett 98(8):082905
41. Tuncer E, Sauers I, James DR, Ellis AR, Duckworth RC (2008) Nanodielectric system for cryogenic applications: barium titanate filled polyvinyl alcohol. IEEE Trans Dielectr Electr Insul 15(1):236–242
42. Dang Z-M, Zhou T, Yao S-H, Yuan J-K, Zha J-W, Song H-T et al (2009) Advanced calcium copper titanate/polyimide functional hybrid films with high dielectric permittivity. Adv Mater 21(20):2077–2082
43. Yang W, Yu S, Sun R, Du R (2011) Nano- and microsize effect of CCTO fillers on the dielectric behavior of CCTO/PVDF composites. Acta Mater 59(14):5593–5602
44. Prakash BS, Varma KBR (2007) Dielectric behavior of CCTO/epoxy and Al-CCTO/epoxy composites. Compos Sci Technol 67(11-12):2363–2368
45. Amaral F, Rubinger CPL, Henry F, Costa LC, Valente MA, Barros-Timmons A (2008) Dielectric properties of polystyrene-CCTO composite. J Non-Cryst Solids 354 (47-51):5321–5322
46. An AL, Boggs SA, Calame J, IEEE (2006) Energy storage in polymer films with high dielectric constant fillers. Conference Record of the IEEE International Symposium on Electrical Insulation, Toronto, Ont
47. Calame JP (2006) Finite difference simulations of permittivity and electric field statistics in ceramic-polymer composites for capacitor applications. J Appl Phys 99(8):084108
48. Song Y, Shen Y, Liu H, Lin Y, Li M, Nan C-W (2012) Enhanced dielectric and ferroelectric properties induced by dopamine-modified $BaTiO_3$ nanofibers in flexible poly(vinylidene fluoride-trifluoroethylene) nanocomposites. J Mater Chem 22(16):8063–8068
49. Song Y, Shen Y, Liu H, Lin Y, Li M, Nan C-W (2012) Improving the dielectric constants and breakdown strength of polymer composites: effects of the shape of the $BaTiO_3$ nanoinclusions, surface modification and polymer matrix. J Mater Chem 22(32):16491–16498
50. Avila HA, Ramajo LA, Goes MS, Reboredo MM, Castro MS, Parra R (2013) Dielectric behavior of epoxy/$BaTiO_3$ composites using nanostructured ceramic fibers obtained by electrospinning. ACS Appl Mater Interfaces 5(3):505–510
51. Tang H, Lin Y, Andrews C, Sodano HA (2011) Nanocomposites with increased energy density through high aspect ratio PZT nanowires. Nanotechnology 22(1):015702
52. Liu S, Xue S, Zhang W, Zhai J, Chen G (2014) Significantly enhanced dielectric property in PVDF nanocomposites flexible films through a small loading of surface-hydroxylated $Ba_{0.6}Sr_{0.4}TiO_3$ nanotubes. J Mater Chem A 2(42):18040–18046
53. Dang Z-M, Wang H-Y, Xu H-P (2006) Influence of silane coupling agent on morphology and dielectric property in BaTiO3/polyvinylidene fluoride composites. Appl Phys Lett 89(11):112902
54. Ramesh S, Shutzberg BA, Huang C, Gao J, Giannelis EP (2003) Dielectric nanocomposites for integral thin film capacitors: Materials design, fabrication, and integration issues. IEEE Trans Adv Pack 26(1):17–24
55. Li J, Khanchaitit P, Han K, Wang Q (2010) New route toward high-energy-density nanocomposites based on chain-end functionalized ferroelectric polymers. Chem Mater 22(18): 5350–5357
56. Xie L, Huang X, Wu C, Jiang P (2011) Core-shell structured poly(methyl methacrylate)/ BaTiO3 nanocomposites prepared by in situ atom transfer radical polymerization: a route to high dielectric constant materials with the inherent low loss of the base polymer. J Mater Chem 21(16):5897–5906
57. Paniagua SA, Kim Y, Henry K, Kumar R, Perry JW, Marder SR (2014) Surface-initiated polymerization from barium titanate nanoparticles for hybrid dielectric capacitors. ACS Appl Mater Interfaces 6(5):3477–3482

58. Jung HM, Kang J-H, Yang SY, Won JC, Kim YS (2010) Barium titanate nanoparticles with diblock copolymer shielding layers for high-energy density nanocomposites. Chem Mater 22(2):450–456
59. Tchoul MN, Fillery SP, Koerner H, Drummy LF, Oyerokun FT, Mirau PA et al (2010) Assemblies of titanium dioxide-polystyrene hybrid nanoparticles for dielectric applications. Chem Mater 22(5):1749–1759
60. Guo N, DiBenedetto SA, Kwon D-K, Wang L, Russell MT, Lanagan MT et al (2007) Supported metallocene catalysis for in situ synthesis of high energy density metal oxide nanocomposites. J Am Chem Soc 129(4):766–767
61. Li Z, Fredin LA, Tewari P, DiBenedetto SA, Lanagan MT, Ratner MA (2010) In situ catalytic encapsulation of core-shell nanoparticles having variable shell thickness: dielectric and energy storage properties of high-permittivity metal oxide nanocomposites. Chem Mater 22(18):5154–5164
62. Yuan J-K, Yao S-H, Dang Z-M, Sylvestre A, Genestoux M, Bai J (2011) Giant dielectric permittivity nanocomposites: realizing true potential of pristine carbon nanotubes in polyvinylidene fluoride matrix through an enhanced interfacial interaction. J Phys Chem C 115(13):5515–5521
63. Nan CW, Shen Y, Ma J (2010) Physical properties of composites near percolation. Annu Rev Mater Res 40:131–151
64. Dang ZM, Lin YH, Nan CW (2003) Novel ferroelectric polymer composites with high dielectric constants. Adv Mater 15(19):1625–1629
65. Sun LL, Li B, Zhao Y, Mitchell G, Zhong WH (2010) Structure-induced high dielectric constant and low loss of CNF/PVDF composites with heterogeneous CNF distribution. Nanotechnology 21:305702
66. Yuan J-K, Yao S-H, Sylvestre A, Bai J (2012) Biphasic polymer blends containing carbon nanotubes: heterogeneous nanotube distribution and its influence on the dielectric properties. J Phys Chem C 116(2):2051–2058
67. Fan P, Wang L, Yang J, Chen F, Zhong M (2012) Graphene/poly(vinylidene fluoride) composites with high dielectric constant and low percolation threshold. Nanotechnology 23:365702
68. Yu J, Huang X, Wu C, Jiang P (2011) Permittivity, thermal conductivity and thermal stability of poly(vinylidene fluoride)/graphene nanocomposites. IEEE Trans Dielectr Electr Insul 18(2):478–484
69. He F, Lau S, Chan HL, Fan JT (2009) High dielectric permittivity and low percolation threshold in nanocomposites based on poly(vinylidene fluoride) and exfoliated graphite nanoplates. Adv Mater 21(6):710–715
70. Dang ZM, Wang L, Yin Y, Zhang Q, Lei QQ (2007) Giant dielectric permittivities in functionalized carbon-nanotube/electroactive-polymer nanocomposites. Adv Mater 19(6):852–857
71. Yao S-H, Yuan J-K, Zhou T, Dang Z-M, Bai J (2011) Stretch-modulated carbon nanotube alignment in ferroelectric polymer composites: characterization of the orientation state and its influence on the dielectric properties. J Phys Chem C 115(40):20011–20017
72. Zhou T, Zha J-W, Hou Y, Wang D, Zhao J, Dang Z-M (2011) Surface-functionalized MWNTs with emeraldine base: preparation and improving dielectric properties of polymer nanocomposites. ACS Appl Mater Interfaces 3(12):4557–4560
73. Wu C, Huang X, Wu X, Yu J, Xie L, Jiang P (2012) TiO_2-nanorod decorated carbon nanotubes for high-permittivity and low-dielectric-loss polystyrene composites. Comp Sci Technol 72(4):521–527
74. Wu C, Huang X, Xie L, Yu J, Jiang P (2011) Morphology-controllable graphene-TiO_2 nanorod hybrid nanostructures for polymer composites with high dielectric performance. J Mater Chem 21(44):17729–17736
75. Zhang S, Wang H, Wang G, Jiang Z (2012) Material with high dielectric constant, low dielectric loss, and good mechanical and thermal properties produced using multi-wall carbon

nanotubes wrapped with poly(ether sulphone) in a poly(ether ether ketone) matrix. Appl Phys Lett 101:012904
76. Liu H, Shen Y, Song Y, Nan C-W, Lin Y, Yang X (2011) Carbon nanotube array/polymer core/shell structured composites with high dielectric permittivity, low dielectric loss, and large energy density. Adv Mater 23(43):5104–5108
77. Wang B, Liang G, Jiao Y, Gu A, Liu L, Yuan L et al (2013) Two-layer materials of polyethylene and a carbon nanotube/cyanate ester composite with high dielectric constant and extremely low dielectric loss. Carbon 54:224–233
78. Wu H, Gu A, Liang G, Yuan L (2011) Novel permittivity gradient carbon nanotubes/cyanate ester composites with high permittivity and extremely low dielectric loss. J Mater Chem 21(38):14838–14848
79. Yuan J, Yao S, Li W, Sylvestre A, Bai J (2014) Vertically aligned carbon nanotube arrays on SiC microplatelets: a high figure-of-merit strategy for achieving large dielectric constant and low loss in polymer composites. J Phys Chem C 118(40):22975–22983
80. Li W, Yuan J, Lin Y, Yao S, Ren Z, Wang H et al (2013) The controlled formation of hybrid structures of multi-walled carbon nanotubes on SiC plate-like particles and their synergetic effect as a filler in poly(vinylidene fluoride) based composites. Carbon 51:355–364
81. Zhou Y, Wang L, Zhang H, Bai Y, Niu Y, Wang H (2012) Enhanced high thermal conductivity and low permittivity of polyimide based composites by core-shell Ag@SiO2 nanoparticle fillers. Appl Phys Lett 101:012903
82. International Technology Roadmap of Semiconductors (2013) http://www.itrs.net.
83. Taa Z, Yang S, Ge Z, Chen J, Fan L (2007) Synthesis and properties of novel fluorinated epoxy resins based on 1,1-bis(4-glycidylesterphenyl)1-(3'-trifluoromethylphenyl)-2,2,2-trifluo roethane. Eur Polym J 43(2):550–560
84. Shamiryan D, Abell T, Iacopi F, Maex K (2004) Low-k dielectric materials. Mater Today 7(1):34–39
85. Ma S, Wang Y, Min Z, Zhong L (2013) Nano/mesoporous polymers based low-k dielectric materials: a review on methods and advances. Adv Polym Technol 32:21358
86. Jiang LZ, Liu JG, Wu DZ, Li HQ, Jin RG (2006) A methodology for the preparation of nanoporous polyimide films with low dielectric constants. Thin Solid Films 510(1-2):241–246
87. Dang Z-M, Ma L-J, Zha J-W, Yao S-H, Xie D, Chen Q et al (2009) Origin of ultralow permittivity in polyimide/mesoporous silicate nanohybrid films with high resistivity and high breakdown strength. J Appl Phys 105:044104
88. Suzuki N, Kiba S, Yamauchi Y (2011) Low dielectric property of novel mesoporous silica/polymer composites using smart molecular caps: theoretical calculation of air space encapsulated inside mesopores. Micropor Mesopor Mater 138(1-3):123–131
89. Shan W, Chen L, Chu Y, Zhao F, Liang G, Gu A et al (2013) Synthesis of a fully capped mesoporous silica and its hybrids with extremely low dielectric constant and loss. Micropor Mesopor Mater 176:199–208
90. Min C-K, Wu T-B, Yang W-T, Chen C-L (2008) Functionalized mesoporous silica/polyimide nanocomposite thin films with improved mechanical properties and low dielectric constant. Compos Sci Technol 68(6):1570–1578
91. Gibson LT (2014) Mesosilica materials and organic pollutant adsorption: part a removal from air. Chem Soc Rev 43(15):5163–5172
92. Kuo S-W, Chang F-C (2011) POSS related polymer nanocomposites. Prog Polym Sci 36(12):1649–1696
93. Ye Y-S, Chen W-Y, Wang Y-Z (2006) Synthesis and properties of low-dielectric-constant polyimides with introduced reactive fluorine polyhedral oligomeric silsesquioxanes. J Polym Sci Part a-Polym Chem 44(18):5391–5402
94. Wang Y-Z, Chen W-Y, Yang C-C, Lin C-L, Chang F-C (2007) Novel epoxy nanocomposite of low Dk introduced fluorine-containing POSS structure. J Polym Sci Part B-Polym Phys 45(4):502–510

95. Wahab MA, Mya KY, He C (2008) Synthesis, morphology, and properties of hydroxyl terminated-POSS/polyimide low-k nanocomposite films. J Polym Sci Part a-Polym Chem 46(17):5887–5896
96. Tseng M-C, Liu Y-L (2010) Preparation, morphology, and ultra-low dielectric constants of benzoxazine-based polymers/polyhedral oligomeric silsesquioxane (POSS) nanocomposites. Polymer 51(23):5567–5575
97. Geng Z, Huo M, Mu J, Zhang S, Lu Y, Luan J et al (2014) Ultra low dielectric constant soluble polyhedral oligomeric silsesquioxane (POSS)-poly(aryl ether ketone) nanocomposites with excellent thermal and mechanical properties. J Mater Chem C 2(6):1094–1103
98. Kuang Z, Chen Y, Lu Y, Liu L, Hu S, Wen S et al (2015) Fabrication of highly oriented hexagonal boron nitride nanosheet/elastomer nanocomposites with high thermal conductivity. Small 11(14):1655–1659
99. Li Y, Huang X, Hu Z, Jiang P, Li S, Tanaka T (2011) Large dielectric constant and high thermal conductivity in poly(vinylidene fluoride)/barium titanate/silicon carbide three-phase nanocomposites. ACS Appl Mater Interfaces 3(11):4396–4403
100. Huang X, Zhi C, Jiang P, Golberg D, Bando Y, Tanaka T (2013) Polyhedral oligosilsesquioxane-modified boron nitride nanotube based epoxy nanocomposites: an ideal dielectric material with high thermal conductivity. Adv Funct Mater 23(14):1824–1831

Chapter 2
Dielectric Loss of Polymer Nanocomposites and How to Keep the Dielectric Loss Low

Yanhui Huang and Xingyi Huang

2.1 Introduction

Dielectric loss is a type of energy dissipation inherent to almost any type of dielectric material. It not only causes attenuation of transmitted signal at high frequency and unnecessary energy loss for energy storage, but could also lead to insulation failure due to thermal instability. Due to the increasing technological importance of polymer nanocomposites as dielectrics, a detailed understanding of the dielectric loss behavior of this type of material is required for efficient material utilization. Dielectric loss in polymer nanocomposites generally arises from two aspects: (1) hysteresis of polarization processes from molecular dipole orientation or mobile charges displacement and (2) ohmic loss from direct current conduction of the mobile charges. Several strategies have been developed to suppress the loss of nanocomposites, including developing polymers with fast dipole polarizations, improving the nanofiller dispersion and fabricating advanced nanostructures. In this chapter, we shall firstly introduce to readers the nature of dielectric loss and outline the specific loss behavior pertaining to each type of mechanism and then thoroughly discuss the strategies as well as particular methods to reduce the loss in nanocomposites.

Y. Huang, PhD (✉)
Department of Materials Science and Technology, Rensselaer Polytechnic Institute, 110 8th Street, Troy, NY 12180, USA
e-mail: huangy12@rpi.edu

X. Huang
Shanghai Key Laboratory of Electrical Insulation and Thermal Ageing, Department of Polymer Science and Engineering, Shanghai Jiao Tong University, Minhang, Shanghai, China
e-mail: xyhuang@sjtu.edu.cn

© Springer International Publishing Switzerland 2016

X. Huang, C. Zhi (eds.), *Polymer Nanocomposites*,
DOI 10.1007/978-3-319-28238-1_2

2.2 The Origin of Dielectric Loss

Dielectrics are different from conductors that all charges in dielectrics are strongly attached to specific atoms or molecules and cannot move freely across the medium. An external electrical field **E** can induce a displacement of bound charges or an alignment of permanent dipoles, known as the polarization **P**. The polarization is an inherent material response of dielectrics to the external electric disturbance that will decrease the internal field inside the material. For many substances, the polarization is proportional to **E,** provided **E** is not too strong:

$$\mathbf{P} = \varepsilon_0 \chi \mathbf{E} \tag{2.1}$$

Here ε_0 is the vacuum permittivity, and the dimensionless constant χ is defined as the electric susceptibility of the medium. Deviation from linearity can happen at very high field and also has been found as an intrinsic feature for some types of materials [1]. The electric displacement is defined as

$$\mathbf{D} \equiv \varepsilon_0 \mathbf{E} + \mathbf{P} = \varepsilon_0 \left(1 + \chi\right) \mathbf{E} \tag{2.2}$$

And then we can define the permittivity ε

$$\varepsilon \equiv \varepsilon_0 \left(1 + \chi\right) \tag{2.3}$$

The ratio of $\varepsilon / \varepsilon_0 = \varepsilon_r$ is known as the relative permittivity ε_r or the dielectric constant.

The polarization is found to be a time-dependent process, and the characteristic time dependence varies for different mechanisms. The delay between the polarization and the field can manifest in the time response of the displacement current to a step-function field,

$$i\left(t\right) = dP / dt = \varepsilon_0 E f\left(t\right) \tag{2.4}$$

where $f(t)$ is the dielectric response function as $\dfrac{d\chi\left(t\right)}{dt}$. In the framework of linear response theory, the polarization to a time-varying signal can be written as a convolution integral

$$\mathbf{P}\left(t\right) = \varepsilon_0 \int_{-\infty}^{t} f\left(t - t'\right) \mathbf{E}\left(t'\right) dt' \tag{2.5}$$

If a harmonic oscillating field $E\left(t\right) = E_0 \exp\left(-i\omega t\right)$ is applied with a radian frequency ω, the Fourier transformation of Eq. 2.5 gives the form of χ in the frequency domain as

$$P(\omega) = \varepsilon_0 \chi(\omega) E(\omega) \tag{2.6}$$

Here, $\chi(\omega)$ is a complex Fourier transform of $f(t)$,

$$\chi(\omega) = \chi'(\omega) - i\chi''(\omega) \tag{2.7}$$

where $i = \sqrt{-1}$, or equivalently we can write it in the form of permittivity

$$\varepsilon(\omega) = \varepsilon_0 (\chi(\omega) + 1) = \varepsilon'(\omega) - i\varepsilon''(\omega) \tag{2.8}$$

The real part represents the component of **P** or **D** in phase with **E**, while the imaginary part represents the component that is 90° out of phase with **E**. The phase lag δ can be calculated from the ratio of $tan\delta = \varepsilon''/\varepsilon'$. So the hysteresis energy loss per radian is just $\varepsilon''(\omega)E_0^2/2$. For material exhibiting direct current (dc) conduction, the total power loss is $(\sigma_{dc} + \omega\varepsilon''(\omega))E^2{}_0/2$, where σ_{dc} is the dc conductivity. This defines the alternating current (ac) conductivity being the form of

$$\sigma(\omega) = \sigma_{dc} + \omega\varepsilon''(\omega) \tag{2.9}$$

So far we know that the dielectric loss in an alternating field essentially comes from two parts, one is the hysteresis of the polarization and other is the joule heating from the dc conduction. Since the stored energy per radian is $\varepsilon'(\omega)E_0^2/2$, the energy efficiency can be quantified by $\frac{\sigma_{dc}/\omega + \varepsilon''(\omega)}{\varepsilon'(\omega)}$.

The time dependence of the polarization response varies for different mechanisms, and each is characterized with a distinctive loss behavior. There are three types of polarization in polymeric materials: (1) the resonance phenomena caused by atomic or molecular vibrations, (2) the relaxation phenomena that are related to the orientation of permanent molecular dipoles, and (3) the propagation of mobile charge carriers (ions, electron/hole, polarons) and the charge accumulation at interfaces. The resonating absorption happens very fast and lies in the optical frequency, resulting in a minimal loss in lower frequencies. The latter two processes cover a wide frequency range from radio frequency to sub-Hertz frequency and are the major sources of the increased permittivity and loss of polymer nanocomposites and thus will be more thoroughly discussed.

2.2.1 Losses from Molecular Polarization

The molecular polarization of a polymer has a dipolar nature that involves the rotation of small dipoles like side groups as well as the cooperative rearrangement of the large backbone chain. It generally shows as a relaxation process: the loss is low

if the external field varies so fast that dipoles can hardly move and do not contribute to polarization; and if the field changes so slow that all molecular motions can follow, the loss is also low. The maximum loss occurs when the frequency of changing field is comparable to the characteristic relaxation time of the molecular segment.

An ideal dipole relaxation can be well described by the Debye model [2]. This model is developed from a scenario where a dipole can jump by thermal activation between two preferred orientations separated by a potential barrier. The application of the electric field lowers the energy potential of one state and changes the average occupation number of each state. This microscopic redistribution process manifests as a macroscopic polarization. For such type of polarization, **P**, after the voltage removal is found to decay with time as

$$\frac{d\mathbf{P}(t)}{dt} = -\frac{1}{\tau}\mathbf{P}(t) \tag{2.10}$$

where τ is the characteristic relaxation time and is inversely proportional to the jump rate. This leads to an exponential time dependence of

$$\mathbf{P}(t) = P_0 \exp(-t/\tau) \tag{2.11}$$

In the frequency domain, the complex permittivity has a form of

$$\varepsilon^*(\omega) = \varepsilon_\infty + \frac{\Delta\varepsilon}{1+i\omega\tau} = \varepsilon_\infty + \frac{\Delta\varepsilon}{1+(\omega\tau)^2} - i\frac{\omega\tau\Delta\varepsilon}{1+(\omega\tau)^2} \tag{2.12}$$

where ε_∞ is the high frequency limit of the real permittivity, and $\Delta\varepsilon$ is known as the relaxation strength. This type of function is characterized with a steplike increase in $\varepsilon'(\omega)$ and a loss peak in $\varepsilon''(\omega)$ with maximal loss at $1/\tau$ (Fig. 2.1). The loss peak is usually found to be broader than it is predicted by the Debye function. One explanation attributes this broadening to the dispersion of relaxation times arising from the structural heterogeneity in polymers including the variation in molecular weight, morphology, etc. The deviation of Debye-type relaxation has been formulated as various empirical functions proposed by Cole and Cole [3], Davidson and Cole [4], and Havriliak and Negami [5], for which additional fitting parameters have been introduced. But the experimentally observed relaxation in real polymer always departs strongly from the Debye model, and Jonscher argues that the nature of this dipolar response is never Debye-like and should be explained under the framework of the "universal dielectric response," which is developed from correlated many body interactions that govern both dipole and charge carrier polarizations [6].

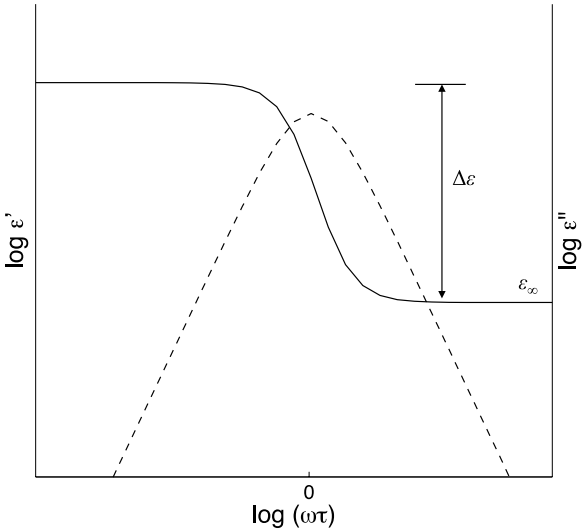

Fig. 2.1 The real (*line*) and imaginary (*dash*) permittivity for a typical Debye relaxation

Table 2.1 The dielectric constant loss factor of selected polymers at 60 Hz

Polymer	ε_r	*tanδ*
Polypropylene [7]	2.25	<0.0005
Polyethylene [8]	2.3–2.7	<0.0002
Polystyrene [7]	2.56	<0.00005
Poly(methyl methacrylate) [9]	4	0.07
Polyvinyl chloride [7]	3.2	0.0115
Polyvinylidene fluoride [10]	7	0.05
Poly(vinylidene fluoride–hexafluoropropylene) [11]	12	0.046

2.2.1.1 Strategies for Loss Reduction

Equation 2.12 shows that the real and imaginary permittivity of a dipolar polarization is actually correlated, and a large increase in dielectric constant is always accompanied by a significant dielectric loss. Table 2.1 summarizes the dielectric constant and loss for various polymers, and it can be seen that polar polymers like polyvinylidene fluoride (PVDF) generally exhibit larger dielectric constant together with greater loss compared to nonpolar polymers like polyethylene (PE) and polypropylene (PP). But since the dipolar loss exhibits as a peak in the frequency spectra, one can reduce the loss by using the polymer in the frequency range far away from the peak. Much attention has been paid to synthesizing special polymers with fast dipolar polarizations pushed up to the gigahertz range [12]. For fillers having larger dielectric constant but smaller loss than the matrix polymer, increasing the filler loading to some extent can increase the composite dielectric constant while maintain a low loss, resulting in a smaller *tanδ* and higher energy efficiency [11]. But further increasing the particle loading may increase the loss instead due to the enhanced conductivity.

2.2.2 *Losses from Charge Carrier Propagation*

Another important type of polarization is the charge carrier polarization. The charge carrier could be electron, hole, polaron, or ion. The engineering polymer dielectrics are never free of impurities like catalyst residues, antioxidants, or even water molecules, which may be ionized and dissociated by the field and become mobile ionic species. For highly purified polymers like polyethylene, an electron or hole hopping mechanism is suggested to be responsible for the charge propagation. The electron or hole can be injected from the electrode and transferred directly between localized electronic states by thermally assisted tunneling [13]. The injection rate and hopping mobility is found to increase superlinearly with the field. Particularly, if the mobility of the charge is small, the induced molecular polarization will travel together with the point charge, which as a whole is known as a polaron [14].

The dc conduction arises from a condition where charges flow without changing the net charge distribution in the space. The leakage current results in an ohmic loss that is proportional to the dc conductivity. Since it is the impedance of the sample that is measured in the dielectric spectroscopy, from Eq. 2.9, we know that the dc conductivity will render the measured ε'' increases with frequency as ω^{-1}. But the real permittivity will have a flat response because the dc conduction does not change the charge distribution and thus has no contribution to the polarization (Fig. 2.2).

Polarization happens when charge carriers have a more limited movement and the net charge distribution is changed. For example, as the injected charge move into the bulk of the sample, the effective distance between two electrodes decreases and it results in an increment of the apparent real permittivity. Polarization can also occur if the ionized species are separated by the field and move toward the opposite electrode. For the charge carrier dominated polarization, the current is usually found to decay with time in a power–law behavior

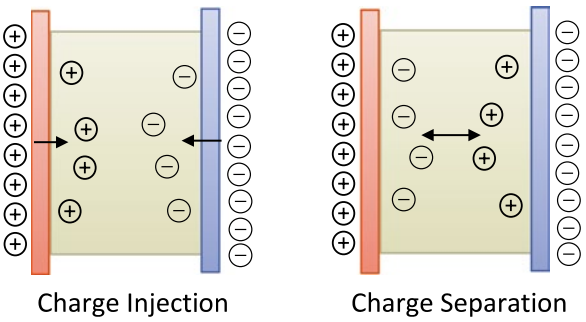

Fig. 2.2 The two mechanisms of the charge carrier polarization

$$i(t) \propto t^{-n}, 0 < n < 1 \tag{2.13}$$

The corresponding response in the frequency domain exhibits as

$$\varepsilon'(\omega) - \varepsilon_\infty \propto \varepsilon''(\omega) \propto \omega^{n-1} \tag{2.14}$$

with a frequency-independent ratio

$$\frac{\varepsilon''(\omega)}{\varepsilon'(\omega) - \varepsilon_\infty} = \cot(n\pi/2) \tag{2.15}$$

where n is usually found smaller than 0.3 which results in a relatively steep increase in both $\varepsilon'(\omega)$ and $\varepsilon''(\omega)$ at low frequencies and this is known as the anomalous low-frequency dispersion (LFD) [15].

If the dielectric material is composed of two or more different phases, like the case of polymer composites or the polymer with water absorption, the charge carrier accumulation can occur at phase boundaries as a result of the difference in the conductivity and permittivity of each phase. This is known as the Maxwell–Wagner–Sillars interfacial polarization [16]. This polarization can be understood using the model consisting of two contiguous layers with equal thickness but different conductivity and dielectric constant (Fig. 2.3). When a steplike voltage is suddenly applied to the sample, the electric displacements in the two layers are equal, and the instantaneous voltage partition is determined by the capacitance or the dielectric constant of each layer, so that the field distribution follows

$$E_1 / E_2 = \varepsilon_2 / \varepsilon_1 \tag{2.16}$$

In contrast, the steady state field distribution is determined by the conductivity of each layer as a result of current continuity, so that

$$E_1 / E_2 = \sigma_2 / \sigma_1 \tag{2.17}$$

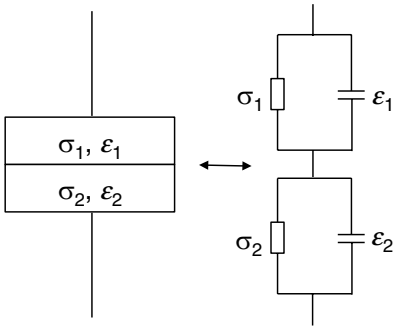

Fig. 2.3 The two-layer model of interfacial polarization and its equivalent circuit

The change of field distribution is a result of charge accumulation at the phase boundaries. The time dependence can be analyzed from its equivalent circuit and a Debye-like relaxation behavior is found [2],

$$\varepsilon^*(\omega) = \varepsilon_\infty + \frac{\Delta\varepsilon}{1 + i\omega\tau_{MW}} \tag{2.18}$$

The characteristic relaxation time is determined by the ratio of permittivity to conductivity as $\tau_{MW} = \frac{\varepsilon_1 + \varepsilon_2}{\sigma_2 + \sigma_1}$; the relaxation intensity is related to the difference between the relative ratios of each phase's permittivity and conductivity as $\Delta\varepsilon = \frac{\left(\sigma_1\varepsilon_2 - \sigma_2\varepsilon_1\right)^2}{\left(\sigma_2 + \sigma_1\right)^2\left(\varepsilon_1 + \varepsilon_2\right)}$ and $\varepsilon_\infty = \frac{\varepsilon_1\varepsilon_2}{\varepsilon_1 + \varepsilon_2}$. The true response in real polymers is much more complicated because of the time dependence of permittivity and conductivity and the irregularities of filler geometry and dispersion.

Nevertheless, the general relation should still hold, and we note that the characteristic relaxation time should decrease with the increasing conductivity of each phase. So by reducing the conductivity, we can shift the polarization to lower frequencies and reduce the loss at the desired frequency range. In addition, Sillars has demonstrated that the magnitude of interfacial loss increases dramatically with the length of the dispersed phase geometry along the direction of the field [16]. A greater polarization effect is usually found in composites containing high aspect ratio fillers like carbon nanotubes [17] and glass fibers [18]. The polarization intensity also depends on the specific spatial distribution of fillers and will become more pronounced and dispersed with frequency for increased degree of agglomeration [19].

2.2.2.1 Strategies for Loss Reduction

In general, the charge carrier propagation in polymer nanocomposites can cause a significant increase of loss with decreasing frequency. The onset frequency and the intensity are strongly affected by the conductivity of the material, which can be significantly altered due to the addition of nanofiller. Nanofillers are usually found to have a relatively high surface conductivity due to the structural defects or absorbed impurities like water. Charge carriers hopping along the filler surface is thus relatively easy compared to the hopping in the pure polymer. The conduction will be further enhanced if fillers are fractal agglomerated and form a percolating network. It has been found that in some cases fillers can form string or sheet like structures either through a particular thermodynamic interaction or by mechanical shearing during the processing [20], and for these types of structures the percolation is more easily to form at low volume fractions. Therefore, it is critical to reduce the impurities introduced during processing and improve the filler distribution to isolate fillers from contacting each other. Recent advances in material chemistry and

polymer physics have provided experimental tools as well as a theoretical guide to specifically tailor the filler surface chemistry and morphology to improve the filler/matrix adhesion and reduce the propensity for agglomeration. Other strategies like constructing special nanostructures like core-shell and bimodal systems with carrier-trapping species have also been developed to limit the charge movement and reduce the dielectric loss. We shall briefly discuss these methods in the following sections.

Improving Filler Dispersion by Surface Modification

The filler distribution in polymer nanocomposites is determined by the Gibbs free mixing energy ΔG, which consists of both enthalpic (ΔH) and entropic (ΔS) interactions between the filler and the polymer matrix as $\Delta G = \Delta H - T\Delta S$. A more positive mixing energy will strongly encourage the particle agglomeration, but it can be mitigated by attaching short ligands or polymer brushes to the nanofiller to change the interfacial interactions.

Grafted with Short Organic Ligands

Nanofillers grafted with short ligands can effectively passivize the unstable surface and reduce the van der Waals (vdW) core–core enthalpic attraction between fillers [21]. An appropriate type of ligand is chosen to match the surface energy of the polymer and provide strong binding with the filler. Silanes are the mostly used and commercially available coupling agent for surface modification. It has shown a great versatility to different substrates including SiO_2 and many metal oxides like TiO_2, ZrO_2, SnO_2, $BaTiO_3$, Al_2O_3, etc. It is available with different end groups like alkoxy-, hydrogen-, and chloro- that vary in reactivity and by-products. Di- or trichlorosilanes have very high reactivity and do not require the water catalysis, but are susceptible to self-condensation which can result in an ill-defined surface structure [22]. Phosphonates, as a another type of ligands, bind strongly with metal oxides like TiO_2, ZrO_3, $BaTiO_3$, etc. by forming stable M-O-P bond and do not undergo of self-condensation [23], but the use is limited to non-siliceous particles due to the easy hydrolysis of Si-O-P bond [24]. Noble metal particles are normally modified with ligands containing thiol, disulfide, amine, nitrile, carboxylic acid, or phosphine end groups [22].

The ligand can bear numerous functionalities on the other end such as amino, epoxy, cyano, thiol, alkyl, vinyl, carboxylic acid, *etc.* These end functionalities can lead to very different interfacial energetics between the filler and matrix and thus largely impact the filler dispersion. Natarajan et al. modified SiO_2 nanoparticles with silanes of different terminal groups and systematically examined the interfacial energetics and particle dispersion in a variety of polymer matrix. It was found that the final state of particle dispersion can be effectively predicted by the ratio of the work of adhesion between the filler and the polymer to the work of adhesion

1)

Polymer	PEMA	PS	PMMA	P2VP
W_{PF}/W_{FF}	0.9	0.95	0.96	1.09
3 wt%	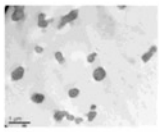	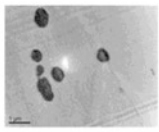	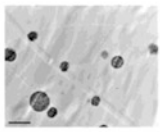	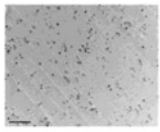
8 wt%	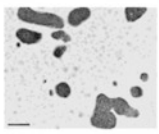	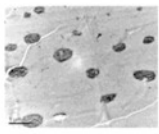	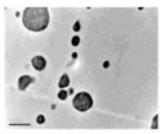	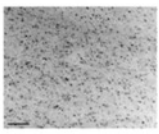

2)

System	Chloro PS	Octyl PS	Octyl PMMA	Chloro PMMA
ΔW_a	6.16	3.48	0.95	0.62
3 wt%	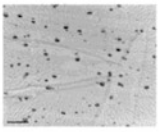	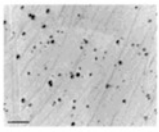	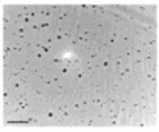	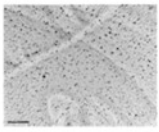
8 wt%	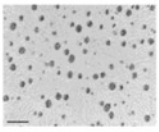	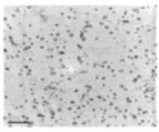	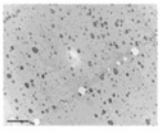	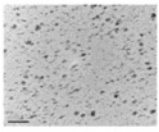

Fig. 2.4 TEM micrographs (20,000×) at 3 and 8 wt % loadings of (*1*) aminosilane silica in the four matrices used, demonstrating the effect of W_{PF}/W_{FF} and (*2*) different silane-treated silicas in PS and PMMA matrices, demonstrating the effect of ΔW_a. All scale bars represent 1 μm (Adapted with permission from Ref. [25]. Copyright 2013 American Chemical Society)

between fillers (W_{PF}/W_{FF}), in conjunction with the relative work of adhesion ($\Delta W_a = W_{FF} + W_{pp} - 2W_{PF}$) (Fig. 2.4) [25]. W_{PF}/W_{FF} is found to determine the initial dispersion during processing and the propensity to dispersion increases with increasing W_{PF}/W_{FF}. ΔW_a is found to be related to the stability of the initial dispersion during the post-mixing steps like drying, pressing, and annealing, and a larger value ΔW_a indicates a larger driving force for reagglomeration [26]. Some functional groups can react with the matrix polymer and form a strong chemical bond, which effectively prohibits the post-annealing reagglomeration. Typical examples include the epoxy group reacting with hardeners in epoxy [27] and the vinyl group participating in the radical polymerization [28]. The great variety of terminal groups

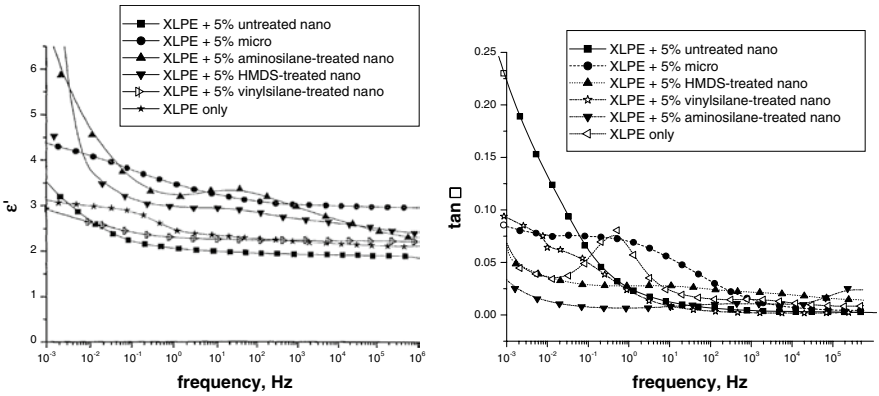

Fig. 2.5 The dielectric constant and loss tangent for XLPE containing different SiO_2 fillers. The nanofiller has a size of 12 nm with a loading of 5 wt%. HDMS stands for hexamethyldisilazane [30]

also open up endless possibilities for further chemical reactions, for example, linking with initiators for *in situ* polymer grafting from the nanoparticle surface [9, 29].

In addition, the terminal groups may also differ in electronic properties such as the dipole moment and the electron affinity which can influence the charge carrier mobility by scattering or trapping, and thus lead to different loss behaviors. Figure 2.5 shows the dielectric spectroscopy of SiO_2/cross-linked polyethylene (XLPE) composites treated with different surface modifications.

Grafted with Long Polymer Brushes

The polymer can be attached to the filler either from the backbone or through the chain end. Covering the surface with short ligands alone does not always warrant a good dispersion, so sometimes long polymer brushes are attached to the filler to provide sufficient enthalpic screening as well as entropic entanglement with the matrix polymer to further decrease the mixing energy.

For the former case, the polymers are absorbed to the nanoparticle through the bonding between the monomer side group and the filler like the case of poly(vinyl pyrrolidone) (PVP) interacting with Ag clusters [31] or the case of the surface-grafted vinyl groups participating in the polymerization [28]. Shen et al. found that coating Ag nanoparticles with a layer of PVP can effectively prevent the direct conduction upon percolation, and the corresponding epoxy composites achieved a very high dielectric constant of more than 100 but maintained the *tanδ* below 0.04 [32].

It has been found that the dispersion state of polymer-grafted nanoparticles is determined by the complex interplay of the enthalpic attraction and entropic entanglement between the grafted brush and the matrix polymer, which is sensitive to parameters like morphology, molecular weight, and graft density [21, 33]. This requires an effective control over the grafting reaction and the grafted brush morphology. This can be more easily achieved by grafting polymers onto the

nanoparticle surface via the chain end to form a better-defined structure and a more uniform covering. Grafting polymer brushes can be more sophisticated and requires more stringent reaction conditions compared to grafting short ligands. The grafting reactions can be generally categorized into two groups: the "graft to" and the "graft from" approaches. In the "graft to" approach, the polymer brush is synthesized separately with an end-functional group that can be used to couple directly with the nanoparticle or with the already attached surface ligand. "Click chemistry" like thiol–ene or azide–alkyne reactions is often employed for its high yield and robustness [34]. But the "graft to" method is limited to the diffusion of the polymer brush to the particle surface, which can suffer from low graft density due to the steric hindrance especially when the brush has a large molecular weight or many bulky side groups. The "graft from" approach, on the hand, can bear much higher graft density. The particle is firstly grafted with appropriate initiators or chain transfer agents (CTA), and then polymers can be grown from the particle surface using the controlled radical polymerization methods like atom transfer radical polymerization (ATRP), nitroxide-mediated polymerization (NMP), or reversible-addition fragmentation chain transfer (RAFT) polymerization [9, 33d, 35] (Fig. 2.6).

The Influence of the Interfacial Region

The specific interaction between the nanoparticle and the matrix polymer gives rise to an interfacial region of different chain mobility, crystallinity, or cross-linked density compared with the bulk polymer and thus exhibit a different relaxation behavior [37]. Due to the large surface-to-volume ratio of nanofillers, this

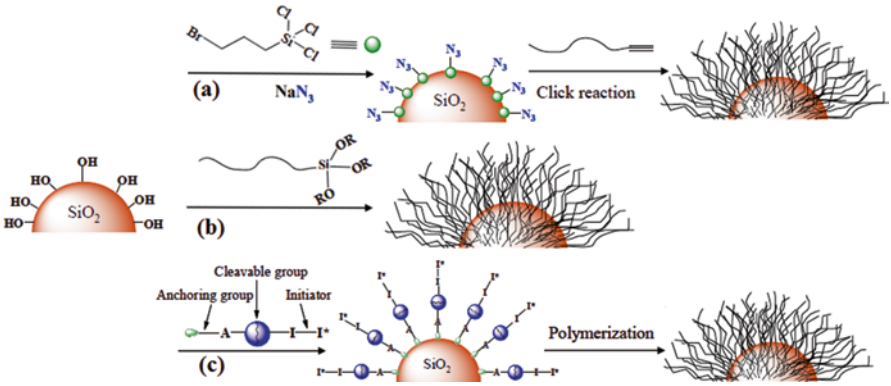

Fig. 2.6 Schematic representation of synthetic procedures used to graft polymer chains onto the surface of SiO_2 particles via (**a**) the "grafting to" approach using silane coupling and click chemistry; (**b**) the "grafting to" approach using direct silane coupling; (**c**) the "grafting from" method by attaching surface initiator (Adapted from Ref. [36])

interfacial region may constitute a significant portion of the material. For example, for a composite containing 5 vol% of monodispersed spherical nanoparticles of 10 nm in diameter, the volume fraction of the interfacial region can be up to 35 vol% even if we assume the thickness of the region as small as 5 nm. The enhanced entanglement of the matrix polymer with the grafted polymer brush can extend this interfacial influence further into the bulk.

A loosely bonded interface would yield a high chain mobility and correspondingly a large loss. To suppress the increase of loss, the molecular relaxation of the interfacial region needs to be effectively controlled. For example, chain mobility can be tuned by modulating the chain length and the size of the side group of the grafted polymer. Yang et al. found that grafted polymers with long rigid side groups tend to more tightly packed and weakly entangled with the matrix polymer. The packing order increases with the molecular weight of the grafted polymer. This leads to an enhanced interface chain mobility and a large dielectric loss. While at the same graft density, the grafted polymers with a short flexible side group favor the entanglement with the matrix polymer and the degree of entanglement increases with the molecular weight of the grafted chain. The enhanced entanglement reduces the interface chain mobility and leads to a lower loss. More interestingly, since the polymer contributes to the majority of the loss but only a small portion of the dielectric constant compared to the $BaTiO_3$ filler, reducing the chain mobility and thus the intensity of molecular polarization does not appreciably decrease the dielectric constant of the composites so that the sample with lowest loss can achieve the highest energy storage density [11] (Fig. 2.7).

Fabricating Special Nanostructures

Core–Shell Structure

In some cases, nanoparticles are grafted with a thick layer of polymer and the composite is directly obtained after solvent removal. This "matrix-free" method avoids problems during further mixing and results in a good material homogeneity [38]. Composites made by this method have an intact core–shell structure and can avoid percolation even at high particle loadings and therefore exhibit a much lower loss. For example, surface-initiated ATRP was used to graft a thick poly(methyl methacrylate) (PMMA) layer around $BaTiO_3$ nanoparticle, and the loss was found to have maintained as low as the polymer matrix even at high particle loadings [38a] (Fig. 2.8).

Other than organic ligands and polymer, an inorganic insulating shell has also been utilized to suppress the leakage current and reduce the dielectric loss. For example, Yu et al. coated a $BaTiO_3$ nanoparticle with an insulating SiO_2 shell, which exhibits 46 % reduced energy loss compared to bare $BaTiO_3$ when filled in PVDF [39] (Fig. 2.9).

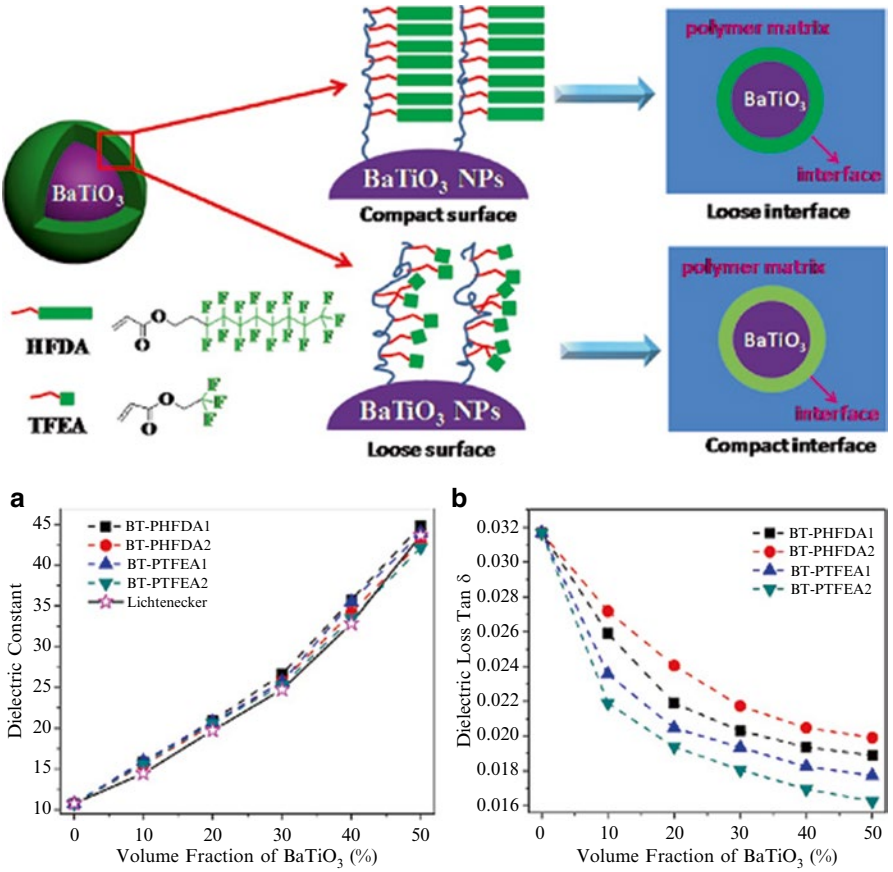

Fig. 2.7 Schematic illustration for the fluoro-polymer@$BaTiO_3$ nanoparticles and the interfacial region within the nanocomposites. Dielectric constant (**a**) and dielectric loss tangent (**b**) of P(VDF-HFP) nanocomposite films with BT-PHFDA1, BT-PHFDA2, BT-PTFEA1, and BT-PTFEA2 at 1 kHz. The particles denoted with "2" have larger molecular weight than those denoted with "1" (Adapted with permission from Ref. [11]. Copyright 2013 American Chemical Society)

Core–Double-Shell Structure

A core–double-shell structure can be formed by grafting a block copolymer or by sequentially grafting two layers of polymers to the nanoparticle [38a, 40]. Xie et al. utilized a high conductivity hyper-branched polymer as the inner shell and a low conductivity PMMA as the outer shell. The dielectric constant was increased in such way due to the interfacial polarization between different layers, while conduction loss was suppressed since charge carriers are mostly confined in the inner shell and long range hopping is prohibited [38a, 41] (Fig. 2.10).

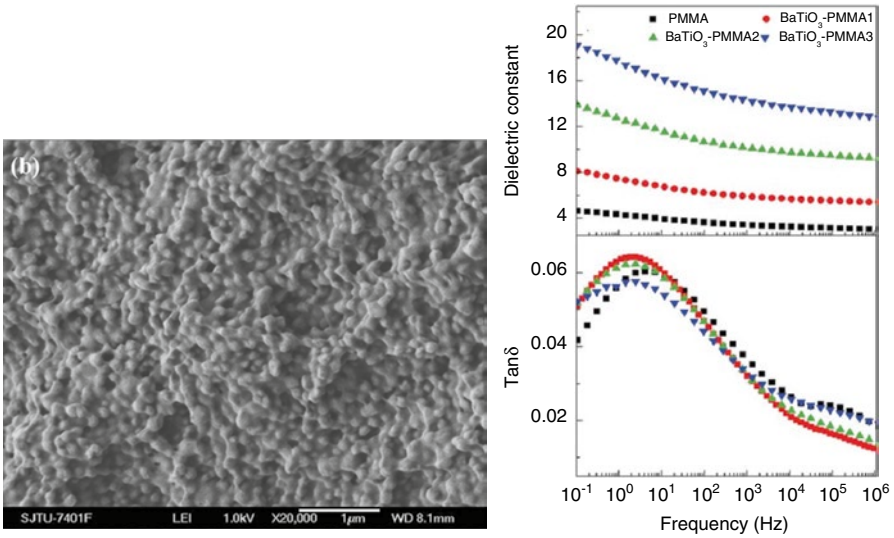

Fig. 2.8 *Left*: The SEM images of core–shell structured $BaTiO_3$@PMMA with 68 wt% $BaTiO_3$. *Right*: The dielectric constant and tan δ for PMMA composites with different $BaTiO_3$ loadings, as 50 wt%, 68 wt%, and 77 wt% and was denoted as 1–3 (Adapted with permission from Ref. [38a]. Copyright 2011 Royal Society of Chemistry)

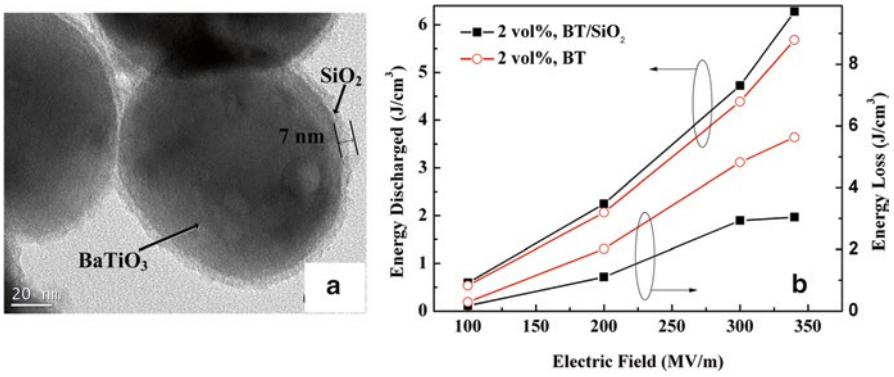

Fig. 2.9 (**a**) The TEM images of the core–shell structured $BaTiO_3$@SiO_2 nanoparticles, (**b**) the energy discharged and energy loss of the nanocomposites of $BaTiO_3$@SiO_2 nanoparticles and BT nanoparticles with a concentration of 2 vol % as a function of applied electric field (Adapted with permission from Ref. [39]. Copyright 2013 AIP Publishing LLC)

Core–Satellite Structure

To suppress the high surface conduction along the nanoparticle, Xie et al. covered a 100-nm diameter $BaTiO_3$ nanoparticle surface with many 2 nm silver clusters, forming a core–satellite structure (Figs. 2.11). The PVDF composites filled with

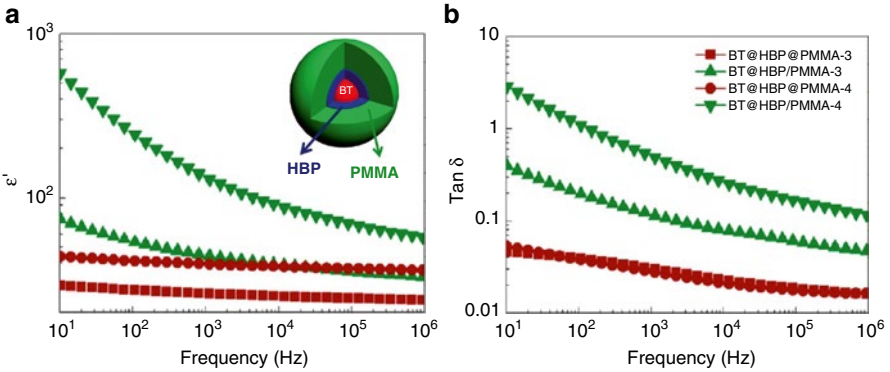

Fig. 2.10 The (**a**) dielectric constant and (**b**) loss tangent of $BaTiO_3$/PMMA composites filled with nanoparticle with single highly conductive hyper-branched shell (denoted as BT@HBP/PMMA) and with double confining shell (denoted as BT@HBP@PMMA) (The sample specifications can be found in Ref. [41]. Reprinted with permission from Ref. [41]. Copyright 2013 American Chemical Society)

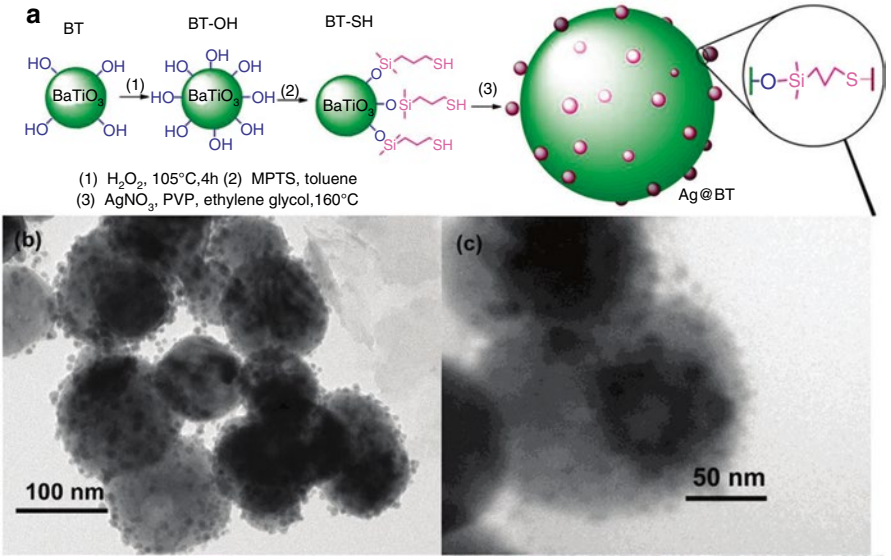

Fig. 2.11 (**a**) Scheme of the preparation process and (**b**) TEM images of the Ag@$BaTiO_3$ core–satellite nanoassemblies; (**c**) TEM image of Ag1 %@BT–PVDF nanocomposite (Reprinted with permission from Ref. [42]. Copyright 2013 Royal Society of Chemistry)

this type of particles exhibits a large increase of breakdown strength as well as a decrease of low-frequency dielectric loss compared to the composites with unmodified $BaTiO_3$ and result in a much higher energy density (Fig. 2.12). The suppression of surface conductivity is attributed to the Coulomb blockade effect

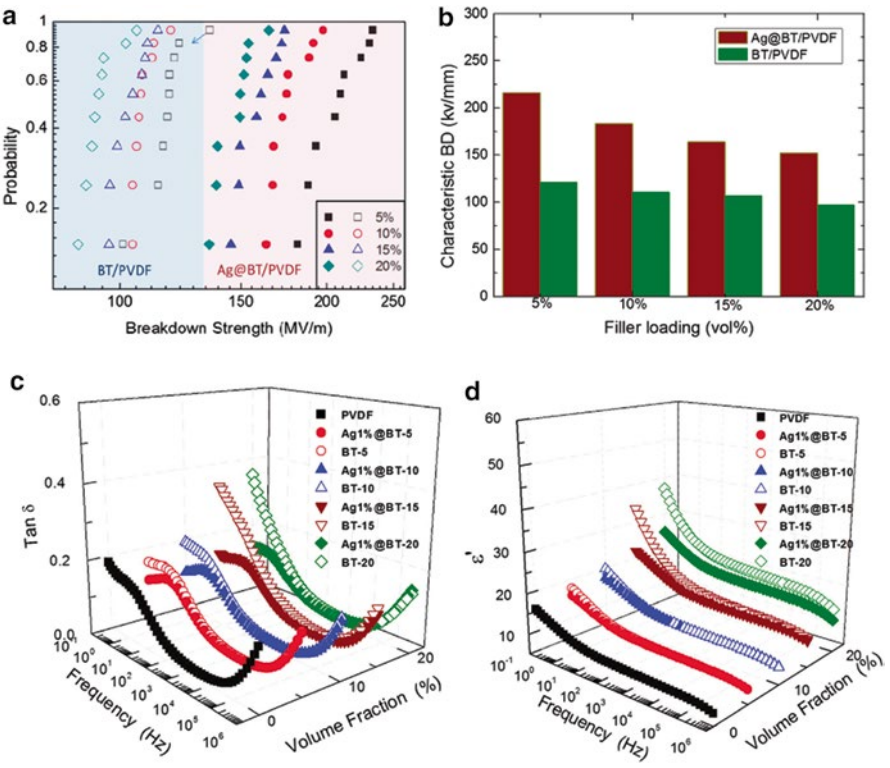

Fig. 2.12 (**a**) Weibull distribution of the breakdown strength (*BD*) and (**b**) characteristic BD (BD at the cumulative failure probability of 63.2 %) of PVDF–BT and PVDF-Ag1%@BT nanocomposites, (**c**, **d**) frequency dependence of dielectric loss tangent, and dielectric constant of PVDF–BT and PVDF–Ag1%@BT nanocomposites (Reprinted with permission from Ref. [42]. Copyright 2013 Royal Society of Chemistry)

from the ultrasmall Ag clusters that the energy barrier for charge hopping is increased due to the large columbic repulsion when two electrons are to be confined at one small cluster [42].

Bimodal System

A bimodal system contains two populations of ligands of different size and functionalities: a sparsely grafted matrix-compatible long polymer brush to increase the entanglement with the matrix polymer and a densely grafted short chain to provide sufficient screening against the inter-particle core–core attraction. This interfacial morphology can greatly increase the propensity to dispersion compared to the monomodal system [21]. The short ligands sometimes can offer additional functionalities [21, 37a]. For instance, some small conjugated organic compounds like anthracene have showed a potential to increase the breakdown strength and

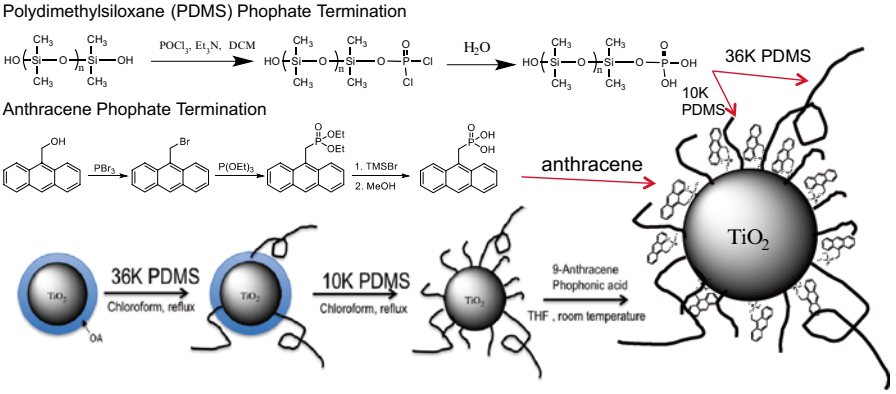

Fig. 2.13 The schematic of the synthesis of PDMS and anthracene-grafted TiO_2 nanoparticle [45]

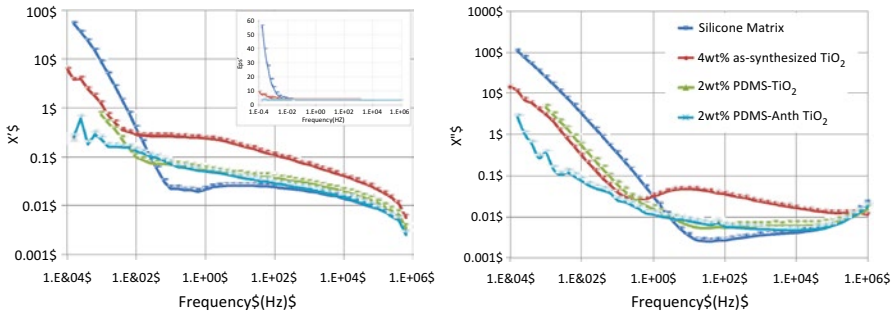

Fig. 2.14 The frequency dependence of electric susceptibility $\chi^* = \left(\varepsilon^* - \varepsilon_\infty\right)/\varepsilon_0$ of silicone matrix and different TiO_2 nanoparticle-filled silicone composites [45]

reduce the carrier mobility by acting as deep trapping sites [37a, 43]. But the immiscibility of these molecules with most dielectric polymers can lead to precipitation or migration toward the surface and thus limit their applications [44]. Using the bimodal method, the functionality and miscibility can be controlled separately by grafting small molecules and long chain matrix-compatible polymers together to the nanoparticle. Virtanen et al. grafted poly(glycidyl methacrylate) (PGMA) and different small conjugated molecules as bimodal brushes to SiO_2 nanoparticles using the "grafting to" method and found a significant improvement of the particle dispersion in epoxy as well as an increased ac breakdown strength up to 40 % [34b]. Similar improvement of nanoparticle dispersion and bulk resistivity was also found in polydimethylsiloxane (PDMS) and anthracene-grafted TiO_2 nanoparticle-filled silicone (Fig. 2.13), and particularly the low frequency dielectric loss was found to have decreased by two orders of magnitude (Fig. 2.14), thanks to the charge-trapping effect of TiO_2 and anthracene [45].

2.3 Concluding Remarks

The dielectric loss is an inherent property of dielectrics under a changing field due to the hysteresis of polarization and the leakage current. The major polarization mechanisms in polymer nanocomposites are molecular polarization and charge carrier polarization. The former has a dipolar nature and exhibits as a relaxation peak in the frequency spectra. One can reduce this type of loss by 1) avoiding using the material in the frequency range close to the characteristic relaxation time, or 2) using nonpolar polymers like polyethylene and polypropylene, or 3) developing fast relaxing polymers to maintain a high dielectric constant and low loss at the desired frequency range. The charge carrier can be generated either in the bulk or be injected from the electrode, whose propagation in the medium is responsible for the leakage current and additional polarization mechanisms like the interfacial polarization and the low-frequency dispersion. The loss of this type is more pronounced in the low-frequency region and increases indefinitely with decreasing frequency. The loss can be suppressed by minimizing the conductivity of the material, which can be achieved by improving the filler distribution through grafting short ligands or polymer brushes to the filler. It has been a hot research topic recently to make materials with high dielectric constant and low loss due to the increasing demand of energy storage. Utilizing special nanostructures like core–shell, core–satellite, and bimodal systems has shown as a promising strategy to achieve this goal, but much still remains to be explored by future research.

References

1. Pirc, R., Blinc, R., & Kutnjak, Z. (2002). Nonlinear dielectric response of relaxor ferroelectrics. Physical Review B, 65(21), 214101
2. Kremer F, Schönhals A (2003) Broadband dielectric spectroscopy. Springer, Berlin/New York
3. Cole KS, Cole RH (1941) Dispersion and absorption in dielectrics I. Alternating current characteristics. J Chem Phys 9(4):341–351
4. Davidson D, Cole R (1951) Dielectric relaxation in glycerol, propylene glycol, and n-propanol. J Chem Phys 19(12):1484–1490
5. Havriliak S, Negami S (1967) A complex plane representation of dielectric and mechanical relaxation processes in some polymers. Polymer 8:161–210
6. Jonscher AK (1977) Theuniversal'dielectric response. Nature 267:673–679
7. International Telephone, & Telegraph Corporation. (1968). Reference data for radio engineers. Howard W. Sams and Co.
8. Liu T, Fothergill J, Dodd S, Nilsson U (2009) Dielectric spectroscopy measurements on very low loss cross-linked polyethylene power cables, J Phys: Conference Series, IOP Publishing. p 012002
9. Xie L, Huang X, Wu C, Jiang P (2011) Core-shell structured poly (methyl methacrylate)/ BaTiO 3 nanocomposites prepared by in situ atom transfer radical polymerization: a route to high dielectric constant materials with the inherent low loss of the base polymer. J Mater Chem 21(16):5897–5906
10. Chanmal C, Jog J (2008) Dielectric relaxations in PVDF/BaTiO3 nanocomposites. Exp Polym Lett 2(4):294–301

11. Yang K, Huang X, Huang Y, Xie L, Jiang P (2013) Fluoro-polymer@BaTiO3 hybrid nanoparticles prepared via RAFT polymerization: toward ferroelectric polymer nanocomposites with high dielectric constant and low dielectric loss for energy storage application. Chem Mater 25(11):2327–2338
12. Zhu L (2014) Exploring strategies for high dielectric constant and low loss polymer dielectrics. J Phys Chem Lett 5(21):3677–3687
13. Brunson J (2010) Hopping conductivity and charge transport in low density polyethylene. Utah State University
14. Cubero D, Quirke N (2004) Computer simulations of localized small polarons in amorphous polyethylene. J Chem Phys 120(16):7772–7778
15. Jonscher A (1978) Low-frequency dispersion in carrier-dominated dielectric. Philos Magazine B 38(6):587–601
16. Bartnikas R, Eichhorn R (1983) Engineering dielectrics volume IIA: electrical properties of solid insulating materials: molecular structure and electrical behavior. American Society for Testing and Materials. American Society for testing and materials, Philadephia
17. Yuan J-K, Yao S-H, Dang Z-M, Sylvestre A, Genestoux M, Bail J (2011) Giant dielectric permittivity nanocomposites: realizing true potential of pristine carbon nanotubes in polyvinylidene fluoride matrix through an enhanced interfacial interaction. J Phys Chem C 115(13):5515–5521
18. Steeman P, Maurer F (1992) An interlayer model for the complex dielectric constant of composites: an extension to ellipsoidally shaped particles. Colloid Polym Sci 270(11):1069–1079
19. Pelster R, Simon U (1999) Nanodispersions of conducting particles: preparation, microstructure and dielectric properties. Colloid Polym Sci 277(1):2–14
20. Akcora P, Liu H, Kumar SK, Moll J, Li Y, Benicewicz BC, Schadler LS, Acehan D, Panagiotopoulos AZ, Pryamitsyn V (2009) Anisotropic self-assembly of spherical polymer-grafted nanoparticles. Nat Mater 8(4):354–359
21. Li Y, Tao P, Viswanath A, Benicewicz BC, Schadler LS (2013) Bimodal surface ligand engineering: the key to tunable nanocomposites. Langmuir: ACS J Surf Colloids 29(4):1211–1220
22. Neouze M-A, Schubert U (2008) Surface modification and functionalization of metal and metal oxide nanoparticles by organic ligands. Monatshefte für Chemie-Chemical Monthly 139(3):183–195
23. Kim P, Jones SC, Hotchkiss PJ, Haddock JN, Kippelen B, Marder SR, Perry JW (2007) Phosphonic acid-modified barium titanate polymer nanocomposites with high permittivity and dielectric strength. Adv Mater 19(7):1001–1005
24. Corbridge DE (2013) Phosphorus: chemistry, biochemistry and technology. CRC Press
25. Natarajan B, Li Y, Deng H, Brinson LC, Schadler LS (2013) Effect of interfacial energetics on dispersion and glass transition temperature in polymer nanocomposites. Macromolecules 46(7):2833–2841
26. Stöckelhuber KW, Das A, Jurk R, Heinrich G (2010) Contribution of physico-chemical properties of interfaces on dispersibility, adhesion and flocculation of filler particles in rubber. Polymer 51(9):1954–1963
27. Ma PC, Kim J-K, Tang BZ (2007) Effects of silane functionalization on the properties of carbon nanotube/epoxy nanocomposites. Composites Sci Technol 67(14):2965–2972
28. Rong MZ, Ji QL, Zhang MQ, Friedrich K (2002) Graft polymerization of vinyl monomers onto nanosized alumina particles. Eur Polym J 38(8):1573–1582
29. Rungta A, Natarajan B, Neely T, Dukes D, Schadler LS, Benicewicz BC (2012) Grafting bimodal polymer brushes on nanoparticles using controlled radical polymerization. Macromolecules 45(23):9303–9311
30. Roy M (2005) An examination of the potential for nano-composites in the formulation of HV cable insulation. Rensselaer Polytechnic Institute
31. Wang H, Qiao X, Chen J, Wang X, Ding S (2005) Mechanisms of PVP in the preparation of silver nanoparticles. Mater Chem Phys 94(2–3):449–453
32. Shen Y, Lin Y, Nan CW (2007) Interfacial effect on dielectric properties of polymer nanocomposites filled with core/shell-structured particles. Adv Funct Mater 17(14):2405–2410

33. (a) Xu J, Qiu F, Zhang H, Yang Y (2006) Morphology and interactions of polymer brush-coated spheres in a polymer matrix. J Polym Sci Part B: Polym Phys 44(19):2811–2820; (b) Takai C, Fuji M, Takahashi M (2007) A novel surface designed technique to disperse silica nano particle into polymer. Colloids Surf A: Physicochem Eng Aspects 292(1):79–82; (c) Ohno K, Morinaga T, Takeno S, Tsujii Y, Fukuda T (2006) Suspensions of silica particles grafted with concentrated polymer brush: a new family of colloidal crystals. Macromolecules 39(3):1245–1249; (d) Kumar SK, Jouault N, Benicewicz B, Neely T (2013) Nanocomposites with polymer grafted nanoparticles. Macromolecules 46(9):3199–3214
34. (a) Yang K, Huang X, Zhu M, Xie L, Tanaka T, Jiang P (2014) Combining RAFT polymerization and Thiol–Ene click reaction for core–shell structured polymer@ BaTiO3 nanodielectrics with high dielectric constant, low dielectric loss, and high energy storage capability. ACS Appl Mater Interfaces 6(3):1812–1822; (b) Virtanen S, Krentz TM, Nelson JK, Schadler LS, Bell M, Benicewicz B, Hillborg H, Zhao S (2014) Dielectric breakdown strength of epoxy bimodal-polymer-brush-grafted core functionalized silica nanocomposites. Dielectrics Electrical Insulation, IEEE Transactions on 21(2):563–570
35. Edmondson S, Osborne VL, Huck WT (2004) Polymer brushes via surface-initiated polymerizations. Chem Soc Rev 33(1):14–22
36. Achilleos DS, Vamvakaki M (2010) End-grafted polymer chains onto inorganic nano-objects. Materials 3(3):1981–2026
37. (a) Natarajan B, Neely T, Rungta A, Benicewicz BC, Schadler LS (2013) Thermomechanical properties of bimodal brush modified nanoparticle composites. Macromolecules 46(12):4909–4918; (b) Todd MG, Shi FG (2003) Molecular basis of the interphase dielectric properties of microelectronic and optoelectronic packaging materials. Components Packaging Tech, IEEE Transactions on 2003 26(3):667–672; (c) Tanaka T, Kozako M, Fuse N, Ohki Y (2005) Proposal of a multi-core model for polymer nanocomposite dielectrics. Dielectrics Electrical Insulation, IEEE Transactions on 2005 12(4):669–681.
38. (a) Xie L, Huang X, Huang Y, Yang K, Jiang P (2013) Core@ double-shell structured BaTiO3–polymer nanocomposites with high dielectric constant and low dielectric loss for energy storage application. J Phys Chem C 117(44):22525–22537; (b) Yang K, Huang X, Xie L, Wu C, Jiang P, Tanaka, T (2013) Core–shell structured polystyrene/BaTiO3 hybrid nanodielectrics prepared by in situ RAFT polymerization: a route to high dielectric constant and low loss materials with weak frequency dependence. Macromolecul Rapid Comm 33(22):1921–1926; (c) Li Y, Wang L, Natarajan B, Tao P, Benicewicz BC, Ullal C, Schadler LS (2015) Bimodal "matrix-free" polymer nanocomposites. RSC Adv 5(19):14788–14795
39. Yu K, Niu Y, Bai Y, Zhou Y, Wang H (2013) Poly(vinylidene fluoride) polymer based nanocomposites with significantly reduced energy loss by filling with core-shell structured BaTiO3/SiO2 nanoparticles. Appl Phys Lett 102(10):102903
40. Laruelle G, Parvole J, Francois J, Billon L (2004) Block copolymer grafted-silica particles: a core/double shell hybrid inorganic/organic material. Polymer 45(15):5013–5020
41. Xie L, Huang X, Huang Y, Yang K, Jiang P (2013) Core-shell structured hyperbranched aromatic polyamide/BaTiO3 hybrid filler for poly (vinylidene fluoride-trifluoroethylene-chlorofluoroethylene) nanocomposites with the dielectric constant comparable to that of percolative composites. ACS Appl Mater Interfaces 5(5):1747–1756
42. Xie L, Huang X, Li B-W, Zhi C, Tanaka T, Jiang P (2013) Core–satellite Ag@ BaTiO 3 nanoassemblies for fabrication of polymer nanocomposites with high discharged energy density, high breakdown strength and low dielectric loss. Phys Chem Chem Phys 15(40):17560–17569
43. (a) Mozer AJ, Sariciftci NS (2004) Negative electric field dependence of charge carrier drift mobility in conjugated, semiconducting polymers. Chem Phys Lett 389(4):438–442; (b) Englund V, Huuva R, Gubanski SM, Hjertberg T (2009) High efficiency voltage stabilizers for XLPE cable insulation. Polym Degrad Stab 94(5):823–833; (c) Zhang H, Shang Y, Wang X, Zhao H, Han B, Li Z (2013) Mechanisms on electrical breakdown strength increment of polyethylene by aromatic carbonyl compounds addition: a theoretical study. J Mol Model 19(12):5429–5438.

44. (a) Yamano Y, Iizuka M (2009) Suppression of electrical tree initiation in LDPE by additives of polycyclic compound. Dielectrics Electrical Insulation, IEEE Transactions on 2009 16(1):189–198; (b) Yamano Y (2006) Roles of polycyclic compounds in increasing breakdown strength of LDPE film. Dielectrics Electrical Insulation, IEEE Transactions on 2006 13(4):773–781
45. Huang Y, Krentz TM, Nelson JK, Schadler LS, Bell M, Benicewicz B, Bimodal Brush Functionalized TiO2/silicone Nanocomposites with Improved Dielectric Properties," in Electrical Insulation Conference (EIC), IEEE, Seattle, USA, 2015, pp. 325–328

Chapter 3
Electrical Conductivity and Percolation Behavior of Polymer Nanocomposites

Qingzhong Xue and Jin Sun

3.1 Introduction

Polymer nanocomposites are a class of nano-sized materials comprising multiple solid phases. Filled with various fillers (semiconductors, metals, ceramics, and carbon-based materials), the properties of polymers such as thermal conductivity, flame resistance, and electrical, magnetic, and mechanical properties can be greatly improved [1–5]. With good processability, strong corrosion resistance, comparatively low weight and low cost, polymer-based nanocomposites containing conducting fillers have aroused great interest in a wide range of potential applications. Compared with the ceramic and metal composites, polymer-based nanocomposites possess low density and high flexibility [6]. Due to their excellent properties of the nanosized carbon fillers, such as carbon nanotubes (CNT), carbon nanofiber and graphene, carbon–polymer nanocomposites are endowed with great possibilities for commercial applications including electromagnetic interference (EMI), electrostatic dissipation (ESD), gas sensors, weight-sensitive aerospace, automobile, and so on.

In the context of EMI applications, electromagnetic waves from the environment interfere with sensitive electronic instruments and the human body. In addition, high-frequency devices, e.g., radiofrequency devices, can enhance such electromagnetic pollution [7]. For instance, cell phone use has been suspected to be one of the major causes for premature cataract [8]. Consequently, in order to prepare efficient EMI shielding materials, a substantial research effort has been undertaken by

Q. Xue (✉) • J. Sun
State Key Laboratory of Heavy Oil Processing, China University of petroleum, No. 66, Changjiang West Road, Huangdao District, Qingdao, Shandong 266580, People's Republic of China

College of Science, China University of Petroleum, Qingdao, Shandong 266580, People's Republic of China
e-mail: xueqz@upc.edu.cn; sunjin2012@126.com

© Springer International Publishing Switzerland 2016

X. Huang, C. Zhi (eds.), *Polymer Nanocomposites*,
DOI 10.1007/978-3-319-28238-1_3

researchers. Electromagnetic radiation-absorbing materials have already been researched widely and been applied to immunize against radar. Recently, people have found that by adding conductive fillers, such as carbon black [9–13], carbon fiber [9–11, 14], nanowire [15], and CNT [16–18], polymers gain shielding property for EMI which is mainly projected for protecting against radiation [19], and these polymer composites have been extensively studied as EMI shielding materials owing to their light weight, flexibility, corrosion resistance, and good shielding efficiency.

ESD is another important application of electrically conductive polymer nanocomposites for which moderate conductivities are required ($\sigma = 10^{-4}$–10^{0} S/m) [20, 21]. The ESD can be used as a good material to prevent harmful arcing discharges through bleeding off charge continuously [19].

Recently, an increasing interest in the use of electrically conductive polymer nanocomposites filled with carbon materials as single gas sensors has emerged. These types of vapor sensors have attracted considerable research interest. Swelling of the polymer upon exposure to various gases causes the dispersed carbon particles to move farther apart from each other. Disruption of formerly formed conductive pathways of carbon particles in the polymer nanocomposites raises the resistance of the sensor, thereby providing an extraordinary simple means for monitoring the presence of a vapor [22].

In weight-sensitive aerospace and automobile industries, the weight of electrically conductive polymer nanocomposites is strictly limited. In order to reach the standards of design, well-controlled voids are introduced into polymer nanocomposites to reduce their densities and increase their electrical properties [8–11, 23–27]. Microcellular foaming is an effective way to introduce well-controlled voids into polymer nanocomposites, and many lightweight polymer nanocomposites were prepared [9, 10, 25–33]. The lightweight polymer nanocomposites not only have ultra lightweight but also have low percolation threshold and excellent conductivity which is one of the hottest topics in polymer nanocomposites.

In addition, electrically conductive polymer nanocomposites are also being explored for novel applications, such as actuators [28, 34], lightning-protection aircraft panels [29], photoconductors [35], flexible and transparent plastic electronics, printable circuit wiring, and variable resistors [20, 36–38].

There are many ways to incorporate conductive fillers into polymer matrix: solution mixing [39, 40], in situ polymerization [41], melt blending, and latex blending [42, 43]. As more conductive fillers are added into the polymer matrix, the polymer matrix becomes conductive as the fillers form a conductive network. The critical concentration of the conductive fillers, allowing for the polymer nanocomposites from insulator to conductor, is defined as the percolation threshold, and this phenomenon can be well explained by percolation theory. Since the electrical conductivity is so closely related to the percolation threshold, researchers describe the relationship between the percolation threshold and electrical conductivity with simple explicit laws. We will use these simple explicit laws to analyze the conductivity and percolation behavior of the polymer nanocomposites in the Sect. 3.2. In addition, we will give special emphasis to the excluded volume theory, which is the most widely used continuum analytical model of percolation.

Preserving the desirable mechanical properties of polymer nanocomposites such as flexibility, low percolation threshold, and high electrical conductivity is our pursuit. To achieve this goal, we need to be clear as to the factors affecting the percolation threshold and electrical conductivity of polymer nanocomposites. It has been demonstrated that the type, size, content, distribution, and alignment of the fillers in a polymer matrix and the type of polymer matrix will affect the percolation threshold and electrical conductivity of polymer nanocomposites. In this chapter, we will review the major affecting factors and discuss the existing experimental data for different polymer nanocomposites.

In the past decade, a lot of work about polymer nanocomposites have been published [44–50]. In this chapter, theoretical and experimental results on the electrical conductivity and percolation behavior of polymer nanocomposites are illustrated by a variety of examples. In addition, we will focus on the lightweight carbon–polymer nanocomposites, which not only have ultra lightweight but also have low percolation threshold and excellent conductivity. Thus, this chapter is organized as follows: In Sect. 3.2, we provide the basics of percolation theory and the excluded volume theory currently used to describe and predict the electrical properties of polymer nanocomposites. In Sect. 3.3, we discuss the factors of affecting the percolation threshold and electrical conductivity of polymer nanocomposites. In Sect. 3.4, we describe the progress of lightweight carbon–polymer nanocomposite foams which is one of the hottest research topics of polymer nanocomposites.

3.2 Percolation Theory

3.2.1 The Basics

The basis of the percolation theory is to describe the connectivity of object, randomly or regularly positioned in some systems, and the effects of this connectivity on the properties of these systems. A key focus of percolation models is the critical probability, called the percolation threshold (f_c), and a connected network is formed causing the system to percolate. In 1957, Broadbent and Hammersley proposed the concept of percolation theory and used a statistical and geometrical way to settle the problem of fluid flow through a static medium [51]. Abundant work over the past years has shown that the model of percolation theory can be well used to interpret the electrical behavior of polymer nanocomposites which have a sharp insulator–conductor transition with increasing the concentration of fillers.

Extensive simulations and theoretical work have shown that the conductivity of polymer nanocomposites σ, the volume fraction of the filler f and the percolation threshold f_c can be described by simple explicit laws [52]:

1. When f just exceeds f_c, the conductive fillers form a continuous percolating path throughout the polymer matrix. So σ is determined mainly by σ_1 of the conductive fillers as follows:

$$\sigma \approx \sigma_1 \left(f - f_c\right)^{\alpha} \tag{3.1}$$

where α is the well-known critical exponent that is different for various systems depending on the connectivity of the systems. In literature, the critical exponent is found between 1.6 and 2.0 for a three-dimensional and between 1.1 and 1.3 in a two-dimensional system.

2. When f is less than f_c, the matrix prevents the formation of a percolating network by the conductive fillers. Thus, the value of σ is determined by the narrow gaps between the adjacent fillers. When f is close to f_c, the conductivity of the composite σ can be calculated as:

$$\sigma \approx \sigma_2 \left(f_c - f\right)^{-\beta} \tag{3.2}$$

where σ_2 is the conductivity of polymer matrix, and β is the critical exponent that is depending on dimensionality of the systems. In literature, the critical exponent is found between 0.7 and 1.0 for a three-dimensional and between 1.1 and 1.3 in a two-dimensional system.

3. For $|f–f_c| \to 0$, i.e., the crossover region of points 1 and 2 above, the conductivity of the composite σ can be described as:

$$\alpha \propto \alpha_2^{\gamma} \alpha_1^{1-\gamma} \tag{3.3}$$

where $\gamma = \alpha / \left(\alpha + \beta\right)$. Many experiments have proven the validity of these simple laws in descriptions of electrical conductivity of composites near percolation [52].

However, considerable spread has been observed in the experimentally obtained values of the critical exponent [52–56], and some studies have attributed it to the complex tunneling transport processes in real composites [57–59].

3.2.2 Excluded Volume Theory of Percolation

The excluded volume theory is the most widely used continuum analytical model of percolation, especially for predicting percolation thresholds of cylindrical fillers [60, 61]. The volume around the object into which another identical object cannot enter without contacting the first object is the excluded volume of the object [57]. Balberg et al. firstly proposed the excluded area of three systems including width-less sticks, finite-width two-dimensional sticks (e.g., rectangles), and a three-dimensional stick (capped cylinder) as follows [62]:

3.2.2.1 Widthless Stick

A stick of length L makes an angle θ_i with respect to a given direction in the plane. At the same time, let another stick j make an angle θ_j with the same given direction. As shown in Fig. 3.1, the excluded area for two given sticks is simply the area of the parallelogram,

$$L^2 \sin\left(\theta_i - \theta_j\right) \tag{3.4}$$

3.2.2.2 A Stick with a Finite Width

For two sticks (rectangles) of length L and width W, the angle between them is $\theta = \theta_i \quad \theta_j$. Moving stick i around stick j and registering the center of the stick i can obtain the excluded area as shown in Fig. 3.2. The shaded area represents the stationary stick, and the curve is the path of the center of the other stick as it is moved around the stationary stick. Balberg et al. obtained the excluded area within the curve. The formula of the excluded area is shown as the following:

$$\left(L\sin\theta + W + W\cos\theta\right)\left(L + W\sin\theta + L\cos\theta\right) - \left(L^2 + W^2\right)\sin\theta\cos\theta \tag{3.5}$$

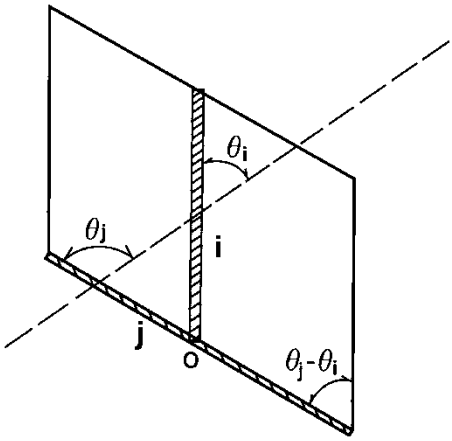

Fig. 3.1 Two "widthless" sticks (*shaded area*) and their corresponding excluded area. This area is the parallelogram which is obtained by following the center o of the stick *j* as it travels around the stick *i* while being parallel to itself and touching stick *i* at a single point (Reprinted with permission from Balberg et al. [62]. Copyright © 1984, American Physical Society)

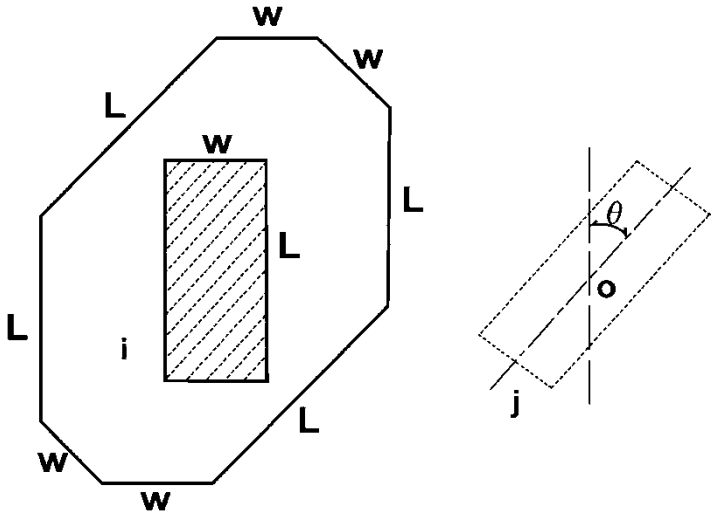

Fig. 3.2 Two sticks of length L and width W, the angle between which is θ. The excluded area is obtained by following the center o as stick j travels around stick i while touching it at least at one point (Reprinted with permission from Balberg et al. [62]. Copyright © 1984, American Physical Society)

3.2.2.3 A Three-Dimensional Stick (Capped Cylinder)

In the three-dimensional space, the γ is the angle between the axes of the two cylinders. Moving stick j around stick i, keeping stick j parallel to itself, the two sticks just touch each other. By moving one capped cylinder (length L and radius W/2) around the other, Balberg et al. obtain a capped parallelepiped with the width of 2W. As shown in Fig. 3.3, the parallelepiped is capped by four half-cylinders, of radius W and length L (instead of rectangles in two dimensions), and by four spherical sectors (rather than circular sectors in two dimensions) which add up to a full sphere [62]. Thus, the excluded volume of the capped cylinder is given by

$$\left(4\pi/3\right)W^3 + 2\pi W^2 L + 2WL^2 \sin\gamma \tag{3.6}$$

The excluded volume theory can be used in both soft-core spherocylinder model and hard-core spherocylinder model based on the above analytical results by Balberg et al.

For soft-core spherocylinder model, Berhan assumed that sticks are straight cylinders, the length is L, the radius is R. The derivation begins with the assumption that the number of objects per unit volume at percolation q is inversely proportional to the excluded volume V_{ex} of one of the objects [63],

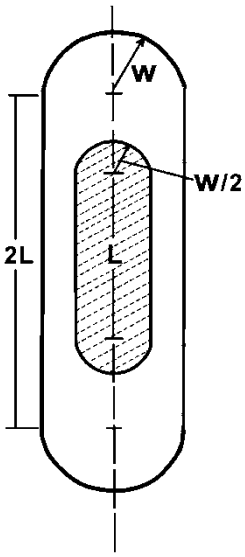

Fig. 3.3 Capped rectangle and the corresponding excluded area which is obtained with $\theta = 0$. In three dimensions, the stick is a capped cylinder and so is the excluded volume. Both the stick and the excluded volume are obtained by rotating the two-dimensional figures around the axis shown (Reprinted with permission from Balberg et al. [62]. Copyright © 1984, American Physical Society)

$$q \propto \frac{1}{V_{ex}} \tag{3.7}$$

According to equation (3.6), the excluded volume of a spherocylinder of length L and radius R can be described as [63]:

$$V_{ex} = \frac{32\pi}{3} R^3 \left[1 + \frac{3}{4}\left(\frac{L}{R}\right) + \frac{3}{8\pi} \sin(\theta) \left(\frac{L}{R}\right)^2 \right] \tag{3.8}$$

where θ is the angle between two sticks, and $\langle \sin(\theta) \rangle$ is the average value of $\sin(\theta)$ for the two sticks. For a random distribution, $\sin(\theta) = \frac{\pi}{4}$, so the excluded volume V_{ex} of a spherocylinder randomly distributed in a medium can be given by:

$$V_{ex} = \frac{32\pi}{3} R^3 \left[1 + \frac{3}{4}\left(\frac{L}{R}\right) + \frac{3}{32}\left(\frac{L}{R}\right)^2 \right] \tag{3.9}$$

For a single spherocylinder, the volume can be described as:

$$V = \frac{4\pi}{3} R^3 + \pi R^2 L \tag{3.10}$$

For very high-aspect-ratio fiber, the analytical solution for q is often described as follows:

$$q = \frac{1}{V_{ex}} \tag{3.11}$$

Since q is the number of objects per unit volume at percolation, the f_c for soft-core spherocylinder model is often expressed as:

$$f_c = \frac{V}{V_{ex}} = \frac{\frac{4}{3}\pi R^3 + \pi R^2 L}{\frac{32}{3}\pi R^3 + 8\pi R^2 L + \pi R L^2} \tag{3.12}$$

According to the excluded volume model, we can see that f_c decreases with increasing aspect ratio in an isotropic network. This theory is consistent with experimental and theoretical results.

Figure 3.4 a, b show the models of the soft-core spherocylinder and hard-core spherocylinder, respectively. The soft-shell model (Fig. 3.4a) has length L and radius r and is assumed to be fully penetrable; thus, objects are allowed to overlap and penetrate each other. The hard-core spherocylinder model (Fig. 3.4b) has an impenetrable core of radius r and length with hemispheric end caps of radius r along with a surrounding spherocylindrical soft shell of length L and radius R and hemispheric end caps of radius R. The parameter t is defined as the ratio of the radius of the core to the outer radius of the soft shell,

$$t = \frac{r}{R} \tag{3.13}$$

The soft-core limit is expressed as $t=0$, and for hard-core limit, $t = 1$. Since the interior spherocylinder is impenetrable, the excluded volume of the hard-core object is equal to the excluded volume of the soft shell minus that of the hard core. The excluded volume can be expressed as

$$V_{ex} = \frac{32\pi}{3} R^3 \left[\left(1 - t^3\right) + \frac{3}{4}\left(\frac{L}{R}\right)\left(1 - t^2\right) + \frac{3}{32}\left(\frac{L}{R}\right)^2 (1 - t) \right] \tag{3.14}$$

Obviously, the width of the shell (selected tunneling distance) has a large impact on the excluded volume of the core–shell model, as shown in Fig. 3.5. However, the width of the shell is difficult to predetermine, which impedes the adoption of the core–shell model. Varying the thickness of the shell in the core–shell model until the simulated threshold is approximately equal to the experimental percolation threshold may be a solution [50].

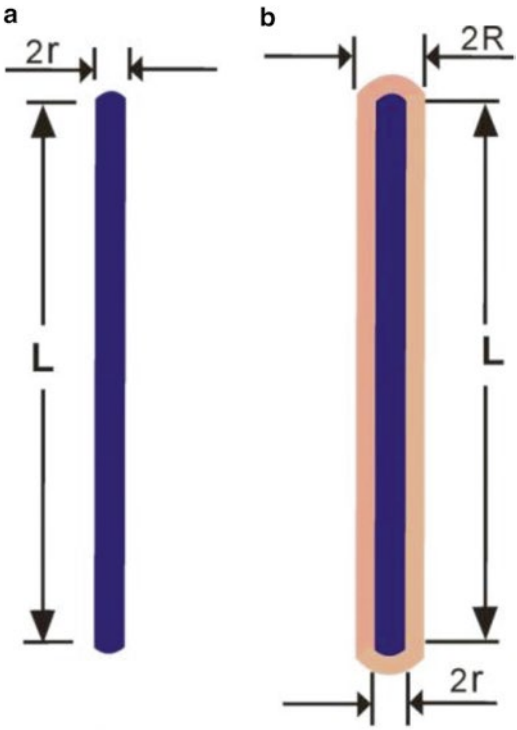

Fig. 3.4 (**a**) Soft-core model and (**b**) hard-core model with soft shell of radius R for a spherocylinder of length L and radius r (Reprinted with permission from Berhan and Sastry [63]. Copyright © 2007, American Physical Society)

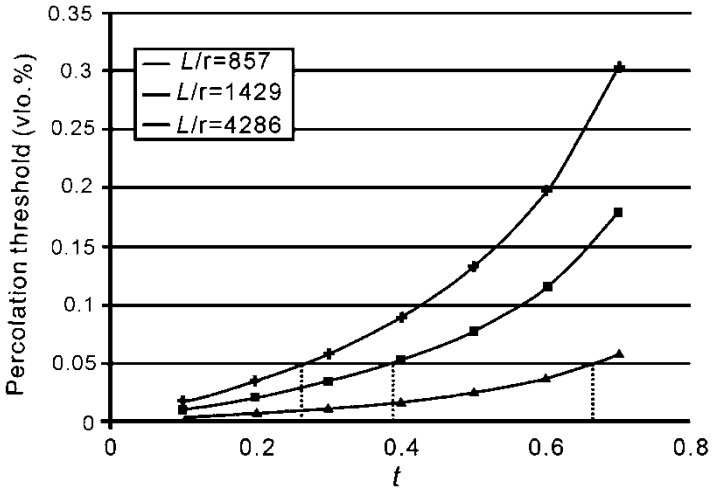

Fig. 3.5 Hard-core analytical solution for percolation threshold versus t for nanotube bundles (Reprinted with permission from Berhan and Sastry [63]. Copyright © 2007, American Physical Society)

3.3 Factors of Affecting Percolation Threshold and Electrical Conductivity of Polymer Nanocomposites

3.3.1 Filler Size, Shape, and Aspect Ratio

The percolation threshold and conductivity of polymer nanocomposites are greatly influenced by the geometric parameters of fillers, such as filler size, shape, and aspect ratio.

For polymer composites filled with two kinds of randomly distributed spherical fillers, the particle size of the major filler R_1 and the particle size of the minor filler R_2 are two factors affecting the f_c as shown in Fig. 3.6 [52]. When $R_1 / R_2 \leq 1$, $f_c \geq 0.16$; when $R_1 / R_2 >> 1$, f_c can be much less than 0.16. In order to obtain low percolation threshold with spherical fillers, researchers can use polymer composites filled with two kinds of randomly distributed spherical fillers, the major filler with large size and minor filler with small size. For instance, Shen et al. reported the effect of size for percolation threshold in Ni/ferrite–polymer composite, the size of Ni particles was much smaller than that of the ferrite particles, and due to the large size ratio, a low percolation threshold (0.095) was obtained [64]. Mezzenga et al. also observed that polyaniline/polystyrene-poly (2-vinylpyridine) composite, the smaller-sized polyaniline particle, was forced into the gaps between the large polystyrene particles, and thus the percolation threshold was reduced by one order of magnitude [65].

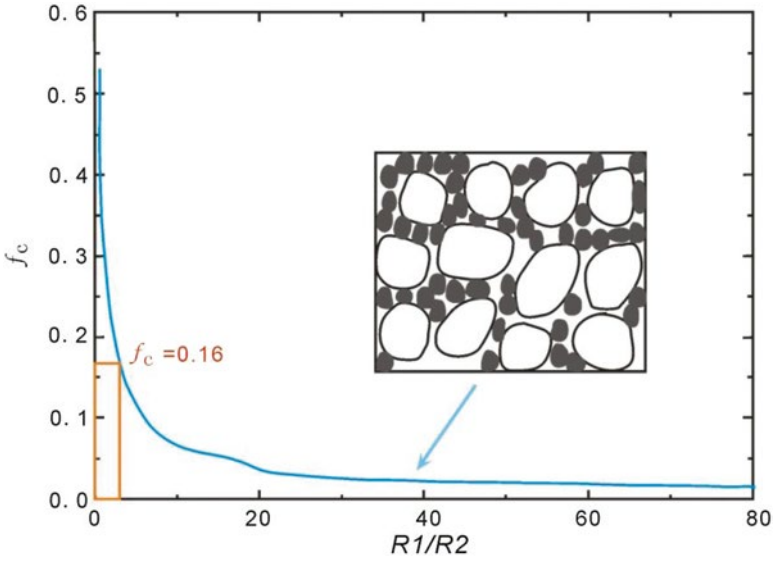

Fig. 3.6 Schematic variation of the percolation threshold f_c with the ratio between the radius R_1 of the matrix-phase particles (*white regions in the inset*) and the radius R_2 of the filler particles (*shadowed region in the inset*). The area above the solid blue line represents where a percolation path of the filler particles forms ($f > f_c$). As $R_1 / R_2 \approx 1$, $f_c \approx 0.16$, i.e., the Sher–Zallen invariant (Reprinted permission from Nan [52]. Copyright © 1993, Elsevier)

For polymer composites filled with one kind of randomly distributed fillers, the size and the aspect ratio of conductive fillers are two principal factors that should be carefully examined when making conductive polymer-based composites. Celzard [66] and Li [67] also pointed out that the aspect ratio of filler is the most dominant factor according to experimental and theoretical models for short carbon–fiber or graphite–nanoplatelet-reinforced polymer nanocomposites. The aspect ratio of fillers is the ratio of the length of the long axis to the length of the short axis. According to the excluded volume model, the percolation threshold of polymer nanocomposites, as Sect. 3.2.2 has pointed out, is inversely proportional to the aspect ratio in isotropic networks of both penetrable (soft core) and impenetrable (hard core) rods [62, 63]. This conclusion is consistent with both experimental and theoretical results. But this excluded volume theory provided an exact analytical solution only for slender-rod fillers with very high aspect ratio fillers, and this theory may not be for large sheet fillers such as graphene.

As mentioned above, for fillers with large aspect ratio, percolation threshold decreases with an increase in the aspect ratio (as shown in Fig. 3.7 [68]), and according to many experimental observations, some researchers even found that percolation threshold is approximately equal to the reciprocal of the aspect ratio [44, 48, 55, 69].

Xue et al. deduced a new formulation for describing the percolation threshold of metal–polymer nanocomposites with the different axial ratio and size of metal. The author proposed that, for metal–polymer nanocomposites, percolation threshold decreases with increasing metal particle axial ratio and decreasing metal particle size, and using metal particles with large axial ratio and smaller size helps to reduce the minimum metal content required reaching a certain conductivity value in theory [70]. Bai et al. reported an experimental investigation of the effect of MWCNT length and size on the mechanical and electrical properties of polymer composites.

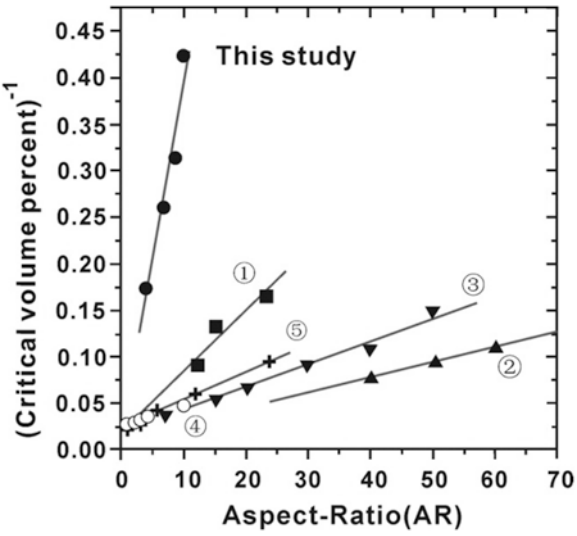

Fig. 3.7 Inverse relationship between critical volume concentration and aspect ratio. The circled numbers represent the same references shown in Fig. 3.5 (Reprinted permission from Yi et al. [68]. Copyright © 1999, Springer)

The author added three kinds of MWNTs with different lengths and sizes into a resin matrix, respectively. The experimental evidence suggested that the length and size had a very clear impact on the percolation threshold, and the percolation threshold decreased with increasing MWNT aspect ratio [71].

By doping fillers with large aspect ratio, polymer composites with ultralow percolation threshold could be obtained, and Li et al. [72] suggests that, for polymer composites filled with short carbon fibers or carbon black, if the aspect ratio of filler is too low, the formation of conduction networks requires a very high content of fillers, no matter how the dispersion state of the fillers is. Bryning et al. suggested that a higher length-to-diameter ratio is important for obtaining low threshold, and they observed conductivity threshold at SWNT volume fraction as low as 5.2×10^{-5}, nearly 10 times lower than values quoted in previous reports on SWNT composites in epoxy matrices [73]. A lower percolation threshold was obtained by Martin; they explored the use of aligned chemical vapor deposition-grown MWNT as a conductive filler in an epoxy system based on a bisphenol-A resin and an amine hardener. The percolation threshold of the MWNT (aspect ratio: 860)–polymer nanocomposites was 0.0039 wt%, which is more than two orders of magnitude lower than the theoretical values predicted by statistical percolation theory [54]. Moisala worked on optimizing the electrical conductivity of composites containing MWNTs and focused on forming a percolated network at low filler content; an ultralow percolation threshold of 0.0025 wt% was developed in MWNT (aspect ratio:1000)–epoxy nanocomposites [74]. Graphene sheets, one-atom-thick two-dimensional layers of sp^2-bonded carbon, have an extremely high aspect ratio. For polymer composites filled with graphene, ultralow percolation threshold could also be obtained. Stankovich presented a general approach for the preparation of graphene–polymer composites. They claimed that a polystyrene–graphene composite exhibits a percolation threshold of 0.1 vol% for room-temperature electrical conductivity, the lowest reported value for any carbon-based composite except for those involving CNT due to the extremely high aspect ratio of graphene [48].

To study the effect of the MWNT aspect ratio on the conductivity of MWNT-epoxy, Ayatollahi et al. choose a filler content of 0.5 wt% [56]. According to the images of scanning electron microscope, a good dispersion state of the fillers is obtained. Therefore, the effect of aggregation on electrical properties is removed and the aspect ratio is the only effective factor. The author then studied the effect of the MWNT aspect ratio on the electrical properties of MWNT–epoxy nanocomposites. They found that the nanocomposites with higher aspect ratio presented better conductivity (as shown in Fig. 3.8), and this phenomenon can be explained by excluded volume theory. In addition, as shown in Fig. 3.8, they found that only when the aspect ratio of MWNT is higher than about 500 did the MWNT–epoxy nanocomposites show conductivity.

Since the aspect ratio has a strong impact on the percolation threshold and conductivity of polymer nanocomposites, researchers should characterize the fillers in polymer and give out the value of the aspect ratio of fillers dispersing in polymer. It is important to note, however, the “value of the aspect ratio of fillers dispersing in

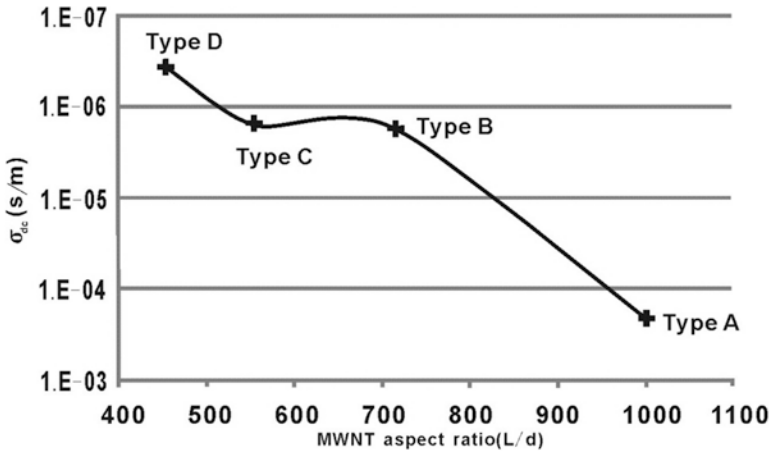

Fig. 3.8 The electrical conductivity of epoxy/0.5 wt% MWNT nanocomposites versus the MWNT aspect ratio (Reprinted permission from Ayatollahi et al. [56]. Copyright © 2011, Elsevier)

polymer" does not equal the "value of the aspect ratio of fillers before dipping in the polymer"; this is because the aspect ratio of fillers is strongly affected by the processing of nanocomposites.

3.3.2 Dispersion State of Fillers

In most theoretical and experimental studies of polymer nanocomposites, it has often pretended that fillers were distributed evenly in polymer matrices. However, fillers with nanoscopic dimensions are inclined to agglomerate in polymer matrices due to the strong inter-van der Waals forces. For CNT and graphene, aggregation during processing of such polymer nanocomposites is one of the major obstacles for their successful exploitation. This is due to the chemical inertness of CNT and graphene caused by their unique sp^2 bonding and their complex entanglement due to strong van der Waals forces.

The dispersion state of fillers in polymer nanocomposites is a key factor of affecting the percolation threshold and conductivity of polymer nanocomposites. Mutiso et al. [50] concluded that the dispersion state of fillers greatly impacts the microstructure of polymer nanocomposites, and the details of the nanofiller microstructure significantly impact the electrical properties of the final composite. As a result, the author claimed that fine control and an in-depth understanding of the dispersion state of fillers in polymer nanocomposites are essential so as to accurately predict composite properties. Nan et al. [69] also pointed out that homogeneously dispersion state of fillers in polymers is critical for the preparation of polymer nanocomposites. In the remainder of this section, we introduce the main

approaches of controlling filler dispersion. Moreover, the effects of the dispersion state of fillers in polymer nanocomposites on the electrical conductivity and percolation threshold of polymer nanocomposites are discussed.

3.3.2.1 Methods to Disperse Fillers in Polymer

To date, researchers have developed many methods to optimize the dispersion of fillers in polymer, and the mainly used methods with commercial viability fall into two categories, kinetic and thermodynamic approaches.

The kinetic approaches include solution mixing, melt processing, and in situ polymerization; in these processes, researchers often used shear forces or ultrasound vibrations to temporarily disperse the fillers followed by a method to trap this state. However, as for the thermodynamic approaches, functionalization of fillers is used involving covalently or non-covalently bonded chemical additives to mediate the interfacial energy; functionalization of fillers can improve the compatibility of filler polymer and/or reduce the attractive interactions between the fillers. In many cases, in order to achieve the most optimal results, combinations of both kinetic and thermodynamic approaches are adopted.

Solution Mixing

Solution mixing is the simplest and most widely used method for processing polymer nanocomposites filled with conductive fillers. Here, the fillers and polymer are mixed with a suitable solvent. In this process, ultrasonication is usually used to enhance the dispersion of fillers. In the experiment conducted by Zheng [75], long time, intensive stirring, and ultrasonic bath were used to promote fine dispersion of expanded graphite in polymethyl methacrylate for the composites, and the composites showed improvements in electrical conductivity.

Zhang et al. stirred GO at 35 °C for 6 h for the dispersion of GO in polymer [76]. In order to achieve better dispersion of functional graphene in polymer, Sun et al. also come into used 5-h ultrasonication before solution mixing [77]. Guo et al. [78] combined surfactant treatment and ultrasonication to ensure the dispersion of fillers in polymer. Grossiord [38] described that ultrasound propagates via a series of compression and rarefaction waves induced in the molecules of the medium through which it passes. Just look at SWNT, as an example, the authors point out that the shock waves promote the "peeling off" of individual SWNTs located at the outer part of the SWNT bundles and thus results in the exfoliation of individualized SWNT. If the ultrasonication treatment is too aggressive and/or too long, it can lead to localized damage of the SWNT walls, or even to SWNT shortening [79]. Localized damage of the SWNTs deteriorates both electrical and mechanical properties of the composite, so it is crucial to control the strength and time of ultrasonication treatment. The solvent, used to disperse fillers and polymer, is then evaporated in a controlled condition after forming nanocomposite on the surface of the substrate.

By this method, a series of polymer composites have been processed [80]. It is worth noting that, in some cases, fillers showed agglomeration again during the process of solvent evaporation. To avoid the agglomeration during the process of solvent evaporation, Du et al. introduced spin casting [80]. Another method can also resolve this problem; Dror et al. adopted electrospinning in which processing of polymer fibers takes place in the presence of electric field [81, 82]. Winey et al. also claimed that nanoparticle agglomeration is avoided by rapidly expelling the good solvent from the system, and a common recovery approach is called the coagulation, or rapid precipitation [50]. The coagulating or precipitating polymer rapidly traps the well-dispersed fillers in polymer. Alternatively, by drying at elevated temperatures or employing special casting techniques, accelerated solvent evaporation can avoid reaggregation of the fillers in polymer [83].

Melt Processing

The method of solution mixing is restricted by the solubility of the polymers into the solvent. In order to solve the problem, melt processing is introduced. This method is often used to deal with thermoplastic polymers such as polypropylene, polystyrene, polycarbonate, and poly (ethylene-2, 6-naphthalate) [80]. Before mixing the polymer and fillers, the polymer is melted into viscous liquid at elevated temperatures. After the melt processing of polymer, the viscous liquid is mixed with fillers. The dispersion state of fillers can be improved by shear mixing, which can be achieved by extrusion and injection molding techniques. Given that high viscosity of polymers leads to hindrance in achieving uniform dispersion of CNTs, melt processing is viewed as a less efficient method than solution mixing. However, melt processing shows great superiority of being the most compatible with the existing industrial practices. Therefore, many experimental efforts are targeted toward dispersion optimization in melt-blending processes.

In Situ Polymerization

This method involves mixing, dispersion of fillers with monomer for polymer, and polymerization of the mixture. This process is able to go on in the presence or absence of solvent. But unlike the solution mixing and melt processing, in the process of in situ polymerization, monomer for polymer is the starting materials rather than polymer. The power of this approach lies in that the fillers have better dispersion due to the grafting of polymer molecules on fillers; in addition, this method results in better interactions between fillers and the polymer matrix. Some insoluble and thermally unstable polymers are not proper to be processed by solution mixing and melt processing, which can be processed by in situ polymerization.

Recently, Fan [84] prepared graphene aerogel–poly(methyl methacrylate) composites via an in situ polymerization process. Typically, methyl methacrylate and 2, 2-Azobis (2-methylpropionitrile) are first mixed and stirred until the mixture

becomes viscous, and it is rapidly cooled to cease the pre-polymerization. The graphene aerogels are then pressed into the mixture, and the mixture with the graphene aerogels immersed is kept at a low temperature to remove air bubbles. Afterward, the above mixture is maintained in a water bath until it completely solidified. Images of field emission scanning electron microscope showed that graphene aerogels are well dispersed in poly(methyl methacrylate). Through the adoption of in situ polymerization process, good dispersion of graphene in polymer was obtained by Aldosari [85] and Yuan [86]. In addition, in situ polymerization is widely used on epoxy composites [74, 87], and the composites are cured by hardener [36]. Although commercial applications for thermoplastic polymers are limited [88], in situ polymerization is well applied to process composites of thermosetting polymers. As expected for a kinetic method of dispersion, the rate of polymerization must exceed the rate of nanoparticle agglomeration for the process to be successful [50].

Through adopting different methods of dispersing fillers in polymer, the percolation threshold of graphene–polymer nanocomposites was studied intensively. Verdejo et al. collected the percolation thresholds described in the literatures and assembled the information in Fig. 3.9. As the figure shows, the percolation thresholds vary from the lowest at 0.07 vol% for ultrahigh molecular weight PE, to 0.1 vol%

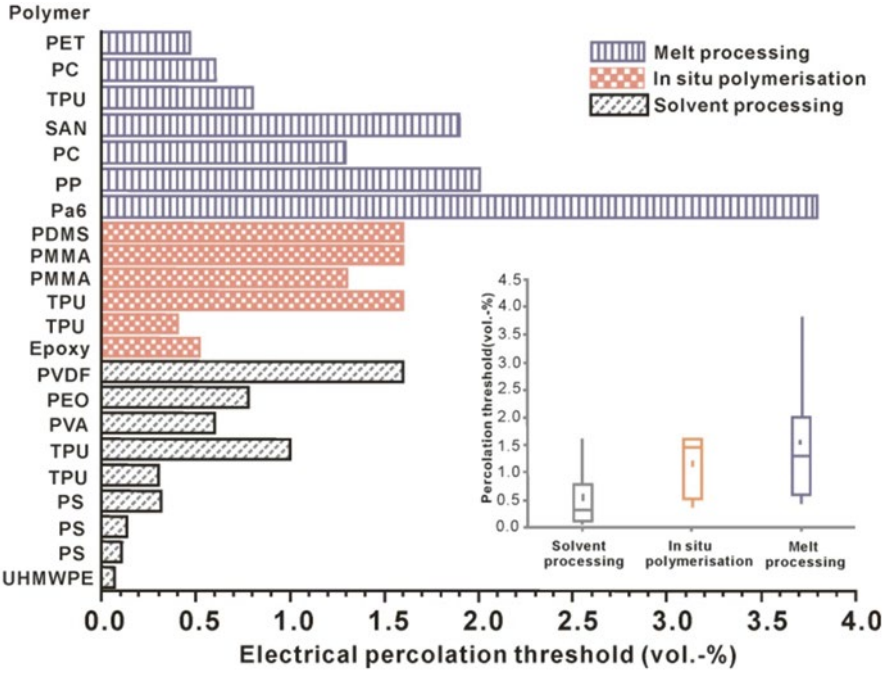

Fig. 3.9 Electrical percolation thresholds of graphene–polymer nanocomposites according to processing strategy. For comparison purposes, the values of loading fraction reported in wt% have been converted to vol% (Reprinted permission from Verdejo et al. [12]. Copyright © 2011, Royal Society of Chemistry)

for PS and 3.8 vol% for polyamide. On average (Fig. 3.9, inset), the lowest percolation threshold was obtained by solvent processing, closely followed by in situ polymerization since these two methods usually enabled better dispersions than melt compounding [12].

The most common method for thermodynamic dispersion is functionalization of fillers. The goal of functionalization of fillers is to reduce the van der Waals force between the fillers and improve the interaction between fillers and polymer matrices and then enhance the properties of filler–polymer nanocomposites. Functionalization of fillers involves covalent functionalization and non-covalent functionalization.

Covalent Functionalization

Covalent functionalization of fillers is based on linkage between various chemical species and the fillers, and there exists a lot of chemistry accomplishing the linkage between them. However, for nano-sized carbon fillers including graphene and CNT, covalent functionalization changes the hybridization of the carbon atoms from sp^2 to sp^3. This transition leads to the disruption of π conjugation in the carbon fillers and then diminishes the intrinsic carbon conductivity owing to electron scattering at the functionalization sites.

Yuan [76] reported an efficient one-step approach to reduce and functionalize graphene oxide (GO) during the in situ polymerization of phenol and formaldehyde. The hydrophilic and electrically insulating GO is converted to hydrophobic and electrically conductive graphene with phenol as the main reducing agent. The composites prepared show excellent electrical conductivity of 0.20 S/m, when the content of GO is 0.85 vol%.

Ding et al. [77] synthesized the polyamide-6 (PA6)-graphene composites. The generated PA6 chains are covalently grafted onto GO sheets through the "grafting to" strategy with the simultaneous thermal reduction reaction from GO to reduce graphene oxide (RGO). The PA6 chain-grafted RGO sheets showed good dispersion in the polymer, and the well dispersion was attributed to the high density of grafting, which enhanced the interfacial interaction between the RGO sheets and the polymer matrix, immensely improving their compatibility.

As mentioned above, covalent functionalization has the drawback of destroying the extended π conjugation in graphene and CNT. While the impact of disrupted π conjugation is limited for mechanical and probably thermal properties, the impact on electrical properties is expected to be profound because each covalent functionalization site scatters electrons [36]. And yet, covalent functionalization can be very effective for improving mechanical properties.

Non-covalent Functionalization

Comparing to the covalent functionalization, the non-covalent functionalization not only improve the dispersion of fillers in polymer but it also keeps the extended π conjugation in graphene and CNT.

By a combinatorial process of non-covalent functionalization of defect-free pristine graphene with poly(amidoamine) (PAMAM) dendrimer and the homogenous attachment of silver nanoparticle (AgNP) on graphene surface, Liu et al. [89] presented a method for a large-scale production of AgNP/pristine graphene hybrid, and the hybrid is used as nano-sized filler to generate epoxy-based conductive composites. Due to the non-covalent functionalization, the intrinsic structure of graphene sheets in the hybrid was maintained, and the hybrid showed homogenous dispersion in the polymer of epoxy. Due to the combined effects of the excellent electrical conductivity of high-quality pristine graphene at low percolation threshold and enhanced contacts between the fillers by low temperature sintering of AgNP, the epoxy composite filled with PMMA/graphene/AgNP exerted low-volume resistivity as shown in Fig. 3.10.

Martin-Gallego et al. [90] functionalized graphene sheets (GNs) with gold nanoparticles by a spontaneous deposition of gold particles on its surface, and the Au–GN hybrids were used as fillers to prepare epoxy-based composites. The conductivity of the epoxy-based composites containing Au-GN was about four orders of magnitude than the conductivity of GN–epoxy nanocomposite. The author illustrated that the excellent conductivity could be attributed to a charge transfer mechanism, which is strongly enhanced by the presence of gold particles.

Recently, Wang et al. [91] proposed a facile and effective method to prepare polymer-functionalized reduced graphene oxide (polymer-FG) from a non-covalently functionalized pyrene-terminal polymer in benzyl alcohol (BnOH). The existence of BnOH simplifies the synthesis process and make the production of polymer-FG easily scalable because the transition of GO to RGO and the non-covalent functionalization proceed simultaneously. The resulting polymer-FG sheets show organo-dispersibility, high electrical conductivity, and good processability.

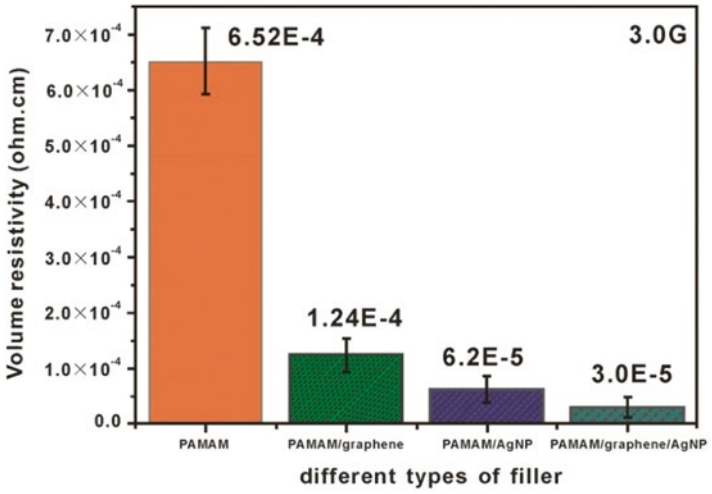

Fig. 3.10 Volume resistivity of different types of epoxy-based composites (Reprinted permission from Liu et al. [89]. Copyright © 2014, Elsevier)

Ryu et al. [92] utilized pyrene moieties containing amide functional groups to modify the surface of MWNTs. The image of Raman spectra showed that the D/G ratio of the MWNTs remained unchanged after the modification, indicating that the structure of MWNTs was not destroyed and the modification was non-covalent functionalization. The modified MWNT-polyamide 6 nanocomposites exhibited better electrical properties due to the preservation of the intrinsic structure of the MWNTs as well as the uniform dispersion of the MWNTs in the polyamide 6 matrix.

3.3.2.2 Effects of Dispersion State of Fillers on Electrical Properties of Polymer Nanocomposites

Until now, a lot of researches have been focused on the effect of dispersion state on electrical properties of polymer nanocomposites. A few researchers found that the electrical properties of polymer nanocomposites are improved as the dispersion state of fillers improves [76, 77, 89–92]; nevertheless, some of these studies have reported that aggregation is good for improving electrical properties of polymer nanocomposites [56, 73, 93].

Bryning et al. [73] showed how the SWNT length/diameter aspect ratio and the spontaneous formation of SWNT networks affect the conductivity of bulk SWNT–epoxy composites. The author concluded that composites in which SWNTs were allowed to reaggregate exhibited lower thresholds and better electrical properties. According to the analysis of electrical percolation in CNT polymer composites by Bauhofer [93], the best dispersions, which mean the formation of a polymer layer around each CNT, do not necessarily result in the highest conductivities. Through reviewing and analyzing research data, the author concluded that solvent-processing technique or shear-induced reaggregation sometimes improves the electrical performance of composites by preventing an overall sheathing or reducing the sheath thickness, respectively. Gojny et al. [94] prepared CNT–epoxy composites and evaluated the electrical and thermal conduction mechanisms in composites. They found that obtaining the statistical percolation suggests good dispersion of filler particles; however, good dispersion results in better mechanical properties, it might lead to lower electrical conductivity.

In many of these researches above, most of the characterizations of the dispersion state of fillers are qualitative, which result that meaningful comparisons to probe the origin of these conflicting findings are difficult to conduct. However, Winey et al. [50] proposed several important factors for shedding light into these seemingly disparate trends; the several important factors are shown below.

First, specifying the length scales involved is requisite condition for discussing the quality of dispersion state; second, any discussion of enhanced or reduced electrical performance based on dispersion state of fillers must conduct the parameter space. The parameter space is valuable for establishing the applicability or generality of the findings of these studies; finally, only when the aspect ratio is not well characterized and the same filler type and polymer matrix are considered, the comparisons of different dispersion states are effective. Correlations between dispersion and

composite conductivity are vague when the dispersion is enhanced by functionalization, which can enhance the dispersion of fillers, but may also inhibit electron transport [50].

It is very important to predict the correlations, and this can be accomplished by theoretical approaches; in addition, predicting the correlations will advance our ability to engineer robust composites. It is important to note, modeling the nonequilibrium structures, which are the norm experimentally, is still a challenge [50].

3.3.3 Orientation of Fillers

Alignment and rational assembly of nanofillers are effective methods to formulate high-performance and multifunctional composite materials. The reinforcing or functional efficiency of the composites containing anisotropic nanofillers can be significantly improved by aligning the nanofillers in the same direction that the composites are intended to be utilized. Nanofillers can be aligned by inducing an external force, such as electrical/magnetic fields or mechanical shear, in the chosen direction before or during consolidation [95]. The relative orientations of fillers influence the excluded volume and then impact the percolation threshold. In addition, the alignment of fillers influences electrical conductivity of polymer nanocomposites.

The effect of CNT alignment on percolation conductivity in SWNT-PMMA composites has been investigated by Du et al. [96]. They systematically address percolation conductivity as a function of alignment, varied in a controlled manner from isotropic to highly aligned. Variable extensional forces were applied to achieve various degrees of SWNT alignment in a polymer matrix. Surprisingly, the electrical conductivity follows a power–law dependence in alignment as well as concentration. As a function of alignment, the conductivity exhibits a power–law behavior. As illustrated in Fig. 3.11, at fixed 2 wt% loading, the electrical conductivity parallel to the alignment direction shows a sharp transition with respect to the degree of SWNT alignment. The conductivity of nanocomposites increases dramatically, from 6.5×10^{-11} to 4.4×10^{-6} S/cm, as the full width at half maximum (FWHM) varies from 20 to 36°. Percolation is also appropriate for describing this behavior. When the SWNTs are highly aligned, they rarely touch each other and thus do not form conductive pathways at small loading. Highest conductivities occur for slightly aligned, rather than isotropic SWNTs. By using Monte Carlo simulations, the effects of CNT alignment on percolation resistivity can be obtained. The theoretical investigation showed that minimum resistivity occurred for a partially aligned rather than a perfectly aligned CNT film [97].

Liu et al. [98] proposed a new 3D percolation network model to study the effects of CNTs alignment on electrical conductivity of polydimethylsiloxane (PDMS)-CNT composites, wherein the polymer-type-dependent formula is employed to adjust the data in comprehensive experiments. The results of their simulation show that randomly distributed MWNTs need 0.1 vol% CNT loading to achieve a stable

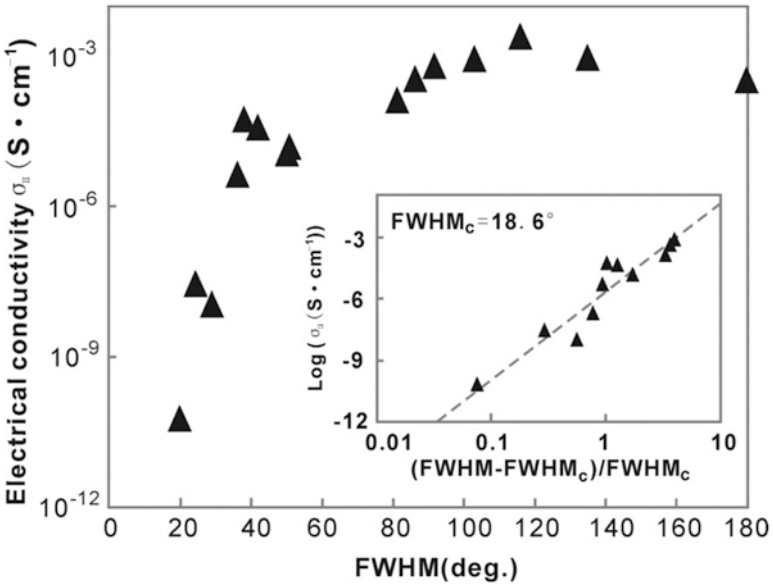

Fig. 3.11 Electrical conductivity of the 2 wt% SWNT–PMMA composite along the alignment direction as a function of alignment. Inset: a log–log plot of conductivity versus reduced FWHM determines the critical alignment, FWHW*c* (Reprinted permission from Du et al. [96]. Copyright © 2005, American Physical Society)

conductive network. The author assumes this is the percolation threshold of PDMS–MWNT composites. Above percolation threshold, different alignments can achieve different electrical conductivities at a fixed CNT loading. The author gives a visual description about the relationship between different alignments and electrical conductivities; with a MWNT loading at 2, 3, and 5 % in PDMS matrix, the electrical conductivity of composites is changing with different alignment angle. For different MWNT loadings, they share the same tendency, and with the alignment angle of 30°, the best electrical conductivity is achieved. On the other hand, with alignment angle of 0°, or when CNTs are aligned in the horizontal direction, the worse electrical conductivity is found.

Through an environmentally benign process, Yousefi et al. [95] produced polyurethane (PU)-based composite films containing highly aligned graphene sheets. An aqueous liquid crystalline dispersion of graphene oxide (GO) is in situ reduced in PU, resulting in a fine dispersion and a high degree of orientation of graphene sheets. The resulting composites show excellent electrical conductivity with an extremely low percolation threshold of 0.078 vol%, which is considered one of the lowest values ever reported for polymer composites containing graphene.

The orientations of fillers can greatly influence the percolation threshold and electrical conductivity of polymer nanocomposites. So, by controlling the orientations of fillers, the electrical properties can be optimized.

3.3.4 Matrix Properties

In addition to the effect of these geometric features of fillers, the percolation threshold may be influenced by a number of characteristics of the matrix, such as viscosity, polarity, and degree of polarization [69]. This effect is particularly apparent when polymers are employed as the matrix in composites. Bauhofer et al. [93] reviewed experimental and theoretical work on the electrical percolation of CNT in different polymers. They found that the conductivity of composites with identical filler concentration seems to almost vary with only one or two orders of magnitude for identical matrices, but by 10 or more orders of magnitude for different matrices.

Despite the variety of viscosity, polarity, and degree of polarization, the mechanisms of how polymer matrix influence percolation threshold are principally the same. First, as the fillers are dispersed in the polymer, the interactions between fillers are largely influenced by the polymer matrices, thus fillers are able to move in response to these medium-mediated interactions when the preparation of composite is in progress in solution or melt. The interactions between fillers influence the formation of conductive networks in polymer nanocomposites. It is important to note that the kinds of polymer have large effects on percolation thresholds as the medium-mediated interactions are strong and the viscosity of polymer is very low. Second, the dispersion state of fillers and the compatibility of the fillers in polymer are determined by the interfacial energy between the filler and polymer, and these factors influence the percolation threshold of polymer composites. Third, crystalline or semicrystalline polymer matrices also influence the electrical properties of polymer nanocomposites. Jeon et al. [99] proposed that polyethylenes are the most affordable polyolefin-based thermoplastics. The author showed a carefully controlled fast crystallization from a dilute solution of a SWNT–high-density polyethylene (HDPE) mixture, maintaining the uniformity of the CNT dispersion in the solvent, and they provided HDPE nanocomposites with improved electrical conductivities. Haggenmueller [100] also studied the effect of polymer on electrical properties of polymer nanocomposites. They probed the electrical conductivity of SWNT–polyethylene nanocomposites by considering the factors about polymer as below: a crystalline matrix (polyethylene), crystalline alignment in the matrix. The effect of the polyethylene crystallinity on conductivity in SWNT–polyethylene composites is studied in isotropic composites made with low-density and high-density polyethylenes. From the studies above, the authors found that, through providing nucleation sites and templating the crystal growth, fillers impact the crystallization behavior of polymers. On the other hand, they also found that crystallization is good for improving the micro- and nanoscale dispersion of fillers, as the crystallites that form along the particles prevent clustering [99]. Beyond the potential effects of matrix crystallinity on filler distribution, there is as yet no compelling evidence that matrix crystallization significantly affects the conductivity of polymer nanocomposites [50].

To increase the percolation threshold of polymer nanocomposites, higher polarity, higher surface tension, higher viscosity, and a lower degree of crystallization are

needed, because these factors hinder the uniform distribution of fillers in the matrix [69].

To decrease the percolation threshold of polymer nanocomposites, adopting two different matrices in composites is also an effective method. In order to enhance the performance of composite, uniformly distribution of fillers including graphene and CNT in polymer matrix is required, but it is often difficult to achieve. Due to the high aspect ratio of fillers and strong van der Waals force between fillers, the fillers have a large tendency of agglomeration. High loading fractions favor agglomeration not only because the particles come into contact more often, but also because there can be a shortage of polymer matrix to wet out the surface of the filler [101, 102]. Hwang et al. proposed that one of the recent trends is to use multiphase polymer blends for reducing the amount of conductive fillers in composites, and they investigated the electrical properties of polypropylene (PP)/polystyrene (PS) blends filled with MWNT. The result showed that adopting two matrices can improve the electrical conductivity of nanocomposites. Sumita et al. [103] claimed that phase separation of polymer blends and selective localization of CNT into one phase can produce conducting composite materials at lower filler content. Gubbels [97] and Tchoudakov [104] prepared composites of carbon black (CB)-PS + high-density polyethylene and CB-polypropylene + polycarbonate, respectively. They found that a preferential distribution of the conductive CB particles was induced by using immiscible polymer blends as matrices and low percolation thresholds were obtained.

3.4 Lightweight Carbon Material–Polymer Nanocomposite Foams with Excellent Conductivity

Being lightweight and having excellent conductivity are key technological requirements for the development of both scientific and industrial communities [8, 9, 11, 31, 32]. Currently, the hot topic of polymer composites is about preparing lightweight carbon material–polymer composite foam, which not only have ultra lightweight but also have low percolation threshold and excellent conductivity.

As an effective way, microcellular foaming was used to reduce the density of polymer materials, and many lightweight polymer foams were prepared [9, 10, 25–33]. Recently, Zhi et al. [8] used microcellular foaming to reduce the density of polymer materials and fabricated lightweight and tough polycarbonate (PC)–CNT composites with improved electrical properties. By melting compounding, the author prepared PC–CNT composites, and by supercritical CO_2 foaming of the composites, they introduced well-controlled voids into the PC–CNT composites. The introduction of numerous voids not only endows the PC composites with higher electrical conductivity but also makes the brittle PC–CNT composites tough. This is because the introduction of numerous voids generates large interfaces in the foams, which facilitates the multiple reflections of microwaves within the foams.

By a phase separation process, Ling et al. [9] produced lightweight microcellular polyetherimide (PEI)–graphene nanocomposite foams with a density of about 0.3 g/cm^3. They observed that the strong extensional flow generated during cell growth induced the enrichment and orientation of graphene on cell walls. Compared to PEI–graphene nanocomposite, microcellular PEI–graphene foam possessed a higher electrical conductivity as shown in Fig. 3.12, which suggested that the presence of microcellular structure might decrease the percolation threshold of the conductive composites and increased the conductivity with same graphene content.

Ameli et al. [31] prepared foamed and solid polypropylene–carbon fiber (PP-CF) composites containing various CF contents (0-10 vol%). They used dissolved pressurized nitrogen gas to get foamed composites. Interestingly, they observed that the introduction of foaming reduced the density of the injection-molded samples by 25 %, lowered the volume fraction of the percolation threshold from 8.5 to 7 vol% CF, and enhanced the through-plane conductivity up to a maximum of six orders of magnitude.

Ma et al. [11] prepared PC nanocomposites by blending PC with thermally exfoliated graphene and p-phenylenediamine (PPD)-functionalized and reduced

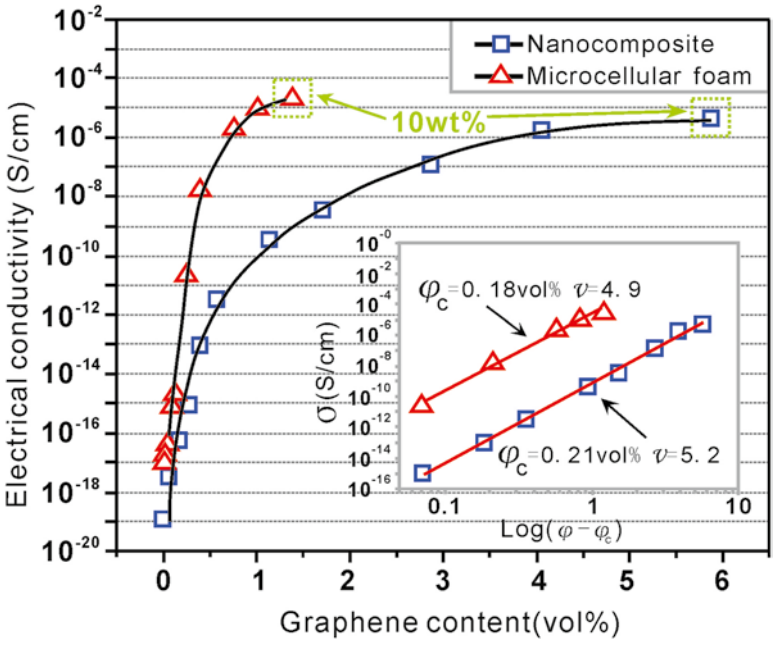

Fig. 3.12 Electrical conductivity for PEI–graphene nanocomposites and microcellular foams as the function of graphene content (Reprinted permission from Ling et al. [9]. Copyright 2013, © American Chemical Society)

graphene oxide (GO-PPD). The author claimed that GO-PPD exhibits a better compatibility with the PC matrix comparing to thermally exfoliated graphene and thus a more homogeneous dispersion due to the presence of PPD in GO-PPD. After being freely foamed with supercritical carbon dioxide as the foaming agent, the PC-(GO-PPD) nanocomposite foams show improved cell structures with higher cell density, smaller cell size, and more regular shapes, which should be attributed to the uniform dispersion of GO-PPD sheets in the matrix, which act as nucleation sites for foaming. Interestingly, the conducting network formed by GO-PPD sheets survives even after mold-limited foaming of PC-(GO-PPD) nanocomposites, and therefore the nanocomposite foams exhibit similar or even higher electrical conductivity in comparison to their solid counterparts.

The results obtained in these investigations reveal that lightweight conductive composites with lower filler content and enhanced electrical properties can be developed by a kind of methods, which can be used as lightweight, flexible, and high-performance EMI shielding material in areas such as aerospace and next-generation flexible electronics [32].

3.5 Conclusion

Polymer-based nanocomposites containing conducting fillers have aroused great interest in a wide range of potential applications. In this chapter, the electrical conductivity and percolation behavior of polymer nanocomposites are briefly illustrated. We give special emphasis to the main factors of affecting percolation threshold and electrical conductivity of polymer nanocomposites. It is shown that filler size, sharp, aspect ratio, dispersion state, orientation, and matrix properties have significant influences on the percolation threshold and electrical conductivity of polymer nanocomposites, which are summarized as following:

3.5.1 Aspect Ratio of Fillers

Percolation threshold decreases with an increase in the aspect ratio. And some researchers even found that percolation threshold is approximately equal to the reciprocal of aspect ratio. By doping fillers with large aspect ratio, polymer nanocomposites with ultralow percolation threshold could be obtained. Aspect ratio of fillers also has an effect on the conductivity of polymer nanocomposites. Nanocomposites with higher aspect ratio usually presented better conductivity, and this phenomenon can be explained by excluding volume theory.

3.5.2 Dispersion State of Fillers

We introduce the main approaches used to control and quantify the dispersion state of fillers, which include solution mixing, melt processing, in situ polymerization, and functionalization of fillers. In many cases, in order to achieve the most optimal results, combinations of these approaches are adopted.

Moreover, the effects of the dispersion state of fillers in polymer nanocomposites on the electrical conductivity and percolation threshold of polymer nanocomposites are discussed. A few researchers found that the electrical properties of polymer nanocomposites are improved as the dispersion state of fillers improves; nevertheless, some of these studies have reported that aggregation is good for improving electrical properties of polymer nanocomposites.

3.5.3 Orientation of Fillers

For CNT–polymer nanocomposites, the highest conductivity occurs for slightly aligned, rather than isotropic CNT. The theoretical investigation also showed that the minimum resistivity occurred for a partially aligned rather than a perfectly aligned CNT film. However, other studies have found that polymer-based composite films containing highly aligned graphene sheets showed excellent electrical conductivity with an extremely low percolation threshold. So, the orientations of fillers could influence the percolation threshold and electrical conductivity of polymer nanocomposites, and by controlling the orientations of fillers, the electrical properties can be optimized.

3.5.4 Characteristics of Matrix

In addition to the effect of these geometric features of fillers, the percolation threshold may be influenced by a number of characteristics of the matrix, such as viscosity, polarity, and degree of polarization. To increase the percolation thresholds of polymer nanocomposites, higher polarity and hence the higher surface tension, higher viscosity, and a lower degree of crystallization are needed, and to decrease the percolation thresholds of polymer nanocomposites, adopting two different matrices in nanocomposites is an effective method.

At last, we give a short description about lightweight carbon–polymer nanocomposite foams. The lightweight carbon–polymer nanocomposite foams not only have ultra lightweight but also have low percolation threshold and excellent conductivity, which is one of the hottest research topics of polymer nanocomposites.

Acknowledgments This work is supported by the Natural Science Foundation of China (41330313), Taishan Scholar Foundation (ts20130929),and the Fundamental Research Funds for the Central Universities (13CX05009A).

References

1. Glushanin S, Topolov VY, Krivoruchko A (2006) Features of piezoelectric properties of 0-3 $PbTiO_3$-type ceramic/polymer composites. Mater Chem Phys 97(2):357–364
2. Pelaiz-Barranco A, Marin-Franch P (2005) Piezo-, pyro-, ferro-, and dielectric properties of ceramic/polymer composites obtained from two modifications of lead titanate. J Appl Phys 97(3):034104
3. Huang ZM, Zhang YZ, Kotaki M, Ramakrishna S (2003) A review on polymer nanofibers by electrospinning and their applications in nanocomposites. Compos Sci Tech 63(15): 2223–2253
4. Jordan J, Jacob KI, Tannenbaum R, Sharaf MA, Jasiuk I (2005) Experimental trends in polymer nanocomposites-a review. Mater Sci Eng A 393(1):1–11
5. O'connell MJ (2006) Carbon nanotubes: properties and applications. CRC Press, Boca Raton
6. Fu X, Chung D (1998) Submicron-diameter-carbon-filament cement-matrix composites. Carbon 36(4):459–462
7. Park SH, Thielemann P, Asbeck P and Bandaru PR (2009) Enhanced dielectric constants and shielding effectiveness of, uniformly dispersed, functionalized carbon nanotube composites. Appl Phys Lett 94:243111
8. Zhi X, Zhang HB, Liao YF, Hu QH, Gui CX, Yu ZZ (2015) Electrically conductive polycarbonate/carbon nanotube composites toughened with micron-scale voids. Carbon 82:195–204
9. Ling J, Zhai W, Feng W, Shen B, Zhang J, Zheng WG (2013) Facile preparation of lightweight microcellular polyetherimide/graphene composite foams for electromagnetic interference shielding. ACS Appl Mater Interfaces 5(7):2677–2684
10. Xu XB, Li ZM, Shi L, Bian XC, Xiang ZD (2007) Ultralight conductive carbon-nanotube-polymer composite. Small 3(3):408–411
11. Ma HL, Zhang HB, Li X, Zhi X, Liao YF, Yu ZZ (2014) The effect of surface chemistry of graphene on cellular structures and electrical properties of polycarbonate nanocomposite foams. Ind Eng Chem Res 53(12):4697–4703
12. Verdejo R, Bernal MM, Romasanta LJ, Lopez-Manchado MA (2011) Graphene filled polymer nanocomposites. J Mater Chem 21(10):3301–3310
13. Dao TD, Erdenedelger G, Jeong HM (2014) Water-dispersible graphene designed as a Pickering stabilizer for the suspension polymerization of poly (methyl methacrylate)/graphene core–shell microsphere exhibiting ultra-low percolation threshold of electrical conductivity. Polymer 55(18):4709–4719
14. Xue QZ (2004) Effective dielectric constant of composite with interfacial shells. Physica B: Condensed Matter 344(1):129–132
15. Xue QZ (2003) Model for effective thermal conductivity of nanofluids. Phys Lett A 307(5):313–317
16. Du F, Scogna RC, Zhou W, Brand S, Fischer JE, Winey KI (2004) Nanotube networks in polymer nanocomposites: rheology and electrical conductivity. Macromolecules 37(24): 9048–9055
17. Pang H, Chen T, Zhang G, Zeng B, Li ZM (2010) An electrically conducting polymer/graphene composite with a very low percolation threshold. Mater Lett 64(20):2226–2229
18. Zhao P, Luo Y, Yang J, He D, Kong L, Zheng P, Yang Q (2014) Electrically conductive graphene-filled polymer composites with well organized three-dimensional microstructure. Mater Lett 121:74–77

19. Huang JC (1995) EMI shielding plastics: a review. Adv Polym Tech 14(2):137–150
20. Glatz-Reichenbach J (1999) Feature article conducting polymer composites. J Electroceramics 3(4):329–346
21. Huang JC (2002) Carbon black filled conducting polymers and polymer blends. Adv Polym Technol 21(4):299–313
22. Danesh E, Ghaffarian SR, Molla-Abbasi P (2009) Effect of porosity on response behavior of carbon black-PMMA conductive composite sensors toward organic vapors, AIP Conference Proceedings, Brescia (Italy), p 361.
23. Zhang HB, Yan Q, Zheng WG, He Z, Yu ZZ (2011) Tough graphene-polymer microcellular foams for electromagnetic interference shielding. ACS Appl Mater Interfaces 3(3):918–924
24. Lee LJ, Zeng C, Cao X, Han X, Shen J, Xu G (2005) Polymer nanocomposite foams. Compos Sci Technol 65(15):2344–2363
25. Yang Y, Gupta MC, Dudley KL, Lawrence RW (2005) Conductive carbon nanofiber-polymer foam structures. Adv Mater 17(16):1999–2003
26. Thomassin JM, Pagnoulle C, Bednarz L, Huynen I, Jerome R, Detrembleur C (2008) Foams of polycaprolactone/MWNT nanocomposites for efficient EMI reduction. J Mater Chem 18(7):792–796
27. Yang Y, Gupta MC, Dudley KL, Lawrence RW (2005) Novel carbon nanotube-polystyrene foam composites for electromagnetic interference shielding. Nano Lett 5(11):2131–2134
28. Xiang ZD, Chen T, Li ZM, Bian XC (2009) Negative temperature coefficient of resistivity in lightweight conductive carbon nanotube/polymer composites. Macromol Mater Eng 294(2):91–95
29. Hermant MC, Verhulst M, Kyrylyuk AV, Klumperman B, Koning CE (2009) The incorporation of single-walled carbon nanotubes into polymerized high internal phase emulsions to create conductive foams with a low percolation threshold. Compos Sci Technol 69(5):656–662
30. Yan DX, Ren PG, Pang H, Fu Q, Yang MB, Li ZM (2012) Efficient electromagnetic interference shielding of lightweight graphene/polystyrene composite. J Mater Chem 22(36):18772–18774
31. Ameli A, Jung P, Park C (2013) Electrical properties and electromagnetic interference shielding effectiveness of polypropylene/carbon fiber composite foams. Carbon 60:379–391
32. Chen Z, Xu C, Ma C, Ren W, Cheng HM (2013) Lightweight and flexible graphene foam composites for high-performance electromagnetic interference shielding. Adv Mater 25(9):1296–1300
33. Chen L, Ozisik R, Schadler LS (2010) The influence of carbon nanotube aspect ratio on the foam morphology of MWNT/PMMA nanocomposite foams. Polymer 51(11):2368–2375
34. Landi BJ, Raffaelle RP, Heben MJ, Alleman JL, VanDerveer W, Gennett T (2002) Single wall carbon nanotube-Nafion composite actuators. Nano Lett 2(11):1329–1332
35. Cao L, Chen H, Wang M, Sun J, Zhang X, Kong F (2002) Photoconductivity study of modified carbon nanotube/oxotitanium phthalocyanine composites. J Phys Chem B 106(35):8971–8975
36. Moniruzzaman M, Winey KI (2006) Polymer nanocomposites containing carbon nanotubes. Macromolecules 39(16):5194–5205
37. Byrne MT, Gun'ko YK (2010) Recent advances in research on carbon nanotube–polymer composites. Adv Mater 22(15):1672–1688
38. Grossiord N, Loos J, Regev O, Koning CE (2006) Toolbox for dispersing carbon nanotubes into polymers to get conductive nanocomposites. Chem Mater 18(5):1089–1099
39. Tkalya E, Ghislandi M, Alekseev A, Koning C, Loos J (2010) Latex-based concept for the preparation of graphene-based polymer nanocomposites. J Mater Chem 20(15):3035–3039
40. Wang J, Shi Z, Ge Y, Wang Y, Fan J, Yin J (2012) Solvent exfoliated graphene for reinforcement of PMMA composites prepared by in situ polymerization. Mater Chem Phys 136(1):43–50

41. Arzac A, Leal GP, Fajgar R, Tomovska R (2014) Comparison of the emulsion mixing and in situ polymerization techniques for synthesis of water-borne reduced graphene oxide/polymer composites: advantages and drawbacks. Part Part Syst Charact 31(1):143–151
42. Steward P, Hearn J, Wilkinson M (2000) An overview of polymer latex film formation and properties. Adv Colloid Interface Sci 86(3):195–267
43. Tian M, Zhang J, Zhang L, Liu S, Zan X, Nishi T, Ning N (2014) Graphene encapsulated rubber latex composites with high dielectric constant, low dielectric loss and low percolation threshold. J Colloid Interface Sci 430:249–256
44. Sandler J, Kirk J, Kinloch I, Shaffer M, Windle A (2003) Ultra-low electrical percolation threshold in carbon-nanotube-epoxy composites. Polymer 44(19):5893–5899
45. Bin Y, Kitanaka M, Zhu D, Matsuo M (2003) Development of highly oriented polyethylene filled with aligned carbon nanotubes by gelation/crystallization from solutions. Macromolecules 36(16):6213–6219
46. Sandler J, Shaffer M, Prasse T, Bauhofer W, Schulte K, Windle A (1999) Development of a dispersion process for carbon nanotubes in an epoxy matrix and the resulting electrical properties. Polymer 40(21):5967–5971
47. Du J, Cheng HM (2012) The fabrication, properties, and uses of graphene/polymer composites. Macromol Chem Phys 213(10-11):1060–1077
48. Stankovich S, Dikin DA, Dommett GH, Kohlhaas KM, Zimney EJ, Stach EA, Piner RD, Nguyen ST, Ruoff RS (2006) Graphene-based composite materials. Nature 442(7100): 282–286
49. Steurer P, Wissert R, Thomann R, Mülhaupt R (2009) Functionalized graphenes and thermoplastic nanocomposites based upon expanded graphite oxide. Macromol Rapid Commun 30(4-5):316–327
50. Mutiso RM, Winey KI (2015) Electrical properties of polymer nanocomposites containing rod-like nanofillers. Prog Polym Sci 40:63–84
51. Broadbent SR, Hammersley JM (1957) Mathematical Proceedings of the Cambridge Philosophical Society. In: Percolation processes. Cambridge University Press, Cambridge, pp 629–641
52. Nan C-W (1993) Physics of inhomogeneous inorganic materials. Prog Mater Sci 37(1): 1–116
53. Regev O, ElKati PN, Loos J, Koning CE (2004) Preparation of conductive nanotube-polymer composites using latex technology. Adv Mater 16(3):248–251
54. Martin C, Sandler J, Shaffer M, Schwarz MK, Bauhofer W, Schulte K, Windle A (2004) Formation of percolating networks in multi-wall carbon-nanotube-epoxy composites. Compos Sci Technol 64(15):2309–2316
55. Ounaies Z, Park C, Wise K, Siochi E, Harrison J (2003) Electrical properties of single wall carbon nanotube reinforced polyimide composites. Compos Sci Technol 63(11):1637–1646
56. Ayatollahi M, Shadlou S, Shokrieh M, Chitsazzadeh M (2011) Effect of multi-walled carbon nanotube aspect ratio on mechanical and electrical properties of epoxy-based nanocomposites. Polym Test 30(5):548–556
57. Balberg I (1987) Tunneling and nonuniversal conductivity in composite materials. Phys Rev Lett 59(12):1305
58. Balberg I (2009) Tunnelling and percolation in lattices and the continuum. J Phys D Appl Phys 42(6):064003
59. Johner N, Grimaldi C, Balberg I, Ryser P (2008) Transport exponent in a three-dimensional continuum tunneling-percolation model. Phys Rev B 77(17):174204
60. Bug A, Safran S, Webman I (1985) Continuum percolation of rods. Phys Rev Lett 54(13):1412
61. Bug A, Safran S, Webman I (1986) Continuum percolation of permeable objects. Phys Rev B 33(7):4716
62. Balberg I, Anderson C, Alexander S, Wagner N (1984) Excluded volume and its relation to the onset of percolation. Phys Rev B 30(7):3933

63. Berhan L, Sastry A (2007) Modeling percolation in high-aspect-ratio fiber systems. I. Soft-core versus hard-core models. Phys Rev E 75(4):041120
64. Shen Y, Yue Z, Li M, Nan CW (2005) Enhanced initial permeability and dielectric constant in a double-percolating $Ni_{0.3}Zn_{0.7}Fe_{1.95}O_4$-Ni-polymer composite. Adv Funct Mater 15(7):1100–1103
65. Mezzenga R, Ruokolainen J, Fredrickson GH, Kramer EJ, Moses D, Heeger AJ, Ikkala O (2003) Templating organic semiconductors via self-assembly of polymer colloids. Science 299(5614):1872–1874
66. Celzard A, McRae E, Deleuze C, Dufort M, Furdin G, Marêché J (1996) Critical concentration in percolating systems containing a high-aspect-ratio filler. Phys Rev B 53(10):6209
67. Li J, Kim JK (2007) Percolation threshold of conducting polymer composites containing 3D randomly distributed graphite nanoplatelets. Compos Sci Technol 67(10):2114–2120
68. Yi JY, Choi GM (1999) Percolation behavior of conductor-insulator composites with varying aspect ratio of conductive fiber. J Electroceramics 3(4):361–369
69. Nan C-W, Shen Y, Ma J (2010) Physical properties of composites near percolation. Ann Rev Mat Res 40:131–151
70. Xue QZ (2004) The influence of particle shape and size on electric conductivity of metal-polymer composites. Eur Polym J 40(2):323–327
71. Bai J, Allaoui A (2003) Effect of the length and the aggregate size of MWNTs on the improvement efficiency of the mechanical and electrical properties of nanocomposites-experimental investigation. Compos Part A: Appl Sci Manuf 34(8):689–694
72. Li J, Ma PC, Chow WS, To CK, Tang BZ, Kim JK (2007) Correlations between percolation threshold, dispersion state, and aspect ratio of carbon nanotubes. Adv Funct Mater 17(16):3207–3215
73. Bryning MB, Islam MF, Kikkawa JM, Yodh AG (2005) Very low conductivity threshold in bulk isotropic single-walled carbon nanotube-epoxy composites. Adv Mater 17(9): 1186–1191
74. Moisala A, Li Q, Kinloch I, Windle A (2006) Thermal and electrical conductivity of single- and multi-walled carbon nanotube-epoxy composites. Compos Sci Technol 66(10): 1285–1288
75. Zheng W, Wong SC (2003) Electrical conductivity and dielectric properties of PMMA/expanded graphite composites. Compos Sci Technol 63(2):225–235
76. Yuan FY, Zhang HB, Li X, Ma HL, Li XZ, Yu ZZ (2014) In situ chemical reduction and functionalization of graphene oxide for electrically conductive phenol formaldehyde composites. Carbon 68:653–661
77. Sun J, Xue Q, Guo Q, Tao Y, Xing W (2014) Excellent dielectric properties of polyvinylidene fluoride composites based on sandwich structured MnO_2/graphene nanosheets/MnO_2. Compos Part A: Appl Sci Manuf 67:252–258
78. Guo Q, Xue Q, Sun J, Dong M, Xia F (2015) Gigantic enhancement in dielectric properties of polymer-based composites using core/shell MWCNT/amorphous carbon nanohybrid. Nanoscale 7:3660–3667
79. Lu K, Lago R, Chen Y, Green M, Harris P, Tsang S (1996) Mechanical damage of carbon nanotubes by ultrasound. Carbon 34(6):814–816
80. Mittal G, Dhand V, Rhee KY, Park SJ, Lee WR (2015) A review on carbon nanotubes and graphene as fillers in reinforced polymer nanocomposites. J Ind Eng Chem 21:11–25
81. Hwang TY, Yoo Y, Lee JW (2012) Electrical conductivity, phase behavior, and rheology of polypropylene/polystyrene blends with multi-walled carbon nanotube. Rheologica Acta 51(7):623–636
82. Sarvi A, Sundararaj U (2014) Enhancing electrical properties of MWCNTs in immiscible blends of poly (methyl methacrylate) and styrene-acrylonitrile copolymer by selective localization. Polym Compos

83. Haggenmueller R, Fischer JE, Winey KI (2006) Single wall carbon nanotube/polyethylene nanocomposites: nucleating and templating polyethylene crystallites. Macromolecules 39(8):2964–2971
84. Fan Z, Gong F, Nguyen ST, Duong HM (2015) Advanced multifunctional graphene aerogel-Poly (methyl methacrylate) composites: Experiments and modeling. Carbon 81:396–404
85. Aldosari MA, Othman AA, Alsharaeh EH (2013) Synthesis and characterization of the in situ bulk polymerization of PMMA containing graphene sheets using microwave irradiation. Molecules 18(3):3152–3167
86. Yuan X, Zou L, Liao C, Dai J (2012) Improved properties of chemically modified graphene/poly (methyl methacrylate) nanocomposites via a facile in-situ bulk polymerization. Exp Polym Lett 6(10):847–858
87. Martin C, Sandler J, Windle A, Schwarz M-K, Bauhofer W, Schulte K, Shaffer M (2005) Electric field-induced aligned multi-wall carbon nanotube networks in epoxy composites. Polymer 46(3):877–886
88. Moniruzzaman M, Chattopadhyay J, Billups WE, Winey KI (2007) Tuning the mechanical properties of SWNT/Nylon 6, 10 composites with flexible spacers at the interface. Nano Lett 7(5):1178–1185
89. Liu K, Chen S, Luo Y, Jia D, Gao H, Hu G, Liu L (2014) Noncovalently functionalized pristine graphene/metal nanoparticle hybrid for conductive composites. Compos Sc Technol 94:1–7
90. Martin-Gallego M, Lopez-Manchado MA, Calza P, Roppolo I, Sangermano M (2015) Gold-functionalized graphene as conductive filler in UV-curable epoxy resin. J Mater Sci 50(2):605–610
91. Wang H, Bi SG, Ye YS, Xue Y, Xie XL, Mai YW (2015) An effective non-covalent grafting approach to functionalizing individually dispersed reduced graphene oxide sheets with high grafting density, solubility and electrical conductivity. Nanoscale 7:3548–3557
92. Ryu J, Han M (2014) Improvement of the mechanical and electrical properties of polyamide 6 nanocomposites by non-covalent functionalization of multi-walled carbon nanotubes. Compos Sci Technol 102:169–175
93. Bauhofer W, Kovacs JZ (2009) A review and analysis of electrical percolation in carbon nanotube polymer composites. Compos Sci Technol 69(10):1486–1498
94. Gojny FH, Wichmann MH, Fiedler B, Kinloch IA, Bauhofer W, Windle AH, Schulte K (2006) Evaluation and identification of electrical and thermal conduction mechanisms in carbon nanotube/epoxy composites. Polymer 47(6):2036–2045
95. Yousefi N, Gudarzi MM, Zheng Q, Aboutalebi SH, Sharif F, Kim JK (2012) Self-alignment and high electrical conductivity of ultralarge graphene oxide-polyurethane nanocomposites. J Mater Chem 22(25):12709–12717
96. Du F, Fischer JE, Winey KI (2005) Effect of nanotube alignment on percolation conductivity in carbon nanotube/polymer composites. Phys Rev B 72(12):121404
97. Behnam A, Guo J, Ural A (2007) Effects of nanotube alignment and measurement direction on percolation resistivity in single-walled carbon nanotube films. J Appl Phys 102(4):044313
98. Liu F, Sun W, Sun Z, Yeow JT (2014) In effect of CNTs alignment on electrical conductivity of PDMS/MWCNTs composites, Nanotechnology (IEEE-NANO). 2014 IEEE 14th International Conference on IEEE, pp 711–714
99. Jeon K, Lumata L, Tokumoto T, Steven E, Brooks J, Alamo RG (2007) Low electrical conductivity threshold and crystalline morphology of single-walled carbon nanotubes–high density polyethylene nanocomposites characterized by SEM, Raman spectroscopy and AFM. Polymer 48(16):4751–4764
100. Haggenmueller R, Guthy C, Lukes JR, Fischer JE, Winey KI (2007) Single wall carbon nanotube/polyethylene nanocomposites: thermal and electrical conductivity. Macromolecules 40(7):2417–2421

101. Antonucci V, Faiella G, Giordano M, Nicolais L, Pepe G (2007) Electrical properties of single walled carbon nanotube reinforced polystyrene composites. Macromolecular Symposia, 247(1):172–181
102. Pötschke P, Fornes T, Paul D (2002) Rheological behavior of multiwalled carbon nanotube/polycarbonate composites. Polymer 43(11):3247–3255
103. Sumita M, Sakata K, Asai S, Miyasaka K, Nakagawa H (1991) Dispersion of fillers and the electrical conductivity of polymer blends filled with carbon black. Polym Bull 25(2):265–271
104. Tchoudakov R, Breuer O, Narkis M, Siegmann A (1996) Conductive polymer blends with low carbon black loading: polypropylene/polyamide. Polym Eng Sci 36(10):1336–1346

Chapter 4
Positive Temperature Coefficient Effect of Polymer Nanocomposites

Haiping Xu

4.1 Introduction

Positive temperature coefficient (PTC) of resistivity is an interesting phenomenon in the field of conductive polymer nanocomposites (CPC) consisting of an insulating polymer matrix and conductive fillers, which change their resistivity at the critical temperature by several orders of magnitude. Because of the commercial significance of such a temperature-activated switching feature, the PTC nanocomposites can be utilized in a wide range of industrial applications, such as self-regulating heaters, current protection devices, microswitch sensors, and other outdoor equipments [1–7]. Polymer-based PTC nanocomposites have been paid more attention because of the advantages of excellent formability, flexibility, and lightweight over the conventional inorganic PTC materials, though they have some shortcomings, such as unstable electrical reproducibility and negative temperature coefficient (NTC) effect phenomena when above the melting temperature of polymers.

Polymer materials incorporated with conductive fillers exhibiting the PTC effect were first discovered by Frydman in a carbon black (CB)-filled low-density polyethylene (LDPE) composite in 1945 [8]. After that, the PTC phenomenon has attracted much interest and studies [9–14], and the mechanism of PTC effect for CPC is also turned into the focus of the study.

In this chapter, several theories as well as their characteristics in polymer PTC nanocomposites are summarized. The key factors that influence the PTC properties such as matrix, kinds of fillers, constructural composition, and process technologies are analyzed.

H. Xu, PhD (✉)
Department of Material Engineering, School of Environmental and Materials Engineering
College of Engineering, Shanghai Second Polytechnic University, Shanghai 201209, China
e-mail: hpxu@sspu.edu.cn

© Springer International Publishing Switzerland 2016

X. Huang, C. Zhi (eds.), *Polymer Nanocomposites*,
DOI 10.1007/978-3-319-28238-1_4

4.2 Conduction Mechanism of CPC

The conductivity of CPC depends critically on the filler volume content f [15]. The conductivity increases as

$$\rho(f) \propto (f - f_c)^{-t} \tag{4.1}$$

with a parameter t between 1.65 and 2 for three-dimensional lattices [16]. f_c is called the critical or percolation threshold. The percolation behavior can be influenced by the shape of fillers. For random packing in three dimensions, f_c turns out to be about 16 %.

Figure 4.1 schematically illustrates the percolation curve of resistivity and the cluster structures of fillers, based on reports by Nakamura et al. [17]. When f is in region I, the resistivity of nanocomposite nearly equals that of the insulating polymer. At a critical filler content, f_c, in region II, the resistivity is dominated by tunneling conduction of electrons between clusters because gaps now exist between the fillers. In contrast, when the filler content is above f_c, in region III, the tunneling

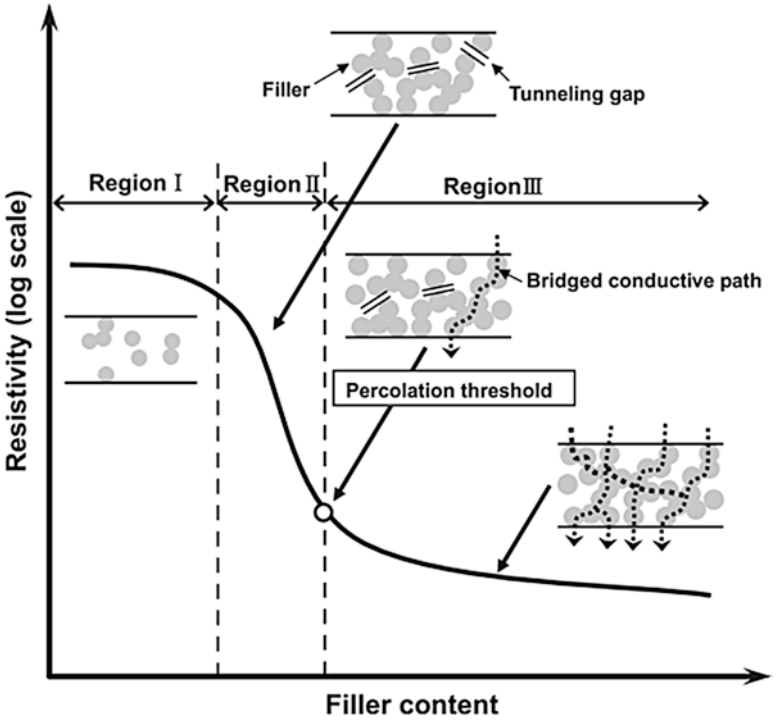

Fig. 4.1 Schematic of the general percolation curve and the presumptive cluster structure of conductive fillers (Reprinted with permission from Ref. [17]. Copyright 2012 Elsevier Ltd.)

gaps between clusters are destroyed by increasing filler content, and an ohmic conductive path is generated due to the bridged cluster between electrodes.

4.3 Theoretical and Phenomenological Background of PTC Effect

It is generally believed that the PTC effect is caused by a breakup of conductive network during sample heating. Several theories have been proposed to elucidate the specific nonlinear shift in resistivity with temperature parameter, such as thermal expansion, electron tunnel effect, electrical field emission, as well as the inner stress and phonon-assisted tunneling models. Nevertheless, these theories still remain in some problems and cannot explain experimental results clearly.

4.3.1 Conducting Chain and Thermal Expansion Theory

Kohler first suggested in 1961 that the PTC mechanism was a function of difference in thermal expansion coefficients between matrix and filler [18]. The sudden expansion, which took place at the melting point of the polymer matrix, resulted in the breakup of the conducting chains with a consequent anomalous increase in the resistivity. However, this model was not able to explain the steep decrease in resistivity above melting temperature (T_m) (so-called NTC effect), when the volume of matrix continued to increase with temperature.

4.3.2 Tunneling Current Mechanism

In contrast, the model proposed by Ohe and Natio assumed that a more uniform distribution of interparticle gaps and the gap width is small enough to allow intensive tunneling to take place at a low temperature [19]. The distribution of gaps became more random at temperatures near T_m, and a significant number of interparticle gaps were too large to allow appreciable electron tunneling, although the average gap width did not change considerably. This resulted in the elimination of many conductive paths with a consequent rise in resistivity. The influence of matrix on the PTC effect and increasing randomness of the interparticle gaps as T_m was approached were unexplained. The NTC effect, which usually took place immediately above the melting point of the matrix, also remained unexplained.

The tunneling model was further modified by Meyer taking the effect of change in crystallinity into consideration [20]. Meyer proposed the conductive particles existing only in amorphous regions being separated by crystalline films, which has

been assumed to be more conductive than amorphous ones. Thus he suggested that the anomalous rise in resistivity near melting point can be attributed to the melting of crystals. He also proposed that the NTC effect might be attributed to the immigration of CB particles, which resulted in the formation of new conductive chains of the filler particles.

Although Meyer's model can explain PTC and NTC phenomena, he has not referred to the effect of crystalline change and the NTC effect.

4.3.3 Mechanism of Congregation and Migration Changes of Filler Particles

Klason et al. explained the PTC and NTC effects on the basis of changes taking place in the carbon congregation structure with temperature [21]. Although they suggested that the NTC effect was due to the formation of new networks of conductive particles, this process was not explained in detail. On the other hand, Voet et al. attributed the PTC effect to the large volume expansion of the polymer in melting range, as well as the migration of CB to the previously CB-free crystalline region as mentioned above, which further diluted the concentration of the filler in matrix and increased resistivity [22].

4.3.4 Electrical Field Emission Mechanism

Based on above viewpoints, Allak H. K. proposed that contact resistance between particles is important in case that filler volume concentration exceeds the percolation threshold, and charge transport through filler phase takes place via direct contact between particles. On the contrary, when a thin, insulating polymer layer separates the filler particles, conductivity is dominated by charge transport via tunneling effect [23].

Additionally, the dynamic factor resulting in reaggregation of CB particles has been considered as the attraction between them (such as Van der Waals interaction or covalent bonds between them), which is too weak to overcome the separation resulting from vigorous macromolecular movement at temperatures over T_m, so NTC effect is caused by a decrease of elastic modules of polymer at high temperature.

4.3.5 Internal Stress Mechanism

During curing of the thermoset matrix or cooling of thermoplastic matrix in polymer composites, internal stresses appear [24]. These stresses increase the pressure between adjacent particles, giving contact pressure and decreasing the contact resistance. Hence, internal stresses in polymer matrix caused by shrinkage, external mechanical actuation, or thermal expansion play an important role in the conductivity of composites. A shrinkage of polymer during processing can induce high internal stresses. This reduces the interparticle resistance. Instead, the observed strong resistivity change is caused by a release of particle–particle contact pressure and a change in gap distance. Polymer and the conducting filler particles are in a state of close packing with intimate contact to next neighbors, forming conducting paths throughout the composite. During heating, the polymer expands much more than the filler particles themselves. The contact pressure between adjacent filler particles is reduced leading to a moderate resistivity increase.

4.3.6 The Percolation Theory and PTC Effect

According to percolation theory and above PTC theories, the PTC effect of polymer nanocomposites strongly depends on filler content. The PTC curve practically coincides with that of percolation curve (as shown in Fig. 4.1). Conductive particles agglomerate in composite as clusters. As the size and number of clusters increase with increasing filler content, at some critical content, the cluster becomes infinite and makes a contribution to the composite conductivity. The agglomerates of particles in infinite cluster can be abruptly separated, and the composite become dielectric by thermal expansion of polymer matrix. So the greatest PTC effect usually takes place in composites with moderate filler content.

In summary, because these theories cannot be observed by experimental techniques, there has been difficulty in finding a comprehensible explanation for the effect, and thus most of mechanisms still remain controversial.

Although there is no satisfactory theory to explain the PTC and NTC phenomena, all of these models suggest that the volume expansion plays an important role in PTC behavior, and the explanation based on tunneling effect is widely accepted. According to this mechanism, electrons pass through the thin gaps between adjacent CB particles, aggregates, and agglomerates at a practical magnitude of the electrical field. The rapid expansion near the melting point of polymer matrix increases the width of gaps and thus hinders the process of electron tunneling. On the other hand, NTC effect is presumably due to the reaggregation of conductive particles in polymer melting state and therefore reparation of disconnected conductive pathways.

4.4 Influence of Polymer Matrix on PTC Effect of Nanocomposites

The polymer is framework of a nanocomposite, and melting expansion is the main role in PTC effect. Therefore the conductivity of polymer nanocomposites is sensitively influenced by characteristics of polymer matrix such as chemical structure, thermal property, morphology, crystallinity, and processing conditions.

4.4.1 Influence of Polymer Crystallinity on PTC Effect

A number of researchers observed strong correlation between crystallinity and PTC effect. The amorphous polymer PTC composites are hard to obtain great PTC effect because the volume thermal expansion of amorphous polymers is too small to produce significant resistivity change. This has led some scientists to suggest that crystallinity has an influence on electrical conductivity [25–27].

The PTC effect is diminished in nanocomposites of semicrystalline polymers if specimens are quenched rapidly to yield low crystallinity or if crystallinity of specimens is reduced by thermal degradation. On the other hand, increased crystallinity of polymer due to annealing promotes PTC effect. Figure 4.2 shows the resistivity as a function of temperature for various polymer composites loaded with 50 wt % CB [28]. For all the polymer/CB composites, the resistivity increased steadily as the temperature was raised and increased more rapidly near the melting temperature when polymer crystal started to melt. When the temperature of composite approached the melting point of polymer resins, the conduction paths formed of the CB interface were damaged because of the partial melting of polymer crystallites; thus, the resistivity of composites increased drastically. The resistivity reached a

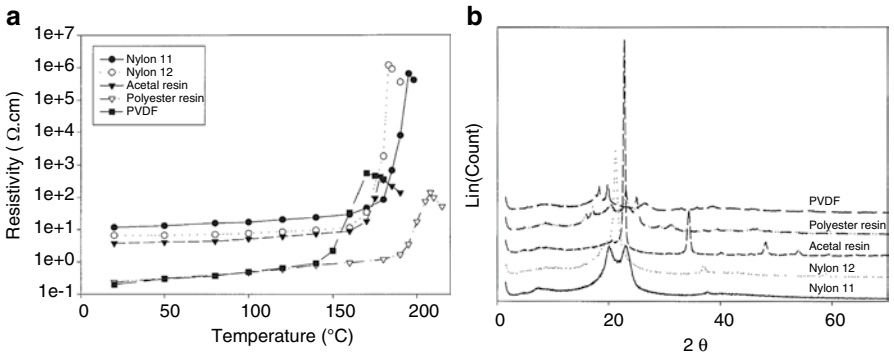

Fig. 4.2 (**a**) Resistivity of various resins/carbon black (50/50 wt %) composites as a function of temperature; (**b**) X-ray diffraction patterns of various polymers (Reprinted with permission from Ref. 28. Copyright 2004 Wiley Periodicals, Inc.)

peak value above the melting temperature and then decreased with a further increase in temperature which is called the NTC effect.

There was a steep increase in resistivity near the melting point of each polymer. The nylon-12 composite had the largest PTC intensity of about 2.0×10^5, although the polyacetal and polyester composites had small PTC intensities. These various PTC intensities were attributed to the difference of crystallinity in the polymer matrix. The larger the crystallinity of the polymer matrix is, the larger the expansion of the polymer becomes when the polymer crystal starts to melt; that is, the conduction path in the composite was effectively interrupted. In these experiments, the crystallinities of the used polymers were measured by X-ray diffractometer at room temperature as shown in Fig. 4.2. As can be seen, the specific crystal peaks of polymer were observed and then were computed. The degrees of crystallinity of the polymer matrices were 48.06 % (nylon-11), 48.30 % (nylon-12), 38.62 % (polyacetal resin), 36.26 % (polyester resin), and 40.91 % (PVDF), respectively. From these data, it was confirmed that the PTC intensity was proportional to crystallinity of polymer.

However, this has been questioned by others. Some experiments do not support a correlation between PTC intensity (the ratio of peak resistivity to the room temperature resistivity) and crystallinity [29–31]. Preparation of an amorphous polymeric PTC composite with PTC intensity of about 10^3 is reported using polyurethane (PU) as matrix and CB as conductive filler and adding reactive low molecular crystals and stearic acid as crystalline phase into polymers [29]. As the stearic acid could melt and expand rapidly in a very narrow temperature range around the melting point, the volume fraction of CB could consequently reduce sharply, which results in the disconnection of conductive channels and cause the amorphous rubbery composite to produce PTC effect. Comparing to crystalline PTC plastics, the amorphous rubbery PTC materials can easily form cross-linking to prevent NTC effect, while it still has rubbery toughness, processability, and moldability. Therefore, it was assumed that the PTC effect is due to the difference of the thermal expansion coefficients between matrix and filler.

4.4.2 Influence of Melting Temperature of Polymer on PTC Critical Temperature

Polymers can show three significant reversible structural transitions, which are thermally induced: crystallization and melting in a semicrystalline phase and a glass transition in the amorphous phase. All three transitions are related to a relative large volume change or to a pronounced change in the thermal expansion.

The improvement on PTC properties of CB-filled semicrystalline polymer composites, such as CB-filled high-density polyethylene (HDPE), poly(vinylidene fluoride) (PVDF), and polypropylene (PP), respectively, has received considerable attention due to its appropriate crystallinity, melting point, processability, and relatively low price [4, 32, 33]. However, one of the great disadvantages that the

semicrystalline used as polymer host is the single temperature at about 130 °C (for HDPE) or 160 °C (for PVDF or PP). From the practical aspect, a difference of the critical temperature at which the PTC anomaly occurs is of special interest in temperature sensor. Recent work in this field has led to a better control of critical temperature.

According to the mechanism mentioned above, the PTC transformation is triggered by the melting of crystalline phase; therefore, the critical transformation temperatures are near the melting points of these polymers and different with the variation of polymer [34, 35]. The PU/CB composite does not have PTC effect in the absence of stearic acid, but it exhibits significant PTC effect and little NTC effect in presence of stearic acid [29]. The critical transformation temperature of PU/CB composites is the melting point of stearic acid (67–71 °C). The critical transformation temperature of polymer-based composites can be adjusted by adding low molecular crystals with different melting points or intermixture immiscible polymer blends to obtain two resistivity jumps which designated as the double-PTC effects. The highest critical transformation temperature was reported above 200 °C [36]. For example, for CB-filled ETFE/HDPE composite, the large thermal expansion owing to the melting of HDPE and ETFE crystallites is responsible for the first and second critical transformation temperature [36]. Akihiko et al. found that the onset of PTC effect with an Ni content of 20 vol.% is approximately 100 °C lower than the melting point of the PVDF matrix [37]. These results are shown in Fig. 4.3.

4.4.3 Influence of Binary-Polymer Blends on Percolation Threshold

It should be strongly stressed that most past investigations on the PTC and NTC effects of CB-filled polymer composites were focused on composites containing CB and a single semicrystalline polymer. However, it is often difficult to reach a suitable conductivity by addition of an amount of CB small enough to preserve the mechanical properties of polymer and to reduce as much as possible the cost of the final composite. Few studies were conducted on the PTC and NTC effects of CB-filled immiscible semicrystalline polymer or multiphase polymeric blends [8, 9, 12–14, 38–41]. The purposes include (1) to obtain a conductive composite with a very low percolation threshold and (2) to provide a new approach to eliminate the NTC effect even at temperatures much higher than the melting point of the polymer.

The selective dispersion of CB in one phase or at the interface of two polymers causes a decrease of the percolation threshold to a very low level. It is proposed that the heterogeneous distribution of CB in immiscible polymer blends is mainly due to the difference in affinity of CB particles to each component of polymer blends, i.e., the difference in the interfacial free energy of the polymer/filler. Gubbels et al. reported the two-step percolation in the LDPE/EVA composite filled with CB [42].

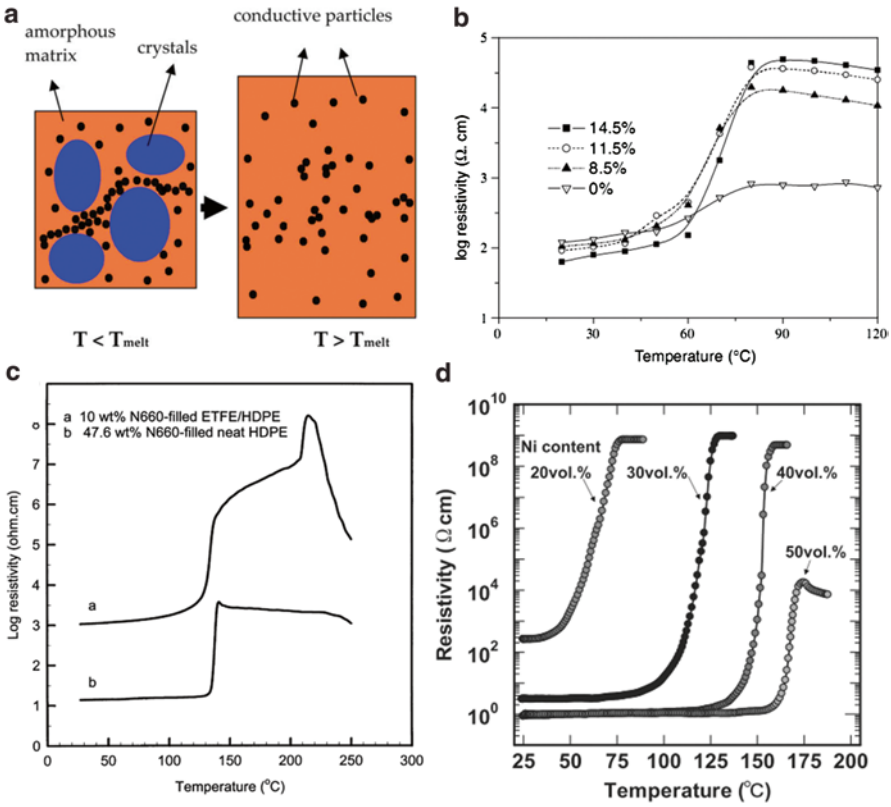

Fig. 4.3 (**a**) Schematic of crystal melting and the origin of the PTC effect in the composites of semicrystalline polymers. Tmelt represents the melting temperature of the crystals. Melting of large amounts of crystals augments the volume and disturbs the connectivity of the conductive particles (Reprinted with permission from Ref. [34]. Copyright 2008 Elsevier Ltd). (**b**) Resistivity of PU/CB composites vs. temperature at different stearic acid content (Reprinted with permission from Ref. [29]. Copyright 2005 Elsevier Ltd). (**c**) Log resistivity of 10 wt% N660-filled ETFE/HDPE(4/1) composite and 47.6 wt% N660-filled neat HDPE composite as a function of temperature (Reprinted with permission from Ref. [36]. Copyright 2000 Elsevier Science Ltd). (**d**) PTC curves of PVDF/Ni composites at Ni content of 20, 30, 40, and 50vol.% (Reprinted with permission from Ref. [37]. Copyright 2012 Elsevier Ltd.)

They thought that CB particles were predominately dispersed in LDPE first due to lower interfacial free energy and then began to be localized at the LDPE/EVA interface when the CB content in LDPE had approached a saturation limit.

Di et al. proposed that the high viscosity of UHMWPE melt will minimize the migration of carbon particles into the polymer matrix and deformation of the polymer particles during the hot compaction [11]. This provides the possibility of reducing the percolation threshold by favoring the heterogeneous distribution of CB particles and eliminating the NTC effect by hindering the movement of CB particles in the UHMWPE melt.

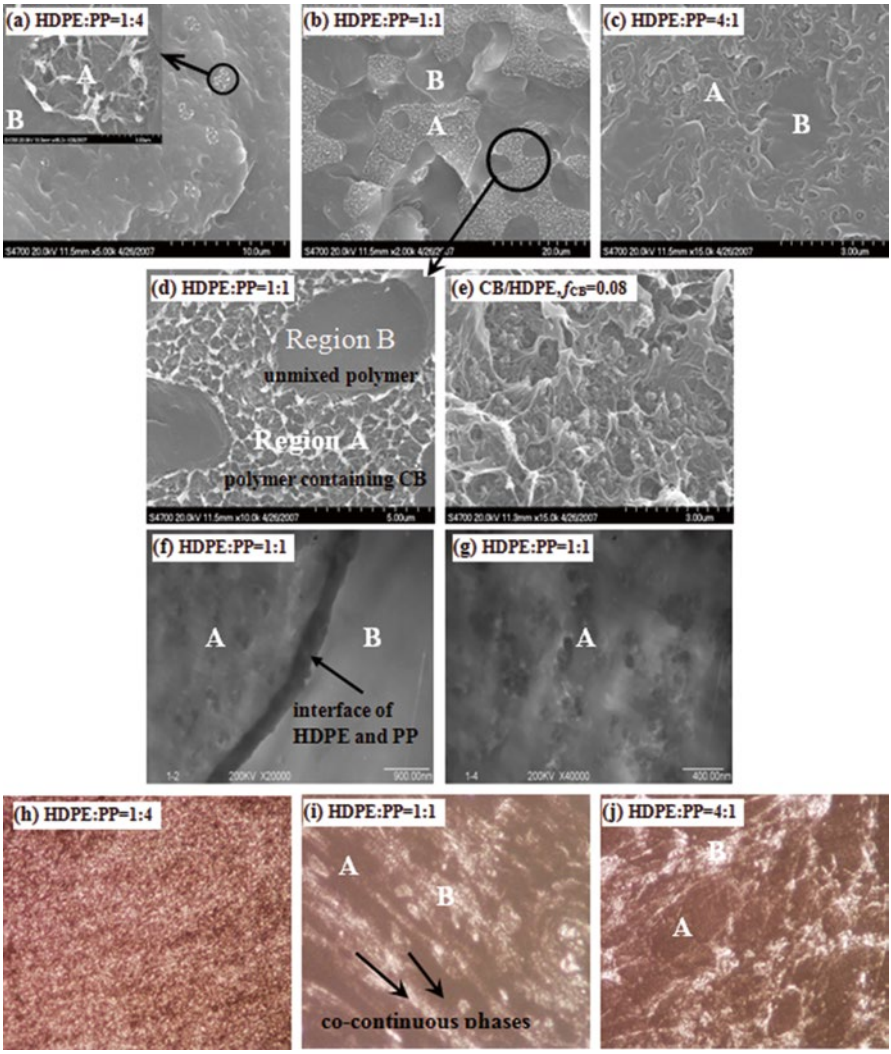

Fig. 4.4 SEM, TEM, and OM images of the (MNCB-HDPE)/PP composites at f_{MNCB} =0.03: (**a**–**c**) SEM images of fracture surfaces of the composites at volume ratios of HDPE:PP =1:4, 1:1, and 4:1; the inset in (**a**) shows a magnified image of the A zone; (**d**) magnified SEM image of the composite at HDPE:PP =1:1; (**e**) SEM image of the fracture surface of the CB/HDPE composite at f_{MNCB} =0.08; (**f**, **g**) TEM images of slices of the composite at the volume ratio of HDPE:PP = 1:1; (**h**–**j**) OM images of the (MNCB-HDPE)/PP thin films at volume ratios of HDPE:PP = 1:4, 1:1, and 4:1, showing that the area of the MNCB-filled HDPE phase (*region A*) increases with increasing volume ratio of HDPE:PP, while the area of the PP phase without MNCB loading (*region B*) decreases (Reprinted with permission from Ref. [39]. Copyright the Royal Society of Chemistry 2008)

Feng et al. have studied the double-PTC effects of CB-filled ETFE/HDPE composites; they observed from the optical microscopy and time-of-flight secondary mass spectrometry results that the CB particles were only selectively localized in the HDPE phase because of the high viscosity of ETFE matrix [13]. Ying et al. also believed that the elimination of the NTC effect and a good reproducibility of LMWPE/UHMWPE blends filled with short carbon fibers were due to the very high viscosity of UHMWPE [11].

Xu et al. present a robust and simple procedure to prepare binary-polymer matrix composites with strong PTC effect [39]. The intuitive and detailed double-percolation structure is observed on basis of morphological evidence as shown in Fig. 4.4. Modified nanoscaled carbon black (MNCB) is often selectively localized in HDPE phase that forms continuous electrically conductive channels in the polymer, and both HDPE and PP phases are also continuous in three-dimensional space. When the volume ratio of the two polymers is very close to 1:1, the remarkable PTC intensity (PTCI), namely, PTCI = 3.3×10^7 in (MNCB-HDPE/PP) nanocomposite, is observed.

4.5 Influence of Conductive Filler on PTC Effect of Nanocomposites

The conventional method of preparing conductive polymer composites is to disperse the conductive fillers such as CB, carbon fiber (CF), graphite, and metal particles, throughout the polymer matrix. The conductivity of polymer composites depends not only on the characteristics of polymer matrix but also on the properties of fillers such as particle size, concentration, dispersion state and aggregate shape, etc. Clarifying the role of all these factors enables us to choose the suitable processing method for obtaining the composites and to improve the electrical characteristics of these systems.

4.5.1 The Kinds of Conductive Filler

The usual conductive fillers used can be classified as carbon system such as CB, CF, graphite, and metallic system such as nickel (Ni), copper (Cu), and zinc (Zn). The superconductive materials can act as a potential filler to be used in PTC materials.

4.5.1.1 Carbon System Filler

The use of polymer conductive composites based on carbon fillers (like carbon black, carbon nanotube, graphite, graphene, carbon fiber, metal-coated carbon fiber, etc.) was found to be superior in many electrical and electronic applications

compared to metals because of their lightweight, low cost, and oxidation resistance. An increasingly important use for CB is as the filler in polymers in order to enhance the electrical conductivity of the polymer. CB varies greatly in their structure. The structural characterization of these materials is difficult because of the very small particle size in the materials. In general, the structures are described as being either a high structure or a low structure. A high-structure CB usually consists of many primary particles of CB fused together in an aciniform aggregate structure. A low-structure CB consists of a small number of CB particles fused together in an aggregate, generally with a larger primary particle size. The use of CB of different structures will affect the conductivity in a given polymer system to varying extents. Normally a polymer loaded with a high-structure CB or a CB with a small particle size will have a lower electrical resistivity than a CB which possesses a low structure or large particle size, at the same CB concentration in a composite [43, 44].

Natural graphite is a well-known material with good electrical conductivity and has been extensively applied to make polymer/graphite composites [45]. The use of expanded graphite in polymer/graphite composites will greatly enhance their electrical conductivity. In addition, it is interesting to note that graphite has different conductivities at different directions.

The electrical conductivity of CF is between CB and graphite. The high aspect ratio of CF would affect the physical and mechanical properties of the synthesizing polymer composites. But the higher cost limits the usage of CF. It can be considered as the second conductive filler, which are considerably longer than the CB particles to bridge distant and unconnected CB particles and which are more likely to form conductive pathways within the polymer blend [46–49].

The PTC effect of electrical resistivity of UHMWPE/LDPE/CF nanocomposites was investigated by Zhang et al. as shown in Fig. 4.5. Figure 4.5a reveals a typical percolation curve of resistivity, and the scaling law demonstrated by Ref. [50] gives f_c of 2.4 vol.%. Comparing with the CB/UHMWPE composites, f_c of UHMWPE/LDPE/CF composites was much lower. The low f_c is mainly attributed to the large aspect ratio of CF and is also influenced by the binary phase of different matrices. From Fig. 4.5b, we can see all specimens exhibited obvious PTC effect. The PTC effect occurred at different temperatures for different samples which increase with CF content evidently, not at a constant temperature. The PTC intensity was enhanced firstly and then decreased with increasing CF content.

The CNTs have been used extensively as conductive filler in different polymer matrices and reported to increase the electrical conductivity of the composites at relatively low concentration [51–55]. Gao et al. reported that the PTC intensity of the CNT/HDPE composites is lower than that of CB/HDPE composites, which is due to the entanglement between CNTs [56]. It is found from Fig. 4.6 that the CNT/HDPE thermistors exhibit much larger hold current and higher hold voltage than the commercial CB/HDPE thermistors; such high voltage-bearing or current-bearing capacity for the CNT/HDPE thermistors is mainly attributed to the high thermal conductivity and heat dissipation of entangled CNT networks. Moreover, the CNT/HDPE also exhibits quick response of current decay to applied voltages, comparable to the commercial CB/HDPE thermistors [57].

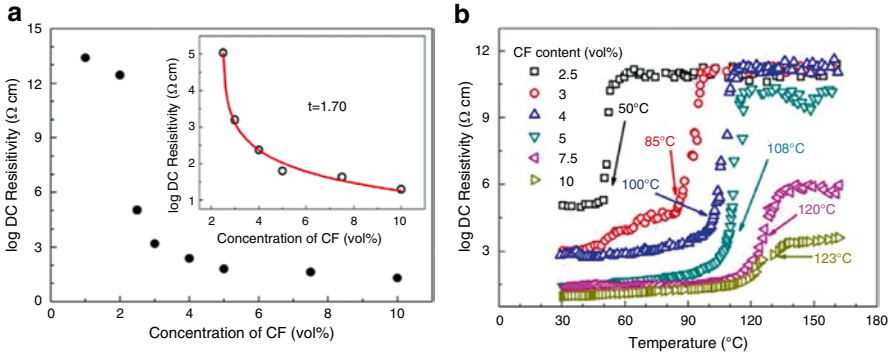

Fig. 4.5 (**a**) DC resistivity of UHMWPE/LDPE/CF composites against CF concentration at room temperature, the inset is the calculation and experimental results (*black open circles*) according to the scaling law; (**b**) PTC effect of UHMWPE/LDPE/CF with CF contents of 2.5–10 vol.% (Reprinted with permission from Ref. [50]. Copyright 2014 Elsevier Ltd.)

Graphene has a large aspect ratio, exceptionally high mechanical strength and superior electrical and thermal conductivity. Thus, it can replace CNTs for reinforcing polymers to form electrically conductive polymer nanocomposites. It has been reported that graphene-based polymer nanocomposites exhibit better electrical and mechanical properties than the CNT/polymer composites [58–60].

In Fig. 4.7, Seung et al. incorporated a novel type of electrochemically exfoliated graphene sheets (EGs) fillers into poly(methyl methacrylate) (PMMA) polymer matrices. Without the conventional oxidation/reduction process to prepare the graphene-based fillers, the EGs/PMMA polymer nanocomposites showed the high electrical conductivity of $417 \pm 83 Sm^{-1}$ at a content loading of 5.8 vol.% and a low percolation threshold of 0.37 vol.% [60].

4.5.1.2 Metal or Metal Ceramic System Filler

Polymer nanocomposites filled with conductive metal particles are of interest for many fields of engineering [61–64]. The interest arises from the fact that the electrical characteristics of such nanocomposites are close to the properties of metals, whereas the mechanical properties and processing methods are typical for plastics. It was observed experimentally that the electrical conductivity and the PTC effect of metal–polymer nanocomposite predominantly depend on the electrical conductivity, the particle shape and size, and the volume fraction and the spatial arrangement of the metal particles. In the present studies, aluminum, nickel, iron, zinc, and copper powders with essentially different particle shapes (irregular, dendritic, and almost spherical) as well as the metal ceramic compounds such as TiB_2, TiC, NbB_2, WSi_2, $MoSi_2$, V_2O_3, and VO_2 were used as conductive fillers. However, the usage of metallic fillers in PTC composites is limited to some extent because of the easy

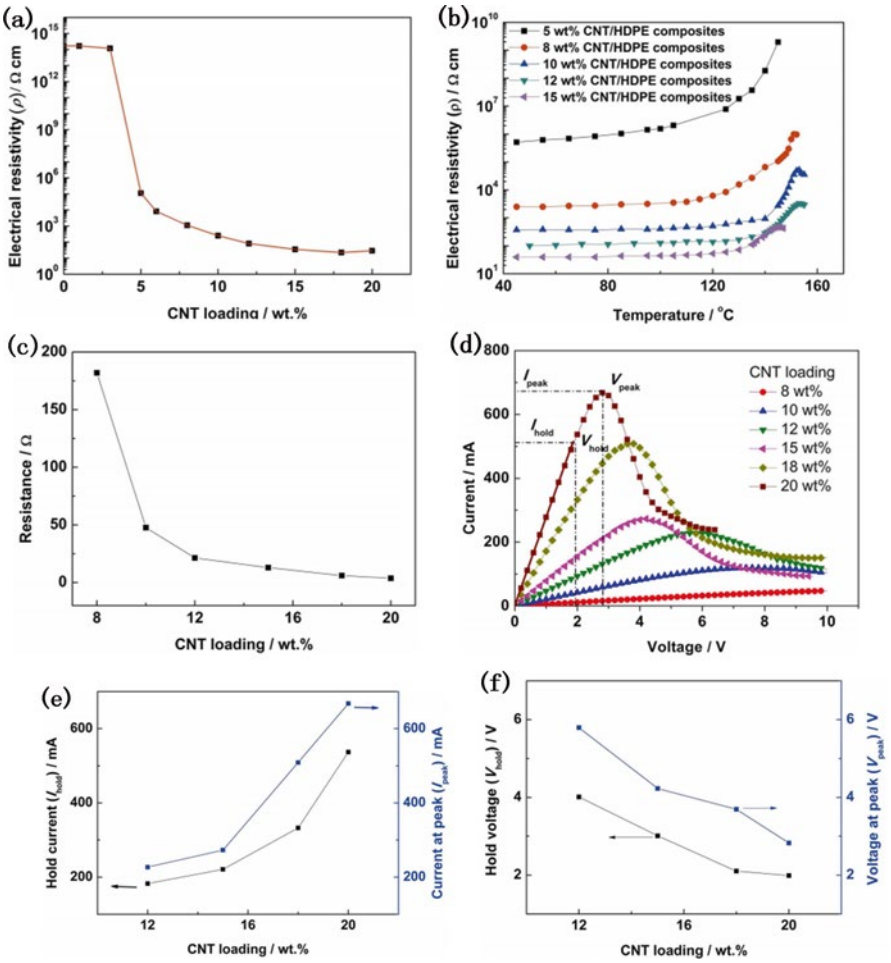

Fig. 4.6 Electrical properties of the CNT/HDPE composites. Electrical resistivity (r) of the CNT/HDPE composites as a function of (**a**) CNT loadings and (**b**) temperature; (**c**) electrical resistance of the CNT/HDPE thermistors at room temperature; (**d**) voltage–current curves of the CNT/HDPE thermistors, implying a typical PTC effect induced by applied voltages; (**e**) hold current and (**f**) hold voltage of the thermistors as functions of CNT loadings (Reprinted with permission from Ref. [57])

oxidation of the surface, and the surface oxide layers formed may decrease the conductivity. Moreover, the high cost of the metallic fillers is another reason for limiting the widely application.

Andrzej et al. studied the nanocomposites based on polymer blends of HDPE and polybutylene terephthalate (PBT), filled with dispersed silver nanoparticles (Ag) [65]. It was found from Fig. 4.8 that depending on the choice of CPC structure,

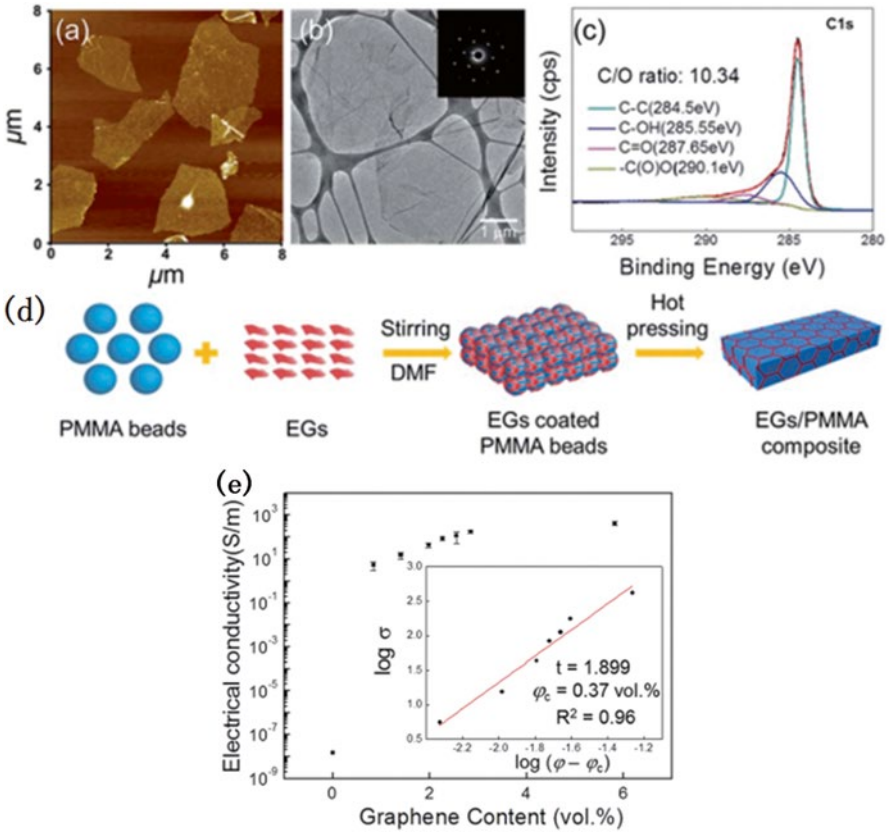

Fig. 4.7 Morphology, thickness, and chemical structure of EGs characterized using (**a**) AFM, (**b**) TEM, and (**c**) XPS; (**d**) schematic illustration of EGs/PMMA composites with the segregated networks of EG fillers. (**e**) Semi-log plot of electrical conductivity of the EGs/PMMA composites as a function of EG filler content (Reprinted with permission from Ref. [60]. Copyright the Royal Society of Chemistry 2015)

the commutation temperature from a conducting state to an insulating state can be observed between 45 and 180 °C. The observed high intensity of PTC effect, i.e., a sharp (narrow temperature range) and strong (10 orders of magnitude) resistivity increase, makes such composites promising for current limiting devices and temperature sensors.

Mitsuhiro et al. have focused on titanium carbide (TiC) from particles with conductivity and thermal conductivity superior to CB as conductive particles to be used in a high-polymer PTC thermistor [66]. Figure 4.9 shows the PTC characteristics of TiC/PE composites. The resistivity showed positive temperature dependence and changed abruptly in the tenth order of its magnitude during the melting transition of PE. The electrical current cutoff characteristics of the samples indicated excellent

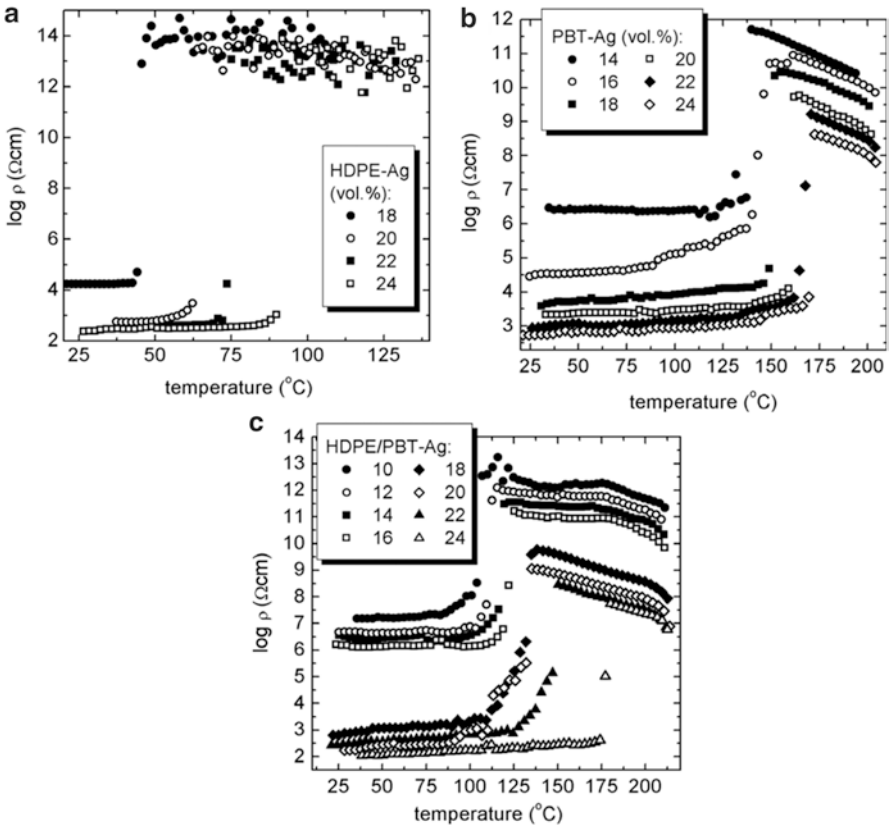

Fig. 4.8 (**a**) The values of the resistivity vs. temperature for HDPE–Ag composites with different contents of the filler; (**b**) temperature dependence of the resistivity of PBT–Ag composites filled with the different volume fractions of Ag; (**c**) temperature dependence of resistivity for the HDPE/PBT–Ag composites with different volume fractions of Ag (Reprinted with permission from Ref. [65]. Copyright 2009 Elsevier Ltd.)

features in the overcurrent response despite their low resistivity values, as compared with those of other PTC materials.

4.5.1.3 Morphological Control Through a Mixed Filler

To achieve a lower percolation threshold or a lower cost, more than one type of fillers, particularly fillers with different aspect ratios, can be used to prepare PTC nanocomposites [33, 67–71]. These hybrid fillers, which contain different carbon fillers, such as CNTs, CF, graphite-based fillers, and CB, are often used due to their distinctly different aspect ratios and similar carbon-based structures.

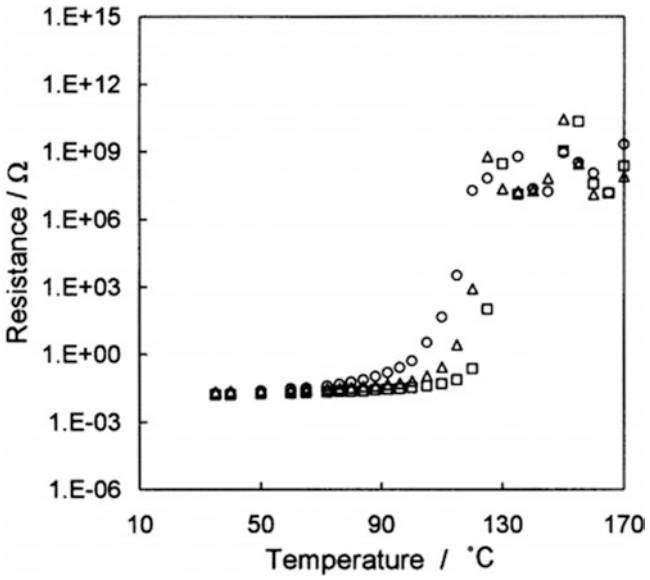

Fig. 4.9 T–R characteristics of TiC/PE composites. f=0.54 (O); 0.58 (Δ); 0.62 (γ) (Reprinted with permission from Ref. [66]. Copyright 2005 Wiley Periodicals, Inc.)

As shown in Fig. 4.10, the percolation thresholds of these systems are often near or below the average of the systems that are filled with a particular type of carbon filler, indicating that a considerable amount of a high aspect ratio and high price filler can be replaced with a low aspect ratio and low price filler [72]. It has been reported that a low aspect ratio filler can act as a bridge between the networks that are formed by the high aspect ratio filler [71] or form special configuration conductive networks with the high aspect ratio filler [33].

In Fig. 4.11, by introducing 0.5 vol.% CNTs into the 4 vol.% CB-filled UHMWPE0.8–PVDF0.2 composites, the initial resistivity decreased by about two orders of magnitude, and the PTC intensity increased by about 30 %. Owing to the three-dimensional conductive networks provided by tube-shaped CNTs and spherical CB and the high viscosity of the UHMWPE matrix, favorable PTC repeatability was also achieved [73].

4.5.2 The Grain Size and Morphology of Conductive Filler

Polymer materials in their pure state are excellent electrical insulators, which can also become conductors when filled with various kinds of conductive particles. In general, the electrical conduction process in conductive polymer composites is

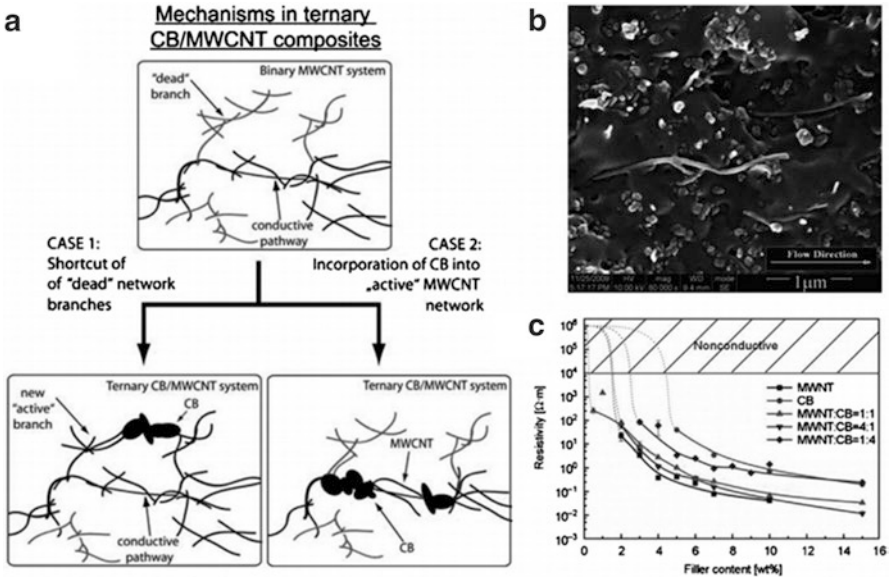

Fig. 4.10 (**a**) The mechanism of synergistic effect between MWNT and CB for the formation of conductive network in CPCs based on epoxy matrix (Reprinted with permission from Ref. [71]. Copyright 2009 Springer Science Business Media); (**b**) the grape cluster-like conductive network constructed by CB and oriented MWNTs in PP matrix (Reprinted with permission from Ref. [33]. Copyright 2012 Elsevier Science Ltd); (**c**) the electrical percolation behavior of CPCs based on PP containing different fillers or hybrid fillers, showing lower percolation threshold can be obtained for CPCs containing MWNT and CB in the ratio of 1:1 (Reprinted with permission from Ref. [68]. Copyright 2012 BME-PT)

complicated and dependent on a large number of parameters, mainly on filler concentration. In addition to the amount of loading, filler particle size and morphology structure, filler–matrix interactions, and processing techniques are key factors in determining the physical properties [74, 75].

4.5.2.1 Effect of Filler Size

Experimental data supported that the composite loaded with the larger average filler size exhibits a higher PTC intensity and room temperature resistivity than those composites with the same filler content. The reason for this difference in the PTC intensity lies on the fact that the entanglement between the particles and polymer chains increases and the number of conductive pathways is smaller and the resistivity of the composite is sensitive to even a small decrease in the number of conductive paths. For example, the degree of entanglement between a large-sized CB and the polymer chains is much higher than that between a small-sized CB and the

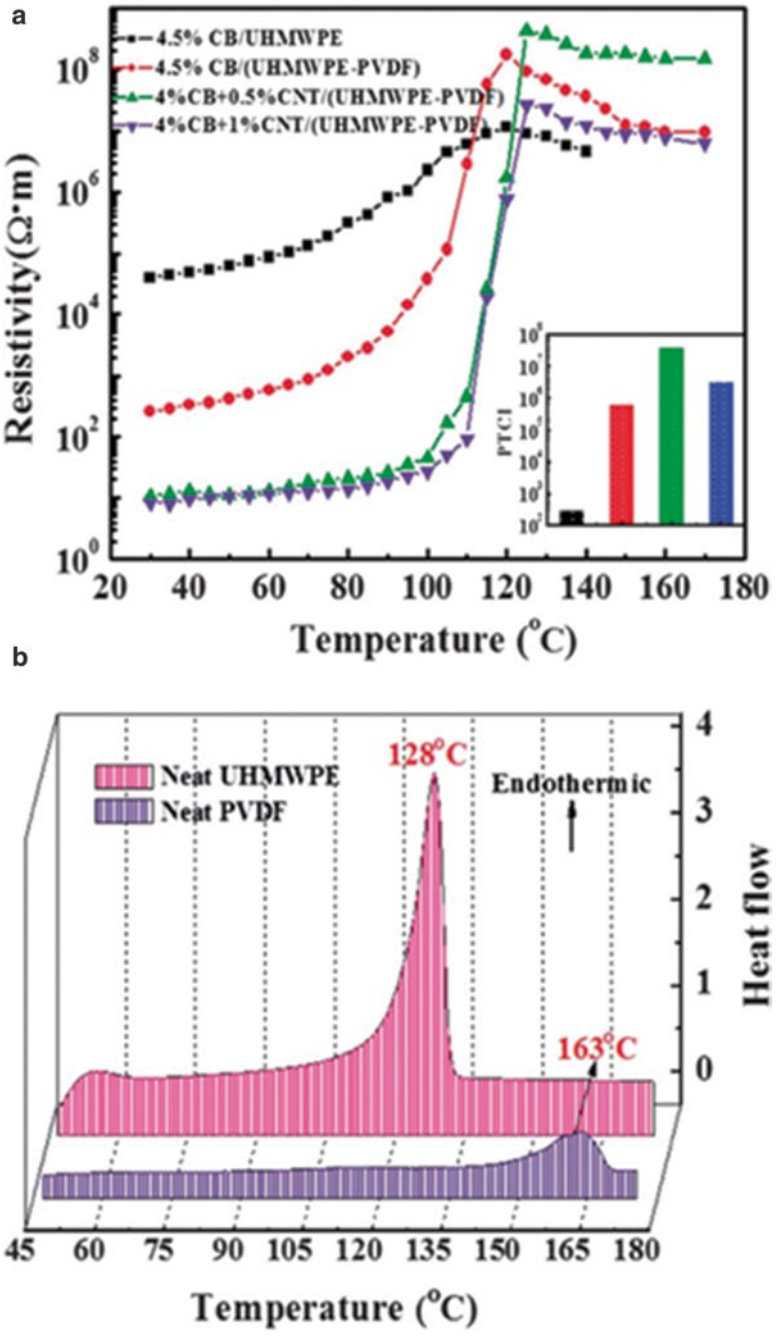

Fig. 4.11 (**a**) Resistivity of the single UHMWPE and UHMWPE0.8–PVDF0.2 based composites with different volume fractions of CB and CNTs as a function of temperature. The inset is their PTC intensities and the same color represents the same system. (**b**) DSC thermograms of neat PVDF and neat UHMWPE (Reprinted with permission from Ref. [73]. Copyright the Royal Society of Chemistry 2013)

polymer chains; thus, the movement of the polymer chains caused by thermal expansion due to the melting of the crystallites may introduce a major deformation of the conductive network structure and break up a large number of the conductive paths. Therefore, composites with a larger particle-size CB show a higher PTC intensity, but their room temperature resistivity is usually higher. This is a major disadvantage for the use of large CB particles in many industrial applications. A balance between the PTC intensity and the room temperature resistivity is then attempted by using a mixture of large-sized and small-sized CB particles in the composites.

4.5.2.2 Effect of Filler Shape

In the previous sections, spherical particles were always assumed in modeling the composites. In practice, however, fillers are often used which have a shape very much different from a sphere. Examples are aluminum flakes, stainless steel fibers, or carbon fibers. The percolation threshold can be drastically reduced for particles with an aspect ratio larger than one. One can easily apperceive that fibers with high aspect ratio can drastically increase the connecting paths and reduce the percolation threshold. Carbon fibers with an aspect ratio of 1000 need only 1.0 vol.%, whereas fibers with an aspect ratio of 10 need a volume fraction of about 10 % in order to achieve the same resistivity [76].

4.5.2.3 Effect of Filler Distribution

The conductive properties depend strongly on the distribution of filler particles in a composite, and the distribution state of filler particles is mainly influenced by the chosen processing technique. For industrial production, extrusion or injection molding processes are used quite often. Using fibers, flakes, or carbon black, the high shear forces occurring at the nozzle, both methods cause an alignment of the filler particles in the flow direction. Hence, the orientation of the fibers or flakes in the final part depends strongly on the form of the mold and the flow of the polymer.

Care must be taken if composite parts are made by compression molding of polymeric and conductive powders. The carbon black particles are much smaller than the polymer particles. This results in a core–shell structure. The polymer particles are surrounded by shells of carbon black, forming a percolating network. The percolation threshold of a core–shell structure is considerably lower than that of homogeneous composite. A controlled orientation of filler particles and an anisotropic conductivity can be achieved by applying electrical or magnetic fields during the processing. This can serve not only for relative high conductivity at low filler content but also for unidirectional conductivity.

4.6 The Effective Ways to Improve the PTC Properties of Nanocomposites

Research and development activities on PTC materials have brought successful industrial applications, and an enormous amount of knowledge has been accumulated in this field. Nevertheless, many problems are not solved yet. Polymer PTC composites have some shortcomings, such as unstable electrical reproducibility due to irregular structure changes in heating/cooling cycles, NTC phenomena, and the slow response rate of PTC effect associated with an adverse effect on desired switching properties. Several ways which include cross-linking, filler treatment, and polymer blends are introduced to increase stability of PTC materials.

4.6.1 Surface Modification of Conductive Filler

The conductive filler, especially for CB, produces large cohesive strength between the individual fine particles, which leads to aggregates of particles, having diameters of not less than several microns. Therefore, it is extremely difficult for CB to be dispersed on the order of submicrons in the medium. So it is very necessary to make a suitable modification on the CB surface in order that it can be more evenly dispersed in the matrix and the interfacial interaction between CB and polymer can be strengthened. Relevant developments in polymer blends based on CB with surface modification such as grafting cross-linking, plasma sputtering, gasification etching, and emulsion polymerization have shown very efficient in improving dispersion behavior and morphological stabilization [77–79], yet the common dispersants would only have a reaction with surface of fillers and not with the molecule of polymers. Grafting a coupling agent to the CB surface can be considered as one of the options to deal with these problems. The coupling agent such as titanate coupling agent (NDZ-102) or silane coupling agent (KH550) has two quite different chemistry reactive groups in the molecule structure, which can react with inorganic filler forming the firm chemical bonds and synchronously link with the organic polymer molecules through physical entanglement or chemical cross-linking, respectively, bridging the filler and polymer tightly together [78]. That is, the filler can be soaked better in the polymer to improve the compatibility of the composite (Fig. 4.12).

He et al. reported a nanocomposite with nanosilver-decorated reduced graphene oxide (Ag–RGO) sheets incorporated into PVDF resulting in a low percolation threshold of 0.17 vol.% [80]. The synthesized Ag–RGO hybrid sheets were proved to be more effective in improving the electrical conductivity of polymer composites when compared to RGO sheets. This was attributed to high intrinsic electrical conductivity of silver. Figure 4.13 illustrated the step procedures of preparing stable Ag–RGO suspension and the PTC effect, making it attractive for a variety of smart device applications.

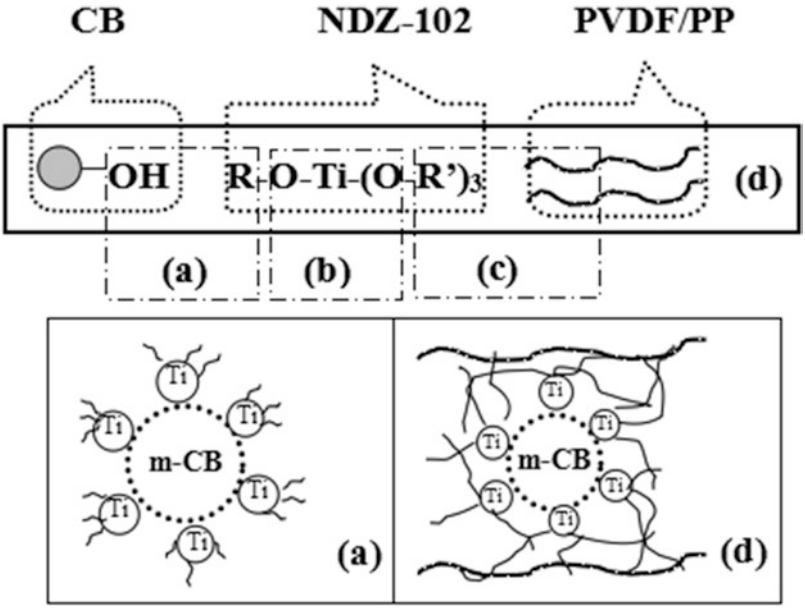

Fig. 4.12 Schematic image of chemical reaction mechanism of NDZ-102 on the interface of CB and polymer (**a**) chemical bond of R groups in NDZ-102 with hydroxyls in CB to form a single molecule layer of coupling agent on CB surface, (**b**) cross-linking action of NDZ-102 with CB and PVDF/PP through conversion reaction of lactones groups, (**c**) physical entanglement and chemical cross-linking of R' with polymer molecules, and (**d**) the enhanced interface between CB and polymer

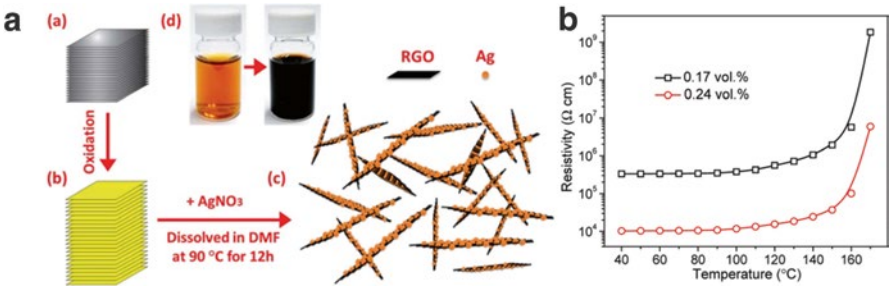

Fig. 4.13 (**a**) Route for synthesizing Ag–RGO hybrid sheets. (*a*) Graphite flake, (*b*) graphite oxide, (*c*) Ag–RGO sheets obtained by dissolving graphite oxide and AgNO3 in DMF and keeping the solution at 90 °C for 12 h, and (*d*) DMF reduction of Ag + and GO to Ag–RGO, changing brown color of the suspension to black; (**b**) effect of temperature on resistivity of Ag–RGO/PVDF composites with 0.17 vol.% and 0.24 vol.% filler loadings (Reprinted with permission from Ref. [80]. Copyright the Royal Society of Chemistry 2015)

4.6.2 The Cross-Linked Polymer Nanocomposites

Researchers have proposed and developed many methods to eliminate the NTC effect of nanocomposites. Among these methods, the first approach used is to cross-link the semicrystalline polymer matrix by a cross-linking agent [81–84]. For instance, Narkis et al. successfully used a peroxide to cross-link CB-filled HDPE composites without sacrificing the PTC intensity [85, 86]. In addition to the use of a cross-linking agent, gamma and electron-beam radiations have been used to cross-link polymer composites [87, 88]. It was mentioned that a third filler could be used to stabilize the polymer matrix and eliminate the NTC effect. The absence of the NTC effect in the cross-linked polymer composites is related to an increase in the viscosity of the polymer matrix, leading to a significant reduction in the mobility of the CB particles in the composites. Based on this idea, it is possible to use a very high viscosity semicrystalline polymer matrix to eliminate the NTC effect.

The effect of electron-beam (EB) irradiation on the PTC/NTC behaviors and the electrical reproducibility of CB/HDPE nanocomposites for PTC switch were investigated by Seo et al. in terms of EB irradiation intensity in a dosage of 30–150 kGy [89]. The NTC behavior was disappeared from a dosage of 60 kGy. It was also found that the EB irradiation led to an improvement of electrical reproducibility of the composites, which was probably due to the reduction of free movement of CB particles at above the melting temperature of HDPE polymer crystalline regions, resulting from increasing the cross-linking structure of CB/HDPE composites. The schematic diagram of electron-beam apparatus for cross-linking, PTC intensity, and electrical reproducibility of polymer nanocomposites is shown in Fig. 4.14.

4.6.3 Heat Treatment of the Nanocomposite

Heat treatment and annealing can improve the crystallization of polymers and enable the fillers to arrange more regularly, so they are good means of improving PTC characteristics of a polymer composite [90, 91]. Cheng et al. prepared a new kind of shape-stabilized phase change materials (PCMs) with PTC effect by adding graphite powder (GP) to the paraffin/LDPE composite (Fig. 4.15) [25]. The heat treatment was done by keeping the temperature of the samples at 70 °C for 5 min. They found that after the process of heat treatment, the NTC effect of the PCMs was eliminated effectively. In addition, the microstructure of the material became more uniform than that without the heat treatment, and the PTC curves were much more stable as a result.

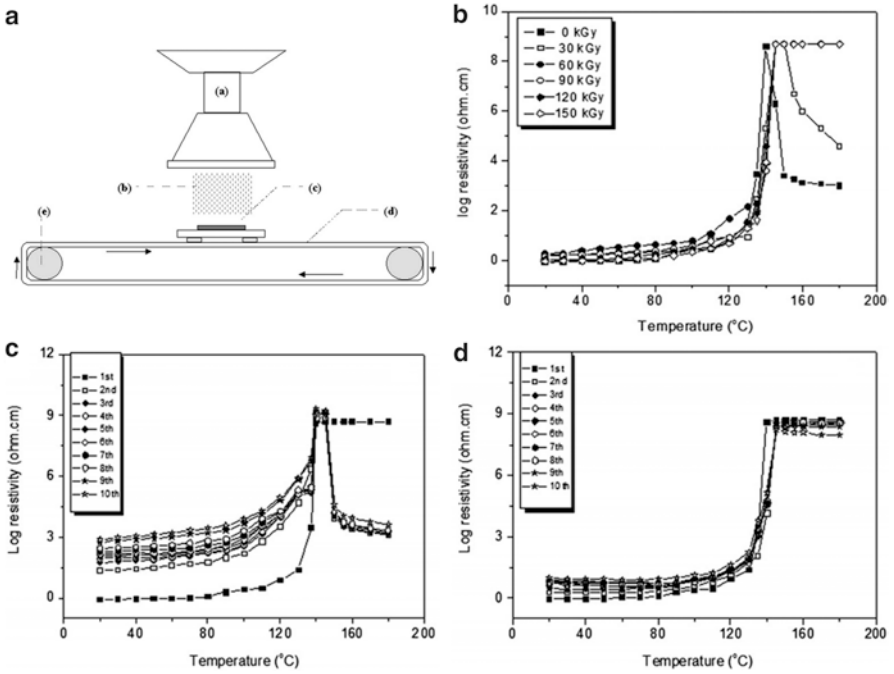

Fig. 4.14 (**a**) Schematic diagram of apparatus for cross-linking of polymer: (*a*) electron-beam accelerator, (*b*) electron beam, (*c*) irradiating sample, (*d*) conveyer, and (*e*) motor; (**b**) PTC intensity of CBs/HDPE conducting polymer composites as a function of irradiation dose; (**c**) electrical reproducibility of unirradiation CBs/HDPE composites; (**d**) electrical reproducibility of CBs/HDPE composites with 60 kGy irradiation dose (Reprinted with permission from Ref. [89]. Copyright 2010 Elsevier B.V.)

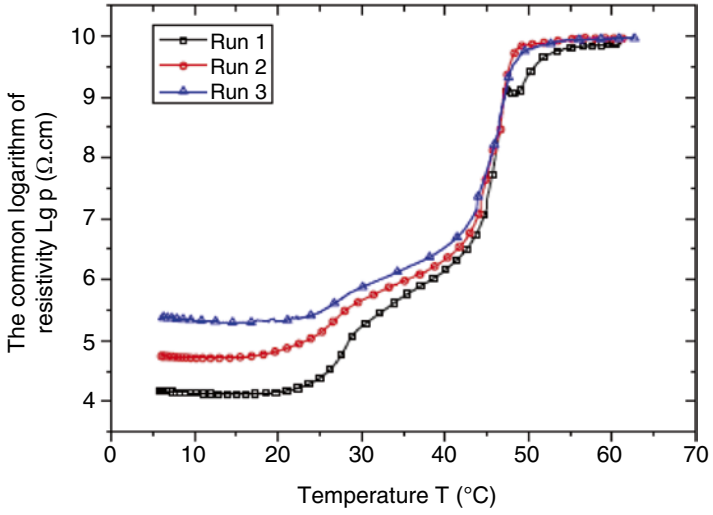

Fig. 4.15 The three runs of the PTC curve for the same sample with the mass fraction (%) of GP/LDPE/Paraffin is 40/18/42. Run 1 was the R–T curve of the sample without heat treatment; Run 2 and Run 3 were the R–T curves of the same sample with heat treatment, which indicated that the NTC effect had disappeared after the heat treatment. In addition, the curve trends of Run 2 and Run 3 in each figure were very similar and much more stable than that of Run 1 (Reprinted with permission from Ref. [25]. Copyright 2014 Published by Elsevier Ltd.)

4.7 Conclusions

In conclusion, research and development activities on PTC nanocomposites have brought successful industrial applications as temperature sensors, self-regulated heaters, and overcurrent protectors. An enormous amount of knowledge has been accumulated in this field. It is assumed that the PTC effect is due to the difference of the thermal expansion coefficients between matrix and filler, and melting expansion of semicrystalline polymer is the main role in PTC effect. Therefore the PTC properties of polymer nanocomposites are sensitively influenced by characteristics of polymer matrix such as thermal property, morphology, crystallinity, and processing conditions. In terms of temperature sensing, the transition temperature can be determined by the melting temperature, the glass transition temperature of the polymer matrix.

Recently, few studies are conducted on the PTC effects of conductive filler-filled immiscible semicrystalline polymer or multiphase polymeric blends. The selective dispersion of fillers in one phase or at the interface of two polymers causes a decrease of the percolation threshold to a very low level, which contributes to being processed with ease, preserving the mechanical properties of the polymer and reducing as much as possible the cost of the final composite. It is proposed that the heterogeneous distribution of fillers in immiscible polymer blends is mainly due to the difference in affinity of fillers to each component of polymer blends, i.e., the difference in the interfacial free energy of the polymer/filler.

The use of PTC nanocomposites based on carbon fillers, such as CB, CNTs, CF, graphite, graphene, metal-coated carbon fiber, etc. is found to be superior in many applications compared to metals because of their lightweight, low cost, and oxidation resistance. In addition to the amount of loading, filler particle size and morphology structure, filler–matrix interactions, and processing techniques are also key factors in determining the PTC properties.

Many efforts to achieve morphological control over the conductive networks in nanocomposites have attracted significant attention due to the vital role that morphology plays in PTC properties. To achieve a lower percolation threshold or a lower cost, more than one type of filler, particularly fillers with different aspect ratios, can be used to prepare PTC nanocomposites. These hybrid fillers, which contain different carbon fillers, such as CNTs, CF, graphite-based fillers, and CB, are often used due to their distinctly different aspect ratios and similar carbon-based structures.

Nevertheless, many problems are not solved yet. Polymer PTC nanocomposites have some shortcomings, such as unstable electrical reproducibility due to irregular structure changes in heating/cooling cycles, NTC phenomena, and the slow response rate of PTC effect associated with an adverse effect on desired switching properties. Recently the extensive progress on several efficient methods for controlling the morphology of conductive networks to increase stability of PTC materials has been developed, which include cross-linking the semicrystalline polymer matrix by a cross-linking agent, gamma and electron-beam radiations, grafting functional chemical groups or polymer molecules onto the surface of the conductive fillers,

etc. It is believed that the elimination of the NTC effect in the cross-linked polymer composites is related to an increase in the viscosity of the polymer matrix, leading to a significant reduction in the mobility of the fillers in the composites. Based on this idea, it is possible to use a very high viscosity semicrystalline polymer matrix to eliminate the NTC effect. Heat treatment and annealing can improve the crystallization of polymers and enable the fillers to arrange more regularity, so they are good means of improving PTC characteristics of a polymer nanocomposite.

References

1. Király A, Ronkay (2015) Polym Test 43:154–162
2. Tan Y, Song Y, Cao Q, Zheng Q (2011) Polym Int 60:823–832
3. Lu C, Hu XN, He YX, Huang X, Liu JC, Zhang YQ (2012) Polym Bull 68:2071–2087
4. Ram R, Rahaman M, Khastgir D (2015) Compos: Part A 69:30–39
5. Brigandi PJ, Cogen JM, Wolf CA, Reffner JR, Pearson RA (2015) Kinetic and thermodynamic control in conductive PP/PMMA/EAA carbon black composites. J Appl Polym Sci 25:132–137
6. Feng C, Jiang L (2013) Compos Part A: Appl Sci Manuf 47:143–149
7. Cheng WL, Zhang RM, Xie K, Liu N, Wang J (2010) Sol Ener Mat Sol Cells 94:1636–1642
8. Frydman E (1945) UK Patent Spec. 604 195 I718 14S, 1945
9. Cheng WL, Song JL, Wu WF (2012) Spacer Eng 21:131–135
10. Kar P, Khatua BB (2011) Polym Eng Sci 51:1780–1790
11. Ying X, Hisako I, Zhen BY (2004) M Masaru Carbon 42:1699–1706
12. Di WH, Zhang G, Peng Y, Zhao ZD (2004) J Mater Sci 39:695–697
13. Chen R, Bin YZ, Zhang R, Dong EY, Ougizawa T, Kuboyama K, Mastuo M (2012) Polymer 53:5197–5207
14. Srivastava S, Tchoudakov R, Narkis M (2000) Polym Eng Sci 40(7):1522–1528
15. Struèmpler R. Glatz-reichenbach J (1999) J Electroceram 3:4, 329–346
16. Sumita M, Sakata K, Asai S, Miyasaka K, Nakagawa H (1991) Polym Bull 25:265–271
17. Nakamura S, Saito K, Sawa G, Kitagawa K (1997) Jpn J Appl Phys 36:5163–5168
18. Kohler F (1966) Resistance element. US Patent, 3,243,753, 1966
19. Ohe K, Natio Y (1971) Jpn J Appl Phys 10:199–208
20. Meyer J (1973) Polym Eng Sci 13:462–486
21. Klason C, Kubat J (1975) J Appl Polym Sci 19:831–845
22. Voet A (1980) Rubber Chem Tech 54:42–50
23. Allak HK, Brinkman AW (1993) J Mater Sci 28:117–120
24. Mamunya YP, Zois H, Apekis L (2004) Powder Tech 140:49–55
25. Cheng WL, Wu WF, Song JL, Liu Y, Yuan S, Liu N (2014) Ener Conversion Manag 79:470–476
26. Brigandi PJ, Cogen JM, Wolf CA, Reffner JR, Pearson RA (2015) J Appl Polym Sci 132:42134
27. Dai K, Zhang YC, Tang JH, Ji X, Li ZM (2012) J Appl Polym Sci 125:561–570
28. Kim J, Kang PH, Nho YC (2004) J Appl Polym Sci 92:394–401
29. Xiong CX, Zhou ZY, Xu W, Hu HR, Zhang Y, Dong LJ (2005) Carbon 43:1778–1814
30. Jiang MJ, Dang ZM, Xu HP (2007) Appl Phys Lett 90:042914
31. Wan Y, Xiong CX, Yu JY, Wen DJ (2005) Comp Sci Tech 65:1769–1779
32. Kar P, Khatua B (2010) J Appl Polym Sci 118:950–959
33. Wen M, Sun X, Su L, Shen J, Li J, Guo S (2012) Polymer 53:1602–1610
34. Gunes IS, Jimenez1 GA, Jana SC (2009) Carbon 47:981–997
35. Ibarrola JMA, Lopez SH, Santiago EV, Pe´rez JA, Valverde MIP (2015) J Thermoplast Compos Mater 28(4):574–590

36. Feng JY, Chan CM (2000) Polymer 41:7279–7282
37. Akihiko K, Katsuya S, Hajime N, Yousuke G, Yusuke K, Toshiaki O, Hideo H (2012) Polymer 53:1760–1764
38. Xu HP, Dang ZM, Yao SH, Jiang MJ, Wang DY (2007) Appl Phys Lett 90:152912
39. Xu HP, Dang ZM, Shi CY, Lei QQ, Bai J (2008) J Mater Chem 18(23):2685–2690
40. Zhang SM, Deng H, Zhang Q, Fu Q (2014) Appl Mater Interfaces 6:6835–6844
41. Dai K, Qu YY, Li Y, Zheng GQ, Liu CT, Chen JB (2014) Tuning of the PTC and NTC effects of conductive CB/PA6/HDPE composite utilizing an electrically superfine electrospun network. Mater lett 114:96–99
42. Gubbels F, Jerome R, Vanlathem E, Deltour R, Blacher S, Brouers F (1998) Chem Mater 10:1227–1235
43. Nicolaus P, Eusebiu G (2002) Carbon 40:201–205
44. Mather PJ, Thomas KM (1997) J Mate Sci 32:401–407
45. Wang WP, Pan CY, Wu JS, Phys J (2005) Chem Solid 66:1695–1700
46. Lee JH, Kim SK, Kim NH (2006) Scripta Mater 55:1119–1122
47. Feller JF, Linossier I, Grohens Y (2002) Mater Lett 57(1):64–71
48. Das NC, Chaki TK, Khastgir D (2001) Adv Polym Tech 20:226–236
49. Zhang YC, Dai K, Pang H, Luo QJ, Li ZM, Zhang WQ (2012) J Appl Polym Sci 124:1808–1814
50. Zhang R, Tang P, Li JF, Xu DG, Bin YZ (2014) Polymer 55:2103–2112
51. Ke K, Wang Y, Luo Y, Yang W, Xie BH, Yang MB (2012) Compos Part B 43:3281–3287
52. Jiang SL, Yu Y, Xie JJ, Wang LP, Zeng YK, Fu M, Li T (2010) J Appl Polym Sci 116:838–842
53. Chen J, Shi YY, Yang JH, Zhang N, Huang T, Chen C (2012) J Mater Chem 22: 22398–22404
54. Huang JR, Mao C, Zhu YT, Jiang W, Yang XD (2014) Carbon 73:267–274
55. Maiti S, Suin S, Shrivastava N, Khatua BB (2014) RSC Adv 4:7979–7990
56. Gao JF, Li ZM, Peng S, Yan DX (2009) Polym Plast Tech Eng 48:478–481
57. Zeng Y, Lu GX, Wang H, Du JH, Ying Z, Liu C (2014) Sci Rep 4:6684
58. Du J, Zhao L, Zeng Y, Zhang L, Li F, Liu P, Liu C (2011) Carbon 49:1094–1100
59. Pang H, Zhang YC, Chen T, Zeng BQ, Li ZM (2010) Appl Phys Lett 96:251907
60. Ryu SH, Kim S, Kim H, Kang SO, Choa YH (2015) RSC Adv 5:36456
61. Thommerel ME, Valmalette JC, Musso J (2002) Mater Sci Eng A328:67–79
62. Tavman IH (1997) Powder Tech 91(1):63–67
63. Rusu M, Sofiana N, Rusu D (2001) Polym Test 20(4):409–417
64. Mamunya YP, Davydenko VV, Pissis P, Lebedev V (2002) Europ Polym J 38(9):1887–1897
65. Andrzej R, Gisele B, Flavien M, Gerard S (2010) Comp Sci Tech 70:410–416
66. Mitsuhiro K, Toru M (2005) Electr Eng Japan 2:1–9 (Translated from Denki Gakkai Ronbunshi, Vol. 124-A, No. 4, April 2004, pp 337–343
67. Sun Y, Bao HD, Guo ZX, Yu J (2009) Macromolecules 42:459–463
68. Zhang SM, Lin L, Deng H, Gao X, Bilotti E, Peijs T, Zhang Q (2012) Exp Polym Lett 6:159–168
69. Otten RHJ, Van DSP (2009) Phys Rev Lett 103:225704/1-4
70. Ma PC, Liu MY, Zhang H, Wang SQ, Wang R, Wang K, Wong YK, Tang BZ, Hong SH, Paik KW, Kim JK (2009) ACS Appl Mater Interfaces 1:1090–1096
71. Sumfleth J, Adroher XC, Schulte K (2009) J Mater Sci 44:3241–3247
72. Deng H, Lin L, Ji MZ, Zhang SM, Yang MB, Fu Q (2014) Prog Polym Sci 39:627–655
73. Zha JW, Li WK, Liao RJ, Bai J, Dang ZM, Mater J (2013) Chem A 1:843–851
74. Chekanov Y, Ohnogi R, Asai S (1999) J Mater Sci 34:5589–5592
75. Xue QZ (2004) Eur Polym J 40:323–327
76. Zhang C, Yi XS, Yui H, Asai S, Sumita M, Appl J (1998) Polym Sci 69(9):1813–1819
77. Xu HP, Dang ZM, Jiang MJ, Yao SH, Bai JB (2008) J Mater Chem 18:229–234
78. Dang ZM, Wang HY, XU HP (2006) Appl Phys Lett 89:112902

79. Bai BC, Kang SC, Im JS, Lee SH, Lee YS (2011) Mater Res Bull 46:1391–1397
80. He LX, Tjong SC (2015) RSC Adv 5:15070
81. Jia SJ, Jiang PK, Zhang ZC et al (2006) Effect of carbon-black treatment by radiation emulsion polymerization on temperature dependence of resistivity of carbon-black-filled polymer blends. Radiat Phys Chem 75:524–531
82. Michael S, Martin B, Jurgen H, Eur J (2005) Ceramic Soc 25:199–204
83. Chen JH, Wei G, Maekawa Y, Yoshida M, Tsubokawa N (2003) Polymer 44(11):3201–3207
84. Yang GC (1997) Polym Comp 18(4):484–491
85. Narkis M, Ram A, Stein Z (1981) Polym Eng Sci 21:1049–1054
86. Narkis M, Vaxman A (1984) J Appl Polym Sci 29:1639–1652
87. Zhang GX, Zhang ZC (2004) Radiat Phys Chem 71(1–2):273–276
88. Yi XS, Zhang JF, Zheng Q, Pan Y, Appl J (2000) Polym Sci 77(3):494–499
89. Seo MK, Rhee KY, Park SJ (2011) Curr Appl Phys 11:428–433
90. Chen JH, Iwata H, Tsubokawa N, Maekawa Y, Yoshida M (2002) Polymer 43(8):2201–2206
91. Hirano S, Kishimoto A (1998) Appl Phys Lett 73:25–27

Part II
Electrical Properties of Polymer Nanocomposites Under High Electric Field

Chapter 5
Dielectric Breakdown in Polymer Nanocomposites

Toshikatsu Tanaka

5.1 Introduction

This article treats with short- and long-time breakdown in nanodielectrics. Short-time breakdown is theoretically established. This is related to more or less intrinsic breakdown of thin insulating films. Such types of breakdown include intrinsic breakdown, electron avalanche breakdown, thermal breakdown, and electromechanical breakdown. Data are collected for pure polymers [2] and polymer nanocomposites [6]. Nanofillers are considered to become carrier traps and play an important role in dielectric breakdown processes. But no breakdown phenomena have been adequately correlated with any of the theoretical models yet, because of their complexity. Long-time breakdown is observed in thick polymer insulations and appears in the shape of electrical treeing. This treeing is especially important from the engineering point of view. Treeing phenomena in nanocomposites can be analyzed from a certain theoretical point of view. Tree initiation takes place in chemical or electronic degradation. Trees grow by partial discharges taking place inside of tree channels and retarded by nanofillers. Under a certain condition such as extremely high electric field, electrons can be accelerated by the field formed by nanofillers.

5.2 Theories of Dielectric Breakdown

Solids are governed by two basic elements, i.e., electrons and phonons (quantum modes of lattice vibration) in electronic conduction. In the case of semiconductors, electrons are available in the conduction band from electron donors and from the

T. Tanaka, PhD (✉)
IPS Research Center, Waseda University,
2-7 Hibikino, Wakamatsu-ku, Kitakyushu, Fukuoka 808-0135, Japan
e-mail: t-tanaka@waseda.jp

© Springer International Publishing Switzerland 2016

X. Huang, C. Zhi (eds.), *Polymer Nanocomposites*,
DOI 10.1007/978-3-319-28238-1_5

valence band. On the other hand, in the case of dielectrics, i.e., electrical insulating materials, electrons are in the conduction band and are usually considered to be supplied form from outside (actually electrodes). Therefore, charge that electrons hold is easily accumulated inside the dielectrics. It is called space charge. Usually electrons are trapped in trapping centers or trap to for such space charge.

Electrons gain energy from electric field and transfer their energy to phonons by collision to reach a steady state. Electronic conduction takes place in this energy balance. This energy balance will collapse if electrons gain more energy than energy loss (energy transferred to phonons). This is an electronic breakdown in solids. This is called dielectric breakdown in solid dielectrics. Dielectric breakdown includes:

1. Intrinsic breakdown
2. Electron avalanche breakdown
3. Thermal breakdown (impulse and steady state)
4. Electromechanical breakdown

5.2.1 Intrinsic Breakdown

Electrons are accelerated by the electric field and lose their energy to the lattice (or phonons) by collision, as shown in Fig. 5.1 [7]. Energy balance in an ensemble of electrons is represented by the formula 5.1

$$A\left(F_c, T_0, E\right) = B\left(T_0, E\right) \tag{5.1}$$

The critical field E, i.e., breakdown strength, is determined by energy balance between the energy gain per unit time from the field and the energy transfer per unit time to phonons. Energy transfer means energy loss of electrons by collisions with phonons or lattice vibrations. Electrons are newly available by impact ionization. Energy transfer B is determined by collision cross sections.

There are several criteria according to mechanisms of energy transfer from the conducting electrons to phonons: there are two categories, i.e., (1) single-electron approximation and (2) collective electron approximation [1]:

1. Single-electron approximation

   - High-energy criterion proposed by Fröhlich
     All electrons fulfill the criterion: Formula 5.1:
   - Low-energy criterion proposed by von Hippel and Callen

   All electrons in the conduction band fulfill the criterion:

$$E_H = \frac{hv}{e\lambda} \tag{5.2}$$

This is called von Hippel electric field for dielectric breakdown.

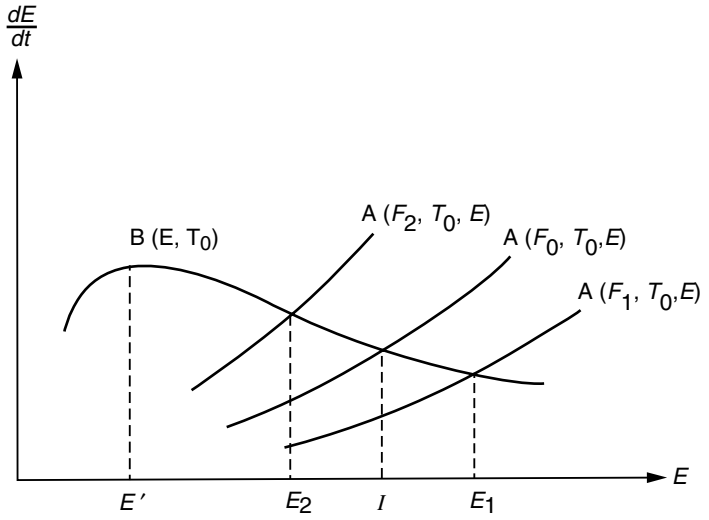

Fig. 5.1 The average rate of energy gain A (F, T_0, E) from an applied field for various field strengths, and the average rate of energy loss to the phonon B (E, T_0) (O'Dwyer [7], p. 21, Fig. 3)

2. Collective electron approximation

- Collective electron criterion: This is proposed by Franz and Stratton. Electrons have an energy distribution. Averaged electrons over energy distribution fulfill the criterion (i) the low density approximation: avalanche theory and (ii) the high-density approximation.
- Electronic thermal breakdown: This is proposed by Fröhlich.

  Electro–electron interaction is larger than electron–phonon interaction.

If electron–electron interactions are strong, electronic thermal breakdown is likely to take place. Electrons can be hot. Such electrons are called hot electrons. This type of breakdown will take place in amorphous or noncrystalline dielectrics when interactions of electrons with impurity levels (donors and/or traps) exceed those with phonons. These results in electron temperature will increase rapidly. This was calculated by Fröhlich. It is considered that this will explain well the high-temperature breakdown characteristics.

5.2.2 Electron Avalanche Breakdown

Successive electron multiplication like avalanche takes place due to the ionization by collision process as shown in Fig. 5.2. This avalanche gives large energy to phonons to cause dielectric breakdown. There are two ways to calculate the critical field, i.e., single-electron approximation and collective electron approximation.

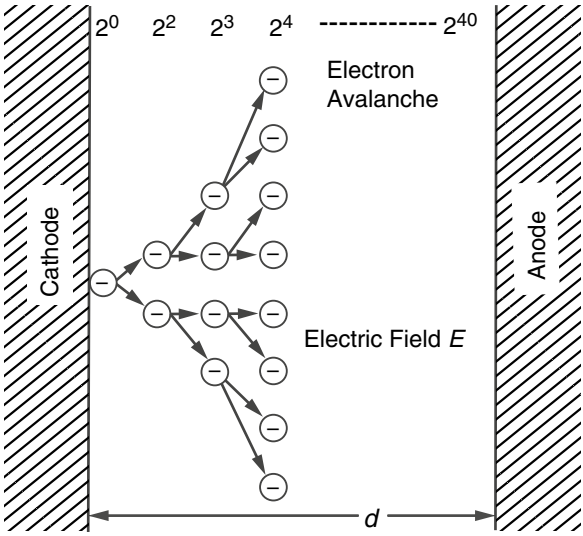

Fig. 5.2 Schematics of electron avalanche process

Here is the simplest case with the single-electron approximation. As electron avalanche in solid dielectrics has no feedback mechanisms including photoionization, the critical field cannot be determined automatically. Therefore, we need some assumption. A condition for 40 generations was given by Seitz [9]:

$$E_c = \frac{H}{\ln\left(\dfrac{d}{40E_c\mu\tau}\right)} \tag{5.3}$$

H: constant, d: insulation thickness, μ: electron mobility, τ: average collision time of electrons

5.2.3 *Thermal Breakdown (Impulse and Steady State) (Fig. 5.3)*

Temperature rise due to Joule heating and heating by dielectric dissipation loss will melt insulation to cause dielectric failure. Intrinsic breakdown is material specific, but this type of breakdown is affected not only by materials but also by heat radiation conditions like electrode sizes and structures. Energy balance in this case is as follows:

$$\underset{\text{Heat Absorption}}{C_v \frac{dT}{dt}} - \underset{\text{Diffusion}}{div\left(k\,grad\,T\right)} = \underset{\text{Joule Hear or Dielectric Heat}}{\sigma E^2} \tag{5.4}$$

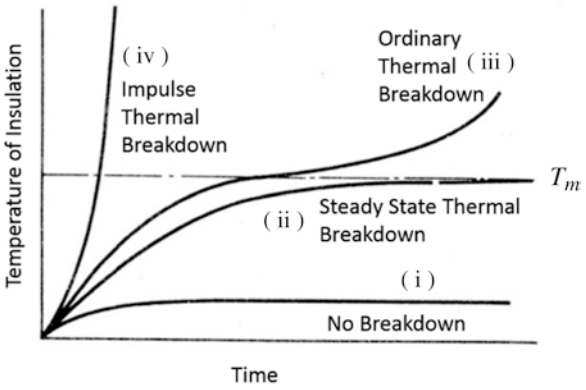

Fig. 5.3 Temperature rise associated with thermal breakdown

C_v, is specific heat at constant volume; T, absolute temperature; t, time; κ, thermal conductivity; σ, electrical conductivity; and E, electric field strength.

In that meaning, thermal breakdown can be called extrinsic breakdown. It takes place at relatively high temperatures. Thermal breakdown strength tends to decrease with the increase of temperature. Thermal breakdown is divided into categories, i.e., steady-state and impulse breakdown modes. Steady-state thermal breakdown, as time dependence can be neglected, is governed by the formula

$$-div\left(k\,grad\,T\right)=\sigma E^2 \tag{5.5}$$

In a plane-parallel electrode system, steady-state thermal breakdown strength is given by

$$V_c=\left(\frac{8\kappa kT}{\sigma_0\phi}\right)^{\frac{1}{2}}\exp\left(\frac{\phi}{2kT}\right) \tag{5.6}$$

where κ is thermal conductivity and $\sigma=\sigma_0\exp(-\phi/kT)$.

Impulse thermal breakdown is determined by the formula 5.7 as the diffusion term can be neglected:

$$C_v\frac{dT}{dt}=\sigma E^2 \tag{5.7}$$

Breakdown takes place in impulse thermal BD before generated heat is dissipated through insulation to outside. All of the generated heat will thermally damage materials directly. If the electrical conductivity is of thermally activated type independent of applied voltage, impulse breakdown strength is given by

$$E_c=\left\{\frac{3C_vkT}{\sigma_0\phi}\bullet\frac{1}{t_c}\right\}\exp\left(\frac{\phi}{2kT}\right) \tag{5.8}$$

$\sigma = \sigma_0 \exp(-\phi/kT)$ is electrical conductivity; k, Boltzmann's constant; ϕ, activation energy for electrical conductivity; and t_c, voltage application time.

Impulse breakdown strength will be lowered, as specific heat becomes smaller, electrical conductivity becomes larger, and temperature becomes higher. The strength is independent of melting point. Time lag for breakdown is relatively long and is in the range of several minutes to several seconds. Ionic conduction, Schottky conduction, and Poole–Frenkel conduction can be taken into consideration.

5.2.4 Electromechanical Breakdown

Soft insulating materials can be reduced in thickness due to Maxwell stress when they are subjected to voltage. In that case, the electric stress is enhanced and then the thickness is further reduced. This causes a positive feedback process to lead to the insulation to electric failure. This is called electromechanical breakdown. Since ordinary solid insulating materials have large Young modulus, they will breakdown via other mechanisms at the lower voltage than the voltage at which they breakdown by the electromechanical breakdown. At high temperatures near softening temperatures, thermoplastic polymers are subject to thermal flow and become thinner due to Maxwell stress and thereby suffer from breakdown:

$$\frac{\varepsilon}{2}\left(\frac{V}{d}\right)^2 = Y \ln\left(\frac{d_0}{d}\right) \quad \text{i.e. } \mathrm{E}_c = 0.607\left(\frac{Y}{\varepsilon}\right)^{\frac{1}{2}} \tag{5.9}$$

5.3 Treeing Breakdown Phenomena

5.3.1 Electrical Trees Electrode Systems for Performance Evaluation

Treeing is a phenomenon whereby partial breakdown or dendritic paths progressively grow and branch into hollow channels in a solid dielectric, as clearly shown in Fig. 5.4. They have the appearance of trees; therefore such breakdown paths are called electrical trees or simply trees. They can occur at rather low applied voltage but possibly at very high electric field. Treelike discharge patterns, sometimes leading to total breakdown of the insulation used, have been observed for many years in oil-impregnated pressboard and oil-impregnated laminate paper cables. They propagate preferentially in a direction parallel to the internal paper interfaces and only occasionally break through layers. Treeing is presently more serious in solid dielectrics such as polyolefinic polymers, rubbers, and epoxy resins, which appear to be

Fig. 5.4 Profile of electrical trees in PMMA

susceptible to treeing. Once a tree starts, it is likely to cause breakdown sooner or later. They have been observed in cables, but rubbers and resins are often pigmented or mineral filled; the existence of treelike channel phenomena may go unnoticed in these materials.

Treeing is observed in thick insulation. It is experimentally evaluated using some electrode systems as shown in Fig. 5.5. Electrical trees are classified into two types, i.e., tree-type trees and bush-type trees, as shown in Fig. 5.6.

Breakdown takes place step by step. Some of the dielectric breakdown processes that are described in subsection 5.2 are involved in each step. Intrinsic breakdown, electron avalanche, or thermal breakdown is taken into consideration. First electrons to be accelerated are supplied from the electrodes. Treeing phenomena in polymer insulating materials were intensively investigated for a long time in the past on mechanisms and well documented [2]. They include two or three stages, i.e., tree initiation, growth, and final breakdown [11, 12, 14, 15]. It should be noted that a tip of trees reaching the opposite electrode does not necessarily mean final breakdown. A certain gaseous discharge process is necessary prior to breakdown. Under these processes, a thin and long tree formed in the beginning is expanded laterally in its radius into a thick tree to be led to the final breakdown.

Treeing takes place in the four stages as indicated below:

Stage 1: Incubation period
Stage 2: Initiation
Stage 3: Growth or propagation
Stage 4: Total breakdown

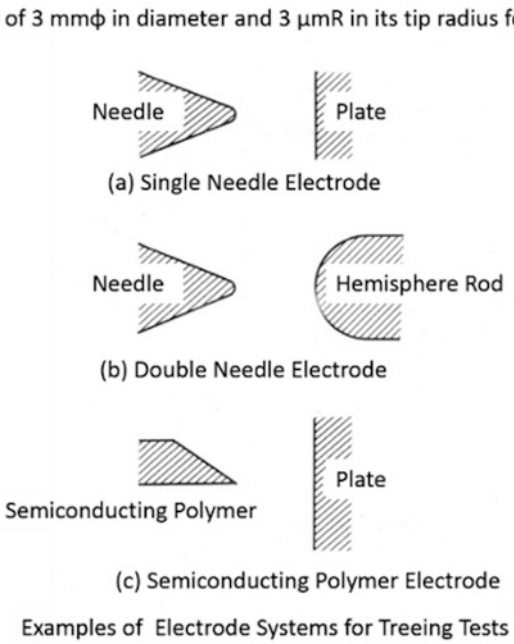

Fig. 5.5 Several types of treeing test electrode systems

5.3.2 Three Possible Processes in Incubation Period

There are two distinct time periods in treeing (stage 1 and stage 2): the first is an incubation period during which nothing appears to happen, and the second is a propagation period during which treelike figures grow in the insulation. A tree appears immediately after the incubation period. Up to the visual appearance of a tree figure and the start of significant measurable partial discharges, no obvious effects may occur. The initiation of electrical trees from sharp point of high electric stress in resins, as contrasted to the propagation, is surely the least understood aspect of electrical tree development. It may be inferred from experimental results obtained thus far that at low stress levels where trees are not immediately observed, cumulative processes are proceeding which eventually foster conditions which initiate a tree channel. Several explanations may be offered for the initiation of an electrical tree:

1. Possible process 1 – Tree initiation by mechanical fatigue
   High Maxwell compressive forces in the dielectric, caused by high electric fields at local areas when ac voltage is applied, produce a mechanical fatigue cracking in the polymer.

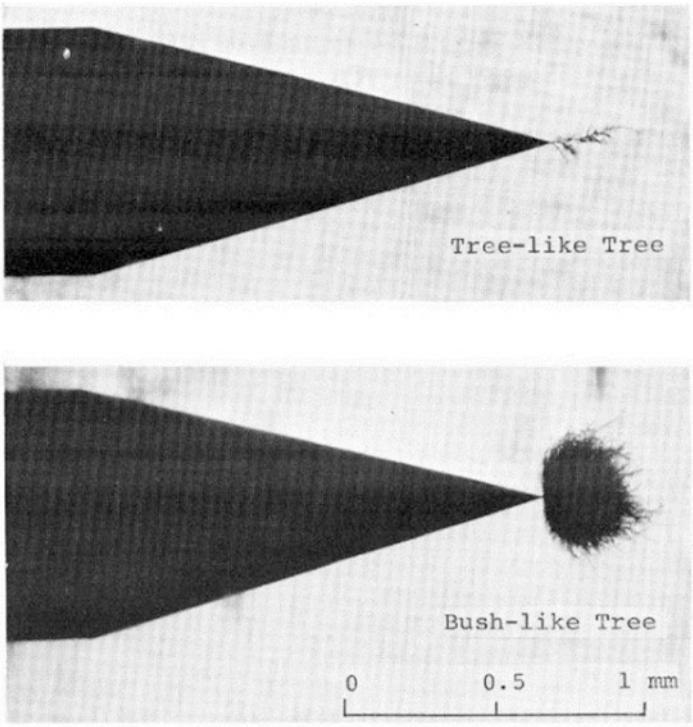

Fig. 5.6 Two types of trees generated in polyethylene

2. Possible process 2 – Tree initiation by partial discharges
   This phenomenon is based on that belief that small cavities exist at tips of foreign particles, asperities, or needles due to different thermal expansion of the resin and the metal or as a consequence of adsorbed or accumulated gas on the surface. It is supported by evidence. Another probable cause is bombardment of the surface of the insulation by high-speed electrons, the source of the electrons being high-intensity ionization in a void or field emission from the surface of a metal point with very small radius of curvature.
3. Possible process 3 – Tree initiation by charge injection and extraction
   Under ac voltage conditions, some electrons will be emitted or injected for a short distance into the dielectric during the negative half cycle, the distance being limited by the declining stress away from the emitting points. If they are not trapped, they will be drawn back into the point on the positive half cycle and re-injected in the following cycle. In each cycle some of the electrons will

gain sufficient energy to cause some resin decomposition to lower molecular weight products and gases.

As an alternative or addition to electrons injected from the electrode, it has been suggested that free electrons within the dielectric may acquire enough energy to cause inelastic collisions with lattices, leading to a molecular degradation and, finally, the initiation of a tree. Electrons may be supplied from deep donors (or trap levels) via the Poole–Frenkel effect and then be accelerated in the conduction level by the external field to become hot electrons.

5.3.3 Charge Injection and Extraction in Tree Incubation Period

Electrons are supplied from inside bulk (the valence band and donors), from the electron reservoir thermodynamically formed in contact, and/or from the outside electrodes via the Schottky and field emission. High-energy electrons working for tree initiation must be injected from the electrode via the field emission [10, 15]. Injected electrons transport in the quasi-conduction band and even in the conduction band with a short distance. They are also trapped in traps, i.e., localized states with trapping capability. Electrons, once injected, travel for a distance called schubweg. It is generally defined as the mean distance traveled by a charge carrier before it is trapped, as shown in Fig. 5.7. This terminology derives from photoconduction in ionic crystals.

Treeing is now a target of interest under ac divergent field condition. After electrons are injected from one electrode via the field emission at extremely high electric filed in a half or quarter cycle of applied ac voltage, they transport in the quasi-conduction band to acquire energy within their schubweg. If it is high enough, a partial breakdown will take place. It is a treeing bud formation process. This can be also called tree initiation. It is generally considered that treeing is a kind of fatigue. Therefore, a repeated electron injection and extraction model was proposed [15], as shown in Fig. 5.7. This model consists of material degradation and charge buildup for tree initiation. Material degradation is caused by polymer chain scission and oxidation under the condition of repeated injection and extraction, and it will lower dielectric breakdown strength. Charge buildup will take place in a distance of schubweg from the tip of the electrode used, as a result of the same repeated process, as shown in Fig. 5.8. Therefore, the length of a tree bud or an initial tree is considered to be around schubweg. Furthermore, it should be noted that a built-up charge will generate higher electric field under opposite cycle of ac voltage, as shown in Fig. 5.9. This will also possibly cause breakdown in some time after voltage application.

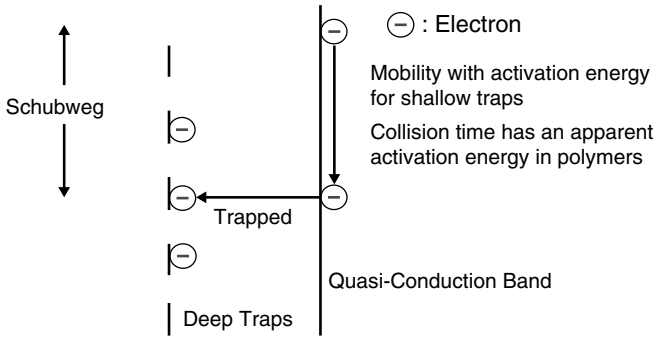

Schubweg $\mathcal{W} = \mu E \tau_t = (e\tau_c / m) E \tau_t$

w: Schubweg, μ: electron mobility, *E*:electric field, τ_t:mean trapping time, *e*: electronic charge, τ_c : mean collision time, *m*: electron mass

Fig. 5.7 Schubweg associated with electron trapping

Fig. 5.8 Electron injection and extraction process for tree initiation

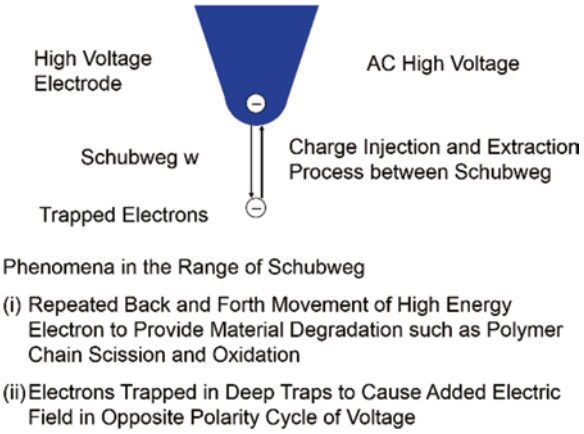

5.3.4 Processes from Tree Initiation to Growth

A treeing breakdown process includes a budding process and a growing process. This budding process can be discussed using the basic understanding of electron behaviors at high electric field. Electron transport mechanisms are described for polymer dielectrics on the basis of a modified energy band model where a quasi-conduction band and localized states in the band gap. Electron injection and extraction processes via the metal electrodes would cause tree initiation, i.e., the formation and growth of tree buds. It is a local dielectric breakdown near the tip of a needle electrode. It must be determined by

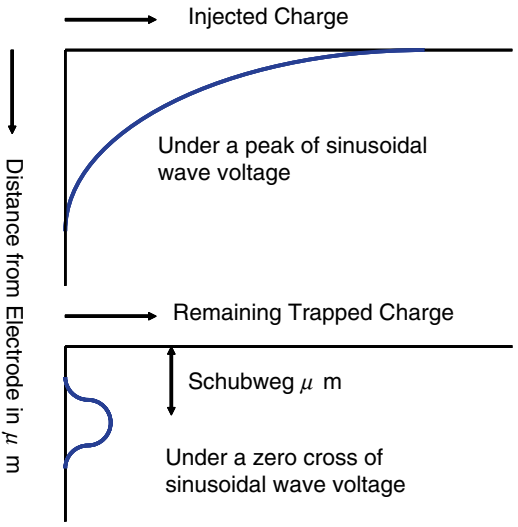

Fig. 5.9 Spatial distribution of electrons produced by their injection and extraction process under ac voltage application

the fact that electrons are injected into a dielectric and extracted back to the electrode via some potential barrier such as the Schottky barrier [15]. Injected electrons transport up to their schubweg to be effectively trapped. This must be a length of a tree bud or an initial tree. SEM observation of the buds of schubweg length must clarify how they will interact with nanofillers in epoxy resins. Buds for treeing are possibly affected by trapping by localized states and the local electric field induced by nanofillers [14].

In the growing process, a tree is extended through the following two major processes:

1. Successive local breakdown
2. Continuous PD attack

Treeing must be a fractal process, because the aforementioned budding process and the above two processes are alternatively and/or successively taking place. A sharp tip of the tree will act as the metal electrode, if the inside of the tip is electrically conductive enough by sufficient energy supply from the electrode, i.e., the outer circuit. This is a budding process in the tree growing process. This results in local breakdown to cause an initial tree. Such a tree will be expanded laterally by partial discharges.

Thus a repeated process of BD-originated tree initiation and PD-originated tree extension will produce tree propagation with a certain speed. Such speed can be measured by a certain technique. Comparison in this speed between neat epoxy and nanocomposites will give us in-depth insight into nanofiller effects on tree propagation.

5.4 Short-Time Dielectric Breakdown of Nanocomposites

Much data are available on short-time dielectric breakdown of nanocomposites. Improvement by nanofiller addition in this type of breakdown is controversial at present. Comprehensive phenomenological review was made (Li Shengtao 2010).

But obtained data are apparently contradictory in many cases, no appropriate conclusion has been reached yet, and furthermore no reasonable mechanistic analysis has been given. This is probably due to that fact that breakdown strength is structure sensitive. It is likely to be influenced by inclusion of unwanted defects. It was confirmed that there is an optimum nanofiller loading content to improve breakdown performances of polymer resin insulation. The degree of nanofiller agglomeration greatly affects breakdown strength, which is closely related to nanofiller mixing techniques.

Figure 5.10 shows a trend of breakdown strength depending on voltage shape under some optimum conditions. When nanofillers are loaded in a certain loading level, there is a tendency that breakdown strength shows an increase for DC, no change for AC, and a decrease for impulse voltage. Increase in DC breakdown strength may be closely related to the formation of barrier and space charge. In the analysis of treeing, electrons can be accelerated by nanofillers under AC high electric field conditions. Similar phenomenon might take place under AC and impulse voltage application. In the case of AC, improved performances are also confirmed. Therefore, if unwanted defects can be removed, it is also possible to increase AC or impulse breakdown strength by the addition of nanofillers.

It is possible to increase even AC breakdown strength if interfaces between nanofillers and surrounding polymer matrices are improved, as polyethylene–silica nanocomposites are observed. In the case of polyethylene–MgO nanocomposites, thermal breakdown is considered to be probable. Nanofiller inclusion will increase electrical resistivity, resulting in the increase of DC breakdown strength. It is also interesting that nanofillers interact with applied electric field. Nanofillers are electrically charged in the range of Debye shielding distance and induce the electric field.

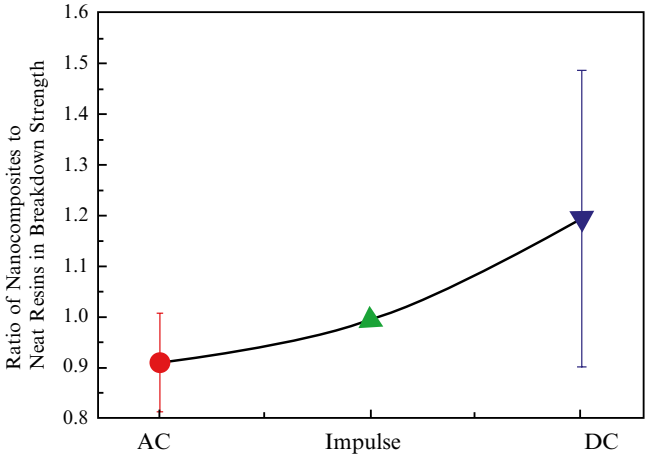

Fig. 5.10 Relative change of breakdown strength due to nanofiller addition as a function of voltage shape [6] p. 1527, Fig. 6)

This field may accelerate or decelerate propagating charge carriers (electrons and holes). This kind of interaction is discussed in Sect. 5.5.

5.5 Long-Term Breakdown Characteristics of Nanocomposites

Long-term breakdown, i.e., treeing in this case, is one of the most important performances from engineering point of view. Treeing characteristics for nanocomposites have been recently investigated to lead to the very interesting conclusion that treeing breakdown time is enormously extended for polymers when they are doped with nanofillers [3–5, 8, 13]. It means that long-term breakdown strength increases due to the inclusion of nanofillers in polymer such as epoxy, polyethylene, and polypropylene. However short-time breakdown strength increases in some cases but decreases in other cases. The short-time breakdown strength is considered to be sensitive to processes for nanocomposite preparation; in other words, it might be influenced by not only possible positive effects of nanofiller loading but also negative effect of accidental or in-process inclusion of impurities. This section deals with long-term breakdown by treeing processes.

Usually final breakdown time is measured and evaluated to compare neat polymers with their nanocomposites, as was done for different kinds of materials in the past. Time for breakdown by treeing can be converted into tree propagation speed by dividing material thickness of interest by breakdown time. In this research, time to three propagation distances, i.e., 10, 100, and 3000 μm, was measured, resulting in obtaining three kinds of speeds that depend on applied voltage. Such speeds are influenced by nanofiller addition, as speculated from *V-t* characteristics. Results obtained from this analysis of three kinds of speeds will give us the deep insight of tree growth in nanocomposites, which is explained in this chapter.

5.5.1 V-t *Characteristics*

Three sets of data are presented by a conventional *V-t* characteristics scheme as shown in Fig. 5.11. This shows a positive effect of nanosilica filler addition on suppression of tree propagation. Actually, values of n increases by the addition of nanofiller. The time of tree propagation to a certain length is increased with the decrease of applied voltage. This tendency is beneficial from the engineering point of view. Inversely, if two curves for a specified tree length are selected, the two curves tend to merge into the same values, and even crossover, as applied voltage is increased. This means that short-time breakdown voltage might be reduced by the addition of nanofillers.

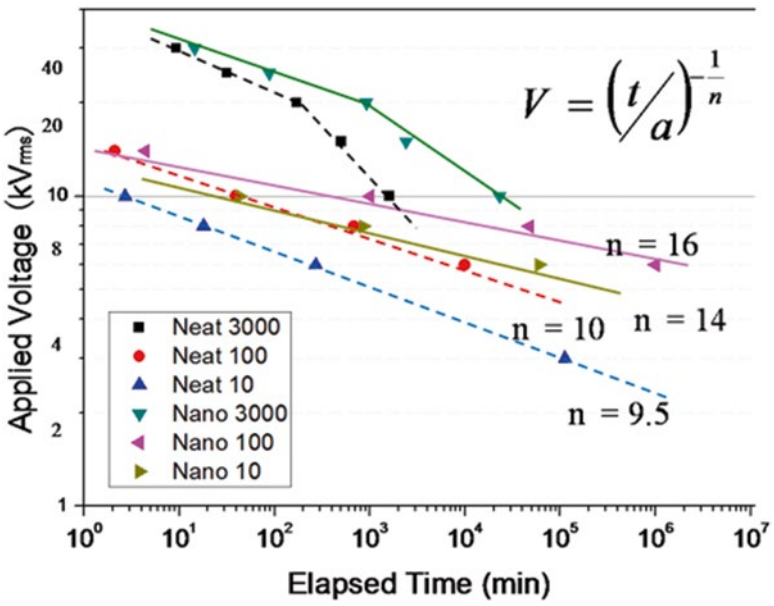

Fig. 5.11 *V-t* characteristics for trees growing up to 10, 100, and 3000 μm in length. Remark: 3000 μm (3 mm) length means breakdown

5.5.2 Derivation of Tree Growth Speed

A small-PD measurement system was developed so that a high voltage source might be shut down by detection of a certain partial discharge magnitude. PD magnitude is considered to be proportional or at least to increase with the increase of tree length. Three kinds of tree lengths, i.e., 10, 100, and 3000 μm (3 mm: sample thickness), can be detected by 10 pC, 100 pC, and breakdown, as shown in Fig. 5.12. Usually conventional *V-t* characteristics can be obtained:

$$V^n t = a\left(\text{constant}\right) \tag{5.10}$$

where V, t, n, and a are applied voltage, time, n-value, and constant, respectively.In order to find out other characteristics of tree growth, a new representation is introduced, i.e., average tree growth speed vs. applied voltage characteristics (S-V characteristics). This representation becomes possible since the time of tree growth up to several lengths is enabled to be measured since the developed small-PD measurement system can shut down a power source when a tree grows up to a specified length. If time and length of a tree are given at a certain applied voltage, S-V characteristics can be represented by the following formula:

$$S = bV^n \tag{5.11}$$

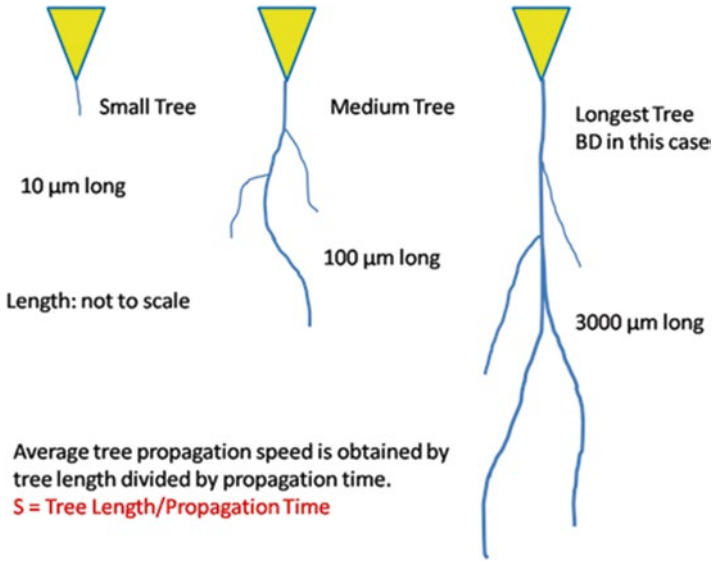

Fig. 5.12 Schematics of tree lengths dependent on applied voltage

where S and b are the average tree growth speed and a constant (tree length/a), respectively. Formula shows the dependence of tree growth speed on applied voltage. It means that the speed is proportional to V^n. Such characteristics experimentally obtained are shown in Fig. 5.2 for trees growing up to 10 μm, 100 μm, and 3 mm. The above relation applies for trees up to 10 and 100 μm length but not for 3 mm length (BD).

5.5.3 S-V *Characteristics*

In order to analyze these characteristics, it would be helpful to look into different aspects such as *S-V* characteristics as described in the formula (2). Figure 5.13 shows tree growth speed vs. applied voltage characteristics (*S-V* characteristics) for trees growing up to 10, 100 and 3 mm. These characteristics can be obtained by the transformation from *V-t* characteristics as shown in Fig. 5.11. It is clearly observed that tree growth speed is a strong positive function of voltage in general. The speed is proportional to the n^{th} power of applied voltage especially for tree length up to 100 μm. It should be pointed out that there are five kinds of cross points found at which tree growth speeds become the same, as indicated as X_1, X_2, X_3, X_4, and X_5 as shown in Fig. 5.13 and in Table 5.1.

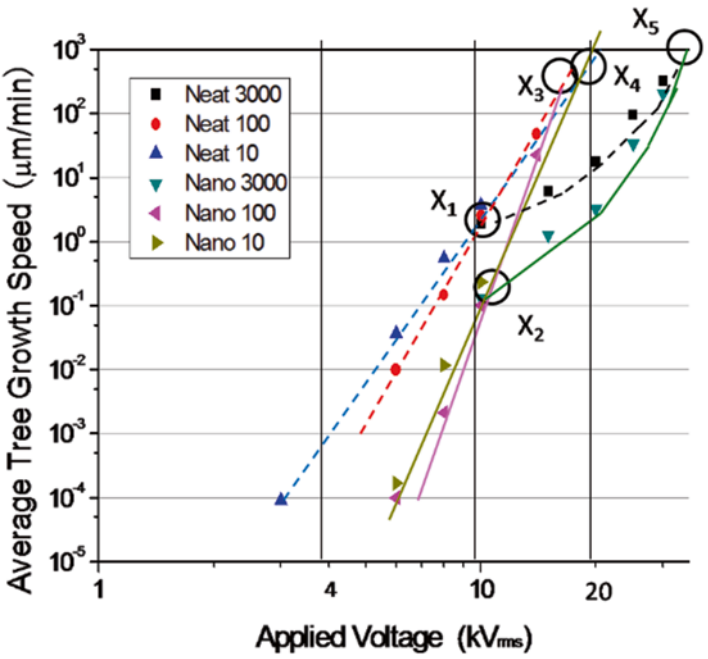

Fig. 5.13 Tree growth speed vs. applied voltage characteristics (S-V characteristics) for trees growing up to 10, 100, and 3 mm

Table 5.1 Four kinds of cross points in *S-V* characteristics

Cross point	Interpretation of cross point at the same speed	Voltage kV_{rms}	Speed μm/min
X_1	Epoxy–epoxy 10, 100 and 3000 μm	10	3×10^0
X_2	Nano–nano 10, 100 and 3000 μm	11	3×10^{-1}
X_3	Epoxy–nano 100 μm	15	3×10^2
X_4	Epoxy–nano 10 μm	18	4×10^2
X_5	Epoxy–nano 3 mm BD	>30	$\backsimeq 10^3$

5.5.4 *Explanation of Cross Points X_1, X_2, X_3, X_4, and X_5*

Triple cross points found as X_1 and X_2 in two groups of three curves as shown in Fig. 5.13 are related to behaviors of trees of 10, 100, and 3000 μm in length within the same material, either neat epoxy or nanocomposite. It is also possible to compare the neat epoxy with the nanocomposite based on the difference in a tree propagation speed and a certain critical voltage at points X_1 and X_2.

Let us take a triple point X1 for neat epoxy at 10 kV_{rms}. There are three kinds of speeds recognized for a 10-μm tree, a 100-μm tree, and a 3000-μm tree, respectively. They are merged into the same speed at 10 kV_{rms}. It is interesting to note that a tree grows at a constant (same) speed (3 μm/min) from the beginning to the end at applied voltage 10 kV_{rms} finally to cause dielectric breakdown. It means that a tree length is proportional to elapsed time, i.e., a linear curve in tree length vs. time characteristics. Below this critical voltage, no breakdown would take place, although a tree grows. A 100-μm (long) tree is slower in speed than a 10-μm (short) tree. This means that a tree grows more slowly as it grows from 10 to 100 nm, resulting in a saturation curve in tree length vs. time characteristics. On the contrary, above the critical voltage 10 kV_{rms}, a tree grows more quickly as it grows from 10 to 100 nm but later drastically slowly as it is reaching to the opposite electrode. This might be a logistic curve in tree length vs. time characteristics.

Then, let us look at another triple point X_2 at 11 kV_{rms} for nanocomposite as indicated in Fig. 5.13. A tree grows at a constant (same) speed (0.3 μm/min) from the beginning to the end at applied voltage 11 kV_{rms} finally to cause dielectric breakdown. The qualitatively same thing with the discovery made to neat epoxy can be said to nanocomposite in regard to a linear curve, a saturation curve, and a logistic curve depending on applied voltage, as observed in the lower three curves in Fig. 5.13. It is thus interesting to propose that a relation between neat epoxy and nanocomposite must be fractal in tree length vs. time characteristics.

It should be pointed out that the speed for tree growth is much reduced by almost one order of magnitude from 3 to 0.3 μm/min by the addition of nanofiller. Furthermore, a critical voltage is shifted a little bit from 10 to 11 kV_{rms}. These findings mean that a tree grows very much slowly in nanocomposite than in neat epoxy and that higher voltage (11 kV_{rms}) is needed for nanocomposite than voltage (10 kV_{rms}) for neat epoxy as for long-term breakdown.

Three kinds of double cross points referred to as X_3, X_4, and X_5 are representative of a relationship between two different materials, i.e., neat epoxy and nanocomposite, under the same condition of tree length, either 10 nm, 100 nm, or 3000 nm in length, respectively. The double cross point X_3 is marked as applied voltage 15 kV_{rms} and tree propagation speed 300 μm/min. Below the critical voltage 15 kV_{rms}, a 100-μm length tree grows more slowly in nanocomposite than in neat epoxy. It is easy to understand. On the contrary, above this critical voltage, a 100-μm length tree gains higher speed in nanocomposite than in neat epoxy.

The double cross point X_4 is marked as applied voltage 18 kV_{rms} and tree propagation speed 400 μm/min. It should be noted that the cross point X_4 (10-μm tree) is smaller the cross point X_3 (10-μm tree) in both the critical voltage and the tree propagation speed. Below the critical voltage 18 kV_{rms}, a 100-μm length tree grows more slowly in nanocomposite than in neat epoxy. On the contrary, above this critical voltage, a 10-μm length tree gains higher speed in nanocomposite than in neat epoxy.

The double cross point X_5 for a 3000-μm tree is designated as a little bit higher voltage than 30 kV_{rms} and 1000 μm/min. Below this critical voltage around 30 kV_{rms}, longer time is needed in nanocomposite for the 3000-μm tree growth than in neat

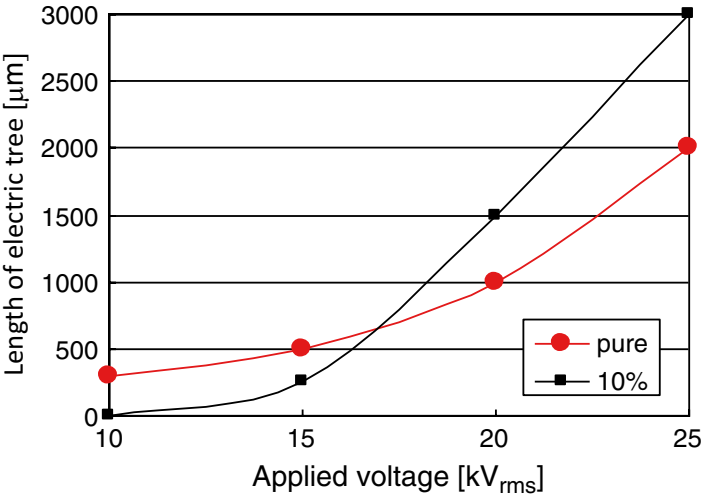

Fig. 5.14 Crossover phenomenon in tree length vs. applied voltage characteristics

epoxy. It is easy to accept this performance. On the contrary, above the critical voltage, it is anticipated that shorter time is needed in nanocomposite for the 3000-μm tree growth than in neat epoxy. In other words, a tree reaches the opposite electrode faster in nanocomposite than in neat epoxy. This might suggest that ac breakdown voltage becomes lower if nanofiller particles are added into epoxy. This is opposite to our expectation.

A similar phenomenon was already observed in short-time breakdown experiments based on a voltage increasing method at a constant speed of 500 V_{rms}/s [5]. Namely, a tree length is smaller in nanocomposite at low voltage than in neat epoxy but becomes larger in nanocomposite above a certain critical 17 kV_{rms} than in neat epoxy, as shown in Fig. 5.14. This was called a crossover phenomenon. This critical voltage 17 kV_{rms} is lower than the other critical voltage around 30 kV_{rms}, because the former was obtained by short-time breakdown tests, while the latter was obtained in long-time breakdown tests (*V-t* characteristics).

A tree reaches the opposite electrode in a needle-plane electrode system in the above discussion. But it does not necessarily mean dielectric breakdown of a whole sample. The tree is too thin in its diameter in the beginning to cause dielectric breakdown. Partial discharges (PDs) are considered to be involved to expand the diameter. PDs erode the inner surface of the tree to expand the diameter of the tree. This increases PDs in turn, which is a positive feedback process for PDs. Finally ac breakdown takes place when a trunk of the tree is spacious enough to form a sufficiently conducting path. Nanocomposite is more resistant to PDs than neat epoxy. Thus short-time ac breakdown voltage can be higher for nanocomposite than for neat epoxy. This is usually obtained experimentally.

5.5.5 *Consideration of X_3 and X_4*

As indicated in Table 5.1, a cross point X_3 appears at a coordinate (15 kV_{rms}, 300 μm/min) for a 100-μm tree, while X_4 is recognized at 18 kV_{rms}, 400 μm/min for a 10 μm tree. Thus, it is concluded that 1.5 s is needed to form a 10-μm tree, while it takes 20 s to form a 100-μm tree. It seems that a 100-μm tree grows faster than a 10-nm tree under this condition of applied voltage. As already observed, voltage at which tree propagation speed in nanocomposite exceeds that in neat epoxy is higher for the 10-μm tree than for the 100-μm tree. Time to be needed to form a 10-μm tree must include tree incubation time to form a tree bud. If this point is taken into consideration, a tree grows more quickly in nanocomposite than in neat epoxy under such a high electric field.

5.5.6 *Initial Tree Length and Tree Buds*

Lengths of initial trees or tree buds are estimated from a relation between tree length and elapsed time at several voltages. This is derived for neat epoxy and epoxy–silica nanocomposite from data obtained for *V-t* characteristics (Fig. 5.11), for tree initiation, and for treeing breakdown. Results are shown in Table 5.2. Then, it is concluded that initial trees possess the following characteristics:

(i) Initial tree length seems to be independent of applied voltage at least up to 10 kV_{rms}.
(ii) Initial tree length seems to be irrespective of presence or absence of nanofiller.
(iii) Average value of initial tree length is 6 μm.

This initial tree is considered to represent the first burst local breakdown in the range of schubweg for charge injection. It should be noted that this value is for relatively low electric field. At high field, it might be modified because it is known that a tree becomes long at high field once it is generated. A somewhat different mechanism will appear under this condition. Furthermore, it is of interest to note that this value for epoxy is shorter than 20 μm for polyethylene presented in the past [15], which suggests some difference in schubweg by different materials.

Table 5.2 Estimated initial tree length for epoxy and nanocomposite

	Estimated initial tree length (μm)		
Applied voltage	6 kV_{rms}	8 kV_{rms}	10 kV_{rms}
Neat epoxy	7.6	7.5	2.3
Nanocomposite	4.3	8.3	6.0
Average	6.0		

Estimated from the dependence of tree length on time

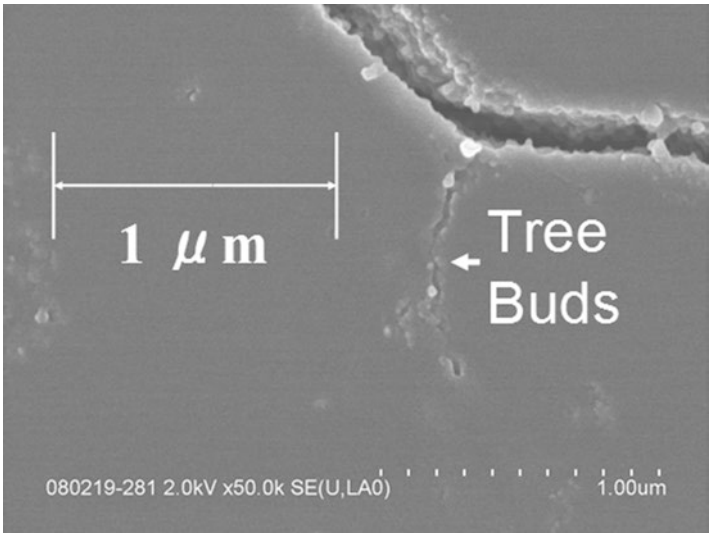

Fig. 5.15 Photo of a tiny thin branch tree from a thick tree trunk that shows some interaction with nanofiller particles

An initial tree or a tree bud generated from an electrode tip has not been directly observed yet. Figure 5.15 shows some tree traces in epoxy–silica nanocomposites including a tree trunk and a tiny tree branch. The tree trunk must be formed due to erosion created by repeated PDs after tree formation, and the tiny tree must be formed by a single shot of voltage. If the latter represents a tree bud, it is 800–900 nm in length, which is smaller than 1 μm. It has further branches in 500 nm apart.

It is to be noted that there is a discrepancy between estimated extrapolated length (6 μm) of an initial tree and the length (1 μm) of a small branched tree. If a tree is fractal, they should be the same. Much ambiguity must remain by the extrapolation method. Therefore, an absolute value of the initial tree length is not conclusive.

5.5.7 Suppression of Treeing by Nanofillers

There is a marked difference in tree growth below and above a critical voltage. Different mechanisms seem to be operative below and above such a voltage. This critical voltage is about 10 kV_{rms} for epoxy and its nanocomposite tested in a specified treeing electrode system used in this research. Maximum electric field in the tip of a needle electrode before a tree starts is 520 kV_{rms}/mm (MV/m) in this case. The following knowledge can be drawn:

1. A tree grows at a constant speed at the critical voltage.
2. A tree starts but stops below the critical voltage.
3. A tree grows up to the opposite electrode above the critical voltage.

Figure 5.16 illustrates the above three characteristics. A tree grows at a constant speed at 10 kV_{rms} for neat epoxy and nanocomposite. Below this voltage, a tree grows at its initial stage but slows down and finally stops growing. In these two cases at least, nanofillers act to suppress tree growth. Above 10 kV_{rms}, a tree grows up to the opposite electrode. At a certain voltage above this voltage, a tree grows slower first and faster later in nanocomposite than in neat epoxy. This performance is described in Fig. 5.16 as two logistic curves. Nanofillers decelerate tree growth in the beginning but accelerate it in the end as described as a crossover point beyond which tree propagation is faster in nanocomposite than in neat epoxy. It means that a tree reaches the opposite electrode in nanocomposite faster than in neat epoxy. This finding must correspond to a crossover phenomenon discovered in tree length vs. applied voltage characteristics (Fig. 5.15).

Figure 5.17 illustrates what are happening in tree growth in the two voltage ranges. At low voltage below 10 kV_{rms}, a tree starts to grow to a certain length such as 100 μm and slows down if nanofiller particles are present. Therefore it will take longer time in nanocomposite than in neat epoxy. Tree shapes with the same length are shown for epoxy and nanocomposite. In epoxy, a tree is easy to grow to have thin channels. In nanocomposite, it is blocked by nanofillers and then subjected to PDs for longer time, resulting in forming thick channels. These characteristics are illustrated in Fig. 5.17(1). The formation tree is governed at low voltage by such a PD dominant mechanism.

At high voltage, a tree is extended fast both in epoxy and nanocomposite by successive local breakdown and then is slowly widened by PD activity. From the experimental results, it grows faster in nanocomposite than in epoxy. A tree is considered to grow in epoxy matrix region between neighboring nanoparticles by successive local breakdown. Thin channels extend rapidly and progressively. This performance is illustrated in Fig. 5.17(2). The formation tree is governed at high voltage by such a treeing dominant mechanism.

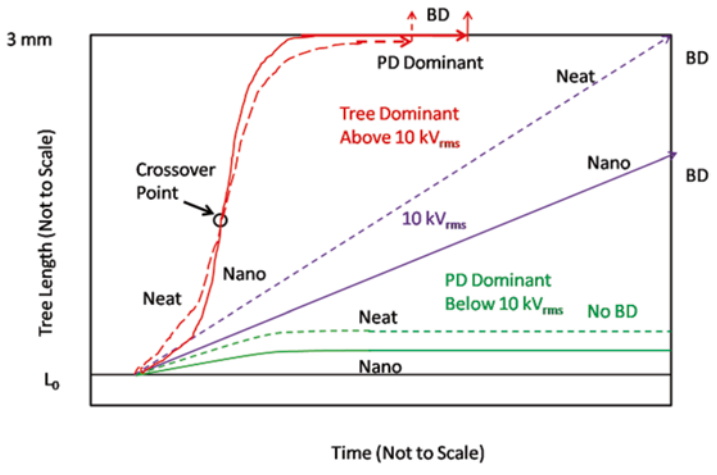

Fig. 5.16 Image of tree growth with time depending on applied voltage

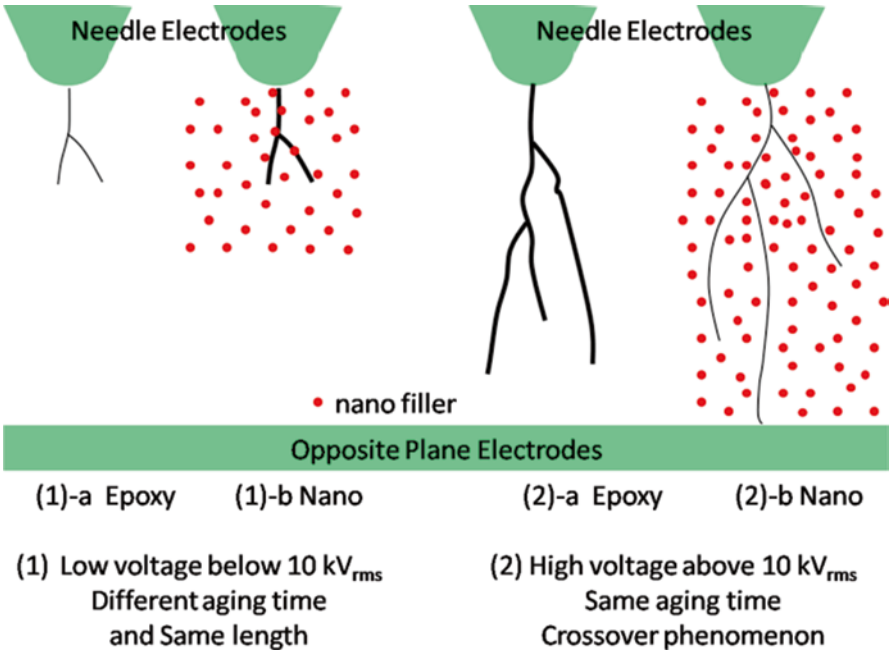

Fig. 5.17 Possible mechanisms for high and low voltage tree growth

An infancy tree at low voltage is estimated to have a 6-μm length that must be equivalent to schubweg. Considering that the incubation period until this growth is prolonged by nanofiller, the following mechanisms are responsible for this:

1. Charge injection is suppressed by nanofiller.
2. Material degradation, especially oxidation, is retarded due to the existence of nanofiller.
3. Schubweg is reduced by nanofiller.

However, as the measured time to be required for 10-μm tree extension includes incubation time or budding time, and the initial tree length 6 μm seems to be independent of applied voltage, there is some contradiction in explanation to be clarified further.

5.5.8 Roles of Nanofillers in Tree Growth Processes

One of the most striking findings is that the existence of nanofillers in epoxy retards tree propagation at low electric field but expedites it at high electric field. Thus a crossover phenomenon is recognized. A tip of thin tree channels reaches the opposite electrode in nanocomposite earlier than in neat epoxy. But it does not mean that

ac breakdown voltage is reduced by the addition of nanofillers. To fulfill the final breakdown, some more time is needed to expand the trunk of a formed tree sufficiently to accommodate gaseous discharges inside the tree channel.

Some other results are obtained as follows:

1. Initial tree lengths are around 6 μm seemingly irrespective of neat epoxy or nanocomposite. But there is an evidence for the fact that filler plays a role to retard the birth of a tree bud.
2. The addition of nanofillers would extend tree initiation time as well as BD time and increase n values as the slope of the curves in log–log plot of *V-t* characteristics.
3. At 10 kV_{rms}, the tree growth speed becomes the same for trees of 10, 100, and 3000 μm (BD) in length. Under this condition, a tree grows at a constant speed of 3 μm/min and 0.3 μm/min for neat epoxy and nanocomposite, respectively.
4. Below 10 kV_{rms}, a tree starts to grow at first but tends to stop growing afterward. It is presumed that PD is predominant to extend a tree but expand in the direction of its diameter at the same time, resulting in forming thick channels. A tree seems to attract nanofillers on its inner surface. Nanofiller is much effective to suppress its growth, because nanofillers are considered to play a significant role against PD attack.
5. Above 10 $kV_{rms,}$ a tree grows rapidly forming thin channels. Tree channels are considered to be extending in matrices by being exerted by some force like Coulombic repulsion force.
6. From *V-t* and *S-V* characteristics, it can be said that nanofiller addition seems to be ineffective to increase short-time breakdown strength at high electric field.

References

1. Froehlich H (1949) Theory of dielectrics – dielectric constant and dielectric loss-, 2nd edn. Clarendon, Oxford
2. Dissado LA, Fothergill JC (1992) Electrical degradation and breakdown in polymers. Peter Peregrinis Ltd., London
3. Iizuka T, Tanaka T (2009) Effects of nano silica filler size on treeing breakdown lifetime of epoxy nanocomposites. Proc. ICPADM. pp 733–736
4. Iizuka T, Uchida K, Tanaka T (2009) Voltage endurance characteristics of epoxy/silica nanocomposites. IEEJ Trans FM 129–3:123–129 (in Japanese)
5. Iizuka T, Uchida K, Tanaka T (2010) Effects of nano silica filler size on treeing breakdown of epoxy nanocomposites. IEEJ Trans FM 130–9:837–842 (in Japanese)
6. Li S (2010) Short-term breakdown and long-term failure in nanodielectrics- reviews. IEEE Trans Dielectr Electr Insul 17–5:1523–1535
7. O'Dwyer JJ (1973) The theory of dielectric breakdown in solids. Clarendon, Oxford
8. Raetzke S, Ohki Y, Imai T, Tanaka T, Kindersberger J (2009) Tree initiation characteristics of epoxy resin and epoxy/clay nanocomposite. IEEE Trans Dielectr Electr Insul 16–5:1473–1480
9. Seitz F (1949) On the theory of electron multiplication in crystals. Phys Rev 76–9:1376–1393
10. Tanaka T, Greenwood A (1978) Effects of charge injection and extraction on tree initiation in polyethylene. IEEE Trans Power Apparatus Syst 97–5:1749–1759

11. Tanaka T (2001) Space charge injected via interfaces and tree Initiation in polymers. IEEE Trans Dielectr Electr Insul 8–5:733–743
12. Tanaka T, Kozako M, Fuse N, Ohki Y (2005) Proposal of a multi-core model for polymer nanocomposite dielectrics. IEEE Trans Dielectr Electr Insul 12–4:669–681
13. Tanaka T, Matsunawa A, Ohki Y, Kozako M, Kohtoh M, Okabe S (2006) Treeing phenomena in epoxy/alumina nanocomposite and interpretation by a multi-core model. IEEJ Trans FM 126–11:1128–1135
14. Tanaka T (2009) Similarity between treeing lifetime and PD resistance in aging mechanisms for epoxy nanocomposites. Proc ICPADM 2:741–744
15. Tanaka T (2010) Buds for treeing in epoxy nanocomposites and their possible interaction with nano fillers. Proc ICSD. pp 159–162

Chapter 6
Polymer Nanocomposites for Power Energy Storage

Qi Li and Qing Wang

6.1 Introduction

Dielectric capacitors that store electric energy through static charge separation between two opposite electrodes induced by the external electric field are ubiquitous in electronics and electric power systems. When a dielectric capacitor is connected to a charging circuit, the amount of electric energy per volume that can be stored in dielectric capacitors is called stored energy density, and when the charged capacitor is then connected to a discharging circuit, the amount of energy per volume that can be released is called dischargeable energy density. These energy densities are usually measured volumetrically in joule per cubic centimeter (J/cm^3).

Energy density is one of the most important criteria for energy storage devices. While dielectric capacitors bear the intrinsic advantage of fast charge and discharge, the energy densities of commercially available dielectric capacitors are much lower relative to their electrochemical counterparts, such as batteries and electrochemical capacitors [1–4]. As the energy density of capacitors is governed by the dielectric materials that separate the opposite static charges between two electrodes, the development of dielectric materials with greatly improved energy density has thus been a major enabling technology for high-energy-density dielectric capacitors.

In general, to compute the energy density of a dielectric material, electric displacement (D) of the material is measured as a function of electric field (E) during the charge–discharge process to plot the D-E loop (Fig. 6.1). The stored energy density is equal to the integral

$$U_s = \int E \mathrm{d}D \tag{6.1}$$

Q. Li, PhD • Q. Wang, PhD (✉)
Department of Materials Science and Engineering, The Pennsylvania State University, University Park, State College, PA 16802, USA
e-mail: qul14@psu.edu; wang@matse.psu.edu

© Springer International Publishing Switzerland 2016

X. Huang, C. Zhi (eds.), *Polymer Nanocomposites*,
DOI 10.1007/978-3-319-28238-1_6

where E is the electric field and D is the electric displacement. As shown in Fig. 6.1, the area of the region that is bounded by the graph of charging, the D-axis, and the horizontal line $y = D_{max}$ defines the stored energy density. Similarly, the area of the region that is bounded by the graph of discharging, the D-axis, and the horizontal line $y = D_{max}$ defines the dischargeable energy density (U_d). The dissipated energy (U_l) caused by electric conduction and/or ferroelectric hysteresis is indicated by the region surrounded by the loop. Apparently, the total charged energy density (U_s) is equal to U_d plus U_l. The charge–discharge efficiency (η) is defined as $U_d/U_s \times 100\ \%$. In particular, for linear dielectrics, the stored energy density can be simply calculated following the equation:

$$U_s = \tfrac{1}{2} DE = 1/2 \varepsilon_r \varepsilon_0 E^2 \tag{6.2}$$

where ε_r is the relative static permittivity, ε_0 is the permittivity of free space, and E is the applied electric field.

Equations 6.1 and 6.2 together suggest that the energy density of a dielectric could be improved by increasing at least one of the two parameters, i.e., the dielectric constant (K) and the electric breakdown strength (E_b). This is because K determines the electric displacement, and E_b defines the highest field that can be applied on the dielectric. Recently, to integrate the complementary advantages of inorganic and organic dielectric materials for high energy storage, attempts to incorporate inorganic nanoparticles with high K into polymer matrices have been made via mechanical blending, solution mixing, or in situ radical polymerization [5–12]. This chapter summarizes the recent progress in polymer nanocomposites for dielectric power energy storage.

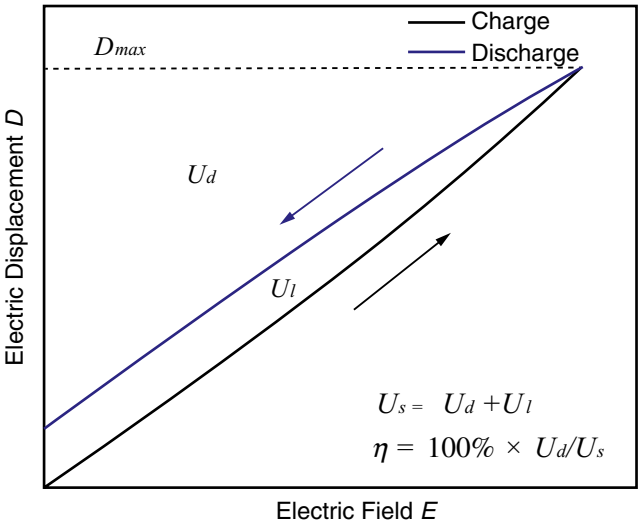

Fig. 6.1 Schematic *D-E* loop for a dielectric material

6.2 Increasing Dielectric Constant of Polymer Nanocomposites

Inorganic materials, such as the barium titanate, enjoy very high-K values (typically ranging from thousands to hundreds of thousands) but are limited by the low E_b (i.e., lower than 100 MV/m) [13]. On the other hand, polymer dielectrics possess good processability, low cost, light weight, high E_b, and graceful failure, although their K values are much lower than those of their inorganic counterparts [14–16]. For example, one of the best commercially available polymer dielectrics, represented by the biaxially oriented polypropylenes (BOPP), has a K of ~ 2.2, and an E_b of > 700 MV/m [17]. As a result, at comparable electric fields, inorganic dielectrics show much higher energy densities in comparison to organic dielectrics. It is thus a promising strategy to incorporate inorganic nanoparticles into polymer dielectrics to increase the effective dielectric constant of the composite material and, at the mean time, preserve the high breakdown strength of the polymer.

6.2.1 Using Ceramics as Fillers

The effective dielectric constant of a two-phase composite system can be predicted by the Maxwell Garnett equation on the basis of the effective medium theory that can be expressed as [18]

$$\varepsilon = \varepsilon_2 \frac{2\varphi_1\left(\varepsilon_1 - \varepsilon_2\right) + \varepsilon_1 + 2\varepsilon_2}{2\varepsilon_2 + \varepsilon_1 + \varphi_1\left(\varepsilon_2 - \varepsilon_1\right)} \tag{6.3}$$

where ε is the effective permittivity of the composite and φ_1 and φ_2 are the volume fractions of filler phase and polymer phase, which have relative permittivities of ε_1 and ε_2, respectively. Equation 6.3 indicates that the incorporation of high-K fillers would directly give rise to an increased K value of the composite material. Besides, the coupling effect occurring at the interface areas in the nanocomposite would create considerable level of interfacial polarization between the filler and matrix phases that advances the energy density of the material [19–21]. Indeed, experimental results have shown that much increased K values of the polymer nanocomposites are attained with high-K inclusions such as $BaTiO_3$, $Ba_xSr_{1-x}TiO_3$, $CaCu_3Ti_4O_{12}$, and Pb(Zr, Ti)O_3, leading to improved energy densities [22–46].

6.2.1.1 Surface Functionalization of Filler Particles

Since nanoscale fillers possessing large surface areas could provide high levels of interfacial polarization, they are the inclusions of the choice for dielectric polymer composites with high energy densities. Because nanoparticles have strong tendency

to aggregate in a polymer matrix due to the high surface energy, they are usually surface functionalized in order to improve the compatibility and achieve homogeneous distributions. This is beneficial in two aspects: (1) uniform dispersion of high-K fillers would minimize the degree of distortion of the local field induced by the large difference in dielectric constant between the filler and matrix phases [47] and (2) elimination of filler aggregation could get rid of the microstructural defects at the filler–matrix interface such as voids and flaws. This is important as either the distortion of the local field or the microstructural defects would result in a significant decrease in breakdown strength of the nanocomposite and thereby offset any potential gain in the energy density from increased K values.

Perry et al. reported phosphonic acid-modified $BaTiO_3$–polymer nanocomposites and concluded that the use of particles modified with suitable phosphonic acid ligands leads to well-dispersed $BaTiO_2$ nanocomposite films with high dielectric constant [25]. The authors examined a series of ligands as the modifier, each bearing an aliphatic octyl chain with a different terminal binding group. It was found that the ligand bearing the phosphonic acid functional group could be firmly bound on $BaTiO_3$ nanoparticles in a tridentate form. To demonstrate the effectiveness of the proposed strategy, the authors provided two examples using these ligands (Fig. 6.2a) to modify $BaTiO_3$ nanoparticles, and two polymer dielectrics were chosen as matrices, i.e., the bisphenol-A-type polycarbonate (PC) and the poly(vinylidenefluoride-*co*-hexafluoropropylene) (P(VDF-HFP)). The obtained nanocomposites showed much higher K values relative to the blank polymers and fairly low dielectric loss (Fig. 6.2b), even though the breakdown strength was also relatively low (~210 MV/m) compared with those of the polymer matrices (e.g., E_b of the P(VDF-HFP) is around 500 MV/m). As a result, the stored energy densities were improved, i.e., 3.9 J/cm^3 for the $BaTiO_3$–PC nanocomposite and 6.1 J/cm^3 for the $BaTiO_3$–P(VDF-HFP) nanocomposite. Following this strategy, a variety of ligands were developed to modify the high-K ceramics for dielectric polymer nanocomposites, such as ethylene diamine [23], dopamine [33], organic titanate coupling agent [44], and silane coupling agent [45, 46].

Another approach to improving the dispersion of filler particles is to directly link the nanoparticles to the molecular chain of the host matrices via covalent bonding. This can be achieved through two different methods which are coined as "grafting from" [48–51] and "grafting to" [26, 30, 52–54] methods, respectively.

The so-called "grafting from" method is referred to describe the initialization of the growth of polymer chains from the surface of nanoparticles. Marks et al. proposed an in situ synthesis of high-energy-density metal oxide nanocomposites [48]. The dielectric nanocomposites were prepared via in situ metallocene polymerization of isotactic propylene from the surface of methylaluminoxane (MAO)-coated inorganic nanofillers (Fig. 6.3). The authors first anchored the MAO onto the nanoparticles via surface hydroxyl group reaction to form covalent Al–O bonds. Then anchored MAO functioned as a co-catalyst to activate the metallocene, and in addition, the hydrophobic MAO functionalization helped disrupt, in combination with ultrasonication, hydrophilic nanoparticle agglomeration in the hydrophobic reaction medium. In virtue of the covalent linkage between the filler and matrix phases, uniform filler distribution was attained in the as-prepared nano-

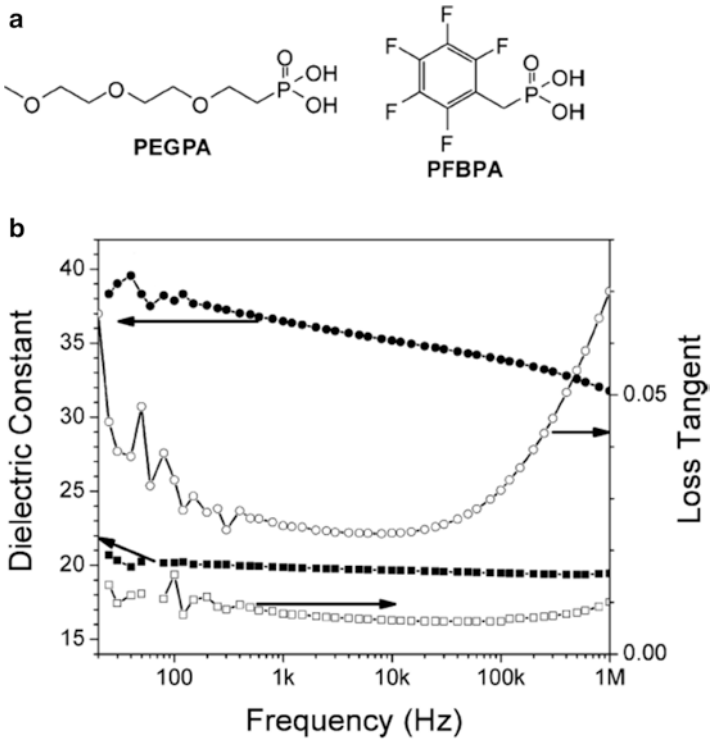

Fig. 6.2 (**a**) Molecular structures of phosphonic acid ligands used to modify $BaTiO_3$ nanoparticles. (**b**) Frequency-dependent dielectric response of capacitor devices fabricated from PEGPA-BT/PC (*squares*) and PFBPA-BT/P(VDF-HFP) (*circles*) (Reprinted from Ref. [25] with permission from John Wiley and Sons)

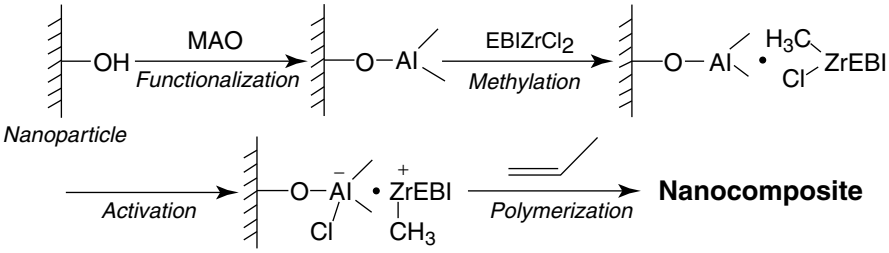

Fig. 6.3 Schematic illustration of synthetic route of isotactic polypropylene–metal oxide nanocomposites (Reprinted with permission from Ref. [48]. Copyright 2007 American Chemical Society)

composites that exhibited moderately increased dielectric constant with high breakdown strength of the polymer matrix being maintained. Consequently, the energy density of the nanocomposite was calculated to be as high as 9.4 J/cm^3. This approach was then extended to other types of polymer matrices by employing different chemistry and polymerizing techniques. For example, Jiang et al. devel-

oped a $BaTiO_3$–poly(methyl methacrylate) (PMMA) nanocomposite that was prepared by in situ atom transfer radical polymerization (ATRP) of methyl methacrylate (MMA) from the surface of $BaTiO_3$ nanoparticles (Fig. 6.4) [49]. By doing so, the dielectric constant of the nanocomposite was improved to ~14.6 from 3.5 of the pure polymer, and in the meantime, the dielectric loss was almost independent of the filler content.

The "grafting to" method involves establishing covalent binding between the filler and polymer phases through functional groups on the polymer chains and the surface of filler particles. A typical example was reported by Wang and coworkers [27]. They prepared the ferroelectric polymers with phosphonic acid end groups (Fig. 6.5a) and subsequently used the reactive terminal groups of the polymer for direct coupling with oxide fillers. The formation of covalent coupling between the polymer matrix and filler particles renders the nanocomposites with good stability and uniform filler dispersion (Fig. 6.5b). Due to the rise of the electric displacement induced by the incorporated nanofillers, the energy storage capability of the nanocomposites was improved (Fig. 6.5c). Another example of the "grafting to" method introduced glycidyl methacrylate (GMA) functionalized P(VDF-HFP) as the matrix to accommodate $BaTiO_3$ nanoparticles, and the covalent linking of the matrix and filler phases was achieved via ring-opening reaction between the epoxy groups of GMA grafted onto P(VDF-HFP) and the amino groups on the surface of $BaTiO_3$ nanoparticles (Fig. 6.6a) [52]. Again, homogeneous filler dispersion and improved dielectric constant were observed in the nanocomposites (Fig. 6.6b, c).

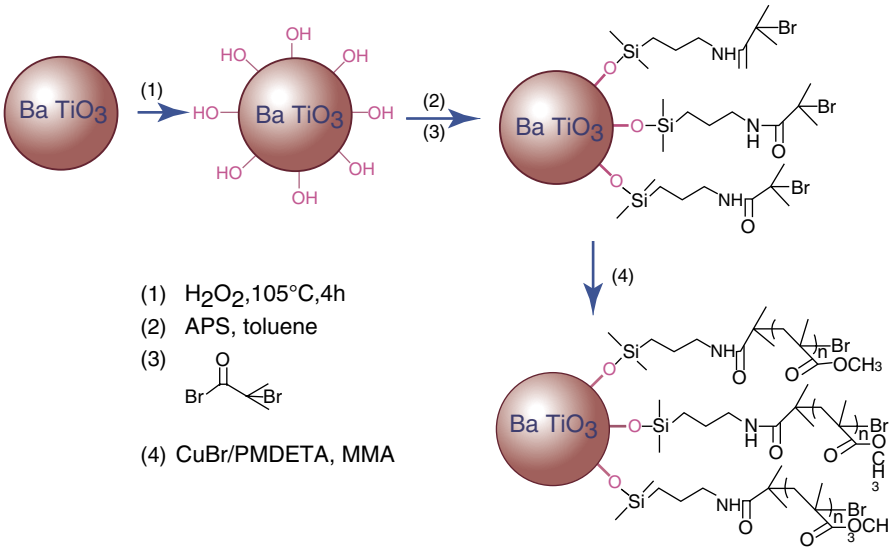

Fig. 6.4 Schematic diagram illustrating the process of ATRP from the surface of $BaTiO_3$ (Reprinted from Ref. [49] with permission from Royal Society of Chemistry)

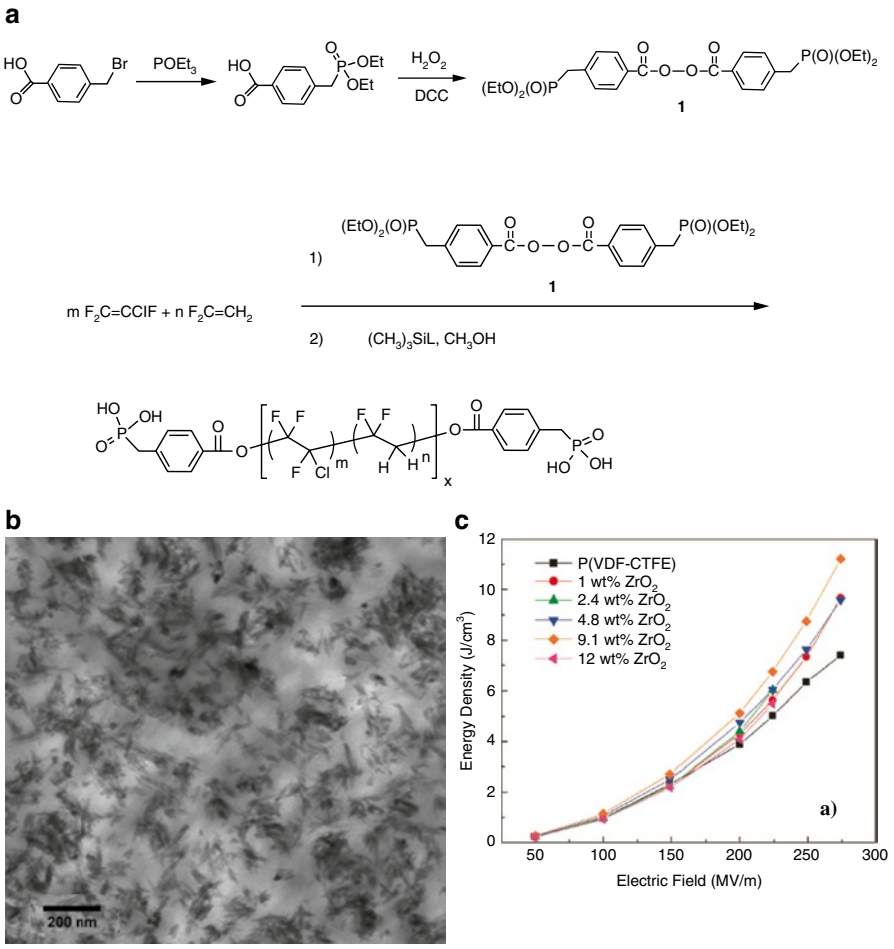

Fig. 6.5 (**a**) Synthesis of the functional initiator and the phosphonic acid-terminated P(VDF-CTFE). (**b**) TEM image of the covalent-bonded P(VDF-CTFE). (**c**) Stored energy density of the polymer and the nanocomposites as a function of the applied field (Reprinted with permission from Ref. [27]. Copyright 2010 American Chemical Society)

6.2.1.2 High Aspect Ratio Fillers

Three-dimensional continuous polymer matrices filled with zero-dimensional nanoparticles is usually referred to as 0-3 polymer nanocomposites. Similarly, those containing one-dimensional inclusions are 1-3 polymer nanocomposites. Recent studies on dielectric nanocomposites have shown that high-*K* nanofillers with high aspect ratios, i.e., one-dimensional nanowires or nanorods, could lead to more significant increase in dielectric constant of dielectric polymers, as compared with zero-dimensional nanoparticles [40, 55–58]. Therefore, composing 1-3 polymer nanocomposites has become a promising strategy toward high-energy-density capacitors.

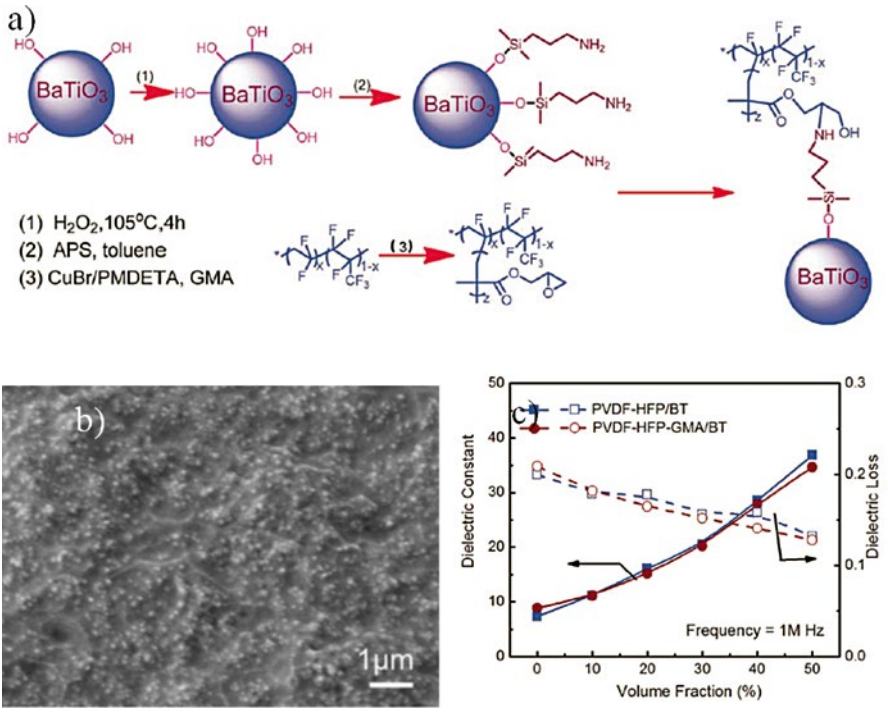

Fig. 6.6 (**a**) Schematic illustration of the preparation process for the PVDF-HFP-GMA–BT nanocomposites. (**b**) SEM images of the fractured surface of the PVDF-HFP-GMA nanocomposite with 20 vol% $BaTiO_3$ nanoparticles. (**c**) Comparison of the dielectric properties for the PVDF-HFP-GMA–BT and PVDF-HFP–BT nanocomposites at 1 MHz (Reprinted from Ref. [52] with permission from Royal Society of Chemistry)

Sodano et al. reported lead zirconate titanate (PZT)–polyvinylidene fluoride (PVDF) dielectric nanocomposites, in which the nanosized inclusions were of different aspect ratios and are termed as nanowires (higher aspect ratio) and nanorods (lower aspect ratio), respectively [40]. The nanocomposite filled with PZT nanowires showed higher dielectric constant and lower loss than that loaded with PZT nanorods, which gave rise to a higher energy density, demonstrating the effectiveness of using high aspect ratio nanofillers for the fabrication of polymer nanocomposites for capacitive energy storage.

By using $BaTiO_3$ nanowires as the filler, the energy density of a ferroelectric terpolymer poly(vinylidene fluoride-trifluoroethylene-chlorofluoroethylene) (P(VDF-TrFE-CFE)) was increased by 45 %, achieving 10.48 J/cc at the electric field of 300 MV/m [55]. Later, $Ba_{0.2}Sr_{0.8}TiO_3$ nanowires were also employed to prepare a composite dielectric using PVDF as the matrix (Fig. 6.7) [56]. The discharged energy density of the nanocomposite, namely, 14.86 J/cc, was 43 % larger relative to the pure PVDF, which was attained at the electric field of 450 MV/m (Fig. 6.8). Because polymer dielectrics filled with high-K nanowires can achieve higher dielectric

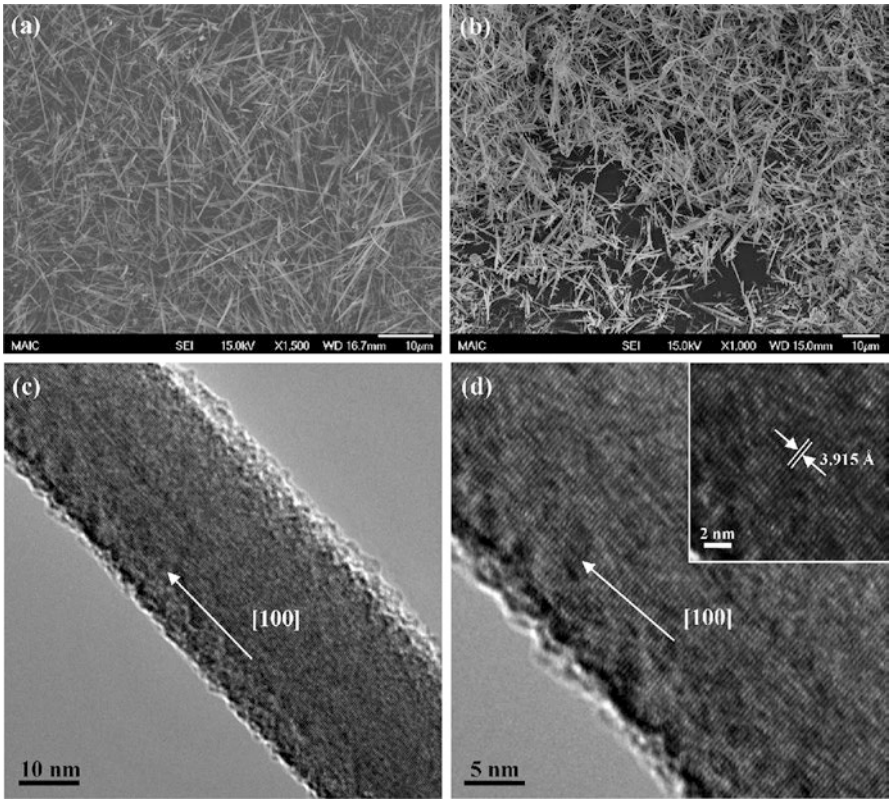

Fig. 6.7 SEM images of (**a**) sodium titanate NWs and (**b**) $Ba_{0.2}Sr_{0.8}TiO_3$ NWs. (**c**) TEM image of a single $Ba_{0.2}Sr_{0.8}TiO_3$ nanowire. (**d**) Representative HRTEM image showing clear crystal lattice fringes of the $Ba_{0.2}Sr_{0.8}TiO_3$ nanowire (Reprinted with permission from Ref. [56]. Copyright 2013 American Chemical Society)

constants than those filled with high-*K* nanoparticles, lower filler content is required for 1-3 systems to induce a similar level of electric displacement as compared with the 0-3 system. This would naturally result in a higher breakdown strength for the 1-3 nanocomposite since breakdown strength decreases with increasing feeding ratio of the high-*K* fillers.

6.2.1.3 Nanofillers with Moderate Dielectric Constant

According to the Maxwell Garnett equation (Eq. 6.3), high-*K* nanofillers would be the dopants of choice for improving the dielectric constant of polymer dielectrics. However, the presence of high-*K* nanofillers in dielectric polymers causes highly inhomogeneous electric field across the nanocomposite due to the large

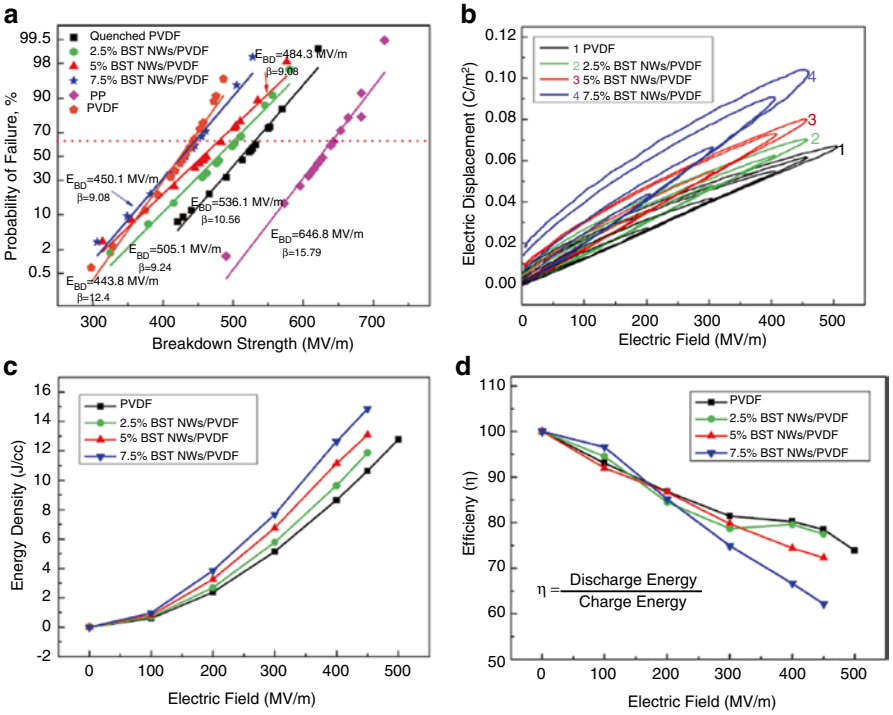

Fig. 6.8 (**a**) Weibull distribution and observed dielectric breakdown strength of nanocomposites with different volume fraction of BST, quenched PVDF, untreated PVDF, and commercial polypropylene films; (**b**) unipolar electric *D-E* loops for nanocomposites with different BST NWs volume fractions; (**c**) energy density of the nanocomposite with different volume fraction as a function of the electric field calculated from *D-E* loops; (**d**) efficiencies of the nanocomposites with different volume fraction as a function of the electric field (Reprinted with permission from Ref. [56]. Copyright 2013 American Chemical Society)

contrast in dielectric constant between the dopant and matrix phases, which drastically decreases the breakdown strength of the composite system [47]. But what if nanofillers with moderate dielectric constant are used as dopants to fabricate dielectric nanocomposites?

To answer this question, Wang et al. proposed a new type of nanocomposites with comparable dielectric constants between the filler and matrix phases, i.e., $K=42$ for the host ferroelectric terpolymer poly(vinylidene fluoride-*ter*-trifluoroethylene-*ter*-chlorotrifluoroethylene) (P(VDF-TrFE-CTFE) and $K=47$ for the fillers (TiO_2 nanocrystals) [22]. Interestingly, the polarization of the nanocomposite was found to be significantly enhanced despite of the moderate dielectric constant of the nanofillers involved. The unexpected improvement in polarization was attributed to the large interfacial polarization, which was supported by the results of temperature dependent dielectric spectroscopy showing an emerging dielectric anomaly (Fig. 6.9). As a result of the enhanced polarization, the energy

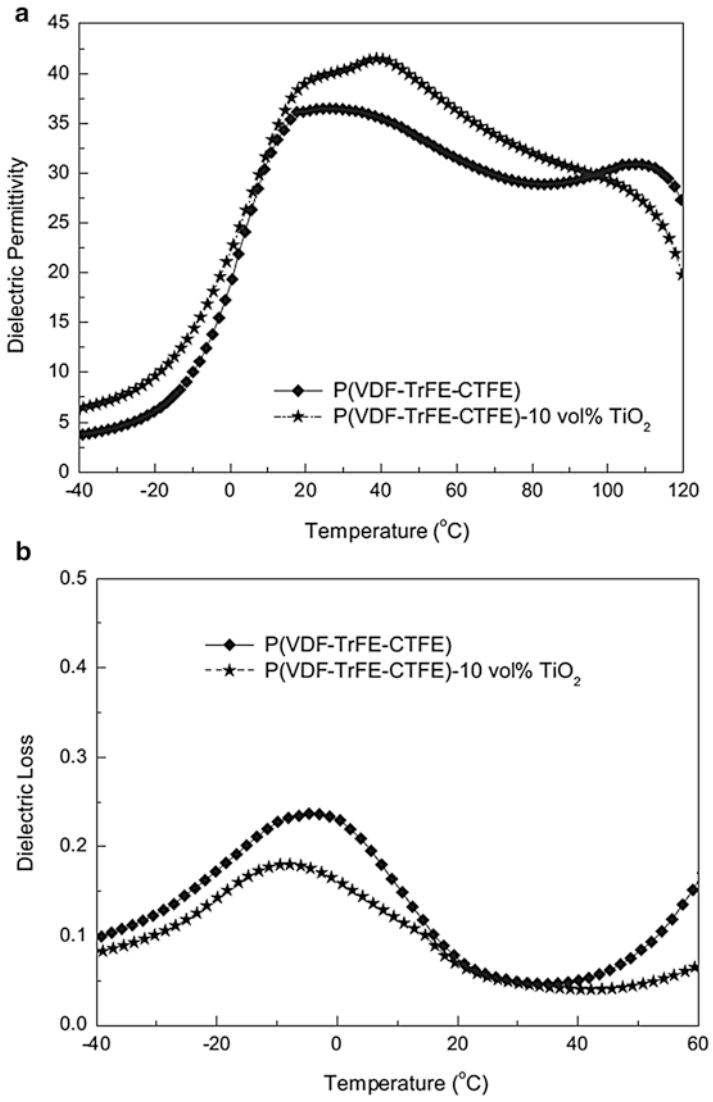

Fig. 6.9 Temperature dependence of the (**a**) dielectric constant and (**b**) dielectric loss of the polymer and nanocomposite measured at 1 kHz (Reprinted from Ref. [22] with permission from John Wiley and Sons)

density of the nanocomposite was found to be 40 % higher than that of the pristine terpolymer under an electric field of 200 MV/m. By employing nanofillers with moderate dielectric constant, the polarization could be increased without compromising breakdown strengths of host polymers and thus leading to much improved capacitive energy storage capabilities. Along this line, polymer nanocomposites

incorporating other nanofillers with moderate dielectric constant were also studied [12, 27, 59–66]. The success of this approach suggests that the usage of high-K nanofillers may not be necessary for producing high-energy-density dielectric polymer nanocomposites.

6.2.2 *Percolative Polymer Nanocomposites*

Percolation theory predicts that in the conductive particle–polymer composite system, dielectric constant increases sharply as the filler content increases to the vicinity of the percolation threshold, which can be expressed by

$$\frac{K}{K_m} = \left| \frac{f_c - f_{fil}}{f_c} \right|^{-q} \tag{6.4}$$

where K is the dielectric constant of the composite, K_m is the dielectric constant of the polymer matrix, f_c is the percolation threshold, and f_{fil} is the filler content [67]. Such abrupt increase in dielectric constant is ascribed to the formation of the so-called microcapacitor networks consisting of a large number of local capacitors [19]. Each of these microcapacitors is formed by the neighboring conductive particles as the two electrodes and a thin layer of dielectric polymer in between. All these microcapacitors contribute to the intensified local electric fields and consequently result in accumulation of charge carriers at the filler–matrix interface responsible for the increased interfacial polarization.

6.2.2.1 Giant Dielectric Constants of Percolative Nanocomposites

By capitalizing on the percolation strategy, numerous percolative polymer composites have been prepared incorporating various conductive fillers including zero-dimensional nanoparticles [68–76], one-dimensional nanotubes [77–88] and nanofibers [89–92], as well as two-dimensional nanoplates [93–98], and all show giant dielectric constants in the neighborhood of the percolation thresholds. For example, Nan et al. reported nickel particles filled polymer composites, in which drastic increase in dielectric constant was observed near the percolation threshold, i.e., from 10 of the host polymer to 400 of the composite with 17 vol.% of conductive fillers [70]. Dang et al. developed carbon nanotube–PVDF percolative polymer nanocomposites that displayed high dielectric constant of 300 at low filler content (2 vol.%) due to the low percolation threshold (1.61 vol.%) [78]. Fan et al. described a sort of percolative composites incorporating exfoliated graphite nanoplates (xGnPs) [93]. At 2.34 vol.% feeding of the xGnPs, the dielectric constant reached as high as 4.5×10^7 (Fig. 6.10).

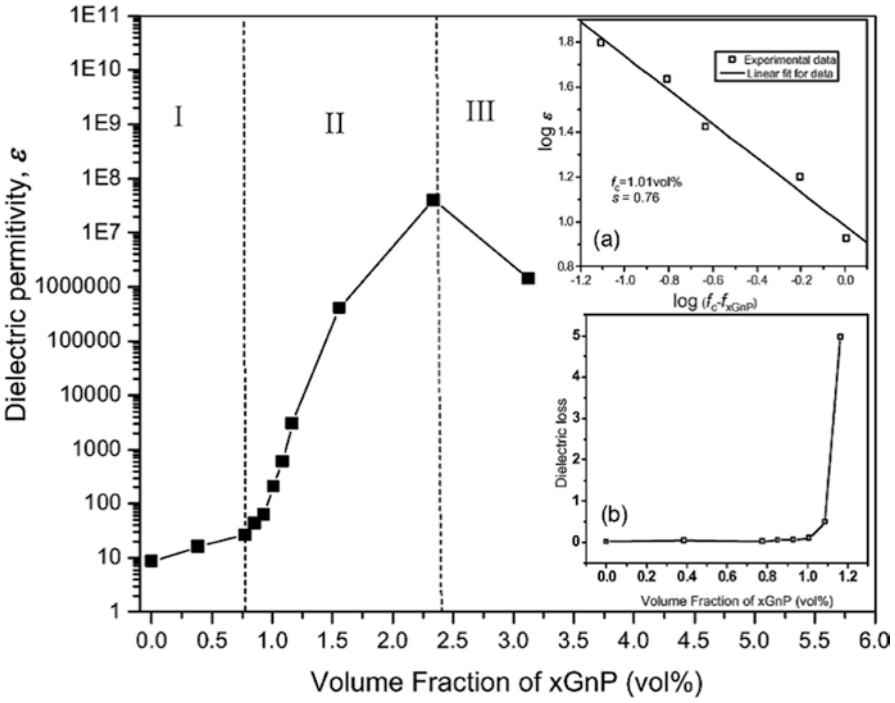

Fig. 6.10 Effective dielectric constant of the PVDF–xGnP nanocomposites as a function of the xGnP volume fraction, measured at 1000 Hz and room temperature. Inset (**a**) shows the best fits of the conductivity to Eq. 6.2. Inset (**b**) shows the loss tangent of PVDF–xGnP nanocomposites as a function of xGnP volume fraction (Reprinted from Ref. [93] with permission from John Wiley and Sons)

6.2.2.2 Conductive Fillers Covered with Insulation Layer

Although much increased dielectric constants have been observed in percolative polymer nanocomposites, the high conduction losses of these materials associated with the involved conductive fillers hindered their applications in power energy storage due to the low breakdown strength. To circumvent this problem, a plenty of efforts have focused on the creation of an insulation layer on the surface of conductive fillers to avoid the formation of conducting pathways. For instance, Nan et al. put forward a strategy using core-shell structured nanofillers with metal particle cores and organo carbon shells (Fig. 6.11) [75]. The presence of the shell structure prevented the conductive metal particles from directly connecting with each other and thus lead to a low dielectric loss (~3 %) even at percolation threshold.

Wang et al. prepared a poly(vinylidene fluoride-co-chlorotrifluoroethylene) (P(VDF-CTFE))-based percolative nanocomposite using SiO_2-coated graphene nanosheets as fillers and studied the dielectric properties at both weak and high fields [95]. While they found a fairly low dielectric loss even beyond the percolation

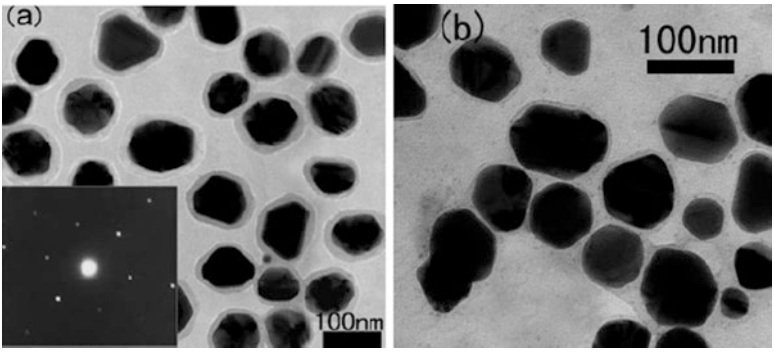

Fig. 6.11 TEM of the Ag–C core-shell particles with (**a**) thicker shells and (**b**) thinner shells (not as clearly visible as the thicker shells), where the inset in (**a**) shows the selected area electron diffraction pattern of the particles, indicating that the Ag cores are single Ag crystals (Reprinted from Ref. [75] with permission from John Wiley and Sons)

threshold, a relatively high dielectric strength was also observed, both of which were attributed to the uniform coating of insulation layer on the surface of graphene nanosheets (Fig. 6.12). Marks et al. used metallic aluminum nanoparticles with a native insulation layer of aluminum oxide as fillers to compose the percolative nanocomposite [76]. Due to the very high dielectric constant achieved and preserved breakdown strength, the energy density was calculated to be as high as 14.4 J/cm^3.

6.3 Increasing Breakdown Strength of Polymer Nanocomposites

In linear dielectrics, U_s scales quadratically with E and linearly with K. A high E is more profitable than a high K for achieving high energy density of dielectric materials. As E_b signifies the maximum E that can be applied on a dielectric material, E_b becomes the very critical parameter that determines the U_s of dielectric materials. One example is that although the K value (~2.2) of BOPP is 100–1000 times lower than those (usually at the level of 10^3–10^4) of typical dielectric ceramics, such as barium titanate, they share a very similar U_s of ~5 J/cm^3, owing to the superior E_b of BOPP (700 MV/m) compared to that of the ceramic films, i.e., ~90 MV/m. For these reasons, efforts have been made in developing high-E_b polymer dielectrics using the composite approach [99–103].

6.3.1 Polymer Nanocomposites with Insulating Nanoparticles

Roy et al. are among the first to observe the improved dielectric strength from insulating nanoparticle-filled polymer composites. They found that XLPE filled with vinylsilane-treated silica nanoparticles had a much higher Weibull

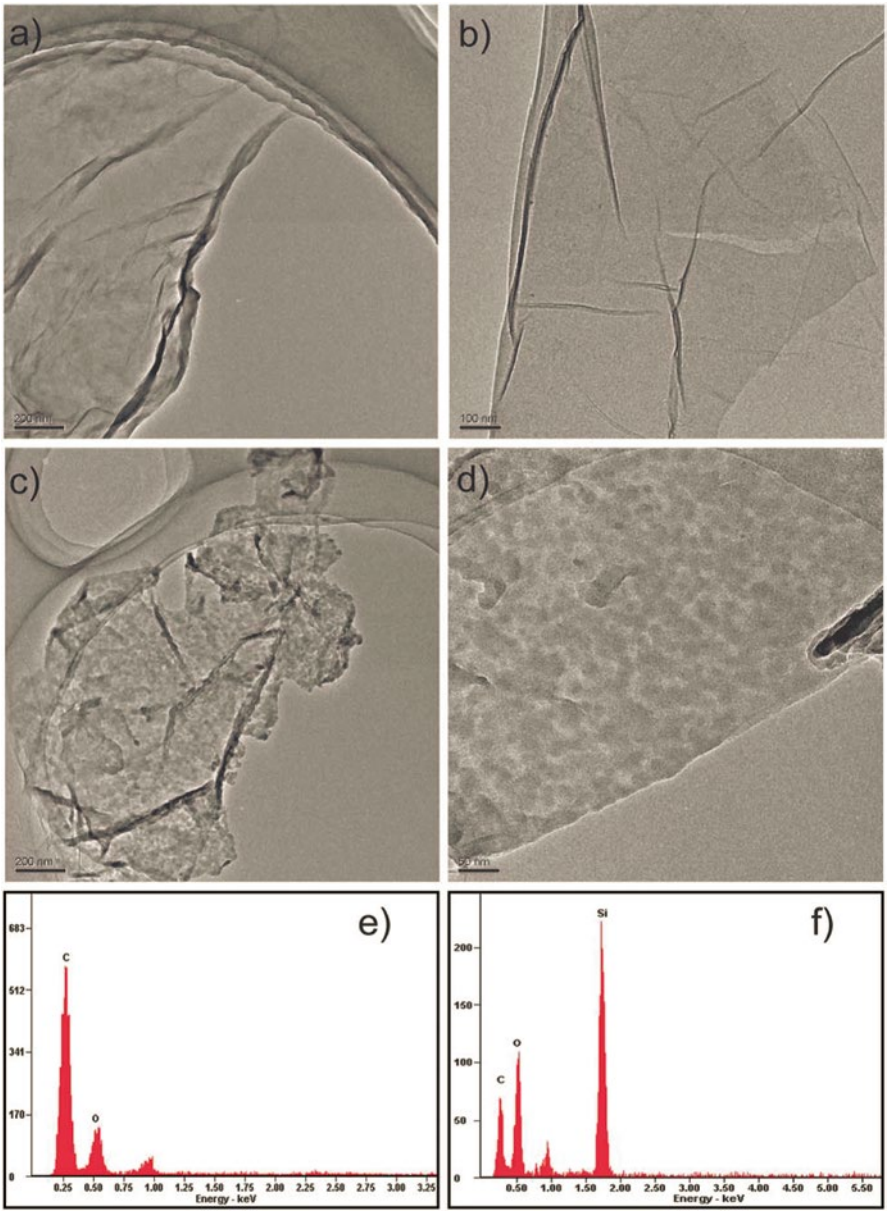

Fig. 6.12 TEM images of (**a**, **b**) GO and (**c**, **d**) r-GO–SiO_2, and EDX analysis of (**e**) GO and (**f**) r-GO–SiO_2. Scale bar: (**a**) 200 nm, (**b**) 100 nm, (**c**) 200 nm, and (**d**) 50 nm (Reprinted from Ref. [95] with permission from Royal Society of Chemistry)

breakdown strength than the bare polymer, i.e., ~500 MV/m *vs*. ~300 MV/m [99]. The authors claimed that physical bonding between nanoparticles and the polymer chain could account for the increase in breakdown strength. Takala et al. then studied silica nanoparticle-filled dielectric composites by use of PP as the matrix [100]. The as-prepared nanocomposites exerted significantly improved breakdown strength relative to the blank polymer. It was believed that the breakdown strength results related to scattering and reduced space charge accumulation, which had an effect on both ac and dc behaviors of the nanocomposite. Nanodispersion of silica also ensured low loss factor of the nanocomposite, which was owing to the large fraction of interface volume and polymer chain entanglement keeping the motion of charge carriers limited.

6.3.2 Incorporation of Insulating Nanolamilates

More recently, it was demonstrated that incorporation of two-dimensional insulating nanostructures in dielectric polymers could lead to essentially increased breakdown strength [101–103].

In a P(VDF-HFP)-based polymer nanocomposite, high aspect ratio two-dimensional kaolinite clays were employed as fillers [101]. The composite films were first cast from solution and then hot-pressed at 200 °C and 55 MPa pressure. After cooling in air, the films were uniaxially stretched mechanically by means of a zone drawing process to five times their original length, which ensured the orientation of the two-dimensional nanofillers. Finally the films were annealed at 120 °C. Unlike the nanocomposites filled with high-K materials, the P(VDF-HFP)–kaolinite clay nanocomposites exhibited decreased loss with increasing filler content, as proved in both the weak field (dielectric spectroscopy) and high field measurements (D-E loop) (Fig. 6.13).

In the meantime, the electric displacement decreased significantly in the nanocomposites compared with that of the blank polymer. Two mechanisms were proposed to rationalize the origin of this trend. First, two-dimensional nanofillers serve as nucleating agents to promote growth of nonpolar crystals in their vicinity. Due to the restricted mobility of the dipoles in these crystals, their reorientation requires higher electric fields. Second, oriented dipole density is reduced because of the incorporation of inorganic fillers, which in turn leads to a lower amount of space charge required for polarization stabilization. The high aspect ratio two-dimensional nanofillers also build up efficient conduction barriers that can limit the charge migration toward the electrodes and hinder the electrical tree growth during breakdown. These aspects contribute to the significantly improved breakdown strength of the nanocomposites, and as such, the discharged energy density increased by 100 % relative to the blank polymer despite of the reduced electric displacement. Similar results were observed using other nanolaminate fillers such as montmorillonites, and filler orientation was found to be able to provide more ordered trapping centers to obstruct the ability of charges to traverse the sample to the opposite electrode [102, 103].

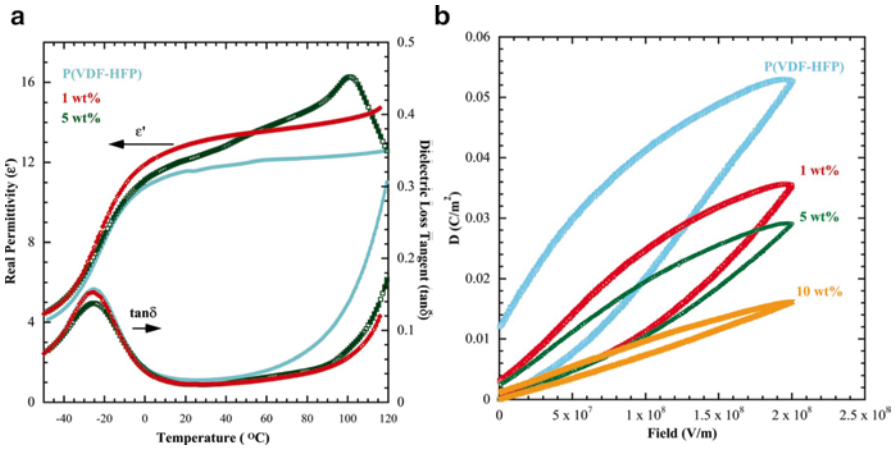

Fig. 6.13 (**a**) Dielectric permittivity and dielectric loss tangent *vs*. temperature, at low electric field and 1 kHz, for the stretched films of unfilled P(VDF-HFP) and two nanocomposites with 1 and 5 wt. % kaolinite. (**b**) Displacement vs. electric field loops of P(VDF-HFP) and of its nanocomposites; all films were uniaxially stretched. Upon kaolinite filler addition, there is a systematic reduction in remnant polarization and an associated improvement in losses (Reprinted from Ref. [101] with permission from AIP Publishing LLC)

6.4 Simultaneous Improvements of Dielectric Constant and Breakdown Strength

It is envisaged that the integration of complementary elements such as large dielectric constant from ceramics and high breakdown strength from polymers in the polymer nanocomposites could lead to an enhanced energy storage capacity. However, it remains elusive how the contradictory criteria of enhancing one parameter while maintaining the other could be balanced in the nanocomposites. For example, a marked decrease in E_b due to a large contrast in K between ceramics and polymers, as shown in current high-K filler involved dielectric nanocomposites, negates any potential substantial increase in energy density under high electric fields. In this regard, the ideal case would be simultaneous improvements of dielectric constant and breakdown strength in the nanocomposites.

This was achieved recently by employing multicomponent filler systems and utilizing either topological-structure or interface engineering [104, 105]. Shen and colleagues expanded the traditional 0-3 nanocomposite system to a multilayered structure fabricated through a simple layer-by-layer tape casting method (Fig. 6.14) [104]. For instance, they demonstrated a 3-layer structure, in which a center layer was designed to be a nanocomposite with higher breakdown strength and the top and bottom layers were both nanocomposites with high dielectric constants. Therefore, the center layer was able to improve the overall breakdown strength of the multilayer-structured nanocomposite, while the outer layers enhanced the electric displacement. As a result, the topological-structured nano-

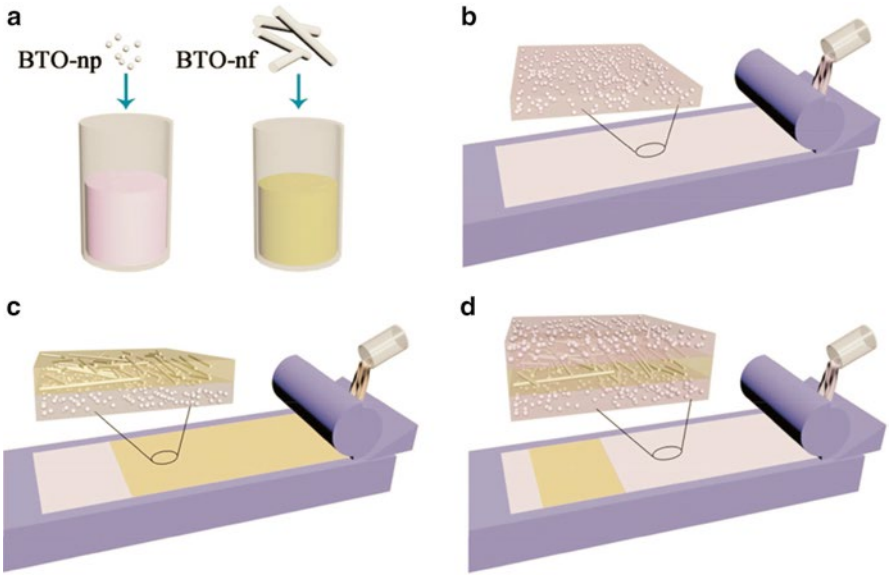

Fig. 6.14 Schematic drawing of the approach of layer-by-layer casting for the fabrication of the sandwich multilayer films. (**a**) Nanofillers were dispersed in the PVDF suspension, (**b**) one layer with BTO-np was cast, (**c**) the central layer with BTO-nf was cast, (**d**) the other layer with BTO-np was cast (Reprinted from Ref. [104] with permission from John Wiley and Sons)

composites were found to show much improved capacitive energy storage performance than the matrix polymer, i.e., a 162 % increase in discharged energy density, which was resulted from the simultaneous improvements of dielectric constant (from 7 to 10) and breakdown strength (from 260 to 450 kV/mm) in the nanocomposite. This approach combines the complementary properties of the constituent layers and thus leads to superior material performance than using traditional nanocomposite systems.

More recently, Shen and colleagues developed another approach to simultaneously improving dielectric constant and breakdown strength in polymer nanocomposites (Fig. 6.15) [105]. They employed a new type of material, i.e., $BaTiO_3$–TiO_2 nanofibers, where $BaTiO_3$ nanoparticles are embedded in TiO_2 nanofibers as inclusions in PVDF-based polymer nanocomposites. The discharged energy density of the nanocomposite was reported to be as high as 20 J/cm^3, which was from the increased electric displacement (72 % increment) and characteristic breakdown strength (8 % increment). While the origin of the increase in breakdown strength was claimed to be the large aspect ratio and partial orientation of nanofibers, the improvement in electric displacement was ascribed to the interfacial effect inside the integrated nanofillers. This was supported by the evidence from simulated atomic-resolution angular bright-field images, from which a clear interfacial layer could be observed at the intermediate region between the embedded $BaTiO_3$ nanoparticles and the host TiO_2 nanofiber. Such interfacial layer possessed a different lattice structure to those of the $BaTiO_3$ and TiO_2 phases. The interpretation made

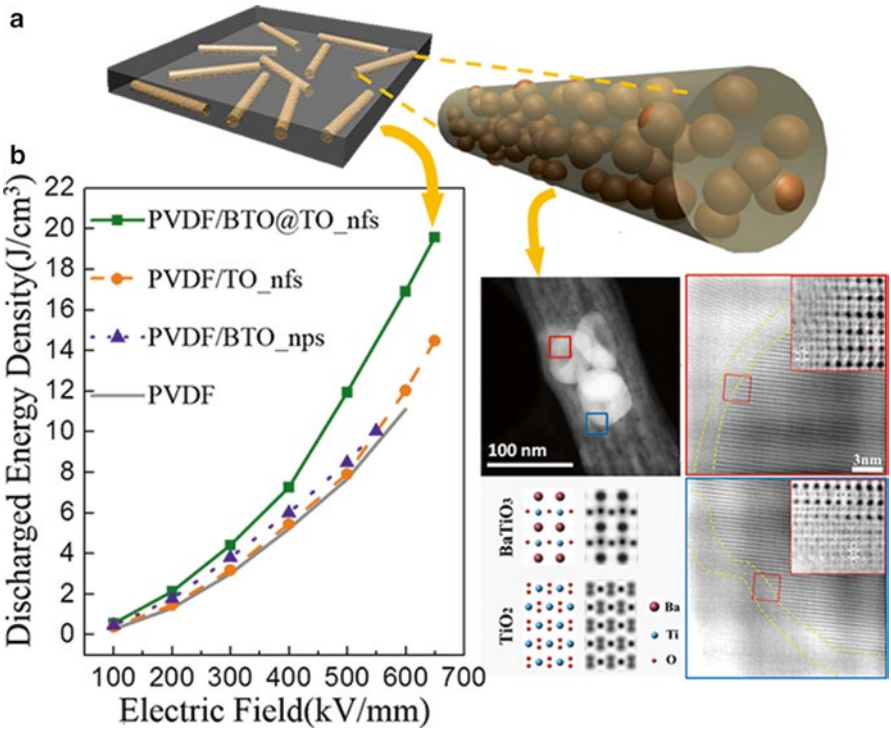

Fig. 6.15 (**a**) Schematic illustration of BTO@TO_nfs and PVDF–BTO@TO_nfs nanocomposites. (**b**) Discharged energy density of PVDF nanocomposites embedded with BTO@TO_nfs, TO_nfs, BTO_nps, and pure PVDF films as a function of electric field, the volume fraction of the three nano-inclusions were fixed at 3 % in all composites. (**c**) Structural models of $BaTiO_3$ and TiO_2 and corresponding simulated atomic-resolution angular bright-field images (Reprinted from Ref. [105] with permission from John Wiley and Sons)

on the basis of this observation was the Ba–Ti mutual occupation at the intermediate regions between $BaTiO_3$ and TiO_2 and thus a large strain should exist in these regions to benefit polarization. This work revealed that, in addition to the interfacial polarization between the inorganic fillers and the polymer matrices, the interfacial effect inside hierarchical multiphase inorganic inclusions could also significantly affect dielectric properties of polymer nanocomposites and therefore be employed to achieve high energy density in dielectric capacitors.

6.5 Conclusions

Recent advances in nanomaterials and nanotechnology have propelled the development of dielectric polymer nanocomposites. The state-of-the-art energy density attained in polymer nanocomposites has already exceeded 20 J/cm^3, which is comparable to those of commercially available electrochemical capacitors. However,

this is far from the end of story as the performance still fall well short of the needs in applications such as electric drive vehicles, pulsed power, and power capacitors, which require not only high energy and power densities but also low loss. It is worth pointing out that while tremendous efforts have been placed on the search for new nano-inclusions with tailored morphologies and electrical properties, minor progress has been gained on the exploitation of high-*K* polymers. Note that a majority of achievements made on high-energy-density polymer nanocomposites are still employing PVDF-based polymers as the host matrix that has been studied over decades. Unfortunately, PVDF-based polymers have high loss values, i.e., >3 % under weak electric fields and could be over 50 % under high electric fields, which is unaccepted for many of the proposed applications. This is somewhat related to the low glass transition temperatures, low Curie temperatures, and low melting points of PVDF-based polymers. On the other hand, the current high-energy-density polymer nanocomposites are exclusively designed for room temperature applications due to the limitation in thermal stabilities of existing high-*K* polymers and are not suitable for harsh condition operations commonly presented in the emerging applications such as electric drive vehicles and deep oil and gas explorations. These concerns raise new challenges in designing the next generation organic capacitor dielectrics. Besides, in-depth knowledge about the matrix–filler coupling effect in dielectric polymer nanocomposites is highly demanded to assist the material selection and engineering as it contributes a major part to the dielectric polarization that defines the energy density. Fundamental understanding of electrical conduction mechanisms in dielectric polymer nanocomposites could help with the optimization of material design, fabrication, and processing in a way high efficiency charge–discharge could be attained. Last but not least, breakthrough could also be made through new designs of composition and structure of polymer nanocomposites. The multilayer-structured polymer nanocomposites proposed by Shen et al. (ref. [104]) stands for a good example along this direction. Multifunctional filler systems may also deserve attentions to realize promoted collective performance. All these efforts together would push this interdisciplinary field onto a new stage to match the needs for electricity in future transportations, portable electronic devices, and storage and conversion of renewable energy sources.

References

1. Pikul JH, Zhang HG, Cho J, Braun PV, King WP (2013) High-power lithium ion microbatteries from interdigitated three-dimensional bicontinuous nanoporous electrodes. Nat Commun 4:1732
2. El-Kady MF, Strong V, Dubin S, Kaner RB (2012) Laser scribing of high-performance and flexible graphene-based electrochemical capacitors. Science 335:1326–1330
3. Wu ZS, Parves K, Feng XL, Müllen K (2013) Graphene-based in-plane micro-supercapacitors with high power and energy densities. Nat Commun 4:2487
4. Burke A (2007) R&D considerations for the performance and application of electrochemical capacitors. Electrochim Acta 53:1083–1091

5. Dang ZM, Wu JB, Fan LZ, Nan CW (2003) Dielectric behavior of Li and Ti co-doped NiO/PVDF composites. Chem Phys Lett 376:389–394
6. Subodh G, Deepu V, Mohanan P, Sebastian MT (2009) Dielectric response of high permittivity polymer ceramic composite with low loss tangent. Appl Phys Lett 95:062903
7. Zhou X, Zhao XH, Suo ZG, Zou C, Runt J, Liu S, Zhang SH, Zhang QM (2009) Electrical breakdown and ultrahigh electrical energy density in poly(vinylidene fluoride-hexafluoropropylene) copolymer. Appl Phys Lett 94:162901
8. Parvatikar N, Ambika Prasad MVN (2006) Frequency-dependent conductivity and dielectric permittivity of polyaniline/CeO2 composites. J Appl Polym Sci 100:1403–1405
9. Afzal AB, Akhtar MJ, Nadeem M, Hassan MM (2009) Investigation of structural and electrical properties of polyaniline/gold nanocomposites. J Phys Chem C 113:17560–17565
10. Schroeder R, Majewski LA, Grell M (2005) High-performance organic transistors using solution-processed nanoparticle-filled high-*k* polymer gate insulators. Adv Mater 17:1535–1539
11. Ginzburg VV, Myers K, Malowinski S, Cieslinski R, Elwell M, Bernius M (2006) High-dielectric-constant self-assembled nodular structures in polymer/gold nanoparticle films. Macromolecules 39:3901–3906
12. Guo N, DiBenedetto SA, Tewari P, Lanagan MT, Ratner MA, Marks TJ (2010) Nanoparticle, size, shape, and interfacial effects on leakage current density, permittivity, and breakdown strength of metal oxide−polyolefin nanocomposites: experiment and theory. Chem Mater 22:1567–1578
13. Love GR (1990) Energy storage in ceramic dielectric. J Am Ceram Soc 73:323–328
14. Cao Y, Irwin PC, Younsi K (2004) The future of nanodielectrics in the electric power industry. IEEE Trans Dielectr Electr Insul 11:797–807
15. Rabuffi M, Picci G (2002) Status quo and future prospects for metallized polypropylene energy storage capacitors. IEEE Trans Plasma Sci 30:1939–1942
16. Chu BJ, Zhou X, Ren KL, Neese B, Lin MR, Wang Q, Bauer F, Zhang QM (2006) A dielectric polymer with high electric energy density and fast discharge speed. Science 313:334–336
17. Ho J, Jow TR (2012) High field conduction in biaxially oriented polypropylene at elevated temperature. IEEE Trans Dielectr Electr Insul 19:990–995
18. Levy O, Stroud D (1997) Maxwell Garnett theory for mixtures of anisotropic inclusions: application to conducting polymers. Phys Rev B 56:8035
19. Nan CW, Shen Y, Ma J (2010) Physical properties of composites near percolation. Annu Rev Mater Res 40:131
20. Wang Q, Zhu L (2011) Polymer nanocomposites for electrical energy storage. J Polym Sci B Polym Phys 49:1421–1429
21. Dang ZM, Yuan JK, Yao SH, Liao RJ (2013) Flexible nanodielectric materials with high permittivity for power energy storage. Adv Mater 25:6334–6365
22. Li J, Seok SI, Chu B, Dogan F, Zhang Q, Wang Q (2009) Nanocomposites of ferroelectric polymers with TiO_2 nanoparticles exhibiting significantly enhanced electrical energy density. Adv Mater 21:217
23. Li J, Claude J, Norena-Franco LE, Il Seok S, Wang Q (2008) Electrical energy storage in ferroelectric polymer nanocomposites containing surface-functionalized $BaTiO_3$ nanoparticles. Chem Mater 20:6304
24. Kim P, Doss NM, Tillotson JP, Hotchkiss PJ, Pan MJ, Marder SR, Li J, Calame JP, Perry JW (2009) High energy density nanocomposites based on surface-modified $BaTiO_3$ and a ferroelectric polymer. ACS Nano 3:2581
25. Kim P, Jones SC, Hotchkiss PJ, Haddock JN, Kippelen B, Marder SR, Perry JW (2007) Phosphonic acid-modified barium titanate polymer nanocomposites with high permittivity and dielectric strength. Adv Mater 19:1001–1005
26. Li Z, Fredin LA, Tewari P, DiBenedetto SA, Lanagan MT, Ratner MA, Marks TJ (2010) In situ catalytic encapsulation of core-shell nanoparticles having variable shell thickness:

dielectric and energy storage properties of high-permittivity metal oxide nanocomposites. Chem Mater 22:5154
27. Li J, Khanchaitit P, Han K, Wang Q (2010) New route toward high-energy-density nanocomposites based on chain-end functionalized ferroelectric polymers. Chem Mater 22:5350
28. Deng Y, Zhang Y, Xiang Y, Wang G, Xu H (2009) Bi_2S_3–$BaTiO_3$/PVDF three-phase composites with high dielectric permittivity. J Mater Chem 19:2058
29. Huang X, Xie L, Jiang P, Wang G, Liu F (2009) Electrical, thermophysical and micromechanical properties of ethylene-vinyl acetate elastomer composites with surface modified $BaTiO_3$ nanoparticles. J Phys D Appl Phys 42:245407
30. Jung HM, Kang JH, Yang SY, Won JC, Kim YS (2010) Barium titanate nanoparticles with diblock copolymer shielding layers for high-energy density nanocomposites. Chem Mater 22:450
31. Dang ZM, Wang HY, Xu HP (2006) Influence of silane coupling agent on morphology and dielectric property in $BaTiO_3$/polyvinylidene fluoride composites. Appl Phys Lett 89:112902
32. Song Y, Shen Y, Liu H, Lin Y, Li M, Nan CW (2012) Enhanced dielectric and ferroelectric properties induced by dopamine-modified $BaTiO_3$ nanofibers in flexible poly(vinylidene fluoride-trifluoroethylene) nanocomposites. J Mater Chem 22:8063
33. Song Y, Shen Y, Liu H, Lin Y, Li M, Nan CW (2012) Improving the dielectric constants and breakdown strength of polymer composites: effects of the shape of the $BaTiO_3$ nanoinclusions, surface modification and polymer matrix. J Mater Chem 22:16491
34. Tuncer E, Sauers I, James DR, Ellis AR, Duckworth RC (2008) Electrical properties of percolative polystyrene/carbon nanofiber composites. IEEE Trans Dielectr Electr Insul 15:236
35. Dou XL, Liu XL, Zhang Y, Feng H, Chen JF, Du S (2009) Improved dielectric strength of barium titanate-polyvinylidene fluoride nanocomposite. Appl Phys Lett 95:132904
36. Dang ZM, Zhou T, Yao SH, Yuan JK, Zha JW, Song HT, Li JY, Chen Q, Yang WT, Bai J (2009) Advanced calcium copper titanate/polyimide functional hybrid films with high dielectric permittivity. Adv Mater 21:2077
37. Yang W, Yu S, Sun R, Du R (2011) Nano- and microsize effect of CCTO fillers on the dielectric behavior of CCTO/PVDF composites. Acta Mater 59:5593
38. Prakash BS, Varma KBR (2007) Dielectric behavior of CCTO/epoxy and Al-CCTO/epoxy composites. Compos Sci Technol 67:2363
39. Amaral F, Rubinger CPL, Henry F, Costa LC, Valente MA, Barros-Timmons A (2008) Dielectric properties of polystyrene–CCTO composite. J Non Cryst Solids 354:5321
40. Tang HX, Lin YR, Andrews C, Sodano HA (2011) Nanocomposites with increased energy density through high aspect ratio PZT nanowires. Nanotechnology 22:015702
41. Yao J, Xiong C, Dong L, Chen C, Lei Y, Chen L, Li R, Zhu Q, Liu X (2009) Enhancement of dielectric constant and piezoelectric coefficient of ceramic–polymer composites by interface chelation. J Mater Chem 19:2817
42. Banerjee S, Cook-Chennault KA (2011) Influence of Al particle size and lead zirconate titanate (PZT) volume fraction on the dielectric properties of PZT-epoxy-aluminum composites. J Eng Mater Technol 133:041016
43. Tang H, Lin Y, Sodano HA (2012) Enhanced energy storage in nanocomposite capacitors through aligned PZT nanowires by uniaxial strain assembly. Adv Energy Mater 2:469
44. Yu K, Wang H, Zhou Y, Bai Y, Niu Y (2013) Enhanced dielectric properties of BaTiO3/poly(vinylidene fluoride) nanocomposites for energy storage applications. J Appl Phys 113:034105
45. Tomer V, Polizos G, Manias E, Randall CA (2010) Epoxy-based nanocomposites for electrical energy storage. I: effects of montmorillonite and barium titanate nanofillers. J Appl Phys 108:074116
46. Xia WM, Xu Z, Wen F, Zhang ZC (2012) Electrical energy density and dielectric properties of poly (vinylidene fluoride-chlorotrifluoroethylene)/BaSrTiO3 nanocomposites. Ceram Int 38:1071–1075
47. Ducharme S (2009) An inside-out approach to storing electrostatic energy. ACS Nano 3:2447

48. Guo N, DiBenedetto SA, Kwon DK, Wang L, Russell MT, Lanagan MT, Facchetti A, Marks TJ (2007) Supported metallocene catalysis for in situ synthesis of high energy density metal oxide nanocomposites. J Am Chem Soc 129:766
49. Xie L, Huang X, Wu C, Jiang P (2011) Core-shell structured poly(methyl methacrylate)/BaTiO3 nanocomposites prepared by in situ atom transfer radical polymerization: a route to high dielectric constant materials with the inherent low loss of the base polymer. J Mater Chem 21:5897
50. Paniagua SA, Kim YS, Henry K, Kumar R, Perry JW, Marder SR (2014) Surface-initiated polymerization from barium titanate nanoparticles for hybrid dielectric capacitors. ACS Appl Mater Interfaces 6:3477
51. Yang K, Huang XY, Xie LY, Wu C, Jiang PK, Tanaka T (2012) Core-shell structured polystyrene/$BaTiO_3$ hybrid nanodielectrics prepared by in situ RAFT polymerization: a route to high dielectric constant and low loss materials with weak frequency dependence. Macromol Rapid Comm 33:1921
52. Xie LY, Huang XY, Yang K, Li ST, Jiang PK (2014) "Grafting to" route to PVDF-HFP-GMA/$BaTiO_3$ nanocomposites with high dielectric constant and high thermal conductivity for energy storage and thermal management applications. J Mater Chem A 2:5244–5251
53. Tchoul MN, Fillery SP, Koerner H, Drummy LF, Oyerokun FT, Mirau PA, Durstock MF, Vaia RA (2010) Assemblies of titanium dioxide-polystyrene hybrid nanoparticles for dielectric applications. Chem Mater 22:1749
54. Maliakal A, Katz H, Cotts P, Subramoney S, Mirau P (2005) Inorganic oxide core, polymer shell nanocomposite as a high K gate dielectric for flexible electronics applications. J Am Chem Soc 127:14655
55. Tang HX, Lin YR, Sodano HA (2013) Synthesis of high aspect ratio $BaTiO_3$ nanowires for high energy density nanocomposite capacitors. Adv Energy Mater 3:451–456
56. Tang HX, Sodano HA (2013) Ultra high energy density nanocomposite capacitors with fast discharge using $Ba_{0.2}Sr_{0.8}TiO_3$nanowires. Nano Lett 13:1373–1379
57. Tang HX, Sodano HA (2013) High energy density nanocomposite capacitors using non-ferroelectric nanowires. Appl Phys Lett 102:063901
58. Zhou Z, Tang HX, Lin YR, Sodano HA (2013) Hydrothermal growth of textured $Ba_xSr_{1-x}TiO_3$ films composed of nanowires. Nanoscale 5:10901–10907
59. Zou C, Kushner D, Zhang S (2011) Wide temperature polyimide/ZrO_2 polyimide/ZrO_2 nanodielectric capacitor film with excellent electrical performance. Appl Phys Lett 98:082905
60. Balasubramanian B, Kraemer KL, Reding NA, Skomski R, Ducharme S, Sellmyer DJ (2010) Synthesis of monodisperse TiO_2-paraffin core-shell nanoparticles for improved dielectric properties. ACS Nano 4:1893
61. Lin S, Kuang X, Wang F, Zhu H (2012) Effect of TiO_2 crystalline composition on the dielectric properties of TiO_2/P(VDF-TrFE) composites. Phys Status Solidi RRL 6:352
62. Ouyang G, Wang K, Chen XY (2012) TiO_2 nanoparticles modified polydimethylsiloxane with fast response time and increased dielectric constant. J Micromech Microeng 22:074002
63. Dang ZM, Xia YJ, Zha JW, Yuan JK, Bai J (2011) Preparation and dielectric properties of surface modified TiO_2/silicone rubber nanocomposites. Mater Lett 65:3430
64. Zha JW, Dang ZM, Zhou T, Song HT, Chen G (2010) Electrical properties of TiO_2-filled polyimide nanocomposite films prepared via an in situ polymerization process. Synth Met 160:2670
65. Zha JW, Fan BH, Dang ZM, Li ST, Chen G (2010) Microstructure and electrical properties in three-component (Al_2O_3–TiO_2)/polyimide nanocomposite films. J Mater Res 25:2384
66. McCarthy DN, Stoyanov H, Rychkov D, Ragusch H, Melzer M, Kofod G (2012) Increased permittivity nanocomposite dielectrics by controlled interfacial interactions. Compos Sci Technol 72:731
67. Nan CW (1993) Physics of inhomogeneous inorganic materials. Prog Mater Sci 37:1
68. Huang XY, Jiang PK, Kim CU (2007) Electrical properties of polyethylene/aluminum nanocomposites. J Appl Phys 102:124103

69. Panda M, Srinivas V, Thakur AK (2011) Role of polymer matrix in large enhancement of dielectric constant in polymer-metal composites. Appl Phys Lett 99:042905
70. Dang ZM, Lin YH, Nan CW (2003) Novel ferroelectric polymer composites with high dielectric constants. Adv Mater 15:1625
71. Panda M, Srinivas V, Thakur AK (2008) On the question of percolation threshold in polyvinylidene fluoride/nanocrystalline nickel composites. Appl Phys Lett 92:132905
72. Huang XY, Jiang PK, Xie LY (2009) Ferroelectric polymer/silver nanocomposites with high dielectric constant and high thermal conductivity. Appl Phys Lett 95:242901
73. Panda M, Srinivas V, Thakur AK (2008) Surface and interfacial effect of filler particle on electrical properties of polyvinyledene fluoride/nickel composites. Appl Phys Lett 93:242908
74. Kofod G, Risse S, Stoyanov H, McCarthy DN, Sokolov S, Kraehnert R (2011) Broad-spectrum enhancement of polymer composite dielectric constant at ultralow volume fractions of silica-supported copper nanoparticles. ACS Nano 5:1623
75. Shen Y, Lin YH, Li M, Nan CW (2007) High dielectric performance of polymer composite films induced by a percolating interparticle barrier layer. Adv Mater 19:1418–1422
76. Fredin LA, Li Z, Lanagan MT, Ratner MA, Marks TJ (2013) Substantial recoverable energy storage in percolative metallic aluminum-polypropylene nanocomposites. Adv Funct Mater 23:3560–3569
77. Yao SH, Dang ZM, Jiang MJ, Xu HP, Bai JB (2007) Influence of aspect ratio of carbon nanotube on percolation threshold in ferroelectric polymer nanocomposite. Appl Phys Lett 91:212901
78. Dang ZM, Wang L, Yin Y, Zhang Q, Lei QQ (2007) Giant dielectric permittivities in functionalized carbon-nanotube/electroactive-polymer nanocomposites. Adv Mater 19:852
79. Wang L, Dang ZM (2005) Carbon nanotube composites with high dielectric constant at low percolation threshold. Appl Phys Lett 87:042903
80. Li Q, Xue QZ, Hao LZ, Gao XL, Zheng QB (2008) Large dielectric constant of the chemically functionalized carbon nanotube/polymer composites. Compos Sci Technol 68:2290
81. Yao SH, Dang ZM, Xu HP, Jiang MJ, Bai J (2008) Exploration of dielectric constant dependence on evolution of microstructure in nanotube/ferroelectric polymer nanocomposites. Appl Phys Lett 92:082902
82. Chang J, Liang G, Gu A, Cai S, Yuan L (2012) The production of carbon nanotube/epoxy composites with a very high dielectric constant and low dielectric loss by microwave curing. Carbon 50:689
83. Simoes R, Silva J, Vaia R, Sencadas V, Costa P, Gomes J, Lanceros-Mendez S (2009) Low percolation transitions in carbon nanotube networks dispersed in a polymer matrix: dielectric properties, simulations and experiments. Nanotechnology 20:035703
84. Yuan JK, Yao SH, Sylvestre A, Bai J (2012) Biphasic polymer blends containing carbon nanotubes: heterogeneous nanotube distribution and its influence on the dielectric properties. J Phys Chem C 116:2051
85. Yuan JK, Yao SH, Dang ZM, Sylvestre A, Genestoux M, Bai J (2011) Giant dielectric permittivity nanocomposites: realizing true potential of pristine carbon nanotubes in polyvinylidene fluoride matrix through an enhanced interfacial interaction. J Phys Chem C 115:5515
86. Yuan JK, Li WL, Yao SH, Lin YQ, Sylvestre A, Bai J (2011) High dielectric permittivity and low percolation threshold in polymer composites based on SiC-carbon nanotubes micro/nano hybrid. Appl Phys Lett 98:032901
87. Zhang S, Wang H, Wang G, Jiang Z (2012) Material with high dielectric constant, low dielectric loss, and good mechanical and thermal properties produced using multi-wall carbon nanotubes wrapped with poly(ether sulphone) in a poly(ether ether ketone) matrix. Appl Phys Lett 101:012904
88. Wu C, Huang X, Wu X, Yu J, Xie L, Jiang P (2012) TiO_2-nanorod decorated carbon nanotubes for high-permittivity and low-dielectric-loss polystyrene composites. Compos Sci Technol 72:521

89. Sun LL, Li B, Zhao Y, Mitchell G, Zhong WH (2010) Structure-induced high dielectric constant and low loss of CNF/PVDF composites with heterogeneous CNF distribution. Nanotechnology 21:305702
90. Sun LL, Zhao Y, Zhong WH (2011) Dependence of dielectric properties and percolative behavior on phase separation structure induced by heterogeneous carbon nanofiber distribution in polymer blend nanocomposites. Macromol Mater Eng 296:992
91. Barick AK, Tripathy DK (2012) Preparation and characterization of carbon nanofiber reinforced thermoplastic polyurethane nanocomposites. J Appl Polym Sci 124:765
92. Sun LL, Zhang ZG, Zhong WH (2011) Fluorination deposition on carbon nanofibers by PTFE decomposition as a facile method to enhance dispersion and interaction in PVDF composites. J Mater Chem 21:944
93. He F, Lau S, Chan HL, Fan JT (2009) High dielectric permittivity and low percolation threshold in nanocomposites based on poly(vinylidene fluoride) and exfoliated graphite nanoplates. Adv Mater 21:710
94. Yu J, Huang X, Wu C, Jiang P (2011) Permittivity, thermal conductivity and thermal stability of poly(vinylidene fluoride)/graphene nanocomposites. IEEE Trans Dielectr Electr Insul 18:478
95. Han K, Li Q, Chen ZY, Gadinski MR, Dong LJ, Xiong CX, Wang Q (2013) Suppression of energy dissipation and enhancement of breakdown strength in ferroelectric polymer–graphene percolative composites. J Mater Chem C 1:7034–7042
96. Fan P, Wang L, Yang J, Chen F, Zhong M (2012) Graphene/poly(vinylidene fluoride) composites with high dielectric constant and low percolation threshold. Nanotechnology 23:365702
97. Wu C, Huang X, Wang G, Wu X, Yang K, Li S, Jiang P (2012) Hyperbranched-polymer functionalization of graphene sheets for enhanced mechanical and dielectric properties of polyurethane composites. J Mater Chem 22:7010
98. Wang DR, Bao YR, Zha JW, Zhao J, Dang ZM, Hu GH (2012) Improved dielectric properties of nanocomposites based on poly(vinylidene fluoride) and poly(vinyl alcohol)-functionalized graphene. ACS Appl Mater Interfaces 4:6273–6279
99. Roy M, Nelson JK, McCrone RK, Schadler LS, Reed CW, Keefe R, Zeneger W (2005) Polymer nanocomposite dielectrics—the role of the interface. IEEE Trans Dielectr Electr Insul 12:629–643
100. Takala M, Ranta H, Nevalainen P, Pakonen P, Pelto J, Karttunen M, Virtanen S, Koivu V, Pettersson M, Sonerud B, Kannus K (2010) Dielectric properties and partial discharge endurance of polypropylene-silica nanocomposite. IEEE Trans Dielectr Electr Insul 17:1259–1267
101. Tomer V, Manias E, Randall CA (2011) High field properties and energy storage in nanocomposite dielectrics of poly(vinylidene fluoride-hexafluoropropylene). J Appl Phys 110:044107
102. Tomer V, Polizos G, Randall CA, Manias E (2011) Polyethylene nanocomposite dielectrics: implications of nanofiller orientation on high field properties and energy storage. J Appl Phys 109:074113
103. Fillery SP, Koerner H, Drummy L, Dunkerley E, Durstock MF, Schmidt DF, Vaia RA (2012) Nanolaminates: increasing dielectric breakdown strength of composites. ACS Appl Mater Interfaces 4:1388–1396
104. Hu PH, Shen Y, Guan YH, Zhang XH, Lin YH, Zhang QM, Nan CW (2014) Topological-structure modulated polymer nanocomposites exhibiting highly enhanced dielectric strength and energy density. Adv Funct Mater 24:3172–3178
105. Zhang X, Shen Y, Zhang QH, Gu L, Hu YH, Du JW, Lin YH, Nan CW (2015) Ultrahigh energy density of polymer nanocomposites containing $BaTiO_3$@TiO_2 nanofibers by atomic-scale interface engineering. Adv Mater 27:819–824

Part III
Thermal Properties of Polymer Nanocomposites

Chapter 7
Thermal Stability and Degradation of Polymer Nanocomposites

T.M. Majka, A. Leszczyńska, and K. Pielichowski

7.1 Introduction

The field of polymer nanocomposites shows tremendous application potential and is currently intensively investigated for new materials fabrication and properties evaluation.

In nanocomposites, one of the components has at least one dimension less than 100 Å. As an example of length scale, carbon fibers, commonly used as a reinforcement in sporting goods, are approximately 7 μm in diameter, and the length of a carbon–carbon chemical bond is about 10^{-10} m [1, 2]. Polymer nanocomposites include, e.g., biomaterials with nanohydroxyapatite, nanostructured drug delivery systems, layer-by-layer self-assembled polymer films, nano-reinforced elastomers, and electrospun nanofibers. The presence of nanostructured additives may considerably enhance barrier properties, thermal stability, flame resistance, electro-optical, and antibacterial properties of polymer matrix.

Nanostructured fillers applied as additives in polymer nanocomposites can be divided into:

- Metal oxides
- Carbon nanotubes
- Nanoclays
- Others, e.g., POSS moieties

It is worth mentioning that polymer-based nanocomposites with, e.g., carbon black have been known since decades in chemical technology; however, their characterization at the nanoscale was not possible due to lack of appropriate experimen-

T.M. Majka (✉) • A. Leszczyńska • K. Pielichowski
Department of Chemistry and Technology of Polymers, Cracow University of Technology, ul. Warszawska 24, 31-155 Kraków, Poland
e-mail: tomasz.m.majka@gmail.com

© Springer International Publishing Switzerland 2016

X. Huang, C. Zhi (eds.), *Polymer Nanocomposites*,
DOI 10.1007/978-3-319-28238-1_7

tal techniques. This has changed at the beginning of 1990s with the first papers on polyamide 6 (PA6)/layered silicate nanocomposites published by Usuki and Okada [3, 4].

As nanofillers can significantly improve various properties of the polymer matrix they are incorporated into, it is of crucial importance to investigate the mechanism of their action. This mechanism may strongly depend on the degree of exfoliation and agglomeration effects of nanoparticulates. It can be clearly seen when considering the thermal and flame retardancy properties of polymer nanocomposites with, e.g., montmorillonite [5–12].

In this chapter, the influence of different types of nanofillers on the thermal stability and decomposition of polymer nanocomposites will be discussed. Mechanisms of thermo-oxidative degradation processes of polymer nanocomposites will be discussed. Although the mechanical reinforcement aspects in the polymer nanocomposites are of the primary interest, thermal stability and flammability resistance get an increased attention. An interesting issue is the search for synergistic actions between the nanofiller and the "classical" thermal stabilizer toward improvement of the final performance of polymer nanocomposites.

7.2 Types of Nanofillers

7.2.1 Nano-oxides

Nano-oxides like metal oxides or nanosilica are spherical particles with diameter in the range of 20–300 nm. Metal nano-oxides, especially titanium dioxide, show photocatalytic properties. Titanium dioxide can be converted by hydrothermal synthesis into titanium nanotubes [13]. These titanium nanotubes have length of 1 μm, an external diameter of 10–20 nm and an internal diameter of 5–8 nm. Nanoalumina spherical particles in sizes from 20 nm are used as fillers with catalytic properties in polymer composites. The use of metal oxides as nanofillers often requires surface functionalization. For instance, Guo et al. have reported the functionalization of nano-oxides by methacryloxypropyl trimethoxisilane [14, 15].

7.2.2 Carbon Nanotubes

Carbon nanotubes (CNT) were discovered by Oberlin and Endo in 1976 [16, 17] and by Iijima in 1991 [18]. The tubes display a nanometric-scale diameter and much larger length in comparison with its diameter. In general, three types of carbon nanotubes are considered:

- Single-walled carbon nanotubes (SWCNT) with diameter between 1 and 2 nm
- Double-walled carbon nanotubes (DWCNT) with diameter between 2 and 4 nm

- Multi-walled carbon nanotubes (MWCNT) with diameter between 4 and 150 nm

Carbon nanotubes are produced by two methods:

- A catalytic chemical vapor decomposition process at temperature in range of 600–1000 °C
- An electric discharge process under helium at temperature in range of 3000–4000 °C

Both processes yield a mixture of SWCNT, DWCNT, and MWCNT. Some surface defects may occur. The proper dispersion of carbon nanotubes in polymer matrices can be achieved via functionalization or by applying high shear rates [19, 20].

7.2.3 Nanoclays

Layered silicate nanofillers can be natural or synthetic clays of transition metals. The most widely used enhancement is clay due to its natural abundance. Clays used in the synthesis of nanocomposites consists of very thin layers that are usually bound together with counterions [19]. The crystal lattice of 2:1 layered silicates consists of two-dimensional layers where a central octahedral sheet of alumina is fused to two external silica tetrahedra by the tip. In tetrahedral sheets, silicon is surrounded by four oxygen atoms, and in octahedral sheets, e.g., aluminum or magnesium is surrounded by eight oxygen atoms. The layer thickness is around 1 nm depending on the particulate silicate, the source of the clay, and the method of preparation [21–24]. The crystal lattice 2:1 structure with silicon in the tetrahedral sheets and aluminum in the octahedral sheet, without any substitution of atoms, is called pyrophyllite. In case when silicon in the tetrahedral sheet is substituted by aluminum, the resulting structure is called mica. Due to this substitution, the clay is characterized by a negative surface charge, which is balanced by interlayer cations [25]. If in the original pyrophyllite structure the trivalent Al-cation in the octahedral layer is partially substituted by the divalent Mg-cation, the structure of montmorillonite is formed. Then overall negative charge is balanced by sodium and calcium ions, which exist hydrated in the interlayer called gallery [26]. A particular feature of the resulting structure is that the layers are held together by relatively weak forces; water and other polar molecules can enter between the unit layers [27, 28]. Layered silicates are only miscible with hydrophilic polymers, such as poly(vinyl alcohol) and poly(ethylene oxide). In order to render them miscible with other polymers, one must exchange the alkali counterions with a cationic-organic surfactant like quaternary alkyl ammonium sulfonium and phosphonium salts [26, 29]. The application of organically modified layered silicates provides some superior properties of nanocomposite material in comparison with systems containing sodium clay [30]. However, ammonium salts that are the most frequently applied salts [31, 32] suffer from thermal degradation during the fabrication and further processing of nanocomposites. This leads to the changes in surface properties of organoclays resulting in alternation of

nanocomposite structure and related properties [33, 34] and facilitates the occurrence of some unwanted side reactions and contamination of polymeric material with the products of thermal degradation of organic modifier that may be responsible for enhanced thermal degradation of polymer matrix [35], color formation, and accelerated aging [36, 37]. The need to improve the thermal stability of organoclays applied for the preparation of polymer nanocomposites has motivated to search for an organic modifier or stabilizer combining high thermal stability with high efficiency in facilitating dispersion of nanofillers in polymer matrix. In Table 7.1, various natural and synthetic nanoclays available and used as fillers in polymers are presented.

7.2.4 Other Nanofillers

Other nanofillers include, e.g., nanosilver, nanozinc, and nanogold. These metal nanoparticles exhibit catalytic behavior and antibacterial properties at the surface. Of interest are also their electrical and magnetic properties [39–41].

Another large group of nanofillers are silsesquioxanes with formula $R-SiO_{3/2}$ with R typically being alkyl or organo-functional groups. They show three-dimensional symmetry and nanometric size making them suitably building blocks for hybrid materials and nanocomposites. The large number of possible functional groups and chemical stability of the cage allows for design of tailored nano-

Table 7.1 Natural and synthetic nanoclays used as fillers in polymers

Family		Group
Double lamellar hydroxide	Synthetic	Hydrotalcite
Polysilicate	Synthetic	Fluorohectorite
		Zeolite
	Natural	Zeolite
		Silhydrite
		Ilerite
		Kanemite
		Magadiite
		Kenyaite
Phyllosilicates	TO(1:1)	Kaolinite
	TOT(2:1)	Smectite
		Sepiolite
	TOT:O(2:1:1)	Chlorite
		Bentonite
		Saponite

Adapted from [38]

architectures in all three dimensions [42–44]. Special attention is focused on polyhedral oligosilsesquioxanes (POSS) as reinforcement for polymer matrices.

7.3 Synthesis of Polymer Nanocomposites

There are four main methods to prepare polymeric nanocomposites:

- In situ template synthesis
- Intercalation of polymer or prepolymer from solution
- In situ intercalative polymerization
- Melt intercalation

Out of these, melt intercalation technique is widely used because it allows to obtain polymer nanocomposites with high yield using all types of nanofillers.

In situ polymerization was the first method used to synthesize polymer–clay nanocomposites based on polyamide 6. The modified layered silicate is swollen by a liquid monomer or a monomer solution. Then, the monomer migrates to interlayer gap of the layered silicate, so that the polymerization reaction can occur between the intercalated sheets. The reaction can be thermally or radiation initiated or by using an initiator located inside the interlayer [5, 22, 24, 45].

Melt intercalation consists of blending the nanoadditive with the thermoplastic polymer matrix in the molten state. If the filler surfaces are sufficiently compatible with the chosen polymer, the macromolecules can, under appropriate conditions, migrate into the interlayer space and form either an intercalated or an exfoliated nanocomposite [5, 22, 24, 46]. Among the abovementioned techniques, in situ polymerization and melt intercalation are considered as commercially attractive approaches for preparing polymer/layered silicate nanocomposites.

An important from technological point of view aspect is the tendency of nanofillers to agglomerate or aggregate. This effect leads to lowering of mechanical and thermal properties, so proper measures have to be taken to prevent or minimize it. Some solutions include [47–50]:

- Functionalization of nanoparticles
- Mixing at a high shear rate to improve the intercalation and then applying vacuum to remove air bubbles
- Sonication

Nanocomposites containing carbon nanotubes can be produced by different techniques, depending on whether or not pre-fiber mat is used [51, 52]. One of the fabrication methods of nanocomposites containing carbon nanotubes is the casting of a large objects subjected to high stresses. Layered hybrid laminates in thermoset matrix containing carbon nanotubes are manufactured in two steps: carbon nanotubes are isolated and dispersed in the mixture containing the matrix. Next, the suspension of polymer/carbon nanotube is added to a mat of fiber. Depending on the matrix and viscosity of the system used, the incorporation of carbon nanotubes could be performed up to 2 wt% [19, 20].

7.4 Degradation Process of Polymer Matrices

The service life of polymer matrices is restricted by their degradation, which can be caused by a number of environmental factors such as humidity, impurities, irradiation, mechanical load, microorganisms, and temperature. Degradation is in most cases an undesired process in the majority of polymer composites applications as it generally leads to changes in the chemical and physical structure of the matrix–nanofiller system resulting in the loss of many useful properties, such as polymer molecular weight [53], color [54], mechanical strength [55], and impact resistance [56]. The understanding of degradation mechanisms of polymer nanocomposites is further complicated by factors such as morphology, diffusion processes, and interactions of nanofillers. The physical behavior of thermoplastic composites in high temperatures is dependent on the degree of crystallinity of polymer matrices. For crystalline matrix-based nanocomposites, there exists a well-defined melting temperature. At the glass transition temperature, the composite material starts a transition toward a soft and rubbery state. For materials requiring stiffness and compressive strength, the glass transition temperature is an upper limit for practical use [57]. Interestingly, numerous polymer matrices could not achieve a viscous state because they begin undergoing thermal decomposition before the material melts (Fig. 7.1). Thermosetting or thermoplastic-based composite materials produce carbonaceous char during the thermal decomposition. It play an important role in stabilization of polymer matrix by inhibiting the flow of heat from the gaseous combustion zone back to the condensed phase and by hindering the access of oxygen [59, 60].

The thermal degradation of polymer nanocomposites could begin with start of oxidative processes that are often auto-accelerated. Oxygen molecules can penetrate the layers well below the surface of polymer matrix [61, 62].

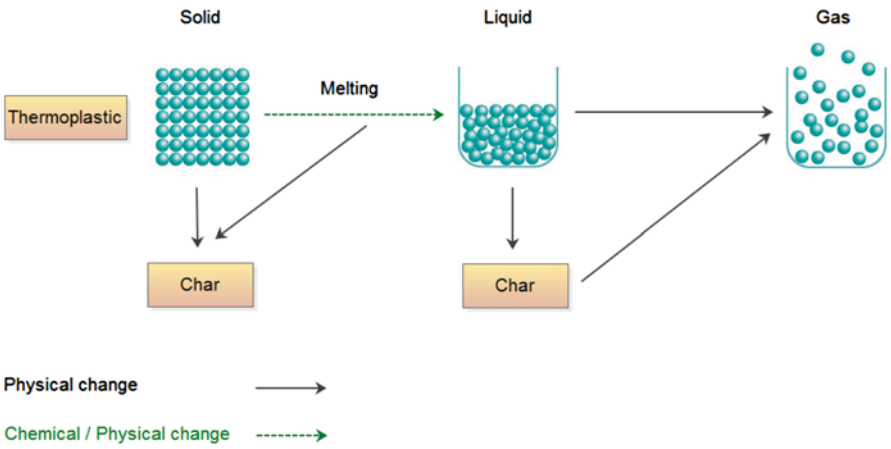

Fig. 7.1 Physicochemical changes during thermal degradation of polymer matrix [58]

Initiation			
	Polymer	→	$P^{\bullet} + P^{\bullet}$
Propagation			
	$P^{\bullet} + O_2$	→	$POO^{\bullet}$
	$POO^{\bullet} + PH$	→	$POOH + P^{\bullet}$
Chain branching			
	$POOH$	→	$PO^{\bullet} + {}^{\bullet}OH$
	$POOH + POOH$	→	$PO^{\bullet} + POO^{\bullet} + H_2O$
	$PH + {}^{\bullet}OH$	→	$P^{\bullet} + H_2O$
	$PH + PO^{\bullet}$	→	$P^{\bullet} + POH$
Termination			
	$P^{\bullet} + P^{\bullet}$	→	Non-radical product
	$P^{\bullet} + POO^{\bullet}$	→	Non-radical product
	$POO^{\bullet} + POO^{\bullet}$	→	Non-radical product + O_2

Fig. 7.2 Auto-oxidation scheme based on free radical chain reaction theory

A number of properties affect the thermal and oxidative degradation of thermoplastic polymers, such as average molecular weight, thermal history, and the presence of weak linkages or irregular structures [63–66].

Oxidation is one of the most important degradation processes and has been thoroughly investigated [67–70]. Oxidation processes may occur in every step of the life cycle of a polymer nanocomposite: during processing, storage, and the service life. In the oxidation process, different polymer decomposition products are formed, e.g., acids, alcohols, aldehydes, esters, ketones, lactones, peracids, peresters, and peroxides [71]. In the presence of impurities or irregular structures, such as branches, functional groups, or unsaturations, the rate of oxidation usually increases. During processing by extrusion or injection/blow molding, peroxy radicals are formed under high temperature and mechanical shear [72]. When certain concentration of hydroperoxides is reached, accelerated oxidation reactions start immediately [72]. The auto-oxidation scheme based on free radical chain reaction theory is shown in Fig. 7.2.

The basic stages include free radical initiation, propagation, chain branching, and termination. At high degree of oxidation, secondary reactions may play important role [73]. During polymerization reactions, catalysts, radical initiators, impurities in monomers, and minute amounts of oxygen could react and form peroxy radicals POO• which separate hydrogen from the polymer chain and form an alkyl radical and hydroperoxides. These hydroperoxides decompose when heated or irradiated to free radicals that initiate auto-oxidation processes [70, 72, 74, 75]. Because the formation reaction of hydroperoxides has a high activation energy, an increase in temperature of oxidation process will increase the rate of reaction, which leads to increase in the number of propagation cycles [76–79]. Chain branching reaction occurs when hydroperoxides undergo thermolysis to produce alkoxy and hydroxy radicals [78]. Termination of the propagation cycle take place, when two radicals recombine to yield non-radical products [80–83] – Fig. 7.3.

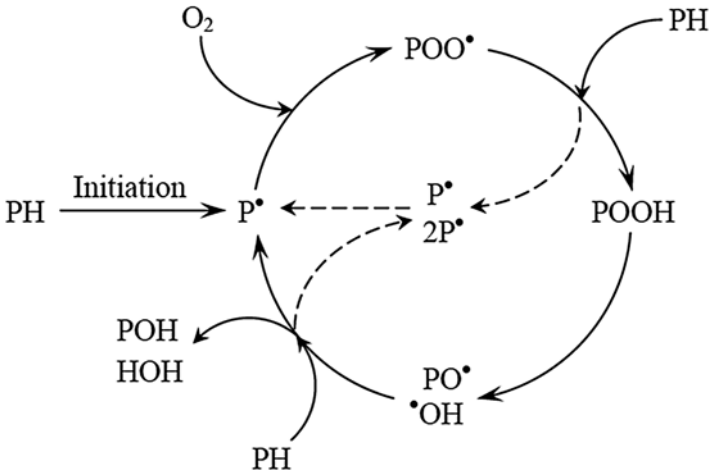

Fig. 7.3 The auto-oxidation cycle of polymer matrix

7.5 Thermal Stability of Polymer Nanocomposites

7.5.1 Polymer/Nano-oxide Nanocomposites

The increase in the thermal stability of polymer/metal or metal oxide nanocomposites is explained by the formation of polymer–nanoparticle network by physical cross-linking of polymer chains through metal particles, which stabilizes the whole system by restriction of the thermal motions of polymer chains. The examples of such systems are polyacrylate/ZnO [84] or polyurethane/TiO_2 [85] nanocomposites. A decrease in the thermal stability, often reported for hybrid materials, could be linked with metal-catalyzed oxidative degradation processes [86, 87].

The inclusion of the ceramic nanofiller into the more flexible polymer matrix with lower thermal resistance can substantially improve its stiffness and thermal stability [88, 89]. The nano-sized silica or alumina particles without any chemical modification could be incorporated into the polymer matrices such as poly(ether ether ketone). The mechanisms of thermal stability enhancement of polymers by silica oxide are referring to molecular dynamics [90], physical cross-linking, and specific interactions between the components. The experiments on the polymaleimide/colloidal silica nanoparticles nanocomposites show that the inorganic networks chemically bound to polymaleimides work for improving the thermal resistance of the nanocomposites [91]. In some cases, incorporation of nanoparticles into polymer matrix causes physical or chemical cross-linking increasing thus the initial decomposition temperature.

7.5.2 *Polymer/Carbon Nanotube Nanocomposites*

The dispersion of carbon nanotubes in polymer matrix can be improved by functionalizing the surface of nanofiller, which improves the interfacial interactions with the matrix [19]. There are three possible ways of functionalization:

- Chemical functionalization
- Physical functionalization
- Surface deposition

Several mechanisms of thermal stability enhancement have been considered for carbon nanotubes and nanofibers. Retardation of mass loss in inert atmosphere is likely to be a result of physical adsorption effect of the macromolecules on the nanotube surfaces that causes slower volatilization of polymer without change in initial degradation temperature [92] or absorption of free radicals generated during polymer degradation [93, 94]. Another scenario is a reduction of mobility of the macromolecules in the presence of CNTs. Although carbon nanotubes do not tend to show an intercalation phenomena, the stabilization effect of carbon nanotubes could be rationalized, similarly to the effect of layered silicates [94, 95]. This effect is clear in inert atmosphere and is displayed by the shift of degradation onset temperature [96]. Marosfői research group found out that the thermal stabilization effect of carbon nanotubes could be attributed to the increased interfacial interactions between the nanoadditive and polymer matrix, which leads to an increase of the activation energy of degradation [97]. They demonstrated that the presence of multi-walled carbon nanotubes slightly delayed thermal volatilization without modification of the thermal degradation mechanism, whereas thermal oxidative degradation in air was delayed by about 100 °C, independently from multi-walled nanotubes concentration [98, 99]. The stabilization effect was ascribed to the formation of a thin protective film of multi-walled carbon nanotubes/polyaromatic carbon char generated on the surface of the nanocomposites. This char was composed by a network of homogeneously dispersed multi-walled nanotubes entangled to form a nonwoven math-like structure [95]. Chipara et al. have shown that the thermal stability of polymer/carbon nanotube nanocomposites is strictly related to the nanoadditive content. They pointed out at an important role of interactions between macromolecular chains and carbon nanotubes that contribute to the formation of polymer–filler interface with enhanced thermal stability [100]. However, carbon nanoparticles could also play an accelerating role at the initiation of polymer decomposition, especially under oxidative conditions [101]. Most of the explanations attributes this effect to the remaining traces of inorganic elements [102]. The degradation behavior of polymer/carbon nanotube nanocomposites strongly depends on the type of modification that carbon nanotubes are subjected to [103, 104]. These reactive chemical modifications can substantially change degradation pathway and offer the increase of the thermal stability due to finer dispersion of nanoparticulates. For instance, the plasma-modified carbon nanotubes with maleic anhydride improved the thermal stability of polyimide nanocomposites through enhancing the dispersion and enabling the modified carbon nanotubes to bond chemically or physically interact with the polymer matrix [105]. Carbon nanotubes modified using amine groups cause significant improvement of thermal stability when covalently bonded to the epoxy matrix [106].

7.5.3 *Polymer/Clay Nanocomposites*

The current literature concerning thermal stability of polymer/clay nanocomposites gives inconsistent conclusions on clay efficiency in improving thermal stability. For instance, Vaia's experimental work revealed that char resulted in an order-of-magnitude decrease in the mass loss rate compared to the pristine polymer matrix, even for as little as 2 wt% of exfoliated layered silicate [107]. In turn, Tidjani [108] reported that the presence of the clay in poly(propylene-*graft*-maleic anhydride)/layered silicate nanocomposites exerted only a minor effect on the thermal degradation and the nanocomposites hardly showed any additional residue. Numerous divergences in results indicate the occurrence of effects of chemical nature that, unlike the physical effects, are different for each polymer–nanofiller system. Thus, the role of the dispersed nanoclay in thermal degradation of a polymer depends critically on the specific mechanisms associated with the polymer degradation reaction as well as chemical properties of nanoadditive [4]. Systematic studies concerning the thermal stability of a number of polymers have put forward the idea that the clay does not only quantitatively but also qualitatively affects the polymer degradation. Great differences in efficiency of clay in improving the thermal stability of various polymeric matrices have been considered in terms of the complexity of degradation mechanisms or in terms of radical stability [109–112]. One can assume that if the stability of free radicals produced during thermal degradation of polymer is high and they exhibit longer lifetimes, the probability that they will undergo secondary intermolecular reactions is also high. The presence of organoclay leads to prevent mass transport from the bulk and to permit radical recombination reactions, exerting thus a stabilization effect in the polymer/layered silicate nanocomposite [113–115]. It should be noted that the free radical trapping model successfully explains why the degradation of polymer/clay systems is slower, but they do not offer direct ways of explaining the changes in the thermal effect. Blumstein reported that the one proposed in literature mechanisms of thermal stability improvement in polymer/layered silicate nanocomposites is the reduction of molecular motions and physical processes in the condensed phase [116]. Recent research works confirm changes in molecular dynamics of macromolecular chains stick to the filler surface that result in, for instance, an increase of glass transition temperature. Since the macromolecular mobility is the major factor that contributes to the transport of reactive species within the polymer matrix, these nanomaterials could have lower reactivity and greater chemical and thermal stability than pristine polymer [117–119].

Montmorillonite is extracted from the bentonite by a process of sedimentation in water and then activated by sodium cations to improve clays swelling. Unmodified sodium montmorillonite exhibits good thermal stability in the temperature range of 20–500 °C, evolving physically adsorbed water at temperatures up to 120 °C, and the water from hydrated ions which is lost in the temperature range of 80–180 °C. The dehydroxylation of crystal lattice of clay was observed at temperatures above 500 °C, at which most of commercial polymers have already decomposed [120–122]. As it was noted, two of the main parameters of nanocomposites that are the dispersion of the nanoadditives and their interaction with the matrix play an important role in thermal stability of polymer nanomaterials [33, 123–126].

Incorporation of appropriate organic links between the matrix and the filler by functionalization improves the intercalation of polymer chains between the layers [49]. These cations reduce the surface energy of organoclay and facilitate macromolecule access between the layers of clays. Hence, the inclusion of layered silicates in a thermoplastic melt needs the exchangeable cations from the clay to be replaced by organophilic cations such as commonly used quaternary ammoniums. In Fig. 7.4, commonly used cations for polyolefin-based and polyamide-based nanocomposites are shown.

Considering the interaction between the nanofiller and the matrix at the nanometric scale, three scenarios are possible, which affect considerably the properties of the polymer composite material:

- The nanofillers are not intimately mixed in the matrix but form regions.
- The macromolecules enter between nanofillers' plates.
- The nanofillers are totally exfoliated and dispersed.

Typically, clays used in polymer nanocomposites have a double catalytic effect on the thermal degradation of organic molecules. If the temperature in inert atmosphere is increasing, carbon–carbon bond scission is accelerated by the clay, which comes in competition with acceleration of carbon–hydrogen bond scission in the presence of oxygen. Consequently, thermal degradation leads to volatiles, whereas thermo-oxidative dehydrogenation leads to unsaturated moieties evolving thermally stable charred nanomaterial [127]. The char formation due to the presence of dispersed montmorillonite layers is suggested as a mechanism of thermal stability improvement; however, under oxidative conditions, exfoliated clay nanoparticles may catalyze the hydroperoxide decomposition [128–132]. It has been shown that nanoadditive induced degradation reactions before the onset of thermal decomposition of the neat polymer. Consequently, charring process slows down the rate of mass loss in a subsequent stages of degradation [132–134]. The catalytic activity of organoclay toward degradation of polymer is also observed during nanocomposite compounding and aging in the thermal oxidative environment [135]. Xie and coworkers showed [136] that quaternary alkyl ammonium organoclays decompose

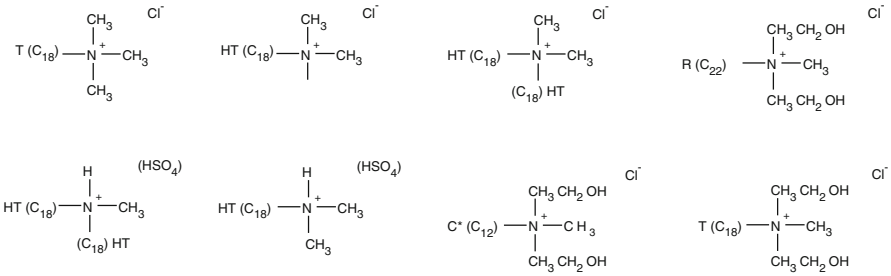

Fig. 7.4 Commonly used cations for polyolefin-based and polyamide-based nanocomposites. The symbols: *T,* tallow (predominantly composed of chains with 18 carbons (ˇ«65 %)); *HT*, hydrogenated tallow; *R*, rapeseed (consisting largely of chains with 22 carbons (ˇ«45 %)); *C**, coco (product made from coconut oil, consisting predominantly of chains with 12 carbons (ˇ«48 %)); *H,* hydrogen designates the substituents on the nitrogen [34]

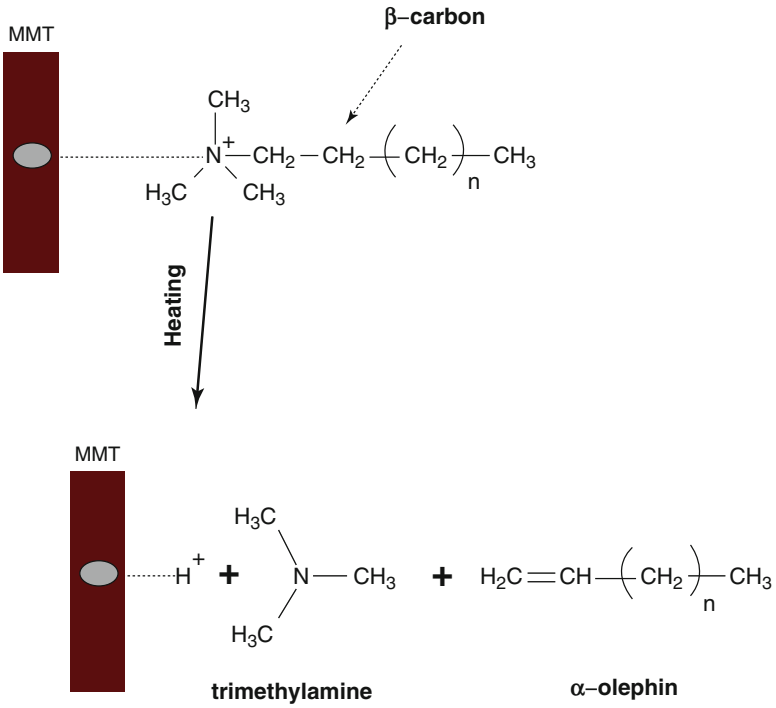

Fig. 7.5 Hofmann elimination reaction for quaternary ammonium compounds [37]

between 200 and 300 °C to produce α-olefins and amines, which is in agreement with Hofmann elimination mechanism [137–142]. This mechanism generally appears when a quaternary ammonium hydroxide or chloride, under high temperatures, is converted into an alkene and an amine, as it is presented in Fig. 7.5.

In the case of organoclays, elimination of the ammonium modifier could result in a substitution of the ammonium linkage on the clay with a hydrogen proton on the β-carbon. Ultimately, the α-olefin intermediates produced in this reaction could attack the polymer [35, 99, 143]. Davis research group also reported a significant level of PA6 degradation during high-temperature melt processing at 300 °C of in situ formed nanocomposites. Authors suggested that the degradation was largely due to hydrolysis caused by water originating from the clay. These authors also proposed other mechanisms – a catalytic degradation caused by unexchanged sodium cations on the surface of the clay [99]. The increased degradation of polymer in the presence of organoclay is often explained in terms of the catalytic activity of acidic sites formed due to the Hofmann degradation of onium compound. It should be emphasized that not only organic modifier and products of its degradation appears to have a catalytic effects on polymer degradation but also acidic sites inherently present on the mineral surface [144]. Several research works evidenced that the metal ions such as Fe^{3+} or Cu^{2+}, naturally present in clay minerals act as catalytic sites increasing the degradation reactions. On the other hand, cations of

some transition metals promote the molecular cross-linking and an increase in the amount of charred residue [145–149].

Kong's group suggested a scheme of successive reactions leading to the formation of char during degradation of hydrocarbon polymers in the presence of Fe-organoclay [150, 151]. Probably the presence of metal species in the clay structure could catalytically enable the oxidative cleavage of alkene substituents in alkyl ammonium compounds to produce aldehydes at high temperatures of processing [136, 152]. Alkylammonium salts which have shown catalytic activity toward degradation reactions are able to create other possible schemes of subsequent events such as an unsaturated and conjugated bond formation, cyclization, aromatization, fusion of aromatic rings, turbostratic char formation, and, finally, graphitization [153–155]. The char formation during the thermal degradation process of polymer nanocomposite is an indication of enhanced flame resistance of material. This is the reason why the thermo-oxidative stability of polymer nanocomposites is often investigated in relation to the fire retardancy [156].

7.5.4 Polymers Reinforced with Other Types of Fillers

Some research studies suggested that gold nanoparticles promote the thermal degradation of the polymer due to its catalytic ability. Metal-containing nanocomposites are more resistive to pyrolytic degradation, but increased mass losses are expected in these nanocomposites under oxidative atmosphere due to the catalytic effects toward oxidation reactions [157–160]. Due to graphite highly anisometric shape of elemental particles and its intrinsic heat resistance, physical barriers for heat and diffusing gases could be produced. Unmodified graphite basically does not interfere with chemical pathways of polymer degradation but operates in a physical mode of action [161, 162]. The commonly performed oxidation of graphite via chemical oxidation enhances the formation of polar groups on the graphite layers [163, 164]. The use of oxidized graphite is better in terms of barrier structure formation leading to improvements in the thermal properties as compared to the pristine graphite [165, 166].

Polyhedral oligomeric silsesquioxane nanoadditives find numerous applications as, e.g., surface modifiers, coating reinforcements, catalysts supports, and membrane materials. Inorganic–organic hybrid materials with POSS possess attractive properties such as better flame and heat resistance, higher glass transition temperature, and increased thermal stability and melt strengths which occur even at low POSS contents [167, 168]. POSS offer versatility both as reaction platforms to which other nanobuilding blocks could be attached and as robust and chemically stable nanostructured silica cages. Multifunctionalized POSS molecules, such as octa(aminophenyl)silsesquioxane, can react with diepoxides or dianhydrides to yield high cross-link density materials with good thermo-oxidative stability and increased compressive strengths [169, 170].

7.6 Synergy Between Stabilizers and Nanofillers

It is well established that the thermophysical properties of polymer nanocomposites depend strongly on the nature, amount, morphology, and dispersion degree of nanofillers. The thermal properties of polymeric nanocomposites are usually different from these of "classical" composites containing fillers of larger size which confirms the importance of the size/shape of filler particles. For fire retarded products, polymeric nanomaterials often require the use of other additives such as stabilizers or antioxidants which help to meet performance criteria against fire. On the other hand, incorporation of nanofillers can become an interesting alternative to traditional flame retardation methods [171–174]. Among numerous studies on the thermal properties and flammability of polymeric nanocomposites, investigations on epoxy resin/carbon nanotube nanocomposites demonstrate an increase in thermal conductivity. However, the addition of multi-walled carbon nanotubes into epoxy resins had no significant effect on the nanocomposites decomposition temperature [175]. Biercuk et al. suggest that epoxy resin reinforced with single-walled carbon nanotubes show an increase in the thermal conductivity of nearly 125 % at room temperature [176]. A larger amount of carbon nanotubes caused a decrease in the thermal conductivity, probably due to poor dispersion of nanotubes at high concentrations [177]. Other studies refer to the thermal properties of nanocomposites with clays and their influence on the initial decomposition temperature and glass temperature [178–180].

A synergy between classical flame retardants or stabilizers and nanofillers could be a desirable effect leading to the decrease in the usually large amounts of flame retardant that need to be applied and better mechanical properties [181, 182]. For instance, organoclay nanoparticles lower the flammability properties of the polymer matrix through formation of a compact layer during the exposure to flames. This layer blocks oxygen access to the fire zone and hinders emission of volatiles. The formed char shield reduces the heat transfer between the flame and the material and lowers the radiative flux by diffusing it into gas phase [130, 183].

In the presence of nanoparticles, the molecular mobility of degradation products and macrochain fragments is lowered which may contribute to the thermal stability of polymer nanocomposites. The incorporation of nanoparticles also causes an increase in viscosity of the melt, which restrict the heat transfer during processing.

The successful flame retardancy effect is obtained by combining the nanoparticles with conventional stabilizers such as metal hydroxides, phosphorous, or halogenated compounds, which mode of action is based on physical or chemical mechanisms [184]. However, during combustion, a portion of nanoparticles may be released to the environment causing some risks [185]. The use of double-layered hydroxides is an alternative to the use of modified organoclays for making nanocomposites with good fire and thermal properties. Our observations suggest that combination of montmorillonite with a phosphorus-based stabilizer leads to major improvements in the thermal and fire properties of polymer nanocomposites. Among different compositions of classical stabilizers and nanoparticulates showing possible synergetic effects, one can select:

- Carbon nanotubes in combination with metallic hydroxides
- Nano-hydroxides and nano-oxides in combination with phosphorous compounds
- Organoclays in combination with metallic hydroxides
- Organoclays in combination with phosphorous compounds to form intumescent structure [181, 182].

The use of modified nanofillers increases the flame retardation efficiency of the hybrid system at constant load of stabilizer. Improving the fire and thermal behavior of polymer materials using nanoparticles is associated with barrier effects but also with radicals scavenging ability. Application of nanoadditives could advantageously be combined with the use of reactive antioxidants. Appropriately selected stabilizers, adsorbed on nanofiller surface, could be added either before or during processing to inhibit the oxidation processes of polymer matrices. Antioxidants are added to the polymeric hybrid systems mostly in order to react with species formed during oxidation in an attempt to suppress the autocatalytic oxidation reactions.

Scavenging antioxidants are mainly used to trap free radicals formed in polymer nanocomposites during decomposition. These types of antioxidants are usually referred to as chain-breaking acceptors and chain-breaking donors [71]. Chain-breaking acceptors are effective at scavenging carbon-centered radicals under oxygen-deficient conditions. Therefore, they are most useful during high-temperature processing of polymeric materials or for the stabilization of the polymer composites [186]. However, they are not effective when molecular oxygen attacks carbon-centered radicals in a very fast reaction. In this case, H-donors such as hindered phenols and aromatic amines could be successfully used [187–190]. Synergistic effects could be achieved if hindered phenols are mixed with a phosphonate as they are preferred hydroperoxide decomposers in, e.g., polyamide nanocomposites stabilization [71]. Phosphonates are able to suppress the chain branching reactions in the auto-oxidative cycle by decomposing hydroperoxides to non-radical products. The hydroperoxides are reduced to an alcohol, while the phosphonate is oxidized in a stoichiometric reaction to phosphates (Fig. 7.6).

7.7 Conclusions and Perspectives

Polymer nanocomposites have considerably application potential in the area of novel advanced materials with improved properties. It is generally agreed that nanofillers can significantly improve various properties of polymer matrix they are incorporated into, but it is of paramount importance to elaborate the mechanism of their action. This is also true for thermal degradation and stabilization actions which mechanism depends strongly on the type of nanofiller, morphology, and polymer–filler interactions. Undesirable effects, such as agglomeration of nanoparticles, may play an important role, too. The results of the research works done so far lead to conclusions that the increase in the thermal stability of polymer/metal or metal

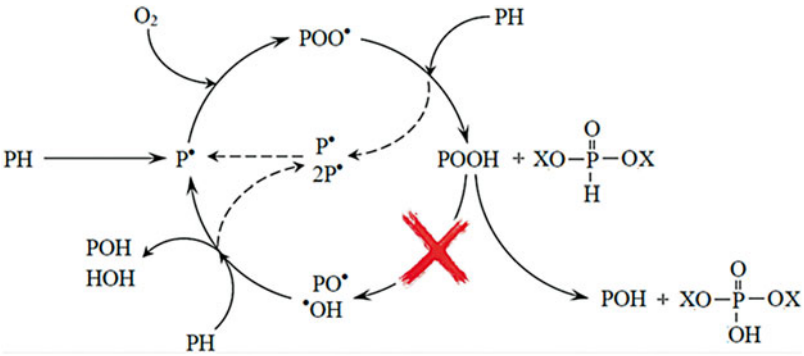

Fig. 7.6 Mechanism of the phosphonates' auto-oxidative cycle

oxide nanocomposites can be explained by the formation of polymer–nanoparticle network by physical cross-linking of polymer chains through metal particles, which stabilizes the whole system by restriction of the thermal motions of polymer chains. The mechanisms of thermal stability enhancement of polymers by silica oxide include slowing down of molecular dynamics, physical cross-linking, and specific interactions between the components. Several mechanisms of thermal stability enhancement have been considered for polymer composites with carbon nanotubes and nanofibers. Retardation of mass loss in inert atmosphere is likely to be a result of physical adsorption effect of the macromolecules on the nanotube surfaces that causes slower volatilization of polymer without change in initial degradation temperature or absorption of free radicals generated during polymer degradation. Another scenario is a reduction of mobility of the macromolecules in the presence of CNTs. For vastly applied polymer/clay nanocomposites, the barrier formation due to the presence of dispersed montmorillonite layers is suggested as a mechanism of thermal stability improvement; however, under oxidative conditions, exfoliated clay nanoparticles may catalyze the hydroperoxides decomposition.

In future developments, a synergy between classical flame retardants or stabilizers and nanofillers could be sought leading to the decrease in the usually large amounts of flame retardant that need to be applied and better mechanical properties of the nanocomposite. Another promising route is surface modification and functionalization of nanoadditives to enhance their dispersion in the polymer matrix or to form covalent bonds in hybrid materials, such as in those with POSS. Other promising area for future research is the use of cheap and abundantly available recyclable polymeric matrices and reinforcing nanomaterials of natural origin. However, materials obtained from renewable raw materials often lack sufficient thermal stability and flame retardancy, so there is a need for novel thermal stabilizers and flame retardants dedicated for this promising class of environmentally friendly nanostructured materials.

Acknowledgments Authors acknowledge funding by the National Science Centre in Poland under contract No. DEC-2011/02/A/ST8/ 00409.

References

1. Berthelot JM (1998) Ling FF (ed) Composite materials: mechanical behaviour and structural analysis. Springer, Berlin/Heidelberg/New York, pp 2–15
2. Twardowski TE (2007) Introduction to nanocomposite materials: properties, processing, characterization. ADEstech Publications book, Lancaster
3. Lan T, Kaviratna P, Pinnavia T (1995) Mechanism of clay tactoid exfoliation in epoxy-clay Nanocomposites. Chem Mater 7(11):2144–2150
4. Lan T, Pinnavaia T (1994) Clay-reinforced epoxy nanocomposites. Chem Mater 6:2216–2219
5. Alexandre M, Dubois P (2000) Polymer-layered silicate nanocomposites: preparation, properties and uses of a new class of materials. Mater Sci Eng R Rep 28:1–63
6. Kumar AP, Depan D, Tomer NS, Singh RP (2009) Nanoscale particles for polymer degradation and stabilization-trends and future perspectives. Prog Polym Sci 34:479–515
7. Mark JE, Jiang CY, Tang MY (1984) Simultaneous curing and filling of elastomers. Macromolecules 17:2613–2616
8. Wilkes GL, Orler B, Huang H (1985) "Ceramers" hybrid materials incorporating polymeric/oligomeric species into inorganic glasses utilizing a sol–gel approach. Polym Prep 26:300–301
9. Wen J, Wilkes GL (1996) Organic/inorganic hybrid network materials by the sol–gel approach. Chem Mater 8:1667–1681
10. Kojima Y, Usuki A, Kawasumi M, Okada A, Kurauchi T, Kamigaito O (1993) Synthesis of nylon 6–clay hybrid by montmorillonite intercalated with ϵ-caprolactam. J Polym Sci Part A Polym Chem 31:983–986
11. Okada A, Fukushim Y, Kawasumi M, Inagaki S, Usuki A, Sugiyama S (1988) Composite material and process for manufacturing same. US Patent 4.739.007
12. Kawasumi M (2004) The discovery of *polymer*-clay hybrids. J Polym Sci Part A Polym Chem 42:819–824
13. Mogilevsky G, Chen Q, Kleinhammes A, Wu Y (2008) The structure of multilayered titania nanotubes based on delaminated anatase. Chem Phys Lett 460(4–6):517–520
14. Guo Z, Lei K, Li Y, Ng H, Prikhodko S, Hahn H (2008) Fabrication and characterization of iron oxide nanoparticles reinforced vinyl-ester resin nanocomposites. Compos Sci Technol 88:1513
15. Guo Z, Wei S, Shedd B, Scaffaro R, Pereira T, Hahn H (2007) Particle surface engineering effect on the mechanical, optical and photoluminescent properties of zno/vinyl-ester resin nanocomposites. J Mater Chem 17:800
16. Endo M, Koyama T, Hishiyama Y (1976) Structure improvement of carbon fibers prepared from benzene. Jpn J Appl Phys 15(11):2073–2076
17. Oberlin A, Endo M, Koyama T (1976) Filamentous growth of carbon through benzene decomposition. J Cryst Growth 32(3):335–349
18. Iijima S (1991) Helical microtubules of graphitic carbon. Nature 354(6348):56–58
19. Song Y, Youn J (2005) Influence of dispersion states of carbon nanotubes on physical properties of epoxy nanocomposites. Carbon 43:1378
20. Ma PC, Siddiqui NA, Marom G, Kim JK (2010) Dispersion and functionalization of carbon nanotubes for polymer-based nanocomposites: a review. Compos Part A 41:1345–1367
21. Miranda-Trevino JC, Coles CA (2003) Kaolinite properties, structure and influence of metal retention on pH. Appl Clay Sci 23:133–139
22. Beyer G (2002) Nanocomposites: a new class of flame retardants for polymers. Plast Addit Compound 4(10):22–27
23. McNally T, Murphy WR, Lew CY, Turner RJ, Brennan GP (2003) Polyamide-12 layered silicate nanocomposites by melt compounding. Polymer 44:2761–2772
24. Solomon MJ, Almusallam AS, Seefeldt KF, Somwangthanaroj A, Varadan P (2001) Rheology of polypropylene/clay hybrid materials. Macromolecules 34:1864–1872
25. Dixon JB (1991) Roles of clays in soils. Appl Clay Sci 5:489–503

26. Manias E, Touny A, Wu L, Strawhecker K, Lu B, Chung TC (2001) Polypropylene/montmorillonite nanocomposites. Review of the synthetic routes and materials properties. Chem Mater 13:3516–3523
27. Chin IJ, Thurn-Albrecht T, Kim H-C, Russell TP, Wang J (2001) On exfoliation of montmorillonite in epoxy. Polymer 42:5947–5952
28. Pramoda KP, Liu T, Liu Z, He C, Sue HJ (2003) Thermal degradation behavior of polyamide 6/clay nanocomposites. Polym Degrad Stab 81:47–56
29. Ishida H, Campbell S, Blackwell J (2000) General approach to nanocomposite preparation. Chem Mater 12:1260–1267
30. Kar S, Maji PK, Bhowmick AK (2010) Chlorinated polyethylene nanocomposites: thermal and mechanical behavior. J Mater Sci 45:64–73
31. Carastan D, Demarquette N (2006) Microstructure of nanocomposites of styrenic polymers. Macromol Symp 233:152–160
32. Liu G, Zhang L, Zhao D, Qu X (2005) Bulk polymerization of styrene in the presence of organomodified montmorillonite. J Appl Polym Sci 96:1146–1152
33. Dharaiya D, Jana SC (2005) Thermal decomposition of alkyl ammonium ions and its effects on surface polarity of organically treated nanoclay. Polymer 46:10139–10147
34. Yoon PJ, Hunter DL, Paul DR (2003) Polycarbonate nanocomposites. Part 1. Effect of organoclay structure on morphology and properties. Polymer 44:5323–5339
35. Monticelli O, Musina Z, Frache A, Bellucci F, Camino G, Russo S (2007) Influence of compatibilizer degradation on formation and properties of PA6/organoclay nanocomposites. Polym Degrad Stab 92:370–378
36. Yoon PJ, Hunter DL, Paul DR (2003) Polycarbonate nanocomposites: part 2. Degradation and color formation. Polymer 44:5341–5354
37. Fornes TD, Yoon PJ, Paul DR (2003) Polymer matrix degradation and color formation in melt processed nylon 6/clay nanocomposites. Polymer 44:7545–7556
38. Marquis DM (2011) Properties of nanofillers in polymer. In: Cuppoletti J (ed) Nanocomposites and polymers with analytical methods. InTech, Rijeka
39. Guo L, Yuan W, Lu Z, Li CM (2013) Polymer/nanosilver composite coatings for antibacterial applications. Colloids Surf A 439:69–83
40. Yeo SY, Tan WL, Abu Bakar M, Ismail J (2010) Silver sulfide/poly(3-hydroxybutyrate) nanocomposites: thermal stability and kinetic analysis of thermal degradation. Polym Degrad Stab 95:1299–1304
41. Habibzade S, Omidvar A, Farahani MRM, Mashkour M (2014) Effect of nano-ZnO on decay resistance and artificial weathering of wood polymer composite. J Nanomater Mol Nanotechnol 3(3):1–5
42. Raftopoulos KN, Janowski B, Apekis L, Pissis P, Pielichowski K (2013) Direct and indirect effects of POSS on the molecular mobility of polyurethanes with varying segment Mw. Polymer 54:2745–2754
43. Raftopoulos KN, Jancia M, Aravopoulou D, Hebda E, Pielichowski K, Pissis P (2013) OSS along the hard segments of polyurethane. Phase separation and molecular dynamics. Macromolecules 46:7378–7386
44. Xu H, Kuo SW, Lee J, Chang FC (2002) Preparations, Thermal Properties, and Tg Increase Mechanism of Inorganic/Organic Hybrid Polymers Based on Polyhedral Oligomeric Silsesquioxanes. Polymer 43:5117–5124
45. Hussain F, Hojjati M, Okamoto M, Gorga RE (2006) Review article: polymer-matrix nanocomposites, processing, manufacturing, and application: an overview. J Compos Mater 40:1511–1575
46. Majka TM, Leszczyńska A, Pielichowski K (2013) Comparison of rheological properties of polyamide-6 and its nanocomposites with montmorillonite, obtained by melt intercalation. Technical transactions 1-Ch:39–46
47. Twardowska H, Dammann L (2005) Hermosetting inorganic clay nanodispersions and their use. US Patent 6(887):931

48. Twardowska H, Singh R, Dammann L (2005) Thermosetting inorganic clay nanodispersions and their use. US Patent 6(841):607
49. Suh D, Lim Y, Park O (2000) The properties and formation mechanism of unsaturated polyester-layered silicate nanocomposite depending on the fabrication methods. Polymer 41:8557
50. Nichols K, Chou C (1999) Polymer composite comprising a inorganic layered material and a polymer matrix and a method for its preparation. US Patent 5(952):093
51. Seyhan A, Gojny F, Tanoglu M, Schulte K (2007) Rheological and dynamic-mechanical behavior of carbon nanotube/vinyl ester-polyester suspensions and their nanocomposites. Eur Polym J 43:2836
52. Seyhan A, Gojny F, Tanoglu M, Schulte K (2007) Critical aspects related to processing of carbon nanotube/unsaturated thermoset polyester nanocomposites. Eur Polym J 43:374–379
53. Rychly J, Matisova-Rychla L, Csmorova K, Achimsky L, Audoin L, Tcharkhtchi A, Verdu J (1997) Kinetics of mass changes in oxidation of polypropylene. Polym Degrad Stab 58:269
54. Grassie N, Weir NA (1965) The photooxidation of polymers. IV. A note on the coloration of polystyrene. J App Polym Sci 9:999
55. Girois S, Delprat P, Audouin L, Verdu J (1997) Oxidation thickness profiles during photooxidation of non-photostabilised polypropylene. Polym Degrad Stab 56:169
56. Ghaemy M, Scott G (1981) Photo- and thermal oxidation of ABS: correlation of loss of impact strength with degradation of the rubber component. Polym Deg Stab 3:233
57. Cullis CF, Hirschler MM (1981) The combustion of organic polymers. Oxford University Press, Oxford
58. Beyler CL, Hirschler MM (2005) Thermal decomposition of polymers. In: Kutz M (ed) SFPE handbook of fire protection engineering. William Andrew Publishing, New York
59. Weil ED, Hansen RN, Patel N (1989) Prospective approaches to more efficient flame retardant systems. In: Nelson GL (ed) Fire and polymers: hazards identification and prevention. ACS Symposium Series 425, American Chemical Society, Dallas, 97108.
60. Hirschler MM (1982) Recent developments in flame-retardant mechanisms. In: Scott G (ed) Developments in polymer stabilisation. Applied Science Publ, London
61. Stuetz DE, DiEdwardo AH, Zitomer F, Barnes BF (1980) Polymer flammability II. J Polym Sci Polym Chem Ed 18:987–1009
62. Brauman SK (1988) Polymer degradation during combustion. J Polymer Sci B 26:1159–1171
63. Kashiwagi T, Hirata T, Brown JE (1985) Thermal and oxidative degradation of poly(methyl methacrylate), molecular weight. Macromolecules 18:131–138
64. Kashiwagi T, Inabi A, Brown JE, Hatada K, Kitayama T, Masuda E (1986) Effects of weak linkages on the thermal and oxidative degradation of poly(methyl methacrylates). Macromolecules 19:2160–2168
65. Kashiwagi T, Nambu H (1992) Global kinetic constants for thermal oxidative degradation of a cellulosic paper. Combust Flame 88:345–368
66. Steckler KD, Kashiwagi T, Baum HR, Kanemaru K (1991) Analytical model for transient gasification of noncharring thermoplastic materials. In: Cox G, Langford B (eds) Fire safety science: proceedings of the third international symposium. Elsevier, London
67. Hoffman AW (1861) Changes of guttapercha under tropical influences. J Chem Soc 13:87
68. Clough RL, Billingham NC, Gillen KT (1996) Polymer durability degradation, stabilization, and lifetime prediction. ASC Adv Chem Ser. doi:10.1021/ba-1996-0249.fw001
69. Allen NS (1983) Degradation and stabilisation of poleolefins. Applied Science Publishers Ltd. Elsevier Applied Science, London
70. Reich L, Stivala SS (1969) Autooxidation of hydrocarbons and polyolefins. Dekker, New York
71. Zweifel H (2001) Plastics additives handbook. Hanser, Munich
72. Scott G (1993) Atmospheric oxidation and antioxidants. Elsevier Publishing Company, Amsterdam
73. Knight JB, Calvert PD, Billingham NC (1985) Localization of oxidation in polypropylene. Polymer 26:1713
74. Scott G (1995) Initiation processes in polymer degradation. Polym Degrad Stab 48:315–324

75. Gugumus F (1998) Novel role for tropospheric ozone in initiation of autoxidation. Polym Deg Stab 62(1998):403–406
76. Miller AA, Mayo FR (1956) The oxidation of unsaturated compounds. The oxidation of styrene. J Am Chem Soc 78:1017–1022
77. Kamiya Y, Niki EG (1978) Aspects of degradation and stabilization of polymers, Jellineck HHG (ed). Elsevier Scientific Publishing Company, Amsterdam
78. McMillen DF, Golden DM (1982) Hydrocarbon bond dissociation energies. Ann Rev Phys Chem 33:493–532
79. Castelhano AL, Griller DJ (1982) Heats of formation of simple alkyl radicals. Am Chem Soc 104:3655–3659
80. Bartlett PD, Guaraldi GJJ (1967) Di-t-butyl trioxide and di-t-butyl tetroxide. Am Chem Soc 89:4799–4801
81. Nangia PS, Benson SW (1980) The kinetics of the interaction of peroxy radicals. I. The tertiary peroxy radicals. Int J Chem Kinetics 1:29–42
82. Nakano M, Takayama K, Shimizu Y, Tsuji Y, Inaba H, Migita T (1976) Spectroscopic evidence for the generation of singlet oxygen in self-reaction of sec-peroxy radicals. J Am Chem Soc 98:1974–1975
83. Howard JA, Ingold KU (1968) Absolute rate constants for hydrocarbon oxidation. J Am Chem Soc 110:1056
84. Liufu SC, Xiao HN, Li YP (2005) Thermal analysis and degradation mechanism of polyacrylate/ZnO nanocomposites. Polym Degrad Stab 87:103–110
85. Chen J, Zhou Y, Nan Q, Ye X, Sun Y, Zhang F, Wang Z (2007) Preparation and properties of optically active polyurethane/TiO_2 nanocomposites derived from optically pure 1,1′-binaphthyl. Eur Polym J 43:4151–4159
86. Sawada T, Ando S (1998) Synthesis, characterization, and optical properties of metal-containing fluorinated polyimide films. Chem Mater 10:3368–3378
87. Rancourt JD, Taylor LT (1987) Preparation and properties of surface-conductive polyimide films via in situ codeposition of metal salts. Macromolecules 20:790–795
88. Goyal PK, Negi YS, Tiwari AN (2005) Preparation of high performance composites based on aluminum nitride/poly(ether-ether-ketone) and their properties. Eur Polym J 41:2034–2044
89. Cassagnau P (2003) Payne effect and shear elasticity of silica-filled polymers in solutions and in molten state. Polymer 44:2455–2462
90. Bershtein VA, Egorova LM, Yakushev PN, Pissis P, Sysel P, Brozova L (2002) Molecular dynamics in nanostructured polyimide-silica hybrid materials and their thermal stability. J Polym Sci Part B Polym Phys 40:1056–1069
91. Lu GT, Huang Y (2002) Synthesis of polymaleimide/silica nanocomposites. J Mater Sci 37:2305–2309
92. Yang J, Lin Y, Wang J, Lai M, Li J, Liu J, Tong X, Cheng HJ (2005) Morphology, thermal stability, and dynamic mechanical properties of atactic polypropylene/carbon nanotube composites. Appl Polym Sci 98:1087–1091
93. Shaffer SP, Windle AH (1999) Fabrication and characterization of carbon nanotube/poly(vinyl alcohol) composites. Adv Mater 11:937–941
94. Chatterjee A, Deopura BL (2006) Thermal stability of polypropylene/carbon nanofiber composite. J Appl Polym Sci 100:3574–3578
95. Kashiwagi T, Grulke E, Hilding J, Harris R, Awad W, Douglas JF (2002) Thermal degradation and flammability properties of polypropylene/ carbonnanotube composites. Macromol Rapid Commun 13:761–765
96. Bikiaris D, Vassiliou A, Chrissafis K, Paraskevopoulos KM, Jannakoudakis A, Docoslis A (2008) Effect of acid treated multi-walled carbon nanotubes on the n the mechanical permeability, thermal properties and thermo-oxidative stability of isolatic polypropylene. Polym Degrad Stab 93:952–967
97. Marosfői BB, Szabó A, Marosi G, Tabuani D, Camino G, Pagliari S (2006) Complex activity of clay and CNT particles in flame retarded EVA nanotube composites. J Therm Anal Calorim 86:669–673

98. Bocchini S, Frache A, Camino G, Claes M (2007) Polyethylene thermal oxidative stabilization in carbon nanotubes based nanocomposites. Eur Polym J 43:3222–3235
99. Davis RD, Gilman JW, VanderHart DL (2003) Processing degradation of polyamide 6/montmorillonite clay nanocomposites and clay organic modifier. Polym Degrad Stab 79:111–121
100. Chipara M, Lozano K, Hernandez A, Chipara M (2008) TGA analysisof polypropylene-carbon nanofibers composites. Polym Degrad Stab 93:871–876
101. Sarno M, Gorrasi G, Sannino D, Sorrentino A, Ciambelli P, Vittoria V (2004) Polymorphism and thermal behaviour of syndiotactic poly(propylene)/carbon nanotube composites. Macromol Rapid Commun 25:1963–1967
102. Hirschler MM (1984) Reduction of smoke formation from and flammability of thermoplastic polymers by metal oxides. Polymer 25:405
103. Mai F, Habibi Y, Raquez JM, Dubois P, Feller JF, Peijs T (2013) Poly(lactic acid)/carbon nanotube nanocomposites with integrated degradation sensing. Polymer 54:6818–6823
104. Di Blasi C, Galgano A, Branca C (2013) Modeling the thermal degradation of poly(methyl methacrylate)/carbon nanotube nanocomposites. Polym Degrad Stab 98:266–275
105. Chou WJ, Wang CC, Chen CY (2008) Thermal behaviors of polyimide with plasma-modified carbon nanotubes. Polym Degrad Stab 93:745–752
106. Chen X, Wang J, Lin M, Zhong W, Feng T, Chen X, Chen J, Xue F (2008) Mechanical and thermal properties of epoxy nanocomposites reinforced with amino-functionalized multiwalled carbon nanotubes. Mat Sci Eng A 492:236–242
107. Vaia RA, Price G, Ruth PN, Nguyen HT, Lichtenhan J (1999) Polymer/layered silicate nanocomposites as high performance ablative materials. J Appl Clay Sci 15:67–92
108. Tidjani A, Wald O, Pohl MM, Hentschel MP, Schartel B (2003) Polypropylene–graft–maleic anhydride-nanocomposites: I—characterization and thermal stability of nanocomposites produced under nitrogen and in air. Polym Degrad Stab 82:133–140
109. Jang BN, Costache M, Wilkie CA (2005) The relationship between thermal degradation behavior of polymer and the fire retardancy of polymer/clay nanocomposites. Polymer 46:10678–10687
110. Jang BN, Wilkie CA (2005) The thermal degradation of polystyrene nanocomposite. Polymer 46:2933–3000
111. Jang BN, Wilkie CA (2005) The effects of clay on the thermal degradation behavior of poly(styrene-co-acrylonitrile). Polymer 46:9702–9713
112. Costache MC, Wang D, Heidecker MJ, Manias E, Wilkie CA (2006) Thermal degradation of ethylene-vinyl acetate copolymer nanocomposites. Polym Adv Technol 17:272–280
113. Chen K, Susner MA, Vyazovkin S (2005) Effect of the brush structure on the degradation mechanism of polystyrene–clay nanocomposites. Macromol Rapid Commun 26:690–695
114. Ghanbari A, Heuzey MC, Carreau PJ, Ton-That MT (2013) A novel approach to control thermal degradation of PET/organoclay nanocomposites and improve clay exfoliation. Polymer 54:1361–1369
115. Feng Y, Wang B, Wang F, Zhao Y, Liu C, Chen J, Shen C (2014) Thermal degradation mechanism and kinetics of polycarbonate/silica nanocomposites. Polym Degrad Stab 107:129–138
116. Blumstein A (1965) Thermal degradation of the inserted polymer. J Polym Sci Part A General Papers 3:2665–2672
117. Chen K, Wilkie CA, Vyazovkin S (2007) Nanoconfinement revealed in degradation and relaxation studies of two structurally different polystyrene-clay systems. J Phys Chem B 111:12685–12692
118. Vyazovkin S, Dranca I (2004) A DSC study of α- and β-relaxations in a PS-clay system. J Phys Chem B 108:11981–11987
119. Vyazovkin S, Dranca I, Fan X, Advincula R (2004) Prepared by surface initiated polymerization. J Phys Chem B 108:11672–11679
120. Gao Z, Xie W, Hwu JM, Wells L, Pan WP (2001) The characterization of organic modified montmorillonite and its filled PMMA nanocomposite. J Therm Anal Calorim 64:467–475
121. Edwards G, Halley P, Kerven G, Martin D (2005) Thermal stability analysis of organosilicates, using solid phase microextraction techniques. Thermochim Acta 429:13–18

122. Ni R, Huang Y, Yao C (2009) Thermogravimetric analysis of organoclays intercalated with the gemini surfactants. J Therm Anal Calorim 96:943–947
123. Kornmann X, Berglund L, Sterte J (1998) Nanocomposites based on montmorillonite and unsaturated polyester. Polym Eng Sci 28:1351
124. Fu X, Qutubuddin S (2004) Synthesis of unsaturated polyester-clay nanocomposites using reactive organoclays. Polym Eng Sci 44:345
125. Chen C, Yebassa D, Raghavan D (2007) Synthesis, characterization, and mechanical properties evaluation of thermally stable apophyllite vinyl ester nanocomposites. Polym Adv Technol 18:574–581
126. Bottino FA, Di Pasquale G, Fabbri E, Orestano A, Pollicino A (2009) Influence of montmorillonite nano-dispersion on polystyrene photo-oxidation. Polym Degrad Stab 94:369–374
127. Bellucci F, Camino G, Frache A, Sarra A (2007) Catalytic charring-volatilization competition in organoclay nanocomposites. Polym Degrad Stab 92:425–436
128. Agag T, Takeichi T (2000) Polybenzoxazine-montmorillonite hybrid nanocomposites: synthesis and characterization. Polymer 41:7083–7090
129. Becker O, Varley RJ, Simon GP (2004) Thermal stability and water uptake of high performance epoxy layered silicate nanocomposites. Eur Polym J 40:187–195
130. Gilman JW (1999) Flammability and thermal stability studies of polymer layered-silicate (clay) nanocomposites. Appl Clay Sci 15(1):31–49
131. Zanetti M, Bracco P, Costa L (2004) Thermal degradation behaviour of PE/clay nanocomposites. Polym Degrad Stab 85:657–665
132. Lomakin SM, Novokshonova LA, Brevnov PN, Shchegolikhin AN (2008) Thermal properties of polyethylene/montmorillonite nanocomposites prepared by intercalative polymerization. J Mater Sci 43:1340–1353
133. Chen W, Feng L, Qu B (2004) Preparation of nanocomposites by exfoliation of ZnAl layered double hydroxides in nonpolar LLDPE solution. Chem Mater 16:368–370
134. Kong Q, Hu Y, Yang L, Fan W, Chen Z (2006) Polymer-matrix composites, impact behaviour, laminate mechanics. Polym Compos 27:49–54
135. Ramos Filho FG, Mélo TJA, Rabello MS, Silva SML (2005) Thermal stability of nanocomposites based on polypropylene and bentonite. Polym Degrad Stab 89:383–392
136. Xie W, Gao Z, Pan WP, Hunter D, Singh A, Vaia R (2001) Thermal degradation chemistry of alkyl quaternary ammonium montmorillonite. Chem Mater 13:2979–2990
137. Dyer JR (1965) Applications of absorption spectroscopy of organic compounds. Prentice Hall, Englewood Cliffs
138. Dintcheva NT, Al-Malaika S, La Mantia FP (2009) Effect of extrusion and photo-oxidation on polyethylene/clay nanocomposites. Polym Degrad Stab 94:1571–1588
139. Stoeffler K, Lafleur PG, Denault J (2008) Thermal decomposition of various alkyl onium organoclays: effect on polyethylene terephthalate nanocomposites' properties. Polym Degrad Stab 93:1332–1350
140. Bertini F, Canetti M, Leone G, Tritto I (2009) Thermal behavior and pyrolysis products of modified organo-layered silicates as intermediates for in situ polymerization. J Anal Appl Pyrolysis 86:74–81
141. Carey FA (1992) Organic chemistry. McGraw-Hill Inc, New York
142. Mittal V (2012) Modification of montmorillonites with thermally stable phosphonium cations and comparison with alkylammonium montmorillonites. Appl Clay Sci 56:103–109
143. Zulfiqar S, Ahmad Z, Ishaq M, Sarwar MI (2009) Aromatic–aliphatic polyamide/montmorillonite clay nanocomposite materials: synthesis, nanostructure and properties. Mater Sci Eng A 525:30–36
144. Pielichowski K, Leszczyńska A (2006) Polyoxymethylene-based nanocomposites with montmorillonite: an introductory study. Polimery 51:60–66
145. Camino G, Tartaglione G, Frache A, Manferti C, Costa G (2005) Thermal and combustion behaviour of layered silicate epoxy nanocomposites. Polym Degrad Stab 90:354–362
146. Cai Y, Huang F, Wei Q, Song L, Hu Y, Ye Y, Xu Y, Gao W (2008) Structure, morphology, thermal stability and carbonization mechanism studies of electrospun PA6/Fe-OMT nanocomposite fibers. Polym Degrad Stab 93:2180–2185

147. Liu J, Hu Y, Wang SF, Song L, Chen ZY, Fan WC (2004) Preparation and characterization of nylon 6/Cu2+–exchanged and Fe3+–exchanged montmorillonite nanocomposite. Colloid Polym Sci 282:291–294
148. Allen NS, Harrison MJ, Ledward M, Fellows GW (1989) Thermal and photo-chemical degradation of nylon 6,6 polymer: part III—influence of iron and metal deactivators. Polym Degrad Stab 23:165–174
149. Chefetz B, Eldad S, Polubesova T (2011) Interactions of aromatic acids with montmorillonite: Ca2+– and Fe3+–saturated clays versus Fe3+–Ca2+–clay system. Geoderma 160: 608–613
150. Dunn P, Sansom GF (1969) The stress cracking of polyamides by metal salts. Part II. Mechanism of cracking. J Appl Polym Sci 13:1657–1672
151. Kong Q, Hu Y, Song L, Yi C (2009) Synergistic flammability and thermal stability of polypropylene/aluminum trihydroxide/Fe-montmorillonite nanocomposites. Polym Adv Technol 20:404–409
152. Xie W, Gao Z, Liu K, Pan WP, Vaia R, Hunter D, Singh A (2001) Thermal characterization of organically modified montmorillonite. Thermochim Acta 367–368:339–350
153. Yariv S (2004) The role of charcoal on DTA curves of organo-clay complexes: an overview. Appl Clay Sci 24:225–236
154. Scaffaro R, Mistretta MC, La Mantia FP (2008) Compatibilized polyamide 6/polyethylene blend-clay nanocomposites: Effect of the degradation and stabilization of the clay modifier. Polym Degrad Stab 93:1267–1274
155. Pielichowski K, Njuguna J (2005) Thermal degradation of polymeric materials. Rapra, Shawbury
156. Takekoshi T (1998) Layered minerals and compositions comprising the same. US Patent 5(707):439
157. Walker CH, John JVS, Wisian-Neilson PJ (2001) Synthesis and Size Control of Gold Nanoparticles Stabilized by Poly(methylphenylphosphazene). Am Chem Soc 123:3846–3847
158. Chang CM, Chang CC (2007) Preparation and characterization of polyimide–nanogold nanocomposites from 3-mercaptopropyltrimethoxysilane encapsulated gold nanoparticles. Polym Degrad Stab 93:109–116
159. Huang HM, Chang CY, Liu I, Tsai H, Lai M, Tsiang RC (2005) Synthesis of Gold Nanocomposite via Chemisorption of Gold Nanoparticles with Poly(p-methylstyrene) Containing Multiple Bonding Groups on the Chain Side. J Polym Sci Part A Polym Chem 43:4710–4720
160. Laachachi A, Ferriol M, Cochez M, Ruch D, Lopez-Cuesta JM (2008) The catalytic role of oxide in the thermooxidative degradation of poly(methyl methacrylate)–TiO_2 nanocomposites. Polym Degrad Stab 93:1131–1137
161. Duquesne S, Bras ML, Bourbigot S, Delobel R, Camino G, Eling B, Lindsayd C, Roels T (2001) Thermal degradation of polyurethane and polyurethane/expandable graphite coatings. Polym Degrad Stab 74:493–499
162. Cerezo FT, Preston CML, Shanks RA (2007) Structural, mechanical and dielectric properties of poly(ethylene-co-methyl acrylate-co-acrylic acid) graphite oxide nanocomposites. Compos Sci Technol 67:79–91
163. George JJ, Bhowmick AK (2008) Ethylene vinyl acetate/expanded graphite nanocomposites by solution intercalation: preparation, characterization and properties. J Mater Sci 43:702–708
164. Xiao M, Sun L, Liu J, Li Y, Gong K (2002) Synthesis and properties of polystyrene/graphite nanocomposites. Polymer 43:2245–2248
165. George JJ, Dyopadhyay AB, Bhowmick AK (2008) New generation layered nanocomposites derived from ethylene-co-vinyl acetate and naturally occurring graphite. J Appl Polym Sci 108:1603–1616
166. Xiong X, Wang J, Jia H, Fang E, Ding L (2013) Structure, thermal conductivity, and thermal stability of bromobutyl rubber nanocomposites with ionic liquid modified graphene oxide. Polym Degr Stab 98:2208–2214
167. Pielichowski K, Njuguna J, Janowski B, Pielichowski J (2006) Polyhedral oligomers silsesquioxanes (POSS)-containing nanohybrid polymers. Adv Polym Sci 201:225–303
168. Blanco I, Abate L, Bottino FA, Bottino P (2014) Thermal behaviour of a series of novel aliphatic bridged polyhedral oligomeric silsesquioxanes (POSSs)/polystyrene (PS) nanocom-

posites: the influence of the bridge length on the resistance to thermal degradation. Polym Degrad Stab 102:132–137
169. Tamaki R, Tanaka Y, Asuncion MZ, Choi J, Laine RM (2001) Octa(aminophenyl)silsesquioxane as a Nanoconstruction Site. J Am Chem Soc 123:12416–12417
170. Blanco I, Bottino FA, Cicala G, Latteri A, Recca A (2013) A kinetic study of the thermal and thermal oxidative degradations of new bridged POSS/PS nanocomposites. Polym Degrad Stab 98:2564–2570
171. Giannelis E (1996) Polymer layered silicate nanocomposites. Adv Mater 8:29
172. LeBaron P, Wang Z, Pinnavaia T (1999) Polymer layered silicates nanocomposites : an overview. Appl Clay Sci 15:11–29
173. Finaa A, Abbenhuisb H, Tabuania D (2006) Metal functionalized poss as fire retardants in polypropylene. Polym Degrad Stab 91:2275–2281
174. Peeterbroech SL, Alexandre B, Bnagy M, Viville J, Lazzaroni P, Dubois R (2007) The influence of the matrix polarity on the morphology and properties of ethylene vinyl acetate copolymers-carbon nanotube nanocomposites. Compos Sci Technol 67:1659–1665
175. Zou W, Liu Y, Yang X, Li H, Zhang C (2008) Functionalization of mwnts using polyacryloyl chloride and the properties of cnt-epoxy matrix nanocomposites. Compos Sci Technol 68:3259
176. Biercuk M, Llaguno M, Hyun J (2002) Carbon nanotube composites for thermal management. Appl Phys Lett 80(15):2767–2769
177. Evseeva L, Tanaeva S (2008) Thermal conductivity of micro and nanostructural epoxy composites at low temperatures. Mech Compos Mater 44(1):87–92
178. Al-Malah K, Abu-Jdayil B (2007) Clay-based heat insulator composites: thermal and water retention properties. Appl Clay Sci 37:90–96
179. Abot J, Yasmin A, Daniel I (2003) Mechanical and thermoviscoelastic behavior of clay/epoxy nanocomposites. Mater Res Soc Symp 740:167–172.
180. Haque A, Hossain F, Dean D (2002) Glass/vinyl ester polymer nanocomposites : manufacturing, structures, thermal and mechanical properties. American Society for Composites, West Lafayette, Indiana, pp 1–9
181. Morgan A, Wilkie C (2007) Flame retardant polymer nanocomposites. Wiley-Interscience, Hoboken, NJ
182. Morgan A (2009) Polymer nanocomposites flammability and flame-retardancy. In Kin-Tak L, Hussain F (eds) Nano and biocomposites. CRC Press, London, New York, Philadelphia
183. Gilman J (2000) Flammability properties of polymer layered silicate nanocomposites polypropylene and polystyrene nanocomposites. Chem Mater 12:1866–1873
184. Le Bras M, Wilkie C, Bourbigot S, Duquesne S, Jama C (2005) New applications of mineral fillers: the use of mineral fillers in micro and nano-composites. In: Fire retardancy of polymers. The Royal Society of Chemistry, London
185. Chivas-Joly C, Guillaume E, Ducourtieux S, Saragoza L, Lopez-Cuesta J, Longuet C, Duplantier S, Bertrand J, Calogine D, Minisini B, Gensous F (2010) Influence of carbon nanotubes on fire behavior and on decomposition products of thermoplastic polymers. INTERFLAM, Nottingham
186. Grassie N, Scott G (1985) Polymer degradation and stabilization. Cambridge University Press, Cambridge
187. Allen NS, Edge M (1992) Fundamentals of polymer degradation and stabilization. Elsevier Applied Science, London
188. Gugumus F (1990) Plastic additives, Gachter R, Muller H (eds). Hanser Publishers, Munich
189. Cerruti P, Rychly J, Matisova-Rychla L, Carfagna C (2004) Chemiluminescence from oxidation of polyamide 6,6: II. The effect of metal salts. Polym Deg Stab 84:199
190. Njuguna J, Pielichowski K, Fan J (2012) Polymer nanocomposites for aerospace applications. In: Gao F (ed) Advances in polymer nanocomposites – types and applications. Woodhead Publishing Ltd., Cambridge

Chapter 8
Thermomechanical Analysis of Polymer Nanocomposites

Engin Burgaz

8.1 Introduction

Polymer nanocomposites have been categorized under new and advanced polymer composite materials which have structural dimensions on the order of 1–100 nm, and these materials with proper additions of nanocylinders, nanospheres, and nanoplatelets have unusual combination of material properties compared to traditional polymer composites. The addition of 1–15 vol.% of nanospheres such as POSS (polyhedral oligomeric silsesquioxane), silica, alumina, magnetite, TiO_2, silver, aluminum nitride, Fe_2O_3, and ZnO; nanoplatelets such as clay, graphite, and graphene; and nanocylinders such as carbon nanotubes and nanofibers provide property enhancements such as better electrical and thermal conductivity [1, 2], higher thermal stability [3, 4], better dispersion and morphology, increased stiffness, strength and modulus [5–7], improved wear and fatigue, enhanced barrier properties [8] and decreased flammability [9], lighter weight, and better physical properties such as magnetic, optic, or dielectric properties [10, 11] in comparison with conventional polymer composites containing 15–50 vol.% of micron-sized inorganic particles. During the past 20 years, academia and industry have invested both time and money on polymer nanocomposites since the properties of these materials can be greatly improved compared with the pure polymer or conventional polymer composites. Polymer nanocomposites can be synthesized by three common methods: (1) The polymer matrix can be mixed with nanofillers and then heated above the glass transition temperature of the polymer (the melt blending) [12, 13]. (2) A suitable monomer can be mixed with nanofillers in situ and then polymerized (in situ polymerization) [14, 15]. (3) Nanofillers can be mixed with the polymer matrix in

E. Burgaz, PhD (✉)
Department of Materials Science and Engineering, Ondokuz Mayis University, Atakum, Samsun 55139, Turkey
e-mail: eburgaz@omu.edu.tr

© Springer International Publishing Switzerland 2016

X. Huang, C. Zhi (eds.), *Polymer Nanocomposites*,
DOI 10.1007/978-3-319-28238-1_8

solution (the solution blending) [16]. During the last two decades, polymer nanocomposites containing nanospheres, nanorods, and nanoplatelets with improved properties have been synthesized by using different types of polymers as matrix materials. The most widely used polymers as the matrix phase in polymer nanocomposites can be expressed as epoxy resins, polyurethanes, polyesters, poly(ethylene oxide), polyolefins, poly(methyl methacrylate), polystyrene, polyamide, polyimide, polylactide, nafion, etc. Besides the matrix material, the most widely used filler materials can be identified as POSS, silica, alumina, and TiO_2 under the category of nanospheres; clay, graphene, and graphite under the category of nanoplatelets; carbon nanotubes and carbon nanofibers under the category of nanocylinders. The ultimate purpose in these polymer nanocomposite studies which have been realized during the past 20 years of time is to improve polymer properties such as mechanical properties, thermal stability, thermomechanical behavior, nanofiller dispersion and morphology, wear and fatigue behavior, barrier properties, magnetic, optical, and dielectric properties. Among these material properties, thermomechanical behavior of polymer nanocomposites is an important issue and has been quite studied in the literature. However, there are still problems and issues need to be resolved toward the development of advanced polymer nanocomposites with improved thermomechanical behavior. In polymer nanocomposites, the most important thermomechanical properties can be defined as stiffness, glass transition, storage and loss modulus, damping coefficient (tan δ), heat distortion temperature, and thermal expansion coefficient. These material properties are usually measured via well-known materials characterization techniques such as dynamic mechanical analysis (DMA), tensile testing, and thermomechanical analysis (TMA).

A significant number of excellent review articles about thermomechanical properties of polymer nanocomposites containing nanoplatelets [17, 18], nanospheres [19, 20], and nanocylinders [21, 22] are available in the literature. These publications not only give a detailed overview of the field but also summarize the potential problems and challenges that need to be resolved by experts who are actively working on thermomechanical characterization of polymer nanocomposites. In the investigation of structure–thermomechanical property relationships, the ultimate aim is to realize the fine distribution and dispersion of nanofillers without any single agglomeration in the matrix. In the last few years, excellent reviews covering the topic of polymer–nanofiller interactions in polymer nanocomposites had been published [23, 24]. Due the large specific surface area of nanofillers, an interfacial polymer layer is formed between the polymer matrix and nanoparticles [25]. Thus, in polymer nanocomposites, to achieve desirable and improved properties, a fine dispersion of nanofillers with an efficient interfacial polymer layer in a polymer matrix is the most important requirement. Intermolecular interactions between nanofillers and polymer chains in the polymer layer can be repulsive or attractive. If interactions are attractive, then the movement of polymer chains in the interface between nanoparticles and polymer matrix will be suppressed, and the glass transition of polymer will increase. If interactions are repulsive, then polymer chains in the polymer layer will gain more mobility, and the glass transition of polymer will decrease.

Thermomechanical behavior of polymer nanocomposites is greatly affected by the molecular interactions between the polymer chains in the interfacial polymer layer with the nanoparticles and polymer chains in the polymer matrix [26]. Therefore, surface modification of nanoparticles and adjusting the properties of the interfacial polymer layer by using proper chemistry and physics are very important criteria in order to improve thermomechanical properties of polymer nanocomposites.

This chapter reviews thermomechanical properties of polymer nanocomposites containing nanoplates, nanospheres, and nanocylinders and focuses on important thermomechanical parameters such as stiffness, glass transition, storage modulus, loss modulus, damping coefficient, heat distortion temperature, and thermal expansion coefficient. Throughout the course of this chapter, new synthesis methods which are very important for improving the thermomechanical behavior of polymer nanocomposites are also reviewed by giving specific and detailed examples from the literature. The most important nanofillers and polymers as matrix materials that have been used in thermomechanical studies of polymer nanocomposites are also reviewed by giving detailed information for each polymer and nanofiller from the literature. The adjustment of polymer–nanoparticle interactions by using new synthesis methods, proper chemistry, physics, and engineering and choosing the right nanofiller and polymer matrix combination was discussed to fabricate new polymer nanocomposite materials with improved thermomechanical properties. The goal of this chapter is not to present a complete literature review in the topic. Interested readers are referred to a number of recent reviews that give detailed analysis of the substantial work published in this area [1–4, 17–26]. However, careful analysis of this chapter can direct researchers to find out promising approaches and further lead the design and production of new and advanced polymer nanocomposites with improved thermomechanical properties.

8.2 Polymer Nanocomposites Containing Nanoplatelets

Nanoplatelets such as clay, graphite, mica, and graphene have been used in diverse polymer matrices such as epoxy resins, polyurethanes, polyesters, poly(ethylene oxide), polyolefins, polystyrene, polyamide, polyimide, polylactide, nafion, etc., for thermomechanical property analysis of polymer nanocomposites. Among polymer–nanoplatelet works in the literature, the most widely studied nanoplatelet has been nanoclay or nanolayered silicate which has established a profoundly important place both in academia and industry due to its remarkable thermal barrier, thermomechanical, and fire-resistance properties achieved at low nanoclay content [27]. The improvement of properties depends on how well clay is dispersed within the polymer matrix. Usually, thermomechanical properties improve if the nanoclay is intercalated or exfoliated. And the formation of these two morphologies is ultimately affected by interactions between nanoclay and polymer matrix and synthesis methods [7, 27–29].

8.2.1 Clay-Based Polymer Nanocomposites

For thermomechanical studies of polymer nanocomposites, 2:1 layered silicates such as montmorillonite and laponite have been mainly used as nanofillers in polymer matrices [5, 7, 12]. In terms of geometry, silicate layers consist of two tetrahedral sheets of silicon atoms which are separated by one octahedral sheet of magnesium hydroxides. The layer thickness of montmorillonite clay with this type of structure is close to 1 nm. The negative charges at the silicate layer are balanced with Ca^{+2}, Na^{+}, Li^{+}, and K^{+} ions that are present inside clay galleries [5, 7, 12]. Since the electrostatic forces are not very strong, polar molecules can be inserted within the clay galleries, and also clay galleries have a strong swelling ability in water. Particularly, montmorillonite (MMT) which is categorized under smectites has a cation exchange capacity (CEC) of 80–150 meq/100 g and a specific surface area of 800 m^2/g [26]. Thus, because of this reason, MMT has been widely used as a nanoplatelet in studies of polymer nanocomposites.

Well dispersion of nanoclay in a polymer matrix mainly depends on the type of interactions between the polymer matrix and clay nanolayers. Based on the difference of these interactions, mainly three types of different structures can be formed: (1) If the physical attraction between clay and polymer is very poor, then the polymer is not intercalated within clay galleries, and the resulting material is not a nanocomposite and has poor properties. Furthermore, particle agglomeration of clay nanolayers tends to reduce strength and produces weaker materials. (2) If the physical attraction between clay and polymer is good, then a single polymer layer is intercalated within clay galleries, and the resulting material is an intercalated nanocomposite with improved properties. (3) If the physical attraction between clay and polymer is relatively strong, then clay galleries are exfoliated and complete dispersion of single silicate nanolayer in a continuous polymer matrix without any agglomeration is realized, and the resulting material is an exfoliated polymer nanocomposite with enhanced mechanical and physical properties [5, 7, 12, 26, 30].

The physical attraction between polymer and clay can be improved by exchanging inorganic cations of clay galleries with various organic cations such as alkylammonium cations and cationic surfactants. Thus, this surface modification changes the normally hydrophilic silicate surface into an organophilic surface. The alkylammonium cations lower the surface energy of the silicate surface and improve the physical attraction between the polymer and clay. In addition to surface energy reduction, organic cations also increase the interlayer distance between clay nanolayers, thus easing the diffusion of polymer chains inside clay galleries [5, 7, 12, 26].

In thermomechanical studies of polymer–clay nanocomposites, pristine or organo-modified MMTs have been used in diverse polymer matrices such as epoxy [31–39], polyolefins [40–42], polyamides [43–46], poly(lactic acid) [47–51], poly(ethylene oxide) [52–54], poly(e-caprolactone) [48, 55], poly(ethylene terephthalate) [56, 57], polystyrene [58], polycarbonate [59], poly(vinyl alcohol) [60, 61], polyurethanes [62], and nafion [63–65]. Laponite which is a small-size clay platelet with a diameter of 25 nm and a thickness of 1 nm has been also used in

polyurethanes [18] and polystyrene [58] for thermomechanical analysis of polymer nanocomposites.

Mechanical and thermomechanical properties of epoxy nanocomposites containing 1–10 wt % of clay particles were investigated via DMA, TMA, and tensile testing by Yasmin et al. [32]. It was found that both the elastic modulus and storage modulus improves with the addition of clay particles. Authors also reported that the thermal expansion coefficient (CTE) was reduced with the addition of clay.

Figure 8.1a, b shows the variation of storage modulus with temperature for Nanomer I.28E/epoxy and Cloisite 30B/epoxy nanocomposites, respectively. At room temperature both nanocomposites showed higher storage modulus as the clay content increases. However, for the same clay content, it is clearly seen that the Cloisite 30B/epoxy shows much higher storage modulus compared to the Nanomer I.28E/epoxy. For 10 wt % clay addition, the Cloisite 30B/epoxy showed an increase

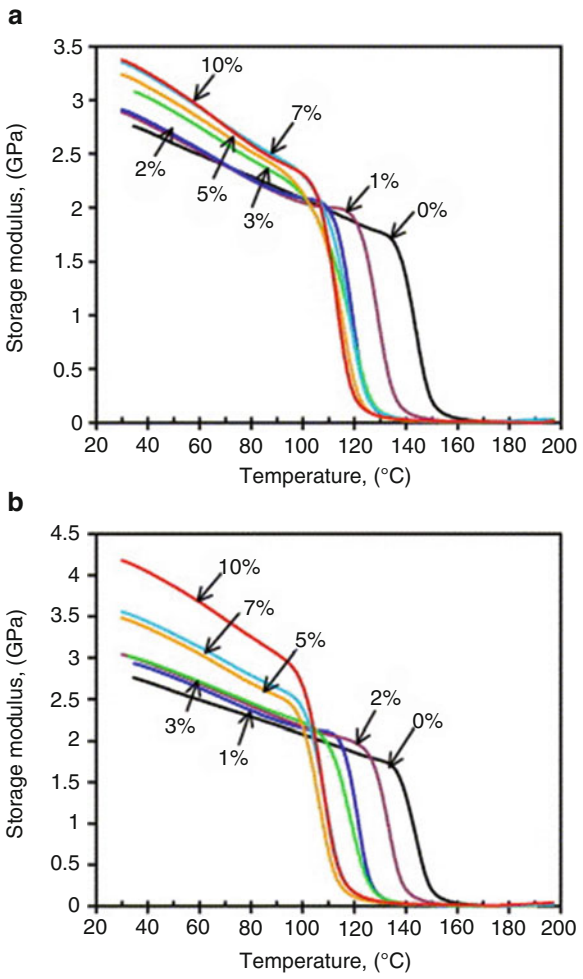

Fig. 8.1 Variation of storage modulus with temperature: (**a**) NanomerI.28E/epoxy; (**b**) Cloisite 30B/epoxy (Reproduced with permission from Ref. [32]. Copyright 2006 Elsevier Ltd)

of 53 % compared to pure epoxy, whereas the Nanomer I.28E/epoxy nanocomposite showed an increase of 22 % compared to pure epoxy. From Fig. 8.1a, b, it is clearly observed that for any clay content, the Cloisite 30B/epoxy always shows higher storage modulus compared to Nanomer I.28E/epoxy system. These DMA results were supported by the fact that better dispersion and intercalation/exfoliation of Cloisite 30B/epoxy nanocomposites leads to a higher storage modulus compared to the intercalated structure of Nanomer I.28E/epoxy system [32]. Yasmin et al. also concluded in Fig. 8.2 that Cloisite 30B/epoxy nanocomposite shows a lower glass transition temperature, T_g in the presence of higher d-spacing compared to the Nanomer I.28E/epoxy system. Chen et al. proposed the interphase formation hypothesis such that the volume fraction of interphase material is higher if the clay content and the d-spacing are higher in the nanocomposite [66]. The flexural and thermomechanical properties of woven carbon–nanoclay–epoxy laminates were studied by Chowdhury et al. [31] via three-point bend flexure and DMA, and their results revealed that maximum improvements in flexural strength and modulus were obtained with 2 wt % nanoclay addition. DMA results also showed that thermomechanical properties improved, and T_g of room temperature cured and thermally post-cured samples showed an improvement of about 9 and 13 °C, respectively, for 2 wt % nanoclay addition [31].

Sharmila et al. fabricated epoxy–clay nanocomposites from diglycidyl ether of bisphenol A (DGEBA) epoxy and modified nanoclay (Cloisite 93A) using triethylenetetramine (TETA) as a curing agent [39]. They examined static and dynamic mechanical properties of epoxy nanocomposites for barrier resistance and thermal stability. Authors showed that tensile strength and flexural strength increased about 15 % and 23 %, respectively, at very low clay additions. This result was explained to be caused by enhanced cross-linking in the epoxy matrix due to partially exfoliated/intercalated clay structure. Their XRD and TEM results revealed that the clay dispersion in the epoxy matrix is partially exfoliated at lower clay loadings and

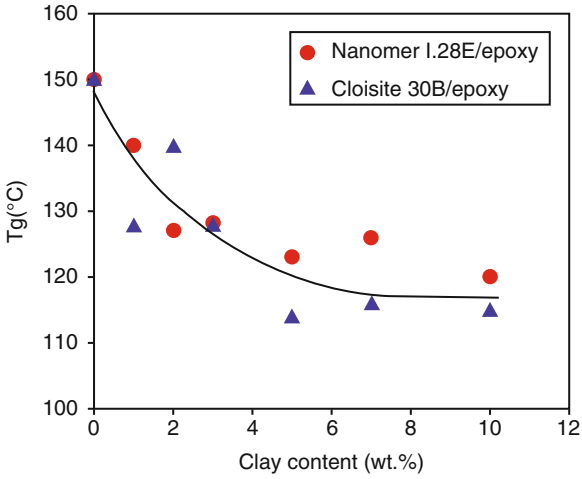

Fig. 8.2 Effect of clay content on Tg (Reproduced with permission from Ref. [32]. Copyright 2006 Elsevier Ltd)

intercalated at higher loadings (Fig. 8.3). Also, the level of clay dispersion in epoxy nanocomposites led to greater thermal stability compared to pure epoxy. In addition to thermal stability improvement, equilibrium swelling experiments revealed that a maximum of 61 % increase in barrier performance was achieved by the addition of 5 phr (per hundred gram of resin) clay. The increase in barrier properties is a definite result of increase in the cross-linking density. Cross-link density (CLD) results showed that the presence of Cloisite increased CLD of epoxy resin up to 1 phr loading and then it decreased with further clay addition. Figure 8.4 shows the schematic representation of nanocomposite's morphology at lower and higher clay loadings. Based on the depiction in Fig. 8.4, the higher clay amount in epoxy nanocomposites increases the organic content of Cloisite. This organic content functions as a plasticizer in the epoxy network and decreases CLD. The interfacial interactions brought about by Cloisite 93A also benefited the thermomechanical properties to a large extent in the form of improved glass transition temperature and an impressive enhancement in storage modulus [39].

Storage and loss modulus vs. temperature at different clay loadings in epoxy–Cloisite nanocomposites were also studied by the authors. The apparent improvement of storage modulus (E′) at lower clay addition was explained by the stiffness enhancement due to the partial exfoliated/intercalated morphology and the homogenous clay dispersion level in epoxy. At high clay loadings, the less improvement of E' was explained to be caused by the change of morphology from partially exfoliated to fully intercalated one. The maximum of loss modulus (E″) shifts slightly to higher temperature for 1 phr Cloisite loading compared to pure epoxy. It was clearly

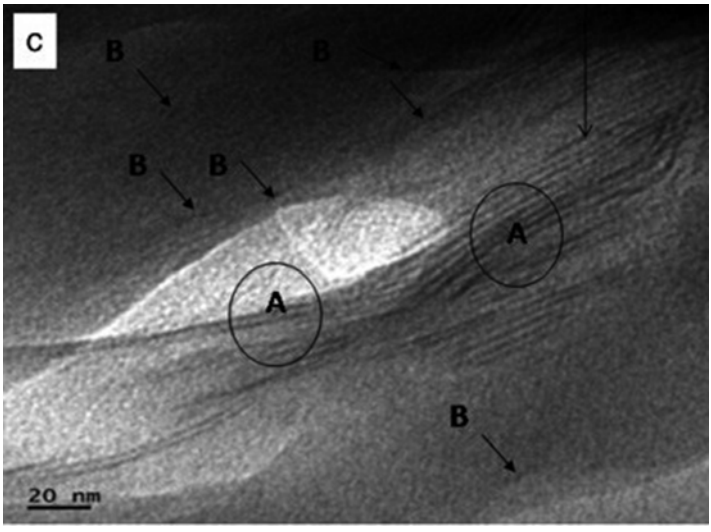

Fig. 8.3 TEM micrograph of cloisite epoxy nanocomposite system containing 1 phr cloisite. Intercalated structure and exfoliated structure are marked by *A* and *B*, respectively (Reproduced with permission from Ref. [39]. Copyright 2014 Elsevier Ltd)

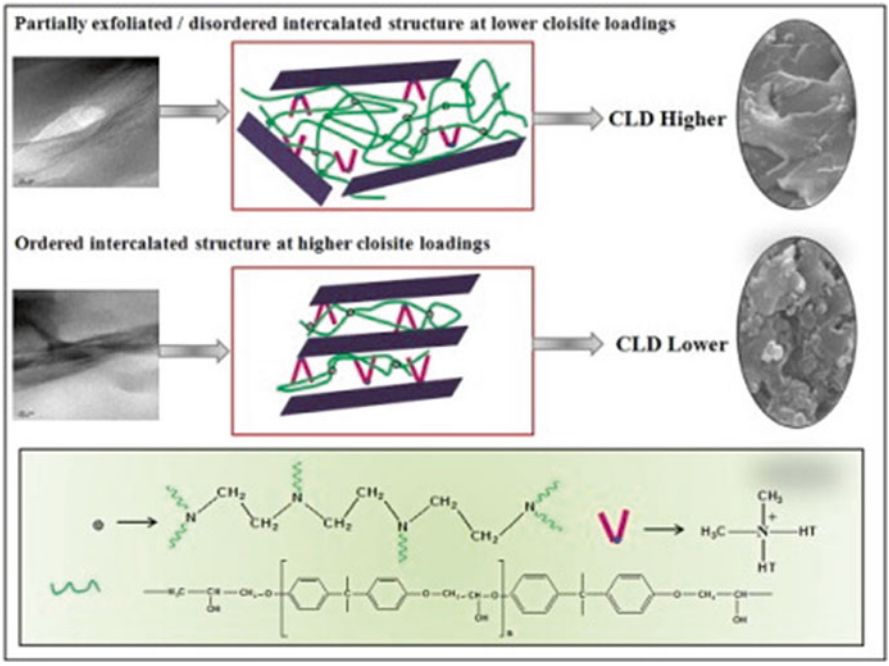

Fig. 8.4 Schematic representation of the structure of cloisite epoxy nanocomposites and its effect on CLD (Reproduced with permission from Ref. [39]. Copyright 2014 Elsevier Ltd)

observed that the damping coefficient (tan δ) peak height of epoxy nanocomposites decreases at lower clay addition compared to pure epoxy which means lower damping, good clay–epoxy interactions, and improvement of interfacial bonding in epoxy nanocomposites [39].

Souza et al. [38] investigated the influence of the MMT content (Cloisite® 30B), clay dispersion and exfoliation on morphology, thermomechanical, and viscoelastic properties of epoxy/MMT systems. The nanocomposite morphology indicated that increasing mixing time caused an improvement in clay dispersion. The use of ultrasonication decreased the dispersion of MMT in the epoxy matrix. Authors reported that the epoxy system containing 5 wt % of MMT exhibited greater homogeneity than that containing 3 wt % clay. The nanocomposites prepared without ultrasonication showed two peaks in tan δ, and the storage modulus decreased with clay addition compared to pure epoxy matrix [38].

Verge et al. [36] used a new ammonium-based bio-sourced surfactant derived from a 3-alkyl phenol glycidyl ether in the surface modification of sepiolite clay in order to enhance the compatibility of clay with the epoxy matrix. Authors showed via SEM that the compatibilization and dispersion of sepiolite in epoxy was achieved. DMA results also revealed that Tg of epoxy was shifted around 20 °C to higher temperatures, and the storage modulus below Tg was enhanced [36]. Yang et al. developed a facile biomimetic method to enhance the interfacial interactions

in epoxy–clay nanocomposites [35]. By mimicking mussel adhesive proteins, authors constructed a monolayer of polydopamine on clay surface by using a coating method. After incorporation of this modified clay into epoxy matrix, it was found out that strong interfacial interactions between epoxy and clay through polydopamine improved the dispersion of modified clay in the epoxy matrix. And as a result of this, thermomechanical properties of epoxy–clay nanocomposites at very low clay loadings were greatly improved. Based on infrared spectroscopy and rheology results, it was shown that the interfacial interactions between the modified clay and epoxy were shown to be dominated by the hydrogen bonds between polydopamine and epoxy. Figure 8.5 shows the schematic illustration of the possible interactions both hydrogen bonds (dashed line) and covalent bond (solid line) in epoxy–clay nanocomposites [35].

Baniasadi et al. studied the morphological, physical, and mechanical properties of polypropylene (PP)–clay nanocomposites that were prepared by in situ polymerization [40]. In their study, they used non-modified smectite type of clay (bentonite) in the preparation of bi-supported Ziegler–Natta catalyst of $TiCl_4/Mg(OEt)_2$/clay. Based on their TEM and XRD results, the formation of exfoliated PP/clay nanocomposites via in situ intercalative polymerization of propylene with bi-supported catalyst was confirmed. Figures 8.6 and 8.7 show the XRD and TEM data of PP/clay nanocomposites, respectively. In Fig. 8.6, from XRD curve of the nanocomposite, it is clearly seen that the clay peak disappeared due to the exfoliation of clay during in situ polymerization. In Fig. 8.7, TEM micrograph of in situ polymerized PP/clay nanocomposite confirms the uniform distribution and exfoliated structure of clay particles in PP. From the storage modulus results, it was clearly observed that exfoliated type of clay dispersion in PP increases stiffness at all temperatures. Also, it was shown that the storage modulus of PP/clay nanocomposites increases with increasing clay content. From tan δ plot, it was clearly observed that T_g increases with increasing clay concentration between 1 and 5 wt % clay. The heights of the tan δ peaks decrease with increasing temperature. Thus, authors suggested

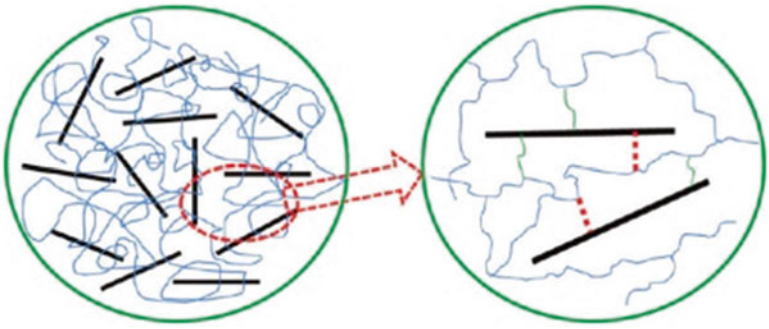

Fig. 8.5 Schematic illustration of the Possible Interactions in Clay/Epoxy Nanocomposites: Dashed Line, Hydrogen bond; Solid Line, Covalent Bond (Reproduced with permission from Ref. [35]. Copyright 2011 American Chemical Society)

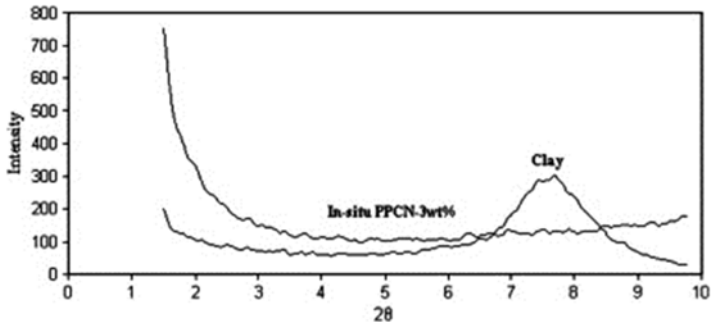

Fig. 8.6 XRD patterns of clay and in situ prepared nanocomposite (3 wt %) (Reproduced with permission from Ref. [40]. Copyright 2009 Elsevier Ltd)

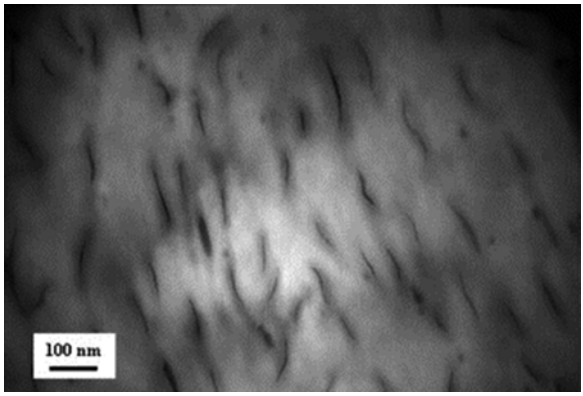

Fig. 8.7 TEM micrograph of prepared in situ nanocomposite (Reproduced with permission from Ref. [40]. Copyright 2009 Elsevier Ltd)

that the damping properties of PP/clay nanocomposites decrease with clay content due to the solid-like behavior of in situ polymerized PP/clay nanocomposites [40].

Passador et al. prepared high-density polyethylene (HDPE)/linear low-density polyethylene (LLDPE) blend-based nanocomposites via melt processing using three different compatibilizer systems (maleic anhydride grafted linear low-density polyethylene (LLDPE-g-MA), maleic anhydride grafted high-density polyethylene (HDPE-g-MA), and 50/50 wt % mixture of these compatibilizers [42]. The influence of these three different compatibilizers on the rheological, thermomechanical, and morphological properties of HDPE/LLDPE/organoclay nanocomposites was evaluated by the authors. The synthesis of these nanocomposites was realized by melt intercalation in a torque rheometer in two steps: first, mixtures of compatibilizer/organophilic MMT (Cloisite 20A) in the ratio of 2:1 were obtained and secondly, these mixtures were mixed with the HDPE/LLDPE matrix to produce nanocomposites with 2.5 wt % clay content. It was found that compatibilized nanocomposites with LLDPE-g-MA or mixture of HDPE-g-MA and LLDPE-g-MA showed better clay dispersion due to stronger interactions between clay and HDPE/

LLDPE blend matrix. Based on TEM, WAXD, and rheological results, it was shown that there are weak interactions between the HDPE/LLDPE matrix and nanoclay, and there is also poor clay dispersion in the nanocomposite without any compatibilizer. Figure 8.8 shows the storage modulus of HDPE, LLDPE, HDPE/LLDPE blend, and the nanocomposites as a function of temperature. The presence of organoclay in HDPE/LLDPE blend caused an increase in the storage modulus, while the presence of relatively soft compatibilizer caused a decrease of the storage modulus. Thus, the storage modulus of compatibilized nanocomposites was lower than that of nanocomposites without any compatibilizer. It was concluded that there is a clear advantage of adding maleic anhydride grafted polyethylene in HDPE/LLDPE/clay nanocomposites since compatibilizers not only cause the exfoliation and/or intercalation of nanoclay but also improve the adhesion of organoclay to the HDPE/LLDPE blend system [42].

Grigoriadi et al. investigated the effect of nanoclay content and aspect ratio on the thermomechanical behavior of unmodified LDPE/clay nanocomposites [41]. Two kinds of organo-modified clays (synthetic laponite with low aspect ratio and MMT with high aspect ratio) were used in the preparation of LDPE/clay nanocomposites. It was shown that the LPDE reinforced with organo-MMT had better

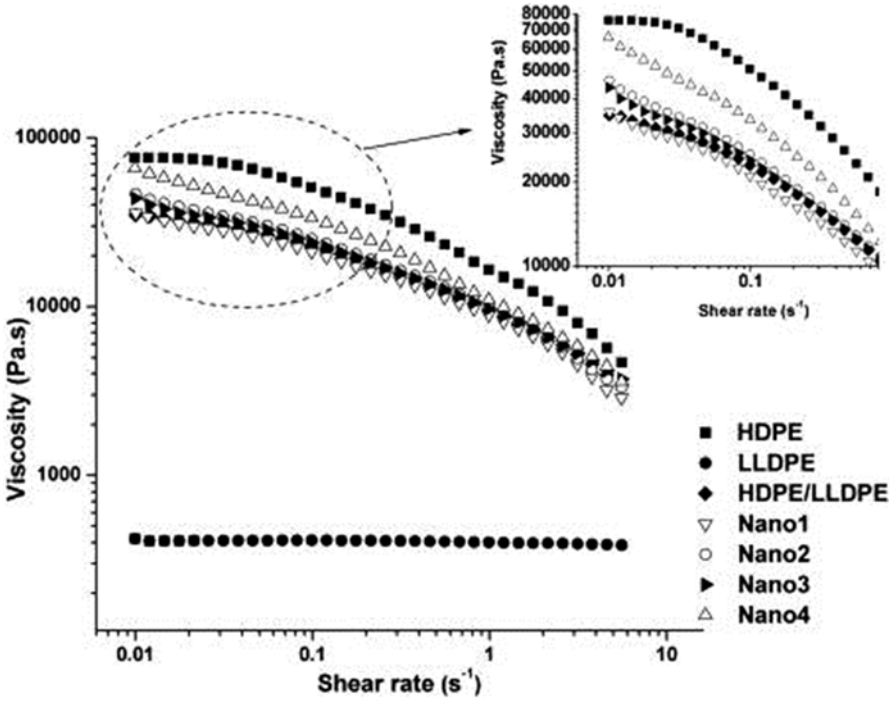

Fig. 8.8 Storage modulus of HDPE, LLDPE, HDPE–LLDPE blend, and the nanocomposites as a function of temperature (Reproduced with permission from Ref. [42]. Copyright 2013 Wiley Periodicals, Inc.)

dynamic mechanical properties in the whole temperature range than those with organo-laponite. This result was explained such that the higher active surface area and preferential orientation of longer MMT nanoplatelets led to higher mechanical enhancement in unmodified LDPE/clay nanocomposites up to clay contents of 5 wt %. DMA experiments of LDPE, LDPE/organo-modified laponite (OLp), and LDPE/organo-modified MMT (OMt) nanocomposites with various organoclay contents of 2–10 wt % were performed by the authors. From DMA results, it was clearly observed that storage modulus of polymer nanocomposites significantly increased compared to that of the unmodified LPDE especially at temperatures below −20 °C. It was shown that the addition of OLp or OMt led to lower damping at temperatures below −20 °C and higher damping at high temperatures. This result was explained such that at temperatures lower than −20 °C, the elasticity characteristics of LDPE/clay nanocomposites increases more compared to their plasticity characteristics [41].

Siengchin et al. studied ternary composites composed of polyamide-6 (PA-6), hydrogenated nitrile rubber (HNBR), and sodium fluorohectorite (FH) or boehmite alumina (BA) that were produced by melt blending with latex precompounding [43]. Their DMA results (Fig. 8.9) showed that the incorporation of FH and BA particles increased the storage modulus in the whole temperature range, compared to that of the PA-6/HNBR blend. This was explained by the reinforcing effect of the nanoparticles leading to increased stiffness. Also, it was observed that the storage modulus of FH is higher than BA nanocomposites. In agreement with SEM results (Fig. 8.10), this result was also attributed to the fact that FH stacks are well dispersed in the PA-6 matrix and have much higher aspect ratio in comparison with BA [43].

Stoclet et al. prepared bio-based nanocomposites made from polyamide 11 (PA11) and sodium montmorillonite via water-assisted extrusion [45]. Their TEM and SAXS results showed that injecting water on nanocomposites during extrusion resulted in a well-exfoliated structure with clay contents as high as 10 % wt. Based on tensile testing and DMA results, it was observed that adding 10 % wt of filler doubled the value of the Young's modulus, and storage modulus increased with clay addition to PA11 nanocomposites. Also, it was shown that the addition of clay drastically enhanced the thermal stability of the nanocomposites by increasing the start of degradation by 35 °C when 10 % wt of filler is added to the system [45]. Wan et al. prepared polyamide 6 nanocomposites consisting of clay and short glass fiber (SGF) filled via a two-step melt compounding process in a twin screw extruder [46]. Based on their DMA results, it was observed that the combination of SGF and clay in polymer matrix had a synergistic effect in modulus, and clay had a significantly higher reinforcing effect compared to SGF in PA/clay/SGF at the same amount of filler content. TMA results showed that exfoliated clay in PA/SGF provided a low coefficient of thermal expansion especially above T_g compared to cases of individual filler composites. Authors also concluded that the synergy of multi-scale reinforcements of clay and glass fiber provided better physical properties for polymer–matrix composites (PMCs) compared to the case where PA-6 was filled with each of individual filler [46].

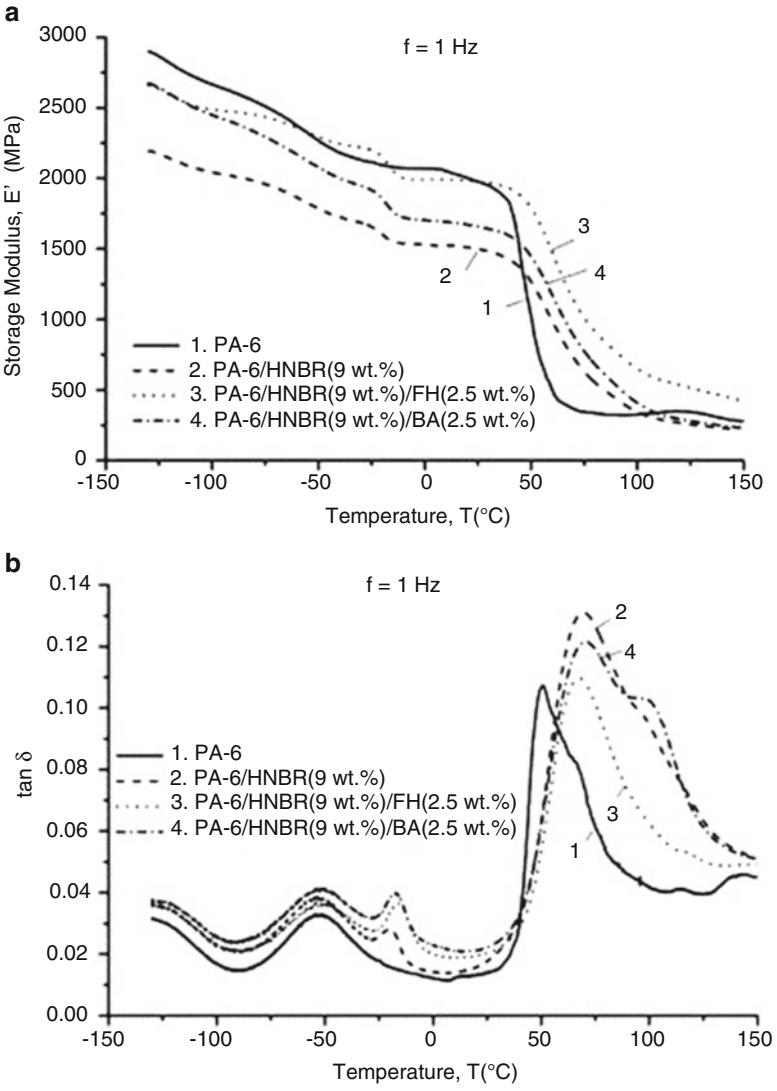

Fig. 8.9 (**a**) E' vs. T and (**b**) tan δ vs. T for the PA-6, PA-6/HNBR, and PA-6/HNBR/FH (BA) composites (Reproduced with permission from Ref. [43]. Copyright 2009 Elsevier Ltd)

Pluta et al. prepared polylactide (PLA)–clay nanocomposites via melt blending by using three kinds of organo-modified MMTs at a concentration level varying from 1 to 10 wt % and 20 wt % of poly(ethylene glycol) (PEG) as a plasticizer [47]. According to their DMA results, the storage modulus increased with the clay content. Glassy PEG which was well dispersed within unfilled PLA matrix increased the storage modulus compared to the case of PLA without any PEG below the glass transition of PEG. The loss modulus of all plasticized samples revealed an additional

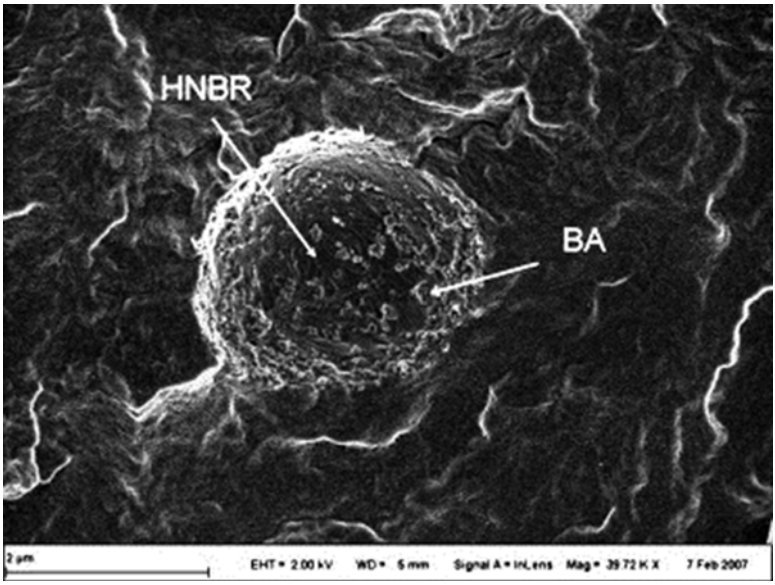

Fig. 8.10 SEM picture from the fracture surfaces of PA-6–HNBR (9 wt %)/BA (2.5 wt %) (Reproduced with permission from Ref. [43]. Copyright 2009 Elsevier Ltd)

peak due to the glass transition of PEG-rich dispersed phase which is a proof for the partial mixing of components in the system. The magnitude of this mechanical loss exhibited a tendency to increase with the filler content was correlated. This increase was related with the intercalation ability of PEG molecules inside clay galleries [47].

Fukushima et al. studied poly(lactic acid) (PLA) and poly(ε-caprolactone) (PCL) nanocomposites that were prepared by adding two organically modified MMTs and one sepiolite via melt blending [48]. Based on WAXS, SEM, and TEM results, it was reported that all clays showed a good dispersion level with both of the polymer matrix. Figure 8.11 shows DMA results of PLA nanocomposites. The storage modulus increases with the incorporation of all clays with increasing temperature. The addition of 5 wt % of these clays was shown to have a considerable effect on the elastic properties of the corresponding PLA matrices, which is more noticeable above T_g. However, the presence of clay particles did not show very significant shifts of tan δ (Fig. 8.11b) for all nanocomposites compared to pure PLA and PCL [48]. Kontou et al. compared the effects of two different types of nano-sized fillers (silica and montmorillonite) and their mixtures on the thermomechanical properties of polylactide (PLA) [49]. Based on DMA results, the storage modulus increased more pronouncedly at temperatures higher than T_g with increasing nanofiller content for each series of PLA nanocomposites. Furthermore, it was pointed out that PLA/MMT nanocomposites exhibited higher values of storage modulus compared to PLA/silica nanocomposites. It was concluded that the nanofiller addition higher than 3 wt % usually does not increase the interphase region and improve properties since the total surface area of nanofiller is counterbalanced by the creation of nano-

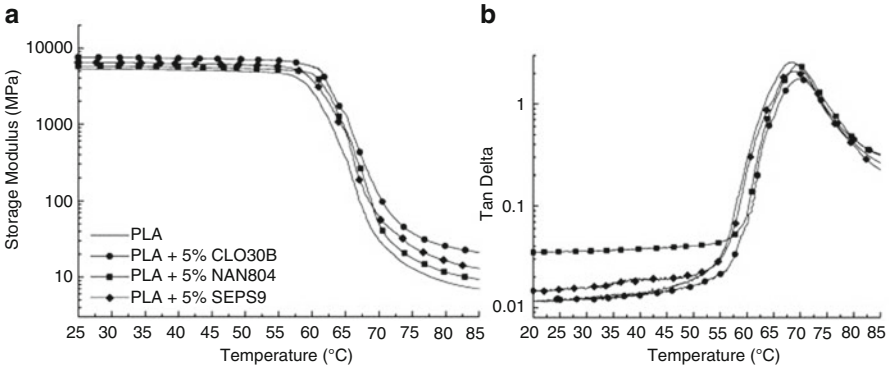

Fig. 8.11 Temperature dependence of (**a**) E′ and (**b**) tan delta for PLA-based nanocomposites (Reproduced with permission from Ref. [48]. Copyright 2008 Elsevier Ltd)

filler aggregates [49]. Wootthikanokkhan et al. prepared poly(lactic acid) (PLA) composites containing three different types of additives (kenaf fiber, nanoclay, and boron nitrile) by using a twin screw extruder before molding [50]. Effects of annealing on thermomechanical properties (heat distortion temperature) of PLA and PLA composites were investigated. Figure 8.12 shows the heat distortion temperature (HDT) results of various PLA composites both before and after annealing. After annealing, the HDT of PLA was improved due to the increase of crystallinity % in the polymer. The highest HDT value (128 °C) was obtained for the PLA sample containing 20 pph kenaf fiber after annealing at 100 °C for 60 min. It was also pointed out that the HDT value reduced to 123 °C by decreasing the annealing time to 10 min. The use of nanoclay and boron nitrile produced composites with relatively low HDT values but with good mechanical properties [50].

Ratna et al. prepared poly(ethylene oxide) (PEO)/organo-modified clay nanocomposites via solution intercalation method by using chloroform as a solvent [52]. Their XRD results showed that intercalated type of morphology was formed in PEO nanocomposites. Further XRD studies on PEO samples containing 5 and 10 wt % clay indicated that the d-spacing between clay layers increased up to 9.5 nm as a result of sonication. This result showed that applying ultrasonication helps nanoclay galleries to swell up, provides more energy, and causes their further separation and dispersion within the polymer matrix. Based on DMA results in Fig. 8.13, it was shown that the storage modulus at all temperatures was found to be higher for nanocomposites compared to the pure PEO. A slight shift in loss tangent peak toward higher temperature was observed in the case of nanocomposites compared to pure PEO. This result was attributed to the confinement of polymer chains as a result of intercalation inside clay galleries [52]. Burgaz prepared poly(ethylene oxide) PEO/clay/silica nanocomposites via solution intercalation by exploiting phase separation based on the bridging of particles by polymer chains [53]. Figure 8.14 shows the schematics of polymer bridging interactions between aggregates of spherical nanoparticles and between intercalated aggregates of clay nanoparticles. Based on

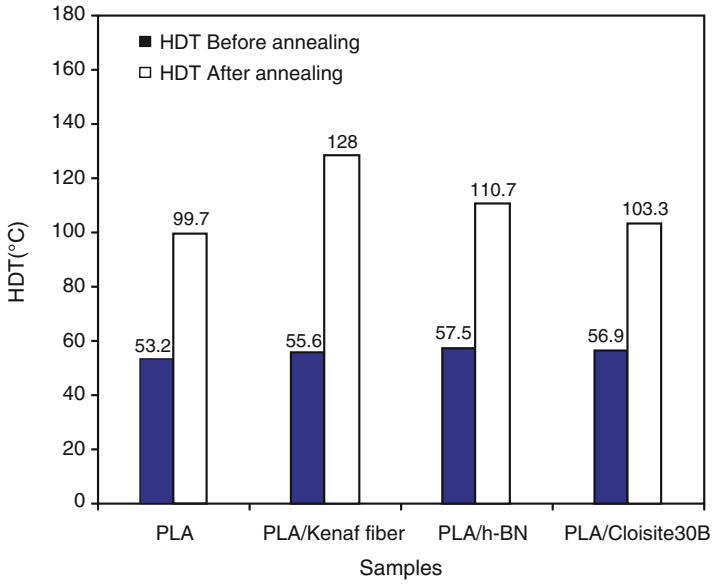

Fig. 8.12 Heat distortion temperature (*HDT*) of various PLA composites both before and after annealing (Reproduced with permission from Ref. [50]. Copyright 2012 Wiley Periodicals, Inc.)

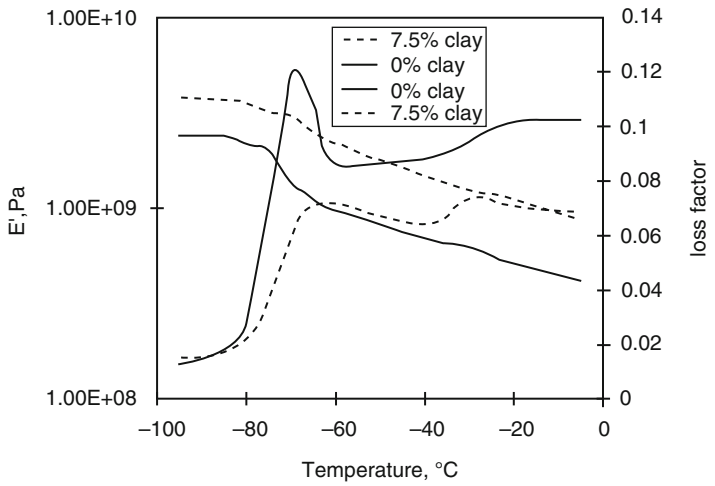

Fig. 8.13 Dynamic mechanical analysis of pure PEO and PEO–clay nanocomposite (Reproduced with permission from Ref. [52]. Copyright 2006 Elsevier Ltd)

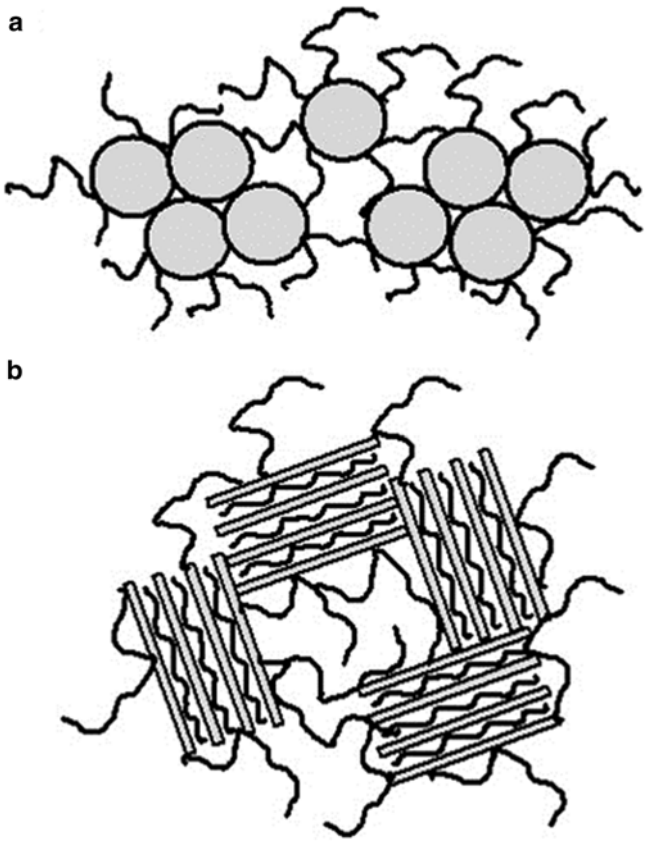

Fig. 8.14 Schematic showing the polymer bridging interactions (**a**) between aggregates of spherical nanoparticles (**b**) between intercalated aggregates of clay nanoparticles (Reproduced with permission from Ref. [53]. Copyright 2011 Elsevier Ltd.)

FT-IR and XRD results, the intercalated morphology of nanocomposites was confirmed. Figure 8.15 shows SEM images of a PEO/clay/silica hybrid containing both 10 wt % clay and 5 wt % silica before any melt crystallization. From SEM images, it was observed that the overall density of particle aggregates in the amorphous region is much higher compared to that inside spherulites. Figure 8.15b shows the formation of a clay–polymer network structure via the edge-to-face aggregation of intercalated clay particles. Based on DMA results, it was shown that the hybrid containing 10 wt % clay and 5 wt % silica has substantially higher storage modulus within the entire temperature range compared to the 15 wt % clay system. It was also reported that in the glass transition region of PEO, tan δ peaks of the nanocomposites are slightly shifted to higher temperatures due to different degrees of PEO/clay and PEO-fumed silica interactions which restrict the mobility of polymer chains. It was also concluded that the higher density of silica aggregates in the amorphous region compared to that inside spherulites and the formation of physical

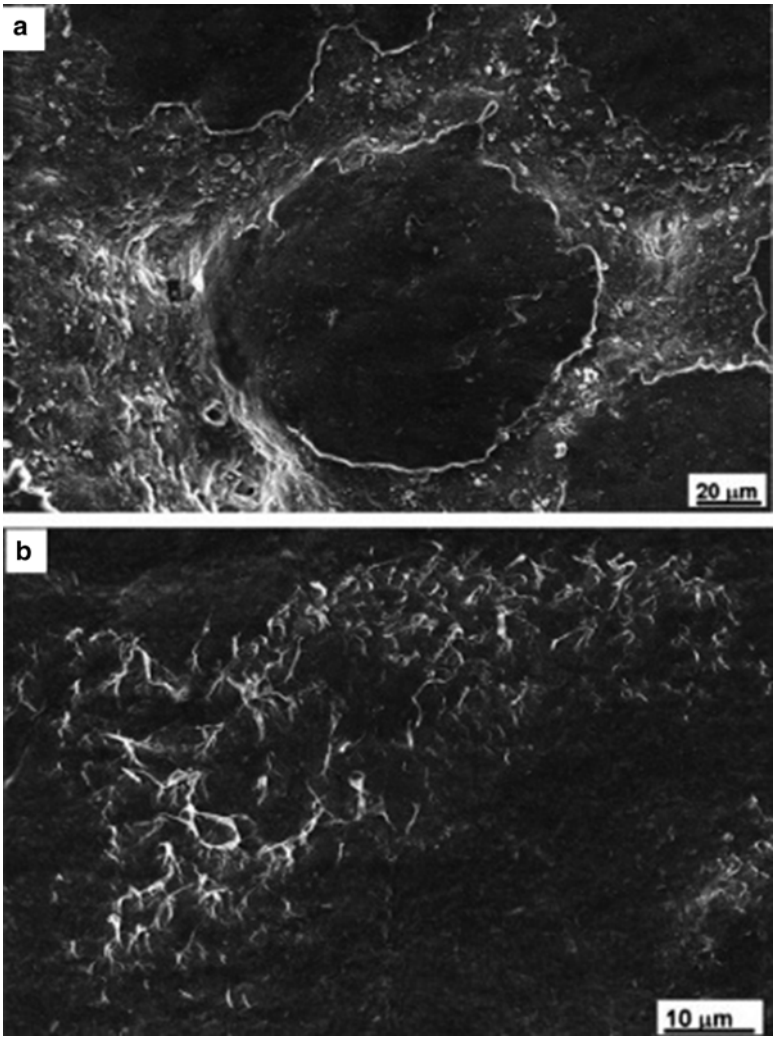

Fig. 8.15 SEM images showing the presence of (**a**) particle aggregates (**b**) edge-to-face aggregation of intercalated clay nanoparticles (Reproduced with permission from Ref. [53]. Copyright 2011 Elsevier Ltd)

cross-link sites by fumed silica via strong H-bonds were shown to be the main reasons for the reinforcement effect in PEO/clay/silica hybrids [53].

Sehaqui et al. assembled polymers such as polyethylene oxide and hydroxyethyl cellulose (HEC) and MMT into hybrid films using water-based filtration process [54]. It was shown that hybrids exhibited storage modulus values above 2 GPa even in severe conditions (300 °C or 94 % relative humidity) despite their high 60–85 wt % MMT content. Based on the DMA data, it was also pointed out that at the end of the DMA test, the PEO hybrid containing 80 wt % MMT did not show any sign of

thermal degradation such as discoloration since its degradation temperature is above 300 °C [54]. Marras et al. prepared poly(e-caprolactone) (PCL) and organically modified MMT by using the solution intercalation technique, and fibrous membranes of pure and nanocomposite PCLs were fabricated via electrospinning [55]. Authors investigated the effect of the applied voltage, solution concentration, and the clay content on the morphology, thermal, and thermomechanical properties of fibrous PCL nanocomposites. In agreement with tensile test results, the storage modulus of the nanocomposites showed much higher values than that of the pure polymer over the entire temperature range. This result was attributed to the fact that organo-modified clay with high aspect ratio was well dispersed due to good polymer–particle interactions within the PCL matrix. Tan δ peaks were also reported to shift slightly to lower temperatures in the glass transition region due to the fact that segmental motions of the intercalated PCL matrix were manipulated by organo-modified nanoclays [55]. Li et al. used in situ polymerization to prepare polyethylene terephthalate (PET) nanocomposites containing ethoquad-modified montmorillonite (eMMT), unmodified hectorite (HCT), or phenyl hectorite (phHCT) in order to study the effect of clay surface properties and loading on thermal, mechanical, and gas barrier properties [56]. On the basis of DMA results, it was shown that for thermally quenched eMMT, nanocomposites had much higher storage modulus values around T_g compared to pure PET, HCT, and phHCT nanocomposites. Thus, this result supports the fact that eMMT acts as a reinforcement agent in thermally quenched eMMT nanocomposites, and eMMT has strong and favorable interactions with PET. Moreover, tan δ peaks or T_g did not show any clear pattern in their shifts as a function of clay loading for any PET nanocomposite [56].

Zengeni et al. investigated the influence of clay size (MMT and laponite) and type of organic modifier (cetyltrimethylammonium bromide (CTAB) and a reactive modifier (vinylbenzyldodecyldimethylammonium chloride (VBDAC)) on highly filled hybrid latex morphology and physical properties of polystyrene/clay nanocomposites [58]. TEM and small-angle X-ray scattering (SAXS) results showed that the degree of clay exfoliation was strongly affected by the reactivity of clay modifier but not by the clay size. Based on DMA results, it was shown that all PS nanocomposites had much higher storage modulus values compared to the neat polymer, independent of the clay or the modifier used, especially in the rubbery region. This result is due to polymer–clay interactions which restrict mobility of polymer chains [63, 65]. However, the dependency behavior of storage modulus on clay content was found to be strongly affected by both the clay size and the type of modifier. It was shown that the tan δ peak decreased in intensity and became broader with increasing clay content. This result was also related to the reduced chain mobility due to presence of nanoclay in polymer nanocomposites [58, 64, 65]. It was also mentioned that there is no direct relation between the damping factor and type of clay or modifier that was used in PS nanocomposites [58]. Poreba et al. studied thermal, thermomechanical, tensile, and gas transport properties of aliphatic polycarbonate-based polyurethanes (PCPUs) and their nanocomposites with bentonite for organic systems [59]. Based on temperature modulated differential scanning calorimeter (TMDSC) and DMA results, three

thermal transitions were observed by the authors. The first one was from −30 to −40 °C which corresponds to the glass transition of soft polymer segments. The second transition was located at the temperature region 50–55 °C. The third transition was located above 100 °C and was shown to be responsible for the disruption of highly organized hard segment domains such as the disruption of hydrogen bonds and other physical cross-linking bonds [59].

Spoljaric et al. prepared nanocomposites of poly(vinyl alcohol) (PVA), nanofibrillated cellulose (NFC), and montmorillonite (MMT) clay via solvent casting and compared the properties of poly(acrylic acid) (PAA) cross-linked PVA matrices with those of linear (non-cross-linked) PVA nanocomposites [60]. It was shown that the effect of cross-linking on restricting chain mobility was evident such that the cross-linked films displayed superior storage modulus values compared to non-cross-linked films. Based on the tan δ data, it was reported that the addition of 10 wt % nanoclay increased T_g to 67 °C, and a maximum T_g value of 82 °C was obtained for PVA–NFC nanocomposite containing 50 wt % nanoclay. The cross-linked nanocomposites displayed T_g values ranging from 69 °C for the sample containing no clay up to 84 °C for the sample containing 50 wt % nanoclay. The moduli of both cross-linked and non-cross-linked PVA films as a function of relative humidity (RH) are displayed in Fig. 8.16. It is clearly seen that the storage moduli gradually increase in value and become constant during the initial 0 % RH period. It was also discussed that as RH goes up to 50 %, the storage modulus decreases sharply due to disruption of intermolecular secondary bonds or plasticization of the polymer matrix by water molecules [60].

Qian et al. prepared polyurethane (PU)/organo-modified vermiculite (OVMT) nanocomposites with good clay dispersion by using in situ intercalative polymerization [62]. In the study, PUs were synthesized starting from a polyol–OVMT dispersion, and this conventional environmentally friendly process was shown to be well suited for both thermoplastic and thermoset elastomers. It was shown that the hydroxyl groups and tertiary amine sites on the surface of OVMT improved interactions between clay particles and the polyol. Based on XRD and FT-IR data, it was

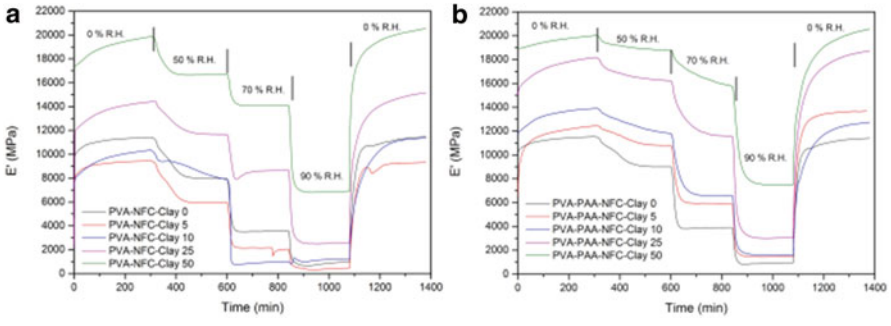

Fig. 8.16 Humidity-step storage modulus curves; (**a**) PVA–NFC–clay nanocomposites, (**b**) PVA–PAA–NFC–clay nanocomposites (Reproduced with permission from Ref. [60]. Copyright 2013 Society of Plastics Engineers)

reported that the industrially friendly in situ intercalative polymerization method produced high degrees of intercalation/exfoliation of OVMT within the PU matrix. According to DMA results, the storage modulus was increased by greater than 150 % with 2.7 wt % addition of catalyst VMT and by greater than 170 % with 5.3 wt % clay loading compared to that of neat PU [62].

In a previous report, Alonso et al. [63] reported the preparation of a series of Nafion/H^+ MMT nanocomposite membranes by using the solution casting method.

Nafion was dissolved in water or low aliphatic alcohols and the dispersion of H^+ MMT in water with Nafion solutions were mixed in an ultrasonic bath for 2 h followed by overnight stirring at room temperature. It was reported that the membranes casted from water led to better clay dispersion and exhibited much lower methanol permeability with increasing clay content compared to samples casted from alcohol [63]. Burgaz et al. also reported the synthesis of Nafion–Na^+ MMT hybrid membranes with a unique morphology using the depletion aggregation of suspended particles [65]. It was shown that a gel was formed by mixing certain concentrations of Nafion solution with clay suspensions. Using cryo-TEM (Fig. 8.17), they showed that clay particles in Nafion hybrid gels formed a network structure with an average cell size of 500 nm. After casting these hybrid gels, authors also performed DMA tests on solid hybrid Nafion–clay membranes. Figure 8.18 shows the DMA of Nafion and Nafion–clay hybrid membranes.

It is clearly seen that the hybrid membranes showed two different relaxations between 75 and 250 °C. The first weak relaxation appears at 75 and 120 °C for the nanocomposites. A much stronger second relaxation appears around 230 °C for all the nanocomposites. It was previously reported that the Na^+ form of Nafion shows a stronger relaxation at 240 °C and a weaker relaxation at around 150 °C [67]. Authors also discussed that a partial ion exchange reaction between the Nafion and the Na^+MMT leading to the formation of Na^+ form of Nafion could be the reason for the shift to higher temperatures. Based on the storage modulus data, it was observed that the sample containing 23 wt % clay showed a storage modulus about ten times that of Nafion.

The overall DMA analysis revealed that Nafion/clay membranes are much stiffer and can withstand higher temperatures compared to pure Nafion. It was also concluded that these enhanced properties are highly desirable for using these Nafion/clay hybrid membranes in fuel cell applications [65].

Liff et al. prepared biomedical polyetherurethane/laponite nanocomposite films by controlled evaporation of PU/laponite solution [18]. It was reported that TEM images of nanocomposites containing 4, 10, and 20 wt % laponite exhibited fully exfoliated, uniformly dispersed, and randomly oriented laponite platelets within the polyurethane matrix. Based on DMA results, before the onset of the soft segment T_g, increasing the laponite wt % in the nanocomposites did not significantly change the flexural storage modulus. However, above this temperature, it was shown that the magnitude of storage modulus increases significantly with laponite concentration. Based on heat distortion temperature measurements, authors stated that pure polyurethane showed little resistance to heat distortion, deformed a great amount with increasing temperature, and reached its maximum extension at 95 °C. On the

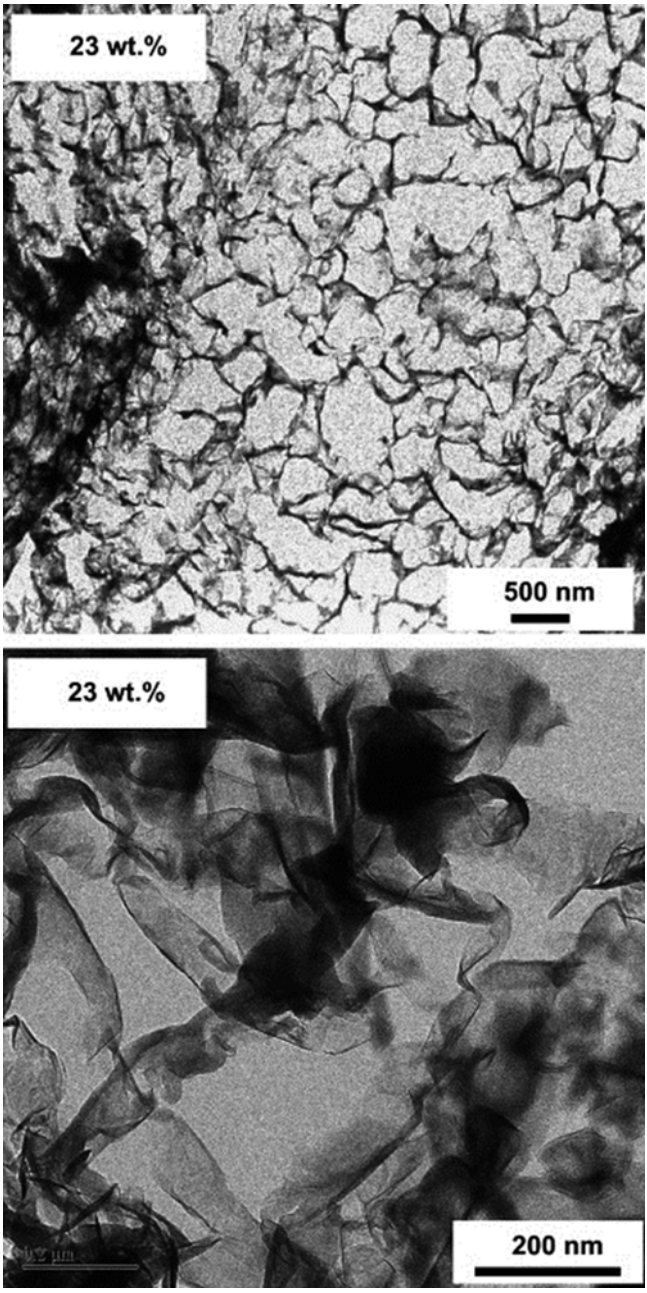

Fig. 8.17 Cryo-TEM of Nafion–clay hybrid gels before any drying (Reproduced with permission from Ref. [65]. Copyright 2009 Elsevier Ltd.)

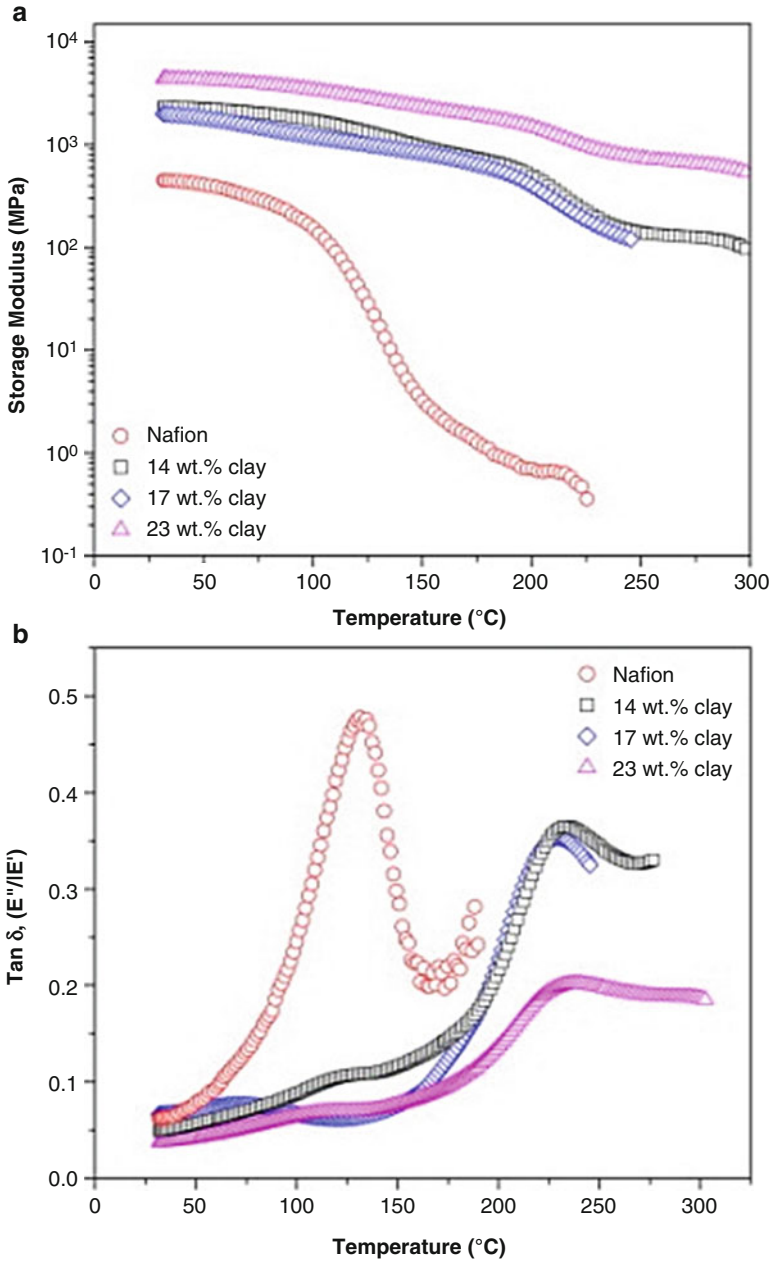

Fig. 8.18 DMA of Nafion and Nafion–clay hybrid membranes: (**a**) Storage modulus and (**b**) tan δ as a function of temperature (Reproduced with permission from Ref. [65]. Copyright 2009 Elsevier Ltd)

other hand, the nanocomposite containing 20 wt % laponite was shown to resist heat distortion and did not visually exhibit any deformation on heating [18].

8.2.2 Graphene or Graphite-Based Polymer Nanocomposites

Graphene or graphite nanoplatelets have been used as one of the most important nanofillers in thermomechanical studies of polymer nanocomposites in recent years [2, 68–72]. In terms of geometry, graphene is a two-dimensional single atomic layer of graphite containing sp^2-hybridized carbon atoms arranged in a honeycomb structure. Like graphite, graphene is an allotrope of carbon. Graphene has been used as a nanofiller in polymer nanocomposites due to its following unique properties: (1) a basal plane with elastic modulus of 1 TPa, (2) an electric conductivity of 10^6 Scm^{-1}, (3) a carrier mobility of 200,000 $cm^2V^{-1}s^{-1}$, (4) a thermal conductivity of 5000 $Wm^{-1}K^{-1}$, (5) a large specific surface area of 2600 m^2g^{-1}, and (6) a low thermal expansion coefficient of -1.2×10^{-6} K^{-1} [73–75]. These improvements in properties can be fully realized when graphene sheets are exfoliated as single isolated layers and well dispersed in the polymer matrix. Graphene can be produced from graphite which is a very cheap and easily found material because graphite is composed of layers of graphene sheets that are stacked on top of each other, and these graphene layers can be separated by using specific techniques [76]. The thickness of graphene nanoplatelets can be given as in the range of 3–100 nm [77]. Thus, because of these reasons, graphene or graphite nanoplatelets have been widely used as nanofillers in studies of polymer nanocomposites. In thermomechanical studies of polymer–graphene nanocomposites, graphene or graphite nanoplatelets (GNPs) have been used in polymer matrices such as epoxy [78–81], poly(methyl methacrylate) [82], polystyrene [83], polyurethanes [74, 84], and poly(D,L-lactic-co-glycolic acid) [85].

Zhang et al. prepared epoxy/magnetic graphene nanocomposites containing graphene nanosheets coated with iron core–iron oxide shell nanoparticles and compared these magnetic nanocomposites with the epoxy containing pure graphene [78]. Based on DMA results, the values of storage modulus for pure epoxy and epoxy nanocomposites with the same content of graphene were observed approximately same both in the glassy and the rubbery plateau. However, the loss modulus was observed to be higher in epoxy/magnetic graphene nanocomposites which was attributed to the interfacial friction between the nanoparticles and the epoxy resin [86]. It was reported that both storage and loss modulus of epoxy nanocomposites became lower compared to those of pure epoxy as temperature was increased to the glass transition temperature region. Thus, this decreased storage modulus was explained such that graphene nanoparticles obstructed the formation of highly cross-linked molecular structure of epoxy [87]. The reduced loss modulus was also attributed to free volume increase between the graphene nanoplatelets and epoxy [88, 89]. It was also shown from tan δ results that compared with pure epoxy, the peak of tan δ of epoxy nanocomposites was shifted to lower temperature due to the enlarged free volume between the epoxy chains and graphene nanoplatelets [78].

Li et al. studied the nanoscopic morphologies, thermomechanical, mechanical, and electrical properties of graphite nanoplatelet (GNP)/epoxy nanocomposites after UV/O_3 treatment of graphite [79]. Well-dispersed GNPs with good amount of exfoliation in epoxy nanocomposites were prepared by using the graphite intercalation and surface modification methods and solvent-assisted ultrasonication. Figure 8.19 shows the DMA results of storage modulus and T_g values obtained from the peaks of loss modulus as a function of UV/O_3 exposure duration. It is clearly seen that increasing the exposure time increased both the Tg and storage modulus. The mobility of epoxy chains was diminished near the surface of GNPs due to enhanced interfacial adhesion and stiffening effect of the interphase material [79]. In a previous study [90], it was shown that UV/O_3 treatment led to the formation of hydroxyl and carboxyl groups on the graphite surface, and these functional groups enhanced the interfacial adhesion via chemical reactions between these functional groups and epoxide function groups of epoxy. Patsidis et al. prepared exfoliated GNP/epoxy resin nanocomposites and analyzed their morphology and thermomechanical properties as a function of different filler content [80]. Based on DMA results, it was shown that storage modulus increased with increasing filler content. Epoxy nanocomposites had higher storage modulus values compared to pure epoxy from ambient temperature up to 100 °C. It was also reported that the height of tan δ peak decreased with the addition of GNP, and the elastic behavior of epoxy nanocomposites was enhanced [80]. The effect of graphene nanoplatelets thickness and lateral size on the morphology and behavior of epoxy composites were studied by Prolongo et al. [81]. Based on the findings of that study, it was revealed that small graphene platelets were more able to make aggregations compared to bigger ones. The glass transition temperature, thermal stability, and stiffness of epoxy nanocomposites increased with the addition of graphene nanoplatelets compared to pure epoxy. It was also concluded that nanocomposites containing larger and thicker nanoplatelets displayed lower T_g, higher storage modulus, and higher decomposition temperature [81].

Potts et al. prepared nanocomposites of PMMA with graphene oxide (G-O) and reduced graphene oxide (RG-O) using in situ polymerization method and processed

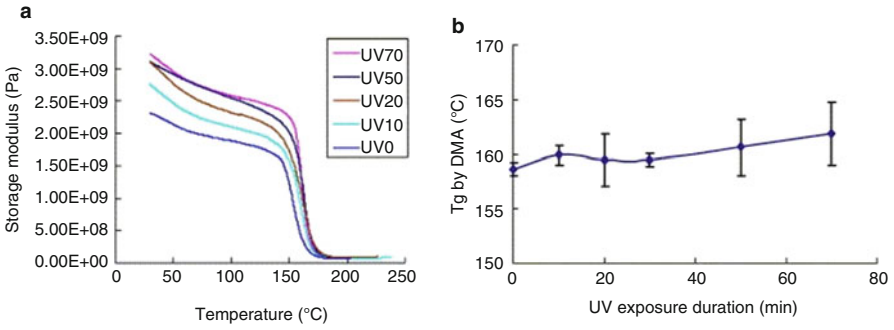

Fig. 8.19 Effect of UV exposure duration on (**a**) storage modulus and (**b**) glass transition temperature. (Reproduced with permission from Ref. [79]. Copyright 2007 Elsevier Ltd)

the nanocomposites by using injection molding or hot pressing [82]. Results from DMA experiments showed that T_g of the nanocomposites increased substantially compared to pure PMMA. The storage modulus of nanocomposites also increased compared to that of PMMA. It was also shown that RG-O/PMMA nanocomposites exhibited a T_g increase of more than 15 °C at 0.05 wt % nanoplatelet loading. Moreover, the reason behind this T_g increase was explained to be caused by the interphase polymer which was formed due to the interactions of polymer chains with the surface of platelets [82]. Hazarika et al. prepared sulfonated polystyrene (SPS)/graphene (GP) nanocomposites containing of 1-nm-thick GP nanosheets by solution blending of exfoliated graphene oxide (GAO) with SPS [83]. Based on X-ray diffraction, Raman spectroscopy and atomic force microscopy results, it was clearly proved that a single layer of 1-nm-thick and 170-nm-long GP nanosheets were synthesized in the presence of SPS nanospheres. It was also shown that spherical SPS particles were adsorbed on graphene nanosheets due to strong interactions between the $-SO_3H$ functionality of SPS and functional group of GAO. Based on DMA results, it was reported that the storage modulus of SPS/GP nanocomposites increased with increasing GP content. Approximately, 90 % increase in mechanical strength was observed with the addition of 7 % GP to SPS. Besides this, authors also observed about 143 % increase of storage modulus at 90 °C which is very close to T_g of the system under study [83]. In another study, nanocomposites of thermoplastic polyurethane (TPU) and ultrathin graphite (UTG) with concentrations ranging from 0.5 to 3 wt % were prepared using a solution compounding strategy. It was shown that storage modulus and shear viscosity of TPU nanocomposites were improved by 300 % and 150 %, respectively, compared to pure TPU with the addition of 3 wt % of UTG [84].

Yoon et al. studied nanocomposite nanofibers of poly(D, L-lactic-co-glycolic acid) (PLGA)/graphene oxide (GO) nanosheets [85]. It was reported that the clear improvement of storage and loss moduli of PLGA nanocomposite nanofibers containing 2 wt % of GO nanosheets was caused by enhanced chemical bonding between the oxygenated functional groups of GO nanosheets. Figure 8.20 shows the thermo-

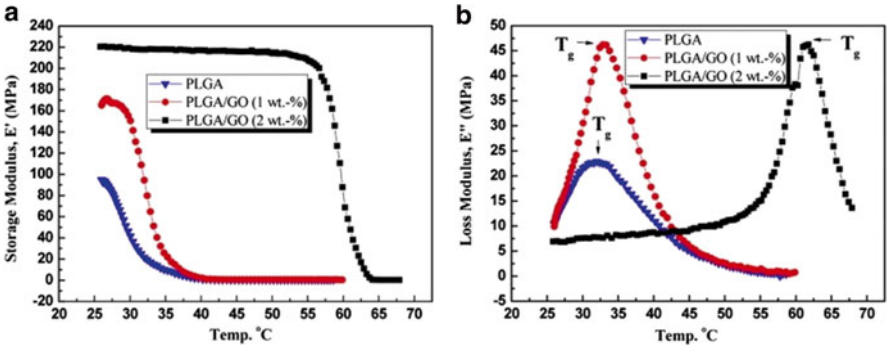

Fig. 8.20 DMA (**a**) storage modulus and (**b**) loss modulus of PLGA and PLGA–GO nanocomposites (Reproduced with permission from Ref. [85]. Copyright 2011 Elsevier Ltd)

mechanical properties of nanocomposite nanofibers measured by DMA by performing temperature sweep experiments at a frequency of 10 Hz. It was reported that the storage modulus at 37 °C increased from 4.1 MPa for pure PLGA and 8.2 MPa for PLGA containing 1 wt % of GO to 217.8 MPa for PLGA containing 2 wt % of GO. It is clearly seen from the loss modulus plot that the T_g of PLGA containing 2 wt % of GO in the rubbery plateau significantly increased to 66.7 °C compared to the values of 32 and 33 °C for pure PLGA and PLGA containing 1 wt % of GO, respectively. It was explained that this huge increase of the T_g in PLGA containing 2 wt % of GO was caused by strong interfacial interactions and chemical bonding between PLGA and GO nanosheets in PLGA nanocomposite nanofibers. Enhanced hydrophilicity of nanocomposite nanofibers caused by embedded GO nanosheets provided good biocompatibility to PLGA bionanocomposite fibers and for this reason, these materials can be used as scaffolds in biomedical applications [85].

8.3 Polymer Nanocomposites Containing Nanospheres

Nanospheres such as silica, POSS, alumina, magnetite, TiO_2, silver, aluminum nitride, Fe_2O_3, and ZnO have been used in diverse polymer matrices such as epoxy resins, polyurethanes, polyesters, poly(ethylene oxide), polyolefins, polystyrene, polyamide, polyimide, polylactide, polysulfone, etc., for thermomechanical property analysis of polymer nanocomposites. In the literature, nanosilica and POSS have been the most widely studied nanospheres both in academia and industry since these nanospheres remarkably have improved abrasion and thermal expansion resistance, dimensional and thermal stability, flame retardancy, stiffness, electrical and thermal conductivity, impact toughness, and thermomechanical properties of polymer nanocomposites at low nanosphere contents [91–96]. The improvement of properties depends on how well silica and POSS are dispersed within the polymer matrix. Usually, thermomechanical properties improve if nanosilica or POSS is surface modified with surface functional groups that are physicochemically compatible with the polymer matrix. And the compatibility between the polymer matrix and nanospheres is ultimately affected by interactions between the surface of nanospheres and polymer matrix and synthesis methods.

8.3.1 Silica-Based Polymer Nanocomposites

Hydrophilic, hydrophobic, and mesoporous nanosilica [97, 98], surface-modified nanosilica with low molecular weight polymers or oligomers [99], and nanosilica prepared via sol–gel methods [100] have been mainly used as nanofillers with different surface properties in thermomechanical studies of polymer nanocomposites. In terms of geometry, nanosilica is a spherical nanofiller with a diameter of 5–50 nm. Among silica nanospheres, fumed silica has been extensively used both

in industry and academia as an active filler for the property improvement of elastomers, as an additive in rheological studies of fluids and as a free flow agent in powders [101]. Fumed silica nanospheres have very high surface area of 50–600 m^2/g and very high Young's modulus on the order of 71.7 GPa, compressive strength greater than 1.1 GPa, and tensile strength of 48.3 MPa and a very low density on the order of 0.19 g/cm^3 [101]. Thus, because of these reasons, nanosilica has been widely used as a nanofiller in improving thermomechanical properties of polymer nanocomposites.

Pristine and surface-modified nanosilicas have been used in epoxy [37, 102], polystyrene [103–106], poly(lactic acid) [49, 107–109], poly(methyl methacrylate) [110], polyamides [91], poly(ethylene oxide) [53], polycarbonate [94], poly(vinyl alcohol) [92], poly(ether ether ketone) [111], polyurethanes [112], poly(e-caprolactone) [113], polysulfone [114] poly(butylene adipate-terephthalate) [107], and poly(2-vinylpyridine) [115, 116] for thermomechanical studies of polymer–silica nanocomposites.

The effect of the filler size, filler loading, and dispersion conditions on the glass transition and relaxation behavior of epoxy nanocomposites were investigated via DMA, DSC, and dielectric relaxation spectroscopy by Sun et al. [102]. The storage and loss modulus of epoxy composites and pure epoxy are shown in Fig. 8.21. Based on DMA results, it is clearly seen that the nanocomposite containing 20 wt % nanosilica showed a T_g depression in comparison with pure epoxy and epoxy containing 20 wt % micron-sized silica. It was discussed that the T_g depression in epoxy nanocomposites was related to the enhanced polymer dynamics due to the extra free volume at the epoxy–nanofiller interface [102]. Shabana et al. used the asymptotic homogenization method (AHM) based on finite element analysis (FEA) to investi-

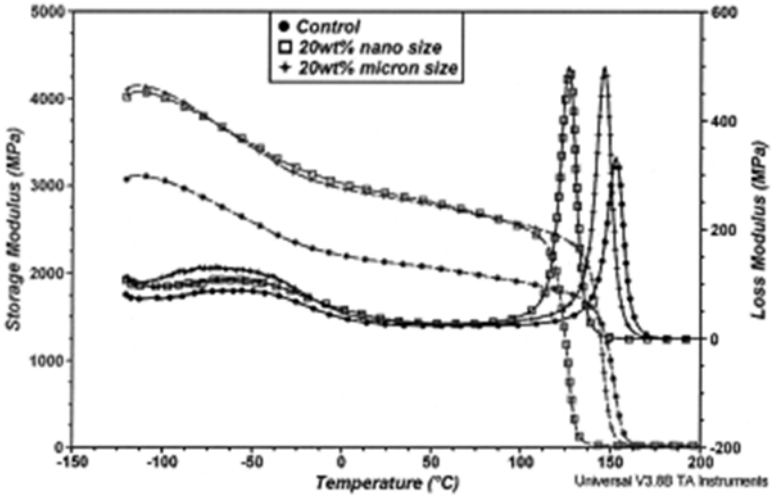

Fig. 8.21 Dynamic moduli of the silica composites and the blank resin (Reproduced with permission from Ref. [102]. Copyright 2004 Wiley Periodicals, Inc.)

gate the effects (nanoparticle weight fraction, material type, distribution, and shape) of adding silica, rubber, and clay nanofillers to the epoxy matrix on thermomechanical properties [37]. Numerical results obtained from AHM modeling were in very good agreement with experimental data for elastic modulus and thermal expansion coefficient. Authors concluded that the AHM modeling technique can be effectively used in the structure–property analysis of polymer nanocomposites containing at least two different nanofillers [37]. Kontou et al. prepared polystyrene (PS) nanocomposites containing fumed nanosilica surface modified with dimethyldichlorosilane by using melt mixing and compression molding, and they investigated the viscoelastic and structure–thermomechanical properties of PS nanocomposites as a function of nanosilica addition (from 4 to 10 wt %) [104]. Based on the results of SEM, DSC, DMA, and tensile testing, the PS nanocomposite containing 4 wt % fumed silica was found to be the best material for the enhancement of the thermomechanical properties [104]. Bansal et al. [106] prepared PS/silica nanocomposites with surface-untreated silica and PS-end-grafted silica and studied the changes in T_g with increasing nanosilica content in a polymer nanocomposite. They found out that for untreated silica surfaces, the T_g changes with nanosilica content like in planar free-standing films. On the other hand, for modified silica surfaces, it was also reported that the T_g changes like in capped surfaces with increasing nanosilica content [106]. Nataran et al. prepared PS nanocomposites containing bimodal and monomodal silica particles with grafted PS brushes [103]. They dispersed bimodal and monomodal particles in the high molecular weight matrix in order to examine the role of the individual PS brush on dispersion and to examine the role of nanosilica dispersion on thermomechanical properties at various silica loadings. They also prepared bimodal particles of the two different grafting densities that were in a polymer matrix of higher molecular weight in order to study the role of entanglement. Based on DMA results, it was shown that the enhancement in mechanical properties of glassy state upon the addition of bimodal particles was greater than that of adding monomodal particles for each grafting density. In agreement with experiments, it was concluded that combining a long entangling brush and a short screening brush leads to excellent nanofiller dispersion and has a great advantage over individual brushes in homopolymer systems [103].

The effect of using nanosilica particles and micro-sized wood-flour on the thermal, mechanical, thermomechanical, and rheological behavior of a blend of poly(butylene adipate-terephthalate) (PBAT) copolyester, and polylactide (PLA) was studied by Georgiopoulos et al. [107]. Based on SEM results, a narrow particle size distribution was observed with larger agglomerates of 300–400 nm coexisting with smaller particles on the order of 20 nm. The better distribution of silica nanoparticles in the matrix was explained such that blending of PBAT with PLA made the matrix much more compatible with silica nanoparticles due to lower interfacial tension and polar interactions between the PBAT and the filler. Based on DMA results, the reinforcing effect of all filler types was observed, and increasing the filler concentration resulted in the increase of loss modulus peak. The T_g shifted to higher temperatures due to the filler addition, and this was attributed to the immobilization of polymer chains near the surface of fillers [107]. Wen et al. prepared

poly(L-lactide) nanocomposites containing 1, 3, 5, 7, and 10 wt % hydrophilic pyrogenic silica nanoparticles by melt compounding in a melt mixer and investigated the phase morphology, thermomechanical properties, and optical transparency in comparison with pure PLA [109]. Hydrogen-bonding interactions between C=O functional groups of PLA and Si−OH groups of silica was observed via Fourier transform infrared analysis by the authors. Based on DMA results, below T_g, all of nanocomposites had higher storage modulus values compared to pure PLA. Figure 8.22 shows the tan δ of PLA nanocomposites and pure PLA as a function of temperature. It is clearly seen from the data that the T_g is shifted to higher temperatures up to the addition of 5 wt % silica and then it decreases with further silica addition [109].

Transparent sol–gel-derived organic–inorganic nanocomposite thin films were prepared by in situ incorporation of a silica network into poly(trimethylhexamethylene terephthalamide) using the solution casting method by Sarwar et al. [91]. It was shown that increasing the silica network structure increases the storage modulus. However, when the concentration of silica increases beyond 10 wt % silica addition, the network in the polyamide matrix formed agglomerated structure leading to a decrease in the storage modulus. Incorporation of the silica network shifted the tan δ peaks to higher temperatures leading to an increase in T_g, also the intensity of tan δ peaks decreased and the peaks became broader with higher amounts of silica addition to the polymer matrix [91]. Zhang et al. prepared poly(methyl methacrylate) (PMMA) nanocomposites containing mesoporous forms of silica (MS) with different framework structures and pore sizes, including hexagonal MCM-41 (2.4 nm), cubic MCM-48 (1.9 nm), hexagonal SBA-15 (7.0 nm), and mesocellular silica foam (MSU-F) (24.8 nm) by using in situ emulsion polymerization and compression molding [110]. Based on DMA and TGA results, it was observed that all of the composites containing 5 wt % MS exhibited improved thermal stability, an increase of T_g, and storage modulus compared to pure PMMA. Among different MS particles used in the study, MSU-F silica with the largest framework pore size led to the best

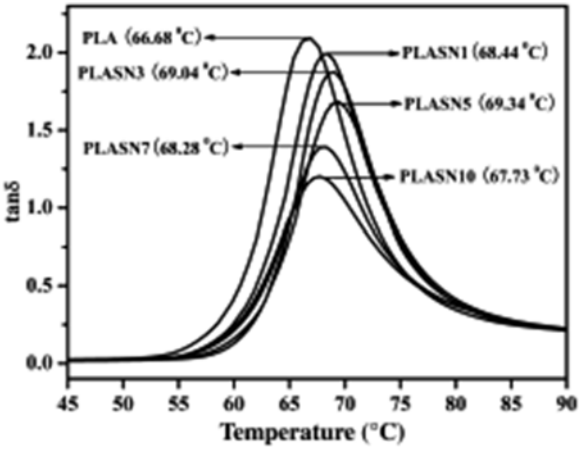

Fig. 8.22 Effect of the SiO2 concentration on the tan δ of the PLASNs (Reproduced with permission from Ref. [109]. Copyright 2009 Wiley Periodicals, Inc.)

improvement in thermomechanical properties. The authors attributed this result to the confinement of polymer chains in large pore channels with a 3D structure [110]. Chrissafis et al. prepared various bionanocomposites via solution casting by dispersing fumed silica nanoparticles in biocompatible polymers such as poly(vinyl pyrrolidone) (PVP), chitosan (Chi), or poly(vinyl alcohol) (PVA) [92]. Based on SEM experiments, a fine dispersion of silica nanoparticles was observed in all three polymer matrices. This well dispersion of nanosilica was further supported by the observation of sufficient interactions between PMMA and the surface hydroxyl groups of silica from FTIR measurements. Finally, DMA tests revealed that for Chi/silica and PVA/silica nanocomposites, the glass transition temperature observed in tan δ curves shifted to higher values with silica addition due to the mobility decrease of PMMA chains in the silica/PMMA interphase [92]. Nanocomposites of polycarbonate (PC) filled with untreated and modified silica nanoparticles were melt mixed and injection molded, and the effects of modified silica and low-temperature melting on the morphology, mechanical property, and thermostability of composites were investigated by Feng et al. [94]. Based on SEM, uniform dispersion of silica agglomerates in the PC matrix was formed by low-temperature melt blending. Based on DMA analysis, the storage modulus of composites with modified silica increased more obviously as a function of silica addition compared to that of composites containing untreated silica, however, the T_g values of PC nanocomposites did not exhibit any considerable change. In addition, TGA results indicated that the incorporation of modified silica into PC matrix showed a more significant improvement compared to pure PC and PC/modified silica nanocomposites at low silica content [94]. The nano-sized silica fillers (both untreated and modified) reinforced poly(ether ether ketone) (PEEK) composites and were fabricated by using the compression molding technique by Lai et al. [111]. Based on SEM and TEM analysis, the modified nanosilica was observed to disperse more uniformly compared to the untreated silica. In addition, XRD results showed that the peaks of PEEK/modified silica composites shifted toward higher 2θ values with silica addition, indicating smaller *d*-spacing of the PEEK crystallites. Based on TMA analysis, the coefficient of thermal expansion (CTE) decreased when the content of the nanosilica increased. Furthermore, PEEK/modified silica nanocomposites showed higher CTE values compared to nanocomposites containing untreated silica. DMA results showed that the storage modulus values of PEEK/modified silica nanocomposites were slightly higher than those of the unmodified counterparts suggesting better dispersion of nanosilica within the PEEK matrix. The PEEK/modified silica nanocomposite showed a lower thermal decomposition temperature compared to the composite filled with untreated silica due to the presence of stearic acid on the modified silica [111].

Neikirk et al. investigated the effects of specific hydrogen-bonding interactions between surface-functionalized silica nanoparticles and ureidopyrimidinone (UPy)-based hydrogen-bonded supramolecular poly(e-caprolactone) in a supramolecular polymer nanocomposite [113]. Based on DMA analysis, it was observed that increasing the extent of UPy surface functionality on the modified nanosilica at a constant nanoparticle content led to a decrease in storage modulus relative to nanocomposites filled with surface-untreated silica nanoparticles. However, TEM inves-

tigation of the nanocomposites filled with modified nanosilica showed an increase in nanoparticle aggregation which provided an explanation for the storage modulus reduction [113]. Recently, Brillouin light scattering (BLS) was successfully used to investigate the influence of processing conditions such as the type of casting solvent and thermal annealing on the thermomechanical properties of bulk poly(2-vinylpyridine) (P2VP)/silica nanoparticles (NPs) nanocomposite films by Zhao et al. [115]. Based on BLS results, it was shown that the P2VP chains are displaced away from the particle surface in solution due to the strong interactions between the solvent and the particle if pyridine (PYR) was used as the casting solvent. On the other hand, if methyl ethyl ketone (MEK) was used as the casting solvent, it was found that the silica surface was covered with a P2VP layer, and for this reason, NPs were bridged at higher particle loadings. Finally, in agreement with DSC results, the T_g measured by BLS was slightly increased for nanocomposites containing 45 wt % nanosilica compared to pure P2VP [115].

8.3.2 POSS-Based Polymer Nanocomposites

In thermomechanical studies of POSS-based polymer nanocomposites, diol, epoxide, acrylic, phenyltrisilanol, octaisobutyl, diol functionalized and an incompletely condensed POSS [117–124], monofunctional and difunctional pendant, a closed cage nonpolar octaisobutyl and an open cage polar trisilanolphenyl POSS, methyl, octavinyl, isobutyl, cyclohexyl, styryl, methacrylate, norbornyl and siloxane-POSS, octamethyl-substituted POSS, octa-isobutyl and octaphenyl POSS [20, 125–129] and glycidylethyl, aminopropylisobutyl and poly(ethylene glycol)-POSS, polyaniline, octyl, octadecyl and cyclopentyl-POSS, aminoethyl aminopropyl, octaphenethyl, aminophenyl, octakis(dimethylsiloxypropylglycidyl ether) and diepoxy-functionalized POSS [95, 96, 130–137] have been mainly used as POSS nanofillers in polymer matrices.

Polyhedral oligosilsesquioxanes (POSS) have been categorized under silsesquioxane molecules. Here, silsesquioxanes refer to molecules whose chemical structures are expressed with the composition of $R_nSi_nO_{1.5n}$ [20, 131]. In terms of geometry, POSS belong to a family of isotropic molecules with diameters ranging between 1 and 3 nm which depend on the number of silicon atoms in the central cage and the peripheral substitution R groups surrounding the core [138]. For example, a cubic silsesquioxane with a cubic core of Si_8O_{12} surrounded by eight substitution groups has the spherical geometry with a diameter of 1.5 nm when R is a cyclopentyl group (Fig. 8.23). One of the R groups on corners of POSS can be efficiently exchanged with a polymerizable functional group X by using various synthesis techniques. Due to this capability of POSS, it has been possible to chemically connect POSS units into polymer chains via covalent bonds [20, 130, 138]. Thus, POSS can be classified both as a spherical nanofiller and a bulky spherical functional group that can go through polymerization reactions. Thus, because of these reasons, POSS have been widely used both as nano-

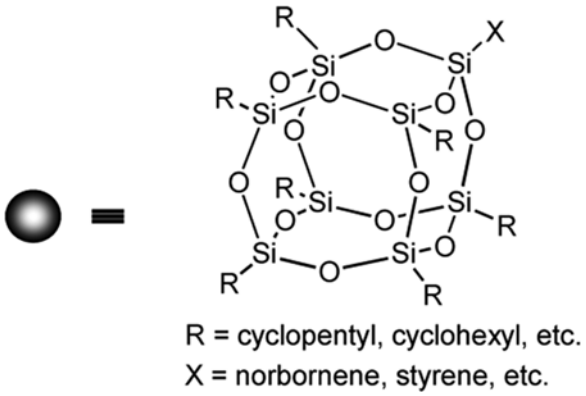

Fig. 8.23 Structure of cubic silsesquioxanes (POSS) (Reproduced with permission from Ref. [138]. Copyright 2004 American Chemical Society)

fillers and constituent units of polymers in improving thermomechanical properties of polymer nanocomposites.

In thermomechanical studies of polymer–POSS nanocomposites, pristine or surface-modified POSS units have been used in diverse polymer matrices such as epoxy [96, 120, 125, 133, 135, 137, 139], polystyrene [132], poly(lactic acid) [ref131], poly(methyl methacrylate) [119, 129, 132], polyamides [126], polycarbonate [123], polyurethanes [95, 117, 124], polyolefins [121], poly(caprolactone) [122], polysulfone [140], poly(amic acid) [118], polyimides [136], polyoxymethylene [130], and polybenzimidazole [128].

Polyhedral oligosilsesquioxane (POSS)-reinforced thermosets based on octaglycidyl epoxy polyhedral oligosilsesquioxane (OG-POSS) cured with 4,4'-diaminodiphenyl sulfone (DDS) were prepared and studied for their curing, thermomechanical, and morphological properties by Kim et al. [96]. Based on DMA analysis, it was shown that T_g of the cured OG–POSS system shifted to higher temperatures with increasing the amount of DDS as a curing agent, and the storage modulus increased below and above the glass transition temperature. TEM studies showed that the morphology of POSS-reinforced thermosets became more homogeneous as the amount of DDS in the OG–POSS system increased. However, the morphology of OG–POSS system consisted of 8–12-nm POSS-rich aggregates [96]. Selected epoxy-functionalized cube nanocomposites were prepared from octa(aminophenyl)-silsesquioxane (OAPS), poly(aminophenyl)-silsesquioxane (PAPS), octa(dimethylsiloxypropylglycidyl ether)-silsesquioxane (OG), diglycidyl ether of bisphenol A (DGEBA), and diaminodiphenylmethane (DDM) by Choi et al. [137]. Based on TGA analysis, char yields and decomposition temperatures increased with tethers having aromatic components. TGA results also suggested that cubes effectively improved network thermal stabilities. Based on DMA analysis, it was revealed that aromatic tether structure, short lengths, and high cross-link densities reduced tether segmental relaxation motions, stiffened the network, and minimized macroscopic glass transitions [137]. Epoxy was modified by an incompletely condensed polyhedral oligomeric silsesquioxane (POSS), and the POSS-triol with a maximum content of 30 wt % was incorporated into the epoxy networks by Liu et al. [120]. They

prepared organic–inorganic hybrid composites via in situ polymerization of epoxy monomers in the presence of POSS-triol, which started from the homogeneous solutions of POSS-triol and epoxy monomers. Based on DMA results, it was shown that the phase-separated composites possessed higher T_g's compared to nanocomposites, while nanocomposites displayed higher storage modulus compared to phase-separated composites in the glassy region. TGA results showed that the nanocomposites displayed higher initial thermal decomposition temperatures compared to phase separated morphologies [120].

Kopesky et al. investigated the miscibility of acrylic-POSS and poly(methyl methacrylate) (PMMA) in order to determine the effect of well-dispersed POSS nanoparticles on the thermomechanical properties of PMMA [119]. They made separate blends of two different acrylic-POSS species (unmodified and hydrogenated) with PMMA at volume fractions up to 0.30. Based on DSC and DMA analysis, it was shown that both POSS species had a plasticizing effect on PMMA by lowering the T_g. However, the unmodified acrylic-POSS had better miscibility with PMMA compared to the hydrogenated form of POSS. Based on wide-angle X-ray diffraction (WAXD) and DMA results, diffraction patterns for the blend systems showed the existence of phase separation at POSS volume fractions of 0.20 and higher, but no significant phase separation was observed at POSS volume fractions of 0.10 and lower. Based on the DMA analysis of unmodified acrylic-POSS–PMMA blends, the storage modulus decreased consistently with increasing POSS loadings at room temperature. However, between −80 and 0 °C, the storage modulus increased with more than 0.10 volume fraction addition of POSS species [119]. Tanaka et al. studied the structure–property relationships between eight kinds of octa-substituted aliphatic and aromatic POSS fillers and the thermomechanical properties of the polymer composites using polystyrene, poly(methyl methacrylate), and ethylene-(vinyl acetate) copolymer [132]. Based on TGA and mechanical property results, it was observed that the longer alkyl chains and unsaturated bonds at the side chains in POSS are favorable to improve the thermal stability and the elasticity of polymer matrices. Based on DMA results, it was shown that POSS fillers had a significant effect on the storage modulus. The highest increase was seen with vinyl-POSS even at 5 wt % POSS addition, increasing modulus dramatically by twofold while modulus with phenyl-POSS increased dramatically by 65 %. Overall, the phenyl-POSS was found to be the best nanofiller in terms of improving the thermomechanical properties [132].

Biodegradable poly(L-lactide) (PLLA)/octa-isobutyl POSS nanocomposite was prepared via solution casting method by Qiu et al. [127]. SEM results showed that octa-isobutyl POSS were homogeneously dispersed in the PLLA matrix. Based on DMA results, the PLLA/POSS nanocomposite showed a clear increase of storage modulus compared with that of neat PLLA in the glassy region. On the other hand, the presence of octa-isobutyl POSS did not lead to a significant shift and broadening in the tan δ curves of PLLA/POSS nanocomposites in comparison with pure PLLA [127]. The morphology and thermomechanical properties of polycarbonate (PC)/polyhedral oligomeric silsesquioxane with phenethyl substituent (Ph-POSS) nanocomposites at POSS loadings between 0 % and 15 wt % were studied by Sánchez-Soto et al. [123]. The DSC and DMA results showed that increasing the amount of

POSS nanocages continuously decreased the T_g of nanocomposites. On the other hand, based on TGA results, it was found that the presence of Ph-POSS did not improve significantly the thermal stability of PC nanocomposites. Based on DMA results, it was also revealed that the storage modulus of PC/POSS hybrid composites slightly increased in comparison with pure PC [123]. Turri et al. synthesized a series of linear ionomeric polyurethanes (PUs) incorporating various contents (6–20 %) of a diol functionalized POSS comonomer [117]. Based on XRD results, it was found that POSS structures consisted of self-assembled nanocrystalline domains with dimensions on the order of 20 nm. Dynamic mechanical analysis and rotational rheometry results showed that the reinforcement effect or the increase in storage modulus was mainly observed when longer soft segments (poly(tetramethylene glycol) 2000) were used in the synthesis of PUs [117]. Mya et al. prepared starlike polyurethane (PU) hybrid films containing octafunctional POSS by polyaddition reaction between octakis(dimethylsilyloxy) silsesquioxane isopropenyldimethylbenzyl isocyanate (OS-PDBI) and octakis(dimethylsilyloxy) hydroxypropyl silsesquioxane (HPS), and between OS-PDBI and hexane diol (HD), and studied the effect of incorporation of nanostructured cubic silsesquioxanes(CSSQ) on the macroscopic properties of PU film and their thermomechanical properties. Their TGA and DMA results indicated that the incorporation of octafunctional POSS in PU hybrid film enhanced thermal stability and increased cross-link density [95].

Lee et al. prepared and studied degradable shape memory POSS-initiated polycaprolactone (PCL) telechelic diol networks, utilizing a POSS diol macromer as the difunctional initiator via ring-opening polymerization [122]. It was shown that using POSS diol as a difunctional initiator at varying contents in the POSS/PCL ratio controlled the physical properties of PCL networks. Based on DMA results, it was revealed that higher POSS content (42 wt %) networks exhibited two distinct rubbery plateaus: the first plateau in the region between $T_{g,PCL}$ and $T_{m,POSS}$, which was attributed to crystalline POSS aggregates, and the second plateau at the temperature region greater than $T_{m,POSS}$, which is due to the chemical cross-links in PCL networks. Thus, authors concluded that POSS forms a physical network in addition to the chemical network of the PCL chains leading to a chemical/physical double network in the PCL matrix [122]. Misra et al. prepared octaisobutyl POSS/polypropylene (PP) nanocomposites at varying POSS concentrations via melt blending and investigated the effects of POSS molecular geometry, composition, and concentration on tribological, nanomechanical, surface energy, and bulk properties of the nanocomposites [121]. Based on AFM, SEM, TEM, and spectroscopy results, significant differences in POSS distribution and aggregation were observed in the surface and the bulk. Figure 8.24 shows the schematic representation of bulk versus surface distribution of POSS nanoparticles in PP nanocomposites. Authors explained that the hydrophobic and low surface energy properties of POSS aggregates led their preferential segregation toward the surface of the nanocomposite. Based on DMA results, it was shown that the storage modulus of the nanocomposites increased about 10 % in comparison to that of pure PP in the glassy regime. Furthermore, the incorporation of POSS led to the broadening of the β-transition peak (the characteristic T_g peak) and a small reduction in the calculated transition temperature of PP nanocomposite compared to that of pure PP [121].

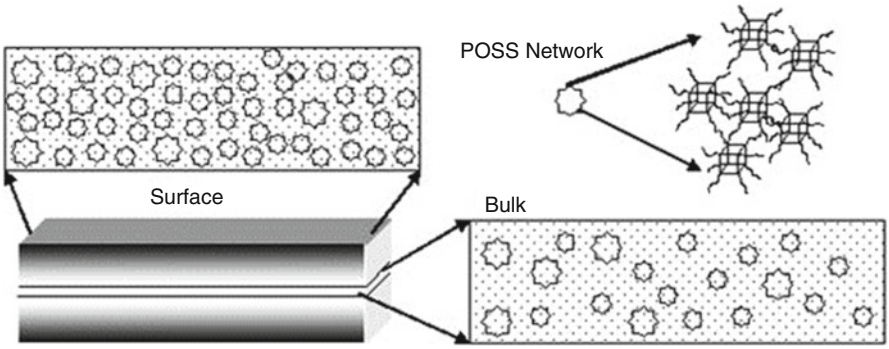

Fig. 8.24 Schematic representation of bulk versus surface distribution of POSS nanoparticles in Oib-POSS/PP nanocomposite (Reproduced with permission from Ref. [121]. Copyright 2007 Wiley Periodicals, Inc.)

Choi et al. prepared imide nanocomposites prepared from octaaminophenyl-silsesquioxane (OAPS) as a model nanobuilding block for rigid, high-temperature hybrid nanocomposite materials [136]. Authors modified tether rigidity, length, and cross-link densities using reactions of OAPS with oxydiphthalic anhydride (ODPA) and diluting with oxydianiline (ODA) in order to control nanocomposite stiffness. FTIR and DMA results of the OAPS/ODPA/ODA nanocomposites suggested that cure temperatures greater than 500 °C are necessary for the optimum imidization. However, increasing only the OAPS loading without curing at high temperatures was stated as an alternative solution for increasing the cross-link density and improving thermomechanical stabilities of organic–inorganic imide nanocomposites [136].

8.4 Polymer Nanocomposites Containing Nanocylinders

Nanocylinders such as carbon nanotubes (CNTs) and carbon nanofibers (CNFs) have been used in diverse polymer matrices such as epoxy and phenolic resins, polyurethanes, polyesters, poly(vinyl chloride), polyolefins, polyamide, polyimide, polysulfone, poly(vinyl alcohol), etc., for thermomechanical property analysis of polymer nanocomposites. In the literature, CNTs have been the most widely studied nanocylinders both in academia and industry due to their high flexibility, low mass density, high aspect ratio, and extraordinary mechanical and electrical properties [141–146]. Nanotubes and nanofibers are similar materials in terms of geometry, but they have a slight difference in terms of the alignment of graphite crystallites within their structure [147]. There are mainly two types of CNTs such as multi-walled carbon nanotubes (MWCNTs) and single-walled carbon nanotubes (SWCNTs). Although CNTs have been widely studied in the literature, CNFs are very important alternative nanocylinders that can be used in the production of polymer nanocomposites since the production costs of CNFs are cheaper compared to

CNTs while their mechanical, electrical, and physical properties are almost same as CNTs. On the other hand, the improvement of properties depends on how well CNTs or CNFs are dispersed within the polymer matrix. Usually, thermomechanical properties improve if CNTs or CNFs are surface modified with surface functional groups that are physicochemically compatible with the polymer matrix. And the compatibility between the polymer matrix and nanocylinders is ultimately affected by interactions between the surface of nanocylinders and polymer matrix and synthesis methods.

8.4.1 Carbon Nanotube-Based Polymer Nanocomposites

For thermomechanical studies of CNT-based polymer nanocomposites, pristine or aminated poly(phenylene sulfide)-functionalized SWCNTs [141, 148], pristine MWCNTs or acyl chloride-grafted, polyoxyethylene octyl phenyl ether, 2-hydroxyethyl triphenyl phosphonium, 1,1,1,3,3,3-hexafluoro-2-phenyl-2--propanol, citric acid, ascorbic acid, carboxylic acid, poly(3-hexylthiophene), amino-terminated linear polypropylene oxide, and aminoethyl aminopropyl POSS-functionalized MWCNTs [133, 143, 145, 146, 149–160] have been mainly used as CNT nanofillers in polymer matrices.

MWCNTs are composed of larger-diameter nanotubes surrounding smaller carbon nanotubes each containing an outer shell with the characteristic rolled graphene structure [147]. In general, carbon nanotubes are composed of graphite structure which is rolled into a cylindrical shape with the diameter of nanometer scale. SWCNTs are composed of a single sheet of graphene rolled perfectly to form a cylinder with a diameter of 1 nm and length of several centimeters [161, 162]. On the other hand, MWCNTs are composed of multiples of nanocylinders formed concentrically and separated by 0.35 nm which is similar to the basal plane separation in graphite [21, 163]. MWCNTs can have diameters from 2 to 100 nm and lengths of tens of microns [21]. Carbon nanotubes in general have remarkable properties. Their densities are very low on the order of 1.3 g/cm^3, and their Young's modulus is much more higher compared to carbon fibers which is more than 1 TPa [164]. In addition, the highest measured strength for a carbon nanotube was around 63 GPa [165]. Thus, because of these reasons, CNTs have been widely used as nanofillers in improving thermomechanical properties of polymer nanocomposites.

Pure or surface-modified CNTs have been used in diverse polymer matrices such as epoxy [133, 143, 149, 151, 153, 166], polyesters [146, 157], poly(methyl methacrylate) [141, 144], polyurethanes [154, 156, 167, 168], polyolefins [150], ethylene-methyl acrylate copolymer [159], polyimides [145, 148, 155, 158], poly(phenylene sulfide) [ref166], and poly(vinyl chloride) [152] for thermomechanical studies of polymer–CNT nanocomposites,

Geng et al. successfully surface-modified CNTs with a nonionic surfactant in order to enhance the dispersion of CNTs in epoxy polymer and analyzed the effects of the dispersion state, surface chemistry, structure, and morphology of CNTs on

thermomechanical, mechanical, and electrical properties of epoxy/CNT nanocomposites [143]. The impact fracture toughness, the flexural strength and modulus, the thermomechanical properties, and the electrical conductivity of the nanocomposites showed significant improvements after the surface treatment of CNTs. Authors explained this finding such that "bridging" effects occurred between CNTs and epoxy due to the hydrophobic and hydrophilic character of the nonionic surfactant. Based on TEM analysis shown in Fig. 8.25, the differences in dispersion state of CNTs before and after surfactant treatment were also clearly shown. It is clearly seen that large agglomerates of CNTs existing in the pristine state significantly disappeared after the surface treatment. Based on the storage modulus and tan δ plots from DMA results, it was shown that the surfactant-treated CNT/epoxy nanocomposites exhibited much higher values of storage modulus and T_g (an increase of about 30 °C) compared to the untreated counterparts for the same CNT content [143].

Chen et al. grafted epoxy-compatible amino-terminated linear polypropylene oxide (A-PPO) molecules of different molecular weight to oxidized multi-walled carbon nanotubes (o-MWCNTs) via ionic bonding and thereby modified the interphase of MWCNT–epoxy nanocomposites [149]. Based on DMA results, both T_g and storage modulus increased steadily with increasing o-MWCNT and 200-MWCNT (with $(PPO)_3$-amine surface grafts) loading. In contrast, T_g and storage modulus decreased in nanocomposites reinforced with 2000-MWCNT (with $(PPO)_{33}$-amine surface grafts). The decrease in the T_g of 2000-MWCNT composites was attributed to the selective surface adsorption. On the other hand, the observed increase in T_g for both o-MWCNT and 200-MWCNT composites was explained by the local confinement effects of CNTs at the interface [149]. Spitalsky et al. studied the effects of three types of CNT surface modifications (end-walled covalent chemical modification at the ends of nanotubes, side-walled covalent chemical modification along the whole length of nanotubes, and non-covalent physical modification of the CNT surface with polyaniline) on the CNT dispersion and mechanical properties of epoxy-amine-based nanocomposites [151]. Based on DMA results, it was found that the nanocomposites with physically modified nanotubes had strong interactions between the nanotube and the polymer matrix. More specifically, the side-walled chemical modification of MWCNTs shows a more significant increase

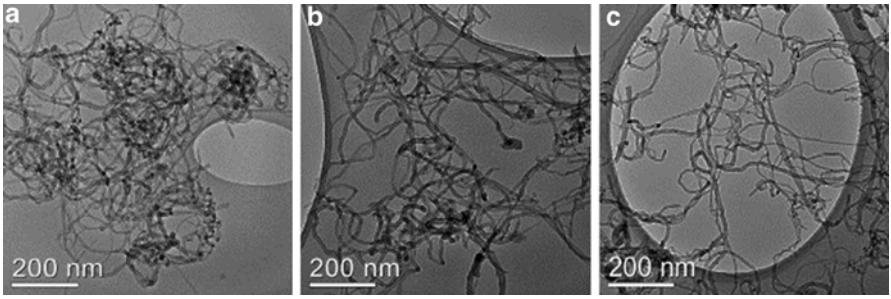

Fig. 8.25 TEM images of (**a**) pristine; (**b**) Triton X-100 (1 CMC) treated; (**c**) Triton X-100 (10 CMC) treated CNTs (Reproduced with permission from Ref. [143]. Copyright 2008 Elsevier Ltd.)

in the storage modulus in comparison with end-walled modified MWCNTs. In the nanocomposites filled with physically modified nanotubes with PANI, the immobilization of epoxy network chains at the CNT interface resulted in a twofold increase of storage modulus [151].

Logakis et al. prepared nanocomposites of poly(methyl methacrylate) (PMMA) containing various MWCNTs contents using melt mixing [144]. It was found out that weak polymer–filler interactions and absence of crystallinity led to high conductivity levels in the nanocomposites. In agreement with DSC and dielectric relaxation spectroscopy (DRS) results, DMA results showed that storage modulus and T_g did not change much with the addition of CNTs, thus indicating absence of strong matrix–filler interactions in the composites [144]. Lasater et al. studied the thermoresistive behavior of nanocomposites with electrically conductive networks of CNTs containing from 0.10 to 1.00 wt % CNT in a vinyl ester polymer matrix and characterized the nanocomposites using an in situ electrical resistance measurement during thermomechanical analysis [146]. Figure 8.26 shows the comparison of volume resistivity and dimensional change curves for CNT/vinyl ester composites during final ramp-up segment. The local minima in both the resistance and resistivity curves in Fig. 8.26 correlate strongly to the T_g measured by TMA. As a result, it was concluded that the thermoresistive analysis of the carbon nanotube network enabled in situ measurement of glass transition in a bulk material without the use of complex thermal analysis instrumentation [146].

The multi-walled carbon nanotube (MWNT) reinforced thermoplastic polyurethane (TPU) nanocomposites were prepared through melt compounding method and compression molding by Barick et al. [156]. SEM and TEM results showed that the CNTs were homogeneously well dispersed within the TPU matrix. Based on DMA results, it was shown that the T_g and storage modulus of the nanocomposites were increased with increasing CNT content. TGA results also showed that thermal stability of TPU nanocomposites was improved in comparison with pure TPU [156]. Lopes et al. investigated composites based on a thermoset polyurethane elastomer

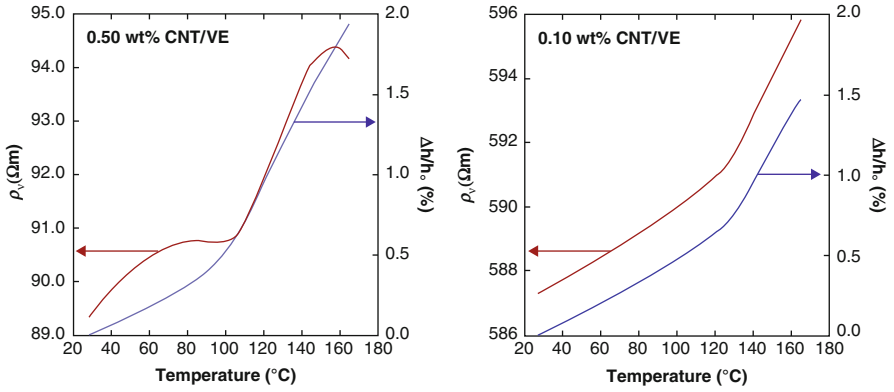

Fig. 8.26 Comparison of volume resistivity and dimensional change curves for CNT/vinyl ester composites (Reproduced with permission from Ref. [146]. Copyright 2012 Elsevier Ltd.)

(PU) with as-grown and modified MWCNTs in the case of a PU of high elastic modulus greater than 200 MPa [167]. DMA results showed that the storage modulus was slightly higher for the oxygenated PU/MWCNT composite below 75 °C compared to pure PU. Authors suggested that the tan δ large peak for all the PU composites revealed a considerable overlap between the thermal transitions associated with the hard and soft domains in PU. It was also shown that there was an increase of 20 °C in the T_g of the hard domains for nanocomposite containing 0.5 wt % CNT in comparison with pure PU [167]. Mamunya et al. investigated dielectric characteristics, conductivity, and thermomechanical properties of poly(vinyl chloride) (PVC)/MWCNT nanocomposites [152]. Based on TMA results (Fig. 8.27), a sharp change of deformation was observed on all TMA curves as a result of transition from glassy to high-elastic state. However, pure PVC and PVC composite with 0.04 % MWCNT showed the biggest values of deformation. TMA results also indicated the formation of a rigid network of CNTs in the polymer matrix which restricts the transition of polymer into the plastic state [152].

Hegde et al. studied two amorphous all-aromatic poly(ether imide)s (aBPDA-P3, a nonlinear matrix and ODPA-P3, a linear matrix) with similar chemical structures but with different backbone geometries as matrix materials for SWCNT-based nanocomposites [148]. Based on DMA results, nanocomposites prepared from aBPDA-P3 nonlinear matrix remained amorphous, and the presence of SWCNTs reduced the T_g by 11 °C. In addition, no change was observed on the storage modulus or stress–strain results with the addition of SWCNTs to this nonlinear matrix. However, when

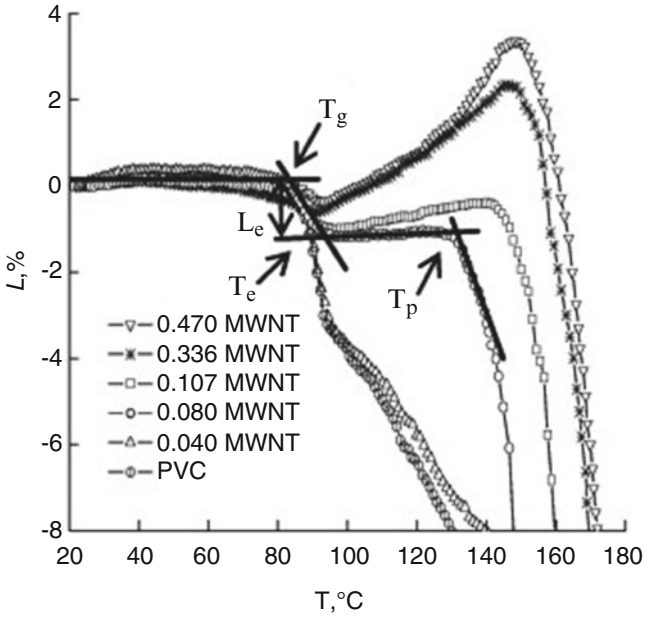

Fig. 8.27 Thermomechanical curves of the PVC/MWNT composites with different contents of filler (Reproduced with permission from Ref. [152]. Copyright 2009 Elsevier Ltd.)

ODPA-P3 linear polymer was used as the matrix, with the addition of SWCNTs, the T_g of polymer was increased by 12 °C due to the induced crystallinity, and the modulus above T_g showed a dramatic increase. It was concluded that the poly(ether imide) backbone geometry directly affects whether the polymer is compatible with SWCNTs or not [148].

8.4.2 Carbon Nanofiber-Based Polymer Nanocomposites

For thermomechanical studies of CNF-based polymer nanocomposites, pristine CNFs [169], triazole, and amine-functionalized CNFs [101, 170–172] have been mainly used as CNFs in polymer matrices. Carbon nanofibers (CNFs) are cylindrical tubes which have a graphite-like structure with nano-scale diameters, and they are synthesized by deposition from carbon vapor [173]. Their nanoscale diameter, cheap production price, high aspect ratio, and excellent mechanical, thermal, and electrical properties made CNFs ideal candidates in various applications such as aerospace, electronic devices, automotive, and defense industries where CNFs are used as effective nanocylinders for the reinforcement. CNFs have usually diameters of 100 nm and lengths between 20 and 100 μm. In comparison with conventional carbon fibers, the nanoscale dimension of CNFs means much more surface area and better intermolecular interactions between the polymer matrix and CNFs. In terms of mechanical properties, CNFs have Young's modulus values in the range of 100–1000 GPa and tensile strengths between 2.5 and 3.5 GPa [174]. Thus, because of these reasons, CNFs have been widely used as nanofillers in improving thermomechanical properties of polymer nanocomposites.

For thermomechanical studies of polymer–CNF nanocomposites, pristine or surface-modified CNFs have been used in diverse polymer matrices such as epoxy [101, 170–172], polyesters [175, 176], poly(methyl methacrylate) [177], polyurethanes [178, 179], and polyolefins [180].

Zhu et al. prepared amine functional group terminated CNF/epoxy nanocomposites by using in situ polymerization and systematically studied the effects of CNF loading, surface treatment, and operating temperatures of rheological tests on the complex viscosity, storage modulus, and loss modulus of epoxy nanocomposites [170]. Figure 8.28 shows the scheme of formation of surface-modified CNF/epoxy nanocomposites. Figure 8.29 shows the storage modulus and tan δ vs. temperature curves for nanocomposites with 0.3 and 0.5 wt % unmodified CNFs (u-CNFs) and surface-modified CNFs (s-CNFs), respectively.

In the glassy region, the storage modulus values of the cured epoxy nanocomposites filled with 0.5 and 0.3 wt % s-CNFs increased in comparison with those of cured pure epoxy and epoxy nanocomposites filled with u-CNFs. Authors explained the improvement of the thermomechanical properties of epoxy nanocomposites filled with s-CNFs due to the covalent bonding between the amine-terminated functional groups of s-CNFs and the epoxide groups of epoxy monomers during in situ polymerization. The peak of tan δ shifted significantly to higher temperatures

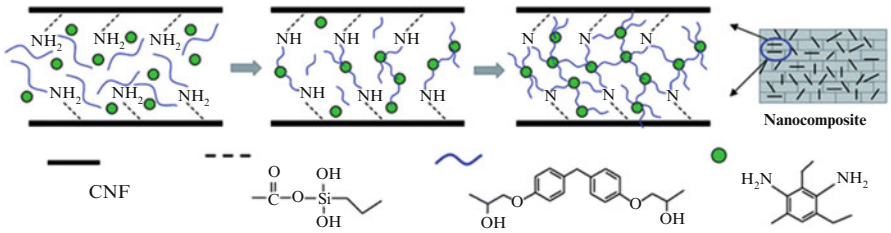

Fig. 8.28 Schematic illustration of the in situ reinforcement of functionalized CNFs in an epoxy matrix, the bottom symbols represent the chemical structures (Reproduced with permission from Ref. [170]. Copyright 2010 The Royal Society of Chemistry)

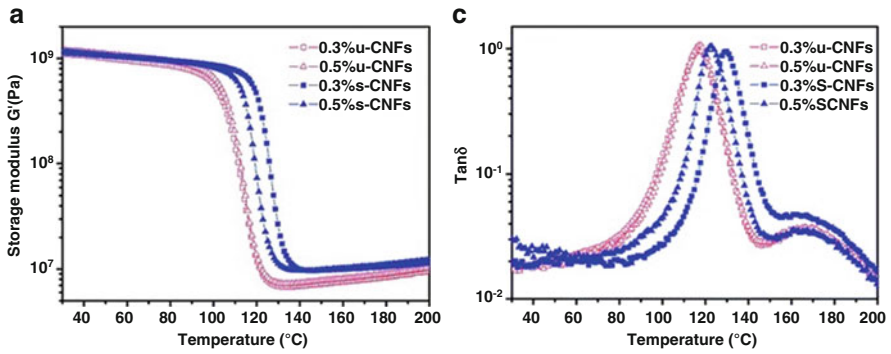

Fig. 8.29 (**a**) Storage modulus and (**c**) tan δ vs. temperature curves for nanocomposites with 0.3 wt % and 0.5 wt % u-CNFs and s-CNFs, respectively (Reproduced with permission from Ref. [170]. Copyright 2010 The Royal Society of Chemistry)

for the cured epoxy nanocomposites containing s-CNFs compared to those of cured epoxy nanocomposites filled with u-CNFs. This result was discussed such that in situ polymerization of epoxy monomers in the presence of s-CNFs led to restrictions on the epoxy mobility, and thus the T_g of epoxy/s-CNF nanocomposites increased compared to those of cured pure epoxy and epoxy/u-CNF nanocomposites [170]. Prolongo et al. synthesized CNF/epoxy nanocomposites containing amino group-functionalized nanofibers and studied the effects of CNF content and surface modification on the morphology and thermomechanical properties of epoxy nanocomposites [171]. Based on TMA results, it was shown that the value of coefficient of thermal expansion (CTE) was not affected by the dispersion degree of CNFs and the morphology of the nanocomposite. DMA results also showed that increasing the CNF amount improved the glassy storage modulus of the nanocomposites up to high CNF contents (5 wt % CNFs and 1 wt % amino CNFs) where agglomerations started to appear. In addition to storage modulus results, at low CNF contents (1 wt % for non-treated CNFs and 0.5 wt % for amino-functionalized CNFs) the glass transition temperature (α-relaxation) of the nanocomposites decreased linearly with increasing contents of CNFs [171]. Green et al. reported the

synthesis and fabrication of multi-scale fiber-reinforced composites (M-FRCs) using glass fiber preforms combined with a low viscosity CNF/epoxy nanostructured matrix, and they investigated the thermomechanical properties such as relaxation behavior (T_g) and dimensional stability (CTE) of the M-FRCs [172]. TMA results showed that CTE values of the M-FRC samples improved compared to the neat FRC. Based on DMA results, M-FRC sample containing 0.1 and 1 % CNF contents exhibited a 17 and 4.5 % increase, respectively, in the glassy shear modulus. Also, from the tan δ results, it was observed that the T_g of both 0.1 and 1 % CNF containing M-FRC samples increased by 25 °C, relative to the neat FRC sample. The improved T_g and CTE properties in the M-FRC samples were attributed to favorable interactions between the CNF/epoxy matrix and glass fibers [172]. Barick et al. prepared CNF-based TPU nanocomposites by melt blending in order to explore the effects of CNF dispersion and addition on the morphology, mechanical, thermal, rheological, and electrical properties of the nanocomposites [178]. TEM results showed that CNFs exhibited a uniformly dispersed morphology in the TPU matrix. Based on DMA results, it was shown that the storage modulus both in the glassy and rubbery regions increased with increasing CNF content. Based on tan δ vs. temperature plots, it was revealed that the tan δ peak position is shifted toward higher temperatures with CNF addition, and also, the peak height decreases with increasing CNF loading [178].

8.5 Conclusions

Clearly, using nanospheres, nanoplatelets, and nanocylinders in various polymer matrices has provided significant thermomechanical property improvements compared to the case of using conventional micron-sized fillers in polymeric materials. In the establishment of good morphology–thermomechanical property relationships, the ultimate aim has been to realize the fine distribution and dispersion of nanofillers while avoiding any type of agglomeration in the polymer matrix. For this reason, in order to achieve desirable and improved properties, a fine dispersion of nanofillers in the polymer matrix has been realized by performing specific types of surface modification techniques on the surface of nanofillers in polymer nanocomposites. Due to the large specific surface area of nanofillers in comparison with their micron-sized counterparts, changing the physicochemical properties of interfacial polymer layer between the polymer matrix and nanofiller by using proper chemistry and physics has resulted in the enhancement of thermomechanical properties. Therefore, the nature of intermolecular interactions between nanofillers and polymer chains can determine the thermomechanical properties of polymer nanocomposites. If interactions are attractive or favorable, then the mobility of polymer chains is usually restricted, and this condition leads to an increase of stiffness or modulus and glass transition of polymer. Also, favorable interactions between the polymer matrix and nanofillers lead to improvement of thermal stability, reduction of the thermal expansion, and damping coefficients. In the literature, so many different types of polymers

as the matrix materials have been used in combination with so many surface-modified nanofillers in order to produce advanced polymer nanocomposites with improved thermomechanical properties. Although a significant amount of work has already been completed on various aspects of thermomechanical property analysis, much research still needs to be done in order to understand the complex structure–property relationships in polymer nanocomposites.

Among polymer–nanoplatelet works in the literature, nanoclay has been successfully incorporated to various polymer matrices with an intercalated or exfoliated morphology in order to improve thermomechanical properties. However, understanding the mechanism for the exfoliation or intercalation of nanoclay in certain polymers is still a challenge that needs to be resolved. Among polymer–nanosphere studies in the literature, surface-modified nanosilica and POSS have been used in so many polymer matrices. However, fine dispersion of POSS and silica nanospheres in certain polymer matrices has not been fully realized. Among polymer–nanocylinder studies in the literature, carbon nanotubes and carbon nanofibers that are surface modified with specific functional groups have been used in diverse polymer matrices. But, certain issues such as the effects of polymer backbone structure, geometry, and architecture on the dispersion level of carbon nanotubes or nanofibers still need to be studied more by researchers who are working in the field of thermomechanical analysis. Especially, in solving the problem of fine dispersion of nanoplatelets, nanospheres, and nanocylinders in polymer matrices, the intermolecular interactions between the polymer matrix and nanofillers have to be adjusted by applying the well-established laws and theories from physics.

For future studies, simultaneous incorporation of at least two types of different nanofillers that are surface modified with different functional groups can be performed to obtain hybrid nanocomposites with enhanced thermomechanical properties. It will be also interesting to systematically prepare and characterize polymer nanocomposites containing these different binary nanofiller combinations and conventional micron-sized fillers in order to see the outcome on the thermomechanical properties of these hybrid materials. Furthermore, the simultaneous use of nanospheres and nanoplatelets or different types of nanofillers in a polymer matrix which is chemically or physically compatible with the surface of nanofillers might also improve the thermomechanical properties much more than the system in which only one type of nanofiller is used. Thus, the concept of using binary mixtures of surface-modified nanofillers in a polymer matrix can be systematically studied and extended to various types of polymers and consequently to different useful applications.

Acknowledgments This work was supported by Ondokuz Mayis University under Grant No. PYO.MUH.1904.11.008.

References

1. Han Z, Fina A (2011) Thermal conductivity of carbon nanotubes and their polymer nanocomposites: a review. Prog Polym Sci 36:914

2. Sengupta R, Bhattacharya M, Bandyopadhyay S, Bhowmick AK (2011) A review on the mechanical and electrical properties of graphite and modified graphite reinforced polymer composites. Prog Polym Sci 36:638
3. Kashiwagi T, Grulke E, Hilding J, Groth K, Harris R, Butler K, Shields J, Kharchenko S, Douglas J (2004) Thermal and flammability properties of polypropylene/carbon nanotube nanocomposites. Polymer 45:4227
4. Gilman JW (1999) Flammability and thermal stability studies of polymer layered-silicate (clay)nanocomposites. Appl Clay Sci 15:31
5. LeBaron PC, Wang Z, Pinnavaia TJ (1999) Polymer-layered silicate nanocomposites: an overview. Appl Clay Sci 15:11
6. Okada A, Kawasumi M, Usuki A, Kojima Y, Kurauchi T, Kamigaito O (1990) Nylon-6 clay hybrid. Mater Res Soc Symp Proc 171:45
7. Giannelis EP, Krishnamoorti R, Manias E (1999) Polymer-silicate nanocomposites: model systems for confined polymers and polymer brushes. Adv Polym Sci 138:107
8. Messersmith PB, Giannelis EP (1995) Synthesis and barrier properties of poly (e-caprolactone)-layered silicate nanocomposites. J Polym Sci Part A Polym Chem 33:1047
9. Gilman JW, Jackson CL, Morgan AB, Harris R, Manias E, Giannelis EP, Wuthenow M, Hilton D, Phillips H (2000) Flammability properties of polymer-layered-silicate nanocomposites. Polypropylene and polystyrene nanocomposites. Chem Mater 12:1866
10. Gleiter H (1992) Nanostructured materials. Adv Mater 4:474
11. Ziolo RF, Giannelis EP, Weinstein BA, O'Horo MP, Ganguly BN, Mehrotra V, Russell MW, Huffman DR (1992) Matrix-mediated synthesis of nanocrystalline ggr-Fe2O3: a new optically transparent magnetic material. Science 257:219
12. Giannelis EP (1996) Polymer layered silicate nanocomposites. Adv Mater 8:29
13. Fisher H, Gielgens L, Koster T (1998) Nanocomposites from polymers and layered minerals, TNO-TPD Report
14. Usuki A, Kojima Y, Kawasumi M, Okada A, Fukushima Y, Kurauchi T, Kamigaito O (1993) Synthesis of nylon 6-clay hybrid. J Mater Res 8:1179
15. Lan T, Pinnavaia TJ (1994) Clay-reinforced epoxy nanocomposites. Chem Mater 6:2216
16. Chang JH, An YU, Cho DH, Giannelis EP (2003) Poly (butylene terephthalate)/organoclay nanocomposites prepared by in situ interlayer polymerization and its fiber (II). Polymer 44:371514
17. Vaia RA, Maguire JF (2007) Polymer nanocomposites with prescribed morphology: going beyond nanoparticle-filled polymers. Chem Mater 19:2736
18. Liff SM, Kumar N, McKinley GH (2007) High-performance elastomeric nanocomposites via solvent-exchange processing. Nat Mater 6:76
19. Zou H, Wu S, Shen J (2008) Polymer/silica nanocomposites: preparation, characterization, properties, and applications. Chem Rev 108:3893
20. Wu J, Mather PT (2009) POSS polymers: physical properties and biomaterials applications. Polym Rev 49:25
21. Coleman JN, Khan U, Blau WJ, Gun'ko YK (2006) Small but strong: a review of the mechanical properties of carbon nanotube–polymer composites. Carbon 44:1624
22. Xia Y, Yang P, Sun Y, Wu Y, Mayers B, Gates B, Yin Y, Kim F, Yan H (2003) One-dimensional nanostructures: synthesis, characterization, and applications. Adv Mater 15:353
23. Ramanathan T, Abdala AA, Stankovich S, Dikin DA, Herrera-Alonso M, Piner RD, Adamson DH, Schniepp HC, Chen X, Ruoff RS, Nguyen ST, Aksay IA, Prud'homme RK, Brinson LC (2008) Functionalized graphene sheets for polymer nanocomposites. Nat Nanotech 3:327
24. Rittigstein P, Priestley RD, Broadbelt LJ, Torkelson JM (2007) Model polymer nanocomposites provide an understanding of confinement effects in real nanocomposites. Nat Mater 6:278
25. Rittigstein P, Torkelson JM (2006) Polymer-nanoparticle interfacial interactions in polymer nanocomposites: confinement effects on glass transition temperature and suppression of physical aging. J Polym Sci Part B-Polym Phys 44:2935
26. Hanemann T, Szabó DV (2010) Polymer-nanoparticle composites: from synthesis to modern applications. Materials 3:3468

27. Ray SS, Okamoto M (2003) Polymer/layered silicate nanocomposites: a review from preparation to processing. Prog Polym Sci 28:1539
28. Chen B, Evans JRG, Greenwell HC, Boulet P, Coveney PV, Bowden AA, Whiting A (2008) A critical appraisal of polymer–clay nanocomposites. Chem Soc Rev 37:568
29. Pavlidou S, Papaspyrides CD (2008) A review on polymer-layered silicate nanocomposites. Prog Polym Sci 33:1119
30. Mittal V (2009) Polymer layered silicate nanocomposites: a review. Materials 2:992
31. Chowdhury FH, Hosur MV, Jeelani S (2006) Studies on the flexural and thermomechanical properties of woven carbon/nanoclay-epoxy laminates. Mater Sci Eng A 421:298
32. Yasmin A, Luo JJ, Abot JL, Daniel IM (2006) Mechanical and thermal behavior of clay/epoxy nanocomposites. Compos Sci Tech 66:2415
33. Leszczynska A, Njuguna J, Pielichowski K, Banerjee JR (2007) Polymer/montmorillonite nanocomposites with improved thermal properties Part I. Factors influencing thermal stability and mechanisms of thermal stability improvement. Thermo Acta 453:75
34. Kaya E, Tanoglu M, Okur S (2008) Layered clay/epoxy nanocomposites: thermomechanical, flame retardancy, and optical properties. J Appl Poly Sci 109:834
35. Yang L, Phua SL, Teo Jun Kai H, Toh CL, Lau SK, Ma J, Lu XA (2011) Biomimetic approach to enhancing interfacial interactions: polydopamine-coated clay as reinforcement for epoxy resin. ACS Appl Mater Interfaces 3:3026
36. Verge P, Fouquet T, Barrère C, Toniazzo V, Ruch D, Bomfim JAS (2013) Organomodification of sepiolite clay using bio-sourced surfactants: compatibilization and dispersion into epoxy thermosets for properties enhancement. Compos Sci Tech 79:126
37. Shabana YM, Wang GT (2013) Thermomechanical modeling of polymer nanocomposites by the asymptotic homogenization method. Acta Mech 224:1213
38. Souza VS, Bianchi O, Lima MFS, Mauler RS (2014) Morphological, thermomechanical and thermal behavior of epoxy/MMT nanocomposites. J Non-Cryst Solids 400:58
39. Sharmila TKB, Ayswarya EP, Abrahamd BT, Beguma PMS, Thachil ET (2014) Fabrication of partially exfoliated and disordered intercalated cloisite epoxy nanocomposites via in situ polymerization: mechanical, dynamic mechanical, thermal and barrier properties. Appl Clay Sci 102:220
40. Baniasadi H, Ramazani SAA, Nikkhah SJ (2010) Investigation of in situ prepared polypropylene/clay nanocomposites properties and comparing to melt blending method. Mater Design 31:76
41. Grigoriadi K, Giannakas A, Ladavos A, Barkoula NM (2013) Thermomechanical behavior of polymer/layered silicate clay nanocomposites based on unmodified low density polyethylene. Polym Eng Sci 53:301
42. Passador FR, Ruvolo-Filho CA, Pessan LA (2013) Effects of different compatibilizers on the rheological, thermomechanical, and morphological properties of HDPE/LLDPE blend-based nanocomposites. J Appl Polym Sci 130:1726
43. Siengchin S, Karger-Kocsis J (2009) Structure and creep response of toughened and nanoreinforced polyamides produced via the latex route: effect of nanofiller type. Compos Sci Tech 69:677
44. Anoukou K, Zaïri F, Naït-Abdelaziz M, Zaoui A, Messager T, Gloaguen JM (2011) On the overall elastic moduli of polymer–clay nanocomposite materials using a self-consistent approach. Part II: experimental verification. Compos Sci Tech 71:206
45. Stoclet G, Sclavons M, Devaux J (2013) Relations between structure and property of polyamide 11 nanocomposites based on raw clays elaborated by water-assisted extrusion. J Appl Polym Sci 127:4809
46. Wan T, Liao S, Wang K, Yan P, Clifford M (2013) Multi-scale hybrid polyamide 6 composites reinforced with nano-scale clay and micro-scale short glass fibre. Comp: Part A 50:31
47. Pluta M, Paul MA, Alexandre M, Dubois P (2006) Plasticized polylactide/clay nanocomposites. I. The role of filler content and its surface organo-modification on the physico-chemical properties. J Polym Sci Part B Polym Phys 44:299
48. Fukushima K, Tabuani D, Camino G (2009) Nanocomposites of PLA and PCL based on montmorillonite and sepiolite. Mater Sci Eng C 29:1433

49. Kontou E, Niaounakis M, Georgiopoulos P (2011) Comparative study of PLA nanocomposites reinforced with clay and silica nanofillers and their mixtures. J Appl Polym Sci 122:1519
50. Wootthikanokkhan J, Cheachun T, Sombatsompop N, Thumsorn S, Kaabbuathong N, Wongta N, Wong-On J, Ayutthaya SIN, Kositchaiyong A (2013) Crystallization and thermomechanical properties of PLA composites: effects of additive types and heat treatment. J Appl Polym Sci 129:215
51. Chang JH, An YU, Sur GS (2003) Poly(lactic acid) nanocomposites with various organoclays. I. Thermomechanical properties, morphology, and gas permeability. J Polym Sci Part B Polym Phys 41:94
52. Ratna D, Divekar S, Samui AB, Chakraborty BC, Banthia AK (2006) Poly(ethylene oxide)/clay nanocomposite: thermomechanical properties and morphology. Polymer 47:4068
53. Burgaz E (2011) Poly(ethylene oxide)/clay/silica nanocomposites: morphology and thermomechanical properties. Polymer 52:5118
54. Sehaqui H, Kochumalayil J, Liu A, Zimmermann T, Berglund LA (2013) Multifunctional nanoclay hybrids of high toughness, thermal, and barrier performances. ACS Appl Mater Interfaces 5:7613
55. Marras SI, Kladi KP, Tsivintzelis I, Zuburtikudis I, Panayiotou C (2008) Biodegradable polymer nanocomposites: the role of nanoclays on the thermomechanical characteristics and the electrospun fibrous structure. Acta Biomater 4:756
56. Li S, Auddy K, Barber P, Hansen TJ, Ma J, Loye HC, Ploehn HJ (2012) Thermal, mechanical, and barrier properties of polyethylene terephthalate-platelet nanocomposites prepared by in situ polymerization. Polym Eng Sci 52:1888
57. Gashti MP, Moradian S (2012) Effect of nanoclay type on dyeability of polyethylene terephthalate/clay nanocomposites. J Appl Polym Sci 125:4109
58. Zengeni E, Hartmann PC, Pasch H (2012) Encapsulation of clay by ad-miniemulsion polymerization: the influence of clay size and modifier reactivity on latex morphology and physical properties. ACS Appl Mater Interfaces 4:6957
59. Poreba R, Spırkov M, Brozov L, Lazic N, Pavlicevic J, Strachota A (2013) Aliphatic polycarbonate-based polyurethane elastomers and nanocomposites. II. mechanical, thermal, and gas transport properties. J Appl Polym Sci 127:329
60. Spoljaric S, Salminen A, Luong ND, Lahtinen P, Vartiainen J, Tammelin T, Seppala J (2014) Nanofibrillated cellulose, poly(vinyl alcohol), montmorillonite clay hybrid nanocomposites with superior barrier and thermomechanical properties. Polym Comp 35:1117
61. Sengwa RJ, Choudhary S (2014) Structural characterization of hydrophilic polymer blends/montmorillonite clay nanocomposites. J Appl Polym Sci 131:40617
62. Qian Y, Liu W, Park YT, Lindsay CI, Camargo R, Macosko CW, Stein A (2012) Modification with tertiary amine catalysts improves vermiculite dispersion in polyurethane via in situ intercalative polymerization. Polymer 53:5060
63. Alonso RH, Estevez L, Lian H, Kelarakis A, Giannelis EP (2009) Nafion–clay nanocomposite membranes: morphology and properties. Polymer 50:2402
64. Cele N, Ray SS (2009) Recent progress on nafion-based nanocomposite membranes for fuel cell applications. Macromol Mater Eng 294:719
65. Burgaz E, Lian H, Alonso RH, Estevez L, Kelarakis A, Giannelis EP (2009) Nafion–clay nanocomposite membranes: morphology and properties. Polymer 50:2384
66. Chen J-S, Poliks MD, Ober CK, Zhang Y, Wiesner U, Giannelis E (2002) Study of the interlayer expansion mechanism and thermal-mechanical properties of surface-initiated epoxy nanocomposites. Polymer 43:4895
67. Cable KM (1996) PhD thesis. The University of Southern Mississippi, Hattiesburg
68. Kim H, Abdale AA, Macosko CW (2010) Graphene/polymer nanocomposites. Macromolecules 43:6515
69. Juilla T, Bhadra S, Yao D, Kim NH, Bosem S, Lee JH (2010) Recent advances in graphene based polymer composites. Prog Polym Sci 35:1350
70. Mahmoud WE (2011) Morphology and physical properties of poly(ethylene oxide) loaded graphene nanocomposites prepared by two different techniques. Eur Polym J 47:1534

71. Potts JR, Dreyer DR, Bielawski CW, Ruoff RS (2011) Graphene-based polymer composites. Polymer 52:5
72. Ajayan PM, Schadler LS, Giannaris C, Rubio A (2000) Single-walled carbon nanotube–polymer composites: strength and weakness. Adv Mater 12:750
73. Allen MJ, Tung VC, Kaner RB (2010) Honeycomb carbon: a review of graphene. Chem Rev 110:132
74. Oh SM, Oh KM, Dung DT, Lee H, Jeonga HM, Kim BK (2012) The modification of graphene with alcohols and its use in shape memory polyurethane composites. Polym Int 62:54
75. Kelly BT (1981) Physics of graphite. Applied Science, London
76. Novoselov KS, Geim AK, Morozov SV, Jiang D, Zhang Y, Dubonos SV, Grigorieva IV, Firsov AA (2004) Electric field effect in atomically thin carbon films. Science 306:666
77. Chu K, Li W, Dong H (2013) Role of graphene waviness on the thermal conductivity of graphene composites. Appl Phys A 111:221
78. Xi Z, Allou O, He Q, Zhu J, Verde MJ, Li Y, Wei S, Guo Z (2013) Strengthened magnetic epoxy nanocomposites with protruding nanoparticles on the graphene nanosheets. Polymer 54:3594
79. Li J, Sham ML, Kim JK, Marom G (2007) Morphology and properties of UV/ozone treated graphite nanoplatelet/epoxy nanocomposites. Compos Sci Tech 67:296
80. Patsidis AC, Kalaitzidou K, Psarras GC (2014) Graphite nanoplatelets/polymer nanocomposites: thermomechanical, dielectric, and functional behavior. J Therm Anal Calorim 116:41
81. Prolongo SG, Jiménez-Suárez A, Moriche R, Ureña A (2014) Graphene nanoplatelets thickness and lateral size influence on the morphology and behavior of epoxy composites. Eur Polym J 53:292
82. Potts JR, Lee SH, Alam TM, An J, Stoller MD, Piner RD, Ruoff RS (2011) Thermomechanical properties of chemically modified graphene/poly(methyl methacrylate) composites made by in situ polymerization. Carbon 49:2615
83. Hazarika M, Jana T (2013) Graphene nanosheets generated from sulfonated polystyrene/graphene Nanocomposite. Compos Sci and Tech 87:94
84. Menes O, Cano M, Benedito A, Giménez E, Castell P, Maser WK, Benito AM (2012) The effect of ultra-thin graphite on the morphology and physical properties of thermoplastic polyurethane elastomer composites. Compos Sci Tech 72:1595
85. Yoon OJ, Jung CY, Sohn IY, Kim HJ, Hong B, Jhon MS, Lee BNE (2011) Nanocomposite nanofibers of poly(D, L-lactic-co-glycolic acid) and graphene oxide nanosheets. Composites: Part A 42:1978
86. Suhr J, Koratkar N, Keblinski P, Ajayan P (2005) Viscoelasticity in carbon nanotube composites. Nat Mater 4:134
87. Pan Y, Xu Y, An L, Lu H, Yang Y, Chen W, Nutt S (2008) Hybrid network structure and mechanical properties of rodlike silicate/cyanate ester nanocomposites. Macromolecules 41:9245
88. Sherely AP, Christoph S, Kuruvilla J, Gem MGD, Laly PA, Sabu T (2010) Dynamic mechanical analysis of novel composites from commingled polypropylene fiber and banana fiber. Polym Eng Sci 50:384
89. Gojny FH, Schulte K (2004) Functionalisation effect on the thermomechanical behaviour of multi-wall carbon nanotube/epoxy-composites. Compos Sci Technol 64:2303
90. Li J, Kim JK, Sham ML (2005) Conductive graphite nanoplatelet/epoxy nanocomposites: effects of exfoliation and UV/ozone treatment of graphite. Scripta Mater 53:235
91. Sarwar MI, Zulfiqar S, Ahmad Z (2008) Polyamide–silica nanocomposites: mechanical, morphological and thermomechanical investigations. Polym Int 57:292
92. Chrissafis K, Paraskevopoulos KM, Papageorgiou GZ, Bikiaris DN (2008) Thermal and dynamic mechanical behavior of bionanocomposites: fumed silica nanoparticles dispersed in poly(vinyl pyrrolidone), chitosan, and poly(vinyl alcohol). J Appl Polym Sci 110:1739
93. Zhu A, Diao H, Rong Q, Cai A (2010) Preparation and properties of polylactide–silica nanocomposites. J Appl Polym Sci 116:2866
94. Feng Y, Wang B, Wang F, Zheng G, Dai K, Liu C, Chen J, Shen C (2014) Effects of modified silica on morphology, mechanical property, and thermostability of injection-molded polycarbonate/silica nanocomposites. J Reinf Plast Compos 33:911

95. Mya KY, Wang Y, Shen L, Xu J, Wu Y, Lu X, He C (2009) Star-like polyurethane hybrids with functional cubic silsesquioxanes: preparation, morphology, and thermomechanical properties. J Polym Sci Part A Polym Chem 47:4602
96. Kim GM, Qın H, Fang X, Sun FC, Mather PT (2003) Hybrid epoxy-based thermosets based on polyhedral oligosilsesquioxane: cure behavior and toughening mechanisms. J Polym Sci Part B Polym Phys 41:3299
97. Maitra P, Ding J, Huang H, Wunder SL (2003) Poly(ethylene oxide) silananted nanosize fumed silica: DSC and TGA characterization of the surface. Langmuir 19:8994
98. Tominaga Y, Asai S, Sumita M, Panero S, Scrosati B (2005) A novel composite polymer electrolyte: effect of mesoporous SiO2 on ionic conduction in poly(ethylene oxide)–LiCF3SO3 complex. J Power Sources 146:402
99. Ding J, Maitra P, Wunder SL (2003) Characterization of the interaction of poly(ethylene oxide) with nanosize fumed silica: Surface effects on crystallization. J Polym Sci Part B Polym Phys 41:1978
100. Kweon JO, Noh ST (2001) Thermal, thermomechanical, and electrochemical characterization of the organic–inorganic hybrids poly(ethylene oxide) (PEO)–silica and PEO–silica–LiClO4. J Appl Polym Sci 81:2471
101. Liu W, Kong J, Toh WE, Zhou R, Ding G, Huang S, Dong Y, Lu X (2013) Toughening of epoxies by covalently anchoring triazole-functionalized stacked-cup carbon nanofibers. Compos Sci Tech 85:1
102. Sun Y, Zhang Z, Moon KS, Wong CP (2004) Glass transition and relaxation behavior of epoxy nanocomposites. J Polym Sci Part B Polym Phys 42:3849
103. Natarajan B, Neely T, Rungta A, Benicewicz BC, Schadler LS (2013) Thermomechanical properties of bimodal brush modified nanoparticle composites. Macromolecules 46:4909
104. Kontou E, Anthoulis G (2007) The effect of silica nanoparticles on the thermomechanical properties of polystyrene. J Appl Polym Sci 105:1723
105. Bansal A, Yang H, Li C, Benicewicz BC, Kumar SK, Schadler LS (2006) Controlling the thermomechanical properties of polymer nanocomposites by tailoring the polymer–particle interface. J Polym Sci Part B Polym Phys 44:2944
106. Bansal A, Yang H, Li C, Benicewicz BC, Kumar SK, Schadler LS (2005) Quantitative equivalence between polymer nanocomposites and thin polymer films. Nat Mater 4:693
107. Georgiopoulos P, Kontou E, Niaounakis M (2014) Thermomechanical properties and rheological behavior of biodegradable composites. Polym Compos 35:1140
108. Huang WM, Yang B, Zhao Y, Ding Z (2010) Thermo-moisture responsive polyurethane shape-memory polymer and composites: a review. J Mater Chem 20:3367
109. Wen X, Lin Y, Han C, Zhang K, Ran X, Li Y, Dong L (2009) Thermomechanical and optical properties of biodegradable poly(L-lactide)/silica nanocomposites by melt compounding. J Appl Polym Sci 114:3379
110. Zhang FA, Lee DK, Pinnavaia TJ (2010) PMMA/mesoporous silica nanocomposites: effect of framework structure and pore size on thermomechanical properties. Polym Chem 1:107
111. Lai YH, Kuo MC, Huanga JC, Chena M (2007) On the PEEK composites reinforced by surface-modified nano-silica. Mater Sci Eng A 458:158
112. Kyoung JM, Hartwig A, Kim BK (2009) Shape memory polyurethanes cross-linked by surface modified silica particles. J Mater Chem 19:1166
113. Neikirk CC, Chung JW, Priestley RD (2013) Thermomechanical behavior of hydrogen-bond based supramolecular poly(e-caprolactone)-silica nanocomposites. RSC Advances 3:16686
114. Olmos D, Prolongo SG, González-Benito J (2014) Thermo-mechanical properties of polysulfone based nanocomposites with well dispersed silica nanoparticles. Composites: Part B 61:307
115. Zhao D, Schneider D, Fytas G, Kumar SK (2014) Controlling the thermomechanical behavior of nanoparticle/polymer films. ACS Nano 8:8163
116. Jouault N, Moll JF, Meng D, Windsor K, Ramcharan S, Kearney C, Kumar SK (2013) Bound polymer layer in nanocomposites. ACS Macro Lett 2:371

117. Turri S, Levi M (2005) Structure, dynamic properties, and surface behavior of nanostructured ionomeric polyurethanes from reactive polyhedral oligomeric silsesquioxanes. Macromolecules 38:5569
118. Huang J, He C, Liu X, Xu J, Tay CSS, Chow SY (2005) Organic–inorganic nanocomposites from cubic silsesquioxane epoxides: direct characterization of interphase, and thermomechanical properties. Polymer 46:7018
119. Kopeskya ET, Haddad TS, McKinley GH, Cohen RE (2005) Miscibility and viscoelastic properties of acrylic polyhedral oligomeric silsesquioxane–poly(methyl methacrylate) blends. Polymer 46:4743
120. Liu H, Zheng S, Nie K (2005) Morphology and thermomechanical properties of organic-inorganic hybrid composites involving epoxy resin and an incompletely condensed polyhedral oligomeric silsesquioxane. Macromolecules 38:5088
121. Misra R, Fu BX, Morgan SE (2007) Surface energetics, dispersion, and nanotribomechanical behavior of POSS/PP hybrid nanocomposites. J Polym Sci Part B Polym Phys 45:2441
122. Lee KM, Knight PT, Chung T, Mather PT (2008) Polycaprolactone-POSS chemical/physical double networks. Macromolecules 41:4730
123. Sánchez-Soto M, Schiraldi DA, Illescas S (2009) Study of the morphology and properties of melt-mixed polycarbonate–POSS nanocomposites. Eur Polym J 45:341
124. Tan J, Jia Z, Sheng D, Wen X, Yang Y (2011) Thermomechanical and surface properties of novel poly(ether urethane)/polyhedral oligomeric silsesquioxane nanohybrid elastomers. Polym Eng Sci 51:795
125. Brus J, Urbanova M, Strachota A (2008) Epoxy networks reinforced with polyhedral oligomeric silsesquioxanes: structure and segmental dynamics as studied by solid-state NMR. Macromolecules 41:372
126. Misra R, Fu BX, Plagge A, Morgan SE (2009) POSS-Nylon 6 nanocomposites: influence of POSS structure on surface and bulk properties. J Polym Sci Part B Polym Phys 47:1088
127. Qiu Z, Pan H (2010) Preparation, crystallization and hydrolytic degradation of biodegradable poly(L-lactide)/polyhedral oligomeric silsesquioxanes nanocomposite. Compos Sci Tech 70:1089
128. Liu Y, Shi Z, Xu H, Fang J, Ma X, Yin J (2010) Preparation, characterization, and properties of novel polyhedral oligomeric silsesquioxane-polybenzimidazole nanocomposites by Friedel-Crafts reaction. Macromolecules 43:6731
129. Kopesky ET, Haddad TS, Cohen RE, McKinley GH (2004) Thermomechanical properties of poly(methyl methacrylate)s containing tethered and untethered polyhedral oligomeric silsesquioxanes. Macromolecules 37:8992
130. Sanchez-Soto M, Illescas S, Milliman H, Schiraldi DA, Arostegui A (2010) Morphology and thermomechanical properties of melt-mixed polyoxymethylene/polyhedral oligomeric silsesquioxane nanocomposites. Macromol Mater Eng 295:846
131. Wang F, Lub X, He C (2011) Some recent developments of polyhedral oligomeric silsesquioxane (POSS)-based polymeric materials. J Mater Chem 21:2775
132. Tanaka K, Adachi S, Chujo Y (2009) Structure–property relationship of octa-substituted POSS in thermal and mechanical reinforcements of conventional polymers. J Polym Sci Part A Polym Chem 47:5690
133. Damian CM, Ciobotaru CC, Garea SA, Iovu H (2013) Effect of POSS-NH_2 functionalization of MWNTs on reinforcing properties in epoxy nanocomposites. High Perform Polym 25:566
134. Wu Y, Li L, Feng S, Liu H (2013) Hybrid nanocomposites based on novolac resin and octa(phenethyl) polyhedral oligomeric silsesquioxanes (POSS): miscibility, specific interactions and thermomechanical properties. Polym Bull 70:3261
135. Matejka L, Kroutilová IA, Lichtenhan JD, Haddad TS (2014) Structure ordering and reinforcement in POSS containing hybrids. Eur Polym J 52:117
136. Choi J, Tamaki R, Kim SG, Laine RM (2003) Organic/inorganic imide nanocomposites from aminophenylsilsesquioxanes. Chem Mater 15:3365
137. Choi J, Kim SG, Laine RM (2004) Organic/inorganic hybrid epoxy nanocomposites from aminophenylsilsesquioxanes. Macromolecules 37:99

138. Zheng L, Hong S, Cardoen G, Burgaz E, Gido SP, Coughlin EB (2004) Polymer nanocomposites through controlled self-assembly of cubic silsesquioxane scaffolds. Macromolecules 37:8606
139. Matejka L, Murias P, Pleštil J (2012) Effect of POSS on thermomechanical properties of epoxy-POSS Nanocomposites. Eur Polym J 48:260
140. Milliman HW, Sanchez-Soto M, Arostegui A, Schiraldi DA (2012) Structure–property evaluation of trisilanolphenyl POSS/polysulfone composites as a guide to POSS melt blending. J Appl Polym Sci 125:2914
141. Liu J, Rasheed A, Minus ML, Kumar S (2009) Processing and properties of carbon nanotube/poly(methyl methacrylate) composite films. J Appl Polym Sci 112:142
142. Stephane B, Peeterbroeck S, Bonduel D, Alexandre M, Dubois P (2008) Mini-review from carbon nanotube coatings to high-performance polymer nanocomposites. Polym Int 57:547
143. Geng Y, Liu MY, Li J, Shi XM, Kim JK (2008) Effects of surfactant treatment on mechanical and electrical properties of CNT/epoxy nanocomposites. Compos Part A 39:1876
144. Logakis E, Pandis C, Pissis P, Pionteck J, Pötschke P (2011) Highly conducting poly(methyl methacrylate)/carbon nanotubes composites: Investigation on their thermal, dynamic-mechanical, electrical and dielectric properties. Compos Sci Tech 71:854
145. He G, Zhou J, Tan K, Li H (2011) Preparation, morphology and properties of acylchloride-grafted multiwall carbon nanotubes/fluorinated polyimide composites. Compos Sci Tech 71:1914
146. Lasater KL, Thostenson ET (2012) In situ thermoresistive characterization of multifunctional composites of carbon nanotubes. Polymer 53:5367
147. Sinnott SB, Andrews R (2001) Carbon nanotubes: synthesis, properties, and applications. Crit Rev Sol St Mater Sci 26:145
148. Hegde M, Lafont U, Norder B, Picken SJ, Samulski ET, Rubinstein M, Dingemans T (2013) SWCNT induced crystallization in an amorphous all-aromatic poly(ether imide). Macromolecules 46:1492
149. Chen W, Lu H, Nutt SR (2008) The influence of functionalized MWCNT reinforcement on the thermomechanical properties and morphology of epoxy nanocomposites. Compos Sci Tech 68:2535
150. Ko JH, Chang JH (2009) Properties of ultrahigh-molecular-weight polyethylene nanocomposite films containing different functionalized multiwalled carbon nanotubes. Polym Eng Sci 49:2168
151. Spitalsky Z, Matejka L, Slouf M, Konyushenko EN, Kovarova J, Zemek J, Kotek J (2009) Modification of carbon nanotubes and its effect on properties of carbon nanotube/epoxy nanocomposites. Polym Compos 30:1378
152. Mamunya YP, Levchenko VV, Rybak A, Boiteux G, Lebedev EV, Ulanski J, Seytre G (2010) Electrical and thermomechanical properties of segregated nanocomposites based on PVC and multiwalled carbon nanotubes. J Non-Cryst Solids 356:635
153. Li H, Zhong J, Meng J, Xian G (2013) The reinforcement efficiency of carbon nanotubes/shape memory polymer nanocomposites. Compos Part B 44:508
154. Rana S, Cho JW, Park JS (2013) Thermomechanical and water-responsive shape memory properties of carbon nanotubes-reinforced hyperbranched polyurethane composites. J Appl Polym Sci 127:2670
155. Shepard KB, Gevgilili H, Ocampo M, Li J, Fisher FT, Kalyon DM (2012) Viscoelastic behavior of poly(ether imide) incorporated with multiwalled carbon nanotubes. J Polym Sci Part B Polym Phys 50:1504
156. Barick AK, Tripathy DK (2011) Preparation, characterization and properties of acid functionalized multi-walled carbon nanotube reinforced thermoplastic polyurethane nanocomposites. Mater Sci Eng B 176:1435
157. Gupta A, Choudhary V (2012) Effect of multiwall carbon nanotubes on thermomechanical and electrical properties of poly(trimethylene terephthalate). J Appl Polym Sci 123:1548
158. Mallakpour S, Zadehnazari A (2014) A convenient strategy to functionalize carbon nanotubes with ascorbic acid and its effect on the physical and thermomechanical properties of poly(amide–imide) composites. J Solid State Chem 211:136

159. Basuli U, Chaki TK, Chattopadhyay S (2011) Thermomechanical and rheological behaviour of polymer nanocomposites based on ethylene–methyl acrylate (EMA) and multiwalled carbon nanotube (MWNT). Plast Rub Compos 40:213
160. Díez-Pascual AM, Naffakh M (2013) Enhancing the thermomechanical behaviour of poly(phenylene sulphide) based composites via incorporation of covalently grafted carbon nanotubes. Compos Part A 54:10
161. Bethune DS, Kiang CH, Devries MS, Gorman G, Savoy R, Vazquez J et al (1993) Cobalt-catalyzed growth of carbon nanotubes with singleatomic-layerwalls. Nature 363:605
162. Iijima S, Ichihashi T (1993) Single-shell carbon nanotubes of 1-nm diameter. Nature 363:603
163. Iijima S (1991) Helical microtubules of graphitic carbon. Nature 354:56
164. Wong EW, Sheehan PE, Lieber CM (1997) Nanobeam mechanics: elasticity, strength, and toughness of nanorods and nanotubes. Science 277:1971
165. Yu M, Lourie O, Dyer MJ, Kelly TF, Ruoff RS (2000) Strength and breaking mechanism of multiwalled carbon nanotubes under tensile load. Science 287:637
166. Hossain MK, Chowdhury MR, Salam MB, Malone J, Hosur MV, Jeelani S, Bolden NW (2014) Improved thermomechanical properties of carbon fiber reinforced epoxy composite using amino functionalized XDCNT. J Appl Polym Sci 131:40709
167. Lopes MC, Castro VG, Seara LM, Diniz VPA, Lavall RL, Silva GG (2014) Thermosetting polyurethane-multiwalled carbon nanotube composites: thermomechanical properties and nanoindentation. J Appl Polym Sci 131:41207
168. Saha S, Saha U, Singh JP, Goswami TH (2013) Thermal and mechanical properties of homogeneous ternary nanocomposites of regioregular poly(3-hexylthiophene)-wrapped multiwalled carbon nanotube dispersed in thermoplastic polyurethane: dynamic- and thermomechanical analysis. J Appl Polym Sci 128:2109
169. Bafekrpour E, Simon GP, Naebe M, Habsuda J, Yang C, Fox B (2013) Preparation and properties of composition-controlled carbon nanofiber/phenolic nanocomposites. Compos Part B 52:120
170. Zhu J, Wei S, Ryu J, Budhathoki M, Liang G, Guo Z (2010) In situ stabilized carbon nanofiber (CNF) reinforced epoxy nanocomposites. J Mater Chem 20:4937
171. Prolongo SG, Campo M, Gude MR, Chaos-Morán R, Ureña A (2009) Thermo-physical characterisation of epoxy resin reinforced by amino-functionalized carbon nanofibers. Compos Sci Technol 69:349
172. Green KJ, Dean DR, Vaidya UK, Nyairo E (2009) Multiscale fiber reinforced composites based on a carbon nanofiber/epoxy nanophased polymer matrix: Synthesis, mechanical, and thermomechanical behavior. Compos Part A 40:1470
173. Endo M, Kroto HW (1992) Formation of carbon nanofibers. J Phys Chem 96:6941
174. Tibbetts GG, Beetz CP (1987) Mechanical properties of vapor grown carbon fibers. J Phys D Appl Phys 20:292
175. Nouranian S, Toghiani H, Lacy TE, Pittman CU, Dubien J (2011) Dynamic mechanical analysis and optimization of vapor-grown carbon nanofiber/vinyl ester nanocomposites using design of experiments. J Compos Mater 45:1647
176. Ma H, Zeng J, Realff ML, Kumar S, Schiraldi DA (2003) Processing, structure, and properties of fibers from polyester/carbon nanofiber composites. Compos Sci Technol 63:1617
177. Zeng J, Saltysiak B, Johnson WS, Schiraldi DA, Kumar S (2004) Processing and properties of poly(methyl methacrylate)/carbon nanofiber composites. Compos B: Eng 35:245
178. Barick AK, Tripathy DK (2010) Effect of nanofiber on material properties of vapor-grown carbon nanofiber reinforced thermoplastic polyurethane (TPU/CNF) nanocomposites prepared by melt compounding. Compos Part A 41:1471
179. Jimenez GA, Jana SC (2009) Composites of carbon nanofibers and thermoplastic polyurethanes with shape-memory properties prepared by chaotic mixing. Polym Eng Sci 49:2020
180. Yang S, Taha-Tijerina J, Serrato-Diaz V, Hernandez K, Lozano K (2007) Dynamic mechanical and thermal analysis of aligned vapor grown carbon nanofiber reinforced polyethylene. Compos B: Eng 38:228

Chapter 9
Applications of Calorimetry on Polymer Nanocomposites

Qingliang He, Xingru Yan, Jiang Guo, Xi Zhang, Huige Wei, Dawei Jiang, Xin Wei, Daowei Ding, Suying Wei, Evan K. Wujcik, and John Zhanhu Guo

9.1 Introduction

The objective of calorimetry is to measure the heat in specific ways. Microscale combustion calorimetry (MCC) is also named as pyrolysis–combustion flow calorimetry [1], which has the dynamic capability to measure maximum rate of heat release and other heat-related parameters using milligram-sized samples. MCC achieves this objective by (1) rapidly heating sample to a controlled pyrolysis state under an inert condition (nitrogen) or a mixture of oxygen and nitrogen followed by (2) rapid high-temperature oxidization (combustion) of the pyrolyzate in excess oxygen, which simulates the combustion [2]. Thus, MCC reproduces both the solid phase state (pyrolysis) and the gas phase state (combustion) chemical processes of flaming combustion of polymeric materials and determines the heat release rate

Q. He • X. Yan • J. Guo • J.Z. Guo (✉)
Integrated Composites Laboratory (ICL), Department of Chemical and Biomolecular Engineering, University of Tennessee, Knoxville, TN 37996, USA
e-mail: zguo10@utk.edu

X. Zhang • H. Wei • D. Jiang
Department of Chemistry and Biochemistry, Lamar University, Beaumont, TX 77710, USA

X. Wei • D. Ding • E.K. Wujcik
Dan F. Smith Department of Chemical Engineering, Lamar University, Beaumont, TX 77710, USA

S. Wei
Department of Chemistry and Biochemistry, Lamar University, Beaumont, TX 77710, USA

Dan F. Smith Department of Chemical Engineering, Lamar University, Beaumont, TX 77710, USA

J.Z. Guo (✉)
Chemical and Biomolecular Engineering Department, University of Tennessee, Knoxville, TN 37996, USA

© Springer International Publishing Switzerland 2016

X. Huang, C. Zhi (eds.), *Polymer Nanocomposites*,
DOI 10.1007/978-3-319-28238-1_9

based on the oxygen consumption in a "non-flaming" oxidation process. Parameters including heat release capacity (HRC), specific heat release rate (HRR) at different temperatures, peak heat release rate (PHRR), temperature at PHRR (T_{PHRR}), and total heat release (THR) can be obtained from MCC. Meanwhile, full width half height (FWHH) and final residual percentage can be calculated [3].

The heat-related parameters collected from MCC, especially the rate of heat release, are the most important and the single key to evaluate the fire hazards of one material. According to its standard testing method ASTM D-7309, the specific HRR at time t can be calculated by Eq. (9.1):

$$\mathrm{HRR}_{(t)} = \frac{EOF}{m_o} \Delta\left[O_2\right]_{(t)} \tag{9.1}$$

The first term E refers to the heat released by complete combustion of a sample per unit mass of O_2 consumed, which is an empirical constant (~13.1 kJ/g-O_2). The second term (ρ) is the density of O_2 at ambient condition. The third term F is the volumetric flow rate of the combustion stream at ambient temperature and pressure measured at the terminal flow meter. The forth term Δ[O2](t) is the change in the concentration (volume fraction) of O_2 in the gas stream due to combustion measured at the oxygen sensor at time t. The last term m_0 is the original mass of one testing sample. It is obvious that the oxygen consumption (Δ[O2](t)) is the key factor to determine the value of HRR.

HRC is another important parameter to determine the flammability of one material. HRC is calculated using Eq. (9.2):

$$\mathrm{HRC} = \frac{PHRR}{\beta} \tag{9.2}$$

PHRR is the maximum specific heat release rate during a controlled thermal decomposition, and β is the average heating rate.

For exploration of multifunctional polymer nanocomposites, especially for the investigation on these flame-retardant-treated polymer nanocomposites, it is useful and necessary to determine the fire risks/hazards based on these combustion parameters. In addition, these parameters are also important guidance for the industrial applications.

Differential scanning calorimetry (DSC) is one of the most widely used calorimetry for determining the endothermic and exothermic heat during the melting and cooling process for one material via measuring the change of the difference in the heat flow rate to one testing sample and to a standard reference sample while they are subjected to a controlled temperature program [4]. In one typical non-isotherm DSC heat-cool-heat cycle, the melting and cooling thermograms including maximum endothermic melting temperature (T_m), the maximum exothermic crystalline

temperature (T_c), the enthalpy of fusion (ΔH_m), and the enthalpy of crystallization (ΔH_c) can be obtained [5]. Meanwhile, the crystallization fraction (F_c) of one semicrystalline polymer or its nanocomposites can also be calculated according to Eq. (9.3):

$$F_c = \Delta H_m / \left[\Delta H_m^\circ \cdot (1 - x) \right] \tag{9.3}$$

where ΔH_m is the measured enthalpy of fusion (integration of the melting peak area under the baseline of DSC curves); ΔH_m° is the enthalpy of fusion of 100 % crystalline polymer (here, e.g., the theoretical value of ΔH_m° for 100 % crystalline polypropylene is 209 J/g [6]; and the theoretical value of ΔH_m° for 100 % crystalline polyethylene is 293 J/g) [5a, 7]. The x is the loading of the fillers in the polymer matrix. If pure polymer is used, the x here equals to zero.

In order to prove the improvement after fabricating one polymer into its polymer matrix nanocomposites, it is of great importance to determine the differences of their physicochemical properties. The calorimetry including both the DSC and MCC is powerful to obtain heat-related parameters, which are useful to evaluate the performance of the obtained polymer matrix nanocomposites in terms of improved melting and crystalline behaviors and reduced flammability and lower fire risks for certain applications.

The synthesis procedures of the HDPE and PP nanocomposites were reported elsewhere [3, 5, 8]. The non-isotherm DSC melting and cooling thermograms of pristine polyolefins and their polymer matrix nanocomposites were carried out by using DSC on a TA Instruments Q-2000 calorimeter. Approximately 5–10 mg sample was encapsulated in a standard aluminum pan and heated from 0 to 250 °C at a heating rate of 10 °C/min under a nitrogen flow rate of 50 mL/min. Prior to cooling down to room temperature, the sample was set to stay isotherm at 200 °C for 3 min. After that, the samples were reheated again from room temperature to 200 °C. The data enclosed were collected from the first cooling and the second heating procedures in order to remove the heat history.

The heat release-related parameters were collected by using a microscale combustion calorimetry (MCC, type 2, Govmark, Inc.) with milligram-sized samples according to the standard testing method ASTM D7309-2007 (Method A). These parameters were recorded and utilized to evaluate the fire hazards [2, 3]. To be specific, the heat release-related parameters including specific heat release rate (HRR) at different temperatures, peak heat release rate (PHRR), temperature at PHRR (T_{PHRR}), and total heat release (THR) were obtained from MCC. Meanwhile, full width half height (FWHH) and final residual percentage were calculated. In a typical measurement, about 3–5 mg sample was heated from 90 to 600 °C under a heating rate of 1 °C/s in a continuous stream of nitrogen flowing at 80 mL/min. The thermal decomposition products (also called as “fuel gases”) were mixed with a 20 mL/min stream of oxygen before entering a 900 °C combustion furnace to complete the non-flaming combustion.

9.2 Discussion

The crystallization behaviors of semicrystalline hydrocarbon polymers like polyethylene and polypropylene have been widely studied. Due to their intrinsic semicrystallinity, the crystallization behaviors can be strongly affected by the nanofillers which have been introduced into these polymer matrices. For example, the DSC melting and crystallization plots of the pristine high-density polyethylene (namely, as HDPE) and its polymer matrix nanocomposites filled with in situ-formed iron@iron oxide ($Fe@Fe_2O_3$) nanoparticles (NPs) were demonstrated in Fig. 9.1a, b. The detailed data including melting peak temperature, T_m; crystallization peak temperature, T_c; enthalpy of fusion, ΔH_m; enthalpy of crystallization, ΔH_c; and crystallization fraction, F_c were summarized in Table 9.1. For 100 % crystalline polyethylene, the best experimental heat of fusion is 4.1 kJ/mol of CH_2, which approximately equals to 293 J/g [7]. The pristine HDPE demonstrates a T_m at 129.8 °C and a T_c at 116.7 °C. The F_c is 62.0 % as calculated from Eq. 9.3. Compared with pristine HDPE, the melting and crystalline peak temperatures of all the nanocomposites with different filler loadings stayed almost unchanged as shown in Fig. 9.1.

These phenomena indicate that the original crystal structure of the hosting HDPE matrix remains unchanged in spite of the incorporation of the in situ-synthesized

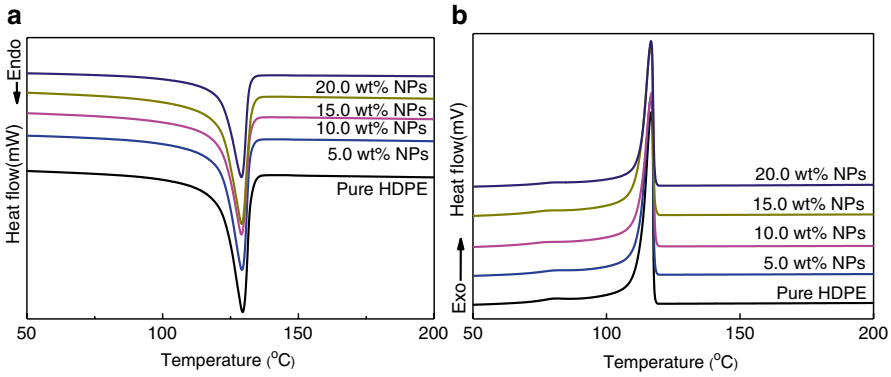

Fig. 9.1 DSC curves of pure HDPE and its nanocomposites: (**a**) second heating and (**b**) first cooling cycle [5a] (Reproduced from Ref. [5a] with permission from the Elsevier)

Table 9.1 DSC characteristics of the HDPE and its nanocomposites [5a]

Composition	T_m (°C)	ΔH_m (J/g)	T_c (°C)	ΔH_c (J/g)	F_c (%)
Pure HDPE	129.8	181.8	116.7	169.3	62.0
5.0 wt% NPs	129.3	167.9	116.7	151.5	60.3
10.0 wt% NPs	129.3	157.2	116.7	139.1	59.6
15.0 wt% NPs	129.3	151.5	116.7	147.0	60.8
20.0 wt% NPs	129.3	140.9	116.7	126.7	60.1

Reproduced from Ref. [5a] with permission from the Elsevier

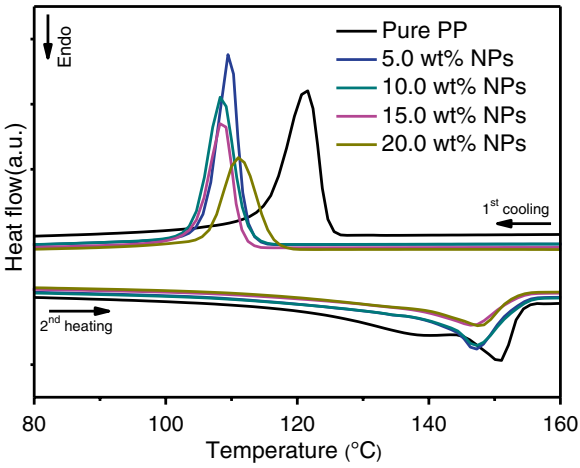

Fig. 9.2 DSC curves of pure PP and its nanocomposites with different loadings of Co@Co_3O_4 NPs [5b] (Reprinted with permission from Ref. [5b]. Copyright (2013) American Chemical Society)

NPs. However, the F_c (Table 9.1) decreased slightly (3–4 %) after the NPs were introduced into the hosting polymer matrix. The ΔH_m of HDPE decreased significantly from 181.8 to 167.9 J/g when 5.0 wt% NPs were incorporated in the HDPE matrix and further decreased to 140.9 J/g in the PNCs with 20.0 wt% particle loading. Since the crystalline structure of HDPE didn't change in all the nanocomposite samples after adding the Fe@Fe_2O_3 NPs as evidenced from X-ray diffraction pattern [5a], the decrease of the enthalpy of fusion was probably caused by the decrease in the crystalline size of HDPE molecules [9].

Upon heating in xylene, the hydrocarbon HDPE chains were relaxed and the NPs were formed among the relaxed chains. The lower F_c of these nanocomposites is attributed to the fact that the NPs are able to disturb the continuity of the HDPE chains and thus introduce more grain boundaries and defects in hosting matrix; and the F_c is suppressed accordingly.

Similar situation was also observed in the polypropylene (PP) magnetic polymer matrix nanocomposites reinforced with in situ-formed cobalt@cobalt oxide (Co@Co_3O_4) NPs in the presence of surfactant maleic anhydride grafted polypropylene (MAPP) [5b]. Compared with the PP matrix, all these polymer matrix nanocomposites show a slightly decreased T_m and a significantly decreased T_c (Fig. 9.2). Meanwhile, significant decreases in ΔH_m and ΔH_c are observed. ΔH_m decreases significantly from 87.0 to 80.8 J/g when 5.0 wt% NPs were introduced into PP matrix. The ΔH_m and ΔH_c were observed to further decrease to 60.1 and 61.7 J/g, respectively, when the particle loading was further increased to 20.0 wt%. The F_c is observed to decrease after the incorporation of the NPs (F_c decreased from 41.6 to 40.7 % when polymer matrix was incorporated with 5.0 wt% NPs, then decreased to 35.9 %, when particle loading was further increased to 20.0 wt% NPs) [5b]. This suggests that the crystallization of PP was partially suppressed, as the Co@Co_3O_4 NPs could act as defects and thus introduced more grain boundaries, which effectively hindered the crystallization of PP segments [10].

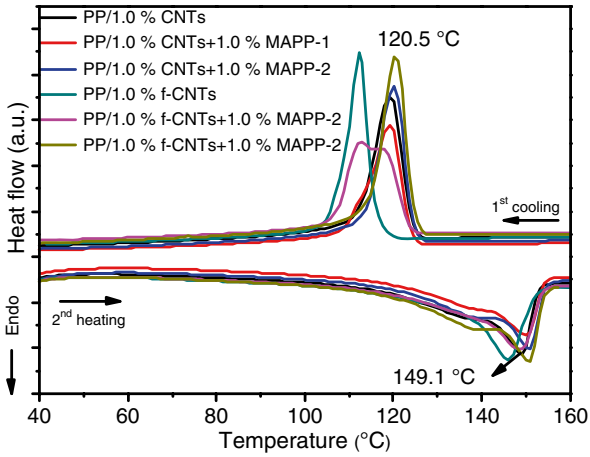

Fig. 9.3 DSC curves of PP/1 % CNTs, nanocomposites of PP/1 % f-CNTs, nanocomposites of PP/1.0 % CNTs/1 % MAPP (1 or 2), and PP/1.0 % f-CNTs/1 % MAPP (1 or 2) [8]. MAPP-1: (molecular weight $M_n = 800$), MAPP-2 ($M_n = 8000$) (Reproduced from Ref. [8] with permission from the John Wiley and Sons)

Another example of the melting and crystallization behaviors of PP polymer matrix nanocomposites filled with untreated and treated carbon nanotubes (with/without the aid of surfactant MAPP) was illustrated in Fig. 9.3 [8]. It can be seen that pure PP has a T_m at 150.7 °C and a ΔH_m of 101.8 J/g with F_c of 48.7 %. When 1.0 wt% untreated carbon nanotubes (CNTs) were added in the PP matrix, the T_m was slightly decreased (149.1 °C); however, ΔH_m was significantly decreased from 101.8 to 83.3 J/g, leading to a decreased F_c of 40.3 %. When adding 1.0 wt% MAPP (type 1 or 2), T_m stayed almost unchanged compared with that of pure PP; however, ΔH_m was further decreased to 74.4 J/g for adding 1.0 wt% MAPP-1 and increased to 88.2 J/g for adding 1.0 wt% MAPP-2, respectively. The corresponding calculated F_c was 36.3 and 42.6 %. For either the PP/1 % CNTs or PP/1 % CNTs/1 % MAPP (type 1 or 2), there was no obvious change of T_c, indicating that no strong restriction of PP crystallization was taken place.

The crystallization of PP main chains was significantly restricted when introducing 1.0 wt% surface-treated CNTs (namely, as f-CNTs) in the PP matrix: T_m decreased to 146.1 °C and T_c decreased to 112.5 °C, which represents 4.6 and 8.8 °C decrease, respectively, along with a decreased F_c of 37.3 %. In combination with 1.0 wt% f-CNTs and 1.0 wt% MAPP-1, all these parameters were slightly changed as shown in Table 9.2. However, when combining 1 % f-CNTs and 1 % MAPP-2, the ΔH_m was increased to 92.1 J/g, corresponding to an F_c of 44.5 %. Meanwhile, T_m (146.1 °C) and T_c (120.5 °C) are similar to those of pure PP.

Usually, for semicrystalline polymer like PP, the introduction of CNTs into the polymer matrix can lead to an earlier crystallization (increase T_c) compared to pure polymer due to the fact that the heterogeneous nucleating effect of CNTs can accelerate the crystallization when polymer is cooled upon melt [11]. However, the decrease of T_c observed here is probably attributed to the non-crystallizable barrier effect of the agglomerated f-CNTs in the PP matrix [11b]. Therefore, the fillers can act as non-crystallizable barriers to disturb the crystal growth of polymer crystallization, which inversely decelerates the crystallization. Furthermore, the fillers may also hinder the mobility of polymer chains, which in turn restricts the growth of the crystallites [12].

Table 9.2 DSC data of pure PP and PP/CNT nanocomposites

Composition	T_m (°C)	ΔH_m (J/g)	T_c (°C)	ΔH_c (J/g)	F_c (%)
PP	150.7	101.8	121.3	104.7	48.7
PP/1 % CNTs	149.1	83.3	119.2	88.8	40.3
PP/1 % CNTs + 1 % MAPP-1	150.3	74.4	119.2	80.6	36.3
PP/1 % CNTs + 1 % MAPP-2	150.6	88.2	120.1	89.7	42.6
PP/1 % f-CNTs	146.1	77.2	112.5	83.4	37.3
PP/1 % f-CNTs + 1 % MAPP-1	148.5	77.7	112.5	85.4	38.0
PP/1 % f-CNTs + 1 % MAPP-2	150.7	92.1	120.5	98.1	44.5

Reproduced from Ref. [8] with permission from the John Wiley and Sons

In addition to the decreased T_c, the peak-broadening effects in the PP/1.0 % f-CNTs and PP/1.0 % f-CNTs/1.0 % MAPP-1 PNCs were also observed during the exothermic crystallization cycle, indicating the formation of imperfect polymer crystallites and the size distribution-broadening effect of thus formed crystallites [13]. The T_c (112.5 °C) of the PP/1.0 wt% f-CNTs/1.0 wt% MAPP-1 was further decreased compared with that (119.2 °C) of the PP/1.0 wt% CNTs, indicating a stronger barrier effect to the PP crystallization, while T_c was not significantly changed when MAPP-2 (120.5 °C) was introduced in the PP matrix since the larger free volume has been introduced (Fig. 9.3).

MCC was utilized to determine the heat release-related flammability parameters and further evaluate the fire hazards of pure PP, PP/20.0 wt% Co, and PP/20.0 % Co polymer matrix nanocomposites stabilized with two different molecular weight surfactants PP-g-MA [3]. PP-g-MA (S) ($M_n \approx 800$) is a gel-like propylene–hexene copolymer with one maleic anhydride (MA) group at one terminal and the other MA grafted on the main chain; and PP-g-MA (L) ($M_n \approx 2500$) is a solid homo-polypropylene with one terminal MA through Alder–ene reaction [14]. Figure 9.4 demonstrated the HRR vs. temperature curves, and Table 9.3 showed the detailed heat release parameters. HRR is the single most important parameter to assess the fire hazard of one flammable material [15]. Pure PP is a highly flammable material as the PHRR observed here of 1513.0 w/g. Adding 5 % PP-g-MA (L/S) slightly decreased the flammability as evidenced by the small amounts of reduction in HRC, PHRR, and THR (Table 9.3), which were apparently due to the less gas fuels generated from the oxygen-containing PP-g-MA (L/S) than pure hydrocarbon PP. In addition, the initial thermal decomposition and T_{PHRR} were similar to these of pure PP.

When adding 20.0 wt% Co NPs into PP matrix, PHRR was decreased from 1513.0 to 1024.0 W/g (~32.3 % reduction), THR was decreased from 40.6 to 27.7 W/g (~31.8 % reduction); and the initial decomposition temperature was enhanced upon adding the Co NPs (Fig. 9.4). Apparently, with excluding the dilution of combustible PP through the 20.0 wt% noncombustible Co loading, an additional 12.3 % decrease in HRR and 11.8 % decrease in THR indicated a flame retardancy effect of these in situ-synthesized Co NPs. Therefore, the HRR reduction

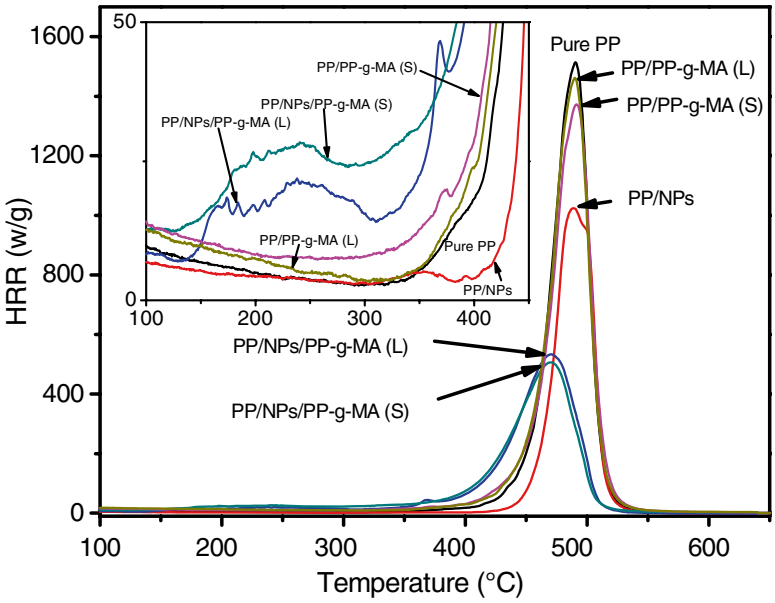

Fig. 9.4 Heat release rate curves of pure PP, PP/PP-g-MA, PP/20.0 % Co PNCs, and PP/20.0 % Co nanocomposites stabilized with two different molecular weight PP-g-MAs. Insert is enlarged initial low-temperature decomposition between 100 and 400 °C [3] (Reproduced from Ref. [3] with permission from the Royal Society of Chemistry)

Table 9.3 Heat release data of the PP and its nanocomposites with Co NPs [3]

Composition	HRC (J/g-k)	PHRR (W/g)	PHRR reduction (%)	T_{PHRR} (°C)	THR (KJ/g)	FWHH (s)
Pure PP	1187.0	1513.0	/	490.4	40.6	24.2
PP/PP-g-MA(L)	1150.0	1454.0	3.9	491.1	40.3	25.1
PP/PP-g-MA(S)	1077.0	1366.0	9.7	489.9	39.8	25.9
PP/20.0 % NPs	809.0	1024.0	32.3	489.9	27.7	23.7
PP/20.0 % NPs/ PP-g-MA(L)	417.0	532.4	64.8	471.0	25.6	39.7
PP/20.0 % NPs/ PP-g-MA(S)	395.0	500.8	66.9	471.0	25.1	41.0

Reproduced from Ref. [3] with permission from the Royal Society of Chemistry

here suggests a slower generation rate of combustible volatiles from the random chain scission of PP backbones in the presence of Co NPs, which can be considered as a barrier effect for the flame retardancy mechanism. During the decomposition, heat and mass transfers between gas and condense phases were slowed down by forming an insulating layer when these PNCs were exposed under heat, and thus fast decomposition of the polymeric PP matrix was suppressed [16].

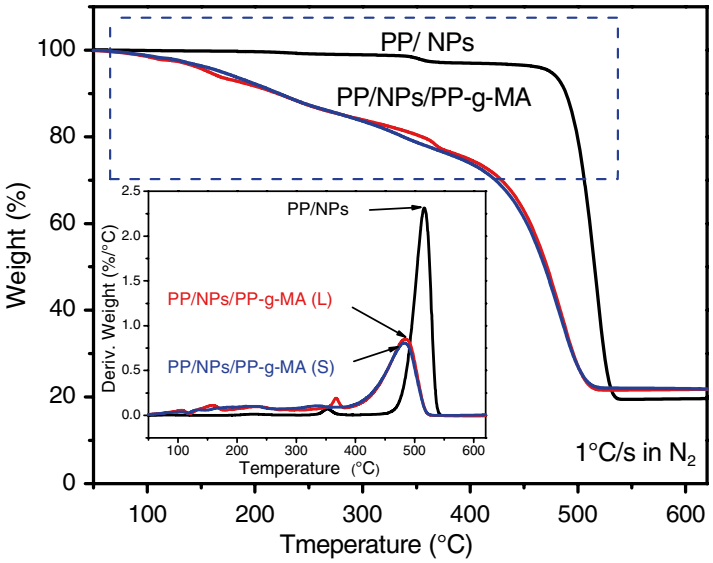

Fig. 9.5 TGA and DTA curves of PP/20.0 % Co MPNCs and PP/20.0 % Co PNCs stabilized with two PP-g-MAs under a heating rate of 1 °C/s (60 °C/min) [3] (Reproduced from Ref. [3] with permission from the Royal Society of Chemistry)

Synergistic effect in reducing flammability was observed when adding 5.0 % to both PP-g-MAs in the PP/20.0 wt% Co NP system (Fig. 9.4). HRC and PHRR were observed to decrease sharply, i.e., PHRR was further decreased from 1024.0 to 532.4 W/g in the case of PP/PP-g-MA (L)/Co PNCs or to 500.8 W/g in the case of PP/PP-g-MA (S)/Co PNCs when 5.0 % PP-g-MA was added in the PP/Co PNCs. Meanwhile, THR was further slightly decreased from 27.7 to 25.6 KJ/g with the addition of 5.0 % PP-g-MA (L) or to 25.1 KJ/g with the addition of 5.0 % PP-g-MA (S) into PP/20.0 % Co PNCs. Since PP-g-MA is only a polymeric additive serving as surfactant, this remarkable decrease in the flammability of PP by Co NPs and PP-g-MA has to be in its unique pathway. Although the conventional synergistic effect (such as nitrogen–phosphorus [17], phosphorus–silicon [18]) on flame-retardant polymer matrix nanocomposites has been extensively studied and reported, the synergistic effect between PP-MA and Co NPs has rarely been demonstrated. In addition, when either PP-g-MA was added in the PP/20.0 % Co system, a small amount of HRR was observed during the initial thermal decomposition stage (around 100–300 °C), and T_{PHRR} was decreased to 471.0 °C (shown in the insert of Fig. 9.4).

In order to further understand the synergism between PP-g-MA and Co NPs in dramatically reducing the flammability of PP matrix, a fast thermal degradation test was performed by thermogravimetric analysis (TGA) and differential thermal analysis (DTA) through using the identical heating condition as MCC measurements – a heating rate of 60 °C/min (1 °C/s) under nitrogen (TGA and DTA curves shown in Fig. 9.5). MCC measurements here were performed through using an inert sample thermal

degradation procedure to pyrolyze the sample into combustible gas volatiles followed by a non-flaming oxidation of these volatiles. The fast thermal degradation by TGA can illustrate the dynamic sample weight loss under temperature ramping at a constant high heating rate (1 °C/s); meanwhile, the derivative weight loss (%/°C) from the insert of Fig. 9.5 can reproduce the thermal degradation stage of MCC clearly. Therefore, the degradation and weight loss processes can be demonstrated simultaneously.

It is observed that the addition of 5.0 % PP-g-MA (L/S) barely decreased the initial thermal degradation temperature of PP, while 20.0 % Co NPs increased the initial thermal degradation of PP as evidenced by the higher thermal degradation temperature than that of pure PP (no detectable HRR increase before 400 °C, shown in the insert of Fig. 9.4). However, the degradation of PP/5.0 % PP-g-MA (L/S)/20.0 % Co NPs was definitely altered by the evidence of: broad HRR peaks appeared in the range of 130–310 °C (insert of Fig. 9.4) and ~18.0 % weight loss within the thermal degradation temperature of 100–310 °C from the TGA curves (Fig. 9.5). When exposed to heat flux at elevated temperature from 80 to 650 °C, the thermal degradation of PP under inert atmosphere was initiated primarily by chain scission and chain transfer; then reductions in molecular weight were first observed at 227 to 247 °C, and gas volatiles became significant above 302 °C. Finally, ignition of PP was observed at a surface temperature of 337 °C [19], consistent with the initial HRR jump at ~330 °C observed from MCC. Meanwhile, the addition of 5.0 % PP-g-MA (L/S) has limited influence on initiating the degradation of the PP matrix. With 20.0 % Co NPs, only shielding effect functioned as barrier for reducing the HRR through slowing and delaying the release of gas volatiles [16]. When adding PP-g-MA together with Co NPs in the PP matrix, the catalytic effect was responsible for lowering the initial thermal degradation temperature of the resulted PNCs (from 330 °C for pure PP to ~100–130 °C for the PNCs) and led to a smaller HRR in the range of 100–310 °C due to a small amount of gas volatiles released from bulk material. Probable mechanism includes the random chain scission of C–C bond of PP backbone to generate hydrocarbon radicals during initial decomposition, the formation of lower hydrocarbons such as propylene from further degradation of these hydrocarbon radicals, the β-scission and abstraction of H radicals from other hydrocarbons to produce a new hydrocarbon radicals during propagation stage, and finally the disproportionation or recombination of two radicals as termination reaction [20]. Meanwhile, slightly similar to the "smoldering" fire, a substantial fraction of the total mass of PP/5.0 % PP-g-MA (L/S)/Co PNCs (~18.0 %) was consumed during 100–310 °C subjected to a slow heat release process, effectively decreased the total available gas volatiles, which would generate large quantity of heat under higher temperatures. In addition, the strong interfacial adhesion between Co NPs and PP matrix through PP-g-MA was responsible for the sharply suppressed mass loss rate as observed reduction in PHRR (Figs. 9.4 and 9.5). Another important parameter, full width half height (FWHH), of the PP/PP-g-MA/Co PNCs was much wider than those of pure PP, PP/PP-g-MA, and PP/Co PNCs (Table 9.3) and further proved a longer combustion period upon introducing the PP-g-MA and Co NPs in the PP matrix. This is another sign of lower fire hazard of the PP/PP-g-MA/Co PNCs.

9.3 Conclusion

To summarize, we have demonstrated the powerful capability of DSC and MCC to study the melting and crystallization behaviors and heat release-related flammability parameters. The melting and crystallization behaviors of both pristine polymers and their polymer matrix nanocomposites are of great importance to understand how and why the nanofillers changed the intrinsic properties of polymer backbones and can thus give further insight to predict and guide material design for optimal industrial applications. The heat release-related parameters including heat release rate and heat release capacity are paramount to determine the flammability of both the polymers and their nanocomposites. Along with other techniques such as thermogravimetric analysis, the change of thermal degradation pathways after introducing nanofillers into polymer matrix can be determined, and the flame retardancy mechanism can thus be understood by this powerful calorimetry.

Acknowledgement This work is financially supported by start-up fund from University of Tennessee. S. Wei acknowledges the donors of the American Chemical Society Petroleum Research Fund (ACS PRF# 53930-ND6) for partial support of this research.

References

1. (a) Lyon RE, Walters R, Stoliarov S (2007) Screening flame retardants for plastics using microscale combustion calorimetry. Polym Eng Sci 47(10):1501–1510; (b) Lyon RE, Walters RN (2004) Pyrolysis combustion flow calorimetry. J Anal Appl Pyrolysis 71(1):27–46; (c) Lyon R, Walters R, Stoliarov S (2007) Thermal analysis of flammability. J Therm Anal Calorim 89(2):441–448
2. Yang CQ, He Q, Lyon RE, Hu Y (2010) Investigation of the flammability of different textile fabrics using micro-scale combustion calorimetry. Polym Degrad Stab 95(2):108–115
3. He Q, Yuan T, Wei S, Guo Z (2013) Catalytic and synergistic effects on thermal stability and combustion behavior of polypropylene: influence of maleic anhydride grafted polypropylene stabilized cobalt nanoparticles. J Mater Chem A 1(42):13064–13075
4. Höhne G, Hemminger W, Flammersheim H-J (2003) Differential scanning calorimetry. Springer Science & Business Media, Berlin - Heidelberg
5. (a) He Q, Yuan T, Zhu J, Luo Z, Haldolaarachchige N, Sun L, Khasanov A, Li Y, Young DP, Wei S (2012) Magnetic high density polyethylene nanocomposites reinforced with in-situ synthesized Fe@ FeO core-shell nanoparticles. Polymer 53(16):3642–3652; (b) He Q, Yuan T, Zhang X, Luo Z, Haldolaarachchige N, Sun L, Young DP, Wei S, Guo Z (2013) Magnetically soft and hard polypropylene/cobalt nanocomposites: role of maleic anhydride grafted polypropylene. Macromolecules 46(6):2357–2368
6. (a) Carlson ED, Krejchi MT, Shah CD, Terakawa T, Waymouth RM, Fuller GG (1998) Rheological and thermal properties of elastomeric polypropylene. Macromolecules 31(16):5343–5351; (b) Rozanski A, Galeski A, Debowska M (2011) Initiation of cavitation of polypropylene during tensile drawing. Macromolecules 44:20–28
7. Wunderlich B, Czornyj G (1977) A study of equilibrium melting of polyethylene. Macromolecules 10(5):906–913
8. He Q, Yuan T, Yan X, Ding D, Wang Q, Luo Z, Shen TD, Wei S, Cao D, Guo Z (2014) Flame-retardant polypropylene/multiwall carbon nanotube nanocomposites: effects of surface functionalization and surfactant molecular weight. Macromol Chem Phys 215(4):327–340

9. Zhu J, Wei S, Li Y, Sun L, Haldolaarachchige N, Young DP, Southworth C, Khasanov A, Luo Z, Guo Z (2011) Surfactant-free synthesized magnetic polypropylene nanocomposites: rheological, electrical, magnetic, and thermal properties. Macromolecules 44:4382–4391
10. Purohit PJ, Huacuja-Sánchez JE, Wang DY, Emmerling F, Thünemann A, Heinrich G, Schönhals A (2011) Structure–property relationships of nanocomposites based on polypropylene and layered double hydroxides. Macromolecules 44(11):4342–4354
11. (a) Yang BX, Pramoda KP, Xu GQ, Goh SH (2007) Mechanical reinforcement of polyethylene using polyethylene-grafted multiwalled carbon nanotubes. Adv Funct Mater 17(13):2062–2069; (b) Xu D, Wang Z (2008) Role of multi-wall carbon nanotube network in composites to crystallization of isotactic polypropylene matrix. Polymer 49(1):330–338
12. (a) Fornes T, Paul D (2003) Crystallization behavior of nylon 6 nanocomposites. Polymer 44(14):3945–3961; (b) Homminga D, Goderis B, Dolbnya I, Reynaers H, Groeninckx G (2005) Crystallization behavior of polymer/montmorillonite nanocomposites. Part I. Intercalated poly (ethylene oxide)/montmorillonite nanocomposites. Polymer 46(25):11359–11365
13. (a) Trujillo M, Arnal M, Müller A, Laredo E, St. Bredeau, Bonduel D, Dubois P (2007) Thermal and morphological characterization of nanocomposites prepared by in-situ polymerization of high-density polyethylene on carbon nanotubes. Macromolecules 40(17):6268–6276; (b) Koval'chuk AA, Shchegolikhin AN, Shevchenko VG, Nedorezova PM, Klyamkina AN, Aladyshev AM (2008) Synthesis and properties of polypropylene/multiwall carbon nanotube composites. Macromolecules 41(9):3149–3156
14. Lei C, Chen D, Wu B, Xu Y, Li S, Huang W (2011) Melt-grafting mechanism study of maleic anhydride onto polypropylene with 1-decene as the second monomer. J Appl Polym Sci 121(6):3724–3732
15. Babrauskas V, Peacock RD (1992) Heat release rate: the single most important variable in fire hazard. Fire Saf J 18(3):255–272
16. Wang X, Song L, Yang H, Xing W, Lu H, Hu Y (2012) Cobalt oxide/graphene composite for highly efficient CO oxidation and its application in reducing the fire hazards of aliphatic polyesters. J Mater Chem 22(8):3426–3431
17. (a) Yang H, Yang CQ, He Q (2009) The bonding of a hydroxy-functional organophosphorus oligomer to nylon fabric using the formaldehyde derivatives of urea and melamine as the bonding agents. Polym Degrad Stab 94(6):1023–1031; (b) He Q, Lu H, Song L, Hu Y, Chen L (2009). Flammability and thermal properties of a novel intumescent flame retardant polypropylene. J Fire Sci 27(4):303–321; (c) Nie S, Hu Y, Song L, He Q, Yang D, Chen H (2008) Synergistic effect between a char forming agent (CFA) and microencapsulated ammonium polyphosphate on the thermal and flame retardant properties of polypropylene. Polym Adv Technol 19(8):1077–1083
18. (a) He Q, Song L, Hu Y, Zhou S (2009) Synergistic effects of polyhedral oligomeric silsesquioxane (POSS) and oligomeric bisphenyl A bis(diphenyl phosphate)(BDP) on thermal and flame retardant properties of polycarbonate. J Mater Sci 44(5):1308–1316; (b) Zhang W, Li X, Guo X, Yang R (2010) Mechanical and thermal properties and flame retardancy of phosphorus-containing polyhedral oligomeric silsesquioxane (DOPO-POSS)/polycarbonate composites. Polym Degrad Stab 95(12):2541–2546
19. Beyler C, Hirschler M (1995) Thermal decomposition of polymers, chapter 7. In: SFPE handbook of fire protection engineering. National Fire Protection Association, and Society of Fire Protection Engineers, Boston, Massachusetts, pp 110–131
20. Singh B, Sharma N (2008) Mechanistic implications of plastic degradation. Polym Degrad Stab 93(3):561–584

Chapter 10
Electrically Conductive Polymer Nanocomposites with High Thermal Conductivity

Prabhakar R. Bandaru, B.-W. Kim, S. Pfeifer, R.S. Kapadia, and S.-H. Park

We review the utility of one-dimensional nanostructures, such as linear and nonlinear carbon nanotubes (CNTs), as fillers in polymer matrices and their influence in modulating the electrical, electromagnetic, and thermal properties of the resulting composites. This chapter will first consider the rationale for the use of structures with a large aspect ratio, based on percolation theory. At the very outset, a large length-to-diameter ratio enables matrix spanning at lower volume fractions, with the implication of observing novel phenomena at relatively dilute filler content. Subsequent geometric effects on significantly affecting DC and AC electrical conductivity, with respect to nonlinearity in the structure will also be considered. A significant new result is the observation of a power–law relation for the thermal conductivity, indicative of percolation, which contradicts earlier assertions and indicates that synthesis methodologies may be adapted to facilitate such behavior. Modeling of the experimentally determined electrical and thermal conductivity anisotropy, in addition to the incorporation of interfacial resistance, provides a better understanding of the underlying mechanisms and variations.

10.1 Introduction

Polymer composites containing conducting fillers [1–4] such as carbon black [5], carbon fiber, and metal fiber have been extensively investigated for multifunctional applications incorporating structural reinforcement [6], electromagnetic interference (EMI) shielding [7, 8], electronic packaging [3], radar-absorbing materials [9, 10], high-charge storage capacitors [11, 12], etc. A concomitant enhancement in the

P.R. Bandaru (✉) • B.-W. Kim • S. Pfeifer • R.S. Kapadia • S.-H. Park
Program in Materials Science, Department of Mechanical and Aerospace Engineering, University of California, San Diego, La Jolla, CA 92093, USA
e-mail: pbandaru@ucsd.edu

© Springer International Publishing Switzerland 2016

X. Huang, C. Zhi (eds.), *Polymer Nanocomposites*,
DOI 10.1007/978-3-319-28238-1_10

mechanical properties was also observed in the composites, e.g., facilitated through load transfer from a low elastic modulus (E) polymer matrix to a high E filler [13]. However, there is a limit to the impregnation of polymers with such traditional filler material due to possible embrittlement beyond a certain loading. Consequently, high aspect ratio (A.R.) fillers, which favor reinforcement and electrical properties/percolation at lower volume fractions, are desirable. Carbon nanotubes (CNTs) offer a most attractive option in this regard, primarily due to their extremely large A.R. – which could be as high as 10^6 [14], e.g., with a 1 μm length and 1 nm diameter, coupled with a large interfacial area >1300 m^2/g [15], with the implication of load transfer over a longer length incorporating superior shear strength. Additionally, the CNT surfaces and interfaces can be functionalized and made to interact suitably with the polymer matrix groups through the use of suitable coupling agents [16].

10.1.1 The Utility of Carbon Nanotubes and One-Dimensional Fillers

The large length to diameter A.R. of one-dimensional nanostructures such as carbon nanotubes (CNTs) or nanowires is expected to enhance both the electrical conductivity (σ) and thermal conductivity (κ) of relatively insulating matrices, e.g., polymers, at relatively low nanostructure filler fractions. Integral to such possible enhancement are (i) the postulated high conductivity of the nanostructures, along the length of the wires, due to the reduced scattering space/probability [14, 17], and (ii) that the fillers span/percolate through the matrix. Moreover, it would be expected that the anisotropy in the σ and the κ of the fillers would be transferred to the composite. For example, a filler with an A.R. which deviates most significantly from that of a sphere could have the greatest effect on the *effective* dielectric constant of polymer nanocomposites. Both DC and AC effects, with respect to the electrical conductivity variation, will be considered in this chapter.

We use an excluded volume percolation theory-based model [18, 19] to estimate the theoretical critical volume percolation threshold, ϕ_c of the CNTs, as a function of L. For this, we assume that the *ith* CNT has a volume, v_i, in a polymer/insulating matrix of unit volume. Now, if the percolation threshold corresponds to the connectivity of N_c CNTs, then the odds of *not* selecting any CNT (corresponding to a point in the matrix) would be:

$$\left(1-\phi_c\right)=\left(1-v_1\right)\left(\frac{1-v_1-v_2}{1-v_1}\right)\left(\frac{1-v_1-v_2-v_3}{1-v_1-v_2}\right)\ldots\left(\frac{1-v_1-v_2-v_{N_c}}{1-v_1-v_2-\ldots v_{N_c}}\right)=1-N_c\sum_{i=1}^{N_c}\frac{v_i}{N_c},$$

implying that

$$\phi_c = N_c.E\left[v\right] \tag{10.1}$$

$E[v]$ denotes the expected value or ensemble average of the CNT volume. It is to be noted that Eq. (10.1) is distinct compared to the critical percolation threshold extant in literature, which assumes that the percolating objects are penetrable, i.e., hitherto

applied to pores in rock, etc. In deriving Eq. (10.1), we have assumed that the CNTs were impenetrable. We then use the identity, $E[v] = \frac{E[V_{ex}]N_c}{E[V_{ex}]}\left(\frac{E[v]}{N_c}\right)$, where V_{ex} is defined as the excluded volume [7]: the space circumscribed around the CNT by the center of another CNT, whereby both CNTs contact each other but do not overlap. For isotropically oriented, spherically capped *sticklike* objects of diameter "D" and random length "L", which we take to be akin to CNTs, $E[V_{ex}] = \frac{4\pi}{3}D^3 + 2\pi D^2 E[L] + \frac{\pi}{2}DE[L^2]$. Also, for the CNT modeled as a capped cylinder, $E[v] = \frac{\pi}{6}D^3 + \frac{\pi}{4}D^2 E[L]$. Note that the CNT diameter is assumed to be constant. For infinitely thin cylinders of deterministic length, Monte Carlo simulations were used [6] to estimate $E[V_{ex}]N_c$. as ~1.4. This is an upper bound when the lengths vary randomly, as $E[V_{ex}]$ should be weighted to favor the longer CNTs. For a given D, the theoretical ϕ_c would be:

$$\phi_c(L) = \frac{E[V_{ex}]N_c}{\frac{4\pi}{3}D^3 + 2\pi D^2 E[L] + \frac{\pi}{2}DE[L^2]}\left(\frac{\pi}{6}D^3 + \frac{\pi}{4}D^2 E[L]\right) \tag{10.2}$$

For a deterministic L, the variation of ϕ_c as a function of the A.R. (= L/D) is shown in Fig. 10.1. Such a depiction necessarily implies that a definitive ϕ_c is obtained at a

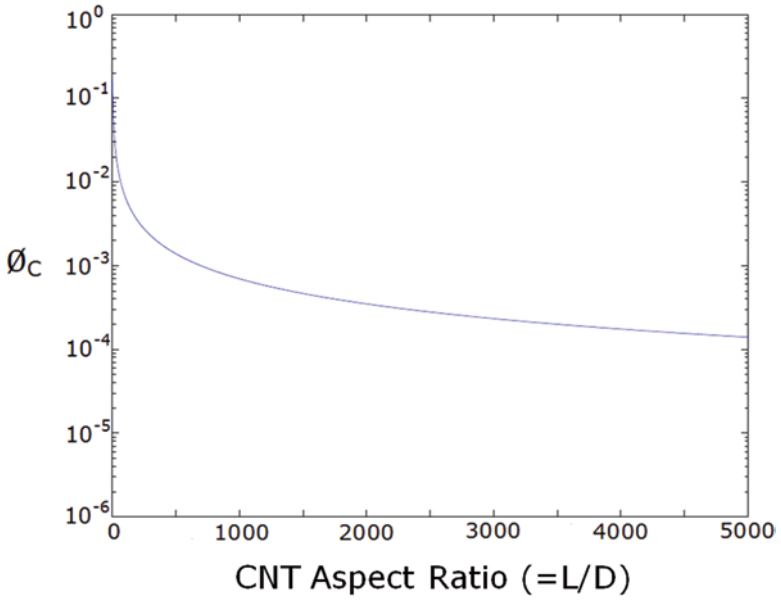

Fig. 10.1 The theoretical variation of the critical percolation threshold (ϕ_c) plotted as a function of the CNT aspect ratio (A.R. = L/D) assuming a deterministic length and diameter (Reproduced from Ref. [20] with permission)

given *L*. We have shown that while the length variation for multiwalled nanotubes (MWNTs) could be fitted very satisfactorily to a Weibull distribution [20] and hence modeled through appropriate probability distributions, for single-walled CNTs (SWNTs), the distributions for CNT length and geometry are more complex. Consequently, with an aim of investigating such percolation-related phenomena in determining the electrical and thermal characteristics of the polymer composites, several nanotube composites with varying nanotube volume fractions were prepared.

10.2 Experimental Methodology: Nanocomposite Synthesis and Characterization

10.2.1 Synthesis

Both single-walled and multiwalled CNTs, of A.R. in the range of 30–1000, in a range of volume fractions (ϕ), i.e., 1–10 vol% (higher fractions rendered the composites brittle), were dispersed uniformly in a reactive ethylene terpolymer (RET) matrix through a careful blend of solution processing and mixing techniques

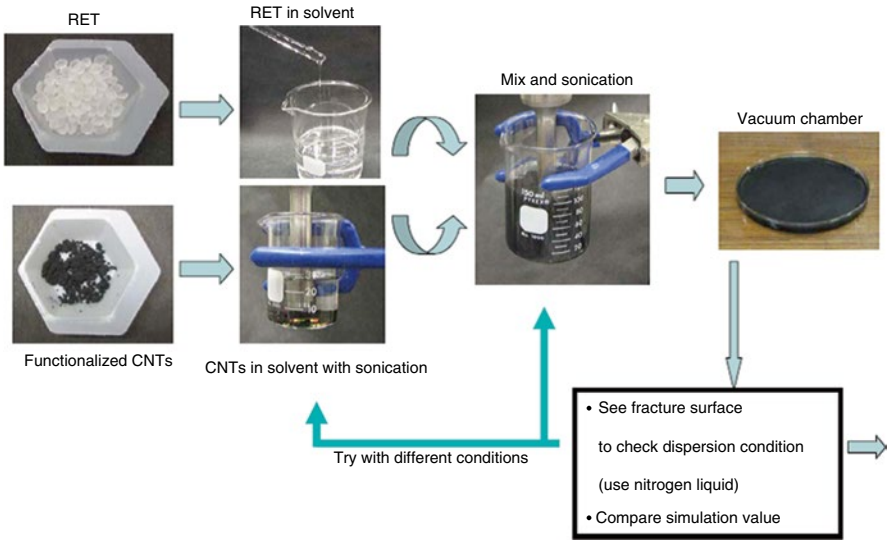

Fig. 10.2 Nanotube–polymer composite fabrication involving (from *left to right*) (1) initial raw materials: RET (reactive ethylene terpolymer) and acid-functionalized carbon nanotubes (CNTs), (2) mixing of RET and CNTs in respective solvents and solubilizing agents, (3) combined sonication of RET and CNTs in solvent mixture, and (4) subsequent drying of solvent and pressing into composite form (also see Fig. 10.5)

over – as outlined in Fig. 10.2. We use both pristine- and carboxyl-functionalized SWNTs (average diameter 1–2 nm, length 5–20 μm, 90 % purity, and density 2.1 g cm^{-3}) and multiwalled carbon nanotubes (MWNTs, average diameter 140 nm, length 5–9 μm, 90 % purity, and density 1.7 g cm^{-3}). A mixture of sulfuric and nitric acids (in a 3:1 ratio) was used both for nanotube surface functionalization, with –COOH groups, and for removing impurities [21]. Subsequently, the nanotubes were rinsed with deionized water, and then dried at 60 °C for 10 h. The MWNTs and SWNTs were then dispersed in toluene with sonication for 20 min. (It was typically seen, through atomic force microscopy (AFM) characterization, that the above procedure, including sonication, reduces the average length of the SWNTs to ~4.3 μm, with a bundle diameter ~4.8 nm, resulting in an A.R. of ~880. On the other hand, the MWNTs had an average length of 5.6 μm, with a bundle diameter ~190 nm (yielding an A.R. of ~30). The RET was then added to toluene solvent with heating, to ~60 °C for 2 h, and subsequent stirring. The nanotube dispersion was then added to the RET solution and sonicated again for ~50 min. To remove excess solvent, the mixture was stirred, at 60 °C for 3 h, and poured into glass dishes, and evacuated in vacuum (10^{-3} Torr) for 12 h. Subsequently, a hot press was used to press the composites into desired thickness. The details of the fabrication steps are shown in Fig. 10.2.

For large-scale processing, it is desirable [1] to ensure effective *mixing* and dispersion of the CNTs within the polymer. The consequent enhanced nanotube–polymer interactions, which are obtained, for example, through chemical functionalization (Fig. 10.3), enable low critical volume fractions for electrical

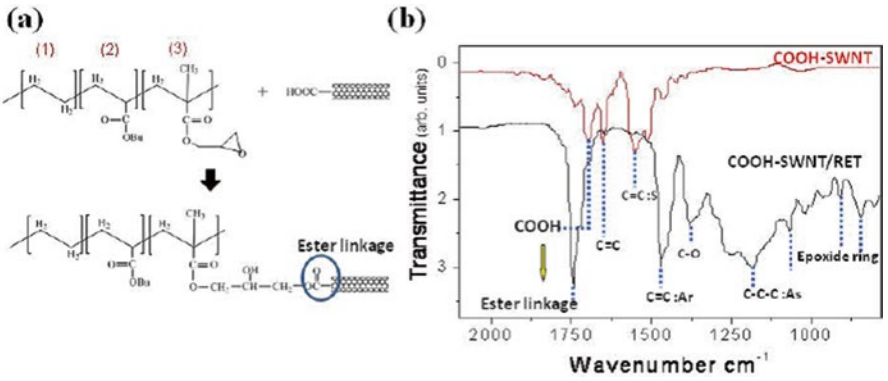

Fig. 10.3 (**a**) Schematic diagram of the reaction between functional groups on the CNTs with the epoxy groups of the reactive ethylene terpolymer (RET) constituted from (1): polyethylene, (2) methyl-methacrylate, and (3) epoxide functional groups. While (1) and (2) contribute to the mechanical robustness, (3) is used for forming ester linkages to the –COOH groups on the functionalized CNTs for enhanced bonding and dispersion, (**b**) Fourier transform infrared (FT-IR) spectrograph of the (i) bare –COOH-functionalized SWNT (COOH-SWNT) and the (ii) functionalized single-walled CNT-RET (COOH-SWNT/RET) composites. The evidence for bonding (through esterification) between the functionalized CNTs and the RET is seen through an energy upshift of the 1700 cm^{-1} peak to 1740 cm^{-1} (*Ar* aromatic, *S* symmetric, *As* antisymmetric) (Reproduced from Ref. [23] with permission)

percolation. We chose for our experiments and for this chapter a composite of CNTs and a reactive ethylene terpolymer (RET: Elvaloy 4170, density 0.94 g cm^{-3}) constituted from (1) polyethylene, (2) a polar methyl-methacrylate group, and (3) epoxide functional groups (Fig. 10.3a). While (1) and (2) contribute to the mechanical characteristics (elastomeric properties) and corrosion resistance underlying the utility of RET as a hot-melt adhesive and coating, the epoxy group has high reactivity [21] and is amenable for effective anchoring of the ring bonds with functional groups (e.g., –OH, COOH, $-NH_2$, etc.) on the carbon nanotubes. The underlying rationale then is that the epoxide ring rupture [22] on the RET would be facilitated by the –COOH groups on the functionalized nanotubes (Fig. 10.3a) [23] and then contribute to bonding between the COOH on the SWNT with the epoxy group of the RET. Fourier transform infrared (FT-IR) spectroscopy (Nicolet Magna-IRTM Spectrometer 550) was used to provide proof of covalent bonding [24] between the nanotubes and the RET and was evidenced by the energy upshift of the C = O stretch (at 1700 cm^{-1}) – due to the carboxyl group of the –COOH functionalized SWNT – to 1740 cm^{-1} due to the bonding/formation of an ester linkage.

The exact location of the functional groups would depend on the defect density on the nanotubes which can be manipulated [25]. However, if the defects are considered randomly dispersed, isotropic bonding of the nanotubes with the polymer matrix is implied and could yield uniform dispersion and mixing. While different strategies have been used for homogeneous dispersion [26, 27], it has been generally observed that covalent stabilization [28] and intimate chemical reaction [21, 24] could be beneficial for enhanced electrical conductivity and electromagnetic shielding effectiveness.

10.2.2 Characterization

Structural Characterization The uniformity of the dispersion was gauged through (a) considering the nanostructure dispersion, through scanning electron microscopy (SEM) micrographs at various length scales (1 μm – 100 μm): Fig. 10.4 [29], as well as through (b) our development and use of an image-processing algorithm for comparing the given distribution to a preferred (e.g., uniform) distribution [30].

We next monitored the electromagnetic characteristics (e.g., the shielding efficiency: SE) of the synthesized composite in the microwave frequency range (8.2–12.4 GHz: X-band) using a two-port vector network analyzer (Agilent 5242A PNA-X). The X-band is used for both civil and military communications with applications as diverse as weather monitoring, vehicular detection, and air traffic control and defense tracking [31]. The desired amount of conducting filler is generally dependent on the required SE, where $SE = 10.\log\frac{p_i}{P_t}$, , where P_i and P_t are the

Electrical and Electromagnetic Characterization Four probe measurements were used for the σ (= x/RA, evaluated from the measured electrical resistance R, with x as the contact spacing and A as the cross-sectional area) of the composites with $R < 1$ GΩ, while for higher resistance composites, two-point measurements (using the Agilent B1500A semiconductor device analyzer, with triaxial probes) were employed. Typical composite plates were 2 mm in thickness. The composites were subject to mild oxygen plasma treatment to remove surface contamination, and subsequently, 5–10 nm of Ti followed by 100 nm of Au were sputtered on for electrical contacts. For such measurements, we used samples with rectangular cross section (5 mm wide × 2 mm thick, typically). The outer current leads were separated by 25 mm, while the inner voltage leads were separated by 15 mm. For higher resistance (>1G Ω) composites, two-point measurements using the Agilent B1500A semiconductor device analyzer, with triaxial probes, were used.

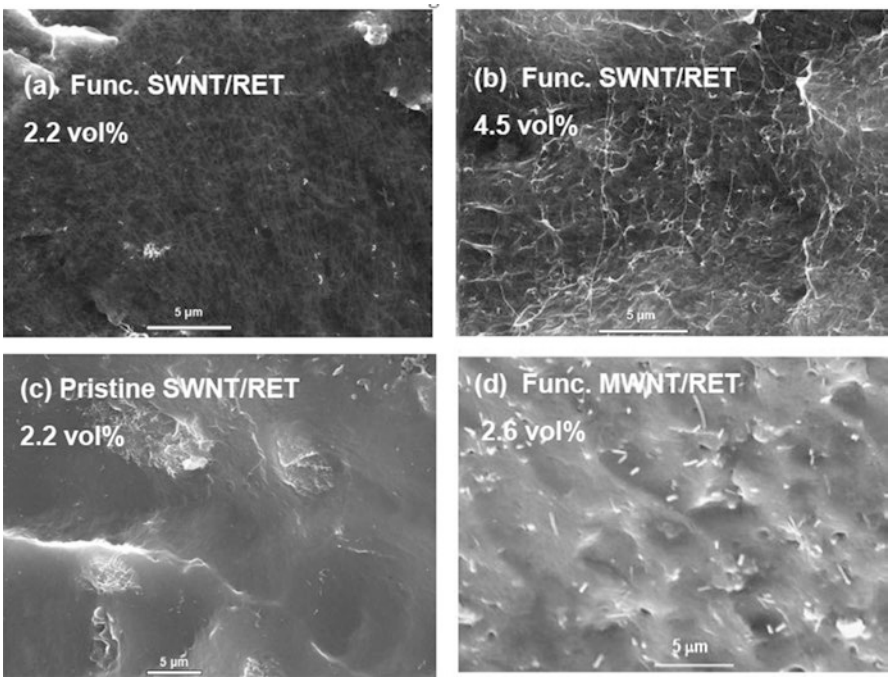

Fig. 10.4 *Uniform* dispersion of functionalized SWNTs in the RET polymer is indicated, through SEM micrographs, at (**a**) 2.2 vol% and (**b**) 4.5 vol% fractions of the SWNTs. Alternatively, (**c**) nonfunctionalized SWNTs dispersed into the polymer matrix exhibit clumping. (**d**) Functionalization was beneficial and necessary to achieve uniform dispersion of MWNTs (Reproduced from Ref. [29] with permission)

magnitudes of the incident and transmitted power densities and were measured through the network analyzer. The initial calibration was performed using the TRL (Thru-Reflect-Line) method [32]. Using the TRL method, the "Thru" measurement was first performed by connecting the two 15-cm waveguide sections directly and measures the total loss and phase delay of the setup, in the absence of the sample. For the "Reflect" calibration, an aluminum short/load was placed between the waveguide sections, while the "Line" calibration was done through the insertion of a quarter-wave section of waveguide (WR-90). The latter measurements accurately delineate the plane of the DUT (device under test) through a consideration of the reflections and other losses prevalent in the test setup including the cabling, waveguide segments, and transitions, in the absence of a sample. The scattering parameters (S_{ij}) obtained from the calibration were then used for the baseline. The total effective shielding effectiveness, SE (Tot), of the composite was composed to be the sum of the contributions due to both the reflective (R) and the absorptive (A) components [31, 33], through: $\mathrm{SE(Tot)} = \mathrm{SE(R)} + \mathrm{SE(A)}$, where SE(R) = −10 log(1 − R) and $\mathrm{SE(A)} = -10\log[31,33]\frac{\mathrm{T}}{1-\mathrm{R}}]$. The R, A, and the T (transmission) were then obtained through the determination of the S-parameters using the vector network analyzer, where $\mathrm{T} = |\mathrm{S_{21}}|^2$, $\mathrm{R} = |\mathrm{S_{11}}|^2$, and $\mathrm{A} = 1 - |\mathrm{S_{11}}|^2 - |\mathrm{S_{21}}|^2$. It was assumed that the effect of multiple reflections on the SE is negligible for our considered composite thickness [7]. The determination of S_{11} and S_{21} also enables the calculation of the relative complex permittivity ($\varepsilon = \varepsilon' + j\ \varepsilon''$) and permeability ($\mu = \mu' + j\mu''$). With respect to the results reported in article, the μ of the polymer nanocomposites was generally close to unity, i.e., $\mu' \sim 1$ and $\mu'' \sim 0$, for both linear and nonlinear, e.g., Fig. 10.10c, nanostructure-constituted composites.

Thermal Characterization Both the *cross plane* ($\kappa_\perp$) and *in-plane* ($\kappa_\parallel$) thermal conductivity values can be estimated through a steady-state method and the 3ω methodology [34], respectively. For $\kappa_\perp$ the experimental apparatus was modeled and constructed in accordance with ASTM (American Society for Testing and Materials) standards E1225 and D 5470 [35]. The accuracy of measurement was estimated to be ~3 % through comparison with standards. For the $\kappa_\parallel$ measurements, employing the 3ω technique, Ti/Au metal lines (70 μm wide and 10 mm long) which serve as both heater and thermometer were deposited on the composites, with the length scales chosen so as to approximate a narrow line heat source [36, 37] (with a ratio of the sample thickness to the metal line width of ~30) (Fig. 10.5) [38]. Using a lock-in amplifier (Stanford Research Systems: SR 830) and a Wheatstone bridge setup, alternating current, $I(\omega)$, of angular frequency ω (in the range of 0.1–1000 Hz), passed through the metal lines, induces resistance oscillations at 2ω : $R(2\omega)$, due to Joule heating ($\sim I^2R$), from which the thermal conductivity can be deduced from the third harmonic voltage, $V(3\omega)$ (= $I(\omega)R(2\omega)$). The temperature change (ΔT) was deduced using the relation [34]: $\Delta T = \frac{2V(3\omega)}{\alpha V(\omega)}$,

where α is the measured temperature coefficient of resistance of the metal line. Assuming an adiabatic boundary condition at the bottom of the composite (which is valid for a thermal penetration depth smaller than 2 mm [37]), the estimated ΔT could be then related to the thermal conductivity product, $\kappa_{\parallel} \cdot \kappa_{\perp}$, obtained through:

$$\Delta T \cong \frac{P}{2\pi\sqrt{\kappa_{\parallel}\kappa_{\perp}}}\left[-\ln(\omega)+G\right] \tag{10.3}$$

In Eq. (10.3), P is the electrical power per unit length of the heater and G is a constant. Combining the steady-state and the 3ω measurements, the individual values of $\kappa_{\parallel}$ and $\kappa_{\perp}$ were computed. Generally, the polymer covers the CNTs and the surface of the composites is not electrically conducting. We ensure that the sample and the metal lines are electrically isolated/mutually insulated at all CNT concentrations through monitoring the electrical capacitance (for any possible shorting) as well as through the variation of the temperature change/oscillation (ΔT) vs. frequency (f). While insulated samples exhibit a well-predicted variation, non-insulated samples (e.g., a bare Si substrate) exhibit irregular behavior.

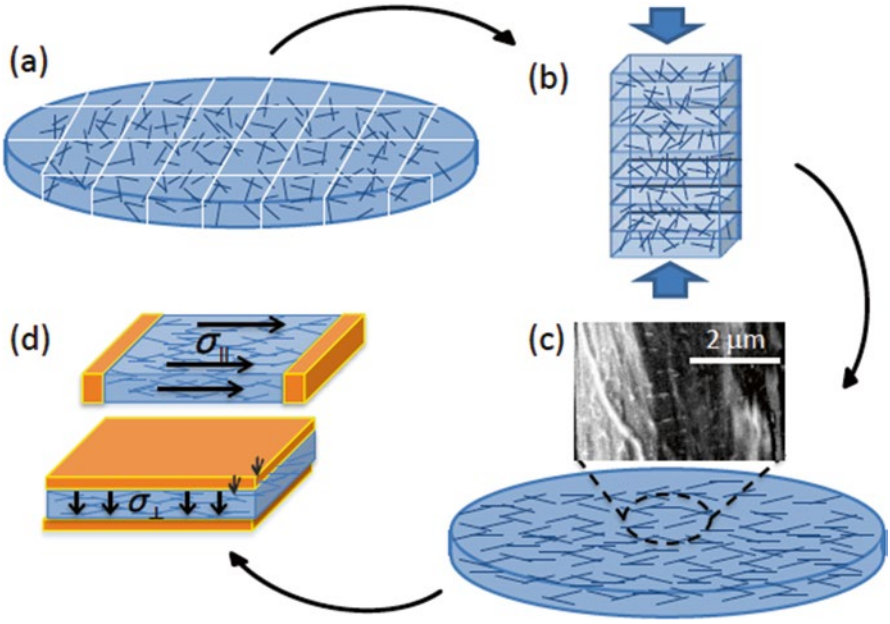

Fig. 10.5 (**a**) Blended CNT–polymer composite material was diced and (**b**) subject to repeated compressive stress. (**c**) The compressed sheet comprises CNTs preferentially aligned in the plane of the sheet. (**d**) *In-plane* (top) *and cross-plane* (bottom) electrical and thermal conductivity measurements were carried out to ascertain anisotropy and percolation (Reproduced from Ref. [38] with permission)

10.3 Experimental Observations

10.3.1 Electrical Conductivity Measurements

For measurements of the *in-plane* conductivity ($\sigma_{\|}$), the contacts were on the *either side* of the composite, while measurements of the *cross-plane* (/through thickness) conductivity ($\sigma_{\perp}$) used contacts deposited on the *top* and *bottom* of the composite – see Fig. 10.5d. Self-heating was negligible due to the low applied power. The measured $\sigma_{\|}$ and $\sigma_{\perp}$ as a function of the CNT concentration are plotted in Fig. 10.6. The variation of both $\sigma_{\|}$ and $\sigma_{\perp}$ could be fitted to power–law relations of the form [39]:

$$\sigma_{DC} \sim \begin{cases} \left(\phi_c - \phi\right)^{-s}, \phi < \phi_c \\ \left(\phi - \phi_c\right)^{t}, \phi > \phi_c \end{cases} \tag{10.4}$$

where ϕ_c is the threshold volume fraction for electrical percolation, while s and t are critical exponents. We estimated, from excluded volume percolation theory [18, 20], that for CNTs with an *A.R.* of ~35, and using Eq. (10.2), we get:

$$\phi_c\left(A.R.\right) = \frac{c}{\frac{4\pi}{3} + 2\pi\left(A.R.\right) + \frac{\pi}{2}\left(A.R.\right)^2}\left[\frac{\pi}{6} + \frac{\pi}{4}\left(A.R.\right)\right] \tag{10.5}$$

C is a constant in the range of 1.4 (for thin rods) to 2.8 (for spherical objects) [40]. Using $C \sim 1.4$, for the nanotubes, a ϕ_c of ~2.2 vol% was estimated. While the fitted ϕ_c was ~2.3 vol% for the $\sigma_{\|}$ change, a value of ~3.3 vol% was noted for the $\sigma_{\perp}$ variation. Moreover, there was a more gradual ($t \sim 4.2$ for $\sigma_{\perp}$ compared with a t value ~ 5.7 for the $\sigma_{\|}$ variation [41]) and smaller net increase. The differing values of ϕ_c for the $\sigma_{\perp}$ and $\sigma_{\|}$ indicate anisotropy, and the $\sigma_{\|}/\sigma_{\perp}$ ratio has been indicated in Fig. 10.6, e.g., the larger value for $\sigma_{\perp}$ could be tentatively understood from the greater deviation from isotropic arrangement [42, 43] of the nanotubes.

The measured $\kappa_{\perp}$ and the estimated $\kappa_{\|}$ are then plotted as a function of the CNT concentration in Fig. 10.3 along with the $\kappa_{\|}/\kappa_{\perp}$ anisotropy ratio. While a fairly linear change was noted for $\kappa_{\perp}$, a percolation-like behavior, similar to the variation in σ, was observed in $\kappa_{\|}$. We then attempted to fit the $\kappa_{\|}$ variation using expressions, analogous to Eq. (10.4), of the form:

$$\kappa_{\|} \sim \begin{cases} \left(\phi_{c,k} - \phi\right)^{-p}, \phi < \phi_{c,k} \\ \left(\phi - \phi_{c,k}\right)^{q}, \phi > \phi_{c,k} \end{cases} \tag{10.6}$$

Where, $\phi_{c,k}$ is now the threshold volume fraction for the onset of *thermal* percolation, and p and q are critical exponents in the respective regimes. We obtained, experimentally, a $\phi_{c,k}$ ~2.2 vol%, close to the theoretically expected

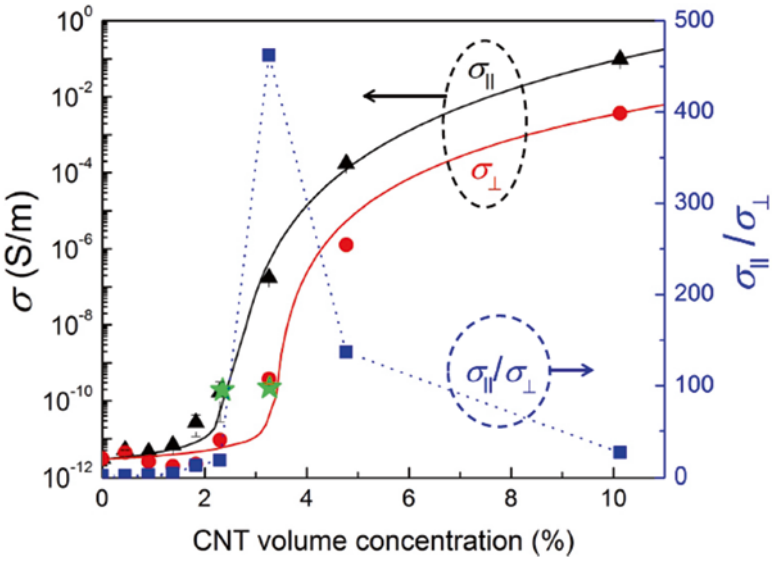

Fig. 10.6 The variation of the measured electrical conductivity with added CNT filler concentration depicted for the *in-plane* ($\sigma_{||}$) and *cross-plane* ($\sigma_{\perp}$) configurations. The anisotropy ratio, i.e., $\sigma_{||}/\sigma_{\perp}$, is indicated on the right-hand axis. The * indicates the results of the Straley model relating the product of the *electrical* resistances of the matrix and the filler to the percolation threshold (Reproduced from Ref. [38] with permission)

value, with $p \sim 0.2$ and $q \sim 0.1$. The value of the exponents in the power laws depends on the particular type of conductivity [41, 44] (i.e., electrical or thermal) as well as on the ratio of the respective conductivities of the constituent phases [45].

The concomitant larger variation in the increase of the σ (10–12 orders of magnitude for $\sigma_{\perp}$ and $\sigma_{||}$) of the CNT/polymer composites compared to the increase of the κ (50 % and 400 % for $\kappa_{\perp}$ and $\kappa_{||}$, respectively) may be attributed to the intrinsically greater range in electrical conductivity. In the former case, one has to consider the much lower electrical resistance of the CNTs compared to the polymers while there is generally a much smaller variation in κ between disparate materials. The substantial enhancement in $\kappa_{||}$ compared to $\kappa_{\perp}$ is also to be noted. We ascribe the $\kappa_{||}$ increase to the effects of percolation. Further evidence was obtained through adapting a Straley model [46] (used for determining the critical exponents for the conductivity of random resistor lattices), where the filler (R_f) and matrix (R_m) could be represented as *thermal* resistors. Through such modeling, the effective thermal conductivity at the percolation threshold fraction could be related to $R_f^u R_m^{1-u}$, where $u = p/(p+q)$, and the estimated value has been indicated through a * in Fig. 10.3. The equivalent σ values, where the filler and the matrix were represented as *electrical* resistors, have been indicated, through the * in Figs. 10.6 and 10.7.

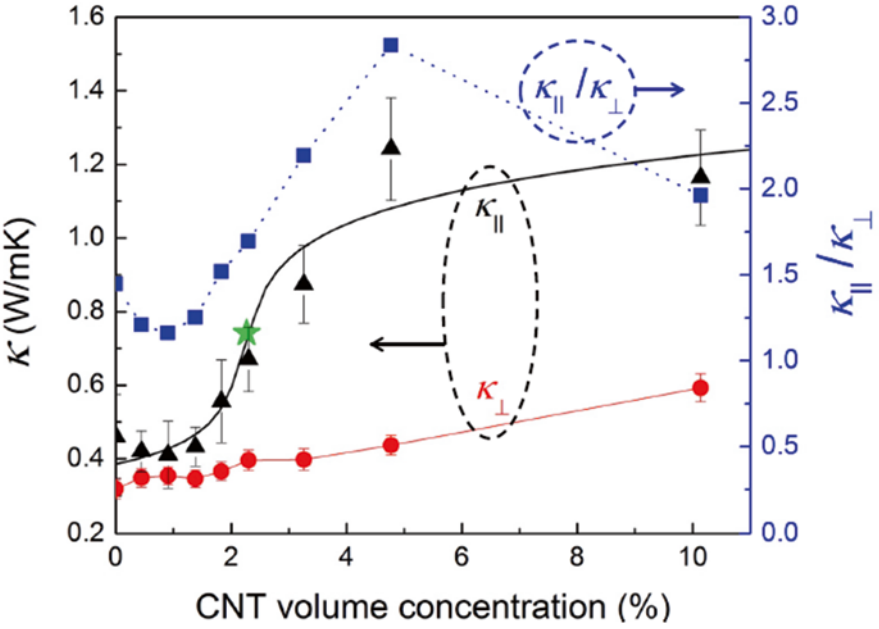

Fig. 10.7 The variation of the measured thermal conductivity with added CNT filler concentration depicted for the *in-plane* ($\kappa_{||}$) and *cross-plane* ($\kappa_{\perp}$) configurations. The anisotropy ratio, i.e., $\kappa_{||}/\kappa_{\perp}$, is indicated on the right-hand axis. The * indicates the results of the Straley model relating the product of the *thermal* resistances of the matrix and the filler to the percolation threshold (Reproduced from Ref. [38] with permission)

10.4 Modeling of Electrical and Thermal Effects in Polymeric Nanocomposites

10.4.1 The Nanotube–Polymer Interface

It has previously been concluded [47] through theoretical analysis (based on the finite element method: FEM and molecular dynamics) that the low thermal conductivity (κ) contrast (of less than 10^4) between the matrix and the filler precludes a "strong percolation threshold effect." A linear variation of the thermal conductivity with volume fraction was consequently predicted based on effective medium theory [48], which may not be valid at/near to the percolation threshold [39, 48]. While the interfacial resistance between fibers and matrix was considered, the value is orders higher than the experimentally determined values [49] (around $(7–8) \cdot 10^{-8}$ m^{2}K/W), which may have precluded the observation of percolation.

Single-walled nanotube (SWNT)–epoxy composites were also studied [50], where the SWNTs were reported where the random orientation of the nanotubes was thought to be the reason for the thermal conductivity increase. An increase in κ was reported

as a function of added SWNT weight content with a 125 % increase at 1 wt% SWNTs. The random orientation was thought to be the reason for the κ increase at a lower wt% compared to previous studies where the nanotubes were aligned perpendicular to the direction of current flow. However, the effects of interfacial resistance between the nanotubes were not considered, as was done in our group.

While an increase in the thermal conductivity in the nanotube–polymer composites was observed [51], a percolation threshold was not observed. Instead, after subtracting the contribution of the polymer matrix (PMMA in their case), the conductivity variation was fit to a scaling law. A major issue was that it does not again consider the influence of the interfacial resistance. A thermal conductivity contrast ratio of ten between the filler and the matrix was thought to be adequate for observing percolation-related effects. The fits of our data to their model equation implied a thermal conductivity of ~1.5 W/mK for the carbon nanotubes, orders of magnitude smaller than what is commonly accepted.

It has long been suspected that possibly large contribution from the CNT–polymer interface may be a determining factor for precluding the observation of percolation-like phenomena. The relative contributions of the interfacial resistance would be a function of the filler geometry and, at a given volume fraction, could be more pronounced in lower A.R. fillers. Indeed, previous work has indicated a proportionally larger κ enhancement in polymer–CNT composites through the use of larger A.R. filers [52]. It had also been previously discussed [51] that the matrix contribution could be subtracted to delineate the CNT contribution to the composite. Consequently, the difference $\Delta\kappa = \kappa_{comp} - \kappa_{poly}\ (1-\phi)$, where ϕ is the volume fraction of the filler could be studied for observing CNT filler effects. However, our data, as presented in Fig. 10.7, for $\kappa_{\perp}$, yielded a thermal conductivity of the CNTs of ~1.3 W/m K, which seemed unrealistically low. A temperature drop over the interfacial layer, which for a given heat flux would yield a proportional interfacial thermal resistance R_{int} [53], would reduce the effective composite conductivity. Such effects may be modeled through a unit cell representation, consisting of the CNT and the interface, and an equivalent circuit model, as depicted in Fig. 10.8.

10.4.2 Rationale for the Percolation Behavior in Thermal Conductivity

We further model such connectivity effects encompassing *both* electrical and thermal conductivity, through a two-dimensional model considering the total number of percolating networks in the *in-plane* and *cross-plane* directions, contributing to an equivalent resistance, $R_{\parallel}$ and $R_{\perp}$, respectively. Following the schematic in Fig. 10.9, we assume that each network is comprised of a series of nanotubes, and many such networks yield a nanostructure-contributed total resistance in the *in-plane* direction ($R_{CNT,\parallel}$). Conduction would occur simultaneously through the polymer matrix of resistance $= R_{M,\parallel}$.

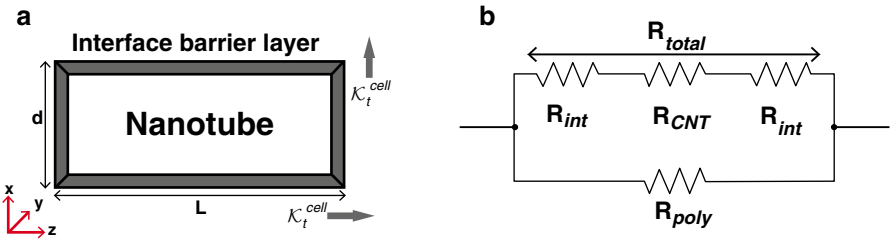

Fig. 10.8 (**a**) A unit cell of a CNT with surrounding interface layer may be used as a constituent to model a nanotube–polymer composite. (**b**) An equivalent circuit model for the thermal transport in a nanotube–polymer composite. The *top branch* indicates the two interfaces in series with a CNT, while the *bottom branch* of the network models heat flow through the polymer matrix (Reproduced from Ref. [35] with permission)

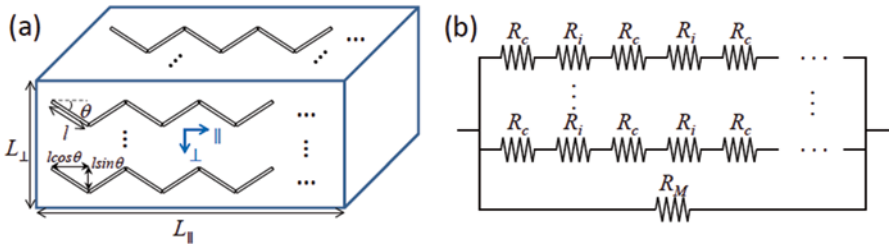

Fig. 10.9 (**a**) Modeling networks of aligned MWCNTs in the polymer matrix, and (**b**) the equivalent electrical/thermal circuit schematic with R_c as the nanotube resistance and R_i as the interfacial resistance (Reproduced from Ref. [38] with permission)

If the resistance of a single nanotube, $R_c = \dfrac{1}{A_c \sigma_c}$, with l being the average nanotube length, A_c as the cross-sectional area, and σ_c the conductivity (which should now be interpreted as an electrical: σ, *or* thermal conductivity: κ) with an interfacial resistance, R_i (in units of Ω m^2), then $R_{CNT,\parallel}$ would be:

$$\frac{1}{R_{CNT,\parallel}} = \frac{1}{\left(R_c + \dfrac{R_i \cos(\theta)}{A_c}\right)\dfrac{L_\parallel}{l\cos(\theta)}} \frac{N_c l \cos(\theta)}{L_\parallel} \tag{10.7}$$

θ is an average orientation angle between the CNT longitudinal axis and the horizontal, $L_\parallel$, is the length of the composite sample, and N_c indicates the total number of CNTs as may be estimated through the incorporated volume fraction (ϕ). The second multiplicative term on the right is a measure of the number of horizontal

networks. The $R_{M,}$ $R_{M,\|} = \dfrac{L_\|}{A_\|(1-\phi)\sigma_m}$, where $A_\|$ is the composite cross-sectional area and σ_m is the matrix (/polymer) conductivity. The *net in-plane* conductivity ($\sigma_\|$) constituted of $R_{CNT,\|}$ and $R_{M,\|}$ would be:

$$\sigma_\| = \frac{\phi\cos^2(\theta)}{\left(\dfrac{1}{\sigma_c} + \dfrac{R_i\cos(\theta)}{l}\right)} + (1-\phi)\sigma_m \tag{10.8}$$

Through similar methodology, the *net cross-plane* conductivity ($\sigma_\perp$) constituted of $R_{CNT,\perp}$ and $R_{M,\perp}$ would be:

$$\sigma_\perp = \frac{\phi\sin^2(\theta)}{\left(\dfrac{1}{\sigma_c} + \dfrac{R_i\sin(\theta)}{l}\right)} + (1-\phi)\sigma_m \tag{10.9}$$

Assuming a range of θ (i.e., $|\theta| < \theta_b$) and a constraint on the anisotropy ratio between the *in-plane* and the *cross-plane* conductivity, i.e., $\dfrac{<\sigma_\|>}{<\sigma_\perp>} \to 1$, as $\theta_b \to \pi/2$, we derive:

$$\frac{<\sigma_\|>}{<\sigma_\perp>} = \frac{\theta_b + \sin(\theta_b)\cos(\theta_b) + \left(\dfrac{1-\phi}{\phi}\right)\left(\dfrac{1}{\sigma_c} + \dfrac{2R_i\sin(\theta_b)}{l}\right)\sigma_m}{\theta_b - \sin(\theta_b)\cos(\theta_b) + \left(\dfrac{1-\phi}{\phi}\right)\left(\dfrac{1}{\sigma_c} + \dfrac{2R_i\sin(\theta_b)}{l}\right)\sigma_m} \tag{10.10}$$

In the case of electrical conductivity, due to the measured small σ_m ($\sim 3\cdot 10^{-12}$ $\Omega^{-1}m^{-1}$), we could ignore the expressions on the far right-hand side of the numerator and denominator, whence we obtain:

$$\frac{<\sigma_\|>}{<\sigma_\perp>} \cong \frac{\theta_b + \sin(\theta_b) + \cos(\theta_b)}{\theta_b - \sin(\theta_b) + \cos(\theta_b)} \tag{10.11}$$

Inserting the corresponding $\sigma_\perp$ and $\sigma_\|$ from Fig. 10.6, at $\phi > \phi_c$ (i.e., at 3.3 vol%, 4.8 vol%, and 10 vol%), we find the θ_b values as 4.6°, 8.5°, and 19°, respectively. These values were then used for interpreting the thermal conductivity variation vis-à-vis the percolation-like behavior of $\kappa_\|$.

However, for modeling the thermal conductivity anisotropy, $\dfrac{<\kappa_\|>}{<\kappa_\perp>}$ the matrix conductivity, κ_m (~ 0.3 W/mK) cannot be neglected, and terms involving the thermal interfacial resistance (R_i^{th} in units of m^2K/W) would remain:

$$\frac{< k_{\parallel} >}{< k_{\perp} >} = \frac{\theta_b + \sin(\theta_b)\cos(\theta_b) + \left(\frac{1-\phi}{\phi}\right)\left(\frac{1}{k_c} + \frac{2R_i^{th}\sin(\theta_b)}{l}\right)k_m}{\theta_b - \sin(\theta_b)\cos(\theta_b) + \left(\frac{1-\phi}{\phi}\right)\left(\frac{1}{k_c} + \frac{2R_i^{th}\sin(\theta_b)}{l}\right)k_m} \quad (10.12)$$

Along with the corresponding $\kappa_{\parallel}$ and $\kappa_{\perp}$ from Fig. 10.3, the θ_b values obtained previously were inserted into Eq. (10.12), to consistently estimate a κ_c (~240 W/mK) and an R_i^{th} (~7×10^{-8} m^2K/W). Such estimates are in excellent accord with previous evaluations of nanotube interfacial thermal resistance [49] and further indicate a significant modulation of the thermal conductivity of nanostructures when they are dispersed into a matrix. While previous reports [47, 50] indicated a lack of percolation due to (i) the relatively low thermal conductivity contrast and (ii) the interfacial resistance between the conducting nanostructure and the matrix (polymer), we have then seen that such characteristics are indeed possible.

We have then shown that it is feasible to adapt a synthesis methodology, e.g., using stacking of nanotube–polymer composite sheets, facilitating percolation-like behavior. We surmise that an increased nanotube A.R., enhanced from that presented here, would yield a corresponding exponential increase of the thermal conductivity. Moreover, a greater degree of isotropy may imply a lower percolation threshold as indicated in Fig. 10.7. Additionally, previous work did not consider the effects of interfacial resistance between the nanotubes and the matrix, the effects of which have been considered in much more detail here.

In summary, we have shown, through detailed experiments and modeling, evidence of anisotropy in both the electrical and thermal conductivity in nanotube–polymer composites. A power–law relation for the thermal conductivity has been indicated, indicative of percolation-like behavior, with implications for tunable thermal conductivity and thermal switching.

10.4.3 Effect of Nonlinear Filler Geometry: Does a Change of Morphology Imply Enhanced Electrical and Electromagnetic Characteristics?

A change in structure and morphology, at the nanoscale, could have a profound influence on macroscopic characteristics, through the paradigm [54] of "function follows shape." For example, in the case of carbon-based nanostructures, nonlinear and coiled carbon nanotubes (CCNTs) [55, 56]/nanowires (CNWs) have been proposed for a variety of applications such as electrical inductors [57], spring-like mechanical elements for energy dissipation [58], novel electronic devices incorporating alternating metallic and semiconductor junctions [59], etc. Additionally, if the degree/extent of coiling can be changed, e.g., through applying mechanical stress, such behavior could form the basis of an electrostrictive actuator [60].

10.4.3.1 Synthesis of CCNTs and CCNT-Based Polymer Nanocomposites

Many of the enhanced attributes of nonlinear nanostructures may arise from the availability of other length scales, e.g., such as the projected length (L_{proj}) and the coil diameter (d_{coil}), *in addition* to the fully extended length (L_{ext}) and the constituent individual CNT diameter (d_{CNT}). For example, a modulation of the electromagnetic characteristics may be expected through a consideration of the length/diameter A.R. of the nanostructures. For instance, the depolarization electric field is enhanced [61] with a smaller A.R. and modifies the effective dielectric permittivity. This implies, for a given electric displacement, a higher ε for the CCNTs when the projected/coiled length L_{proj} and coil diameter d_{coil} is considered, compared to the use of L_{ext} and d_{CNT}. The latter lengths should be used for the A.R. of linear nanostructures, such as SWNTs, dispersed in polymer matrices. Concomitantly, characteristics intrinsic and unique to the coiled structure, e.g., the capacitive couplings between alternate windings of the CCNT (see, e.g., Fig. 10.13), which is absent in a single-walled CNT, may afford enhanced utilities in electromagnetic shielding efficiency.

At the very outset, the formation of CCNTs was explained as due to a combination of (1) specific metal catalyst (e.g., In/Sn)–nanotube interactions, as well as (2) entropy-driven interactions. More specifically, as In and Sn have large wetting angles of ~160° with respect to the graphitic surface [55, 56] (note that commonly used metal catalysts for the growth of linear CNTs such as Fe, Co, and Ni have wetting angles of <75°), it was hypothesized that the former promote coiling of the CNTs, so as to avoid contact and reduce the surface-free energy. Alternatively, a greater overlap between alternate segments, obtained through coiling of the nanotube, could increase the entropy of the ambient. It was then estimated that the nonwetting behavior of In/Sn could provide a large enough driving force, which could overcome the bending energy.

The CCNT fillers were uniformly dispersed into a reactive ethylene terpolymer (RET: Elvaloy 4170) polymer matrix – as previously discussed [62] (See Sect. 10.2.1 and Figs. 10.2 and 10.4). Linear CNT (both single and multiwalled)/RET composites were also synthesized for comparison. While the L_{proj} and the coil diameter d_{coil} were ~15 μm and ~0.5 μm, respectively – see Fig. 10.10c, the L_{ext} was recorded to be ~50 μm and the d_{CNT} was ~20 nm. Subsequently, the dc electrical conductivity (σ_{DC}) was measured on the composite samples through four-point electrical measurements. The *S*-parameters (S_{ij}) were measured in the microwave frequency ($f = \omega/2\pi$) range (8.2–12.4 GHz: X-band). The determination of S_{11} and S_{21} enables the calculation of the complex permittivity ($\varepsilon = \varepsilon' + j\,\varepsilon''$) and permeability ($\mu = \mu' + j\mu''$), where $j = \sqrt{-1}$, along with the reflection and transmission coefficients, as previously discussed in Sect. 10.2.2.

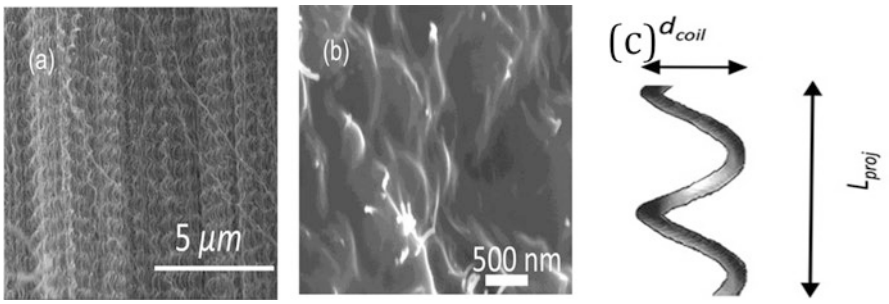

Fig. 10.10 Scanning electron microscope (SEM) micrographs of synthesized (**a**) coiled carbon nanotubes (CCNTs) on a Si substrate, and (**b**) uniformly dispersed into a RET polymer matrix. (**c**) The CCNT is defined with an average projected length (L_{pro}) and the coil diameter (d_{coil}) and is constituted from individual CNTs of average diameter: d_{CNT} and a fully extended length (L_{ext}) (Reproduced from Ref. [62] with permission)

10.4.3.2 DC Conductivity Measurements

DC conductivity (σ_{DC}) measurements were used to first ensure that the σ_{DC} was similar at ~10^{-3} $\Omega^{-1}m^{-1}$ for the polymer composites constituted from CCNTs and single-walled CNTs, for appropriate comparison. A percolation-like behavior in the variation of the σ with CCNT volume fraction (Fig. 10.11a) was observed and fit to an expression of the form: $\sigma \sim \sigma_0 \left(p - p_c\right)^{\beta}$, where p_c is the percolation threshold volume fraction (p) and β, a critical exponent. σ_0 is a constant for a particular filler–polymer combination. The obtained values of p_c (~ 0.1 %) and β (~ 4.2) are appropriate for a thick film resistor-like configuration with elongated fibers [7]. The comparison was made between the CCNTs and the single-walled CNTs dispersed in polymers, as we found that the use of multiwalled CNTs did not significantly enhance the composite electrical properties.

10.4.3.3 Dielectric Constant Measurements

A monotonic variation of the ε' and ε'' with increasing CCNT content was seen (Fig. 10.11b, c). As seen here and also later in Fig. 10.12, the CCNT–polymer nanocomposites exhibit enhanced electromagnetic properties, e.g., a larger dielectric constant, ε', indicating increased polarizability compared to the use of pristine/non-functionalized CNTs. Also shown in the graphs, for comparison, is the behavior of functionalized SWNTs where the superiority of CCNTs, with increased ε, is evident. The ε increase could be related to the CCNT structure, where pentagons on the outer/convex side of the coil (see as well as Refe(c)) and heptagonal structures on the inner/concave side are invoked to accommodate for the curvature: The change in the interactions of the $\pi-$orbitals in the non-hexagonal structures could then result in a charge transfer from the concave to the convex side, inducing local dipole

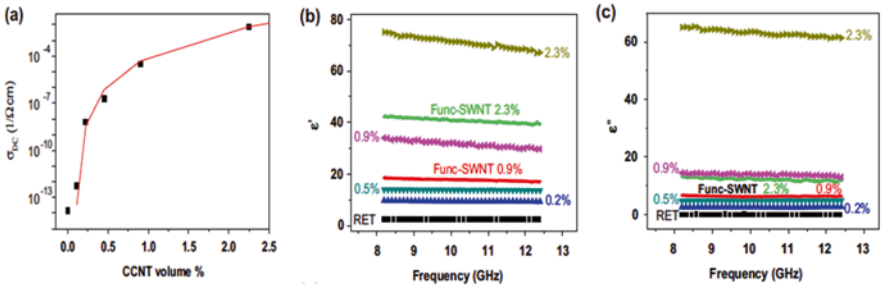

Fig. 10.11 (**a**) The DC electrical conductivity (σ_{DC}) of the CCNT-constituted polymer composites was observed and fit to a percolation-like behavior. The X-band frequency variation of the (**b**) real (ε') and (**c**) imaginary (ε'') permittivity of CCNT-constituted composites (numbers indicate % volume fractions) was much larger compared to single-walled CNTs (SWNTs) (Reproduced from Ref. [62] with permission)

moments [63]. The orbital rehybridization along with the multi-shell characteristics of multiwalled CNTs have also been implicated in curvature-induced interfacial electric fields [64]. Additionally, the smaller projected length A.R. (i.e., L_{proj}/d_{coil} for the CCNT, ~30) in contrast with that of a SWNT (typically ~ 1000) would also imply a larger depolarization electric field. Such characteristics may translate to a larger electromagnetic interference (EMI) shielding efficiency for the CCNT-based composites. We also found that the use of multiwalled CNTs/nonfunctionalized SWCNTs was not useful for enhancing the electrical properties, yielding ε' and ε'' close to those of RET. The increase in ε' with increased SWNT volume fraction may also be ascribed to the formation of an increased number of SWNT–RET dielectric–SWNT capacitors, while the increase in ε'' (= Re $\left[\frac{\sigma}{\omega\varepsilon_0}\right]$), where ε_0 (= $8.854 \bullet 10^{-12}$ C^2/Nm^2) is the permittivity of free space, may be due to an increased σ at increased SWNT filling fractions. Additionally, enhancement of ε'', through dielectric loss, could be related to interfacial polarization at the grain boundary and the formation of an interphase region at the CNT–RET interface.

10.4.3.4 AC Conductivity Measurements (Beyond Percolation Theory?)

Generally, the ac conductivity, σ_{AC} (computed through $\sigma_{AC} = \omega\varepsilon_o\varepsilon''$, where $\omega = 2\pi f$), as well as the related EMI shielding efficiency would be specific to the CNT geometry: see Fig. 10.11b, c. To this end, we have discovered that alternative electrical conduction mechanisms, which go beyond the conventional percolation theory model, are feasible and sometimes necessary.

We interpret σ_{AC} later, through the ε' and ε'' values determined from the *S*-parameter measurements. As previously considered in Fig. 10.11b, c, and again in Fig. 10.12, the ε' and ε'' of the CCNT-based composites was larger, by approximately a factor of two, compared to SWCNT-dispersed composites (Fig. 10.12a).

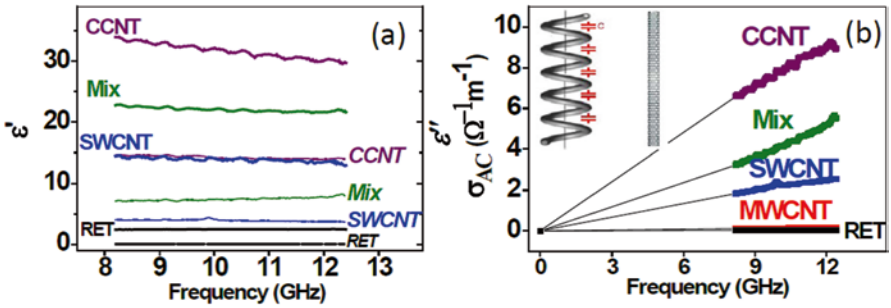

Fig. 10.12 (**a**) The X-band frequency variation of the real (ε') – *left axis* and imaginary (ε'') – *right axis* permittivity of the polymer composites, with CCNT (coiled CNTs). Mix (a mixture of coiled and SWCNT (single-walled CNTs) fillers compared to RET polymer matrix (with a nominal permittivity ~2.4 + *j* 0.054). The higher ε for the CCNTs arises from a smaller A.R. ($=L_{proj}/d_{coil}$) of ~33, with a decreased depolarization field, compared to a much larger A.R. ($=L_{ext}/d_{CNT}$), i.e., ~1000, for the linear SWCNT structures dispersed in the polymers. (**b**) The frequency variation of σ_{AC} of the CNT composites, with CCNTs, Mix, SWCNTs, and multiwalled CNT (MWCNT) fillers compared with the RET polymer. The *inset* shows capacitive coupling between alternate windings of the CCNT, which is absent in a SWCNT (Reproduced from Ref. [62] with permission)

In the figure is also shown the corresponding variation for a mixture of linear and coiled CNTs (with an approximately 1:1 distribution) – which was observed to be intermediate to the CCNTs and SWCNTs. The increased ε' in the coiled CNTs over linear CNTs (SWCNTs/MWCNTs) was tentatively explained on the basis of enhanced capacitive coupling between alternate windings/segments of the coil in the former – see Fig. 10.12b, inset, which effectively increases the ε'. The relatively weak f dependence of ε'' could be due to a smaller volume % of CNTs; a greater variation was found, for example, with higher loading/vol%. The higher ε for the CCNTs arises from a smaller A.R. ($=L_{proj}/d_{coil}$) of ~33, with a decreased depolarization field, compared to a much larger A.R. ($=L_{ext}/d_{CNT}$), i.e., ~1000, for the linear SWCNT structures dispersed in the polymers.

The larger σ_{AC} of the CCNT-based materials may be rationalized based on the formation of parallel resistors and capacitors in the composite, as considered in Fig. 10.12b. In such a model, the CNTs contribute to the electrical resistance, while the polymer matrix serves as the capacitor dielectric and contributes to the ac conductance. The increased number of parallel resistors and capacitors in the CCNTs due to the coiled structure (Fig. 10.13), compared to linear CNTs, decreases the overall resistance and capacitive impedance, $X_c = |1/2\pi fC|$, of the composite due to the availability of several alternative electrical conduction paths. Here, as the SWNT concentration in the matrix increases, equivalent to an increasing number of parallel resistors and capacitors (constituted from CNT–polymer dielectric–CNT), the net resistance and X_c could decrease due to the availability of alternative electrical conduction paths. Using a simple parallel plate capacitor model – as in the inset to Fig. 10.12b, we estimated a capacitance/unit area of ~0.1 mF/m^2 with a coil pitch of ~1 μm. We estimate from the CCNT geometry and sample volume (with ~10^{12} nanocoils) a substantial capacitance, which leads to a low X_c and large σ_{AC}. Such

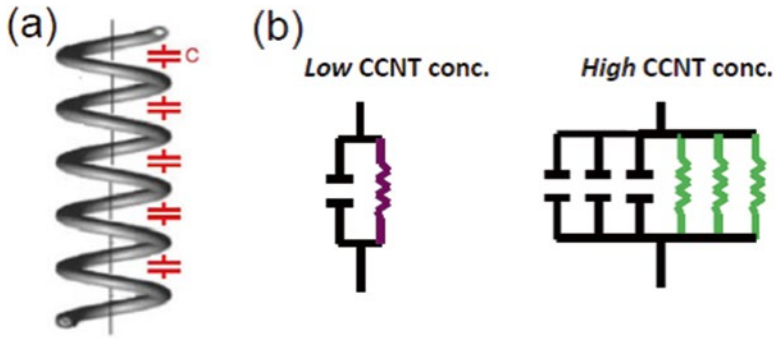

Fig. 10.13 (**a**) While there could be capacitive coupling, i.e., C, as noted between alternate windings of an individual CCNT, (**b**) increasing the CCNT concentration (ϕ_{CNT}) would be equivalent to increasing the number of parallel resistors and capacitors. The net resistance and capacitive impedance, $X_c = \left|1/2\pi fC\right|$, could decrease due to the availability of several alternative electrical conduction paths (Reproduced from Ref. [62] with permission)

effects may be less significant in composites constituted from linear CNTs. As the CNTs are much smaller than the incident EM wavelengths, it is unlikely that the chirality would affect the magnetic characteristics [57, 65–67]. Consequently, the μ of the CCNT-constituted polymer nanocomposites was generally close to unity, i.e., $\mu' \sim 1$ and $\mu'' \sim 0$.

In summary, *both* σ_{DC} and σ_{AC} would increase with increasing filler content, with a diminishing difference at higher *f*. We have noted, for example, (see, for example, Fig. 10.12b, that (1) σ_{AC} varies *linearly* with ϕ_{CNT}, (2) $\sigma_{AC} > \sigma_{DC}$, even below the ϕ_c, and, that (3) σ_{DC} approaches σ_{AC} at high (> 4 vol%) filling fraction of the SWNTs. Such observations indicate a frequency-dependent mechanism of electrical conduction. However, many details are missing from the invoked supporting models, e.g., (a) the values of *R* and *C* that can be used to fit the experimental data, (b) effective ε values of the equivalent capacitor, (c) the dependence of the *R* and *C* on CNT concentration, etc. Consequently, the validity of such models, through assignment of suitable parameter values, should be a major topic of investigation.

10.4.3.5 Electromagnetic Shielding Efficiency

As previously discussed, in Sect. 10.2.2, we probed the components of the total EMI shielding efficiency, SE (*T*) through decomposition into contributions from reflection, SE(*R*) and absorption, and SE (*A*), by a consideration of their frequency (*f*) dependence. We notice that at low (/high) CNT filling fractions, the SE decreases (/increases) with *f* while exhibiting a minimum at intermediate filling fractions (e.g., ~2.3 vol%). This is further illustrated through Fig. 10.14a, b for low (0.5 vol%) and high (4.5 vol%) CNT loading. One could understand such variation by considering the total SE(*T*) of the composite to be the sum of the individual contributions

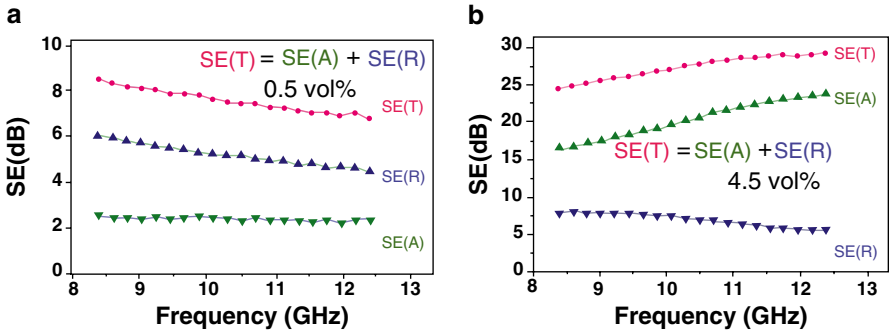

Fig. 10.14 (**a**) Reflective losses dominate the total SE for low (~ 0.5 vol%) nanotube filling fractions, while (**b**) the absorption is more important at larger (~ 4.5 vol%) CNT fractions (Reproduced from Ref. [23] with permission)

through SE (*T*) = SE (*R*) + SE(*A*), where SE(*R*) = −10 log(1-*R*) and SE(*A*) = −10 log $\left[\frac{T_r}{1-R}\right]$. The *R*, *A*, and the *Tr* (transmission) were obtained through the determination of the *S*-parameters, for example, it was seen generally that SE(*R*) > SE (*A*) for low volume % CNT loading (Fig. 10.14a), while SE(*A*) > SE(*R*) for higher filling fractions (Fig. 10.14b). A preliminary explanation, and fit to experiment, where SE (*R*) *decreases* with *f* while SE (*A*) *increases* with *f* could be obtained by positing that SE (*R*) varies as ~$\log_{10}\left(\frac{\sigma}{f}\right)$ and SE (*A*), varies as $t\sqrt{f\sigma}$. The determination of the volume fraction at which crossover from reflection-dominated shielding to absorption-dominated shielding occurs would be of interest. Moreover, the enhanced EMI shielding could again be correlated to a greater L_{ext}/d_{CNT} aspect ratio, while higher ε would arise from a smaller L_{proj}/d_{coil}, as previously considered. Such novel attributes would be possible through nonlinear structures.

10.5 Conclusions

This chapter has probed many frontier issues related to the electrical and electromagnetic characteristics coupled with thermal conductance attributes of nanostructure-infiltrated polymer composites. These include seminal observations of percolation of thermal conductivity and frequency-dependent effects correlated to linear and nonlinear nanostructures. However, as would be typical to any real scientific investigation [68], there are many issues that still remain to be considered, explored, and understood. For example, while percolation theory may be applied (strictly only close to the percolation threshold), it is apparent that the average properties of a composite may deviate considerably from the law of mixtures. Alternative mixing models incorporating Maxwell–Wagner or Hashin–Shtrikman-type theories [69] for determining bounds on the characteristic property variation need to be

probed. Additionally, the variation and characterization of the nanostructure–polymer interfacial thickness and conductivity still represents a formidable barrier and obstacle for rationalizing observed characteristics. The extent to which the nanostructure–polymer mixtures can be considered an effective electrical medium [70] or an effective thermal medium [71, 72] would also be relevant to such investigations and seems to depend both on the composite synthesis (as indicated in Fig. 10.5) as well as the use of such considerations.

While such fundamental studies are imperative, to keep the excitement alive through forays into new fields, we have also indicated novel avenues of exploration related to the study of nonlinear structures, such as coiled CNTs. Such exercises may pave the way to explore new paradigms in polymer composites, where function could follow structure. To provide examples of study and application, analogy to the optical rotation concepts prevalent in organic chemistry [73] may indicate polarization sensitivity for the coiled CNTs and the use of the constituted nanocomposites in optical applications. The harmonious combination of fundamental studies coupled with possible new applications would keep the field of nanostructure–polymer composites relevant and vibrant.

Acknowledgments The support from the National Science Foundation (Grant CMMI 1246800) is acknowledged.

References

1. Breuer O, Sundararaj U (2004) Big returns from small fibers: a review of polymer/carbon nanotube composites. Polym Compos 25:630–645
2. Ajayan P, Schadler LS, Giannaris C, Rubio A (2000) Single-walled carbon nanotube-polymer composites: strength and weakness. Adv Mater 12:750–753
3. Rashid ESA, Ariffin K, Akil HM, Kooi CC (2008) Mechanical and thermal properties of polymer composites for electronic packaging application. J Reinf Plast Compos 27:1573–1584
4. Thomas S, Joseph K, Malhotra SK, Goda K, Sreekala MS (2013) Polymer composites. Wiley-VCH, Weinheim
5. Chung DDL (2001) Electromagnetic interference shielding effectiveness of carbon materials. Carbon N Y 39:279–285
6. Ci L, Suhr J, Pushparaj V, Zhang X, Ajayan PM (2008) Continuous carbon nanotube reinforced composites. Nanoletters 8:2762–2766
7. Li N, Huang Y, Du F, He X, Lin X, Gao H, Ma Y, Li F, Chen Y, Eklund PC (2006) Electromagnetic interference (EMI) shielding of single-walled carbon nanotube epoxy composites. Nanoletters 6:1141–1145
8. Bigg DM, Stutz DE (1983) Plastic composites for electromagnetic interference shielding applications. Polym Compos 4:40–46
9. Liu Z, Bai G, Huang Y, Ma Y, Du F, Li F, Guo T, Chen Y (2007) Reflection and absorption contributions to the electromagnetic interference shielding of single-walled carbon nanotube/polyurethane composites. Carbon N Y 45:821–827
10. Liu Z, Bai G, Huang Y, Li F, Ma Y, Guo T, He X, Lin X, Gao H, Chen Y (2007) Microwave absorption of single-walled carbon nanotubes/soluble cross-linked polyurethane composites. J Phys Chem C 111:13696–13700

11. Hoefer M, Bandaru PR (2009) Determination and enhancement of the capacitance contributions in carbon nanotube based electrode systems. Appl Phys Lett 95:183108
12. Hughes M, Schwarz JA, Contescu CI, Putyera K (2004) Carbon nanotube-conducting polymer composites in supercapacitors. In: Dekker encyclopedia of nanoscience and nanotechnology. Taylor & Francis, London, pp 447–459
13. Halpin JC, Kardos JL (1976) The Halpin-Tsai equations: a review. Polym Eng Sci 16:344–352
14. Bandaru PR (2007) Electrical properties and applications of carbon nanotube structures. J Nanosci Nanotechnol 7:1239–1267
15. Peigney A, Laurent C, Flahaut E, Basca RR, Rousset A (2001) Specific surface area of carbon nanotubes and bundles of carbon nanotubes. Carbon N Y 39:507–514
16. Ni C, Chattopadhyay J, Billups WE, Bandaru PR (2008) Modification of the electrical characteristics of single wall carbon nanotubes through selective functionalization. Appl Phys Lett 93:243113
17. Berber S, Kwon Y-K, Tomanek D (2000) Unusually high thermal conductivity of carbon nanotubes. Phys Rev Lett 84:4613–4616
18. Balberg I, Anderson CH, Alexander S, Wagner N (1984) Excluded volume and its relation to the onset of percolation. Phys Rev B 30:3933–3943
19. Balberg I (1985) 'Universal' percolation-threshold limits in the continuum. Phys Rev B 31:4053–4055
20. Pfeifer S, Park SH, Bandaru PR (2010) Analysis of electrical percolation thresholds in carbon nanotube networks using the Weibull probability distribution. J Appl Phys 108:24305
21. Tasis D, Tagmatarchis N, Bianco A, Prato M (2006) Chemistry of carbon nanotubes. Chem Rev 106:1105–1136
22. Antoniotti S, Antonczak S, Golebiowski J (2004) Acid-catalyzed oxidative ring-opening of epoxide by DMSO. Theoretical investigation of the effect of acid catalysts and substituents. Theor Chem Acc 112:290–297
23. Park S-H, Theilmann P, Asbeck P, Bandaru PR (2010) Enhanced electromagnetic interference shielding through the use of functionalized carbon nanotube-reactive polymer composites. IEEE Trans Nanotechnol 9:464–469
24. Bekyarova E, Thostenson ET, Yu A, Itkis ME, Fakhrutdinov D, Chou T-W, Haddon RC (2007) Functionalized single-walled carbon nanotubes for carbon fiber-epoxy composites. J Phys Chem C 111:17865–17871
25. Nichols J, Deck CP, Saito H, Bandaru PR (2007) Artificial introduction of defects into vertically aligned multiwalled carbon nanotube ensembles: application to electrochemical sensors. J Appl Phys 102:64306
26. Lin Y, Meziani MJ, Sun Y-P (2007) Functionalized carbon nanotubes for polymeric nanocomposites. J Mater Chem 17:1143–1148
27. Haggenmueller R, Fischer JE, Winey KI (2006) Single wall carbon nanotube/polyethylene nanocomposites: nucleating and templating polyethylene crystallites. Macromolecules 39:2964–2971
28. Bryning MB, Islam MF, Kikkawa JM, Yodh AG (2005) Very low conductivity threshold in bulk isotropic single-walled carbon nanotube-epoxy composites. Adv Mater 17:1186–1191
29. Park S-H, Thielemann P, Asbeck P, Bandaru PR (2009) Enhanced dielectric constants and shielding effectiveness of, uniformly dispersed, functionalized carbon nanotube composites. Appl Phys Lett 94:243111
30. Pfeifer S, Bandaru PR (2014) A methodology for quantitatively characterizing the dispersion of nanostructures in polymers and composites. Mater Res Lett, 2(3):166–175
31. Pozar DM (1998) Microwave engineering, 2nd edn. Wiley, New York
32. Engen GF, Hoer CA (1979) 'Thru-reflect-line': an improved technique for calibrating the dual six-port automatic network analyzer. IEEE Trans Microwave Theory Tech MTT-27:987–993
33. Kim HM, Kim K, Lee CY, Joo J, Cho SJ, Yoon HS, Pejakovic DA, Yoo JW, Epstein AJ (2004) Electrical conductivity and electromagnetic interference shielding of multiwalled carbon nanotube composites containing Fe catalyst. Appl Phys Lett 84:589–591

34. Cahill DG (1990) Thermal conductivity measurement from 30 to 750K: the 3w method. Rev Sci Instrum 61:802–808
35. Kapadia RS, Louie BM, Bandaru PR (2013) The influence of carbon nanotube aspect ratio on thermal conductivity enhancement in nanotube–polymer composites. J Heat Transf 136(1):011303
36. Carslaw HS, Jaeger JC (1986) Conduction of heat in solids, 2nd edn. Oxford University Press, New York
37. Borca-Tasciuc T, Kumar AR, Chen G (2001) Data reduction in 3w method for thin-film thermal conductivity determination. Rev Sci Instrum 72:2139–2147
38. Kim B-W, Park S-H, Kapadia RS, Bandaru PR (2013) Evidence of percolation related power law behavior in the thermal conductivity of nanotube/polymer composites. Appl Phys Lett 102(24):243105
39. Kirkpatrick S (1973) Percolation and conduction. Rev Mod Phys 45:574–588
40. Celzard A, McRae E, Deleuze C, Dufort M, Furdin G, Mareche JF (1996) Critical concentration in percolating systems containing a high-aspect ratio filler. Phys Rev B 53:6209–6214
41. Stauffer D, Aharony A (2003) Introduction to percolation theory, 2nd edn. Taylor and Francis, London
42. White SL, DiDonna BA, Mu M, Lubensky TC, Winey KL (2009) Simulations and electrical conductivity of percolated networks of finite rods with various degrees of axial alignment. Phys Rev B 79:24301
43. Du F, Fischer JE, Winey KL (2005) Effects of nanotube alignment on percolation conductivity in carbon nanotube/polymer composites. Phys Rev B 72:121404(R)
44. Foygel M, Morris RD, Anez D, French S, Sobolev V (2005) Theoretical and computational studies of carbon nanotube composites and suspensions: electrical and thermal conductivity. Phys Rev B 71:104201
45. Shklovskii BI, Efros AL (1984) Percolation theory. In: Electronic properties of doped semiconductors. Springer, New York
46. Straley JP (1977) Critical exponents for the conductivity of random resistor lattices. Phys Rev B 15:5733–5737
47. Shenogina N, Shenogin S, Xue L, Keblinski P (2005) On the lack of thermal percolation in carbon nanotube composites. Appl Phys Lett 87:133106
48. Landauer R (1978) Electrical conductivity in inhomogeneous media. AIP Conf Proc 40:2–45
49. Huxtable ST, Cahill DG, Shenogin S, Xue L, Ozisik R, Barone P, Usrey M, Strano MS, Siddons G, Shim M, Keblinski P (2003) Interfacial heat flow in carbon nanotube suspensions. Nat Mater 2:731–734
50. Biercuk MJ, Llaguno MC, Radosavljevic M, Hyun JK, Johnson AT, Fischer JE (2002) Carbon nanotube composites for thermal management. Appl Phys Lett 80:2767–2769
51. Bonnet P, Sireude D, Garnier B, Chauvet O (2007) Thermal properties and percolation in carbon nanotube-polymer composites. Appl Phys Lett 91:201910
52. Deng F, Zheng Q-S, Wang L-F, Nan C-W (2007) Effects of anisotropy, aspect ratio, and nonstraightness of carbon nanotubes on thermal conductivity of carbon nanotube composites. Appl Phys Lett 90:021914
53. Swartz ET, Pohl RO (1989) Thermal boundary resistance. Rev Mod Phys 61:605–668
54. Bandaru PR, Rao AM (2007) Electrical Applications for Novel Carbon Nanotube Morphologies: Does function follow shape? J Mater (Special Issue Nanomater Electron Appl) 7:33–38
55. Wang W, Yang K, Gaillard J, Bandaru PR, Rao AM (2008) Rational synthesis of helically coiled carbon nanowires and nanotubes through the use of tin and indium catalysts. Adv Mater 20(1):179–182
56. Bandaru PR, Daraio C, Yang K, Rao AM (2007) A plausible mechanism for the evolution of helical forms in nanostructure growth. J Appl Phys 101:094307
57. Faraby HM, Rao AM, Bandaru PR (2013) Modeling high energy density electrical inductors operating at THz frequencies based on coiled carbon nanotubes. IEEE Electron Device Lett 34(6):807–809

58. Daraio C, Nesterenko V, Jin S, Wang W, Rao AM (2006) Impact response by a foam like forest of coiled carbon nanotubes. J Appl Phys 100:64309
59. Castrucci P, Scarselli M, De Crescenzi M, El Khakani MA, Rosei F, Braidy N, Yi J-H (2004) Effect of coiling on the electronic properties along single-wall carbon nanotubes. Appl Phys Lett 85:3857–3859
60. Newnham RE (2005) Properties of materials. Oxford University Press, Oxford, UK
61. Landau L, Lifshitz EM, Pitaevskii LP (1995) Electrodynamics of continuous media, 2nd edn. Butterworth-Heinemann Ltd., Bosto
62. Park SH, Theilmann P, Yang K, Rao AM, Bandaru PR (2010) The influence of coiled nanostructure on the enhancement of dielectric constants and electromagnetic shielding efficiency in polymer composites. Appl Phys Lett 96:43115
63. Dumitrică T, Landis CM, Yakobson BI (2002) Curvature-induced polarization in carbon nanoshells. Chem Phys Lett 360:182–188
64. Liu K, Roth S, Düsberg G, Kim GT, Popa D, Mukhopadhyay K, Doome R, Nagy JB (2000) Antilocalization in multiwalled carbon nanotubes. Phys Rev B 61:2375–2379
65. Li Z, Mutlu M, Ozbay E (2013) Chiral metamaterials: from optical activity and negative refractive index to asymmetric transmission. J Opt 15(2):023001
66. Lindell IV, Sihvola AH, Kurkijarvi J (1992) Karl F. Lindman: the last Hertzian, and a harbinger of electromagnetic chirality. IEEE Antennas Propag Mag 34(3):24–30
67. Li Z, Alici KB, Colak E, Ozbay E (2011) Complementary chiral metamaterials with giant optical activity and negative refractive index. Appl Phys Lett 98(16):161907
68. Bush V (1945) Science, the endless frontier. US Government Printing Office, Washington, DC
69. Torquato S (2006) Random heterogeneous materials. Springer Science, New York
70. Pendry JB, Holden AJ, Robbins DJ, Stewart WJ (1999) Magnetism from conductors, and enhanced non-linear phenomena. IEEE Trans Microwave Theory Tech 47:2075
71. Vemuri KP, Bandaru PR (2013) Geometric considerations in the control and manipulation of conductive heat flux in multilayered thermal metamaterials. Appl Phys Lett 103:133111
72. Vemuri KP, Canbazoglu FM, Bandaru PR (2014) Guiding conductive heat flux through thermal metamaterials. Appl Phys Lett 105(19):193904
73. Morrison RT, Boyd RN (1983) Organic chemistry. Allyn & Bacon, Boston

Chapter 11
Thermally Conductive Electrically Insulating Polymer Nanocomposites

Zifeng Wang and Chunyi Zhi

11.1 Introduction

11.1.1 High Thermal Conductive Polymer Composite Materials

The demands for polymer composite material with high thermal conductivity arise from the integration and miniaturization of microelectronic devices. As a result of smaller but more functional devices, dissipation of heat generated from millions of tiny transistors becomes a non-ignorable issue, which greatly affects the performance of certain electronic equipment. Malfunction, poor reliability, and premature failure happen time by time due to accumulated heat generated in local area of the devices. There are different ways to dissipate heat such as applying a heat sink, for which a metal plate is used conventionally, and a cooling fan to blow away local heat. In order to keep good thermal contact between heat sources and heat sinks as well as improve heat transfer efficiency, thermal interface materials (TIMs) with high thermal conductivity are filled into the gaps [1]. This is a typical application of high thermal conductive polymer composite materials (Fig. 11.1).

Z. Wang • C. Zhi (✉)
Department of Physics and Materials Science, City University of Hong Kong,
83 Tat Chee Avenue, Kowloon, Hong Kong
e-mail: cy.zhi@cityu.edu.hk

© Springer International Publishing Switzerland 2016

X. Huang, C. Zhi (eds.), *Polymer Nanocomposites*,
DOI 10.1007/978-3-319-28238-1_11

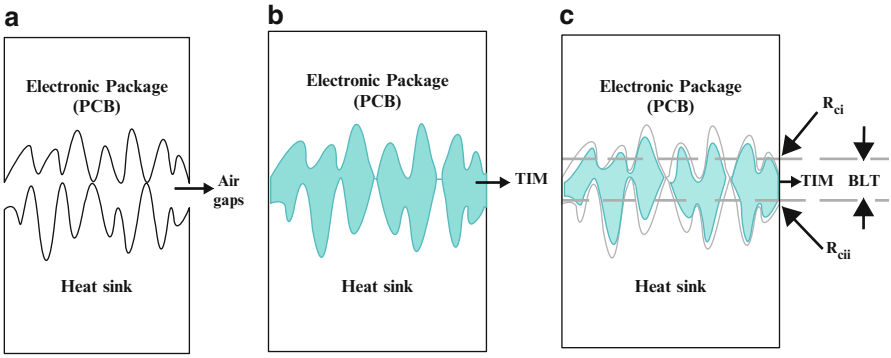

Fig. 11.1 Schematic illustration of thermal interface materials (TIMs) and its application to facilitate heat dissipation (Reproduced with permission from [2])

11.1.2 Overview of Thermally Conductive Electrically Insulating Polymer Composites

The nature of polymer renders its composite materials with well-appreciated processability, low density, as well as low-cost economically. However, the intrinsically low thermal conductivity of polymers makes them inappropriate for heat conduction applications. Commonly applied polymer materials like epoxy resin, polyurethane (PU), silicone, and polyacrylic resin usually get thermal conductivity value ranges from 0.1 to 0.3 W/mK, which is too insufficient to satisfy the required thermal conductivity level. The intrinsically low thermal conductivity of polymeric materials can be understood as follows.

In general, in the existence of defects, polymer chain entanglement and random orientation, and voids and impurities, unfortunately, the transport of heat by means of phonon is greatly suppressed as a result of phonon scattering at these defect sites. S Shen and colleagues tried to restructure polyethylene chains by stretching method and got an ultrahigh thermal conductivity value of 104 W/mK that was comparable to the thermal conductivity of idea of single crystalline fiber [3] (Fig. 11.2).

In spite of the attractive number and the inspiring idea, however, this discovery can hardly fulfill the requirement of TIMs because the stretched polyethylene may lose the property of polymer that is of essential importance. In order to improve the thermal conductivity and simultaneously preserve the advantages of polymeric materials, inorganic fillers with high thermal conductivities are introduced as fillers. As some of the review papers suggested, inorganic fillers like aluminum oxide, aluminum nitride, boron nitride, silicon carbide, and silicon nitride as well as beryllium oxide are of great interests because of their high intrinsic thermal conductivities and high electrical insulation, which make them very suitable for fabrication of high thermal conductive electrically insulating polymer composites. Thermal conductivity values of commonly applied polymers and inorganic compounds are presented in Table 11.1. For beryllium oxide (BeO), the high toxicity nature and expensive cost make it unpreferable for practical applications, although it possesses high thermal conductivity. Detailed discussions of different fillers and their polymer composite materials will be presented in the following sections.

Fig. 11.2 Schematics of stretched polyethylene microfibers (Reproduced with permission from [2])

11.1.3 Theory of Heat Conduction in Electrically Insulating Solid-State Materials

Heat exchange can be completed through different approaches, for example, heat conduction, convection, and radiation. In the case of heat conduction, the thermal energy is exchanged by certain carriers in the materials, such as electrons and phonons. While the conduction of heat by either electron or phonon functions in conductors and semiconductor materials, however, the transport of heat by means of phonon, which is lattice vibration wave, dominates in insulators. The latter is the main conduction mechanism we will discuss in this chapter. Because of the wave nature of phonon, scattering and interference happen so that the propagation of phonon is influenced by various reasons. As a result, thermal conductivity of ordered materials is usually much higher than those with disordered or defective structure even at the same elemental compositions.

In this chapter, we will review the following contents as shown below:

1. High thermal conductivity of electrically insulating inorganic fillers
2. Thermally conductive electrically insulating polymer composite materials
3. Factors that influence the thermal conductivity of polymer composite materials

11.2 High Thermal Conductivity Inorganic Fillers

As mentioned above, materials with good electrically conductivities are usually not surprisingly good thermal conductors as the flow of electrons also carries thermal energy with even higher efficiency. Examples like copper and silver are good electrical conductors and heat conductors. These types of materials are discussed in the other chapter. Here we will focus on thermally conductive but electrically insulating materials. Ceramics, such as aluminum oxide (Al_2O_3), silicon dioxide (SiO_2), zinc oxide (ZnO), aluminum nitride (AlN), boron nitride (BN), silicon nitride (Si_3N_4),

silicon carbide (SiC), and graphene oxide (GO), which has been explosively studied, are ideal candidates in terms of their wide band gap and high thermal conductivity.

11.2.1 Oxides

We will firstly start with oxides. Typical materials in this category are alumina (Al_2O_3), silica (SiO_2), and zinc oxide (ZnO).

11.2.1.1 Alumina (Al_2O_3)

As shown in Table 11.1, the thermal conductivity of alumina (Al_2O_3) is in the range between 38 and 42 W/mK, which is relatively high compared with most of the inorganic compounds and much higher than polymers. There are several types of naturally formed aluminum oxide with different crystal structures, which are the cubic γ and η phases, the tetragonal or orthorhombic δ phase, the orthorhombic κ phase, monoclinic θ phase, and α phase. The α-Al_2O_3 is most frequently used as filler in polymer composite for thermal conductivity applications. Crystal structure of α-Al_2O_3 can be described as follows: the alumina ions stay in two-third of the octahedral interstices of the close-packed hexagonal cage formed by oxygen ions. One of the most commonly seen crystalline forms of alumina is corundum, which is the thermostable form of alpha-Al_2O_3. Famous for its superior hardness and high melting temperatures as well as relatively high thermal conductivity, alumina is frequently used as abrasive material, refractory material, and thermally conductive material (Fig. 11.3).

Basically, as for materials for heat conduction purpose, there are several major applications that have been intensively investigated, which are thermally conductive nanofluid and thermally conductive polymer composite.

Nanofluid, as the name suggests, is a kind of liquid with the addition of nanosized particles dispersed in, of which the physical properties like viscosity, density, and thermal conductivity change as a result of nanoparticle additives. According to some of the research papers, the thermal conductivity of such nanofluid is influenced by several factors such as the nature of nanoparticle additives, volume fraction of nanoparticles in the base liquid, the nature of base liquid, the distribution of nanoparticles in the base liquid, temperature, and even pH value of base liquid, which implies the complexity of nanofluid systems [4] (Fig. 11.4).

Al_2O_3 nanoparticles, among several other competitive candidates like CuO and SiC nanoparticles as well as carbon nanotubes, have attracted much attention of research interests due to its low price. Lee and coworkers [6] produced and measured the thermal conductivity of CuO and Al_2O_3 nanoparticle-suspended nanoflu-

Table 11.1 Thermal conductivity and linear coefficient of thermal expansion (CTE) of various electrically insulating materials at room temperatures

Materials	Thermal conductivity (W/mK)	Coefficient of thermal expansion (CTE)
Polystyrene (PS)	0.04–0.14	90–150
Polypropylene (PP)	0.14	143
Polyvinyl chloride (PVC)	0.12–0.17	90–180
Polymethyl methacrylate (PMMA)	0.15–0.25	90–162
Polycarbonate (PC)	0.19	122
Epoxy	0.17–0.21	81–117
Silicone elastomer	0.17–0.26	270
Polytetrafluoroethylene (PTFE)	0.25	126–216
Polyetheretherketone (PEEK)	0.25	72–85
Polybutylene terephthalate (PBT)	0.25	108–171
Nylon 6,6	0.25	144
Polyethylene terephthalate (PET)	0.29	117
Low-density polyethylene (LDPE)	0.33	180–400
Nylon 1,1	0.36	184
High-density polyethylene (HDPE)	0.45–0.52	106–198
Fused SiO_2	1.5–1.6	0.4–0.5
Crystalline silica	3	10
$BaTiO_3$	6.2	6
Al_2O_3	38–42	7
ZnO	60	2.0–3.0
SiC	85	4.1–4.7
Si_3N_4	86–120	2.7–3.1
AlN	150–220	2.5–5
BN	29–300	1.1–4.3
BeO	300	5.5
Diamond	2000	0.11–1.23

ids, and they found an improved thermal conductivity of that nanofluids compared to nanofluids without nanoparticles. Besides, they found that there is a strong correlation between nanoparticle size and the corresponding thermal conductivity of nanofluids. Coincidentally, Wang [7] and Li [8] and their collaborators had similar discoveries, respectively, according to their papers. They also demonstrated that the thermal conductivity of nanofluid system was also affected by the volume fraction of nanoparticles as thermal conductivity of nanofluids increases with particle volume fraction, to a certain extent. For example, at 34.7 °C, thermal conductivity of 10 vol% Al_2O_3/water suspension reaches nearly 1.30-fold of that of base fluid, which is around 0.6 W/mK [8]. In contrast to the studies mentioned above, temperature dependence of thermal conductivity of nanofluids seems to be more controversial as a positive correlation between temperature and thermal conductivity was shown by some of the published results while others found no anomalous effective

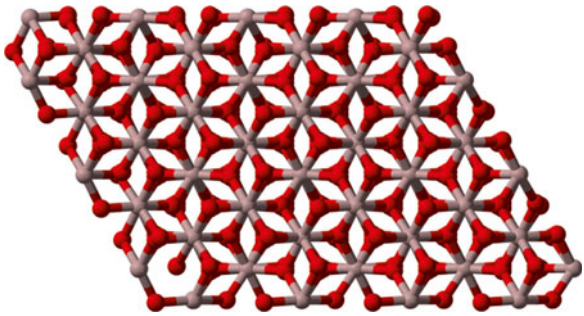

Fig. 11.3 Schematic illustration of the crystalline structure of Al_2O_3 (Reproduced with permission from Wikipedia)

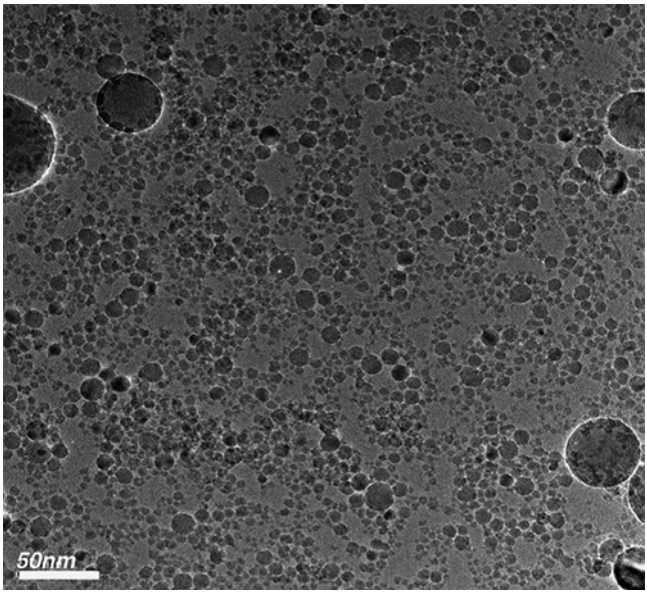

Fig. 11.4 Transmission electron microscopy image of Al_2O_3 nanoparticles dispersed in water (Reproduced with permission from [5])

thermal conductivity improvement when increases the system temperature [9–13]. Other factors like base fluid type and pH value of the fluid have also been studied.

Apart from Al_2O_3 nanofluid, thermally conductive polymer composite with Al_2O_3 filler is also a hot topic and much research efforts have been put in this particular area, which will be discussed in detail in the later section.

11.2.1.2 Silica (SiO_2)

The crystalline form of silica, which is also called silicon dioxide (SiO_2), consists of tetrahedral SiO_4^- in each of the unit cell while each of the vertices oxygen atoms is shared by two adjacent unit cells, yielding the net SiO_2 formula. Similar to alumina,

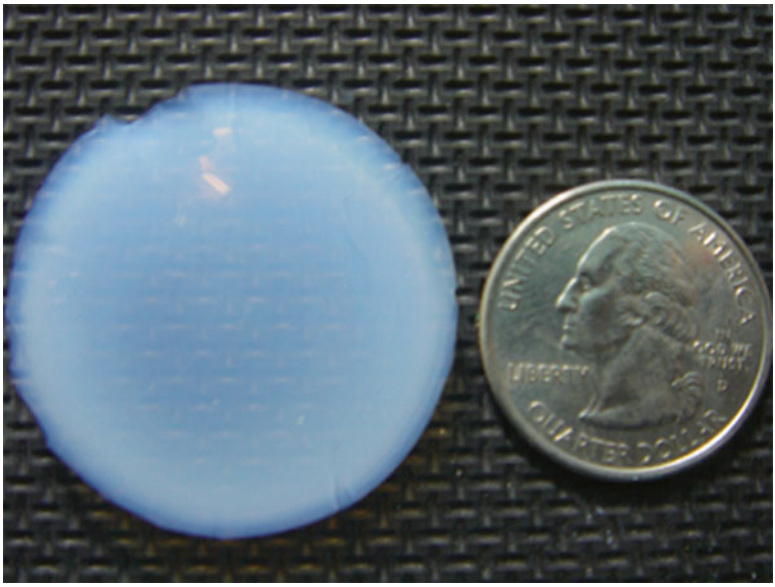

Fig. 11.5 Example image of silica aerogel (Reproduced with permission from [17])

silica presents various crystal structures and one of the most stable forms is α-quartz. Silica has been studied intensively in the recent years, either in fabrication methods or its applications. Approaches for producing silica can be generally classified as fumed silica [14], precipitated silica [14], thin film silica [15] and other special laboratory methods. Applications of silica occupy various fields including substrate of microelectronics, optical fiber in optoelectronics, composite materials, heat conduction, carrier and protective shell for drug delivery, silica aerogel, etc. Among those applications, silica for aerogels, composite materials, and heat conduction will be discussed.

Silica aerogel, which was the first aerogel and was first created by Kistler in 1931 [16], is a kind of highly porous material prepared by replacing the liquid with air in a gel without significant volume shrinkage, resulting in ultralow density in the final product. Light but strong, silica aerogel with high-specific surface area shows attractive mechanical and other properties since its emerging. By virtue of its high porosity and high thermal insulation value, silica aerogel is also a well-acclaimed thermal insulator and much work has been done in this aspect (Fig. 11.5).

Usually, the synthesis of silica aerogel can be classified into the following three steps, according to the literature [18]: (1) preparation of silica gel, (2) aging of the gel, and (3) drying of the gel. Varieties of precursors and fabrication methods, following the three general steps, were developed to make the microstructure and properties of final aerogel tunable. Silicon alkoxides, such as tetramethoxysilane (TMOS), tetraethoxysilane (TEOS), polyethoxydisiloxane (PEDS), methyltrimethoxysilane (MTMS), and methyltriethoxysilane (MTES) are those mainly used as the precursors for silica aerogel by different research groups around the world

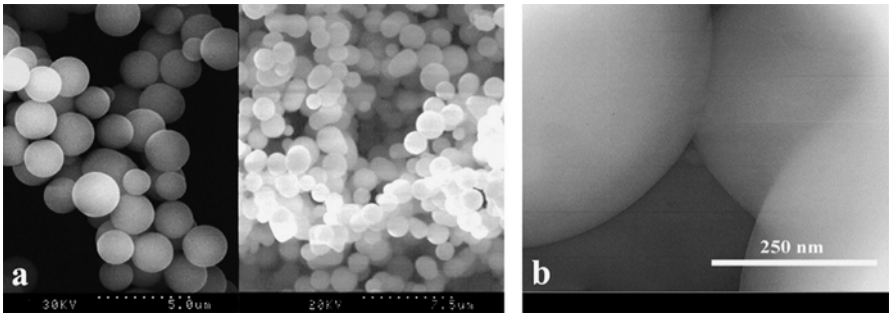

Fig. 11.6 Scanning electron microscope images of silica aerogel (Reproduced with permission from [18])

[19–23]. The aging process has a crucial role in the synthesis of silica aerogel, and two main mechanisms may influence the final structure and property of the gel: neck growth from reprecipitation of silica dissolved from particle surface onto necks between particles and dissolution of smaller particles and precipitation onto larger ones [24]. Other factors, such as the effect of fluid composition, the effect of solvent, and the effect of concentration of aging solution and aging time, were systematically investigated by different groups, respectively [25–27]. Drying process is critical in the formation of aerogel, and significant volume shrinkage caused by capillary force resulting from the evaporation of solvent happens during normal drying method. In the aerogel fabrication process, generally, there are three types of drying methods that are widely used which are supercritical drying (SCD), ambient pressure drying (APD), and freeze drying, while it can be further subdivided into high-temperature supercritical drying (HTSCD) and low-temperature supercritical drying (LTSCD) for the supercritical drying (SCD) method. The problem of capillary pressure, which is essential reason for the volume shrinkage of aerogel during drying, is circumvented in the supercritical drying (SCD) and freeze drying, while it is inevitable in the ambient pressure drying (APD) [18]. After successful preparation, silica aerogel presents unique material properties, such as porous structure with high surface area, low-density while preserved moderate mechanical strength, optical properties, low thermal conductivity for thermal insulation, and hydrophobicity [18] (Fig. 11.6).

11.2.1.3 Zinc Oxide (ZnO)

Famous for its applications in semiconductor industry, zinc oxide (ZnO) has received substantial research interest for its large exciton binding energy (60 meV), wide energy bandgap (3.37 eV), and piezoelectricity, which originates from the noncentral symmetry of wurtzite structure [28–30]. Besides, zinc oxide has got another two crystal structures which are cubic zinc blende and cubic rock salt structures. Among these three structures, wurtzite is the most stable form at ambient condition, while zinc blende structure can be stably obtained on the cubic substrate,

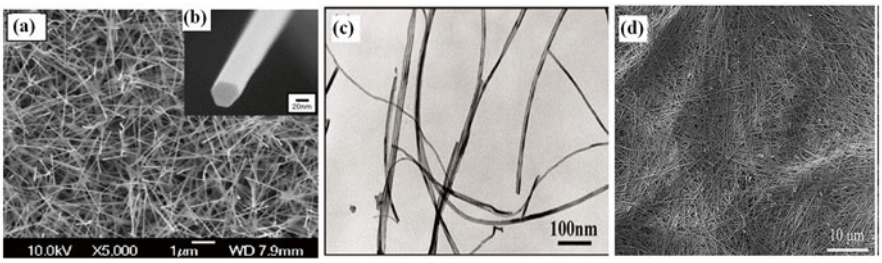

Fig. 11.7 Representative images of ZnO nanostructures (**a**) and (**b**) SEM images of ZnO nanorods; (**c**) TEM image of ZnO nanobelts; (**d**) SEM image of ZnO nanowires (Reproduced with permission from [31–33])

and the one with rock salt structure might not be easily obtained unless at high-pressure condition around 10 GPa [28] (Fig. 11.7).

One of advantages of ZnO as fillers for polymer composites is that the growth or synthesis of ZnO nanostructures has received so much attention that various nanostructures, such as nanowires, nanorods, and even nanobelts with different shapes, have been successfully synthesized through different methods [32, 34–38].

Although famous for its applications in semiconductor industry, parameters related to the thermal properties, which are the main topics in this section, such as the coefficient of thermal expansion, thermal conductivity, and specific heat of ZnO, also drew much attention of researchers. As for thermal conductivity, the value varies from different synthesized nanostructures and treatment. For the bulk counterpart, however, the value of thermal conductivity is around 60 W/mK, while those with modified structures and special treatment reach 100 W/mK [39–41]. Doping has a significant effect on changing the thermal conductivity of pure ZnO by providing impurities that work as carriers for heat transport [42–44].

11.2.2 Nitrides

Nitrides, such as aluminum nitride (AlN), boron nitride (BN), and silicon nitride (Si_3N_4), are another important category of insulating material with high intrinsic thermal conductivity in the family of inorganic compounds. Nitride materials usually have a large energy bandgap and therefore are widely used as insulating and dielectric materials.

11.2.2.1 Aluminum Nitride (AlN)

Aluminum nitride (AlN), which is usually white to pale yellow in color, is a wide bandgap semiconductor material (more than 6.0 eV) that has been intensively studied in different research fields. Owing to its superior thermal properties, for

example, high intrinsic thermal conductivity, good thermal stability in inert atmosphere, high dielectric constant, and low coefficient of thermal expansion, AlN has received the most attention as electronic packaging materials, TIMs, insulators, and materials for high-temperature applications.

Normally, there are two crystal structures for aluminum nitride, known as β-AlN and α-AlN, which are zinc blende and wurtzite structures, respectively [45]. Pure single crystalline aluminum nitride exhibits a thermal conductivity value of nearly 300 W/mK at room temperature, while that for its polycrystalline counterpart is much lower, probably caused by randomly oriented grains, impurity atoms, and precipitated second phase with poor thermal properties [45]. It has been reported that the thermal conductivity value of single crystal aluminum nitride is inversely proportional to the oxygen content [46], while the content of other impurities like CaO and Y_2O_3 enhances the thermal conductivity of aluminum ceramics by improving their densification [47] (Fig. 11.8).

The fabrication of AlN with high thermal conductivity value is of great interest by researchers. However, because of the strong covalent bonding nature of AlN, it is difficult to realize high densification AlN monolith with traditional fabrication approaches. Adding other materials, such as rare earth oxides and alkaline earth oxides in most cases, as sintering aids, is one of the most direct methods for fabrication high densification AlN. The oxide additives form eutectic liquid phase with Al_2O_3 and remove dissolved oxygen thus increasing the thermal conductivity of the AlN, according to the work of Komeya and coworkers [48]. The purification by the

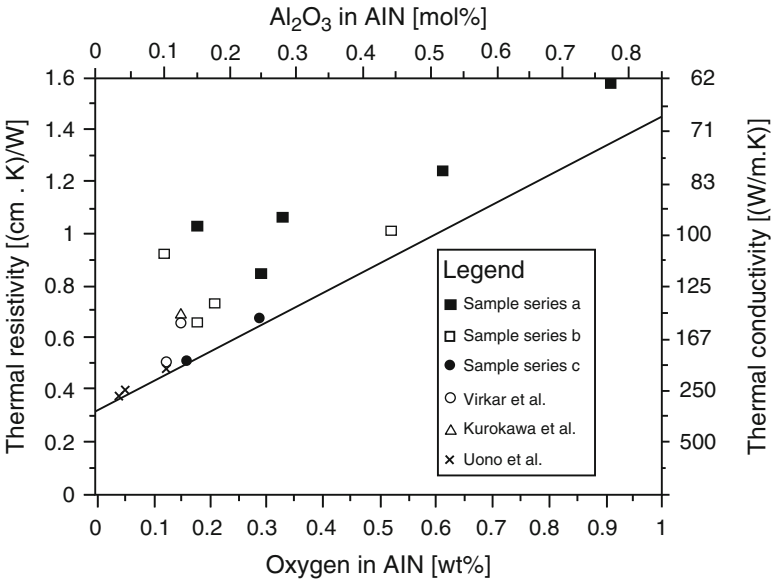

Fig. 11.8 Thermal resistivity and thermal conductivity at room temperature as a function of the oxygen content in the AlN lattice. *Line* represents correlation in single-phase AIN ceramics (Reproduced with permission from [44])

scavenging of dissolved oxygen in the AlN, which is a thermodynamic and phase equilibrium-determined process, has a great effect to the thermal conductivity of the final AlN because those oxygen atoms serve as phonon scattering sites that decrease the thermal conductivity of AlN [45]. Annealing, after the completion of sintering, occurring by either solid-state diffusion or dissolution–reprecipitation or even both, is another important process which determines the thermal conductivity of AlN [45].

Owing to its attractive high thermal conductivity, AlN is used as filler material for fabricating composites with various types of polymer matrices, which will be further discussed in the later section.

11.2.2.2 Boron Nitride (BN)

Boron nitride (BN) is another important inorganic compound belonging to the nitride family. Both boron (B) and nitrogen (N) appear as the neighbor of carbon (C) in a periodic table, and there are in general four types of crystalline structures of BN, which are hexagonal boron nitride (h-BN), cubic boron nitride (c-BN), wurtzitic boron nitride (w-BN), and rhombohedral boron nitride (r-BN) [49]. All those four types of BN were not discovered in nature until a naturally occurred mineral named qingsongite that contains micron-sized c-BN was discovered in Tibet in 2009. Among its allotropes, h-BN, which is the analog to graphite, has attracted much attention due to superior high thermal conductivity, low dielectric constant, high-temperature stability, and relatively low density, which are the ideal candidates for electronic packaging applications [39]. Due to its intriguing properties and non-natural occurrence, the synthesis of h-BN has ever been a hot topic for material scientists. The first report of successful synthesis of h-BN was by Balmain in 1842 by the reaction of potassium cyanide and molten boric acid [49] (Fig. 11.9).

Till now, h-BN has been used in various types of applications in different fields, such as high-temperature ceramic crucibles, various cosmetics, lubricants, and electronic packaging materials. Yoshitsugu Kimura and coworkers designed a series of sliding experiments to investigate and analyze the lubrication property h-BN-added lubricant oil, and they discovered that h-BN can effectively reduce the wear of the bearing steel when using as lubricant additive. They found that an order of magnitude of wear reduction was achieved with merely 1 wt% h-BN addition although the coefficient of friction is slightly increased [50]. Z. Pawlak and coworkers studied h-BN micro-particles as lubricating additives for self-lubricated sliding bearing. The coefficient of friction of the oil with h-BN micro-particles decreases about as twice as much of that of the oil-lubricated self-lubricated bearings [51].

As for applications for the electronic packaging material, h-BN is often incorporated into polymer matrix because of the intrinsically high thermal conductivity value (about several hundred W/mK) and forms a composite material with varieties of shapes and forms, such as thin films, bulk monoliths, greases, and flexible parts. The composites are then used as thermal interface materials (TIMs) for heat dissipation in electronic devices and components, which has gained much scientific research interests. This topic will be discussed in detail in the later section.

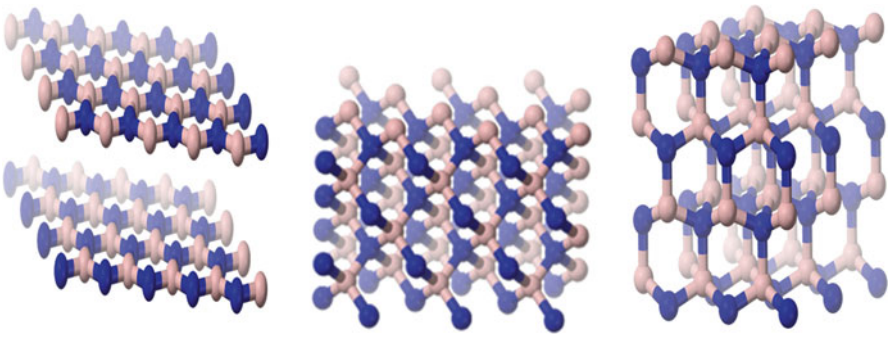

Fig. 11.9 Crystal structures of h-BN, c-BN, and w-BN (Reproduced with permission from Wikipedia)

Besides, in the field of nanomaterial and nanotechnology, research efforts have been put on the discovery or synthesis of novel boron nitride nanostructures, and the results seem to be satisfactory. So far, plenty of novel nanostructures of boron nitride have been reported, such as nanotubes [52, 53], nanosheets [54, 55], nanoparticles [56], nanoribbons [57], nanowires [58], and even nanoflowers [59]. The springing up of novel nanostructures of boron nitride brings not only new materials but also new properties and applications, which is quite appealing to the technology development nowadays.

11.2.2.3 Silicon Nitride (Si_3N_4)

Famous for its low coefficient of thermal expansion, good mechanical strength at high temperature and good resistance to oxidation and creep, silicon nitride (Si_3N_4) is a kind of ceramic material with very high melting temperature (about 1900 °C) and high hardness. Owing to the nature of easy dissociation of silicon and nitrogen atom at about 1850 °C that is just below the melting point of silicon nitride (1900 °C), the production of Si_3N_4 by conventional hot press and sintering process is difficult. Therefore, to solve this problem, adding an appropriate sintering aid is necessary, which is similar to the case of AlN mentioned above.

Generally, there are three different crystalline structures of Si_3N_4, designated as α-Si_3N_4, which is trigonal structure, β-Si_3N_4, which is hexagonal structure, and γ-Si_3N_4, which is a cubic structure. Due to its good high-temperature performances, Si_3N_4 is used to manufacture internal engine parts. Apart from that, Si_3N_4 is also frequently used to fabricate bearings for its superior shock resistance and hardness, which reduces friction by nearly 80 %, resulting in longer service life. In the high-temperature application, Si_3N_4 is also one of the few candidates for hydrogen/oxygen rocket engine because of its excellent thermal shock resistance. Furthermore, Si_3N_4 get its application in many other fields, such as medical, electronics and various tools, which proves their popularity and versatility.

By virtue of its good mechanical strength and potentially high thermal conductivity (around 200 W/mK theoretically), Si_3N_4 is a promising substrate material for electronic devices [60]. However, the realistic thermal conductivity of commercially available Si_3N_4 is usually as low as 60 W/mK, which is caused by the following reason. Owing to the liquid sintering process, the existence of sintering additives results in low thermal conductivity grain boundary phase and lattice defects, which reduces the overall thermal conductivity of the finally Si_3N_4 ceramics [60]. In order to partly solve the problem and increase the thermal conductivity of Si_3N_4, there are several potential methods, such as coarsening the grains, use sintering aids with high oxygen affinities, applying long time heat treatment and increase nitrogen-to-oxygen ratio while sintering [60]. The obtained Si_3N_4 ceramics acquires thermal conductivity value around 140–170 W/mK.

Wei Xu and coworkers investigated the correlation between thermal conductivity and microstructure of Si_3N_4 ceramics [61]. According to their work, the thermal conductivity of obtained Si_3N_4 ceramics varies greatly (46–79 W/mK) when sintered at different temperatures because of the formation of $Mg_5Y_6Si_5O_{24}$ phase when sintered at 2123 K [61]. By changing the variables in the preparation process, Angel de Pablos and coworkers studied the thermal conductivity of Si_3N_4 with distinct microstructures, and they also found that the value of thermal conductivity varies greatly, from 15 to 82 W/mK, for Si_3N_4 with different microstructures [62]. The obtained Si_3N_4 with coarsest grains acquires highest thermal conductivity, which is consistent with the results reported by Wei Xu and coworkers.

Adding Si_3N_4 into polymeric materials to fabricate high thermal conductivity composites for electronic packaging and other applications is another useful application, which will be presented in the later section.

11.2.3 Graphene Oxide (GO)

Graphene oxide (GO), also called graphitic oxide or graphitic acid, is an oxide form of graphene, the single-layer carbon sheet. While graphene is an excellent electric conductor, because of the oxidation process that creates a lot of hydroxyl and carboxyl groups and also defects, graphene oxide (GO) is an electrical insulator that preserves a certain degree of thermal conductivity (Fig. 11.10).

After the successful preparation of graphene by scotch tape by Andre Geim and Kostya Novoselov in 2004 [64], which was then awarded with Nobel Prize in 2010, people realized that the unique properties of graphene can be utilized by human beings only after the realization of large-scale fabrication process. One of the potential approaches for obtaining graphene is by the reduction of graphene oxide (GO), which is much easier than the direct synthesis of graphene. The efforts for obtaining graphene oxide can be traced back to 1860s when Benjamin C. Brodie prepared graphite oxide successfully for the first time by treating graphite with potassium chlorate and fuming nitric acid. Among the methods reported for the synthesis of graphene oxide, William S Hummers and coworkers developed a more efficient way

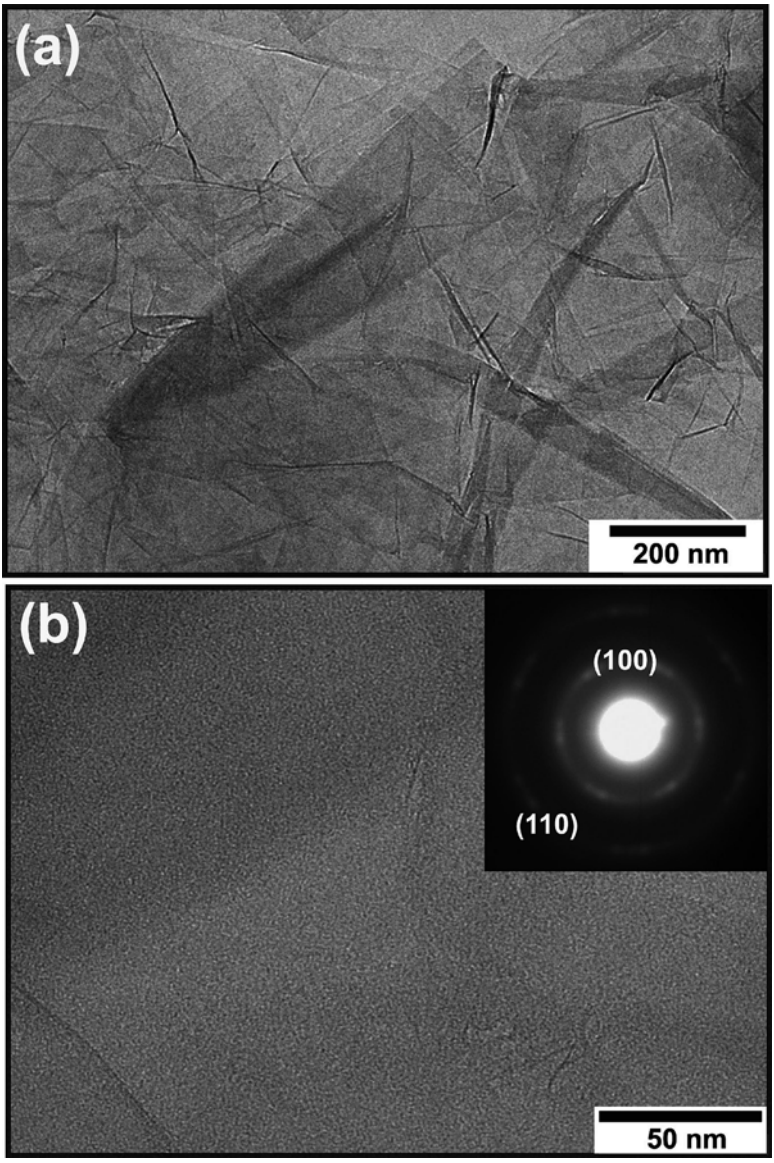

Fig. 11.10 Transmission electron microscope image of graphene oxide nanosheets (Reproduced with permission from [63])

to synthesize graphene oxide that has been widely used nowadays and greatly enhance the yield of GO platelets, which is the famous Hummers' method [65]. According to Hummers' method, concentrated sulfuric acid (H_2SO_4), sodium nitrate ($NaNO_3$), and potassium permanganate ($KMnO_4$) are applied in a certain sequence to oxidize, intercalate, and finally exfoliate graphite layers. Although Hummers'

method is applied with some modifications now and many other methods have been proposed [66–68], it is still one of the most important methods for realizing large-scale preparation of graphene oxide.

By inheriting part of the structural characteristics of graphene, graphene oxide itself has got many attractive applications, such as for water purification [69], protective coatings [70], battery and electrode materials [71, 72], and graphene oxide papers [73], which again demonstrate the versatile functionalities and the value of research of graphene oxide.

Because of the insulating nature of graphene, which is on the contrary to that of graphene, it has been used for electrically insulating and thermally conductive polymer composite for electronic packaging, and we will further discuss on this in the later section.

11.2.4 Silicon Carbide (SiC)

Silicon carbide (SiC) has nearly 250 crystalline forms, which are known as polytypes. One of the most commonly seen polymorphs of SiC is the hexagonal crystalline structure α-SiC, while the β-SiC presents zinc blende crystalline structure that is similar to the structure of diamond. SiC has been intensively studied by material scientists and engineers and has got plenty of applications in different fields. It has been used as abrasive material by virtue of its high hardness, such as grinding materials and various tools, for many years. Besides, it has also been used as structural materials for its good mechanical strength and relatively low density. Moreover, there are a certain number of applications of SiC in the electric and electronic systems and devices, for example, lighting arresters, Schottky diodes, MOSFET, and LEDs.

SiC has high thermal conductivity. The value of thermal conductivity of pure single-crystalline SiC can be as high as 3000 W/mK, according to the work of Glen A. Slack [74]. However, commercially available SiC has thermal conductivity values in the range of several tens W/mK or even lower as the existence of impurities and defects, which act as phonon-scattering sites. There are currently four types of methods for large-scale preparation of SiC, which greatly affect the thermal conductivity of the product SiC–hot press followed by sintering, siliconized or reaction bonded, single crystal, and chemical vapor deposited [45]. The hot pressed and successively sintered SiC usually obtains good mechanical strength while its thermal conductivity and other properties are not satisfying [45]. As for the reaction bonded produced SiC, however, the quality of the final product SiC is strongly influenced by the content of Si, which is used to fill in pores and voids of the porous structure of SiC [45]. In contrast, the un-doped SiC single crystals usually get superior physical properties, except for high thermal conductivity. However, this method is fairly expensive and is only able to produce crystals of relatively insufficient size, which is not favorable for commercializing. On the contrary, chemical vapor-deposited SiC materials acquire not only optimized physical properties but is also a cost-effective approach for scalable production of SiC materials [45].

Owing to the intriguing properties of SiC, the research on this material has attracted many people and so far not only has been put into new applications, in the field of nanomaterial and nanostructure, some novel SiC nanostructures have been discovered and then successfully synthesized in laboratory. For example, porous SiC has been successfully fabricated by various etching methods [75–77] for sensor and luminescence applications [78, 79]. Apart from that, SiC nanoparticles, which are also called SiC quantum dots, can be synthesized by chemical reactions in solution or vapor phase reactions [80, 81]. What's more, the synthesis of SiC nanowires also arouses widely spread research interests, and many growth mechanisms and special nanowire structures have been reported. Basically, there are two main mechanisms that are vapor–solid growth mechanism and vapor–liquid–solid growth mechanism. Aside from various SiC with core–shell structures [82–85], YJ Hao and coworkers reported a success synthesis of bamboo-like SiC nanofibers by carbothermal reduction reaction [86]. Besides, SiC nanowires with other structures, such as beaded-like structure, helical structure, and other periodic structures, can be synthesized, according to the published literatures [87–90].

As mentioned above, SiC has high intrinsic thermal conductivity and therefore has been used for various heat conduction or management applications. One of those that have been intensively studied is for fabricating thermally conductive polymer composite materials, which will be further discussed in the later section.

11.3 High Thermal Conductive Electrically Insulating Polymer Composites

The demand for high thermal conductivity polymer composite materials arises from the need for heat management and heat dissipation in electronic packaging as the elements and components of electronic devices become more and more miniaturized. Incorporating high thermal conductivity inorganic fillers into polymer matrix yields composite material with advantages of both of the constituents, i.e., the high thermal conductivity of the filler and the processability and low density of the matrix. As for the choices of polymer matrix materials, there are several commonly used types for electronic packaging applications and thermal interface material, such as epoxy resin, silicone, polyethylene, polyamide, and so on. The research of incorporating high thermal conductivity filler into polymer has been studied for many years, and we will discuss this topic based on the classification of filler types.

11.3.1 Oxides as Fillers

11.3.1.1 Al_2O_3

Al_2O_3 particles possess moderate thermal conductivity and have been widely used as filler material for fabricating polymer composites with improved thermal conductivity.

Fu Jifang and coworkers investigated the effect of the incorporation of Al_2O_3 nanoparticles on the thermal conductivity of epoxy resin [91]. They fabricated epoxy resin with micro-sized and nano-sized Al_2O_3 filled and compared the thermal conductivity of the two types of composites. The nano-sized Al_2O_3-filled epoxy resin presented higher overall performances, such as thermal conductivity, electrical insulation, and mechanical strength than their micro-sized counterpart. They also found that surface modification of the filler by silane or diisocyanate is advantageous for the improvement of the thermal conductivity of the composites as they decrease the thermal contact resistance between the matrix and filler materials [91].

Mengdie Liu and coworkers fabricated nano-sized and micro-sized Al_2O_3 particle-filled poly(arylene ether nitriles) (PEN-t-ph) composites and achieved a 2.7-fold improvement of thermal conductivity for 30 wt% n-f-Al_2O_3 and 30 wt% m-f-Al_2O_3 loaded composite (0.467 W/mK) compared with that of pure PEN-t-ph polymer (0.206 W/mK) [92]. In their study, the micro-sized Al_2O_3 is used to form main conductive path, while nano-sized Al_2O_3 is used to connect micro-sized particles. The combination of micro-sized and nano-sized particles leads to synergistic effect, which further improves the thermal conduction performance of the composites compared with that of individual filler. Besides, Masahiro Kozako and his coworkers tried to prepare high thermal conductive epoxy-based composites with high filler loading fractions [93]. For industrial application, sometimes, a thermal conductivity value higher than 10 W/mK is necessary, which is not easy to obtain with low filler loading content, and therefore, they focused on this topic and successfully fabricated epoxy composites with 60 vol% micro-Al_2O_3 loaded and achieved a thermal conductivity around 4.3 W/mK [93]. Although they tried to fill epoxy with 80 vol% filler, the result was not satisfactory enough as the suspension containing high content of filler cannot stably and homogenously exist. Apart from that, they found methyl cellusolve is an effective solvent that helps enhance interfacial bonding between matrix and filler materials [93].

Similarly, P. Bujard and his colleagues investigated the thermal conductivity of alumina particle-loaded epoxy resin as a function of filler loading fractions, from 0 to 80 vol% [94]. A 4.5 W/mK thermal conductivity was achieved with 80 vol% alumina-loaded epoxy resin while the uptake of water was smaller than 0.2 wt%, and coefficient of thermal expansion around 10 ppm/K was realized as well [94]. C. P. WONG and colleagues fabricated micro-sized alumina-filled epoxy resin composites with filler loading fractions ranging from 0 to 50 vol%, with 10 vol% increments, and compared the result with theoretical and semi-theoretical models [95]. A thermal conductivity value around 1.3 W/mK was achieved in composite with 50 vol% alumina particle loaded, and the model proposed by Agari gave the best estimation of the prediction of thermal conductivity of composites to the experimental results among several other models proposed by Maxwell and Bruggeman, respectively [95].

11.3.1.2 SiO_2

As one of the most commonly seen substances in microelectronic industries, silica is frequently used as material for electronic packaging for its highly electrical resistive and low dielectric constant nature [39]. The intrinsic thermal conductivity of

silica is not high, which greatly limits its application as filler material for high thermal conductivity polymer composites. However, there are still some people who investigate the thermally conductive behavior of silica-filled polymer composites.

Ming xia Shen and coworkers investigated the thermal conduction performances of SiO_2-filled polyvinyl acetate (EVA) composite film and compared the experimental results with several theoretical models [96]. A thermal conductivity value around 1.5 W/mK was achieved with filler loading fraction about 50 vol%. Besides, they found that thermal conductivity of SiO_2/EVA composites was sophisticatedly influenced by many factors, such as the nature of the filler material, interaction between matrix and filler materials, dispersion of fillers in the matrix, and even interfacial distance among fillers [96]. Theoretical model to predicting thermal conductivity of the as-fabricated co-films was also successively examined and the Agari's model, mixed empirical model, and percolation model, which presented the best predictions to the experimental results [96]. Nevertheless, C. P. WONG and colleagues fabricated epoxy resin filled with silica and silica-coated aluminum nitride and measured the corresponding thermal conductivity of the composites [95]. The thermal conductivity of the silica used in their study was 1.5 W/mK, which is much lower compared with that of other high thermal conductivity filler like aluminum nitride. A maximum thermal conductivity value about only 0.5 W/mK was achieved with 50 vol% silica-filled sample, while that of the silica-coated aluminum nitride-filled sample reached 1.96 W/mK at 50 vol% loading fraction. However, in terms of coefficient of thermal expansion (CTE), silica-filled composites showed the lowest value of CTE, which was primarily due to the intrinsically low CTE of silica, according to their explanations [95]. Woong Sun Lee and coworkers filled spherical silica-filled underfill for electronic packaging at 10, 30, 50, and 60 wt% loading fractions [97]. Thermal conductivity value increased linearly with filler loading fractions. Additionally, it was also observed that thermal conductivity increased slightly at elevated temperature, which can be probably ascribed by the increase of heat capacity of the underfill material [97].

11.3.1.3 ZnO

As mentioned above, ZnO is a wide gap semiconductor material that has been intensively studied in different fields. ZnO has got a moderate intrinsic thermal conductivity, around 60 W/mK, but it can hardly be used as HV electronic packaging material, and this can be ascribed to its high dielectric constant nature [39].

As one of the most important additives for silicone rubber industry, the high thermal conductivity nature of ZnO renders improved thermal performance for rubber. L.C. Sim and colleagues investigated properties of ZnO-filled silicone rubber as elastomeric thermal pads [98]. It was found that the incorporation of ZnO affects the thermal conductivity, thermal stability, and coefficient of thermal expansion (CTE) of the silicone rubber. The increased amount of ZnO resulted in the increase of thermal conductivity and thermal stability but a decrease of CTE of the composites. A linear increase of thermal conductivity values up to 0.26 W/mK with 10 vol% ZnO loaded was observed [98].

Nonetheless, Filiz and coworkers studied the effect of particle size and the electrical resistivity on the overall thermal, mechanical, and electrical performances of the ZnO-filled linear low-density polyethylene (LLDPE) composites [99]. In this work, three types of ZnO filler with different dimensions and electrical resistivities, which were micro-sized ZnO (mZnO), with resistivity of 1.5×10^6, submicron ZnO (sZnO), with resistivity of 1.5×10^9, and nano-sized ZnO (nZnO), with resistivity of 1.7×10^8, were used as fillers for the preparation of composites. The addition of ZnO particles reduced the tensile strength while increasing the elastic modulus of composites. The final electrical resistivity of the composites was affected by the aspect ratio, rather than the size of the particles, and the initial electrical resistivity of the ZnO fillers. 2.5 to 3 times improvement of thermal conductivity of the composites compared with that of original polymer was obtained with 20 vol% addition of ZnO with various dimensions. The authors demonstrated the potential application of this type of LLDPE-ZnO composites for electrostatic and heat dissipation functions [99].

Apart from the aforementioned works, Lijun Fang and colleagues successfully prepared hydrangea-like ZnO superstructure by solvothermal method and used successively as filler material for fabricating PVDF composite materials [100]. The as-prepared ZnO nanostructure provided the polymer matrix with not only significantly enhanced thermal conductivity with a maximum value of 1.13 W/mK with 60 wt% filler loading fraction, resulting in more 270 % enhancement compared with pure PVDF, but also an improved dielectric constant. It was claimed by the author that the hydrangea-like ZnO nanostructure could readily form conductive paths and reached percolation threshold at lower filler loading fractions with respect to those of commercially available ZnO nanoparticles [100].

In addition, Bin Lee and Gance Dai verified the importance or effect of the surface modification of ZnO fillers on the thermal conduction performance of ZnO–ethylene–vinyl acetate copolymer (EVA) composites materials [101]. In their work, several different surface-treating agents, such as stearic acid, OLAT16, KH-560, or NDZ-132, were investigated, and they found that a right dosage of agents treating at appropriate temperatures could greatly enhance the thermal conductivity of the composites. Exceeding usage of surface-treating agent, however, would cause decrease of thermal conductivity of the composites in return [101]. The phenomena could be explained as the filler–matrix interaction improvement given by the surface modification agent, i.e., improve affinity between matrix and filler materials, provide effective adhesion, as well as reduce faults and tiny voids [101].

Zhenhua Wang and colleagues fabricated ethylene propylene diene monomer (EPDM) composites filled with nano-sized zinc oxide and compared their mechanical and thermal properties with that of traditional reinforcing filler material, such as carbon black and silica [102]. They also investigated the influence offered by silane coupling agent Bis-(3-thiethoxy silylpropyl)-tetrasufide (Si69) on the nano-ZnO-filled composites. As a result, it was indicated that nano-ZnO-filled EPDM composites presented better overall performance and surface modification provided by silane coupling agent that rendered better interfacial interaction between the rubber matrix and fillers [102]. Qiuhong Mu and coworkers have also studied the thermal conductivity of ZnO-filled silicone rubber composites, and their results suggested better overall thermal conduction performance by incorporating ZnO fillers [103].

11.3.2 Nitride as Fillers

11.3.2.1 AlN

Because of the emerging high-heat output semiconductor or electronic devices, thermal interface materials with high thermal conductivity and high heat dissipation ability are demanding. As for AlN, because of its intrinsically high thermal conductivity, there were a large number of research works and publications on high thermal conductivity polymer/AlN composites for electronic packaging application [104].

Eun-Sung Lee and coworkers fabricated epoxy-based polymer composites with the incorporation of high thermal conductive AlN [105]. In their study, in order to achieve high filler loading content, dispersant chemistry was applied to avoid high viscosity of the blende system before the cross-linking of epoxy monomer. A maximum of 3.39 W/mK thermal conductivity was achieved with AlN filler loading fraction of 57 vol%, which was around 15-fold of that of epoxy resin. The as-fabricated epoxy–AlN composites were found to be effective for integrated circuit encapsulation [105]. Yongcun Zhou and colleagues fabricated polymethyl methacrylate (PMMA) composites filled with AlN by powder processing for electronic packaging [106]. They fabricated a series of AlN-filled PMMA composites with filler loading fractions ranging from 0.1 to 0.7 and investigated the effect of filler volume fraction to the physical properties, such as thermal conductivity, relative permittivity, and dielectric loss. The value of thermal conductivity was found to increase with increasing filler volume fraction, and a maximum of 1.87 W/mK thermal conductivity as well as a 4.4 relative permittivity (at 1 MHz) were achieved at 0.7 filler volume fraction [106]. Hui Yu and coworkers synthesized epoxy-based adhesive thermal interface material with high AlN filler loading fractions, up to 60 vol%, and acquired a maximum thermal conductivity value of 2.70 W/mK, which was around 13-fold of that of pure epoxy [107]. Moreover, in their research, an appropriate coupling agent, KH560, was applied to reduce the viscosity of the blende system, which was essentially important to obtain good filler dispersion and matrix–filler interface. The as-fabricated composites showed their potential as thermal interface materials for high powder applications [107].

Instead of mixing different constituents of the composites simply, Suzhu Yu and colleagues fabricated polystyrene–AlN composites while keeping aluminum nitride particles surrounding PS matrix particles [108]. Several factors, such as aluminum nitride concentrations, polystyrene particle size, and temperature were investigated to determine their correlation with thermal conductivity of the composites. Furthermore, they discovered that composites with larger matrix polymer size (2 mm) showed higher thermal conductivity than that with smaller matrix polymer particle size (0.15 mm). Polystyrene with 2 mm particle size filled with 20 vol% of AlN particle exhibited 5 times higher value of thermal conductivity compared with that of pristine polymer material [108].

Apart from sole filler material, Yunsheng Xu and colleagues synthesized polyvinylidene fluoride (PVDF)/AlN whisker/AlN particle hybrid filler composites, achieving a maximum thermal conductivity value of 11.5 W/mK at 60 vol% of total

filler loading fraction and AlN whisker/particle ratio of 1:25.7 [109]. In addition, it was also found that filler material with larger particle size could enhance the thermal conductivity of the composites to a larger extent, and silane coupling agent was found to be effective for interfacial modification thus reducing thermal contact resistance between matrix and filler material. While the incorporation of AlN filler improving the thermal conductivity and reducing CTE of the composite material at optimal ratio, the mechanical properties, such as tensile strength, modulus, and ductility, decrease as there is increase addition of filler, which is not favorable to the overall performances of the material [109]. Shu-Hui Xie and coworkers applied in situ polymerization to prepare polyimide–AlN composites based on pyromellitic dianhydride (PMDA) and 4,40-oxydianiline (ODA) [110]. c-glycidoxypropyltrimet hoxysilane (GPTS) was used as coupling agent for realizing homogenous filler dispersion. The enhancement of the thermal conductivity and thermal stability can be ascribed to the addition of AlN filler and coupling agent [110]. Gu, Junwei, and collaborators fabricated thermally conductive linear low-density polyethylene composites with AlN filled and investigated the effects of AlN concentration and surface modification to the thermally conductive and mechanical properties of the final composite materials [111]. The thermal conductivity coefficient was measured to be 1.0832 W/mK at 30 vol% filler fraction, and a maximum tensile strength of 17.42 MPa was achieved at 20 vol% filler loading fraction, respectively. What's more, an apparent increase in thermal stability of LLDPE was observed by TGA analysis, and the melting temperature and crystallinity of LLDPE were influenced by the addition of AlN particles [111]. Masayoshi Ohashi and collaborators investigated the effect of AlN particles with different shapes, or aspect ratio, to the thermal conductivity of AlN-filled epoxy resin [112]. They fabricated single-crystalline spherical AlN particles by solution reprecipitation technique and found it to be more fluidic compared with that of commercially available angular AlN when filling into epoxy matrix. Polymer composites with very high filler content (74 vol%) were successfully fabricated, and a maximum of 8.2 W/mK thermal conductivity was achieved, which in return demonstrated the ability of spherical AlN-filled epoxy composites as electronic encapsulation material. However, they also claimed the importance of improving the moisture resistance of AlN because of its easily inherent hydrolysis nature [112].

Wenyi Peng and collaborators fabricated AlN-filled epoxy resin composites and systematically studied the effect of surface modification of AlN particles on a set of physical properties of the composites, such as morphology, glass transition temperature, electrical property, and thermal conductivity [113]. Enhanced thermal conductivity values were observed for surface-modified AlN-filled epoxy composites compared with epoxy resin without filler modification, which demonstrated the positive effect on thermal conduction and dielectric properties of the composites by surface modification of filler material [113].

The incorporation of AlN not only improves thermal conduction and dielectric property of composites but also results in evolution of other material properties of polymer, such as thermal degradation temperature, duration of curing, etc. J. H. Yu and coworkers investigated the morphology, thermal conductivity, thermal stability,

and curing behavior of AlN-filled epoxy resin/TMPTMA composites [114]. Experimental results showed that incorporation of small amount of nano-sized AlN particles improved thermal stability and increased thermal degradation temperature of the composites. Only 1 wt% nano-AlN increased around 8 °C over epoxy–TMPTMA system. Differential scanning calorimetry (DSC) studies revealed that the curing mechanism of epoxy/TMPTMA system was not changed when filled with nano-AlN, and the incorporation of AlN could even reduce the duration for curing and lower down the curing temperature, which were preferable for composite processing [114].

11.3.2.2 BN

As one of the most high thermal conductive insulating inorganic solids, BN is one of the ideal filler candidates for high thermal conductivity composite material for electronic packaging, and there were extensive research attention and publications on this topic.

The effort of improving the thermal conductivity of h-BN-filled polymeric composite materials starts with particulate h-BN. In 1988, P. BUJARD studied hexagonal BN-filled epoxy resin composites and investigated several factors that influence the thermal conductivity of the composites, such as sample preparation procedures, which may result in agglomeration of fillers, volume fraction of fillers, as well as the temperature dependence [115]. It was found in his research that the thermal conductivity of the composites depends on the arrangement of fillers, which form preferential heat-flow path that determines the magnitude of heat conduction. A positive correlation between temperature and thermal conductivity, when testing temperature $T < T_g$, was also verified from the experimental results [115]. Wenying Zhou and coworkers fabricated BN particulates reinforced with high-density polyethylene (HDPE) composites and discussed the effect of BN content, HDPE particle size, and temperature dependence on the thermal conductivity of the composites [116]. It was indicated by the experimental results that the size of HDPE particle influences the thermal conductivity of the composite, i.e., large size particle provides the composite with higher thermal conductivity compared with that of HDPE with smaller particle size. Moreover, thermal conductivity of PE composites filled with BN generally decreases with increasing temperature and increases with BN filler content, according to the experimental results [116]. Hsiao Yen Ng and colleagues discussed the effect of the properties of different fillers and processing conditions on the thermal conductivity of BN-filled thermoplastics as electronic packaging material [117]. Series of BN-filled poly(butylene terephthalate) (PBT) specimens were fabricated, and thermal conductivity as a function of particle dimensionalities, particle surface chemistries, and filler concentration as well as processing condition was systematically discussed. It was found that large surface area of BN, which may act as phonon-scattering sites, causes lower thermal conductivity at low filler concentration, while at high filler concentration regime, however, high aspect ratio BN reaches percolation threshold easier which gives rise to high thermal conductivity. Shearing

force produced during the extrusion procedure may result in better dispersion of filler, which provides the composites with higher heat conduction performance, compared with that produced by injection molding. A maximum thermal conductivity of approximately 1.2 W/mK was reached for PT180 with BN filler loading fraction no more than 25 vol% [117].

Thermal conductive performance of silicone rubber composites loaded with BN fillers was studied by researchers from different groups, respectively, focusing on different research aspects. Sebnem Kemaloglu and colleagues investigated thermal conductivity and mechanical and morphological properties of silicone rubber reinforced with nano- or micro-sized boron nitride as a function of filler loading level [118]. The thermal conductivity, coefficients of thermal expansion (CTE), and mechanical properties were found to be strongly correlated to the loading fraction, aspect ratio, and dispersion of the filler BN with various dimensions. Nano-sized BN fillers presented much better improvement to the mechanical properties, such as tensile strength and strain at breakage, than their micro-sized counterpart [118]. Wen-Ying Zhou and coworkers have also studied the thermal conductive behavior of h-BN-filled silicone rubber composite materials [119]. Similarly, they found that further improvement of thermal conductivity of the silicone rubber composites can be realized by filling filler material with different distribution of dimensionalities [119].

Apart from silicone rubber composites, Sebnem Kemaloglu and coworkers also investigated the evolution of series of properties of styrene–ethylene–butylene–styrene terpolymer (SEBS)/poly(ethylene-co-vinyl acetate) (EVA) blends as the incorporation of h-BN fillers [120]. Similar trend of evolution of thermal and mechanical properties of the composites has been observed compared with those of silicone rubber composites aforementioned [118], i.e., thermal conductivity, moduli, and hardness of the composites increase with h-BN loading level while tensile strength decreases. It was also found that h-BN can be more thermodynamically stable dispersed in SEBS than EVA, which was proved by surface energy measurement and the calculation of wettability coefficient [120]. Polymeric composites filled with hybrid filler shape or dimensions, i.e., synergistic effect, have been studied by many people, which will be further discussed in the following section [118, 119, 121, 122].

In addition to filling high content h-BN, changing the surface chemistry of filler may also give rise to an improvement of thermal conductivity of polymeric composites. In order to realize this purpose, usually different silane coupling agents and various solvents will be used because the modification provided by silane should often be completed under solution condition. In fact, many researchers have ever tried to improve the filler–matrix interface, which could be a reason for the overall enhancement of properties, to obtain better thermal conductivity [123–125].

Nevertheless, as one of the hottest studied materials with two-dimensional nanostructure, boron nitride nanosheets (BNNSs) are thought to be suitable for using as filler material for thermally conductive polymeric composites, mostly for its ultrahigh aspect ratio. Except for BNNS, there is another one nanostructure belonging to the family of h-BN, namely, boron nitride nanotube (BNNT), that also presents ultra-

high aspect ratio, which is suitable for preparing high thermal conductive polymer composites. Chunyi Zhi and collaborators did elaborate study on the synthesis, functionalization, and as filler material for composites [126]. Toward achieving high thermal conductivity for thermal interface materials (TIMs), they have tried different combinations of polymeric materials and BNNT, for example, PMMA–BNNT composites [127], epoxy–BNNT composites [128], and other polymeric materials filled with BNNT [129–132]. By virtue of its high aspect ratio and ultrahigh intrinsic thermal conductivity, usually very high thermal conductivity can be obtained with relative small amount of BNNT loading fractions, which proves the effectiveness of BNNT as ideal filler material for thermal interface polymeric composite materials.

11.3.2.3 Si_3N_4

The other filler material for thermally conductive polymer composites, which belongs to the category of nitrides, is silicon nitride (Si_3N_4.)However, because of its non-prominent intrinsic thermal conductivity, there were limited numbers of papers discussing Si_3N_4-filled polymer composites for thermal interface materials, which will be summarized below.

Wenying Zhou and coworkers fabricated ultrahigh molecular weight polyethylene-linear low-density polyethylene composite material filled with silicon nitride particulate [133]. Several factors, such as filler size and dispersion as well as filler concentration, which affect the thermal conductivity and relative dielectric property, were systematically studied. Thermally conductive pathway formed by percolated silicon nitride particles provides the composites with enhanced thermal conductivity. Thermal conductivity of the composite can be improved up to 1.2 W/mK loaded with 20 vol% Si_3N_4 with 0.2 μm size. Further improvement of thermal conductivity reached 1.8 W/mK with silane-coupling agent treatment, owing to modified interfacial adhesion [133]. Hong He and colleagues designed and fabricated novel-structured epoxy composite filled with Si_3N_4 fillers [134]. The matrix epoxy resin was pre-fragmented into small particles with different sizes and selected by sieves. Thermally conductive pathway of the composites percolated at relatively low filler concentration and a maximum thermal conductivity of 1.8 W/mK was achieved at 30 vol% filler loading fractions [134]. Besides, they also fabricated other polymeric composites using silicon nitride as fillers. Hot pressing molding method was applied to fabricate polystyrene–Si_3N_4 composites [135]. The effect of particle size of PS polymer, Si_3N_4 loading fraction, and silane surface modification of filler on the thermal conductivity and dielectric property of as-fabricated composites were investigated. Highest thermal conductivity value of the series of composites reached 3.0 W/mK at 40 vol% filler loading fraction. Larger PS particle size, high filler volume fraction, and silane surface treatment render the composites with higher thermal conductivity, according to the measured thermal conductivity values [135]. Jun Zeng and collaborators investigated thermal conductivity and dielectric property of epoxy-molding compound (EMC) filled with different fillers, i.e., Si_3N_4, Si_3N_4/SiO_2, and SiO_2 [136]. EMCs loaded with Si_3N_4 presented exceeding thermal conductivity, reaching 2.5 W/mK at 80 vol% filler volume fraction, than EMC loaded with SiO_2.

11.3.3 Graphene Oxide as Fillers

As aforementioned, graphene oxide (GO), which contains a certain number of surface functional groups, such as carboxylic group and hydroxyl group, is the oxide form of graphene. This renders GO electrically insulating property while preserving the thermal conductivity of graphene to some extent. As a result, by incorporating graphene oxide into polymeric materials, composite materials with enhanced thermal conductivity can be fabricated and applied as thermal interface materials.

Min-Chien Hsiao and coworkers prepared epoxy nanocomposites filled with hybrid nanosheet filler, which is made of sandwiched thermally reduced graphene oxide (TRGO) and silica, of which the composites present enhanced thermal conductivity while maintaining electric insulation property [137]. As the addition of 1 wt% of TRGO coated with silica, the as-prepared composites preserve high electrical resistivity of 2.96×10^{11} Ωm, and the thermal conductivity was increased up to 0.322 W/mK, which was 61 % higher than that of neat epoxy [137].

Coincidentally, Xue Pu and colleagues used similar idea to fabricate electrically insulating and thermally conductive epoxy-based composite by in situ coating silica on functionalized reduced GO and subsequently loading the filler [138]. The reduction and functionalization of graphene oxide were conducted by reacting 3-aminopropyltriethoxysilane (APTES) with GO, which was essentially different with conventional methods. The existence of APTES not only provided interfacial bonding between graphene oxide and the in situ-coated silica but also modified their thermal interface. Seventy-two percent improvement of thermal conductivity was observed by filling 8 wt% of silica-coated graphene oxide, reaching 0.3 W/mK while still retaining electric resistance [138].

Wei-Fu Ji and coworkers prepared PMMA polymeric composites filled with thermally reduced graphene oxide and investigated the effect of the content of carboxylic group on the graphene oxide on the physical property of the composites [139]. It was observed and verified by TEM and FTIR that thermally reduced graphene oxide containing higher content of carboxylic groups formed better dispersion than those containing less carboxylic groups. As a result, physical properties like thermal stability, thermal conductivity, mechanical strength, and permeability varied with carboxylic group content. In terms of thermal conductivity, which was measured by transient plane source (TPS) method, thermally reduced graphene oxide with higher content of carboxylic group PTC-55 presented better thermal conduction performance, and 15 % enhancement in thermal conductivity was seen compared with that of neat PMMA [139].

In addition, Kim, Tae-Eon, and coworkers introduced graphene nanoplatelets into silicon carbide fiber-reinforced phenolic resin composites in order to obtain high thermal conductivity polymer composites [140]. According to their studies, composites without introducing graphene nanofiller showed 4.1 W/mK at 50 vol% filler loading fraction, while the graphene nanoplatelet-loaded one presented much higher value of thermal conductivity, up to 5.5 W/mK, which was primarily due to the synergistic effect of SiC and graphene filler [140].

When it comes to hybrid fillers, there were some other works aiming at demonstrating the effectiveness of improvement of thermal conductivity by incorporating hybrid filler materials [141–144]. Synergistic effect offered by hybrid fillers, which exists not only in different filler composition but also in different filler size and shape distribution, generally modifies the interfacial circumstances between matrix and filler materials, giving rise to better overall properties of the composites.

11.3.4 SiC as Fillers

The last type of filler for fabricating thermally conductive polymer composite material is SiC. As what we have mentioned above, the thermal conductivity of commercially available SiC is usually in the range of tens of W/mK, owing to the existing impurities and defects. Therefore, the thermal conductivity of polymer composites with commercial SiC filled is as high as that obtained from h-BN- or AlN-filled polymer composites. However, the cost-effective characteristics of SiC have attracted much research attention on it.

Hwang, Yongseon, and coworkers fabricated epoxy-based composites with SiC filled by wetting process [145]. In their presented work, SiC cake was preliminarily made and followed by the infiltration of epoxy droplet, resulting in a relative homogenous dispersion of filler, compared with conventional methods. As a result, a maximum thermal conductivity up to 3.85 W/mK was achieved with 70 wt% filler loading fraction [145].

SR Kim and colleagues prepared polyetheretherketone (PEEK)/SiC and PEEK/carbon–fiber composites and successively measured the thermal conductivity value from ambient temperature to 200 °C via laser flash method [146]. A maximum thermal conductivity value of 2.4 W/mK was achieved with 50 vol% SiC loaded while 40 vol% carbon fiber loading rendered the composite 3.1 W/mK, compared with the thermal conductivity of neat PEEK (0.29 W/mK) [146].

In addition, Lisa Ekstrand and collaborators developed an anisotropic conductive adhesive (ACA) with improved thermal conductivity by the addition of thermally conductive but electrically insulating inorganic filler, such as alumina, silicon carbide, and carbon nanotube, into epoxy matrix phase [147]. Finally, measured by transient hot wire method, thermal conductivity of epoxy adhesive was increased 100–150 %, which was more than 0.5 W/mK, with filler loading fraction less than 20 vol% [147].

Perfluoromethyl vinyl ether (PMVE) rubber filled with inorganic fillers was fabricated by Li Wang and coworkers, and thermally conductive behavior of the composites was investigated successively [148]. It was revealed by both theoretical model and their experimental results that there would be less obvious improvement of thermal conductivity when the difference of thermal conductivity between matrix and filler material is bigger than 100 times. It was also found in their study that thermal resistance from the interface will result in deficiency in thermal conductiv-

ity improvement, and therefore filler with large size or aspect ratio can more effectively enhance the thermal conductivity of polymer matrix, compared with smaller filler. Apart from that, thermal conductivity value above 2 W/mK was achieved with 80 vol% 74 micron-SiC loaded [148].

Furthermore, Fang Ren and colleagues filled SiC particles with various dimensions into linear low-density polyethylene (LLDPE) to fabricate composite materials and subsequently tested the thermal, mechanical, and electrical properties of the composites [149]. Prepared by mixing the blende powder and successive hot press molding, effects of filler content and particle diameter on the thermal conduction performance of the composites were investigated. Thermal conductivity of the composite was increased from 0.32 W/mK to 0.98 W/mK at 50 wt% filler loading fraction while the dielectric constant was also increased [149]. However, according to their report, filler with large diameter provided the composites with less thermal conductivity enhancement compared with that of filler with smaller diameter, which was essentially different with the finding mentioned above [148]. This can be ascribed to the effect of aspect ratio of the filler and we will further discuss in the later section.

11.4 Essential Factors to Achieve High Thermal Conductivity

From the discussion above, it is clear that the thermal conductivity of polymer composites filled with inorganic fillers is influenced by certain factors, such as intrinsic thermal conductivity of the filler and matrix materials, the size and shape, i.e., aspect ratio, of the filler, surface modification of the filler, and even the use of hybrid fillers that caused synergistic effect as well as the orientation of the fillers in the matrix. We will discuss the listed factors in detail and try to comprehensively understand the mechanisms related.

11.4.1 Nature of Polymer and Thermal Conductivity of Fillers

The intrinsic thermal conductivity of the constituents plays important role to thermal conductivity of the final-obtained composites. Polymeric materials usually possess low thermal conductivity due to strong phonon-scattering effect. However, there are still some variations of thermal conductivity values among different polymers, which then reflect in variation in the thermal conductivity value of obtained composites. Hatsuo Ishida and coworkers fabricated polybenzoxazine composites with BN as filler material, and an extraordinary high thermal conductivity of 32.5 W/mK was obtained at 88 wt% [150]. The impressive value obtained can be ascribed to the superior properties of the polymer matrix and filler BN material (Fig. 11.11).

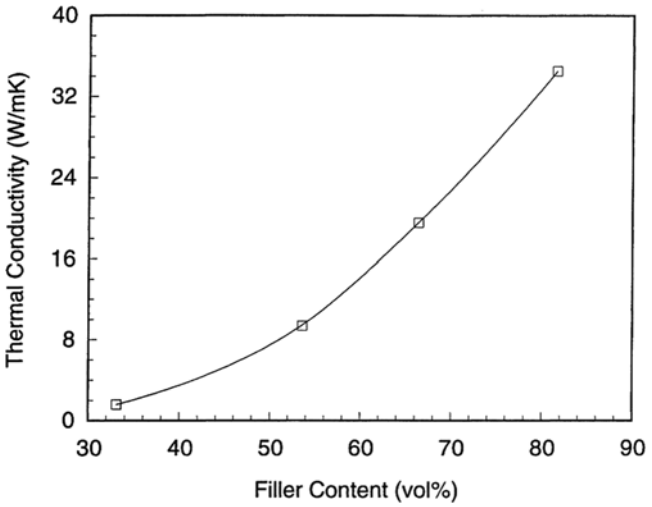

Fig. 11.11 Thermal conductivity of BN-filled polybenzoxazine as a function of filler contents (Reproduced with permission from [146])

As for filler material, as shown in the Table 11.1, the intrinsic thermal conductivity of different inorganic fillers can be lined in the order: h-BN (or AlN) > Si_3N_4 (SiC) > ZnO > Al_2O_3 > SiO_2, therefore, thermal conductivity of the composites fabricated with those different filler varies. For example, according to the experimental results, polymer composites with h-BN filled can feasibly achieve thermal conductivity value above 2 W/mK with moderate filler loading fraction [121, 123, 132], while for Al_2O_3 or SiO_2 filled polymer composites, it is not easy to obtain such value at the same loading level [92, 95, 97]. However, according to the research of Richard F. Hill and coworkers, the enhancement of thermal conductivity of the composites has almost no correlation with the intrinsic thermal conductivity of the filler material when the thermal conductivity value of filler is in the range of 30–300 W/mK [151]. He also claimed that composites filled with filler of high stiffness usually acquire lower thermal conductivity value compared to that of composites filled with soft filler, such as h-BN. The soft platelet-like filler could undergo deformation which is helpful to obtain high packing density and better filler connectivity [151].

Although it is commonly acknowledged that thermal conductivity of the composites increases with increasing filler loading fraction, there will be no significant improvement of thermal conductivity when the difference in thermal conductivity between matrix polymer and filler is greater than 100 [39]. All this research work provided evidence that it is not a necessity to have filler material with very high thermal conductivity.

11.4.2 Filler Size and Shape

Apart from the factor mentioned above, the size and shape of filler also play an important role in the thermal conduction performance of the composites. Yet, contradictive opinions and experimental phenomena have been reported that some people hold the view that smaller and fine particles provide the composites with higher thermal conductivity while others think that particles with larger dimensions conduct heat more efficiently [109, 117, 133, 152].

For a generally point of view, fillers with larger dimensions possess smaller surface area, which corresponds to smaller surface energy. Moreover, smaller surface area meanwhile implies less matrix–filler interfaces, which act as thermal barrier and cause more phonon scattering and therefore reduce thermal conductivity. These opinions are proposed and held by Hsiao Yen Ng et al. and Yunsheng Xu et al., according to their papers [109, 117].

On the other hand, however, Sebnem Kemaloglu et al. and Wenying Zhou et al. believed that fillers with smaller size result in higher thermal conductivity of the composites, as they thought that smaller particles could for thermally conductive paths easier than their bulk counterpart [120, 133].

In general, it is reasonable to hold different views when the experimental results of themselves match the opinions proposed. However, after comparing different experimental results and ideas of many published papers, it is more rational to believe that it is the aspect ratio that really plays the essential role, in terms of heat conduction performance.

As for fillers with particulate shape, aspect ratio can be the ratio of length in the longitudinal and transverse direction. As for fillers with two-dimensional structures, the aspect ratio could be the ratio of the length of lateral size versus in-through distance, while in the aspect ratio of one-dimensional materials, such as nanotubes and nanowires, the aspect ratio can be defined as the length versus diameter. The thermal conductivity can be dramatically enhanced if the high thermal conductivity filler material interconnects with each other and forms continuous conductive paths, i.e., reaching percolation threshold. Therefore, the ability for filler materials to get connected really weighed importantly. Fillers with high aspect ratio interconnect with each other easier at relatively lower concentration, i.e., conductive paths form readily compared with filler that possesses low aspect ratio. As a result, both large size and small size filler have the opportunity to conduct heat more efficiently as long as they acquire satisfying aspect ratios [118, 132, 144]. The effect of size and shape of different fillers can therefore be ascribed into the influence of aspect ratio, to a certain extent.

11.4.3 Surface Modification

In order to improve the thermal conductivity of polymeric materials, inorganic fillers with high thermal conductivity are incorporating into the polymer matrix. Yet, the differences in the physical or chemical nature between polymeric materials and

inorganic materials always make it difficult to tailor or improve the performance of their composites as the affinity between the two constituents is bad.

Interfacial modification or surface modification of the filler materials or both matrix and filler materials could be a solution to solve the problem of improving dissatisfactory interface between matrix and filler. In fact, many researchers dedicate in modifying the surface chemistry of materials to improve some sort of performance of materials.

Hsien Tang Chiu and coworkers coated polysilazane and SiOC on aluminum nitride surface by dip-coating method for surface modification and subsequently filled the modified AlN into silicone rubber matrix [153]. An improved thermal conductivity of the composites was found as a result of modified interfacial adhesion and reduced thermal contact resistance between the rubber matrix and filler. Nevertheless, Mousam Choudhury and colleagues tried to modify the surface of AlN by c-aminopropyltriethoxysilane-coupling agent to tailor the interface of AlN-filled epoxy resin composites [154]. The silane treatment resulted in high-density AlN compared with untreated one, and enhanced thermal conductivity was then obtained.

Moreover, Mengdie Liu and coworkers functionalized alumina with hybrid chemical agent phthalonitrile-terminated poly(arylene ether nitriles) (PEN-t-ph) by solution-casting method and obtained a 2.7-times increase of thermal conductivity compared with pure polymer material at 30 wt% filler loading level [92]. Besides, Bin Lee and coworkers systematically studied the effect of surface modification of ZnO filler on the thermal conductivity of EVA composites by treating ZnO with a variety of agents at certain dosages [101]. By surface treatment, compatibility between filler–matrix improves which effectively provides interfacial adhesion and decreases potentially existing voids as well as suppressing phonon scattering; thermal conductivity of the composites can be therefore improved (Fig. 11.12).

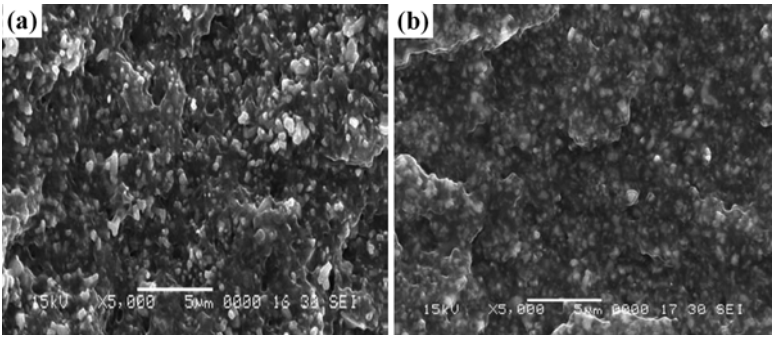

Fig. 11.12 (**a**) The SEM image of the fractured surface morphology of EVA composites filled with untreated ZnO. (**b**) The SEM image of the fractured surface morphology of EVA composites filled with KH-560-treated ZnO (Reproduced with permission from [97])

Additionally, Xingyi Huang and collaborators delicately investigated the role of interfacial modification to the improvement of thermal conductivity of high loading fraction AlN epoxy composites [104]. Six types of surface-treated AlN as well as non-treated ones were filled into epoxy matrix and the effectiveness of different treating methods was examined as a result of thermal conductivity improvements. It was found that covalent-bonding treatment works more effective below certain filler loading volume fraction as individual filler contacts with each other directly after reaching percolation threshold. Apart from that, voids and defects originally existing in the matrix can be effectively removed by mercapto-terminated silane treatment, according to their findings [104].

It can be summarized that surface modification of filler is of great importance in acquiring high thermal conductive polymer composites, according to the discussion above (Fig. 11.13).

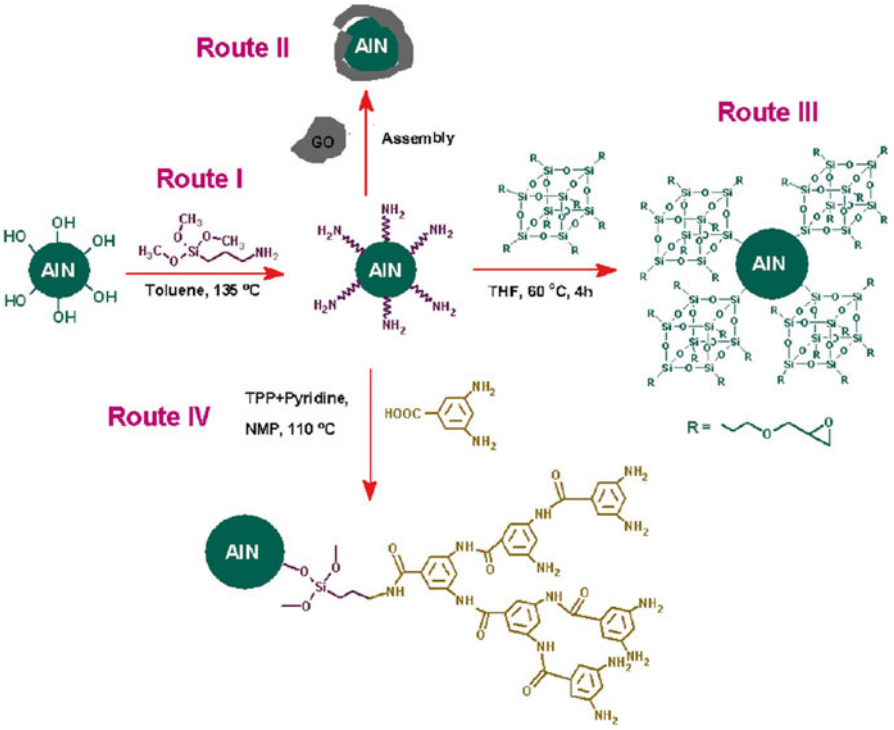

Fig. 11.13 Surface treatment and assembly procedures of AlN particles. Route I: preparation process of amino-functionalized AlN. Route II: assembly of amino-functionalized AlN and GO. Route III: reaction between amino-functionalized AlN and POSS. Route IV: preparation of hyperbranched polymer-modified AlN (Reproduced with permission from [100])

11.4.4 Synergistic Effect

Hybrid fillers are usually used, which provides the so-called synergistic effect, when sole type of filler could hardly fulfill the wanted function or performance of material. In terms of improving thermal conductivity of polymer composites, there are potentially two reasons for the utilization of hybrid fillers. One of the reasons is to improve the packing density and achieving more effectively conductive paths, leading to higher thermal conduction performance. The other one is to use hybrid filler to lower down percolation threshold and realize cost-effectiveness.

Usually, the selected hybrid fillers have different characteristics, for example, elemental composition, dimensions, and geometrical parameters [155] (Fig. 11.14).

K Gaska and coworkers fabricated epoxy–matrix composites filled with BN and AlN with different size distributions [156]. By combination of the two filler materials with different average particle size and shape, it can be observed from experimental results that there was more than 100 % improvement in thermal conductivity compared with epoxy composites filled with sole-type filler. In addition, Tung-Lin Li and coworkers filled nano- and micro-sized BN into polyimide (PI) for fabricating composite thin film with enhanced thermal conductivity [122]. A maximum thermal conductivity value up to 1.2 W/mK was achieved with only 30 wt% of micro- and nano-BN at weight ratio of 7:3, which was nearly doubled value compared with thermal conductivity values obtained from single micro-sized or nano-sized BN fillers.

Mei-Hui Tsai and colleagues functionalized boron nitride and graphene oxide with coupling agent and glycidyl methacrylate, respectively, and then blended them into polyimide to fabricate flexible thin film with enhanced thermal conductivity [141]. As a result of synergistic effect, the gaps or voids between PI and f-BN were successfully filled by the soft graphene oxide nanosheets, forming effective thermally conductive network. Compared with the thermal conductivity obtained from pure PI, the values of thermal conductivity were 16 times higher with the addition

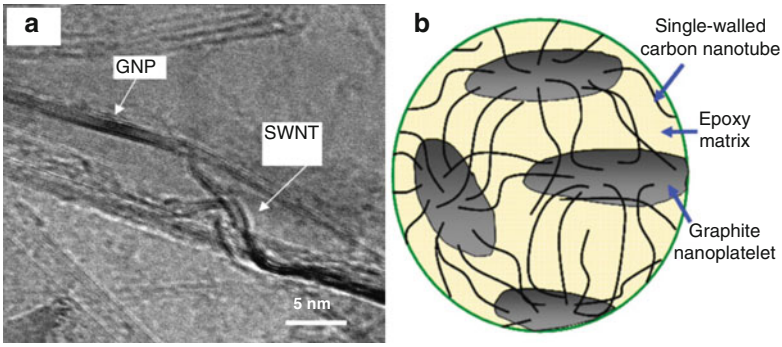

Fig. 11.14 Schematic representation of GNP–SWNT network in polymer matrix showing the synergetic effect (Reproduced with permission from [151])

of 1 wt% g-GO. What's more, even compared with f-BN-filled PI, at any given filler weight fractions, thermal conductivity values were more than doubled with additional 1 wt% g-GO filled. A maximum value of thermal conductivity was 2.11 W/mK with 1 wt% g-GO and 50 wt% f-BN filled.

Besides, Chih-Chun Teng and coworkers fabricated epoxy composites with functionalized carbon nanotubes and aluminum nitride and investigated the improvements of thermal conductivity as a result of synergetic effect [157]. According to the measured thermal conductivity values, epoxy composite containing 25 vol% AlN and 1 vol% functionalized CNT acquired comparable thermal conductivity (1.21 W/mK) compared with that of 50 vol% AlN-filled epoxy composite, which demonstrated the effectiveness of hybrid filler in thermal conductivity improvement.

11.4.5 Orientation of Fillers

Last but not the least, the way how the fillers have been arranged in the matrix also influences the thermal conduction performance of the composites. For two-dimensional nanomaterials, such as GO and hexagonal BN, the intrinsic thermal conductivity along the atomic plane direction and that perpendicular to the in-plane direction sees much difference. Inspired by this, researchers try to align fillers in the preferred direction and expect an anisotropic heat conduction performance along with different directions.

Ho Sun Lim and collaborators connected iron oxide (Fe_3O_4) nanoparticles to BN and utilized magnetic field to align the filler materials in preferred direction in the epoxy resin matrix [158]. Reoriented by external magnetic field, Fe_3O_4-coated BN platelet-filled epoxy presented exceptional in-plane thermal conductivity while sacrificing the thermal conductivity in the vertical direction. A maximum value of thermal conductivity of 4.7 W/mK was obtained at 20 vol% Fe_3O_4-coated BN loading fraction, which was 23.5-times higher than pure epoxy, while thermal conductivity of filled with randomly oriented filler acquired thermal conductivity lower than 1.0 W/mK at the same filler fraction [158].

Haiyan Yan and coworkers applied similar idea of aligning graphene nanosheets in epoxy resin by magnetic field to make full use of the ultrahigh in-plane thermal conductivity of graphene atomic plane [159]. In order to fulfill this purpose, graphene nanosheets and iron oxide (Fe_3O_4) were co-precipitated and then been filled into epoxy resin under magnetic field provided by two parallel aligned magnets. Thermal conductivity measurements were then performed to confirm the effectiveness of improvement and anisotropic thermal conductivity along different testing directions, i.e., either parallel or perpendicular to the direction of filler been aligned. Finally, as shown in the experimental results, at 1 vol% graphene loading fraction, epoxy composites filled with aligned filler presented 139 % and 41 % enhancement of thermal conductivity along the parallel direction and vertical direction, respectively [159].

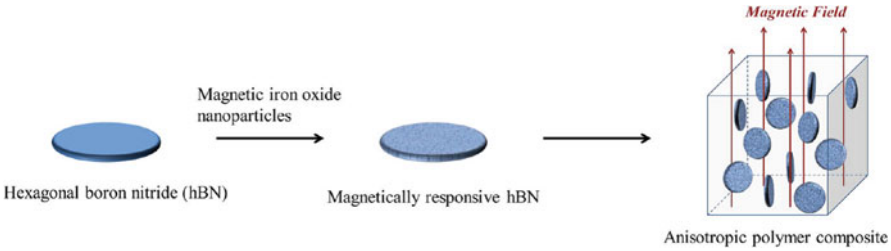

Fig. 11.15 Schematic illustration of alignment of h-BN in the polymer matrix by magnetic field (Reproduced with permission from [161])

Similarly, Ziyin Lin and colleagues also applied magnetic field to align superparamagnetic iron oxide nanoparticle-modified h-BN nanosheets in epoxy resin and achieved 104 % thermal conductivity enhancement at 20 wt% filler loading fraction compared with that of composites filled with randomly oriented filler [160, 161]. Other similar study includes work reported by Hong-Baek Cho and coworkers [162] (Fig. 11.15).

11.5 Summaries and Future Prospects

In summary, numerous efforts have been made on fabrication of thermally conductive electrically insulating polymer composites. Typical fillers for these kinds of nanocomposites include oxides, nitrides, and some newly discovered materials, such as graphene oxides. In general, nitrides, including AlN and BN (they possess thermal conductivity of hundreds of W/mK or even higher) may provide much better thermal conductivity enhancement in comparison with oxides (they usually have thermal conductivities of tens of W/mK), but nitrides are also much more expensive than oxides.

In recent years, various nanostructures, such as nanotubes, nanowires, and nanosheets have been fabricated. With their unique structures and high aspect ratio, they possess much higher efficiency for thermal conductivity improvement than traditional micro-sized ceramic powders with easily formed thermally conductive paths. As fillers with different morphologies available, the filler architecture design, such as using fillers with different sizes and different morphologies to generate synergetic effects, were found to be effective to reach high thermal conductivity. In addition, filler alignments utilizing different mechanisms were found to be very effective to enhance thermal conductivity of a composite along one direction (anisotropic thermal conductivity). The other interesting approach to fabricate high thermal conductive composites facilitated by nanomaterials is formation of 3D network in the composites directly. This is usually realized by fabrication of GO aerogel, followed by filling the gel with polymers.

Although great progresses have been achieved in this field, it seems the materials fabricated still cannot meet the requirements of industry. This is partially because the development of electronic devices is too fast, which makes the related material study much laggard. On the other hand, most reported high thermal conductive composite materials are not industrially useful because their overall performance is scarified to achieve the reported high thermal conductivity. For example, although embedding high fraction fillers in matrix or built-up 3D filler architecture in composites is useful to achieve high thermal conductivity, it will deteriorate the mechanical properties or processability of the polymer. Therefore, it is extremely important to optimize overall performance of the thermally conductive composite materials instead of only thermal conductivity. It is believed that with the advance of nanomaterials and nanotechnologies, high thermal conductive insulating composite materials with well-maintained overall performance can be achieved to meet requirements of highly powered electronic devices in near future.

References

1. Prasher R (2006) Thermal interface materials: historical perspective, status, and future directions. Proc IEEE 94(8):1571–1586
2. Otiaba KC et al (2011) Thermal interface materials for automotive electronic control unit: trends, technology and R&D challenges. Microelectron Reliab 51(12):2031–2043
3. Shen S et al (2010) Polyethylene nanofibres with very high thermal conductivities. Nat Nanotechnol 5(4):251–255
4. Kleinstreuer C, Feng Y (2011) Experimental and theoretical studies of nanofluid thermal conductivity enhancement: a review. Nanoscale Res Lett 6(1):1–13
5. Lee J-H et al (2008) Effective viscosities and thermal conductivities of aqueous nanofluids containing low volume concentrations of Al 2 O 3 nanoparticles. Int J Heat Mass Transf 51(11):2651–2656
6. Lee S et al (1999) Measuring thermal conductivity of fluids containing oxide nanoparticles. J Heat Transf 121(2):280–289
7. Wang X, Xu X, Choi SUS (1999) Thermal conductivity of nanoparticle-fluid mixture. J Thermophys Heat Transf 13(4):474–480
8. Li CH, Peterson G (2006) Experimental investigation of temperature and volume fraction variations on the effective thermal conductivity of nanoparticle suspensions (nanofluids). J Appl Phys 99(8):084314
9. Das SK et al (2003) Temperature dependence of thermal conductivity enhancement for nanofluids. J Heat Transf 125(4):567–574
10. Williams W, Buongiorno J, Hu L-W (2008) Experimental investigation of turbulent convective heat transfer and pressure loss of alumina/water and zirconia/water nanoparticle colloids (nanofluids) in horizontal tubes. J Heat Transf 130(4):042412
11. Rusconi R, Rodari E, Piazza R (2006) Optical measurements of the thermal properties of nanofluids. Appl Phys Lett 89(26):261916
12. Putnam SA et al (2006) Thermal conductivity of nanoparticle suspensions. J Appl Phys 99(8):084308
13. Venerus DC et al (2006) Study of thermal transport in nanoparticle suspensions using forced Rayleigh scattering. J Appl Phys 100(9):094310
14. Greenwood NN, Earnshaw A (1984) Chemistry of the elements. Oxford: Pergamon Press.

15. Nishi Y, Doering R (2000) Handbook of semiconductor manufacturing technology. New York: Taylor & Francis.
16. Kistler SS (1931) Coherent expanded aerogels and jellies. Nature 127:741
17. Wei TY et al (2007) Preparation of monolithic silica aerogel of low thermal conductivity by ambient pressure drying. J Am Ceram Soc 90(7):2003–2007
18. Dorcheh AS, Abbasi MH (2008) Silica aerogel; synthesis, properties and characterization. J Mater Process Technol 199(1–3):10–26
19. Nakanishi K et al (1998) Structure design of double-pore silica and its application to HPLC. J Sol-Gel Sci Technol 13(1–3):163–169
20. Nakanishi K et al (1997) Double pore silica gel monolith applied to liquid chromatography. J Sol-Gel Sci Technol 8(1–3):547–552
21. Ishizuka N et al (2000) Performance of a monolithic silica column in a capillary under pressure-driven and electrodriven conditions. Anal Chem 72(6):1275–1280
22. Wagh P et al (1999) Comparison of some physical properties of silica aerogel monoliths synthesized by different precursors. Mater Chem Phys 57(3):214–218
23. Rao AV et al (2006) Synthesis of flexible silica aerogels using methyltrimethoxysilane (MTMS) precursor. J Colloid Interface Sci 300(1):279–285
24. Strøm R et al (2007) Strengthening and aging of wet silica gels for up-scaling of aerogel preparation. J Sol-Gel Sci Technol 41(3):291–298
25. Titulaer M et al (1994) The increase in pH during aging of porous sol–gel silica spheres. J Non-Cryst Solids 170(2):128–133
26. Chou K, Lee B (1994) Solvent effect on ageing of silica gels. J Mater Sci 29(13):3565–3571
27. Smitha S et al (2006) Effect of aging time and concentration of aging solution on the porosity characteristics of subcritically dried silica aerogels. Microporous Mesoporous Mater 91(1):286–292
28. Özgür Ü et al (2005) A comprehensive review of ZnO materials and devices. J Appl Phys 98(4):041301
29. Wang ZL (2004) Zinc oxide nanostructures: growth, properties and applications. J Phys Condens Matter 16(25):R829
30. Morkoç, H., & Özgür, Ü. (2008). Zinc oxide: fundamentals, materials and device technology. John Wiley & Sons.
31. Zhang Y et al (2005) Zinc oxide nanorod and nanowire for humidity sensor. Appl Surf Sci 242(1):212–217
32. Yang H-J et al (2015) Ultralong mesoporous ZnO nanowires grown via room temperature self-assembly of ZnO nanoparticles for enhanced reversible storage in lithium ion batteries. RSC Adv 5(42):33392–33399
33. Wang ZL (2004) Nanostructures of zinc oxide. Mater Today 7(6):26–33
34. Gao P, Wang ZL (2002) Self-assembled nanowire-nanoribbon junction arrays of ZnO. J Phys Chem B 106(49):12653–12658
35. Gao P, Ding Y, Wang Z (2003) Crystallographic orientation-aligned ZnO nanorods grown by a tin catalyst. Nano Lett 3(9):1315–1320
36. Lao J et al (2003) ZnO nanobridges and nanonails. Nano Lett 3(2):235–238
37. Pan ZW, Dai ZR, Wang ZL (2001) Nanobelts of semiconducting oxides. Science 291(5510):1947–1949
38. Hashimoto S, Yamaguchi A (1996) Growth morphology and mechanism of a hollow ZnO polycrystal. J Am Ceram Soc 79(4):1121–1123
39. Huang X, Jiang P, Tanaka T (2011) A review of dielectric polymer composites with high thermal conductivity. IEEE Electr Insul Mag 27(4):8–16
40. Olorunyolemi T et al (2002) Thermal conductivity of zinc oxide: from green to sintered state. J Am Ceram Soc 85(5):1249–1253
41. Özgür Ü et al (2006) Thermal conductivity of bulk ZnO after different thermal treatments. J Electron Mater 35(4):550–555
42. Tsubota T et al (1997) Thermoelectric properties of Al-doped ZnO as a promising oxide material for high-temperature thermoelectric conversion. J Mater Chem 7(1):85–90

43. Katsuyama S et al (2002) Thermoelectric properties of (Zn1− yMgy) 1− xAlxO ceramics prepared by the polymerized complex method. J Appl Phys 92(3):1391–1398
44. Ong KP, Singh DJ, Wu P (2011) Analysis of the thermoelectric properties of n-type ZnO. Phys Rev B 83(11):115110
45. Shinde SL, Goela J (2006) High thermal conductivity materials. Berlin: Springer
46. Slack GA (1973) Nonmetallic crystals with high thermal conductivity. J Phys Chem Solids 34(2):321–335
47. Buhr H et al (1991) Phase composition, oxygen content, and thermal conductivity of AIN (Y2O3) ceramics. J Am Ceram Soc 74(4):718–723
48. Komeya K, Tsuge A, Inoue H (1984) High density and thermal conductivity. Google Patents US4435513 A
49. Haubner, R., Herrmann, M., Lux, B., Petzow, G., Weissenbacher, R., & Wilhelm, M. (2003). High performance non-oxide ceramics II (Vol. 102). M. Jansen (Ed.). Springer.
50. Kimura Y et al (1999) Boron nitride as a lubricant additive. Wear 232(2):199–206
51. Pawlak Z et al (2009) A comparative study on the tribological behaviour of hexagonal boron nitride (h-BN) as lubricating micro-particles—an additive in porous sliding bearings for a car clutch. Wear 267(5):1198–1202
52. Chopra NG et al (1995) Boron nitride nanotubes. Science 269(5226):966–967
53. Golberg D et al (2007) Boron nitride nanotubes. Adv Mater 19(18):2413–2432
54. Golberg D et al (2010) Boron nitride nanotubes and nanosheets. ACS Nano 4(6):2979–2993
55. Lin Y, Williams TV, Connell JW (2009) Soluble, exfoliated hexagonal boron nitride nanosheets. J Phys Chem Lett 1(1):277–283
56. Tang C et al (2008) Synthetic routes and formation mechanisms of spherical boron nitride nanoparticles. Adv Funct Mater 18(22):3653–3661
57. Zeng H et al (2010) "White graphenes": boron nitride nanoribbons via boron nitride nanotube unwrapping. Nano Lett 10(12):5049–5055
58. Huo K et al (2002) Synthesis of boron nitride nanowires. Appl Phys Lett 80(19):3611–3613
59. Lian G et al (2011) Facile synthesis of 3D boron nitride nanoflowers composed of vertically aligned nanoflakes and fabrication of graphene-like BN by exfoliation. J Mater Chem 21(25):9201–9207
60. Hirao K et al (2012) High thermal conductivity silicon nitride ceramics. J Korean Ceram Soc 49(4):380–384
61. Xu W et al (2003) Study on the thermal conductivity and microstructure of silicon nitride used for power electronic substrate. Mater Sci Eng B 99(1):475–478
62. Pablos A, Osendi MI, Miranzo P (2002) Effect of microstructure on the thermal conductivity of hot-pressed silicon nitride materials. J Am Ceram Soc 85(1):200–206
63. Wang G et al (2008) Facile synthesis and characterization of graphene nanosheets. J Phys Chem C 112(22):8192–8195
64. Novoselov KS et al (2004) Electric field effect in atomically thin carbon films. Science 306(5696):666–669
65. Hummers WS Jr, Offeman RE (1958) Preparation of graphitic oxide. J Am Chem Soc 80(6):1339
66. Marcano DC et al (2010) Improved synthesis of graphene oxide. ACS Nano 4(8):4806–4814
67. Bao C et al (2012) Preparation of graphene by pressurized oxidation and multiplex reduction and its polymer nanocomposites by masterbatch-based melt blending. J Mater Chem 22(13):6088–6096
68. Shen J et al (2009) Fast and facile preparation of graphene oxide and reduced graphene oxide nanoplatelets. Chem Mater 21(15):3514–3520
69. Sreeprasad TS et al (2011) Reduced graphene oxide-metal/metal oxide composites: Facile synthesis and application in water purification. J Hazard Mater 186(1):921–931
70. Su Y et al (2014) Impermeable barrier films and protective coatings based on reduced graphene oxide. Nat Commun 5
71. Zhu XJ et al (2011) Nanostructured reduced graphene oxide/Fe2O3 composite as a high-performance anode material for lithium ion batteries. ACS Nano 5(4):3333–3338

72. Ji LW et al (2011) Graphene oxide as a sulfur immobilizer in high performance lithium/sulfur cells. J Am Chem Soc 133(46):18522–18525
73. Dikin DA et al (2007) Preparation and characterization of graphene oxide paper. Nature 448(7152):457–460
74. Slack GA (1964) Thermal conductivity of pure and impure silicon, silicon carbide, and diamond. J Appl Phys 35(12):3460–3466
75. Shor JS, Kurtz AD (1994) Photoelectrochemical etching of 6 H-SiC. J Electrochem Soc 141(3):778–781
76. Takazawa A, Tamura T, Yamada M (1993) Porous β-SiC fabrication by electrochemical anodization. Jpn J Appl Phys 32(7R):3148
77. Cambaz GZ et al (2006) Anisotropic etching of SiC whiskers. Nano Lett 6(3):548–551
78. Matsumoto T et al (1994) Blue-green luminescence from porous silicon carbide. Appl Phys Lett 64(2):226–228
79. Connolly E et al (2005) A porous SiC ammonia sensor. Sensors Actuators B Chem 109(1):44–46
80. Klein S, Winterer M, Hahn H (1998) Reduced-pressure chemical vapor synthesis of nanocrystalline silicon carbide powders. Chem Vap Depos 4(4):143–149
81. Lin H et al (2008) Synthesis of amorphous silicon carbide nanoparticles in a low temperature low pressure plasma reactor. Nanotechnology 19(32):325601
82. Meng G et al (1998) Preparation of β–SiC nanorods with and without amorphous SiO2 wrapping layers. J Mater Res 13(09):2533–2538
83. Wang ZL et al (2000) Side-by-side silicon carbide–silica biaxial nanowires: synthesis, structure, and mechanical properties. Appl Phys Lett 77(21):3349–3351
84. Ryu Y, Tak Y, Yong K (2005) Direct growth of core–shell SiC–SiO2 nanowires and field emission characteristics. Nanotechnology 16(7):S370
85. Tang C, Bando Y (2003) Effect of BN coatings on oxidation resistance and field emission of SiC nanowires. Appl Phys Lett 83(4):659–661
86. Hao Y-J et al (2006) Synthesis and characterization of bamboo-like SiC nanofibers. Mater Lett 60(11):1334–1337
87. Wei J et al (2006) Growth and morphology of one-dimensional SiC nanostructures without catalyst assistant. Mater Chem Phys 95(1):140–144
88. Hao Y-J et al (2006) Beaded silicon carbide nanochains via carbothermal reduction of carbonaceous silica xerogel. Nanotechnology 17(12):2870
89. Li Z et al (2008) Large-scale synthesis and Raman and photoluminescence properties of single crystalline β-SiC nanowires periodically wrapped by amorphous SiO2 nanospheres 2. J Phys Chem C 113(1):91–96
90. Zhang H-F, Wang C-M, Wang L-S (2002) Helical crystalline SiC/SiO2 core-shell nanowires. Nano Lett 2(9):941–944
91. Fu J et al (2010) Effect of nanoparticles on the performance of thermally conductive epoxy adhesives. Polym Eng Sci 50(9):1809–1819
92. Liu M, Jia K, Liu X (2015) Effective thermal conductivity and thermal properties of phthalonitrile-terminated poly (arylene ether nitriles) composites with hybrid functionalized alumina. J Appl Polym Sci 132(10):1–8
93. Kozako M et al (2010) Preparation and evaluation of epoxy composite insulating materials toward high thermal conductivity. In: Solid Dielectrics (ICSD), 2010 10th IEEE international conference on 2010 IEEE, Potsdam
94. Bujard P et al (1994) Thermal conductivity of molding compounds for plastic packaging. In: Electronic components and technology conference, 1994. Proceedings, 44th, 1994, IEEE, Washington, DC
95. Wong C, Bollampally RS (1999) Thermal conductivity, elastic modulus, and coefficient of thermal expansion of polymer composites filled with ceramic particles for electronic packaging. J Appl Polym Sci 74(14):3396–3403
96. Shen M-X et al (2011) Thermal conductivity model of filled polymer composites. Int J Miner Metall Mater 18(5):623–631

97. Lee WS, Yu J (2005) Comparative study of thermally conductive fillers in underfill for the electronic components. Diam Relat Mater 14(10):1647–1653
98. Sim LC et al (2005) Thermal characterization of Al 2 O 3 and ZnO reinforced silicone rubber as thermal pads for heat dissipation purposes. Thermochim Acta 430(1):155–165
99. Özmıhçı FÖ, Balköse D (2013) Effects of particle size and electrical resistivity of filler on mechanical, electrical, and thermal properties of linear low density polyethylene–zinc oxide composites. J Appl Polym Sci 130(4):2734–2743
100. Fang L et al (2015) Hydrangea-like zinc oxide superstructures for ferroelectric polymer composites with high thermal conductivity and high dielectric constant. Compos Sci Technol 107:67–74
101. Lee B, Dai G (2009) Influence of interfacial modification on the thermal conductivity of polymer composites. J Mater Sci 44(18):4848–4855
102. Wang Z et al (2011) Preparation of nano-zinc oxide/EPDM composites with both good thermal conductivity and mechanical properties. J Appl Polym Sci 119(2):1144–1155
103. Mu Q, Feng S, Diao G (2007) Thermal conductivity of silicone rubber filled with ZnO. Polym Compos 28(2):125–130
104. Huang X et al (2012) Role of interface on the thermal conductivity of highly filled dielectric epoxy/AlN composites. J Phys Chem C 116(25):13629–13639
105. Lee ES et al (2008) Enhanced thermal conductivity of polymer matrix composite via high solids loading of aluminum nitride in epoxy resin. J Am Ceram Soc 91(4):1169–1174
106. Zhou Y et al (2012) Fabrication and characterization of aluminum nitride polymer matrix composites with high thermal conductivity and low dielectric constant for electronic packaging. Mater Sci Eng B 177(11):892–896
107. Yu H et al (2012) Thermal and insulating properties of epoxy/aluminum nitride composites used for thermal interface material. J Appl Polym Sci 124(1):669–677
108. Yu S, Hing P, Hu X (2002) Thermal conductivity of polystyrene–aluminum nitride composite. Compos A: Appl Sci Manuf 33(2):289–292
109. Xu Y, Chung D, Mroz C (2001) Thermally conducting aluminum nitride polymer-matrix composites. Compos A: Appl Sci Manuf 32(12):1749–1757
110. Xie S-H et al (2004) Preparation and properties of polyimide/aluminum nitride composites. Polym Test 23(7):797–801
111. Gu J et al (2009) Thermal conductivity and mechanical properties of aluminum nitride filled linear low-density polyethylene composites. Polym Eng Sci 49(5):1030–1034
112. Ohashi M et al (2005) Spherical aluminum nitride fillers for heat-conducting plastic packages. J Am Ceram Soc 88(9):2615–2618
113. Peng W et al (2010) Electrical and thermophysical properties of epoxy/aluminum nitride nanocomposites: Effects of nanoparticle surface modification. Compos A: Appl Sci Manuf 41(9):1201–1209
114. Yu J et al (2011) Influence of nano-AlN particles on thermal conductivity, thermal stability and cure behavior of cycloaliphatic epoxy/trimethacrylate system. Express Polym Lett 5(2):132–141
115. Bujard P (1988) Thermal conductivity of boron nitride filled epoxy resins: temperature dependence and influence of sample preparation. In: Thermal phenomena in the fabrication and operation of electronic components: I-THERM'88, InterSociety conference on, 1988, IEEE, Los Angeles, CA
116. Zhou W et al (2007) Thermal conductivity of boron nitride reinforced polyethylene composites. Mater Res Bull 42(10):1863–1873
117. Ng HY, Lu X, Lau SK (2005) Thermal conductivity of boron nitride-filled thermoplastics: effect of filler characteristics and composite processing conditions. Polym Compos 26(6):778–790
118. Kemaloglu S, Ozkoc G, Aytac A (2010) Properties of thermally conductive micro and nano size boron nitride reinforced silicon rubber composites. Thermochim Acta 499(1):40–47
119. Zhou WY et al (2007) Thermally conductive silicone rubber reinforced with boron nitride particle. Polym Compos 28(1):23–28

120. Kemaloglu S, Ozkoc G, Aytac A (2010) Thermally conductive boron nitride/SEBS/EVA ternary composites: "processing and characterization". Polym Compos 31(8):1398–1408
121. Yung K, Liem H (2007) Enhanced thermal conductivity of boron nitride epoxy-matrix composite through multi-modal particle size mixing. J Appl Polym Sci 106(6):3587–3591
122. Li T-L, Hsu SL-C (2010) Enhanced thermal conductivity of polyimide films via a hybrid of micro-and nano-sized boron nitride. J Phys Chem B 114(20):6825–6829
123. Wang Z et al (2014) Solvent-free fabrication of thermally conductive insulating epoxy composites with boron nitride nanoplatelets as fillers. Nanoscale Res Lett 9(1):1–7
124. Yu J et al (2012) Interfacial modification of boron nitride nanoplatelets for epoxy composites with improved thermal properties. Polymer 53(2):471–480
125. Xu Y, Chung D (2000) Increasing the thermal conductivity of boron nitride and aluminum nitride particle epoxy-matrix composites by particle surface treatments. Compos Interfaces 7(4):243–256
126. Zhi C et al (2008) Boron nitride nanotubes: functionalization and composites. J Mater Chem 18(33):3900–3908
127. Zhi C et al (2008) Mechanical and thermal properties of polymethyl methacrylate-BN nanotube composites. J Nanomater 2008
128. Zhi CY et al (2010) Dielectric and thermal properties of epoxy/boron nitride nanotube composites. Pure Appl Chem 82(11):2175–2183
129. Terao T et al (2009) Thermal conductivity improvement of polymer films by catechin-modified boron nitride nanotubes. J Phys Chem C 113(31):13605–13609
130. Terao T et al (2010) Alignment of boron nitride nanotubes in polymeric composite films for thermal conductivity improvement. J Phys Chem C 114(10):4340–4344
131. Zhi C et al (2009) Towards thermoconductive, electrically insulating polymeric composites with boron nitride nanotubes as fillers. Adv Funct Mater 19(12):1857–1862
132. Huang X et al (2013) Polyhedral oligosilsesquioxane-modified boron nitride nanotube based epoxy nanocomposites: an ideal dielectric material with high thermal conductivity. Adv Funct Mater 23(14):1824–1831
133. Zhou W et al (2009) A novel fiber-reinforced polyethylene composite with added silicon nitride particles for enhanced thermal conductivity. Compos A: Appl Sci Manuf 40(6):830–836
134. He H et al (2007) High thermal conductive Si3N4 particle filled epoxy composites with a novel structure. J Electron Packag 129(4):469–472
135. He H et al (2007) Preparation and properties of Si 3 N 4/PS composites used for electronic packaging. Compos Sci Technol 67(11):2493–2499
136. Zeng J et al (2009) High thermal conductive epoxy molding compound with thermal conductive pathway. J Appl Polym Sci 113(4):2117–2125
137. Hsiao M-C et al (2013) Thermally conductive and electrically insulating epoxy nanocomposites with thermally reduced graphene oxide–silica hybrid nanosheets. Nanoscale 5(13):5863–5871
138. Pu X et al (2014) Thermally conductive and electrically insulating epoxy nanocomposites with silica-coated graphene. RSC Adv 4(29):15297–15303
139. Ji WF et al (2014) Preparation and comparison of the physical properties of PMMA/thermally reduced graphene oxides composites with different carboxylic group content of thermally reduced graphene oxides. Compos A Appl Sci Manuf 65:108–114
140. Kim T-E et al (2013) Thermal conductivity behaviour of silicon carbide fiber/phenolic resin composites by the introduction of graphene nanoplatelets. Asian J Chem 25(10):5625–5630
141. Tsai M-H et al (2014) Flexible polyimide films hybrid with functionalized boron nitride and graphene oxide simultaneously to improve thermal conduction and dimensional stability. ACS Appl Mater Interfaces 6(11):8639–8645
142. Li Z et al (2014) Enhancement of the thermal conductivity of polymer composites with Ag–graphene hybrids as fillers. Phys Status Solidi A 211(9):2142–2149
143. Qian R et al (2013) Alumina-coated graphene sheet hybrids for electrically insulating polymer composites with high thermal conductivity. RSC Adv 3(38):17373–17379

144. Khan MO et al (2013) Effects of microsized and nanosized carbon fillers on the thermal and electrical properties of polyphenylene sulfide based composites. Polym Eng Sci 53(11):2398–2406
145. Hwang Y, Kim J, Cho W (2014) Thermal conductivity of thermally conductive ceramic composites and silicon carbide/epoxy composites through wetting process. Polymer-Korea 38(6):782–786
146. Kim SR et al (2007) Study on thermal conductivity of polyetheretherketone/thermally conductive filler composites. Solid State Phenom 124:1079–1082
147. Ekstrand L, Kristiansen H, Liu J (2005) Characterization of thermally conductive epoxy nano composites. In: Electronics technology: meeting the challenges of electronics technology progress, 2005. 28th International Spring seminar on. 2005, IEEE, Wiener Neustadt
148. Wang L, Li F, Su Z (2008) Effective thermal conductivity behavior of filled vulcanized perfluoromethyl vinyl ether rubber. J Appl Polym Sci 108(5):2968–2974
149. Ren F et al (2011) Thermal, mechanical and electrical properties of linear low-density polyethylene composites filled with different dimensional SiC particles. Polym Plast Technol Eng 50(8):791–796
150. Ishida H, Rimdusit S (1998) Very high thermal conductivity obtained by boron nitride-filled polybenzoxazine. Thermochim Acta 320(1):177–186
151. Hill RF, Supancic PH (2002) Thermal conductivity of platelet-filled polymer composites. J Am Ceram Soc 85(4):851–857
152. Lu X, Xu G (1997) Thermally conductive polymer composites for electronic packaging. J Appl Polym Sci 65(13):2733–2738
153. Chiu HT et al (2014) Surface modification of aluminum nitride by polysilazane and its polymer-derived amorphous silicon oxycarbide ceramic for the enhancement of thermal conductivity in silicone rubber composite. Appl Surf Sci 292:928–936
154. Choudhury M, Mohanty S, Nayak SK (2013) Effect of surface modification of aluminum nitride on electrical and thermal characterizations of thermosetting polymeric nanocomposites. Polym Compos 34(1):1–14
155. Yu A et al (2008) Enhanced thermal conductivity in a hybrid graphite nanoplatelet–carbon nanotube filler for epoxy composites. Adv Mater 20(24):4740–4744
156. Gaska K et al (2015) Enhanced thermal conductivity of epoxy–matrix composites with hybrid fillers. Polym Adv Technol 26(1):26–31
157. Teng C-C et al (2012) Synergetic effect of thermal conductive properties of epoxy composites containing functionalized multi-walled carbon nanotubes and aluminum nitride. Compos Part B 43(2):265–271
158. Lim HS et al (2013) Anisotropically alignable magnetic boron nitride platelets decorated with iron oxide nanoparticles. Chem Mater 25(16):3315–3319
159. Yan H et al (2014) Enhanced thermal conductivity in polymer composites with aligned graphene nanosheets. J Mater Sci 49(15):5256–5264
160. Lin Z et al (2013) Enhanced thermal transport of hexagonal boron nitride filled polymer composite by magnetic field-assisted alignment. In: Electronic components and technology conference (ECTC), 2013 IEEE 63rd, 2013, IEEE, Las Vegas, NV
161. Lin Z et al (2013) Magnetic alignment of hexagonal boron nitride platelets in polymer matrix: toward high performance anisotropic polymer composites for electronic encapsulation. ACS Appl Mater Interfaces 5(15):7633–7640
162. Cho H-B et al (2013) Thermal anisotropy of epoxy resin-based nano-hybrid films containing BN nanosheets under a rotating superconducting magnetic field. Mater Chem Phys 139(2):355–359

Chapter 12
Polymer–Clay Nanocomposites: A Novel Way to Enhance Flame Retardation of Plastics and Applications in Wire and Cable Industry

Tie Lan and Günter Beyer

12.1 Introduction

Polymer nanocomposites are a new class of materials that have demonstrated unique performance properties which conventional composites cannot offer. These properties can be achieved with minimum addition of the nanodimensional fillers/additives. Polymer nanocomposites are commonly defined as the combination of a polymer matrix and fillers that have at least one dimension in the 100-naomerter or smaller-size range. Polymers with nano-sized inorganic fillers are the most widely researched materials in the last 15–20 years. Flame retardation is one of the most significant performance properties of polymer nanocomposite materials along with other enhanced properties such as mechanical reinforcement, barrier properties, and dimensional stability.

Polymer–clay nanocomposites are the most studied materials up to date. Montmorillonite is the widely used clay particle as filler/additives to make polymer–clay nanocomposite. Addition of a few percentage of organic-modified montmorillonite can effectively reduce the peak heat release rate (HRR) of the polymer in a standard cone calorimeter testing. The reduced HRR indicates the reduction of the flammability of the plastic and allows formulators to form new flame-retardant plastics in combination with the reduced amount of the traditional flame retardants. The formation of polymer–clay nanocomposite in low-smoke halogen-free (LSOH) compounds also reduces the heat generated in the cable burning test. This allows cables to pass newly approved EU's Construction Product Regulation.

T. Lan
Nanocor, LLC, A Minerals Technologies Inc Company,
2870 Forbs Ave., Hoffman Estates, IL 60192, USA
e-mail: Tie.Lan@nanocor.com

G. Beyer (✉)
Kabelwerk Eupen AG, Malmedyer Strasse 9, B – 4700 Eupen, Belgium
e-mail: gbeyer@euregio.net

© Springer International Publishing Switzerland 2016

X. Huang, C. Zhi (eds.), *Polymer Nanocomposites*,
DOI 10.1007/978-3-319-28238-1_12

12.2 Bentonite Clay Surface Chemistry

Montmorillonite clays can be extracted or purified from mined bentonite ores. The best purification method is disclosed in AMCOL's patent US Patent 6,050,509 [1]. Purified montmorillonite has more than 98 % purity with defined cation exchange capacity for the subsequent clay surface modification. Montmorillonite has layered structure (Fig. 12.1), with each platelet consisting of octahedral alumina sheets sandwiched between two tetrahedral silica sheets. The alumina sheet has partial replacement of aluminum cations (Al^{3+}) by magnesium (Mg^{2+}) which provides a net negative charge to the platelet. The negative charge is balanced by inorganic cations like Na^{+} or Ca^{2+}, and these cations are typically hydrated and the clay inner surface is hydrophilic. Ion exchange reaction is the easiest way to modify the montmorillonite clay to hydrophobic. Hydrophobic montmorillonite clays are also commonly called as organoclay. Various alkyl ammonium cations are used to modify the montmorillonite clay to allow inner layer compatibility with various polymer resins. The organic modification is the key modifying montmorillonite from hydrophilic to hydrophobic. Figure 12.2 shows the schematic ion exchange diagram. The exchange reaction is carried out in a media like water or mixture of water and some organic solvents.

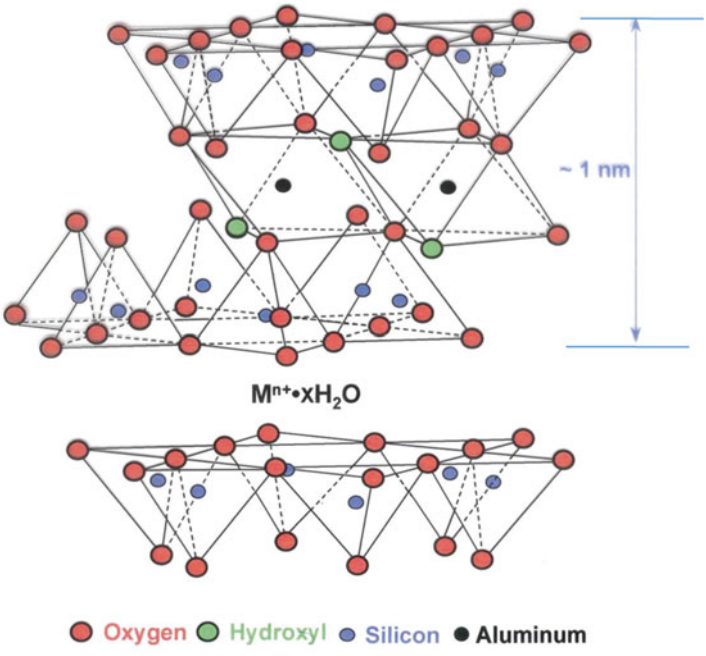

Fig. 12.1 Structure of 2:1 layered silicate like montmorillonite clay

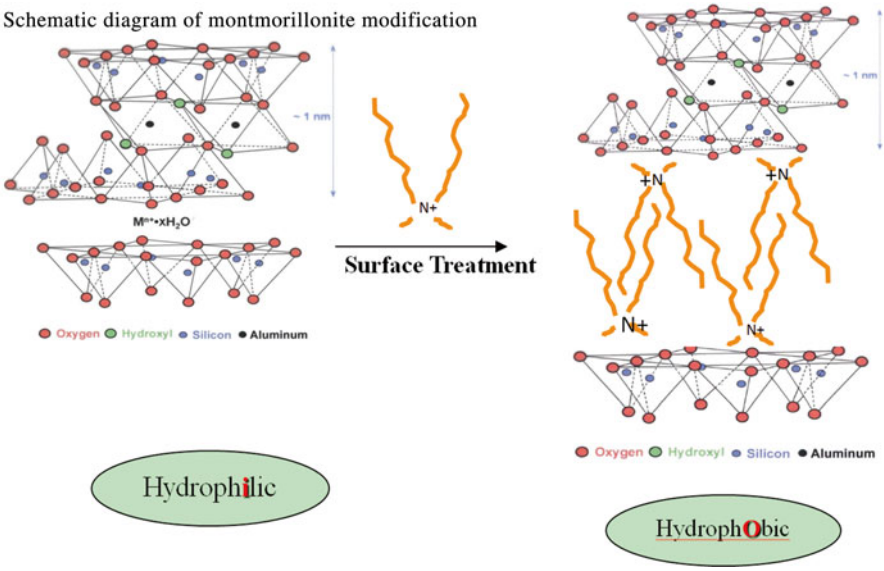

Fig. 12.2 Schematic of the formation of organoclay via ion exchange reaction

Quaternary ammonium, dimethyl dihydrogenated tallow ammonium chloride (DMDHT), is one of the most commonly used surface modifications. The ionic bonding of DMDHT to the clay negatively charged surface is quite strong. NaCl, as the ion exchange reaction by-product will be washed out from the clay. After surface modification, the inner layer region of the clay is hydrophobic. After ion exchange with organic treatment, montmorillonite clays are supplied in an agglomerate form. There are a few commercial products based on DMDHT treatment chemistry, like Nanomer® I.44P, Cloisite® 15A, and 20A. Other quaternary ammoniums like trimethyl hydrogenated tallow ammonium (TMHT), dimethyl benzyl hydrogenated tallow (DMBHT), and methyl benzyl di-hydrogenated tallow (MBDHT) are also used to make organoclay products. Although alkyl quaternary ammonium is suitable for most of the organoclay modification, however, the nature of the chemical also creates a limitation. The most significant limitation is the heat stability. Traditional organoclays with quaternary ammonium like DMDHT as exchange cations were considered with a heat stability only up to 200 °C [2]. Even with special selection of chemical and refined processing, the heat stability can only be improved to 240 °C. This is mainly due the Hoffman elimination reaction associated to the quaternary ammonium. Attempt to increase the heat stability has been a hot topic with emphasis on the use of quaternary phosphonium chemistry (Fig. 12.3).

We selected primary amine (octadecyl amine, ODA) to improve the heat stability of our organoclay due to the fact that primary amine does not undergo Hoffman elimination reaction upon heating. Octadecyl amine was protonated by HCl and dissolved in water for the cation exchange reaction. Octadecyl amine-modified

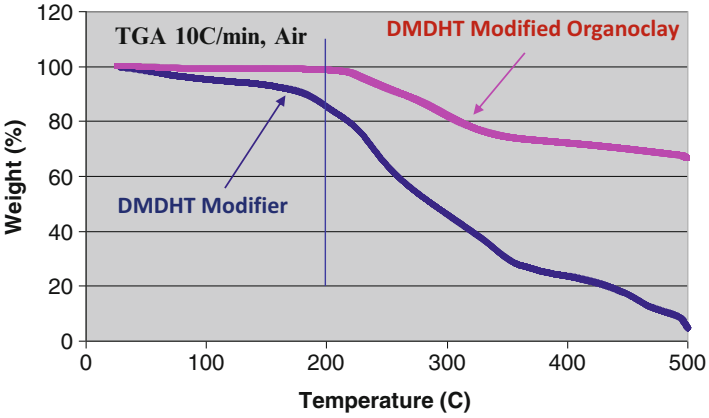

Fig. 12.3 TGA of dimethyl dihydrogenated tallow (DMDHT) ammonium chloride and DMDHT-modified organoclay, 10C/min, in air

organoclay has good hydrophobic properties like other organoclays to allow polymer to invade its interlayer resign to form nanocomposite materials.

Isothermal TGA was used to study the heart stability of the organoclay. In this method, we heat the sample rapidly at 50 °C/min to 250 °C or 300 °C and then hold the temperature to record the weight loss of the organoclay at these temperatures. This testing is similar to the heat experience of an organoclay experienced in a polymer extrusion process. In Fig. 12.4a, b, we report the weight losses of the traditional DMDHT-modified organoclay and the weight loss of ODA-modified montmorillonite clay. The ODA-modified organoclay has much better improved heat stability. Table 12.1 summarizes the heat stability results of DMDHT- and ODA-modified organoclays. For ODA-modified clay, the weight loss at 250 °C isotherm is only 0.8 % at 5 min compared to 8 % weight loss of DMDHT-modified organoclay. At 300 °C isotherm, ODA-modified organoclay has 5 % weight loss versus 15 % weight loss of DMDHT-modified organoclay. Considering 5 min as residence time of a typical plastic processing, the organoclay with ODA can be used for processing up to 280 °C, whereas organoclay with DMDHT can only be used at 220 °C. Organoclay with ODA may be suitable to use in engineering thermal plastics like polyamides and polyester to create new flame-retardant compounds.

After ion exchange reaction, the organoclay was dewatered and dried and milled. The final process should yield final product in a fine powder form. Air classification is recommended to remove the large particle in these milled products. The mean particle size is normally in the range of 15–20 μm. Given that particle size is a distribution of particles, the top size (99 % of the clay particle sizes) should be less than 60 μm.

Coordination chemistry has able been used to modify the bentonite clay inner surface with dipole–dipole interaction [3]. Combination of flame-retardant like resorcinol diphenyl phosphate oligomer with pristine Na-montmorillonite shows potential use as resin compatibilizer and flame-retardant additives [4]. The reaction is carried out is semisolid environment. Phosphate ester was mixed with montmorillonite with addition of water. The mixture was processed in a continuous mixer or

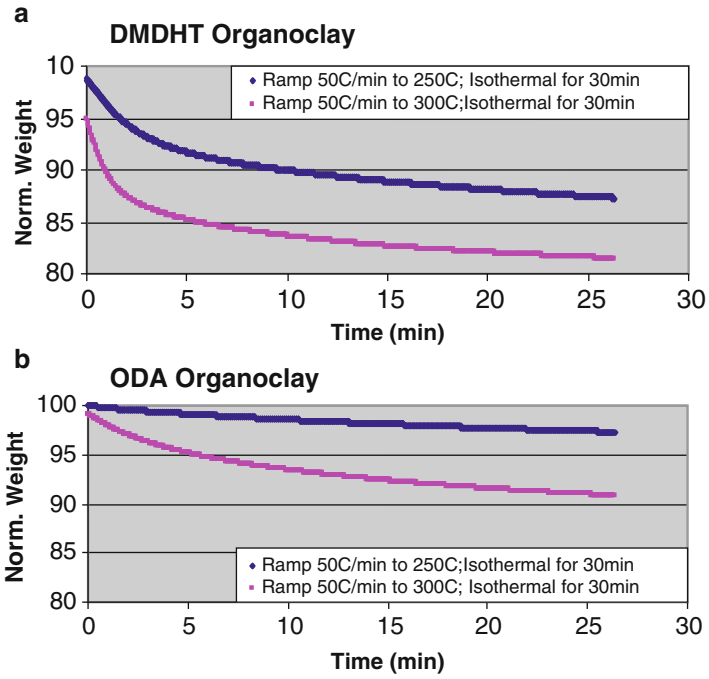

Fig. 12.4 (**a**, **b**) Isothermal TGA of DMDHT- and ODA-modified montmorillonite clays

Table 12.1 Weight loss of DMDHT and ODA organoclays

Samples (TGA, 50C/min to ISO temperature)	Weight loss at 250 °C 5 min	Weight loss at 300 °C 5 min	Max. compounding temp (°C)
DMDHT organoclay	8.0 %	15 %	220
ODA organoclay	0.8 %	5 %	280

extruder. Finished products were obtained with subsequent drying and milling. Figure 12.5 shows the phosphate ester Phosflex® 418-modified montmorillonite (Charex 418515). The d_{001} was increased to 26 Å from 12 Å of the original clay. TGA of Phosflex® 418-modified montmorillonite is shown in Fig. 12.6. The decomposition profile is quite similar to the phosphate ester decomposition. SEM image (Fig. 12.7) reveals the morphological nature of the modified clay.

12.3 Nanocomposite Formation and Structure

Preparation of polymer–clay nanocomposite has been a hot topic for polymer chemist and polymer-processing engineers in the two decades. Generally speaking, the process involves de-agglomerate micron-size organoclay and introduces nanoscale

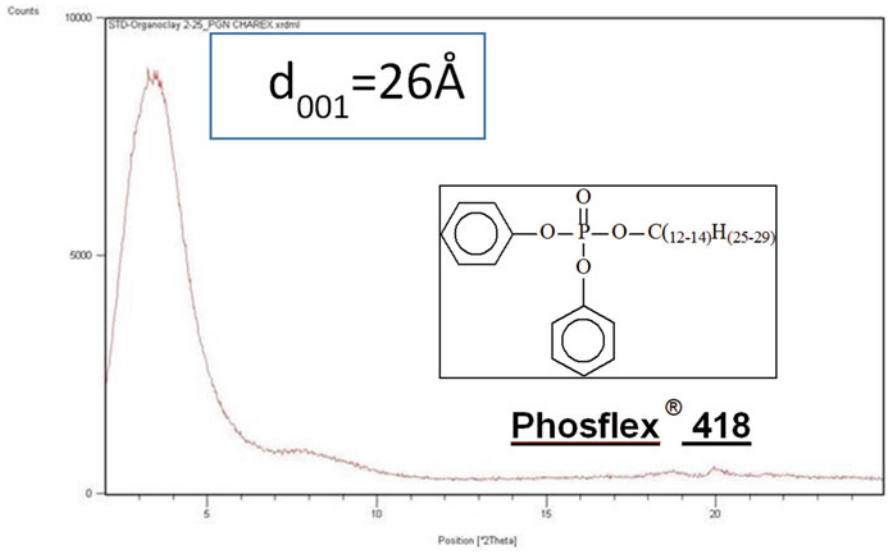

Fig. 12.5 XRD of dialkyl phosphate ester (Phosflex 418)-modified montmorillonite clay

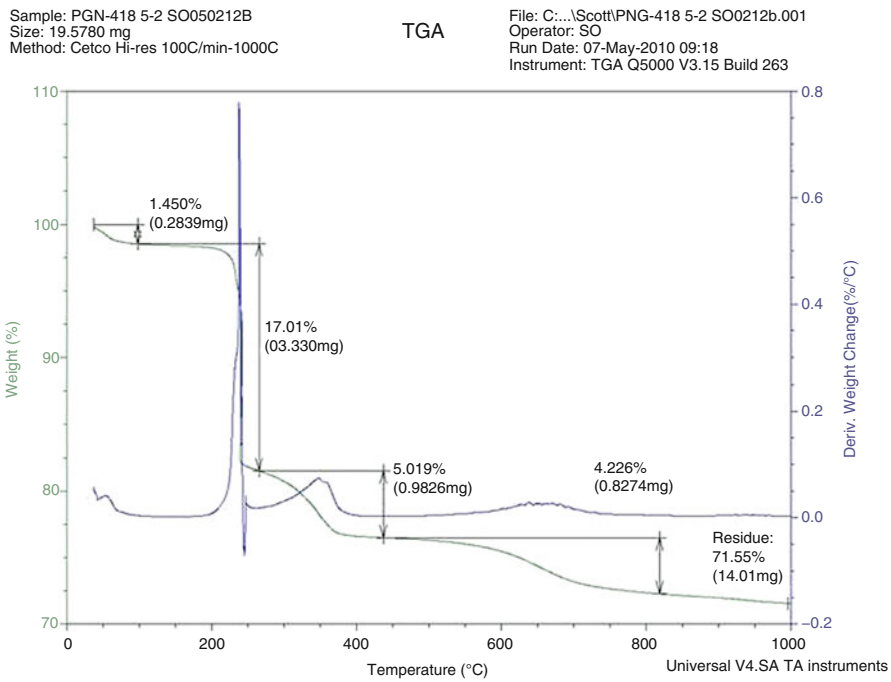

Fig. 12.6 TGA of dialkyl phosphate ester (Phosflex 418)-modified montmorillonite clay

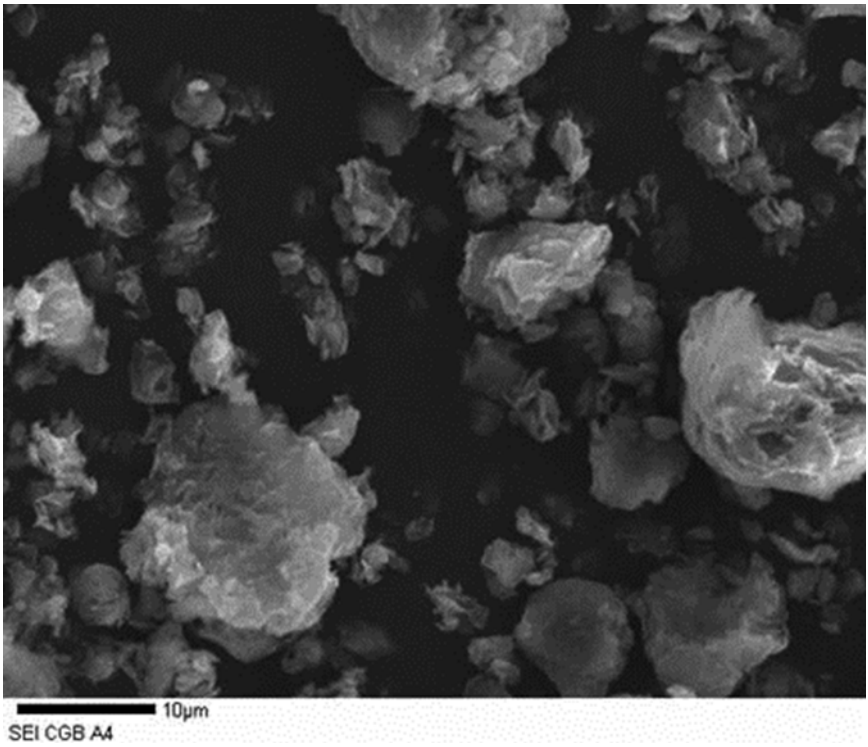

Fig. 12.7 SEM of dialkyl phosphate ester (Phosflex 418)-modified montmorillonite clay

interaction between polymer matrix and organoclay. The nanoscale interaction is caused by the insertion or intercalation of melt polymers into the hydrophobic region of the inner layer space of the organoclays. Monomer or oligomer can be used as starting materials to achieve the interaction followed by polymerization induced by heat or other means. This process is called in situ polymerization process. The first commercial polymer–clay nanocomposite technology developed by Toyota researchers was to use monomer in situ polymerization in organoclay [5]. It has been proven that the polyamide 6 monomer, caprolactam molecules, can enter the inner gallery resigns before the polymerization. In the polymerization process, due the presence of polymer catalyst in the clay gallery, continuous migration of monomers into the gallery resin will expand the organoclay gallery further to a degree of delamination or exfoliation. The clay silicate clay stacking was disturbed by the presence of the polymers formed in the inner layer gallery region. Several attempts to use in situ polymerization of polymer–clay nanocomposites have been reported for both thermoset and thermoplastic resins.

Polymer–clay nanocomposite can also be formed with preformed polymer interaction with organoclays. The hydrophobicity of the organoclay provides an organic moiety to allow nanoscale interaction of resin molecules with silicate layers of the

organoclay. The inner layer spacing expends to a certain degree to accommodate the intercalated polymer. However, most of the case, the silicate layer stacking is still regular. The regular stacking can be measured by standard powder X-ray diffraction technique. The polymer melt interaction into the organoclay is illustrated in Fig. 12.8. The X-ray basal spacing (d_{001}) will increase to d'_{001}. Similarly to d_{001}, which is determined by the clay charge density and chain length of the alkyl ammonium in the bentonite clay treatment, d'_{001} is governed by the chain length of the alkyl chain in the surface treatment. In addition, it is also determined by the shear force in the melt extrusion. The X-ray diffraction peak may become broad under high-shear processing condition, indicating less stacking order of the silicate layer in the composite. For flame retardation, the intercalation is more important than exfoliation. The intercalation enables the polymer to form smaller domain size in the composite. It is unlikely the polymers existing in separated intercalated clay layer regions to have a chance to recombine to form bulk polymer. Therefore, the presence of the silicate clay layers reduces the tendency of the dripping when the composite is exposed to fire or other heat sources. In addition, the polymer also has different decompose mechanisms once they are intercalated into the clay inner layer region. The restricted space enables free radicals to reform stable molecules. This process will eventually allow the polymer to form large amount of char deposited on the clay layer surfaces. Figure 12.9 shows the surface morphology of burned EVA–clay nanocomposite. The EVA–clay nanocomposite was lighted by a burner in ambient condition and allows it to burn to the end naturally. The residual sample is char-like. The char is about two to three times as the loading level of the organoclay in the sample. For instance, the remaining weight is 10–15 wt% of original sample weight with 5 wt% organoclay loading. Clearly, not all EVA was burned into H_2O and CO_2 in burning process. The presence of the clay enables char formation of the EVA in the burning process. The reduced burning fuel and burning intensity allows regular flame retardant to perform better to stop extinguish the fire.

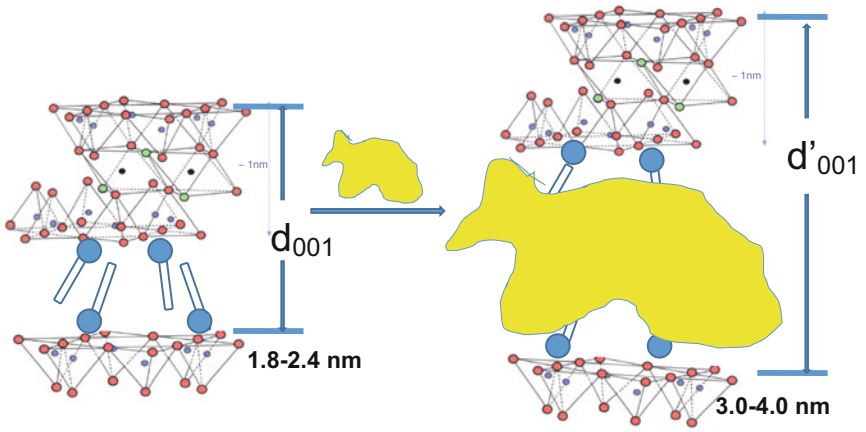

Fig. 12.8 Schematic of the polymer interaction into organoclay and nanocomposite formation process

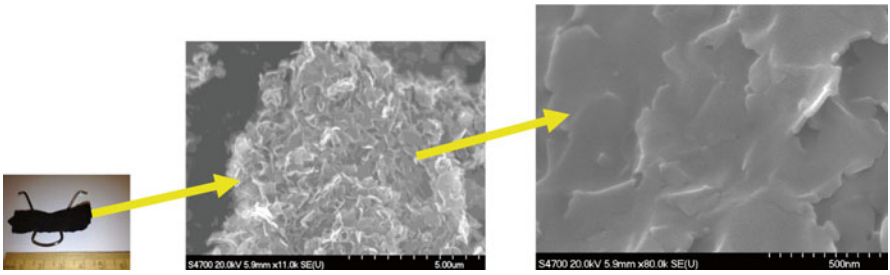

Fig. 12.9 Morphology of burned EVA–clay nanocomposite

Polar polymers like EVA (ethylene vinyl acetate) or EBA (ethylene butyl acrylate) are very easy to form nanocomposite under regular melt-compounding process. Low-polarity polymers like polyethylene and polypropylene have difficulty to enter the organoclay inner gallery region until assisted by modified polyethylene and polypropylene. Maleic-anhydride grafted PE or PP resins are commonly used as compatibilizer to facilitate organoclay dispersion and polymer insertion to the inner gallery region. The selection of PP-g-MA and processing conditions has significant impact in the performance of final PP nanocomposites [6]. Masterbatch process has been developed to minimize and eliminate these concerns [7]. A typical nanoclay masterbatch product contains 30–50 % of organoclay. These organoclay masterbatch products can be used with ease in commercial processing equipment. For flame retardation compounds, these master batches can be used as regular additive masterbatch at the compounding and injection molding process in combination with other additives and fillers.

12.4 Flame Retardation of Polymer–Clay Nanocomposites

The first flame retardation of polymer–clay nanocomposite material was reported by Dr. Jeff Gilman and others at NIST publication [8] "Interactions of Polymers with Fillers and Nanocomposites, NIST, June 18-19, 1998: A Workshop Report." In their report, they disclosed that both exfoliated and intercalated nanocomposites reduce the flammability of polymer-layered silicate (clay) nanocomposites. In studying the flame-retardant effect of the nano-dispersed clays, XRD and TEM analysis identified a nano-reinforced protective silicate/carbon-like high-performance char from the combustion residue that provides a physical mechanism of flammability control. The report also disclosed that "the nanocomposite structure of the char appears to enhance the performance of the char layer. This char layer may also act as an "insulation and mass transport barrier slowing the escape of the volatile products generated as the polymer decomposes." Cone calorimetry was used to study the flame retardation. The HRR (heat release rate) of thermoplastic and thermoset polymer-layered silicate nanocomposites are reduced by 40–60 % in

delaminated or intercalated nanocomposites containing a very low silicate mass fraction of only 2–6 wt%. Based on their expertise and experience in the plastic flammability, they concluded that the polymer–clay nanocomposite is a very promising new method for flame retarding polymers. In addition, they predict that the addition of organoclay into plastics has little or no drawbacks associated with other additives. That is, the physical properties are not degraded by the additive (silicate); instead, they are improved. Regarding to the mechanism of flame retardation of organoclay, they concluded that the nanocomposite structure of the char appears to enhance the performance of the char layer. This layer may act as an insulator and a mass transport barrier showing the escape of the volatile products generated as the polymer decomposes.

Nanocomposites based on EVA are the most widely studied system for flame retardation due to easy processing and wide use in low smoke halogen-free compound (LSOH) [9]. Flame retardation of EVA–clay nanocomposite was reported from Cone calorimetry study (Fig. 12.10) with a heat flux of 35 kW/m^2. Under such conditions, the flame-retardant effect of the organoclay was already observed for 3 % organoclay loading level. With increased amount of the organoclay to 5 %, a significant decrease by 47 % of the PHRR compared to the neat EVA was achieved. In addition, the time to reach the PHRR was also delayed. Further increasing the organoclay content from 5 to 10 % did not significantly improve the reduction of the PHRR. However, the higher clay loading level prolongs the onset of the second burning peak. Most of the case, the second burning peak is related to the fracture of the char to allow new flame to develop. This also quantitatively confirms the char forming and char reinforcement by the formation of the nanocomposite. As a decrease in

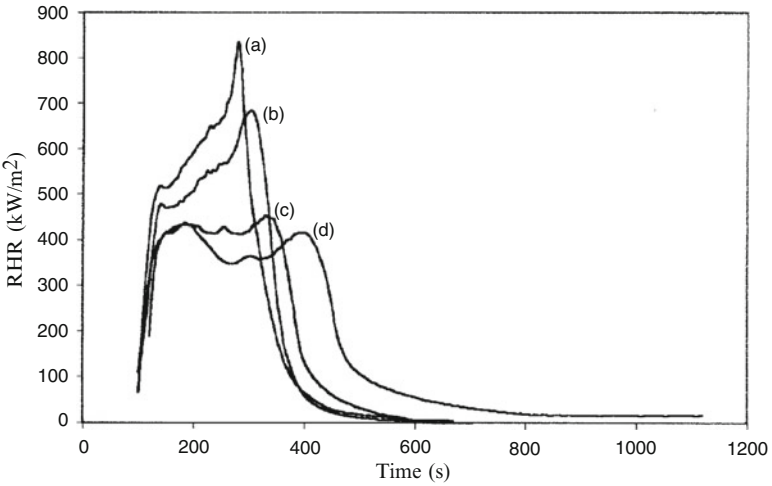

Fig. 12.10 Rate of heat release rate at heat flux = 35 kW/m^2 for various EVA (Escorene UL 00328 with 28 % vinyl acetate content)-based materials. (*a*) Neat EVA, (*b*) EVA + 3 % organoclay; (*c*) EVA + 5 % organoclay; (*d*) EVA + 10 % organoclay (From Ref. [9]; John Wiley & Sons Limited. Reproduced with permission)

PHRR indicates a reduction of burnable volatiles generated by the degradation of the polymer matrix, such a decrease clearly showed the flame-retardant effect due to the presence of the organoclays and their "molecular" distribution throughout the matrix. Furthermore, the flame-retardant properties were improved by the fact that the PHRR was spread over a much longer period. The flame-retardant properties were due to the formation of a char layer during the nanocomposite combustion. This char acted as an insulating and non-burning material and reduced the emission of volatile products (fuel) into the flame area. The silicate layers of the organoclay played an active role in the formation of the char but also strengthened it and made it more resistant to ablation.

The degradation of EVA and EVA nanocomposites was investigated by solid phase cross-polarization magic angle spinning carbon-13 nuclear magnetic resonance spectroscopy (CP-MAS-^{13}C-NMR). Bourbigot [10] described the measurement method in detail. EVA (Exxon's EVA Escorene UL 00112 with 12 wt% vinyl acetate content) and a nanocomposite based on the same EVA with 5 wt% of the organoclay were degraded by irradiation in a cone calorimeter with a heat flux of 50 kW/m^2. Chemical shifts of $-CH_2-$, $-CH_3$, and $-C=O$ were used as evidence of the existence of EVA during the burning process. Neat EVA samples lost the presence of EVA functional groups after irradiation of 150 s, whereas the EVA nanocomposite remains good signal of EVA even after 200 s irradiation. Clearly, formation of EVA nanocomposite has prolonged the surviving time of the EVA in fire. The char formation reduced the heat transfer to the sample and slowed down the diffusion of degraded combustible matters from the bulk phase to the surface. The recombination of radicals in the nanoclay inner gallery may also contribute the slow burning process.

Camino et al. [11] described the synthesis and thermal behavior of layered EVA nanocomposites; the nanofiller was an organoclay based on fluorohectorite, which is a synthetic layered silicate, and protection against thermal oxidation and mass loss was observed in air. The modified silicates accelerated the deacetylation of the polymer but reduced the thermal degradation of the deacetylated polymer due to the formation of a barrier at the surface of the polymer. Zanetti et al. [12] mixed modified fluorohectorite with EVA in an internal mixer and indicated that the accumulation of the filler on the surface of a burning specimen created a protective barrier to heat and mass loss during combustion. In the vertical combustion test, their nanocomposites had much reduced dripping of burning droplets and reduced the hazard of flame spread to surrounding materials. Melt intercalated and additionally gamma-irradiated PE/EVA nanocomposites were prepared by Hu et al. [13, 14] based on a modified montmorillonite; increasing the clay content from 2 to 10 % was beneficial for the improvement of flammability properties. Thermogravimetric analysis (TGA) data showed that nano-dispersion of the modified montmorillonite within the polymer inhibited the irradiation degradation of the PE/EVA blend, which led to nanocomposites with better irradiation-resistant properties than those of the standard polymer blend. Concerning the reaction mechanism of degradation and FR behavior of EVA nanocomposites, Wilkie et al. [15] found that in the early EVA degradation, the loss of acetic acid seemed to be catalyzed by the hydroxyl groups which were

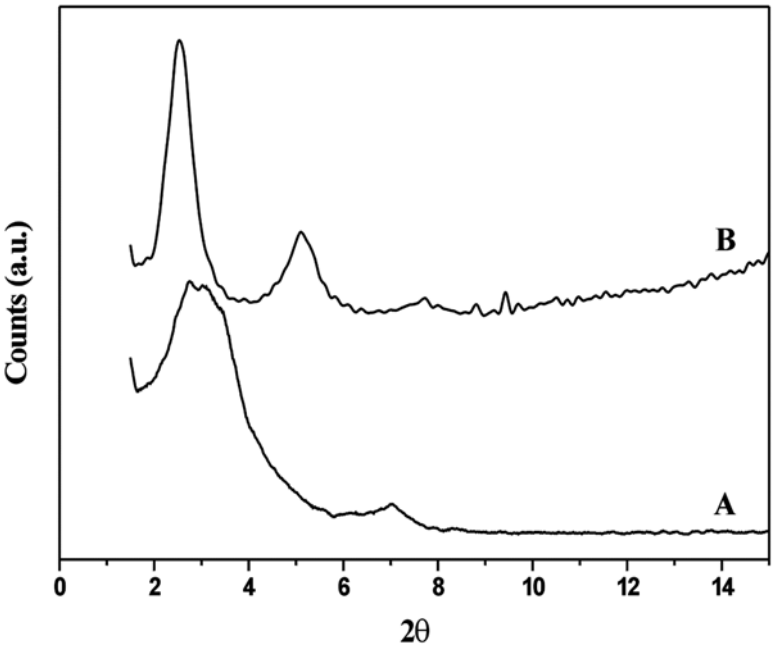

Fig. 12.11 X-ray diffraction of starting organoclay (DMDHT type) *Curve A* and TPU nanocomposite (5 %), *Curve B* (From Ref. [17]; SAGE. Reproduced with permission)

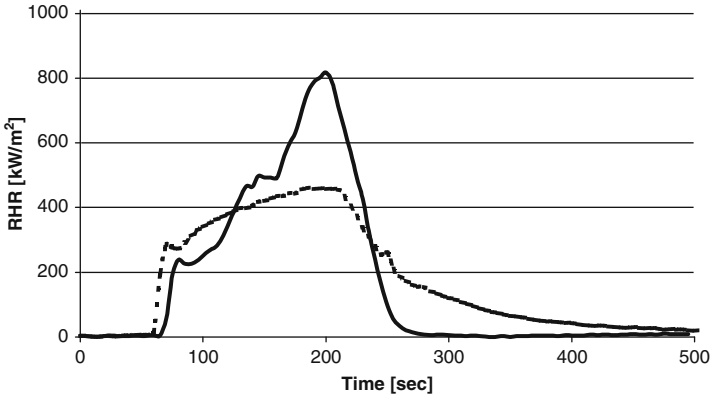

Fig. 12.12 Rate of heat release at heat flux: 35 kW/m^2\ for various TPU and TPU nanocomposite (5 % organoclay) based materials: ——— : Neat TPU. - - - - - - : TPU nanocomposite (5 % organoclay) (From Ref. [17]; SAGE. Reproduced with permission)

present on the edges of the montmorillonite. The thermal degradation of EVA in the presence and in the absence of the organoclay showed that the formation of reaction products differed in quantity and identity. The products were formed as a result of radical recombination reactions that could occur because the degrading polymer was contained within the layers for a long enough time to permit the reactions. The formation of these new products explained the variation of heat release rates. In cases with multiple degradation pathways, the presence of the modified montmorillonite could promote one of these at the expense of another and thus led to different products and hence a different rate of volatilization.

TPU (thermoplastic polyurethane) is a polymer offering a good balance of mechanical properties such as tensile strength, flexibility, and abrasion resistance. One of the TPU applications is for cables used in industrial control automation and medical devices. Despite the possible adjustment property portfolio by combination of polymer segments, TPUs have only moderate thermal stability and low flame retardance. The first of TPU organoclay nanocomposites was reported by Mc Laughlin [16]. Due to the polar nature of the TPU resins, the dispersion of traditional DMDHT-treated organoclay into a TPU (polyether or polyether based) is relatively easy. The formation of intercalated TPU clay-based nanocomposites was investigated by Beyer [17]. X-ray diffraction patents of the (Fig. 12.11) starting organoclay and TPU nanocomposite indicate very similar structure like the EVA–clay nanocomposite we discussed early in this chapter. The organoclay in the nanocomposite has an interacted structure. The d_{001} spacing of the organoclay increased from 30 to 36 Å after the TPU compounding. It seems that the TPU polymer also helps to bring order to the clay stacking with narrower peak and possible observation of d_{002} and d_{003} spacing/peaks. TGA studies of the TPU and TPU nanocomposite indicated the nanocomposite has higher heat stability particularly about 350 °C due to the heat-induced oxidative decomposition. Cone calorimetry study (Fig. 12.12) on TPU and TPU nanocomposite shows similar reduction of HPRR with 5 % organoclay addition. However, the early ignition of the TPU nanocomposite is quite visible from the cone curve. This may be related to the early Hofmann elimination reaction of the quaternary ammonium compound within the organoclay under heat [2].

12.5 Synergy of Nanocomposite with Traditional Flame Retardant

Since fire burning is a very complicated process, it typically involves multiphase flame retardants to stop the flame. For plastics, the burning typically involved with plastic heat decomposition, diffusion of flammable gases from bulk to surface, and surface gas burning. It is very common to combine various flame retardants to reduce the flammability of the plastic to eventually extinguish the fire to achieve certain industrial rating like UL or IEC. Nanocomposite has demonstrated a great

potential in the flame-retardant formulations from traditional halogen-containing systems (PVC and Br-containing chemistry) to new low smoke zero halogen (LSOH) compounds.

PVC is one of the most used plastics with its excellent cost performance ratio and easy formulation and processing. However, regular organoclay made with quaternary ammonium modification cannot be used in PVC system due to unzipping of PVC by the presence of quaternary ammonium. Phosphate ester is a typical plasticizer and flame retardant in PVC. Therefore, we chose to evaluate flame retardance of the phosphate ester-modified montmorillonite in PVC system. Flame-retardant PVC formulations typically contain antimony trioxide (Sb_2O_3 or ATO) as synergist. ATO is a heavy metal oxide with unknown toxicity to human being. In addition, the current mining and extraction methods to obtain ATO have very negative impact to the environment. There is a strong demand to find ATO replacement in the PVC and other flame-retardant compounds. Phosphate ester-modified clay Charex 418515 was used in various FR PVC systems to study the efficiency as ATO replacement. Table 12.2 shows the PVC flame retardation study with Charex 418515 as atrial replacement to ATO. In this study, fire performance parameters like LOI (Limited Oxygen Index, PHHR, and Smoke Density, are used to evaluate the addition of Charex 418515 to the PVC formulations. The limiting oxygen index (LOI) is the minimum concentration of oxygen, expressed as a percentage, that will support combustion of a polymer. Polymers or compounds with higher LOI will not easily burn since it will need more oxygen in the ambient condition to be on fire. Different phosphate esters were used as plasticizer and flame retardant. Phosflex 71B is more flame-retardant phosphate ester, and it can help the PVC to achieve LOI at 35. Three PHR (part per hundred of resin) of ATO was replaced with Charex 418515. Comparing PVC-1 and PVC-2, both of them have very similar measured LOI, PHRR, and smoke density. In addition, they

Table 12.2 FR and mechanical properties of FR PVC with ATO replacement by Charex 418515

	PVC-1	PVC-2	PVC-3	PVC-4
Composition (PHR)				
PVC	100	100	100	100
Phosflex 418	50	50		
Phosflex 71B			50	50
Charex 418515		3		3
Antimony trioxide	6	3	6	3
Flammability				
LOI	27.5	28.0	35.8	35.8
Peak HRR, kW/m^2	310	320	245	225
Smoke, SEA m^2/kg	1150	1140	1290	1150
Physical properties				
Tensile strength, MPa	18.2	17.3	22.9	24.8
Modulus, MPa	6.5	6.9	11.1	12.3
Elongation, %	480	450	380	390
Shore A hardness	89–85	89–85	94–90	92–88

also have comparable mechanical properties such as strength, stiffness, and hardness. Comparing PVC-3 and PVC-4, it is very encouraging to see the PVC-4 has the identical LOI as PVC-3 even with 3 PHR ATO replacement. PVC-4 also has somewhat reduced PHHR and smoke density. UL VW-1 wire flame retardation test evaluated the effectiveness of ATO replacement with Charex 418515. Formulation and testing results are listed in Table 12.3. With addition of 1.5 PHR Charex 418515, the wire samples achieved excellent flame retardation in significant reduced burning time and passed the UL VW-1 test.

Metal hydrates like aluminum trihydrate (ATH) and magnesium hydroxide (MDH) are the most common flame retardants for low smoke zero halogen (LSOH) cable formulations. Typical formulation will need 65 % of ATH or MDH to achieve certainly flame retardation standards. High loading level of the flame retardant in the formulation limits the compound processing and flexibility of the finished wires and cables. EVA and polyethylene are the most common polymers to formulate LSOH compounds. Combinations of organoclay with ATH were also studied by cone calorimeter tests. ATH and organoclay were premixed before compounding with EVA in a batch mixer at 145 °C for 15 min. Cone testing samples were prepared by compression molding and cut to fit the testing aluminum sample holder. With the same loading level of organoclay at 3 %, two loading levels of ATH were used at 58 and 60 %, respectively. A sample containing 65 % ATH was made and tested for comparison purpose.

From cone testing (at a heat flux 35 kW/m^2) data on HRR (Fig. 12.13a), the samples containing organoclays show significantly reduced value. More importantly, the secondary burning of the samples containing organoclay was reduced and diminished eventually with higher ATH loading, like the combination of 60 % ATH with 3 % organoclay. This was attributed by the strong char formation of compounds containing organoclay in the burning process. In contrast, the sample containing only higher amount of ATH does not have strong char formation and had quite heat release and smoke generation associated with the secondary burning after the crack of the original char occurred. The rate of smoke production (RSP) (Fig. 12.13b) of these testing samples showed corresponding patterns like the HRR graph. Smoke generation associated with the secondary burning of the samples containing organoclay was nearly eliminated.

Table 12.3 UL VW-1 testing results with addition of Charex 418515

	Units	Control-1	Control-2	Formulation-1
OxyChem 240	PHR	100	100	100
DINP Jayflex 911	PHR	50	50	50
$CaCO_3$	PHR	50	50	50
ATO	PHR		1.5	1.5
Charex 418515	PHR			1.5
Additive package	PHR	8	8	8
Max burn time	Sec	45	10	4
Paper flag burned	%	100	30	0
Rating		Fail	Fail	Pass

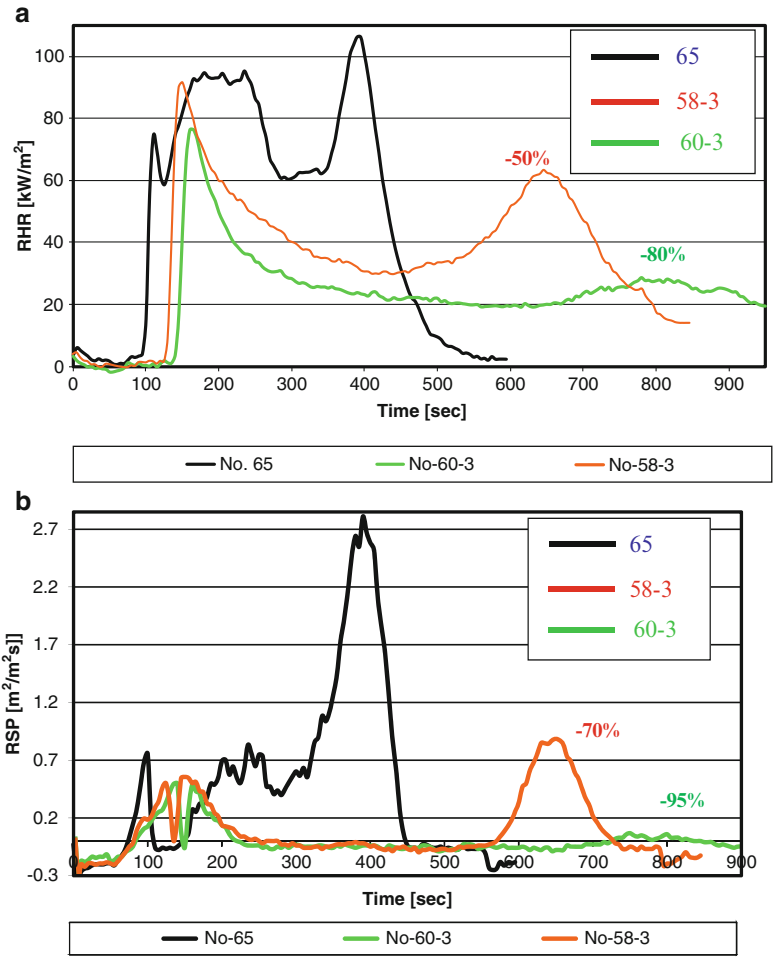

Fig. 12.13 (**a**) Heat release rate (HRR) of EVA–ATH compounds containing organoclay. *65*: 65 % ATH, 35 % EVA ; *60–3*: 60 % ATH, 3 % organoclay, 37 % EVA; *58–3*: 58 % ATH, 3 % organoclay, 39 % EVA. EVA: Escorene UL 00328 with 28 % vinyl acetate content. Heat flux = 35 kW/m^2; polymer plates of 100 × 100 × 3 mm^3 within aluminum dishes. (**b**) Rate of smoke production (RSP) of EVA–ATH compounds containing organoclay. *65*: 65 % ATH, 35 % EVA; *60–3*: 60 % ATH, 3 % organoclay, 37 % EVA; *58–3*: 58 % ATH, 3 % organoclay, 39 % EVA. EVA: Escorene UL 00328 with 28 % vinyl acetate content. Heat flux = 35 kW/m^2; polymer plates of 100 × 100 × 3 mm^3 within aluminum dishes

Combination of MDH with organoclay was carried in PP matrix. FR PP compounds containing MDH and organoclay were prepared in a corotating twin screw extruder [18]. Compatibilizer, like PP-g-MA, was used according to the MDH manufacturer's recommendations. UL 94 vertical test results indicate the addition of 2.5 wt% organoclay, and all the compounds pass the standard test with

self-extinguishing and non-flame dripping. Cone data (Table 12.4) indicates that the compounds containing organoclay can have delayed ignition compared with standard compound. Also the addition of the organoclay significantly increased the char yield from 34.6 wt% to 46.7 wt%. More importantly, the addition of organoclay reduced the CO release 50–75 %. CO_2 release rates for all compounds are essentially the same. CO has been recognized as one of the silent killers in fire due to its being colorless and odorless, and it often contributes to fire death [19]. The reduced CO yield from burning may be caused by the altered decomposition mechanism of the polymer once they enter the clay inner gallery. HRR and RSP results are shown in Fig. 12.14a, b. The benefit of the organoclay is reducing HRR and RSP on the compounds. The reduction features are quite high for the second burning.

Ammonium polyphosphate (APP) is another halogen-free flame retardant. APPs are inorganic salts of *polyphosphoric acid* and *ammonia*. APP is a common flame retardant using the intumescent mechanism. APP decomposes upon exposing to the heat of a fire-form ammonia and phosphoric acid. The phosphoric acid acts as a catalyst in the formation of carbonaceous char and releases nonflammable carbon dioxide which helps to dilute the air of oxygen. The formation of a coherent char is important for the intumescent FR system to pass any regulations. With sufficient amount of APP on the sample surface, it is possible to form a coherent char. However, the APP has certain processing limitation with possible degradation when surface concentrate reaches to high concentration. Addition of organoclay will bridge the carbonaceous char formed from the intumescent agent like APP to form coherent char. Thus, it is possible to a combination of organoclay with APP to create flame-retardant compounds. Table 12.5 lists our recent study in the combination of organoclay with APP in PP systems. All components were fed into a corotating twin screw extruder. UL94 rating increases with increased loading levels of APP from 24 to 28 %. When 1 % organoclay was added to the 24 % APP system, the compound

Table 12.4 UL-94 and cone results of MDH-PP compounds containing organoclay

Sample ID	Control	Nano-1	Nano-2
Co-PP	30.0	32.5	32.5
MDH	65.0	60.0	60.0
Ma-PP 1	5.0		5.0
Ma-PP 2	(5.0)	5.0	
Organoclay		2.5	2.5
UL-94 @ 1/16″	–	–	–
Rating	Failure	V-0	V-0
Time to ignition (s)	49.9	51.6	57.4
Peak RHR (kW/m^2)	238	222	235
Char yield (%)	34.6	46.7	46.7
Mass loss (kg/m^2)	3.19	2.80	2.79
CO yield	0.015	0.005	0.007
CO_2 yield	2.54	2.46	2.53

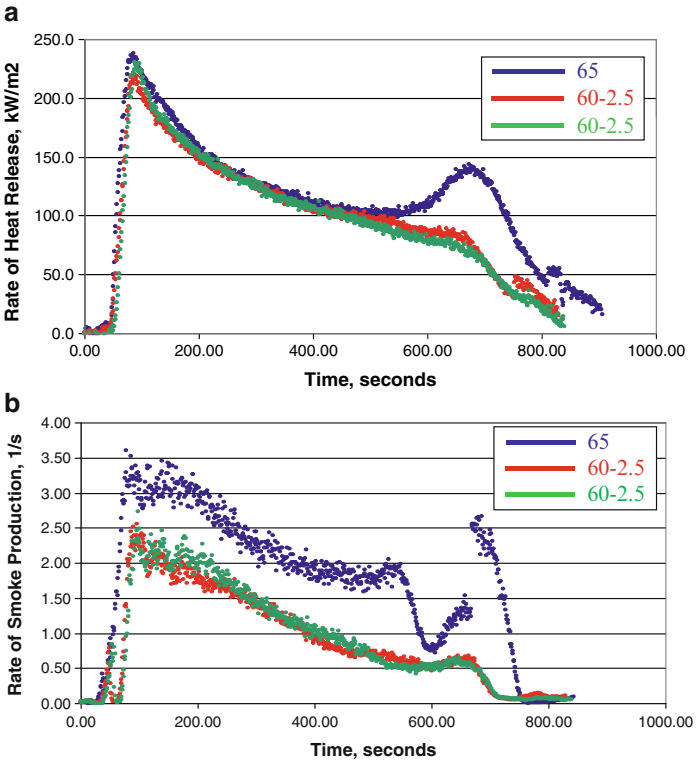

Fig. 12.14 (**a**) Heat release rate (HRR) of PP–MDH compounds containing organoclay and MDH. (**b**) Rate of smoke production (RSP) of PP–MDH compounds containing MDH and organoclay

Table 12.5 Effect of organoclay in PP/APP flame-retardant systems

Components	Sample-1	Sample-2	Sample-3	Sample-4	Sample-5	Sample-6
APP 752 (wt%)	24	26	28	24	24	24
PP (wt%)	76	74	72	75	73	72
Organoclay (wt.)	0	0	0	1	3	4
UL-94 rating (1/8 in)	V2	V-1	V-0	V0	V-0	Fail

could reach V-0 high FR rating which could be achieved with 28 % APP loading level. With further increase of the amount of organoclay to 3 %, the compound still achieved V-0 rating. However, once we increased the organoclay level to 4 %, the compound was no longer classified by the UL-94 test. Therefore, there is a limitation for the intumescent system to accept organoclay as char-forming agent. Once the organoclay level reached 4 %, there were too much organoclay on the surface; this could limit or interfere with char forming by the intumescent agents. Therefore, for intumescent system, it is necessary to start with low level of organoclay. Most

likely, low organoclay level will help the compounds to form coherent char during burning process to achieve good UL-94 FR ratings.

Combination of organoclay with ATH is EVA based. LSOH compound was the first commercial application reported by Kabelwerk Eupen. A coaxial cable containing an outer sheath made with EVA, ATH, and organoclay was studied under UL 1666 fire test. There are many applications for indoor cables passing the large-scale fire test UL 1666 (riser test for cables) with a 145 kW burner in a two-story facility. This very severe fire test defines the following important points of measurements:

1. Maximal temperature of fire gases at 12 feet: 850 °F
2. Maximal height for flames: 12 feet

Compounds with halogenated flame retardants are often used to pass this test, but more and more low smoke halogen-free cables are requested by the market for the riser test. Cables based on nanocomposites compounds demonstrate their promising performances for this fire test.

An example for LSOH cables passing UL 1666 is shown in Fig. 12.15. The outer sheath was based on a nanocomposite with an industrial EVA/ATH/organoclay composition. The analogous coaxial cable was tested with an outer sheath based on regular EVA/ATH compound. In both compounds, the relation of polymer/filler was the same and Table 12.6 presents the fire testing results. The improved flame-retardant properties were due to the formation of a char layer during the combustion process. This insulating and non-burning char reduced the emission of volatile products from the polymer degradation into the flame area and thus minimized the maximal temperature and height of the flames. The fundamental benefit of addition of organoclay in LSOH compounds has been transferred into real application and testing. The reduced heat release allows position lower gas temperature about the cable. This could reduce the fire risk hazard level in case of electrical fire.

European countries are leading the development and applications of LSOH compounds. The first halogen-free flame-retardant (HFFR) cables were introduced to London underground use in the early 1970s. HFFR was replaced by low smoke version in the late 1990s after the Düsseldorf Airport Fire in 1996. Furthermore, in 2010s, the technical and regulatory developments reached a new higher level when European Union Commission started to implement the new Construction Products Regulation (CPR). In a fire, the heat released from a burning article has been considered as the source to spread the fire to harm human life and damage properties. Reduction of heat released from burning articles will reduce the fire risk to provide safer products. The new European *C*onstruction Products *R*egulation (CPR), adopted in 2011, is now mandatory since July 1, 2013. This European regulation 305/2011 describes the conditions to make available a broad range of construction products including power, control, and communication cables for the market. The new CPR substitutes the old Construction Products Directive (CPD), which needed a revision because as a directive, it was not applied in a harmonized way throughout the European Union (EU). The new regulation will remove existing barriers to trade

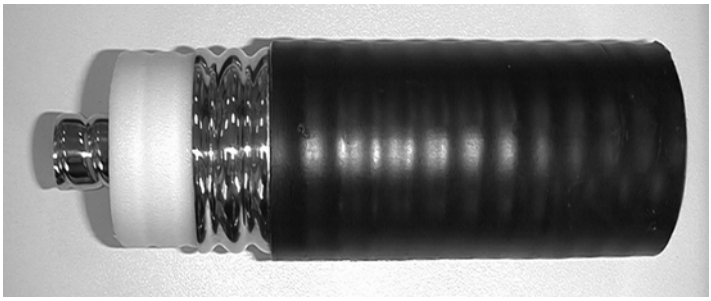

Fig. 12.15 Coaxial cable (1/2″) with a nanocomposite-based outer sheath passing the UL 1666 cable fire test

Table 12.6 Fire performances of LSOH coaxial cables with EVA/ATH and EVA/ATH/organoclay outer sheaths

UL 1666 requirements	EVA/ATH compound	EVA/ATH/organoclay compound
Maximal temperature at 12 feet		
<850 °F	1930 °F	620 °F
Maximal flame height		
<12 feet	>12 feet	6 feet

in the EU where member nations of the EU each had their own fire standards (Fig. 12.16).

The European Commission's Fire Regulators Group, consisting of representatives from each member country, have reviewed various proposals to create a new fire performance hierarchy for products like cables installed in buildings within the governing document known as the *Construction Products Regulation* (CPR). Input was received from its own sponsored studies as well as from investigations by industry groups. The European Commission's FIPEC study (Fire Performance of Electrical Cables) presented a fire hazard assessment methodology for both communications and energy cables in buildings based primarily on modifications to the international cable fire test protocol according to different categories defined by IEC 60332-3 [20]. The revised testing procedures enabled measurements of heat release rate by oxygen consumption technique, smoke release rate, and the possibility of measuring toxic gas production rates by FTIR instrumentation. Parameters are flame spread (FS), peak heat release rate (PHRR), total heat released (THR), fire growth rate (FIGRA), smoke production rate (SPR), and total smoke production (TSP). The ranking of cables is summarized in Table 12.7 and the tests are described by the norm EN 50399. Products in Class A demonstrate the highest fire performances, while products with no fire performances are ranked in class F. This test setup will allow testing of cables in one of the most advanced test arrangements available in Europe.

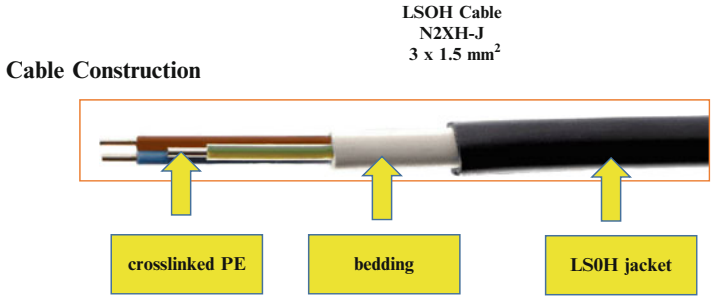

Fig. 12.16 LSOH cable construction for IEC and CPR testing

The value FIGRA is defined as the growth rate of the burning intensity, HRR, during a test. FIGRA is calculated as the maximum value of the function (heat release rate)/(elapsed test time). It should work as an indication of the propensity to cause a quickly growing fire. It is reported from cone calorimeter investigations that nanocomposites showed impressive reductions of peak of heat release rates and FIGRA, especially for higher external heat fluxes [21].

Two detailed test methods were developed for CPR: scenario 1 according to EN 50399-2-1 and scenario 2 according to EN 50399-2-2, the former being slightly more severe than IEC 60332-3-24, and the latter being much more severe and suitable for cables used in high hazard conditions. The conclusions reached by the FIPEC study were that current tests (e.g., IEC 60332-3-24, category C) are not sensitive enough to differentiate the enhanced fire performances needed for high-density telecommunication cable installations, and the parameter that has the most effect on the test results is the method of mounting cables on the ladder.

Cables with the following specification were tested according the FIPEC scenarios 1 and 2 (designation: NHXMH-J, 4 × 16 mm^2; insulation: cross-linked polyethylene; filling sheath: a flame-retardant non-halogen compound; outer sheath: a flame-retardant non-halogen EVA compound either based on classic ATH only or based on a nanocomposite by combination of organoclays and ATH [22]). The values listed in Table 12.8 clearly demonstrate the improvements seen both for flame spread and FIGRA due to the nanocomposite-based outer sheath. In addition, during the fire tests (Table 12.8), there was no dripping of burning polymer from the cable with the nanocomposite-based outer sheath; this is an additional important requirement within the CPR regulation, and it shows that nanocomposites are essential to meeting the new fire test regulations.

12.6 New Development and Outlook

The use of nanocomposites based on organoclays in combination with metal hydroxides is now regularly seen in the cable industry. Kabelwerk EUPEN AG from Belgium, the inventor of this technology, has used it over a number of years for their

Table 12.7 New EU CPR for wire and cable flame retardance rating and classification

Class	Test method(s)	Classification criteria	Additional classification
A_{ca}	EN ISO 1716	PCS ≤ 2.0 MJ/kg (1)	
$B1_{ca}$	FIPEC20 Scen 2 (5)	FS ≤ 1.75 m *and*	Smoke production (2, 6) and flaming droplets/particles (3) and acidity (4)
		THR_{1200s} ≤ 10 MJ *and*	
	and	Peak HRR ≤ 20 kW *and*	
		FIGRA ≤ 120 Ws^{-1}	
	EN 50265-2-1	H ≤ 425 mm	
$B2_{ca}$	FIPEC20 Scen 1 (5)	FS ≤ 1.5 m; *and*	Smoke production (2, 7) and flaming droplets/particles (3) and acidity (4)
		THR_{1200s} ≤ 15 MJ; *and*	
	and	Peak HRR ≤ 30 kW; *and*	
		FIGRA ≤ 150 Ws^{-1}	
	EN 50265-2-1	H ≤ 425 mm	
C_{ca}	$FIPEC_{20}$ Scen 1 (5)	FS ≤ 2.0 m; *and*	Smoke production (2, 7) and flaming droplets/particles (3) and acidity (4)
		THR_{1200s} ≤ 30 MJ; *and*	
	and	Peak HRR ≤ 60 kW; *and*	
		FIGRA ≤ 300 Ws^{-1}	
	EN 50265-2-1	H ≤ 425 mm	
D_{ca}	$FIPEC_{20}$ Scen 1 (5)	THR_{1200s} ≤ 70 MJ; *and*	Smoke production (2, 7) and flaming droplets/particles (3) and acidity (4)
		Peak HRR ≤ 400 kW; *and*	
	and	FIGRA ≤ 1300 Ws^{-1}	
	EN 50265-2-1	H ≤ 425 mm	
E_{ca}	EN 50265-2-1	H ≤ 425 mm	
F_{ca}	No performance determined		

(1) For the product as a whole, excluding metallic materials, and for any external component (i.e., sheath) of the product

(2) **s1** = TSP_{1200} ≤ 50 m^2 *and* Peak SPR ≤ 0.25 m^2/s
s1a = **s1** and transmittance in accordance with EN 50268–2 ≥ 80 %
s1b = **s1** and transmittance in accordance with EN 50268–2 ≥ 60 % < 80 %
s2 = TSP_{1200} ≤ 400 m^2 *and* peak SPR ≤ 1.5 m^2/s
s3 = not s1 or s2

(3) For $FIPEC_{20}$ scenarios 1 and 2: **d0** = no flaming droplets/particles within 1200 s; **d1** = no flaming droplets/particles persisting longer than 10 s within 1200 s; **d2** = not d0 or d1

(continued)

Table 12.7 (continued)

(4) EN 50267-2-3: **a1** = conductivity < 2.5 μS/mm *and* pH > 4.3; **a2** = conductivity < 10 μS/mm *and* pH > 4.3; **a3** = not a1 or a2. No declaration = no performance determined
(5) Air flow into chamber shall be set to 8000 ± 800 l/min
FIPEC$_{20}$ scenario 1 = EN 50399-2-1 with mounting and fixing as below
FIPEC$_{20}$ scenario 2 = EN 50399-2-2 with mounting and fixing as below
(6) The smoke class declared for class $B1_{ca}$ cables must originate from the FIPEC$_{20}$ Scen 2 test
(7) The smoke class declared for class $B2_{ca}$, C_{ca}, D_{ca} cables must originate from the FIPEC$_{20}$ Scen 1 test

Table 12.8 Flame-retardant properties of cables by FIPEC scenarios 1 and 2 according to EN 50399

	NHXMH-J 4 × 16 mm^2	NHXMH-J 4 × 16 mm^2
	Classical purely ATH-based outer sheath	Nanocomposite-based outer sheath
FIPEC scenario 1	Flame spread = 0.49 m	Flame spread = 0.48 m
20.5 kW flame	PHRR = 27.1 kW	PHRR = 22.9 kW
0 min burning time	63.2 W s^{-1}	FIGRA = 20.3 W s^{-1}
FIPEC scenario 2	Flame spread = 1.85 m	Flame spread = 1.21 m
30 kW flame and plate	PHRR = 58.6 kW	PHRR = 55.8 kW
30 min burning time	FIGRA = 53.5 W s^{-1}	FIGRA = 47.9 W s^{-1}

range of flame-retardant non-halogen cables. The company also has worldwide patents on this technology. Other companies will follow this way for their flame-retardant product ranges. In Europe, one can expect a wider application of the nanocomposite-based flame-retardant technology driven by the enhanced requirements of the Construction Product Regulation (CPR). It is also likely that countries including China, South Korea, and Japan which are following the European trends toward non-halogenated flame-retardant products will adopt this technology in the near future.

Nanocomposite materials were developed in the last two decades. Significant progress has been made to adopt the technology in the standard plastic processing methods. Currently, most of the commercial uses of nanocomposites are based on layered silicates. However, with more research on carbon nanotube and graphene materials, one would expect these materials will move into the market place with new featured properties. Design of advanced flame-retardant plastics has taken advantage of this new class of materials. Flame-retardant plastic compounds using nanocomposite technology offer significantly improved char forming and reduced toxic substance emission while keep the same processing as the traditional flame retardant. With the implementation of the new fire retardation standard like the CPR in EU, we expect the growth of the use of nanocomposites in flame-retardant compounds will be substantial in the coming years. Development with other nano-sized

additives is also emerging, such as tubular nanoclay, graphene, and three-dimensional zeolite-like inorganic frameworks.

References

1. Amcol International Corporation (2000) Method of manufacturing polymer-grade clay for use in nanocomposites. US Patent 6,050,509
2. Xie W, Gao WZ, Pan W, Hunter D, Singh A, Vaia R (2001) Thermal degradation chemistry of alkyl quaternary ammonium montmorillonite. Chem Mater 13:2979–2990
3. Beall G, Tsipursky W, Sorokin A, Goldman A (1999) Intercalates and exfoliates formed with oligomers and polymers and composite materials containing same. US Patent 5,877,248
4. Pack S, Kashiwagi T, Cao C, Korach C, Levin M, Rafailoich M (2010) Role of surface interactions in the synergizing polymer/clay flame retardant properties. Macromolecules 43:5338–5351
5. Okada A, Kawasumi M, Usuki MA, Kojima Y, Kurauchi T, Kamigaito TO (1990) Synthesis and properties of nylon-6/clay hybrids. In: Schaefer DW, Mark JE (eds) Polymer based molecular composites, vol 171. MRS Symposium Proceedings, Pittsburgh, pp 45–50
6. Amcol International Corporation (2002) Intercalates formed with polypropylene/maleic anhydride-modified polypropylene intercalants. US Patent 6,462,122
7. Liang Y, Qian G, Cho J, Psihogios V, Lan T (2002) Applications of plastic nanocomposites. Additives, Clearwater Beach
8. NIST-IR 6312 (1998) Interactions of polymers with fillers and nanocomposites
9. Beyer G (2001) Flame retardant properties of EVA-nanocomposites and improvements by combination of nanofillers with aluminium trihydrate. Fire Mater 25:193–197
10. Bourbigot S, Le Bras M, Leeuwendal R, Shen K, Schubert D (1999) Recent advances in the use of zinc borates in flame retardancy of EVA. Polym Degrad Stab 64:419–425
11. Camino G, Mülhaupt R, Zanetti M, Thomann R (2001) Synthesis and thermal behaviour of layered silicate–EVA nanocomposites. Polymer 42:4501–4507
12. Zanetti M, Camino G, Mülhaupt R (2001) Combustion behaviour of EVA/fluorohectorite nanocomposites. Polym Degrad Stab 74:413–417
13. Hu Y, Tang S, Wang Z (2002) Preparation and flammability of ethylene-vinyl acetate copolymer/montmorillonite nanocomposites. Polym Degrad Stab 78:555–559
14. Hu Y, Lu H, Kong Q, Chen Z, Fan W (2004) Influence of gamma irradiation on high density polyethylene/ethylene-vinyl acetate/clay nanocomposites. Polym Adv Technol 15:601–605
15. Wilkie C, Costache M, Jiang D (2005) Thermal degradation of ethylene–vinyl acetate copolymer nanocomposites. Polymer 46:6947–6958
16. Mc Laughlin E, Koene B (2002) Twin screw extrusion of polyurethane nanocomposites. Conference proceedings of the SPE annual technical conference (ANTEC), 2002, San Francisco
17. Beyer G (2007) Flame retardancy of thermoplastic polyurethane and polyvinyl chloride by organoclays. J Fire Sci 25:67–78
18. Lan T (2008) Nanoclay as flame retardant additives, flame resistance in plastics by AMI, Cologne, Germany, 8–10 Dec 2008.
19. M. M. Hirschler, Fire safety, smoke toxicity and halogenated materials, Commentary in: Flame Retardancy News, Business Communications Co., Norwalk, CT, USA, April 2005
20. International Electrotechnical Commission (IEC) 60332-3-24. Tests on electrical cables under fire conditions – Part 3–24: Test for vertical flame spread of vertically-mounted bunched wires or cables; Category C, 2000-10-0040
21. Schartel B, Hartwig A, Putz D, Bartholmai M, Wendschuh-Josties M (2003) Combustion behavior of epoxide based nanocomposites with ammonium and phosphonium bentonite. Mol Chem Phys 204:2247–2257
22. Beyer G (2005) Flame retardancy of nanocomposites – from research to technical products. J Fire Sci 23:75–87

Index

© Springer International Publishing Switzerland 2016
X. Huang, C. Zhi (eds.), *Polymer Nanocomposites*,
DOI 10.1007/978-3-319-28238-1